



HAL
open science

Développement de nouveaux matériaux de protection pour outils de coupe lors d'usinage cryogénique d'alliages pour l'aéronautique

Yutao Zhang

► **To cite this version:**

Yutao Zhang. Développement de nouveaux matériaux de protection pour outils de coupe lors d'usinage cryogénique d'alliages pour l'aéronautique. Mécanique des matériaux [physics.class-ph]. HESAM Université, 2022. Français. NNT : 2022HESAE009 . tel-03635214

HAL Id: tel-03635214

<https://pastel.hal.science/tel-03635214>

Submitted on 8 Apr 2022

HAL is a multi-disciplinary open access archive for the deposit and dissemination of scientific research documents, whether they are published or not. The documents may come from teaching and research institutions in France or abroad, or from public or private research centers.

L'archive ouverte pluridisciplinaire **HAL**, est destinée au dépôt et à la diffusion de documents scientifiques de niveau recherche, publiés ou non, émanant des établissements d'enseignement et de recherche français ou étrangers, des laboratoires publics ou privés.

ÉCOLE DOCTORALE SCIENCES DES MÉTIERS DE L'INGÉNIEUR
[Laboratoire des Matériaux et Procédés – Campus de Cluny]

THÈSE

présentée par : **Yutao ZHANG**

soutenue le : **26 Janvier 2022**

pour obtenir le grade de : **Docteur d'HESAM Université**

préparée à : **École Nationale Supérieure d'Arts et Métiers**

Spécialité : **Mécanique-Matériaux**

Développement de nouveaux matériaux de protection pour outils de coupe lors d'usinage cryogénique d'alliages pour l'aéronautique

Tool materials development for improved performance of cutting tools in cryogenic machining of Aeronautic Alloys

THÈSE dirigée par :
Mme. Corinne NOUVEAU

et co-dirigée par :
M. José OUTEIRO

Jury

M. Nicolas MARTIN, Professeur des Universités, FEMTO-ST, UBFC

Mme Nicole FRETY, Professeur des Universités, Université de Montpellier

M. Aldo ATTANASIO, Professeur des Universités, Université de Brescia

M. Joël RECH, Professeur des Universités, ECL - ENISE

M. Guenaël GERMAIN, Professeur des Universités, LAMPA, Arts et Métiers d'Angers

Mme Corinne NOUVEAU, MCF-HDR, LABOMAP, Arts et Métiers de Cluny

M. José OUTEIRO, MCF-HDR, LABOMAP, Arts et Métiers de Cluny

M. Aurélien BESNARD, MCF, LABOMAP, Arts et Métiers de Cluny

M. Sébastien DEZECOT, Docteur, Responsable R&D, EVATEC-TOOLS

Président du jury

Rapporteuse

Rapporteur

Examineur

Examineur

Examinatrice

Examineur

Invité

Invité

A mes amis du LaBoMaP, merci pour votre amitié et votre aide chaleureuse, je dédie ce
mémoire.

A toute ma famille, merci pour votre soutien et votre patience, je dédie ce mémoire.

Remerciements

Une thèse est un travail personnel durant une longue période de temps pour travailler sur un sujet spécifique et réaliser certains buts. Cependant il est aussi autant important d'avoir les soutiens et aides d'autres personnes qui sont présentes pendant la thèse. Je souhaiterais remercier tous ceux qui ont contribué à la réussite de ma thèse.

Je tiens à remercier tous les membres du jury, M. Guenael GERMAIN et M. Nicolas MARTIN pour participer à mon comité de suivi, M. Aldo ATTANASIO et Mme Nicole FRETY pour avoir accepté d'être mes rapporteurs, M Joël RECH et M Sébastien DEZECOT pour avoir accepté de participer à ma soutenance.

Je tiens à remercier également mes encadrants, MME. Corinne NOUVEAU et M. José OUTEIRO pour leur suivi pendant ma thèse, dans un aspect global et détaillé, pour leur attention à toutes les démarches pendant ces 4 années. Je voudrais surtout vous remercier pour m'avoir aidé à passer les temps difficiles, pour finalement m'avoir suppléé pour l'aboutissement de ma thèse.

Je tiens aussi à remercier M. Denis LAGADRILLERE, M. Aurélien BESNARD et M. Bertrand MARCON pour leur aide respective et continue tout au long de ma thèse, pour leurs connaissances spécifiques, leur accompagnement sur le terrain et leurs efforts maximums pour contribuer à ma thèse.

Je tiens à remercier M. Romaric MASSET et M. Gilles DETROYAT pour leur aide précieuse qui m'a permis de réaliser un travail transversal dans deux secteurs disciplinaires très différents. Je tiens à remercier tous les doctorant(e)s de notre laboratoire, avec lesquels(elles) j'ai passé beaucoup de temps et partagé de très bons moments.

Je tiens enfin à remercier toutes les personnes du ou extérieures LABOMAP, qui ont participé à un moment ou à une période, à mes travaux de recherche ou pour m'aider à passer les temps difficiles pendant ma thèse : MME. Nathalie LAROCHE, MME. Laurence BRETON, MME Lamice DENGUIR, M. Dominique COTTON, M. Philippe JACQUET, M. Frédéric ROSSI, M. Benjamin ROUX, M. Guillaume FALCO, M. Damien EGLI, M. Alex MONTAGNE. Vous êtes nombreux et je ne pourrai pas tous vous citer, mais vous resterez dans mon souvenir.

Je vous remercie !

Résumé

Des préoccupations environnementales et la réduction des coûts de fluides de coupe utilisés en usinage ont conduit à l'accroissement de l'intérêt industriel dans le remplacement de ces fluides par des liquides cryogéniques écologiques comme l'azote liquide (LN2). Cependant, la recherche en usinage dans des conditions cryogéniques (aussi appelé « usinage par assistance cryogénique ») a montré une grande dispersion d'usure et de durée de vie des outils. Ceci s'expliquerait par la faible performance des outils utilisés actuellement à des températures cryogéniques.

L'objectif de ce projet est d'améliorer la performance des outils de coupe lors du tournage d'alliage de Titane Ti6Al4V sous assistance cryogénique en améliorant leurs propriétés chimiques/mécaniques/physiques. Une solution est l'application de traitements de surface, comme les dépôts PVD. Beaucoup d'études ont été faites quant à l'application de dépôts sur des outils de coupe en usinage mais jusqu'ici l'objectif principal était d'obtenir des couches présentant une stabilité thermique à de hautes températures (plus de 1000°C). Ceci est typiquement le cas de TiAlN. Cette étude va donc consister à optimiser des dépôts stables thermiquement à de hautes températures (e.g. 400-500°C) tout en supportant des chocs thermiques. En effet, pendant l'usinage par assistance cryogénique, même sous une atmosphère à -196°C, la température locale au contact outil/copeau peut être extrêmement élevée. Cette étude peut être divisée selon les tâches suivantes :

- Optimisation de monocouches telles que CrN et AlCrN, en faisant varier 2 paramètres : la température de dépôt et la tension de polarisation du substrat.
- Développer des multicouches comme Cr/CrN/AlCrN, en faisant varier 2 paramètres : l'épaisseur de chaque monocouche et le nombre d'interfaces (ou le nombre de chaque monocouche).
- Caractériser ces différents revêtements (MEB + EDS, DRX, contraintes, dureté, adhérence, XPS, propriétés thermiques etc) pour déterminer les mono et multicouches optimales à appliquer sur les pions pour les tests de tribologie.
- Réaliser des essais tribologiques avec des pions en carbure non revêtus et revêtus par PVD, en utilisant les stratégies de refroidissement/lubrification avec azote liquide (LN2) et émulsions (mélange huile-eau), afin d'analyser les performances des revêtements en termes de coefficient de frottement, adhésion de l'alliage de Titane Ti6Al4V sur les pions et sa température.

- Réaliser des essais d'usure en tournage d'alliage de titane Ti6Al4V, afin d'évaluer la durée de vie des outils en carbure revêtu par PVD dans des conditions de refroidissement cryogénique avec LN2 et comparer avec la durée de vie des outils avec les émulsions.

Mots-clefs : Revêtements PVD, Usinage par assistance cryogénique, Alliage de titane Ti6Al4V, Tribologie, Usure d'outil.

Abstract

Environmental concerns and cost reduction of metal working fluids (MWF) used in machining operations result in ever-growing industrial interest in replacing these fluids with eco-friendly cryogenic fluids such as liquid nitrogen (LN₂). However, research on machining under cryogenic conditions (also referred to as “cryogenic assisted machining”) using existing cutting tools (developed for use with common MWF) have shown a large scatter in tool wear, and thus tool life. This scatter can be partially attributed to the subpar performance of the existing cutting tools under cryogenic temperatures. The proposed project aims to develop of the next generation of cutting tools for cryogenic assisted machining. The objective is to enhance the performance of the cutting tools for cryogenic assisted machining by improving the chemical/mechanical/physical properties of the tool materials. One solution to improve the tool life is surface treatments, such as PVD hard coatings. Many studies have been made regarding this topic of research, but so far, the main objective is to obtain coatings that have a high thermal stability at high temperatures (more than 1000°C). This is typically the case of TiAlN. This study is innovative, because it deals with hard protective coatings that will have a high thermal stability at high temperature (around 400-500C) but that could also support thermal shocks. Indeed, during cryogenic machining, even under a -196°C atmosphere, the local temperature at tool-chip/workpiece interface can be extremely high.

This study can be divided into the following tasks:

- To optimize monolayers such as: CrN and AlCrN, by varying 2 parameters: deposition temperature and bias voltage on substrate.
- To develop multilayers such as Cr/CrN/AlCrN, by varying 2 parameters: thickness of each monolayer and the number of interfaces (or number of each monolayer).
- To characterize these different coatings (SEM+EDS, XRD, stress, hardness, adhesion, XPS, thermal properties etc) to determine the optimal mono and multilayers to be applied on pins for tribological tests.
- To conduct tribological tests using uncoated and PVD-coated carbide pins under flood (mixture oil-water) and cryogenic (LN₂) conditions, in order to analyse the performance of the hard coatings in terms of apparent friction coefficient, volume of build-up material (adhesion) to the pins, and their temperature.

- To conduct tool wear tests in turning of Ti6Al4V titanium alloy, in order to evaluate the tool life of PVD-coated carbide tools under cryogenic cooling conditions and compare with the tool life under flood conditions.

Keywords: PVD coatings, Cryogenic Assisted Machining, Ti6Al4V titanium alloy, Tribology, Tool Wear.

Table of content

Résumé.....	I
Abstract	III
Table of content.....	V
List of tables	XI
List of figures	XIV
List of appendix.....	XXV
Glossary.....	XXVI
Abbreviations	XXVI
Symbols.....	XXVII
Introduction	1
Chapter 1. State of the art.....	5
1.1. Introduction	6
1.2. Metal cutting	6
1.2.1. Metal cutting definition and cutting system.....	6
1.2.2. Turning operation.....	7
1.2.3. Metal Working Fluids	9
1.3. Cryogenic assisted machining.....	10
1.3.1. History and definition.....	10
1.3.2. Comparison between different cooling and lubrication methods.....	11
1.3.3. Cooling methods in cryogenic assisted machining	12
1.4. Ti6Al4V titanium alloy	13
1.4.1. Types of titanium alloys, properties and applications.....	13
1.4.2. Machinability	17
1.4.3. Surface integrity	18
1.5. Tribology and tool wear	19
1.5.1. Contact conditions in metal cutting.....	19
1.5.2. Friction coefficient	19
1.5.3. Tool wear in metal cutting	21
1.6. Tool material	23
1.7. Hard coatings.....	24
1.7.1. Coatings deposition.....	25

1.7.1.1.	PVD (Physical Vapor Deposition)	25
1.7.1.2.	Magnetron sputtering	26
1.7.1.3.	Hard coatings for cutting tools	28
1.7.1.4.	Monolayers	30
1.7.1.5.	Multilayers	33
1.7.2.	Conclusion.....	36
1.8.	Résumé du Chapitre 1	37
Chapter 2. Experimental methods		38
2.1.	Introduction	39
2.2.	PVD deposition system	39
2.2.1.	General view of PVD system	39
2.2.2.	Substrates and targets	41
2.2.2.1.	Substrates materials.....	41
2.2.2.2.	Substrates cleaning	42
2.2.2.3.	Targets cleaning	42
2.3.	Coating Characterizations	43
2.3.1.	Surface morphology: Scanning electron microscope.....	43
2.3.2.	Chemical composition: X-ray photoelectron spectroscopy	44
2.3.3.	Structure :X-ray diffraction.....	46
2.3.4.	Residual stress: Optical profilometer	47
2.3.5.	Hardness and elastic modulus: Nanoindentation	50
2.3.6.	Adhesion: Scratch test.....	53
2.3.7.	Tribology: Rotative tribometer.....	55
2.3.8.	Thermal properties: Modulated photothermal radiometry	56
2.4.	Experimental setup for tribological tests.....	59
2.5.	Experimental setup for tool wear	61
2.6.	Preparation of the pins and inserts for temperature measurements.....	62
2.7.	Characterization methods	64
2.7.1.	Micro-hardness and microstructure of the work material	64
2.7.2.	Observation of the work material (Ti6Al4V) adhesion to the pins.....	65
2.7.3.	Pin's profile inspection.....	66
2.7.4.	Surface roughness measurements.....	67
2.8.	Résumé du Chapitre 2	68

Chapter 3. Optimization of Cr-based mono and multilayers	70
3.1. Introduction	71
3.2. Optimization of the monolayer films	72
3.2.1. Cr underlayer.....	72
3.2.1.1. Deposition conditions.....	72
3.2.1.2. Physico-chemical properties	73
3.2.1.2.1. Chemical composition by EDS.....	73
3.2.1.2.2. Surface morphology and microstructure	73
3.2.1.2.3. Structure.....	74
3.2.1.3. Tribological properties	75
3.2.1.4. Mechanical properties	76
3.2.1.5. Partial conclusion	77
3.2.2. CrN coatings.....	78
3.2.2.1. Deposition conditions.....	78
3.2.2.2. Physico-chemical properties	79
3.2.2.2.1. Deposition rate and thickness of the CrN layers	79
3.2.2.2.2. Chemical composition	80
3.2.2.2.3. Surface morphology and microstructure	83
3.2.2.2.4. Structure.....	85
3.2.2.3. Tribological properties	89
3.2.2.4. Mechanical properties	92
3.2.2.4.1. Residual stress	92
3.2.2.4.2. Hardness and elastic modulus.....	94
3.2.2.4.3. Adhesion.....	98
3.2.2.5. Partial conclusion	103
3.2.3. Cr _{1-x} Al _x N coatings	103
3.2.3.1. Optimization of the Al content.....	103
3.2.3.1.1. Deposition conditions	104
3.2.3.1.2. Physico-chemical properties.....	106
3.2.3.1.2.1. Deposition rate and thickness of the CrAlN layers	106
3.2.3.1.2.2. Chemical composition by EDS microanalyses.....	107
3.2.3.1.2.3. Chemical composition by XPS analyses	109
3.2.3.1.2.4. Surface morphology and microstructure	112

3.2.3.1.2.5. Structure.....	115
3.2.3.1.3. Tribological properties	118
3.2.3.1.4. Mechanical properties.....	120
3.2.3.1.4.1. Residual stress	120
3.2.3.1.4.2. Hardness and elastic modulus.....	122
3.2.3.1.4.3. Adhesion.....	126
3.2.3.1.5. Partial conclusion	130
3.2.3.2. Optimization of the substrate bias voltage and deposition temperature.....	130
3.2.3.2.1. Deposition conditions	131
3.2.3.2.2. Physico-chemical properties.....	132
3.2.3.2.2.1. Deposition rate and thickness of the AlCrN layers	132
3.2.3.2.2.2. Chemical composition by EDS microanalyses.....	132
3.2.3.2.2.3. Surface morphology and microstructure	134
3.2.3.2.2.4. Structure.....	136
3.2.3.2.3. Tribological properties	139
3.2.3.2.4. Mechanical properties.....	142
3.2.3.2.4.1. Residual stress	142
3.2.3.2.4.2. Hardness and elastic modulus.....	144
3.2.3.2.4.3. Adhesion.....	148
3.2.3.2.5. Partial conclusion	154
3.3. Cr/CrN/AlCrN and Cr/CrN/CrAlN multilayers	154
3.3.1. Deposition conditions.....	155
3.3.2. Physico-chemical properties	158
3.3.2.1. Deposition rate and thickness.....	158
3.3.2.2. Chemical composition by EDS microanalyses	158
3.3.2.3. Surface morphology and microstructure	159
3.3.2.4. Structure	162
3.3.3. Tribological properties	165
3.3.4. Mechanical properties	167
3.3.4.1. Residual stress	167
3.3.4.2. Hardness and elastic modulus	168
3.3.4.3. Adhesion.....	172
3.3.5. Thermal properties	175

3.3.6.	Partial conclusions.....	176
3.4.	Conclusions	177
3.5.	Résumé du Chapitre 3	182
Chapter 4.	Tribological analysis.....	188
4.1.	Introduction	189
4.2.	Determination of contact conditions in machining of Ti6Al4V alloy	189
4.2.1.	Determination of the sliding speeds	189
4.2.2.	Determination of the normal force acting in the pins.....	191
4.2.2.1.	Determination of the contact pressure in machining of Ti6Al4V alloy	192
4.2.2.2.	Determination of the normal force acting in the pins.....	194
4.3.	Surface roughness of the pins.....	201
4.4.	Design of experiments.....	203
4.5.	Results of the tribological tests	205
4.6.	DoE analysis and discussion	210
4.7.	Conclusion.....	215
4.8.	Résumé du Chapitre 4	216
Chapter 5.	Tool wear analysis	219
5.1.	Introduction	220
5.2.	Tool wear tests and results	220
5.2.1.	Description of the tool wear tests	220
5.2.2.	Results and discussion.....	223
5.2.2.1.	Cryogenic conditions.....	223
5.2.2.2.	Flood conditions	227
5.2.2.3.	Cryogenic vs flood	231
5.3.	Statistical analysis	232
5.3.1.	Statistical approach	233
5.3.1.1.	Pearson's correlation analysis.....	233
5.3.1.2.	Principal Component Analysis (PCA)	234
5.3.2.	Results of the statistical analysis.....	235
5.3.2.1.	Results of the Correlations of Pearson	236
5.3.2.2.	Centered reduced form	236
5.3.2.3.	Forces based flank wear models for each (coating, cooling method) pair	240
5.4.	Conclusions	243

5.5. Résumé du Chapitre 5	245
Conclusions and perspectives.....	247
1. General conclusion	248
2. Perspectives	252
References	254
Appendix	279

List of tables

Table 1. Comparison of effectiveness and application of various cooling and lubricating methods [16].....	11
Table 2. Mechanical properties of Ti6Al4V [58].....	16
Table 3. Tool materials' properties at room temperature [165].....	35
Table 4. Geometry and dimension of substrates	41
Table 5. Etching condition for the substrates	42
Table 6. Etching condition for the targets	42
Table 7. Summary of the coatings' characterization techniques.....	59
Table 8. Techniques de caractérisation des couches minces utilisées lors de notre étude	69
Table 9. Deposition conditions of the Cr underlayer	72
Table 10. Tribological properties of the chromium underlayer	75
Table 11. Mechanical properties of the Cr underlayer.....	76
Table 12. Deposition conditions of the CrN monolayers.....	79
Table 13. Deposition rate and thickness of the CrN monolayers.....	79
Table 14. Chemical composition of the CrN monolayers.....	80
Table 15. Chemical composition of the CrN monolayer (300°C-500V) by XPS	82
Table 16. Grain size of the CrN monolayers.....	88
Table 17. Wear rates of the CrN monolayers.....	90
Table 18. Residual stress of the CrN monolayer as a function of the deposition conditions... 92	
Table 19. Hardness, elastic modulus, elastic and plastic deformation resistance H/E and H^3/E^2 of the CrN monolayers on silicon substrate and mirror-polished WC substrate.....	95
Table 20. Critical load and work of adhesion of CrN monolayers	99
Table 21. Deposition conditions of the $Cr_{1-x}Al_xN$ monolayers at different target power density	104
Table 22. Thickness and deposition rate of the $Cr_{1-x}Al_xN$ monolayers as a function of the targets power density	106
Table 23. Chemical composition of the $Cr_{1-x}Al_xN$ monolayers	108
Table 24. Chemical composition of the CrAlN layer with 61.5 at.% of Al from XPS.....	109
Table 25. Chemical composition of the CrAlN layer with 73.9 at.% of Al from XPS analyses	111
Table 26. Grain size and diffraction peaks of the $Cr_{1-x}Al_xN$ monolayers	117

Table 27. Wear rate of the Cr _{1-x} Al _x N monolayers.....	119
Table 28. Residual stress of the Cr _{1-x} Al _x N coatings at different Al content	121
Table 29. Hardness, elastic modulus, elastic and plastic deformation resistance H/E and H ³ /E ² of Cr _{1-x} Al _x N monolayers with varied Al content	123
Table 30. Critical loads and work of adhesion of Cr _{1-x} Al _x N coatings at different Al content	127
Table 31. Deposition conditions of the AlCrN monolayers.....	131
Table 32. Deposition rate and thickness of the AlCrN monolayers.....	132
Table 33. Chemical composition of the AlCrN monolayers.....	133
Table 34. Grain size of the AlCrN monolayers.....	138
Table 35. Wear rate of the AlCrN monolayers	140
Table 36. Residual stress of AlCrN monolayers as a function of the deposition conditions. .	143
Table 37. Hardness, elastic modulus, elastic and plastic deformation resistance H/E and H ³ /E ² of the AlCrN monolayers on silicon and mirror-polished WC substrate.....	146
Table 38. Critical load and work of adhesion of AlCrN monolayers	150
Table 39. Deposition conditions of the multilayers	157
Table 40. Theoretical and experimental diffraction peaks position and grain size of as-deposited multilayers.....	164
Table 41. Wear rate of the multilayers	166
Table 42. Residual stress of the multilayers.....	167
Table 43. Hardness, elastic modulus, elastic and plastic deformation resistance H/E and H ³ /E ² of the multilayers on WC substrates	169
Table 44. Critical loads and work of adhesion of the multilayers.....	173
Table 45. Thermal conductivity of as-deposited monolayers and multilayers (WC substrate as reference).....	176
Table 46. Properties of the mono and multilayers	181
Tableau 47. Propriétés des mono et multilcouches	186
Table 48. Sliding velocities and correlated cutting speeds determined in tribological tests..	191
Table 49. Experimental data taken from the work of Outeiro et al. [304].	193
Table 50. Determination of the contact pressure.....	193
Table 51. Mechanical properties of the pin and workpiece used in the pin-on-bar model[309].	195
Table 52. Minimum element size tested pin and workpiece	196

Table 53. Equivalent radius (R_{eq}) calculated considering the bar with an initial diameter of 80 mm and a final one of 58 mm.	199
Table 54. Factors and levels used in the multilevel factorial DoE.....	204
Table 55. Additional tests for an average contact pressure of 1329 MPa.....	205
Table 56. Optimized type of MWF and sliding speed for a reduced adhesion of volume of Ti6Al4V material to the pins and apparent friction coefficient.	215
Table 57. Cutting conditions used in the tool wear tests.....	221
Table 58. Order of the tool coatings used in the wear tests.	235
Table 59. Pearson's correlations between cutting tests output and tool flank wear.	236
Table 60. Centered Reduced table corresponding to the M2 insert, LN2 cooling (unitless).	237
Table 61. Correlation matrix corresponding to the coating M2 insert, LN2 cooling.....	238
Table 62. Eigenvectors and eigenvalues corresponding to the correlation matrix (M2 insert, LN2 cooling).	238
Table 63. Eigen values and their implication percentage for wear tests with (M2 insert, LN2 cooling).....	238
Table 64. Percentage of implication of every variable in fact1 (M2 insert, LN2 cooling). ...	239
Table 65. Forces based flank wear models for three types of inserts and two lubrication/cooling strategies.....	243
Table 66. Surface roughness of the coated pins.	vi
Table 67. Surface roughness of the workpiece	vii

List of figures

Figure 1. Drilling system [6].....	6
Figure 2. Global market of cutting tools distribution and growth by metal cutting operation type [9].....	7
Figure 3. Schematic illustration of turning operation [10].....	8
Figure 4. Brief history of cryogenic assisted machining.....	11
Figure 5. Publication number of cryogenic assisted machining (source from www.sciencedirect.com, updated until 7/11/2021).....	13
Figure 6. Cross section of a jet engine [53].....	14
Figure 7. Structural weight percentage of modern commercial aircraft and gas turbine engine, including aluminium, titanium, steel alloys and CFRP (Carbon Fiber Reinforced Polymer) [52].....	14
Figure 8. Crystalline structure of titanium: a) HCP and b) BCC [55].....	15
Figure 9. Titanium phases and properties [56].....	15
Figure 10. Crystallographic structure of Ti6Al4V : a) lamellar structure and b) equiaxial structure [50].....	16
Figure 11. Mechanical properties of Ti6Al4V at low temperature [60].....	17
Figure 12. Wear mechanisms [83].....	21
Figure 13. Different types of tool wear [86].....	22
Figure 14. PVD processing techniques: a) vacuum evaporation, b) and c) sputter deposition in plasma environment, d) sputter deposition in a vacuum, e) Ion plating in a plasma with a thermal evaporation source, f) Ion plating with a sputtering source, g) Ion plating [101].....	25
Figure 15. Coating deposition technologies for cutting tools [102].....	26
Figure 16. Schematic diagram of a cathodic magnetron sputtering.....	28
Figure 17. World market of hard and super-hard cutting materials [9].....	29
Figure 18. Evolution of monolayer coating materials and related deposition technologies for cutting tools [100].....	30
Figure 19. Thermal conductivity of different cutting tool materials as a function of the temperature [165].....	36
Figure 20. Deposition system of KENOSISTEC-KS40V-113K12, 1) chamber, 2-a) power supply and 2-b) automate [178].....	39

Figure 21. Operating system diagram of KENOSISTEC-KS40V-113K12 [178]	40
Figure 22. Planetary carousel system and targets [111].....	41
Figure 23. a) Interaction between radiation and material, b) Interaction zone between radiation and material [182]	44
Figure 24. Example of: a) cross-section and b) EDS spectra of a CrN/CrAlN multilayer	44
Figure 25. XPS emission process [112, 153]	45
Figure 26. Principle of X-ray diffraction	46
Figure 27. Bragg-Brentano configuration	47
Figure 28. Method to determine the thickness of coatings on silicon substrate.....	48
Figure 29. Deformation of coating-substrate: a) compressive residual stress and b) tensile residual stress [112].....	49
Figure 30. Post-treatment example of curvature measurement.....	50
Figure 31. Schematic illustration of indentation load–displacement data [188].....	51
Figure 32. Cross-section of indentation process showing the parameters characterizing the contact geometry [188].....	52
Figure 33. Typical friction force and acoustic emission curve obtained after scratch test and observation of scratch path under optical microscope [151, 191].....	54
Figure 34. Method to calculate the wear volume	56
Figure 35. Modulated photothermal radiometry experimental setup [196]	57
Figure 36. The assembly of tribological tests	60
Figure 37. Nozzle position in MWF and cryogenic assisted tribological tests	60
Figure 38. SONIM CNC lathe machine and the assembly of tool wear tests	62
Figure 39. Drilling EDM machine and drilling position on pins and cutting tools.....	63
Figure 40. Detail of thermocouple position in the pin and in the insert.....	63
Figure 41. Micro-hardness of Ti6Al4V bar	64
Figure 42. Microstructure of Ti6Al4V bar on a) longitudinal and b) axial section	65
Figure 43. Optical surface observation setup with the digital microscope Keyence	65
Figure 44. Alicona 3D measurement system	66
Figure 45. Vertical profile projector	67
Figure 46. Contact profilometer Surfscan	68
Figure 47. a) SEM images of the Cr underlayer surface morphology on WC substrate and b) cross-section of the Cr underlayer on silicon substrate.....	73
Figure 48. Schematic view of extended SZM [207]	74

Figure 49. XRD pattern of the Cr underlayer and the WC substrate	75
Figure 50. Wear track of the Cr underlayer and WC substrate	76
Figure 51. Optical images of Lc1 and Lc2 critical loads for the Cr underlayer.....	77
Figure 52. Chemical composition of the CrN monolayers as a function of the deposition temperature and substrate bias voltage.....	80
Figure 53. XPS spectra of the CrN monolayers (300°C-500V) on WC substrate	81
Figure 54. XPS N1s spectra of the CrN monolayer (300°C-500V) on WC substrate	82
Figure 55. Surface morphology of the CrN monolayers on WC substrates: a) amb-0V, b) amb-500V, c) 150°C-500V, d) 300°C-500V, e) 300°C-250V and f) 300°C-0V	83
Figure 56. Surface morphology of the CrN monolayers on silicon substrates: a) amb-0V, b) amb-500V, c) 150°C-500V, d) 300°C-500V, e) 300°C-250V and f) 300°C-0V.....	83
Figure 57. Cross-section of the CrN monolayers on Silicon substrate obtained at: a) amb-0V, b) amb-500V, c) 150°C-500V, d) 300°C-500V, e) 300°C-250V and f) 300°C-0V.....	85
Figure 58. XRD patterns of CrN monolayers.	86
Figure 59. Grain size of the CrN monolayers as a function of the deposition conditions	88
Figure 60. Friction coefficient of CrN monolayers as a function of the deposition conditions.....	89
Figure 61. Wear rate of the CrN monolayers as a function of the deposition conditions	90
Figure 62. Wear tracks of the CrN monolayers as a function of the deposition conditions	91
Figure 63. Residual stress of the CrN monolayers as a function of the deposition conditions	92
Figure 64. Grain size and residual stress of the CrN monolayers	93
Figure 65. Hardness and elastic modulus of the CrN monolayers under different coating conditions on silicon substrate	94
Figure 66. Residual stress and hardness of the CrN monolayers on silicon substrate	96
Figure 67. Grain size and hardness of the CrN monolayers.....	97
Figure 68. Wear rate and plastic deformation resistance of the CrN monolayers	98
Figure 69. Classification of different failure mode of thin films after scratch test [262]	98
Figure 70. Relation between residual stress and work of adhesion work for CrN monolayers.....	99
Figure 71. Optical images of critical load Lc1 of the CrN monolayers on rough WC substrate obtained at: a) Ambient-0V, b) Ambient-500V, c) 150°C-500V, d) 300°C-500V, e) 300°C-250V, f) 300°C-0V	100
Figure 72 Optical images of critical load Lc2 of the CrN monolayers on rough WC substrate obtained at: a) Ambient-0V, b) Ambient-500V, c) 150°C-500V, d) 300°C-500V, e) 300°C-250V, f) 300°C-0V	101

Figure 73. Optical images of critical loads of the CrN monolayers obtained on WC polished substrates at: a1) Lc1 300°C-500V, a2) Lc2 300°C-500V, b1) Lc1 300°C-250V and b2) Lc2 300°C-250V	101
Figure 74. Critical loads of the CrN monolayers as a function of the deposition conditions	102
Figure 75. Evolution of the Lc1, Lc2 critical loads of the CrN monolayers and their elastic modulus as a function of the deposition temperature.....	103
Figure 76. Glow discharge at the surface field of a target [270].....	105
Figure 77. Deposition rate of the Cr _{1-x} Al _x N monolayers as a function of the targets power density	107
Figure 78. Chemical composition of Cr _{1-x} Al _x N monolayers as a function of the Al content	108
Figure 79. XPS analyses of the CrAlN monolayer with 61.5 at.% of Al.....	110
Figure 80. XPS spectra of the CrAlN monolayer containing 73.9 at.% of Al	110
Figure 81. XPS analyses of the CrAlN monolayer with 73.9 at.% of Al.....	111
Figure 82 Deconvolution of N1s peaks: a) 61.5 at.% of Al, b) 73.9 at.% of Al	112
Figure 83 Surface morphology of Cr _{1-x} Al _x N monolayers on WC substrate with varied Al content: a) x=0.14, b) x=0.57, c) x=0.62, and d) x=0.74	113
Figure 84 Surface morphology of Cr _{1-x} Al _x N monolayers on silicon substrate with varied Al content: a) x=0.14, b) x=0.57, c) x=0.62 and d) x=0.74	114
Figure 85. Cross-section images of Cr _{1-x} Al _x N monolayers on silicon substrate with varied Al content: a) x=0.14, b) x=0.57, c) x=0.62 and d) x=0.74	114
Figure 86. XRD patterns of the Cr _{1-x} Al _x N monolayers with varied Al content	115
Figure 87. Grain size of the Cr _{1-x} Al _x N monolayers at different Al content	117
Figure 88. Friction coefficient of the Cr _{1-x} Al _x N monolayers at different Al content.....	118
Figure 89. Wear rate of the Cr _{1-x} Al _x N monolayers at different Al content.....	119
Figure 90. Wear tracks of the Cr _{1-x} Al _x N monolayers at different Al content and of the WC substrate.....	120
Figure 91. Residual stress of the Cr _{1-x} Al _x N monolayers at different Al content.....	120
Figure 92. Grain size and residual stress of the Cr _{1-x} Al _x N monolayers at different Al content	122
Figure 93. Hardness and elastic modulus of the Cr _{1-x} Al _x N monolayers at different Al content on silicon substrate	123
Figure 94. Correlation between residual stress and hardness of Cr _{1-x} Al _x N monolayers at different Al content	124

Figure 95. Grain size and hardness of the $\text{Cr}_{1-x}\text{Al}_x\text{N}$ monolayers at different Al content	125
Figure 96. Correlation between plastic deformation resistance and wear rate of the $\text{Cr}_{1-x}\text{Al}_x\text{N}$ monolayers at different Al content.....	125
Figure 97. Optical images of critical load of the $\text{Cr}_{1-x}\text{Al}_x\text{N}$ monolayers on WC substrate: a1) Lc1 $x=0.14$, a2) Lc2 $x=0.14$ b1) Lc1 $x=0.57$, b2) Lc2 $x=0.57$, c1) Lc1 $x=0.62$, c2) Lc2 $x=0.62$, d1) Lc1 $x=0.74$ and d2) Lc1 $x=0.74$	126
Figure 98. Correlation between residual stress and work of adhesion of the $\text{Cr}_{1-x}\text{Al}_x\text{N}$ monolayers at different Al content.....	127
Figure 99. Critical loads of the $\text{Cr}_{1-x}\text{Al}_x\text{N}$ coatings at different Al content at different Al content	128
Figure 100. Evolution of the Lc2 critical load of the $\text{Cr}_{1-x}\text{Al}_x\text{N}$ monolayers and their grain size (x^2) as a function of the Al content.....	129
Figure 101. Correlation between residual stress and critical load of the $\text{Cr}_{1-x}\text{Al}_x\text{N}$ coatings at different Al content	129
Figure 102. Hardness of CrN and CrAlN layers as a function of the temperature [230].....	131
Figure 103. Chemical composition of the AlCrN monolayers as a function of the deposition temperature and substrate bias voltage.....	133
Figure 104. Surface morphology of the AlCrN monolayers on WC substrate a) amb-0V, b) amb-500V, c) 150°C-500V, d) 300°C-500V, e) 300°C-250V and f) 300°C-0V	134
Figure 105 Surface morphology of the AlCrN monolayers on silicon substrate a) amb-0V, b) amb-500V, c) 150°C-500V, d) 300°C-500V, e) 300°C-250V and f) 300°C-0V	134
Figure 106. Cross-section of the AlCrN monolayers on Si obtained at: a) amb-0V, b) amb-500V, c) 150°C-500V, d) 300°C-500V, e) 300°C-250V and f) 300°C-0V	136
Figure 107. XRD patterns of AlCrN monolayers with different deposition conditions	137
Figure 108. Grain size of the AlCrN monolayers as a function of the deposition conditions	139
Figure 109. Friction coefficient of AlCrN monolayers as a function of the deposition conditions	140
Figure 110. Wear tracks of the AlCrN monolayers as a function of the deposition conditions	141
Figure 111. Wear rate of the AlCrN monolayers as a function of the deposition conditions	141
Figure 112. Residual stress of the AlCrN monolayers as a function of the deposition conditions	142

Figure 113. Residual stress of the CrN and AlCrN monolayers as a function of the deposition conditions	144
Figure 114. Grain size and residual stress of the AlCrN monolayers	144
Figure 115. Hardness and elastic modulus of the AlCrN monolayers as a function of the deposition conditions on silicon substrate.....	145
Figure 116. Correlation between residual stress and hardness of the AlCrN monolayers.....	147
Figure 117. Grain size and hardness of the AlCrN monolayers.....	147
Figure 118. Wear rate and plastic deformation resistance of the AlCrN monolayers	148
Figure 119. Optical images of the critical load Lc1 of the AlCrN monolayers on rough WC substrate: a) Ambient-0V, b) Ambient-500V, c) 150°C-500V, d) 300°C-500V, e) 300°C-250V, f) 300°C-0V	149
<i>Figure 120 Optical images of the critical load Lc2 of the AlCrN monolayers on rough WC substrate: a) Ambient-0V, b) Ambient-500V, c) 150°C-500V, d) 300°C-500V, e) 300°C-250V, f) 300°C-0V</i>	<i>149</i>
Figure 121. Optical images of the critical loads of AlCrN monolayers obtained at 300°C-250V on polished substrate: a1) Lc1 and a2) Lc2.....	150
Figure 122. Relation between residual stress and work of adhesion of AlCrN monolayers obtained on silicon substrate	151
Figure 123. Critical loads of AlCrN monolayers	151
Figure 124. Evolution of the Lc1, Lc2 critical loads and elastic modulus of the AlCrN monolayers as a function of the deposition temperature at a substrate bias voltage of -500V	152
Figure 125. Evolution of the Lc2 critical load of the AlCrN monolayers and the grain size as a function of the deposition conditions	153
Figure 126. Correlation between residual stress and critical load Lc2 of the AlCrN monolayers	153
Figure 127. Architecture of the multilayers	156
Figure 128. Chemical composition of multilayers (cross-section EDS scanning profiles) ...	159
Figure 129. Surface morphology of multilayers on rough and mirror-polished WC substrates	160
Figure 130. Cross section of the multilayers on silicon substrates	161
Figure 131. XRD patterns of the multilayers	162
Figure 132. Grain size of the multilayers	164

Figure 133. Friction coefficient of the multilayers	165
Figure 134. Wear rate of the multilayers.....	166
Figure 135. Residual stress of the multilayers	167
Figure 136. Grain size and residual stress of the multilayers.....	168
Figure 137. Hardness and elastic modulus of the multilayers.....	169
Figure 138. Correlation between residual stress and hardness of the multilayers	170
Figure 139. Grain size and hardness of the multilayers	171
Figure 140. Wear rate and plastic deformation resistance of the multilayers	172
Figure 141. Optical images of the critical loads (Lc1 and Lc2) of the multilayers	172
Figure 142. Relation between residual stress (absolute values) and adhesion work of the multilayers.....	173
Figure 143. Critical loads of the multilayers.....	174
Figure 144. Evolution of the Lc2 critical load of the multilayers and their grain size	174
Figure 145. Correlation between residual stress and critical load Lc2 of the multilayers	175
Figure 146. Thermal conductivity of as-deposited monolayers and multilayers (substrate as reference).....	176
Figure 147. Single-shear plan model [10].....	190
Figure 148. Chip compression ratio (CCR) in orthogonal cutting of Ti6Al4V alloy using uncoated cemented carbide tools [303].....	191
Figure 149. Flowchart of the procedure to determine the normal force to be applied into the pins.	192
Figure 150. Force diagram in orthogonal cutting [301].....	193
Figure 151. Model and mesh of the pin-on-bar tribological test.....	196
Figure 152. Normal forces in function of the time for several minimum element size.	197
Figure 153. Contact stress distribution in function of the minimum element size.....	198
Figure 154. Normal forces in function of the time for different pin radius.	199
Figure 155. Contact stress distribution for different pin radius.	200
Figure 156. Normal forces in function of the time for several sliding speeds.	201
Figure 157. Contact stress distribution for several sliding speeds.	201
Figure 158. Arithmetic average roughness (R_a) of the pins for different coatings.....	202
Figure 159. Root mean square roughness (R_q) of the pins for different coatings.....	203
Figure 160. Maximum height of the roughness profile (R_t) of the pins for different coatings.	203

Figure 161. Apparent friction coefficient in function of the sliding speed and for different coatings, for (a) flood and b) LN2 (average contact pressure of 872 MPa).....	206
Figure 162. Volume of build-up layer of Ti6Al4V alloy in the pins in function of the sliding speed and for different coatings, for (a) flood and b) LN2 (average contact pressure of 872 MPa).....	207
Figure 163. Apparent friction coefficient in function of the sliding speed, for two average contact pressures (872 MPa and 1329 MPa), and for a) flood conditions using coated (M2) and uncoated pins, and b) for LN2 conditions using uncoated pins.	208
Figure 164. Volume of build-up layer of Ti6Al4V alloy in the pins in function of the sliding speed, for two average contact pressures (872 MPa and 1329 MPa), and for a) flood conditions using coated (M2) and uncoated pins, and b) for LN2 conditions using uncoated pins.	208
Figure 165. Apparent friction coefficient in function of the sliding speed obtained by current tribological tests and from the Courbon et al. [62] (Uncoated pin; average contact pressure of 1329 MPa; LN2 cooling).	209
Figure 166. Temperature in the pins for different coatings (average contact pressure of 872 MPa and a sliding speed of 60 m/min)	210
Figure 167. Pareto analysis of the factors affecting the (a) apparent friction coefficient and (b) volume of build-up layer of Ti6Al4V alloy in the pins.....	212
Figure 168. Influence of the (a) type of MWF and sliding speed, and (b) their interactions on apparent friction coefficient.	213
Figure 169. Influence of the (a) type of MWF and sliding speed, and (b) their interactions on the volume of build-up layer of Ti6Al4V alloy in the pins.....	214
Figure 170. Schematic representation of the workpiece preparation for the tool wear tests.	221
Figure 171. Types of wear in turning tools.	222
Figure 172. Uncoated inserts (a) new and (b) worn showing the tool wear (VB) measurements.	223
Figure 173. Tool flank wear VB_B in function of the time for the three inserts under cryogenic cooling.....	224
Figure 174. Tool flank wear VB_C in function of the time for the three inserts under cryogenic cooling.....	225
Figure 175. Tool life for the three inserts under cryogenic cooling (uncoated = 8.4 min, M2 = 11.2 min and M4 = 9 min).....	225

Figure 176. Worn inserts at the end of the wear tests using LN2: a) uncoated, b) M2 and c) M4.	226
Figure 177. Worn inserts at the end of the tests using LN2: a) rake face of uncoated, b) rake face of M2, c) rake face of M4, d) nose region of uncoated, e) nose region of M2, f) nose region of M4.....	226
Figure 178. Tool temperature for the uncoated, M2 and M4 coated inserts under cryogenic cooling.....	227
Figure 179. Tool flank wear VB_B in function of the time for the three inserts under flood conditions.	228
Figure 180. Tool flank wear VB_C in function of the time for the three inserts under flood conditions.	228
Figure 181. Tool life for the three inserts under flood conditions (uncoated = 8 min, M2 = 4.5 min and M4 = 9 min).....	229
Figure 182. Worn inserts at the end of the tests under flood conditions: a) uncoated, b) M2 and c) M4.	230
Figure 183. Worn inserts at the end of the tests under flood conditions: a) rake face of uncoated b) rake face of M2 c) rake face of M4 d) nose region of uncoated e) nose region of M2 f) nose region of M4.	230
Figure 184. Tool temperature for the uncoated, M2 and M4 coated inserts under flood conditions.	231
Figure 185. Summary of tool life for the three inserts under cryogenic (LN2) and flood conditions.	232
Figure 186. Tool wear VB_B and VB_C as a function of the time for the M2 insert under flood and LN2 conditions, respectively.....	232
Figure 187. Statistical approach.	233
Figure 188. Principle of the PCA applied to a simple sample [316].....	234
Figure 189. Comparing results issues from experimental measurements and forces based models concerning VB_B and VB_C of the uncoated insert during tests under flood conditions.	241
Figure 190. Comparing results issues from experimental measurements and forces-based models concerning VB_B and VB_C of the M2 insert during tests under flood conditions.	241

Figure 191. Comparing results issues from experimental measurements and forces-based models concerning VB_B and VB_C of the M4 insert during tests under flood conditions.	241
Figure 192. Comparing results issues from experimental measurements and forces based models concerning VB_B and VB_C of the uncoated insert during tests under LN2.....	242
Figure 193. Comparing results issues from experimental measurements and forces-based models concerning VB_B and VB_C of the M2 insert during tests under LN2.....	242
Figure 194. Comparing results issues from experimental measurements and forces-based models concerning VB_B and VB_C of the M4 insert during tests under LN2.....	242
Figure 195. TAP assembly of pin-on-disc tribological test on CNC turning machine (Baizeau, Ramirez, Rossi / Lournand, LABOMAP, Cluny, Arts et Métiers).	i
Figure 196. Technical draw of pin used in tribological tests.	ii
Figure 197. (a) Tool holder PCLNL 2525M-12-JHP, (b) schematic diagram of the channels to deliver the LN2 (c) and the nozzles positions and diameters [61].	iii
Figure 198. Example of extracting the adhesion volume: a) determination of background, b) information after subtracting background, c) adhesion volume after removing supplementary information d) 3D view of adhesion volume.....	iv
Figure 199. EDS analysis of wear tracks of worn WC substrate coated by: a) Cr underlayer, b) CrN 300°C-500V, c) $Cr_{1-x}Al_xN$ with $x=0.14$ and d) AlCrN 300°C-250V in pin-on-disc friction test without lubricant.	v
Figure 200. SEM images of the surface morphology of: CrN (a) AlCrN (b) M2 (c) and M4 (d) coated pins.....	vi
Figure 201. Normal force as a function of the sliding speed and for different coatings in flood conditions (Average contact pressure equals to 872 MPa).	vii
Figure 202. Tangential force as a function of the sliding speed for different coatings in flood conditions (Average contact pressure equals to 872 MPa).	viii
Figure 203. Normal force as a function of the sliding speed for different coatings under LN2 conditions (average contact pressure equals to 872 MPa).	viii
Figure 204. Tangential force as a function of the sliding speed and for different coatings under LN2 conditions (Average contact pressure equals to 872 MPa).	ix
Figure 205. Temperature measured in pins as a function of time for different coatings under flood conditions (Average contact pressure equals to 872 MPa, sliding speed equals to 60 m/min).	x

Figure 206. Temperature measured in pins as a function of time for different coatings under LN2 conditions (Average contact pressure equals to 872 MPa, sliding speed equals to 60 m/min). xi

Figure 207. SEM images and EDS cartography of the worn: a) uncoated, b) M2-coated and c) M4-coated inserts at the end of the tests under flood conditions on rake face xii

Figure 208. SEM images and EDS cartography of the worn: a) uncoated, b) M2-coated and c) M4-coated inserts at the end of the tests under LN2 conditions xiii

List of appendix

Appendix A : Tribometer	i
Appendix B : Pin technical draw.....	ii
Appendix C : Tool holder.....	iii
Appendix D : Method of determination for adhesion volume	iv
Appendix E : Wear tracks of pin-on-disc friction tests	v
Appendix F : Surface topography of the pins used in the tribological tests.....	vi
Appendix G : Forces acting in the pins in the tribological tests	vii
Appendix H : Temperatures of the pins in the tribological tests.....	x
Appendix I : EDS analysis of worn inserts in tool wear tests	xii

Glossary

Abbreviations

AC	Alternate current
B	Billion
BCC	Body-Centered Cubic
BUE	Built-up edge
cBN	Cubic boron nitride
CAD	Computer Aided Design
CCD	Charge-coupled device
CCR	Chip compress ratio
CFRP	Carbon Fiber Reinforced Polymer
CMOS	Complementary metal-oxide-semiconductor
CNC	Computer Numerical Control
COF	Coefficient of friction
CSM	Continuous stiffness measurement
CVD	Chemical vapor deposition
DC	Direct current
DLC	Diamond like carbon
EDS	Energy-dispersive X-ray spectroscopy
FWHM	Full width at half maximum
GB	Grain boundary
GLAD	Glancing angle deposition
HCP	Hexagonal Close-Packed
HRSEM	High resolution scanning electron microscopy
HSS	High speed steel
IBAD	Ion beam assisted deposition
IWS	Integrated wear scope
LN2	Liquid nitrogen
MPTR	Modulated photothermal radiometry
MQL	Minimum quantity lubrication
MRR	Metal Removal Rate
MWF	Metal Working Fluid
NIST	National Institute of Standards and Technology (US)
PA	Polyamide
PCA	Principal Component Analysis
PE	Polyethylene
PVD	Physical vapor deposition
RC	Reduced correlation

RF	Radio frequency
SEM	Scanning electron microscopy
WC	Tungsten Carbide
XPS	X-ray photoelectron spectroscopy
XRD	X-ray diffraction

Symbols

a_p	mm	Depth of cut
a_s	$\text{m}^2 \cdot \text{s}^{-1}$	Thermal diffusivity of substrate
A	m^2	Residual deformed surface
A_i, A_j	mm^2	Single/assemble area section
c_p	$\text{kJ} \cdot \text{kg}^{-1} \cdot \text{K}^{-1}$	Specific heat capacity
d	μm	Width of track (scratch-test)
d_{hkl}	\AA	Interplanar distance, (h, k, l) is the Miller index
D_w, D_{w1}	mm	Diameter of raw workpiece/machined surface
e		Euler's number
E, E_r	GPa	Elastic modulus, reduced elastic modulus
E_B	J	Binding energy (XPS)
E_i, E_s	GPa	Elastic modulus of indenter/substrate
E_k	eV	Kinetic energy of the photoelectrons (XPS)
E_c^f, E_p^i	eV	Initial kinetic energy of target/projectile particles
f	mm/rev	Feed
F_c, F_n, F_t	N	Cutting/normal/tangential force
F_{ny}	N	Normal force (tool/chip interface)
h	J·s	Planck's constant (XPS)
h_f, h_{max}, h_s	nm	Final/maximum load/sink-in depth (Nanoindentation)
H	GPa	Hardness
j		Imaginary unit
k_d, k_s	$\text{W} \cdot \text{m}^{-1} \cdot \text{K}^{-1}$	Thermal conductivity of the coating/substrate
K		Dimensionless shape factor
K_c	$\text{MPa} \cdot \text{m}^{1/2}$	Rupture toughness
l_c	mm	Contact length (tool-chip interface)
Lc_1, Lc_2	N	Force corresponding to cracking/delamination of coating
M_c, M_p	uma	Mass of atom/projectile particle
n		Integer number (XPS)
N	rev/min	Rotation speed
P	MPa	Contact pressure (orthogonal cutting)
P_{max}	N	Maximum applied force (Nanoindentation)
P_{ny}	MPa	Average contact pressure (tool/chip interface)

r_ε	μm	Nose radius
R_0, R	m	Curvature of silicon before/after deposition
R_a, R_q, R_t	μm	Arithmetical mean/Root mean square roughness, maximum height
R_{ds}, R_{th}	$\text{m}\cdot\text{K}\cdot\text{W}^{-1}$	Thermal resistance at coating and substrate interface/coating
S	N/m	Stiffness
T_m, T_β	$^\circ\text{C}$	Melting/ β transus temperature
ν	Hz	Frequency of the X-ray (XPS)
ν_f	m/min	feed rate
ν_i, ν_s		Poisson ratio of indenter/substrate (Nanoindentation)
V_c, V_s, V_1	m/min	Cutting speed, sliding/chip velocity
VB_B, VB_C	mm	Flank wear
W_{ad}	$\text{J}\cdot\text{m}^{-2}$	Work of adhesion
$x_i, x_{i+1}; y_i, y_{i+1}$		Abscissa/Ordinate coordinate of area section
β		Line broadening at FWHM (XRD)
ΔT	$^\circ\text{C}$	Temperature variation
ε		Indenter geometry depended constant value (Nanoindentation)
$\varepsilon_p, \dot{\varepsilon}$		Plastic strain, strain rate
ζ		Chip compress ratio
θ	$^\circ$	Incident angle (XPS/XRD)
κ_r	$^\circ$	Cutting edge angle
λ	\AA	X-ray wavelength (XPS/XRD)
Λ		Multilayer period
$\mu_{app}, \mu_{loc}, \mu_{plast}$		Apparent friction coefficient, local adhesive/macrosopic part
P	$\text{kg}\cdot\text{m}^{-3}$	Density
τ	nm	Mean size of the ordered crystalline domains (XRD)
ϕ		Work function term (XPS)
ω	$\text{rad}\cdot\text{s}^{-1}$	Angular frequency
wt. %		Weight percentage

Introduction

Machining operations such as turning, milling, drilling and grinding consume a big quantity of money annually worldwide. Environmental concerns and cost reduction of metal working fluids (MWF) used in machining operations result in ever-growing industrial interest in replacing these fluids with eco-friendly cryogenic fluids such as liquid nitrogen (LN₂). However, research on machining under cryogenic conditions (also referred to as “cryogenic assisted machining”) using existing commercial cutting tools (developed for use with common MWF) have shown a large scatter in tool wear/life.

Titanium can be used in many fields due to its outstanding properties, including high strength, high toughness, biocompatibility, and good corrosion resistance. This material is not only used in the aerospace industry, but also for biomedical applications, and for chemical and oil industries. However, the major problem of this material is its poor machinability. Cryogenic assisted machining is a promising solution to improve machinability and surface integrity of the machined part. Many research works have shown the advantages of cryogenic cooling compared to conventional dry or flood conditions, including reduction of the temperature, reduction of the forces, improvement of surface finishing, etc [1]. However, as mentioned above, there are still some drawbacks associated to this technology, which can be partially attributed to the subpar performance of current commercial cutting tools under very low/cryogenic temperatures [2].

The current research work aims to develop the next generation of high-performance cutting tools for cryogenic machining. The objective is to enhance the performance of the cutting tools for cryogenic machining by improving the chemical/mechanical/physical properties of tool materials. One solution to improve such tool performance/life is by applying surface treatments, such as PVD hard coatings. Many studies have been made regarding this topic of research, but so far, the main objective is to obtain coatings that have a high thermal stability at high temperatures (more than 1000°C). This is typically the case of TiAlN coating. This study is innovative, because it deals with hard protective coatings that will have a high thermal stability at high temperature (around 400-500°C) but that could also support thermal shocks. Indeed,

during cryogenic machining, even under -196°C atmosphere, the local temperature at the tool-chip/workpiece interface can be extremely high.

This manuscript is divided into five chapters as described as follows:

Chapter 1 introduces a state-of-the-art on metal cutting, cryogenic assisted machining, Ti6Al4V alloy, tribology, tool wear, tool materials and hard coatings. This chapter ends by justifying the selection of the Cr/CrN/AlCrN multilayers tool coating to be optimized for cryogenic machining.

Chapter 2 starts by describing the experimental techniques related to coatings synthesis and physicochemical, structural, mechanical, tribological, thermal characterizations, including: magnetron sputtering system, SEM+EDS, XPS, XRD, nanoindentation, scratch test, stress determination, rotative tribometry, optical profilometry etc. This chapter ends with the description of the experimental setup and conditions used in the tribological and tool wear tests.

Chapter 3 presents the results and discussion about the optimization of the Cr, CrN and AlCrN monolayers. Three types of coatings were deposited on silicon and tungsten carbide substrates: a pure Chromium coating as underlayer, Chromium nitride coatings, Chromium Aluminum nitride with varied Aluminum content. The influence of deposition conditions such as deposition temperature and substrate bias voltage on the CrN and AlCrN properties are discussed in this chapter. Numerous characterizations were investigated to determine the coatings properties like structure by XRD, observation of surface morphology by SEM, mechanical properties analysis with Nanoindentation and scratch test, tribological performance with a rotative tribometer, etc. These characterizations permit to study the physicochemical, structural, tribological and mechanical performances of the coatings. Then the best monolayers were determined to be the constituent of the Cr/CrN/CrAlN or Cr/CrN/AlCrN multilayers. In this section of Chapter 3, we studied the effect of the number of interface as well as the thickness of each monolayer on the multilayer's properties. Thus, the properties of the obtained multilayers were investigated by the same characterization methods mentioned above. The optimized mono and multilayer coatings were chosen to be applied on carbide pins for the tribological tests described in the following Chapter 4.

Chapter 4 is dedicated to the tribological tests, the analysis between Ti6Al4V titanium alloy and uncoated/PVD-coated carbide pins, under several sliding speeds, two contact pressures, and two cooling/lubrication strategies: flood (mixture oil-water) and cryogenic (LN2) conditions. The pins were previously coated using the optimized monolayers and multilayers determined in Chapter 3. A multilevel factorial design of experiments (DoE) was applied to analyse the performance of the hard coatings in terms of apparent friction coefficient, volume of build-up material (adhesion) to the pins, and their temperature. Tribological tests were performed using a special designed pin-on-bar tribometer to reproduce the contact conditions in machining, followed by analysis to the pins' surface using digital microscopy, SEM and optical profilometry. The chapter ends with the analysis of the DoE and the determination of the contact conditions that reduce the adhesion of Ti6Al4V material to the pins and the apparent friction coefficient.

Chapter 5 is dedicated to the tool wear tests in turning of Ti6Al4V titanium alloy using uncoated and selected PVD-coated tools (inserts) based on the results of chapter 3 and chapter 4. The main objective is to evaluate the tool life of these tools under cryogenic cooling conditions and compared with the tool life under flood conditions. Tool flank wear measurements were performed using both home-made tool wear inspection system integrated into a CNC lathe machine and using optical microscopy. Tool life was determined based on ISO 3685:1993 using reduced VB values. SEM and EDS analysis were conducted on worn inserts to investigate the wear type and mechanisms. Tool temperature was measured for the three inserts and under both cryogenic cooling and flood conditions using thermocouples embedded in the cutting insert. This chapter ends with a statistical analysis to identify the relation between tool flank wear and other machining outcomes measured during the machining tests (forces and roughness of the machined surface) by applying the Pearson's correlation analysis. The statistical analysis was also used to build models for predicting the flank wear in function of the measured forces using the Principal Component Analysis (PCA) methodology.

PhD dissertation finishes with the general conclusions and perspectives of future research.

*Tool materials development for improved performance of cutting tools in
cryogenic machining of Aeronautic Alloys*

Chapter 1. State of the art

1.1. Introduction

This chapter presents the state of the art on metal cutting process, cryogenic assisted machining, Ti6Al4V titanium alloy, tribology, tool wear, tool materials in general, and in particular recent advances in hard protective coatings for cutting tools (monolayers, multilayers systems).

1.2. Metal cutting

1.2.1. Metal cutting definition and cutting system

Industry productions play a main role in our daily lives. Indeed, as estimation, 80% of manufactured products are machined before they are presented on the market [3]. In 2019, the total machining tool consumption worldwide was about US \$82.1 B [4], 36% of them was used in Europe [5].

Metal cutting should be viewed as a system composed by several components, including: machine, tool, workpiece, fixtures, regime, and MWF. For example, *Figure 1* shows the case of the drilling system proposed by Astakhov [6].

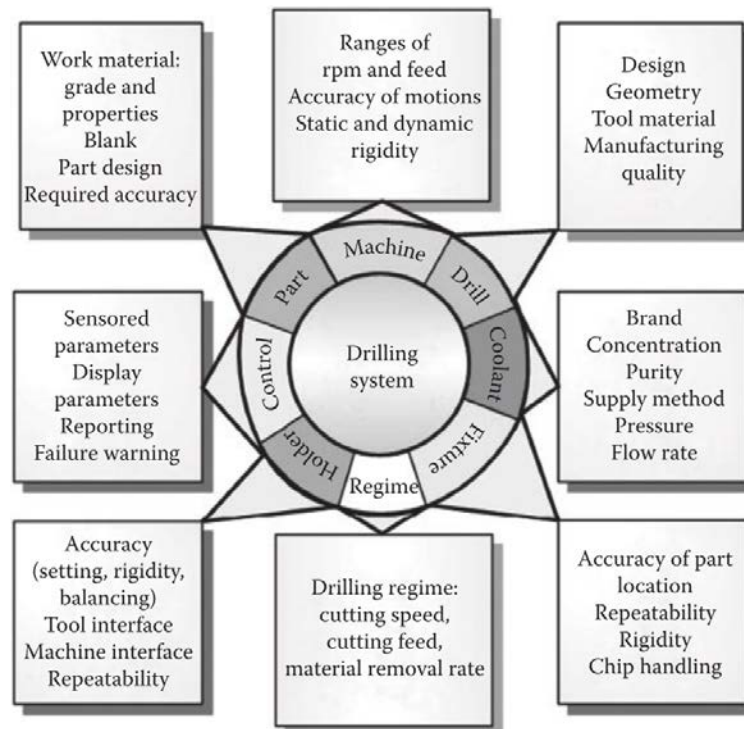


Figure 1. Drilling system [6]

According to Astakhov [7], metal cutting can be regarded as a forming process, where the components are so arranged that by their means the applied external energy causes the

purposeful fracture of the layer to be removed from the bulk material. The principal difference between metal cutting and other metal forming processes is the physical separation of the layer removed as chips from the rest of the workpiece. Different from fracture, in which an external force causes a separation of a solid body into two parts, metal cutting operation usually provides a continuous change of the state of stress in the first deformation zone causing a cyclic nature of the process. With foregoing reasons, the main purpose of metal cutting should be minimizing the external energy applied, therefore, generating adaptive state of stress to reduce the energy required for the separation of material [8].

1.2.2. Turning operation

Metal cutting includes several kinds of operations such as turning, milling, drilling, and grinding. Among them, turning is one of the most performed operation. It represents about 30% profit of cutting tools in global market, in which a total value of US \$16.33 B, the growth of turning operation in forecast reaches 4.4% in 2018 (Figure 2).

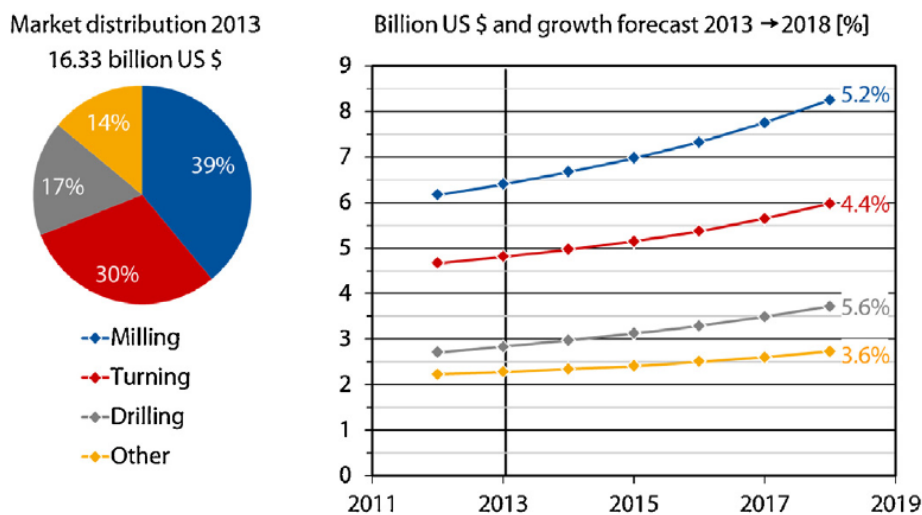


Figure 2. Global market of cutting tools distribution and growth by metal cutting operation type [9]

Generally, during turning operation, a cylindrical workpiece rotates around its axis of revolution, while a cutting tool carries out a translation motion.

Figure 3 illustrates a common turning configuration. The motion of the cutting tool is called feed, presented by f and the unities are mm/rev. In longitudinal turning the feed direction is parallel to workpiece axis. The primary motion of the workpiece is rotation N , the units are rev/min. D_w and D_{w1} are the diameter of raw workpiece and the machined surface, respectively (unities are millimeters). a_p represents the depth of cut (unities are millimeters). The cutting speed, namely V_c , can be calculated by Equation 1:

$$V_c = \frac{\pi D_w N}{1000} \quad \text{Equation 1}$$

where D_w is diameter of workpiece in millimeter (mm) and N is the rotation speed of workpiece in rev/min (or r.p.m). The unities of V_c are m/min.

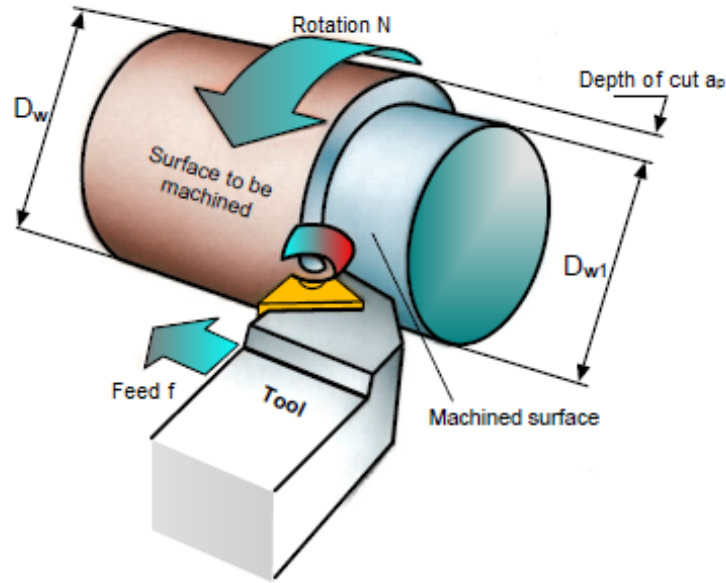


Figure 3. Schematic illustration of turning operation [10]

The feed rate can be calculated using Equation 2:

$$v_f = f \cdot N = f \cdot \frac{1000V_c}{\pi D_w} \quad \text{Equation 2}$$

As productivity becomes more and more important in industrial production, evaluating how fast one turning operation can remove the material from workpiece is represented as MRR (Metal Removal Rate) in mm^3/min . MRR depends on the cutting speed, feed and depth of cut according to Equation 3:

$$MRR = V_c \cdot f \cdot a_p \quad \text{Equation 3}$$

1.2.3. Metal Working Fluids

The metal working fluids (MWF) is integrated in the metal cutting system. They play an important role in cutting, including:

- Evacuation of the heat generated during the metal cutting process;
- Lubrication, which contributes to decrease of friction coefficient at the tool-chip and tool-workpiece interfaces;
- Remove the chips from the cutting zone.

Recent years in the market, the available lubricants are conventional MWF (oil-based, aqueous-based, synthetic and semi-synthetic), and most recently developed MWF (vegetable-based, cryogenic-based, etc.). Minimum quantity lubrication (MQL) and cryogenic assisted machining attract more and more attention of the industries. Regarding the methods of application of MWF in metal cutting, they can be classified into wet, mist cooling and high-pressure (HPJ) techniques [11].

The inconveniences of conventional MWF on health and environment are well known. It is reported around 80% of occupational infections of operators are due to contact of skin with cutting fluids [12], this may even cause skin cancer [13]. The recent developed MWF, for example the vegetable-based oils are preferable because they are biodegradable than mineral oils [14]. Furthermore, the vegetable-based oils not only provide high strength lubricant film to interact strongly with metallic surface, but also reduce the friction and wear. However, low thermal stability, low oxidative stability, high freezing points and poor corrosion protection are the main limitations of these vegetable-based oils in relation to the conventional MWF [11].

In dry machining no cutting fluid is used, thus avoids the health contamination and pollution problems of conventional MWF. However, it reduces enormously the productivity especially in cutting of refractory alloys, where the lubrication and cooling actions are strongly required. To minimize the quantity of lubricants (mineral, vegetal, etc.), MQL is introduced, which substantially reduces the environmental impact and cost associated to conventional MWF. MQL is also called near-dry machining and micro-lubrication due to the very low quantity lubricant mixed in high pressure jet of air. Comparing to traditional flood conditions, the flow rate of MQL is 50 ml/h – 2 l/h, which is one thousandth of the other [15]. Still, the inconvenient of MQL is obvious, it cannot provide an effective cooling and lubrication effects as the traditional MWF in flood conditions.

As mentioned by Jawahir et al. [16], although cryogenic machining is known for more than decade and a half as explained by Uehara and Kumagai [17], no significant progress was reported on it until the work by Chattopadhyay et al. [18]. This cooling method uses low temperature fluids like liquid nitrogen (LN2) and carbon dioxide (CO2) instead of conventional MWF. The LN2 evaporates almost harmlessly into atmosphere when it absorbs the heat generated from metal cutting. Moreover, the chip is removed by the LN2 jet during process, the cooling fluid contains no oil so there is no need to clean the surface of workpiece. Several studies reported a delay of various types of wear such as abrasion, adhesion and diffusion and an increase of tool life when machining with carbide tools [19–25].

As so many benefits are shown by cryogenic assisted machining, the following section will present the cryogenic assisted machining in detail.

1.3. Cryogenic assisted machining

1.3.1. History and definition

Cryogenic is referred to science and technology of producing low temperature environments. Its applications are various; thus, it has different meanings in different domain. This temperature is generally considered as a point below -150°C (123 K), where stands the end of refrigeration. Others (e.g. NIST) divide this line at -180°C in reason that it is the normal boiling points of numerous gases (e.g. helium, hydrogen, neon, nitrogen, oxygen and air) [16]. Particularly, liquid nitrogen boils at -196°C . At the beginning of the 19th century, liquid oxygen and hydrogen were first discovered and employed but the “cryogenic” name appeared at the end of the century [26]. Despite these established definitions and practices, various researchers have used the term cryogenics to refer to temperatures below 0°C , largely including CO2 applications [16].

In domain of machining, the first use of CO2 as coolant in machining is in early 20th century [27]. Through, the term ‘cryogenic assisted machining’ was first used in 1968 by Uehara et al. [17], cryogenic assisted machining using e.g. LN2 and CO2 as an alternative cooling method of traditional MWF [28]. Since the beginning of 21st century, the application of cryogenic was in diverse industrial domains, leading to enrichment of research field on this topic. Same in machining domain, the use of high flow rate liquid nitrogen and carbon dioxide can increase the productivity and product quality but it increases the machining cost [29, 30]. The following

flow diagram (Figure 4) shows the brief history of development in cryogenic assisted machining.

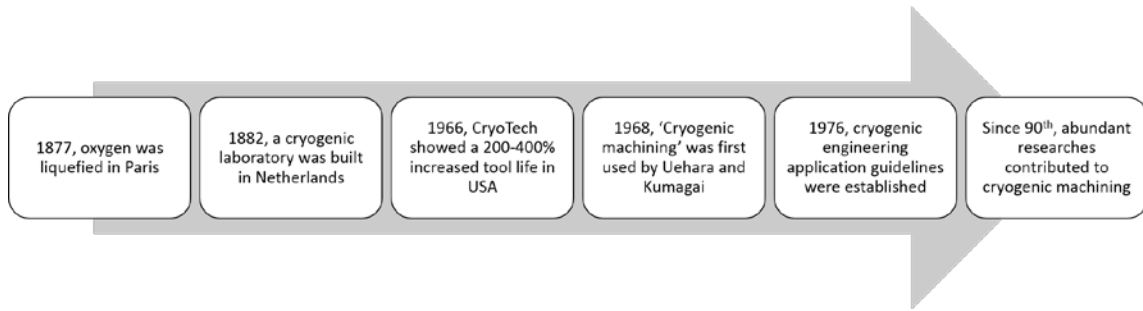


Figure 4. Brief history of cryogenic assisted machining

1.3.2. Comparison between different cooling and lubrication methods

There are abundant (flood) methods for cooling the cutting tool and workpiece during machining operations. The objective of this section is to compare the cryogenic assisted machining with other cooling and lubrication methods. Their applications and effectiveness are listed in Table 1.

Table 1. Comparison of effectiveness and application of various cooling and lubricating methods [16]

Effects of cooling and lubrication method		Dry	Flood (mixture oil-water)	MQL	LN2	CO2	MQL+LN2
Primary	Cooling	Poor	Good	Marginal	Excellent	Good	Excellent
	Lubrication	Poor	Excellent	Excellent	Marginal	Marginal	Excellent
	Chip removal	Good	Good	Marginal	Good	Good	Good
	Tool life	Poor	Good	Marginal	Excellent	Good	Good
Secondary	Machine cooling	Poor	Good	Poor	Marginal	Marginal	Marginal
	Workpiece cooling	Poor	Good	Poor	Good	Good	Good
	Spray control	Poor	Good	Marginal	Marginal	Marginal	Marginal
	Surface integrity	Poor	Good	Marginal	Excellent	Good	Excellent
Sustainability		Thermal damage	Pollution, high cost	Harmful vapour	Reference	Technical difficulties	Oil vapour, Technical difficulties

The cryogenic assisted machining owns several advantages in comparison to other cooling and lubrication methods. On cooling aspect, its thermal capacity is excellent ($c_p = 2 \text{ kJ/kg}\cdot\text{K}$ at 77 K), on the aspect of final products quality, cryogenic assisted machining brings 20% beneficial comparing to dry machining [31]. The industrial productivity increases thanks to the longer tool

life. On environmental and ecological aspect, cryogenic assisted machining is one of the best solutions. Meanwhile, the negative impact to human body like respiratory diseases is minimized [32–34].

1.3.3. Cooling methods in cryogenic assisted machining

LN₂ and CO₂ are the two most frequent very low temperature cooling methods used in machining operations. The use of these two liquified gases as cutting fluid should be considered separately because of their mechanisms of refrigeration. CO₂ is stored in medium pressure tanks (approx. 57 bar) as liquid, the phase transformation from liquid to mixture of gaseous and solid of this substance occurs when the pressure drops. Temperature can reaches -78.5°C due to phase transformation and to the Joule-Thomson effect [16]. Nitrogen is stored in insulated tanks because at ambient pressure it is solidified at -210°C and boiled at -196°C [35]. It is an omnipresent (78% of the air that we breathe), colorless, odorless, nontoxic and inert gas. The production of this gas is by fractional distillation [36] and the cost of production is low [29]. These characteristics make LN₂ a suitable choice for very low temperature cooling. Nevertheless, the needs of thermal insulation of delivery system, longer ready-to-start time and unstable phase makes it weaker than CO₂ [16].

The main objective of both LN₂ and CO₂ in metal cutting is to dissipate the heat generated by this process. A big part of the energy consumed during metal cutting is transformed into heat in the cutting zone [37]. This is critical in machining refractory alloys like Titanium alloys and Nickel based alloys due to their low thermal conductivity, which leads to a very high temperature in cutting zone [38–40]. It is also important to mention that titanium is pyrophoric, so aggressive cutting conditions may cause fire during cutting. Cryogenic assisted machining provides the solution for the problem.

Jerold and Kumar [1] reported that both LN₂ and CO₂ resulted in lower cutting temperature compared to conventional flood MWF, but LN₂ (reduction of 47%) is more effective in reducing the temperature than CO₂ (reduction of 36%). Pahlitzsch [41] reported that LN₂ and CO₂ resulted 240% and 150% longer tool life compared to dry machining, respectively. Klocke et al. [42] reported that in turning Ti6Al4V titanium alloys, the use of LN₂ and CO₂ significantly improves the tool life compared to conventional flood MWF, especially the LN₂ increases the tool life five times. LN₂ can extend the tool life in machining of titanium alloys at higher cutting speeds [23, 43–48].

Numerous scientific publications about cryogenic assisted machining are available and they are increasing due to the strong practical benefits for this technology. *Figure 5* shows an increase of the number of publications on this topic over last 20 years.

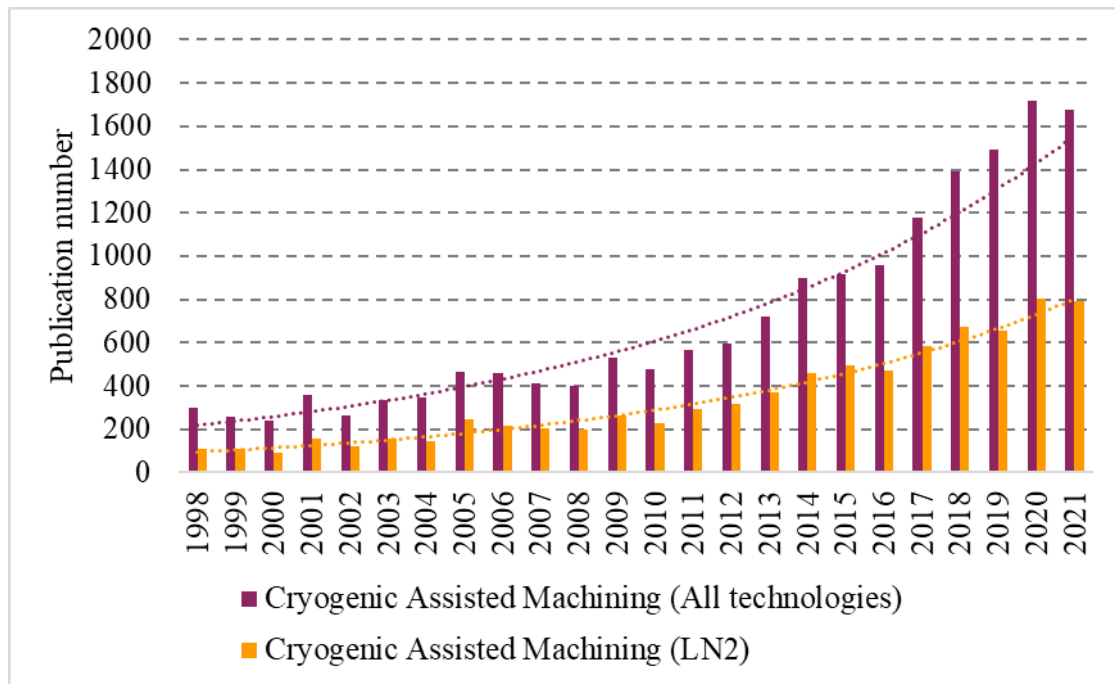


Figure 5. Publication number of cryogenic assisted machining (source from www.sciencedirect.com, updated until 7/11/2021)

Comparing with CO₂, the results of liquid nitrogen are more significant and more satisfied [1, 28, 49].

1.4. Ti6Al4V titanium alloy

1.4.1. Types of titanium alloys, properties and applications

The titanium -based alloys have excellent mechanical properties (high strength/weight ratio) until 600°C, meanwhile, it is still efficient at cryogenic temperature [50]. Comparing to nickel-based alloys, titanium alloys are two times less dense (at 25°C, Ti6Al4V and Inconel 718) and have a lower toughness. Comparing to stainless steel, it has higher corrosion resistance, especially for pitting corrosion, acid corrosion and stress corrosion. Between 300°C and 500°C, the strength of titanium alloys is ten times higher than aluminum alloys [51].

Ti6Al4V alloys are nowadays the mainly used titanium alloy worldwide, because of its high strength/weight ratio, elevated fatigue strength, intermediate fracture toughness and corrosion

resistance. This type of alloy is employed in plenty fields, such as aerospace, automobile, dentistry and other biomedical application. Specifically in aerospace industry, the main application of this type of alloy is the jet engine. About one third of the weight of the jet engine is from titanium [52], the fan blades of jet engine are made from it. *Figure 6* and *Figure 7* illustrate the cross-section of a commercial jet engine and the weight percentage of some frequently used alloys and CFRP (Carbon Fiber Reinforced Polymer) composite on large commercial aircraft.

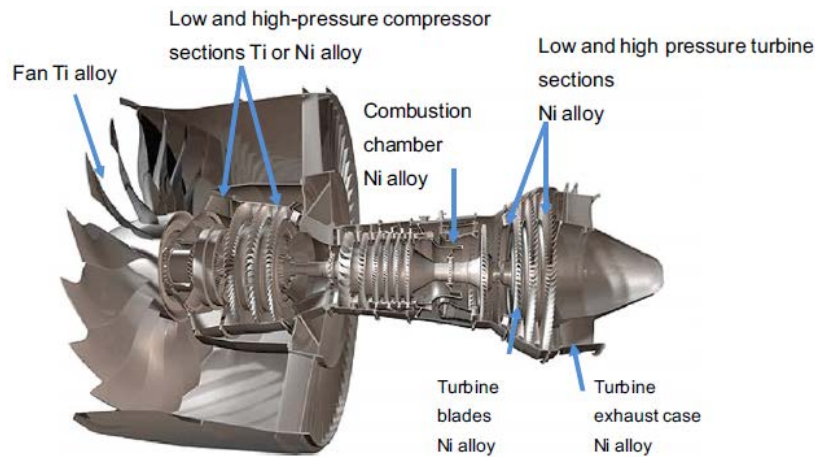


Figure 6. Cross section of a jet engine [53]

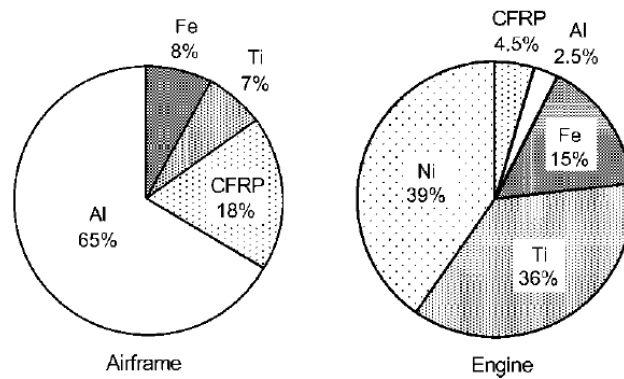


Figure 7. Structural weight percentage of modern commercial aircraft and gas turbine engine, including aluminium, titanium, steel alloys and CFRP (Carbon Fiber Reinforced Polymer) [52]

It exists two crystallographic structures of titanium [54], the illustrations are presented in *Figure 8*. The HCP (Hexagonal Close-Packed) is called phase α , the BCC (Body-Centered Cubic) is called phase β . At ambient temperature, the only phase of pure titanium is α , for temperature higher than 883°C , it transforms into β , this temperature is called transus β (T_{β}).

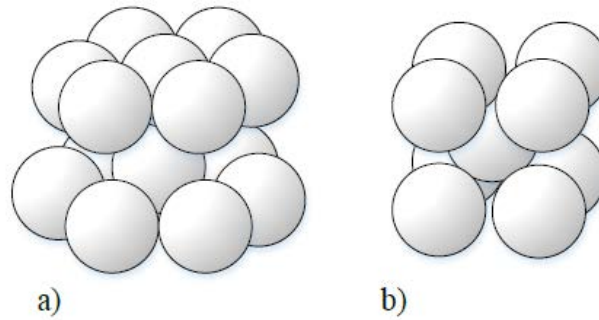


Figure 8. Crystalline structure of titanium: a) HCP and b) BCC [55]

Titanium alloys can be classified into 3 classes, depending on the proportion of phases:

- The α alloy only constituted with α phase
- The β alloy only constituted with β phase
- The $\alpha+\beta$ alloy which can be classified again into 3 subclasses (according to the proportion of β phase equilibrium):
 - Quasi α : portion of β phase $< 5\%$
 - $\alpha+\beta$: portion of α phase is between 5% to 20%
 - Quasi β : few α phase

The additional elements influence the equilibrium diagram. *Figure 9* illustrates some characteristics and properties of titanium alloys in function of their microstructure.

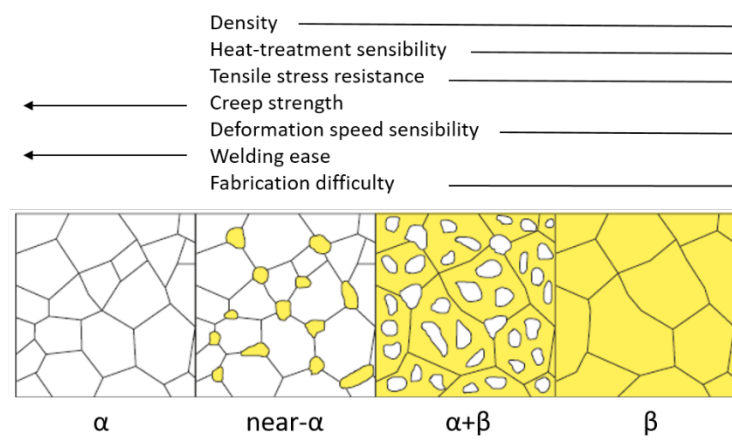


Figure 9. Titanium phases and properties [56]

The cooling kinetics plays an important role on properties of titanium alloys except the chemical composition. For example, the $\alpha+\beta$ alloy is obtained by a quick cooling, thus exhibiting a thin needle structure. In contrast, the kinetic induced increasing diameter of the needles then transform into slats [57]. The presentation of these transformations is illustrated in *Figure 10*.

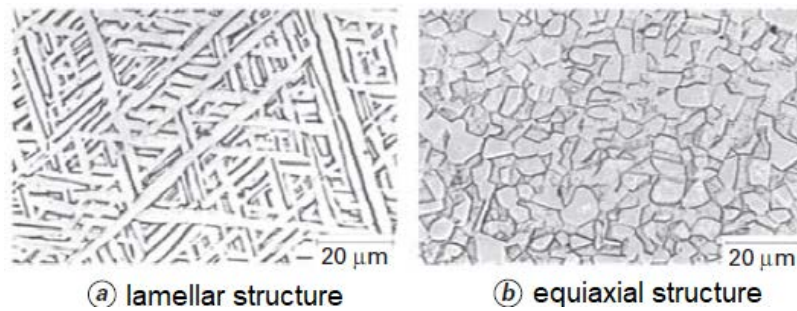


Figure 10. Crystallographic structure of Ti6Al4V : a) lamellar structure and b) equiaxial structure [50]

The titanium alloys have some very interesting thermo-mechanical properties comparing to other engineering metals, such as low density, low elastic modulus, low thermal conductivity, high corrosion resistance, and good mechanical properties until 600°C.

The most frequently used titanium alloy in worldwide market is Ti6Al4V, which represents 50% values of titanium alloys, especially in aerospace sector (about 80%).

Table 2 listed the main mechanical properties of this alloy.

Table 2. Mechanical properties of Ti6Al4V [58]

Properties	Values
Density, ρ (kg/m ³)	4430
Young modulus, E (GPa)	113.8
Poisson coefficient, ν	0.342
Tensile strength, σ (MPa)	950
Elongation to break, A (%)	14%
Thermal conductivity, λ (W·m ⁻¹ ·C ⁻¹)	6.7
Heat capacity, C_p (J·kg ⁻¹ ·C ⁻¹)	526.3
Thermal expansion coefficient at 20, 250, 500°C (10 ⁻⁶ ·°C ⁻¹)	8.6, 9.2, 9.7
Rupture toughness, K_{Ic} (MPa·m ^{1/2})	75
Melting temperature, T_m (°C)	1660
β transus temperature, T_β (°C)	980

The properties of Ti6Al4V at low temperature is also worth to study. Figure 11 illustrates some mechanical properties of Ti6Al4V at low temperature. The observation from these figures are as follows:

- Elasticity modulus remains almost constant
- Rupture dilatation increases with temperature
- Fracture energy remains almost constant
- Fatigue limit decreases with temperature
- Yield and rupture strengths decrease as the temperature increases

Hong et al. [59] also showed the increase of tensile strength and elastic limit when the temperature decreases.

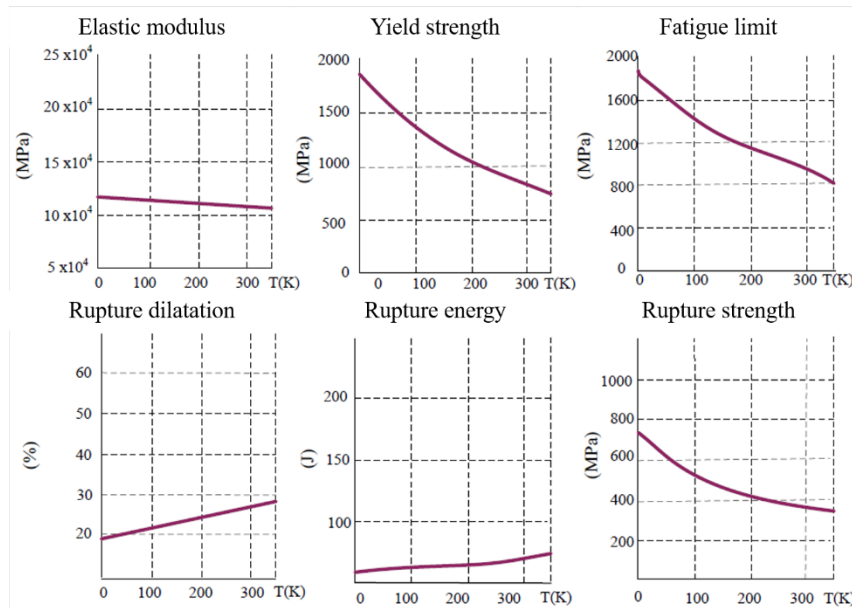


Figure 11. Mechanical properties of Ti6Al4V at low temperature [60]

1.4.2. Machinability

Several standards evaluate the machinability of a material, including cutting tool life, metal removal rate and surface integrity of final product. Titanium alloys are considered as difficult to machine material, due to their mechanical and physical properties. The main problems associated to titanium alloys during machining are the following:

- High sensitivity to strain and strain rate, generating high forces.
- Low thermal conductivity, causing very high local temperatures at tool-chip interface.
- High chemical affinity with cutting tool, causing rapid tool wear.
- Low elastic modulus, leading to spring back after deformation.
- Tool vibrations caused by combination of previous properties.

The low density and high mechanical resistance make them excellent for many applications, but also make them difficult-to-cut. Besides, the low thermal conductivity of titanium alloys (only 10 to 20% of the steels) leads just a minor part of generated heat during machining evacuated by chips [61]. In fact, the heat generated in machining of Ti6Al4V is 20 to 30% superior compared to a common steel (thermal conductivity of 6.7 W/m · K for Ti6Al4V and 50.2 W/m · K for a low alloyed steel at 293 K)[62]. As a consequence, the cutting parameters should be substantially reduced when compared to those used to cut the steel, thus longer operation time and lower productivity [37].

1.4.3. Surface integrity

As the reason of the wide application of titanium alloys, the demand of high-quality products induces continuous study of the surface integrity. According to Field and Kahles [63], surface integrity is the inherent or enhanced condition of a surface produced in machining or other surface generation operation. It includes : i) the topological state (surface roughness and defects); ii) the metallurgical state (microstructure, phase transformation and grain size, shape); iii) the mechanical state (residual stress and hardness) [51]. The reliability of machined titanium alloys is required to be maintained but due to its poor machinability, it can be damaged during machining.

Cryogenic assisted machining can help to improve the surface integrity of machined part in titanium alloys. Agrawal et al. [64] compared the surface roughness of Ti6Al4V under dry, wet and cryogenic environment. They found that R_a reduced up to 71% and 64% with cryogenic assisted machining. Other researchers also found the same improvement in surface integrity with cryogenic assisted machining. Shokrani et al. [65] compared the influence among dry, flood and cryogenic assisted machining with varying cutting speed, feed rate and cutting depth, the results revealed that the cryogenic assisted machining leads to lower surface roughness in any cutting conditions. Ayed et al. [24] measured the surface residual stress of final workpiece, the workpiece machined under dry condition does not exceed -200 MPa while the one machined under high pressure reaches -433 MPa. Bordin et al. [23] found that cryogenic assisted machining helps to decrease the surface roughness at severe cutting condition when the cutting speed is 80 m/min and the feed rate is 0.2 mm/rev, cryogenic assisted machining provides better surface integrity than dry and wet cutting conditions.

1.5. Tribology and tool wear

1.5.1. Contact conditions in metal cutting

The contact between the tool and the chip/workpiece strongly affects tool life and the surface integrity. This contact strongly depends on several factors (contact conditions), including: sliding speed, contact pressure, temperature, lubrication/cooling, etc. The friction coefficient is often used to model this contact by correlating the shear stress with the normal stress at the interface. This coefficient should be determined experimentally through special designed tribological tests able to reproduce the contact conditions observed in metal cutting [66]. This is essential for accurate simulation of the metal cutting process.

Unfortunately, classical methods for determining the friction coefficient between two instances are not suitable for metal cutting process. The standard pin-on-disc tribometer uses a pin to rub repeatedly over a rotating disc to obtain the friction coefficient and the worn volume. However, the pins rub over the same surface of the disc at lower speed and pressure when compared to metal cutting process [67]. Two main approaches to investigate the tribological phenomena (including the determination of the friction coefficient) at tool-chip interface can be found in the literature. One is using the cutting process itself [68–70]. The limits of these methods based on cutting tests can only provide a trend, they are not able to provide quantitative results usable in a finite element cutting model [71]. The second is based on special designed tribometers able to reproduce the contact conditions in metal cutting [72–74]. As mentioned by Rech et al. [66] such tribometers are able to reproduce the pressure, temperature and velocity between the tool and the chip in metal cutting, thus contributing for a better understanding of the tribological phenomena in this process.

1.5.2. Friction coefficient

Friction coefficient is described by *Equation 4*:

$$\mu_{app} = \frac{F_t}{F_n} \quad \text{Equation 4}$$

where μ_{app} is the ‘apparent friction coefficient’, F_t is tangential force and F_n is the normal force in N.

The term ‘apparent friction coefficient’ used here differs from ‘interfacial friction coefficient’ that includes the adhesion at the pin-work material interface. The macroscopic forces include the adhesive phenomena affected by properties such as hardness, chemical reactivity and asperities, non-negligible severe plastic deformation caused by contact conditions [66]. Challen and Oxley [75] propose a simple decomposition for the ‘apparent friction coefficient’ in *Equation 5* :

$$\mu_{app} = \mu_{loc} + \mu_{plast} \quad \text{Equation 5}$$

where μ_{loc} and μ_{plast} are the local adhesive and macroscopic parts, respectively.

The apparent friction coefficient is strongly correlated to the sliding speed and the contact pressure. A lot of researchers reveal that the friction coefficient drops when increasing the sliding speed. Rech et al. [66] conducted tribological tests on various work materials with TiN coated carbide tool, the friction coefficient drops significantly with increasing sliding speeds. Other researchers found the similar results [67, 71, 76, 77]. Besides, the contact pressure between pin and workpiece is also a crucial parameter that infects the tribological condition thus the friction coefficient. Meier et al. [78] tested the friction coefficient using different normal forces between 5 N and 400 N, under dry and flood conditions. With the lower load, the friction coefficient shows increasing trends when the sliding velocity increases. However, with the higher load, the friction coefficient decreases when the sliding speed increases.

Several studies of friction behavior on several metal and non-metal materials at low temperatures in gaseous, liquid nitrogen and ambient air conditions show that the friction coefficient is lowest in liquid nitrogen, followed by gaseous nitrogen and ambient air. It is also revealed that for some metal based materials, like aluminum-, brass-lead pairs and self-mating niobium, the reduction of the friction coefficient and wear rate is significant [79]. Gradt et al. [80] found that the friction coefficient and wear rate reduced significantly in cryogenic environment than in ambient environment for polymer materials. In contrary, a modeling of cryogenic frictional behavior of titanium alloys [81] concludes that the friction coefficient for

Ti6Al4V at high level of load and speed is higher under cryogenic conditions than under dry air condition.

1.5.3. Tool wear in metal cutting

Tool wear is a geometrical change of the cutting tool that is caused by the metal cutting process. Tool failure is due to at least one of the following reasons [82]:

- Gradual wear caused by the interaction between workpiece and the cutting tool.
- Mechanical fracture due to the exposing of cutting edge to high thermomechanical loading or periodic transient thermal and mechanical loading (chatter)
- Plastic deformation of the tool, which changes the geometrical form of the cutting edge

Tool wear is due to several wear mechanism according to their physical based phenomena.

These wear mechanisms can be classified as:

- Abrasive wear
- Diffusion wear
- Adhesion wear
- Fatigue wear

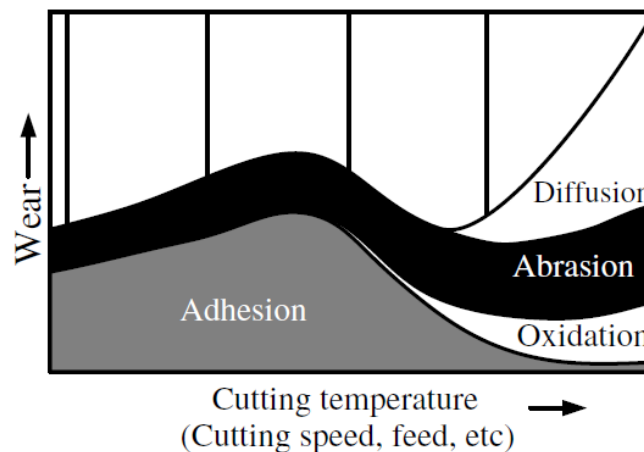


Figure 12. Wear mechanisms [83]

Wear mechanisms change with the temperature as shown in *Figure 12*. *Figure 13* shows different types of tool wear. The abrasive wear mechanism occurs when hard particles slide over the tool faces (rake and clearance face) and plough the surfaces of cutting tools. Generally, these particles are harder than the workpiece and cutting tool materials.

Abrasive wear mechanism is normally the cause of flank and notch wear, but also may be the reason of crater wear [84].

The diffusion wear mechanism is a thermo-chemical process that depends on cutting temperature and chemical stability of tool material. The description of this mechanism is an atomic interchange with two-ways transfer, which can be atoms from the tool diffusion into the flow of material or vice versa. The development of this wear mechanism is determined by chemical properties, such as the affinity of the tool material to the work material. Meanwhile, the wear process accelerates with the cutting speeds due to the increase of the temperature [85]. The typical tool wear generated by this mechanism is the crater wear.

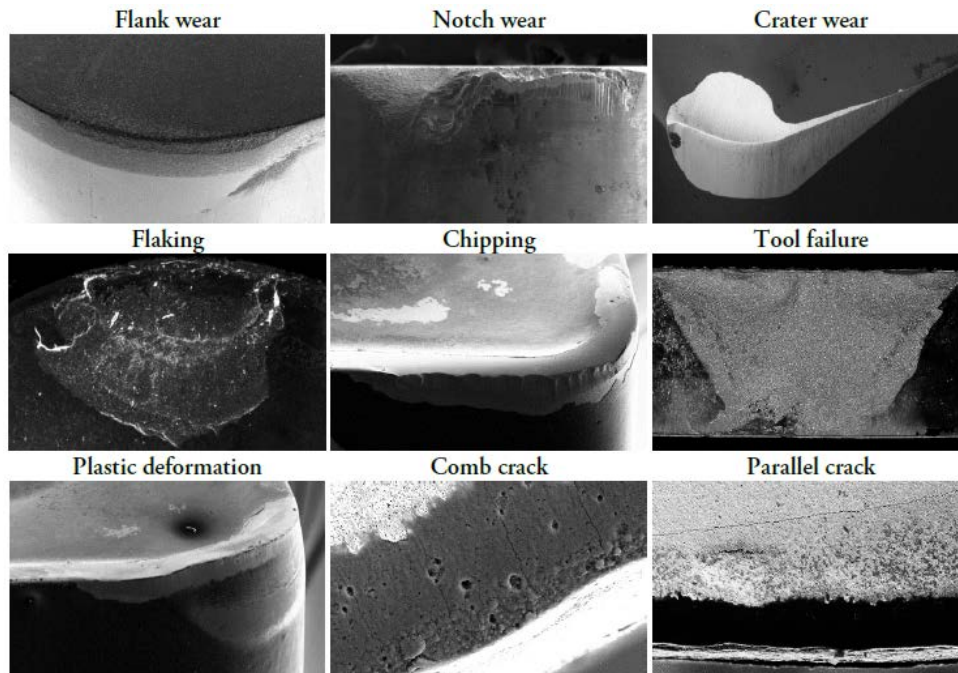


Figure 13. Different types of tool wear [86]

The adhesion wear mechanism is determined by the temperature and affinity between workpiece and tool material. This happens when two asperities are in contact. The local pressure at certain contacted points could be higher than yield strength of the softer material. Low temperature (or low cutting speed) and relatively good affinity lead to BUE (built-up edge), this means a part of the chip being welded and hardened on the rake face. This phenomenon changes the geometry of cutting edge and may deteriorates surface finishing. Since the BUE is a periodical phenomenon (appearance and disappearance), the cutting edge or coating can be taken away with the BUE.

The fatigue wear mechanism occurs when cracks are formed and propagated in the tool when applying cyclic loading, including temperature, forces and stress on the cutting edge. The combination of severe cutting conditions and strong mechanical properties of the workpiece,

the cutting edge suffers constant high thermal and mechanical loadings, causing its plastic deformation.

As foregoing mentioned, the main wear mechanism in machining titanium alloys are abrasive and adhesion wear. The heat generated during machining of titanium alloys are significant, thus a higher thermal loading is applied to the cutting tool, generating one or both wear mechanisms.

Tool life depends on several factors, including tool material (substrate and coating), tool geometry, work material, cutting regime parameters (cutting speed, feed, depth of cut), and MWF. The most well-known equation to estimate tool life is the Taylor's equation [87], which only takes into account the cutting speed, as shown in *Equation 6*.

$$V_c T^n = C \quad \text{Equation 6}$$

where V_c is the cutting speed in m/min, T is the tool life in min, n is an exponent depending on work material, tool material, tool geometry and cutting fluid, C is a constant indicating v for T equals to one of a straight log-log line, depending on feed, depth of cut and the physical quantities of n.

1.6. Tool material

Tool material includes both substrate and coating. This section is focused on the substrate material, by providing significant information from the literature to select the suitable substrate material and microstructure for the cryogenic machining Ti6Al4V alloy.

The selection of substrate of tool material was based on an extensive literature review. Compared to carbides tools, ceramic tools are generally inert, but highly reactive with titanium alloys [88]. Due to extreme chemical reactivity of titanium, it is hard to find an inert tool material that could be totally stable. An analysis by Auger spectroscopy showed that when machining of titanium alloys with diamond or cemented carbide, the titanium from the chip reacts chemically with the carbon of the tool to form a titanium carbide interlayer [89]. Moreover, ceramic tools exhibit inadequate fracture toughness for thermal shock [90]. Thus, the suitable substrate of tool material should be tungsten carbides, as it is now the most common and economical cutting tool material in the market. An ideal cutting tool should provide good wear resistance, high strength and toughness, good resistance to thermal shock and adequate chemical stability at elevated temperature [91].

Dearnley et al. [92] showed that the most suitable grade of tungsten carbide for machining titanium alloys is so called 'straight grade', which means a cobalt content of 6 wt.% and a WC grain size of 0.8-1.4 μm . Higher cobalt content promotes plastic deformation while lower cobalt content increases notch wear formation. Finer grain size (0.8 μm) offers increased hardness hence higher resistance to plastic deformation. Other researchers suggest similar results in their studies [93–96].

The selection of suitable tool material for cryogenic assisted machining was investigated by several researchers. Zhao et al. [97] tested the performance of several cutting tool materials under cryogenic environment. The hardness tests show 60% increase of cutting tools under cryogenic temperature (-120°C) comparing to ambient temperature. The tungsten carbide tools exhibit 15% increasing resilience and 25% better transversal rupture resistance. Another study conducted by Shokrani [34] demonstrates the improvement of mechanical performance of tungsten carbides at cryogenic temperature, 40% increase of hardness is observed for the cutting tool. Besides, Lattemann [98] demonstrates that a modified cobalt content near the surface (200 μm) improves the wear resistance of cutting tool. Wang [99] revealed a linear relation between the thermal expansion of WC-Co material and its cobalt content as follows: higher cobalt levels lead to larger expansion. Furthermore, lower cobalt and coarser WC grain size lead to higher thermal conductivity. In fact, lower thermal conductivity of interface originates the lower thermal conductivity of smaller grain size.

For the foregoing reasons, a 'straight grade' tungsten carbide, grain size of 0.8 μm and cobalt content of 7 wt.% was selected for this study.

1.7. Hard coatings

In addition to verify the feasibility of cryogenic assistance in turning of titanium alloy, the second objective of this work was to verify the efficiency of hard coatings on cutting tools under cryogenic assisted machining. Then, below is described the PVD (Physical Vapor Deposition) method commonly used to realize hard coatings, especially magnetron sputtering technique, the process used during this research work. Then, a State of the Art of hard coatings (mono and multilayers) commonly employed as protective layers on cutting tools under MWF or other lubricant is detailed. Finally, the type of hard coatings proposed to improve the service life of cutting tools during cryogenic assisted machining is justified.

1.7.1. Coatings deposition

1.7.1.1. PVD (Physical Vapor Deposition)

PVD covers broad range of vacuum deposition process. The employed material is physically removed from a target by evaporation or sputtering. Generally, the atoms, ions or molecules of target materials are vaporized by high-temperature vacuum or gaseous plasma. Then they are transported by the energy of vapor particles and condensed on the substrate as a film. For deposition of chemical compounds, either using a similar target source or introducing reactive gases (nitrogen, oxygen, ammonia, etc.) are common methods. The PVD processes are known by their acronyms or various phrases, named with their physical vapor source, e.g. diode or triode sputtering, planar or cylindrical magnetron sputtering, direct current (DC) or radio frequency (RF) power supplies, electron beam evaporation, activated reactive evaporation and ARC evaporation (DC or alternate current (AC)) [100]. The main categories of PVD process can be classified into vacuum deposition (evaporation), sputter deposition, arc vapor deposition and ion plating, as depicted in *Figure 14*.

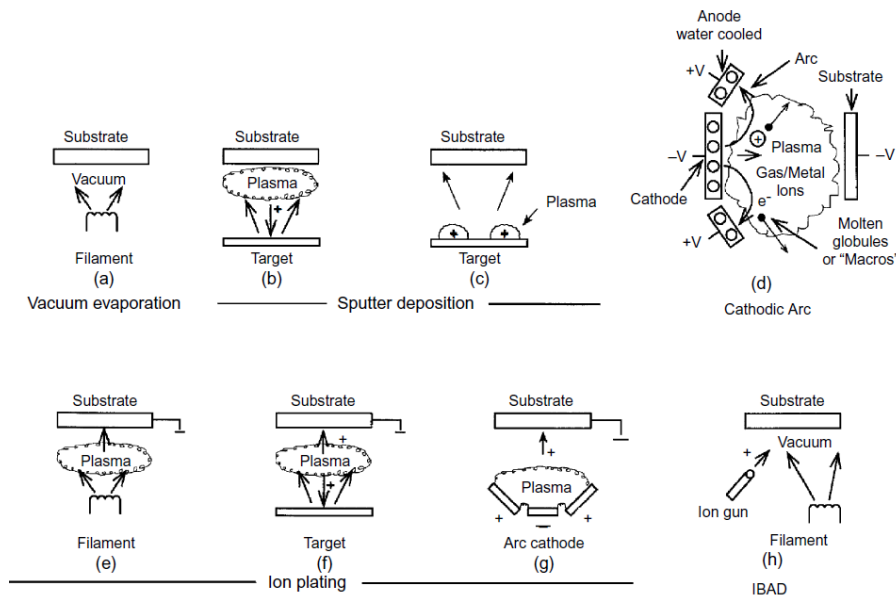


Figure 14. PVD processing techniques: a) vacuum evaporation, b) and c) sputter deposition in plasma environment, d) sputter deposition in a vacuum, e) Ion plating in a plasma with a thermal evaporation source, f) Ion plating with a sputtering source, g) Ion plating [101]

It is noteworthy that CVD (Chemical Vapor Deposition) is another major process to obtain coatings. It is a heat-activated process, the basic is the reaction of gaseous chemical compounds with suitably heated and prepared substrates. Most of the reactions is conducted in an anhydrous

and anaerobic environment and sub-atmospheric pressure. The typical deposition temperature intervals are from 800 to 1200°C.

CVD coatings were commercialized in the 1960s while PVD coatings came 20 years later. Now both PVD and CVD coatings share the market of coated cutting tools. PVD coatings are able to be conducted in low temperature, lying from 250-550°C, which permits the deposition of coatings on HSS (high speed steel) or thermal treated low alloy steel. Moreover, the PVD technique allows the control of coating thickness on cutting edge to avoid the sharp change of cutting tools, which makes it suitable for semi-finish and finish machining operation. The high intrinsic hardness and compressive stresses provides by PVD process inhibit the crack growth on substrate. It hardly reacts with substrate, while CVD coatings may occasionally produce brittle carbides at interfaces [100]. *Figure 15* presents the coating deposition technologies according to pressure and temperature requirement.

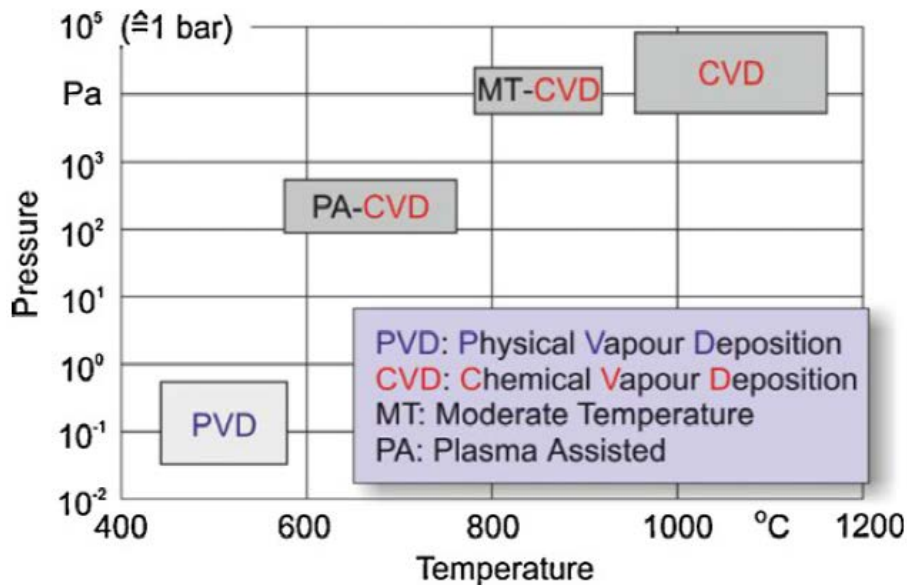


Figure 15. Coating deposition technologies for cutting tools [102]

1.7.1.2. Magnetron sputtering

In basic sputtering process, a target plate is bombarded by energetic ions generated in a glow discharge plasma in front of the target. The bombardment process causes the etching (sputtering) of the target atoms then condensate a thin film on a substrate [103]. Alongside with the ion bombardment, secondary electrons are also emitted from the target surface, which helps to maintain the plasma. Although this technique has been used for many years and was

successful to product many coatings, it has some limitation such as low deposition rate for certain materials, low ionization efficiencies and high substrate heating effects.

Magnetron sputtering has developed rapidly over the last three decades, it became one of the most chosen methods for the deposition of a wide range of coatings in industry [104]. Power supplies like direct current, pulsed direct current or radio frequency are used to produce large-scale and high-quality films [105, 106]. A large number of materials can be sputtered such as metals, alloys, polymers or ceramic. Magnetron sputtering has a lot of advantages, such as reasonable deposition rate, good reproducibility, reliable adhesion on substrate, controllable composition and homogeneity of film on large substrate and it is an environmental-friendly method [101]. This technology also has the ability to synthesize materials out of thermodynamic equilibrium. As a result, a wide range of applications can be achieved, like wear-resistant coatings, low friction coatings, corrosion-resistant coatings, decorative coatings and coatings with specific optical or electrical properties [104].

The main modification of magnetron sputtering to conventional sputtering process is an additional magnetic field parallel to the surface. This helps to keep secondary electron close to the target. One pole is at the central axis of target and another is a ring magnet around the near edge of the target. The magnetron field traps the electrons near the surface of the target thus it increases the probability of an ionizing electron-atom collision. Then it results in a dense plasma near the target and finally a stronger ion bombardment of the target. Higher sputtering rate and higher deposition rate are available with this technology in comparison to classical ones. The increased ionization also allows the discharge maintained at lower working pressures (typically 0.1 Pa compared to 1 Pa) and lower working voltages (typically -500 V compared to -2 to -3 kV) [104].

Figure 16 illustrates the principle of cathodic magnetron sputtering. A pumping group (primary and secondary pumps) permits to reach a residual pressure of around 10^{-4} Pa. Low residual pressure is preferred in reason of maintaining high ion energies, providing enough mean free path to prevent atom-gas collision and reducing gaseous contamination for final coatings. An inert gas (normally Ar) is introduced into the chamber to initiate the plasma with a differential potential field between the target and the wall of the chamber. The working pressure is generally between 0.1 to 10 Pa. The ionized Ar^+ are attracted by the cathode (target) and etch its surface. The energy received by the atom is expressed by momentum equation (*Equation 7*) [107]:

$$E_c^f = E_p^i \frac{4M_p M_c \cos^2 \theta}{(M_p + M_c)^2} \quad \text{Equation 7}$$

where M_p is the mass of projectile particle in uma, its initial kinetic energy is E_p^i in eV; M_c is the mass of atoms from target in uma, its initial kinetic energy is $E_c^f = 0$ in eV. It is clear when $\theta = 0$ and $M_p = M_c$ that the transferred energy reaches the maximum value.

The secondary electrons emission is constrained by the magnetron field to help the ionization. A denser plasma is formed near the target surface region to result in a higher sputtering rate. Some inconvenient of the magnetron sputtering also exist, e.g. the heterogeneous attrition of the target in form of the magnetron field, heating problem caused by strong bombardment [108].

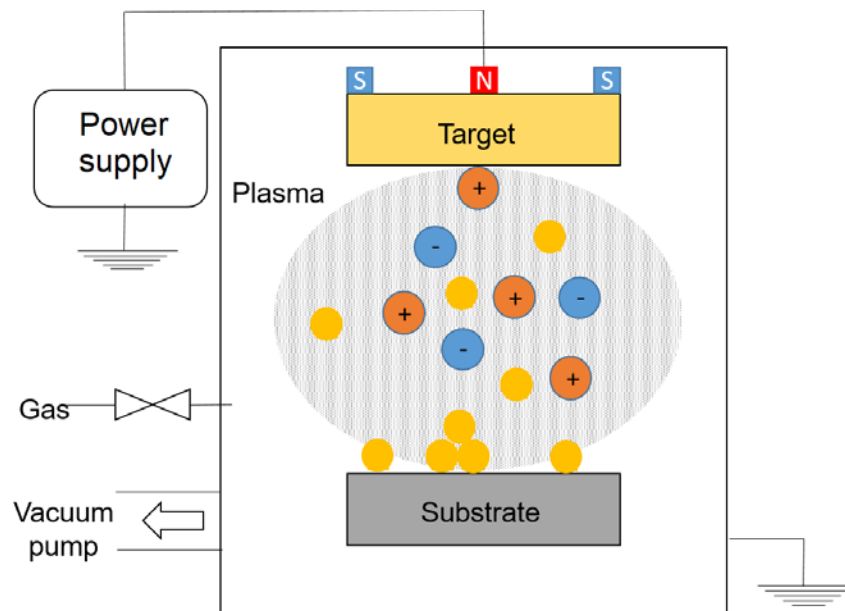


Figure 16. Schematic diagram of a cathodic magnetron sputtering

1.7.1.3. Hard coatings for cutting tools

The progression of human society needs production and consummation of many kinds of materials, such as iron, alloys and carbon fibers. In parallel with the widely use of steam powered machine in 19th century, the needs of large quantities of precise dimension and high-quality components result in the invention of long-last cutting tools, which accelerate the machining process. At the end of the 19th century, high-speed steel (HSS) was invented. Then in early 20th century, Dr. Schroter invented cemented carbide [109], which is much harder than high-speed steel. This kind of cutting tool merchandised quickly after coming out. Then the

cutting tool materials go through an increasing period of development, tungsten carbide in the 1930's, alloyed carbide in the 1940's, ceramic and synthetic diamond in the 1950's and coated carbide in the 1970's [82]. *Figure 17* shows the world market share of cutting tool materials, the PVD coatings has a continuous increase trend on the total percentage.

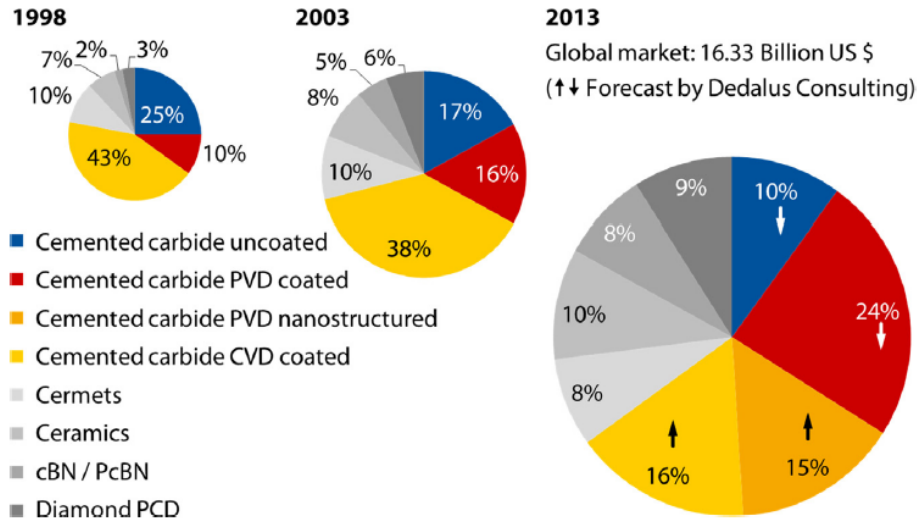


Figure 17. World market of hard and super-hard cutting materials [9]

Regarding the massive use of cutting tools in industry and its importance to productivity, the tool life becomes a major factor to choose a proper cutting tool. Tool life is a function of different parameters, e.g. coatings, geometry and cutting conditions (cutting parameters, lubricant, workpiece material). The tool life depends also on different wear mechanisms. That is why the aim of coatings is to overcome tool wear and to extend tool life as long as possible. The requirement of coatings is focused on protection against abrasion and adhesion from very beginning of the machining process. Then it shifts to the attention of the coating's performance at elevated temperature. Indeed, the coatings should have enough strength in high temperature environment, both mechanical and thermal loads are crucial [110].

Nowadays, we can find different types of commercial coatings such as monolayers (metallic, binary, ternary, quaternary, etc.) or multilayers (Me/MeN, Me/MeC, Me/MeCN or even Me/MeN/MeMe'N, Me/MeC/Me'C etc with Me = metal and Me' = another metal) [111–118]. Besides, we can find some nanocomposites such as nc-CrN/a-SiN_x, nc-TiC/a-C and nc-TiN/aSi₃N₄, etc. [119–121] or superlattices such as CrN/AlN, TiN/VN, TiN/NbN [122–125].

Generally, the performance of the multilayers, nanocomposites and superlattices coatings are better than the monolayer components. Barshilia et al. [126] studied the multilayers coating CrN/CrAlN comparing with CrN and CrAlN monolayers. The hardness of the multilayer

reaches 31 GPa while the hardness of the monolayers is 23 GPa and 28 GPa, respectively. The multilayers coating also retains hardness of 22.5 GPa after heat treatment up to 600°C. Cheng et al. [127] obtained high hardness and elastic modulus of TiSiN nanocomposite coating, until 51 GPa and 449 GPa, respectively. The oxidation resistance of TiSiN nanocomposite coating studied by Kacsich et al. [128] revealed that the coating decreases the oxidation speed at very high temperature (1000°C). Moreover Park et al. [125] showed that AlN/CrN superlattices coating has more promising hardness (40 GPa) than single AlN and CrN monolayer coatings, around 16 GPa and 26 GPa, respectively. Yang et Zhao [129] found that the tribological behavior of superlattices coating TiN/CrN is much better than the monolayers, COF of the superlattices coating is between 0.75 to 0.95, while the COF of TiN is between 1 to 1.2.

As we can see, there are numerous types and combinations of systems. That is why in the following part the discussion is focused on specific monolayers and multilayers in relation to this research work.

1.7.1.4. Monolayers

A monolayer coating is a single homogeneous and continuous layer. As foregoing mentioned, it may be constituted with a single element, for example pure metals, or with synthesized ceramic, for examples nitride, carbide, oxide layers. Regarding the application history of monolayer coatings on the cutting tools market, the first CVD coating on cutting tool proposed in the market was TiC in 1969 [130], followed by TiCN, TiN and Al₂O₃ [131, 132]. TiN was the first PVD coating used in industry in 1980 [133], then TiAlN was developed 9 years later [134]. *Figure 18* presents the developing procedure of monolayer coatings for cutting tools.

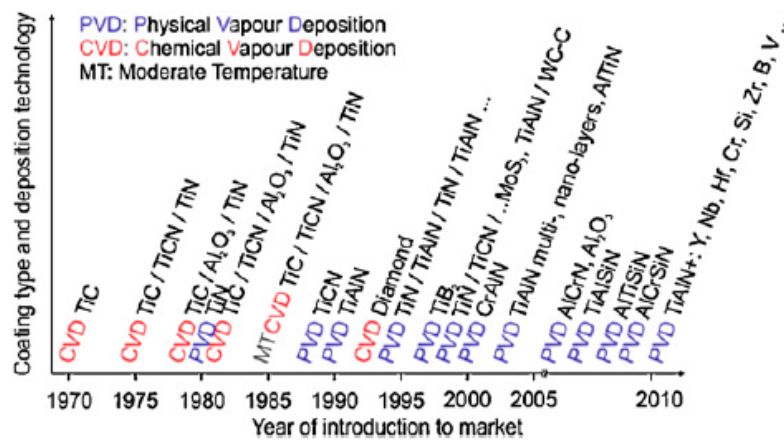


Figure 18. Evolution of monolayer coating materials and related deposition technologies for cutting tools

It is known that TiN is the most commonly used coating on cutting tool since it has been introduced in the market. Molarius et al. [135] made a study of the performance of NbN, ZrN, TiN and TiAlN coatings deposited on HSS, in dry turning of AISI 4140 steel. Although the best coating is ZrN, but TiN still improves the cutting performance. Aihua et al. [136] compared the friction and wear properties of TiN, TiAlN, AlTiN and CrAlN coatings deposited on cemented carbide substrates against SiC ball. The results showed that the TiN and TiAlN coatings present lower COF and lower wear rate than the two others. Cselle et al. [137] summarized the TiN coating performance on many machining applications, such as drilling, tapping, milling, reaming, etc. as follows: it gives reliable high performance for many applications and workpiece materials, the gold color makes it easy to control tool wear, the price of this coating is acceptable.

Since the coming out of TiN coating, various new coating materials based on it were created, like TiAlN, TiZrN, TiAlVN. In particular, TiAlN attracted a lot of attention because of its improvement of hardness, chemical stability and low friction coefficient [138–140]. Despite the improvement of Al content added into TiN system, some researchers revealed that there is no evident benefits in severe metal cutting conditions as it cannot reduce heat flux transmission in cutting tools. Kusiak et al. [141] studied the coatings influence on the heat transfer in the cutting tool during machining, the tests investigated several coatings such as Al₂O₃, TiN, TiAlN and TiAlN-based multilayers, as well as the uncoated tool. The results indicate a slight heat flux diminution by Al₂O₃ coating whereas the others do not modify it significantly. Rech [142] made a research on the tribological characterization of cutting tools coatings for steels in high-speed dry turning. TiAlN seems to lead to a higher temperature at the tool-chip interface and to higher heat fluxes transmitted to the insert, which weakens its resistance.

TiAlN is also the first hard coating applied on cutting tools for machining under cryogenic assistance. A review shows that a majority of studies on cryogenic milling used coated tungsten carbides [143]. Shokrani et al. [65] used TiAlN coated tools for the milling of Ti6Al4V. Sadik et al. [25] reported that no contribution of TiAlN coating was found on tool life in milling Ti6Al4V.

Nevertheless, TiN-based coatings present some limitation: a lower corrosion resistance or poor thermal properties than some alternative coatings such as CrN layers for example. Indeed, Rech et al. [144] investigated the tribological and thermal functions of various cutting tools coated by TiAlN, TiN and TiAlN+MoS₂. The results show that these coatings do not have a significant

influence on heat transmission on substrate. CrN is also a very interesting layer because it is hard, it presents a good adhesion [145], a lower COF [146–148] and a better corrosion resistance [149, 150] in comparison to TiN.

That is why CrN is a very known layer developed and modified for more than 20 years at the LABOMAP. Numerous and rich research work have been done concerning this outstanding coating. Nouveau [112] studied the CrN binary system with its cubic and hexagonal structure and tested the coating during wood machining. According to her results, CrN coating is more wear resistant than the CrN+Cr₂N coatings and presents stronger adhesion than Cr₂N. The wood machining tests also revealed that the CrN coating has the best performance. Benlatreche [151] studied the CrAlN and CrVN ternary system also for wood machining. The additional Al content increases the nitride ratio in CrN system and improves the stoichiometry of CrN. Meanwhile, the CrAlN coating presents good mechanical properties like a hardness of 36 GPa and an elastic modulus of 520 GPa. The natural slight compressive residual stress and good adhesion on WC-Co tool were also obtained. The wood machining test also showed a slight improvement with the ternary coatings compared to the binary coatings. Rahil [152] studied the physico-chemical and tribological behavior of CrN, MoN and CrMoN coatings, as well as their applications in wood machining. The ternary system has the highest density, the best adhesion, the highest hardness, the smallest wear rate and the best thermal stability after annealing between 600 and 700°C under vacuum. The wood machining test demonstrated the effectiveness of this ternary coating. Besides Zairi [153] studied the addition of Si into the CrN system. She showed a significant improvement of the mechanical and tribological properties. Indeed, the hardness and the elastic modulus of CrN are 12 GPa and 198 GPa, respectively, while the CrSiN ones are 27 GPa and 345 GPa. The COF of CrN is 0.65 and the COF of CrSiN is 0.2. Moreover Aissani [154] studied the addition of Zr as a third element in the CrN system. The new ternary system exhibits improved mechanical and tribological properties, regarding hardness, elastic modulus and COF. More recently Aouadi [111] studied the effect of Al content added into CrN binary system and developed a new generation of ultra-hard multilayers coating system. He determined the optimal deposition conditions for CrN and CrAlN monolayer coatings. It is noteworthy that a bright new multilayer structure with decreasing thickness of the CrN/CrAlN pairs was found extremely effective according to its various properties such as mechanical, tribological and anti-corrosion properties.

Previous studies realized in the LABOMAP showed the efficiency of a third element in the CrN system (CrVN, CrZrN, CrAlN, CrSiN etc) but it is also known that a multilayer architecture can lead to higher mechanical properties. This part is discussed in the following paragraph.

1.7.1.5. Multilayers

As mentioned above, multilayers such as hard/soft coatings are full of interest because of the advantages of combining both monolayers to obtain a final multilayer more effective than the monolayers alone.

Indeed, the improvement of multilayers instead of monolayers were reported frequently. Various kinds of multilayer coatings were studied. Barshilia et al. [126, 155] as previously mentioned worked on multilayers coating of CrN/CrAlN and TiN/NbN. They showed that TiN/NbN multilayers coating had a better corrosion resistance compared to monolayer coatings. Another main result is the decrease of the corrosion resistance with the total number of interfaces in the multilayers coating. Warcholinski et al. [156] studied tribological properties of CrCN/CrN multilayers coating. The hardness and adhesion (L_{C2} critical load) of this multilayers coating is 25 GPa and 120 N, respectively. Comparing to CrN monolayer coating, it has a relatively low COF, a lower wear rate, higher critical load and hardness. Okumiya [157] compared the CrN/CrAlN, TiN/CrAlN and their monolayer coatings after tribological test: CrN/CrAlN multilayers coating showed the most promising results among all tested coatings.

Some research works focus on the influence of the bilayer period (λ) in multilayers coating on their mechanical and tribological performance. Kim et al. [158] varied the thickness of CrN/CrAlN bilayer from 4.4 to 44.1 nm. The highest hardness and resistance to plastic deformation were obtained with a bilayer thickness of 5.5 nm. Moreover Yousaf et al. [118] varied the thickness of TiAlN/MoN bilayer from 21 to 124 nm. The highest hardness and elastic modulus are obtained with the thickness of 25 nm. These results reveal that a critical period (λ_c) for the multilayers coating exists, regarding the repetition of bilayers.

Besides these previous results, a new generation of ultra-hard multilayers coating was developed in LABOMAP by Aouadi [111]. He showed that CrN/CrAlN multilayers have some very good mechanical properties. With the increasing of bilayer periods, the grain size of coatings decreases; the hardness of the multilayers coating reaches 43 GPa, the elastic modulus is up to 417 GPa; the adhesion of multilayers coating is excellent with a L_{C2} critical load up to 97 N.

According to these results and regarding the functionality of the layers to develop in this study, the objective is to enhance the performance of the cutting tools for cryogenic assisted machining by improving the chemical/mechanical/physical properties. Outstanding mechanical, tribological and thermal properties should be the main characterization of this coating. Especially for the thermal property, as the developed coating will be employed under extreme thermal shock (high temperature in tool-chip/workpiece interface and low temperature in surrounding environment), the coating should present:

- high thermal stability
- relatively stable mechanical and tribological properties encountering extreme cutting conditions
- low thermal expansion coefficient
- low chemical reactivity.

As foregoing mentioned, heat generated during cutting titanium alloys will be transferred to the substrate and then weaken the cutting tool, the coating should have a good ability to reduce the heat flux at tool-chip interface. Although researchers tested numerous traditional coatings in turning of steel and the results showed no significant reduction of the heat flux, but they also pointed out that the temperature on tools could be influenced by different materials, especially when the thermal properties between coating and substrate are very different [141]. Further, another study showed that the coatings allow an important reduction of the heat flux transmitted into the cutting tools [144]. That is why a new generation of protective coatings for reducing the heat generated during machining process is urged and good thermal properties (e.g. low thermal conductivity) is needed. The ideal situation would be that the cryogenic coolant attenuates the heat flow without damaging the cutting tool.

Based on the scientific results from the researchers and the results from LABOMAP, as well as the needs on current application, it was decided to study the Cr/CrN/AlCrN multilayers system. First, almost all the commercial coatings or laboratory coatings realized has an underlayer to insure the adhesion of the upper layer(s). Generally, the underlayer is made of the metallic compound of the binary (MeN, with Me=metal) or ternary (MeMe'N with Me=metal≠Me') layer. An appropriate adhesive underlayer permits the immobilization of the WC carbides in reacting with high energy ions of the film material during their deposition on the substrate [159–161]. The effectiveness of underlayer coatings to improve the adhesion and tool life is also guaranteed by the roughness of the cemented carbide substrates and the thickness of underlayer

[162]. Beliardouh et al. [163] demonstrated the tribological and anti-corrosion abilities of Cr/CrN/CrAlN compared to CrN/CrAlN without the Cr underlayer. Hong et al. [164] worked on the effects of Cr underlayer for CrAlSiN coating. As a result, the adhesion of Cr/CrAlSiN layer is improved of 20 N (critical load). The wear resistance is also greatly enhanced in spite of the decreased microhardness when introducing the Cr underlayer. The thickness influence of the Cr underlayer is also mentioned. Second, AlCrN monolayer coating replaces the CrAlN monolayer coating in the Cr/CrN/CrAlN multilayers coating studied by Aouadi [111]. Indeed, AlCrN was studied by many researchers and it showed better mechanical properties and thermal stability than CrAlN. As previously explained, the developed coating aims to reduce the heat flux to protect the cutting tool.

Consequently, it should have a very low thermal conductivity. Many commercial coatings and Ti6Al4V workpiece are compared according to their hardness, elastic modulus and thermal conductivity (*Table 3*). Among the investigated coatings, only NbN, TiAlN and AlCrN provide lower thermal conductivity than Ti6Al4V titanium alloy. Moreover, only AlCrN exhibits decreasing thermal conductivity tendency when temperature increases [165] (*Figure 19*).

Table 3. Tool materials' properties at room temperature [165]

Coating	Thermal conductivity (W/m.K)	Hardness (HV)	Elastic modulus (GPa)	Melting point (°C)
TiC	21	2855-3570	410-510	3067
TiN	19.2	1835-2140	251	2950
TiAlN	11 (estimated)	4000	370	2930
AlTiN	4.5	4500	510-560	-
AlCrN	4	2000-4000	500-640	-
Al₂O₃	25.08	3000	344.83-408.99	2034
Ti₃Al	6 (estimated)	700-800	182	1600
NbN	3.76	1356-2400	493	2400
CBN	300-600	3048-4397	650	3000
WC	40	2400	534	2870
Ti6Al4V	6.7	350	113.8	1600-1660

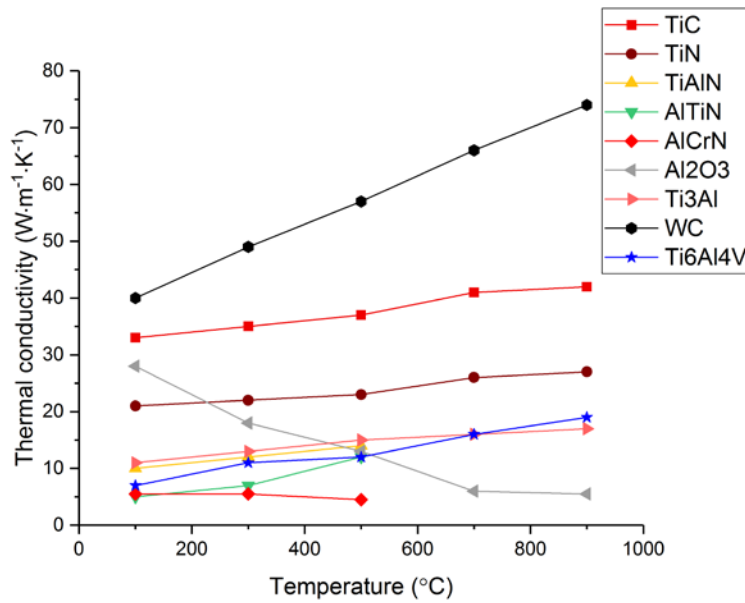


Figure 19. Thermal conductivity of different cutting tool materials as a function of the temperature [165]

In fact, the aluminum content added into CrN binary system should be well controlled. Hasegawa et al. [166] made numerous coatings of $\text{Cr}_{1-x}\text{Al}_x\text{N}$ ($0 \leq x \leq 1.0$). The study concludes that the $\text{Cr}_{1-x}\text{Al}_x\text{N}$ coating changed its structure from cubic at $x = 0.6$ to hexagonal at $x = 0.7$, the lattice parameter changed from 0.416 nm at $x = 0$ to 0.413 nm at $x = 1$, the maximum hardness was 27 GPa when $x = 0.6$. Lin et al. [167] studied the variation of x from 0 to 0.68. They observed similar results to the previous study: the highest value of hardness and elastic modulus are 36 GPa and 370 GPa respectively when $x = 0.585$. When x exceeds 0.64, the ternary coating changes its crystal structure from B1 cubic to B4 hexagonal phase. The tribological tests revealed that the wear resistance increased gradually with the Al content until $x = 0.585$. Plenty of research works prove the above results [168–172]. Regarding of the thermal stability, Kawate et al. [173] compared the oxidation behavior of three $\text{Cr}_{1-x}\text{Al}_x\text{N}$ coatings, at $x = 0.4, 0.6$ and 0.7 , respectively. It is shown that higher Al content improves the oxidation resistance of $\text{Cr}_{1-x}\text{Al}_x\text{N}$. He et al. [174] also studied the thermal stability and oxidation resistance of $\text{Cr}_{1-x}\text{Al}_x\text{N}$ when $x = 0, 0.52$ and 0.68 , respectively. The conclusion is that additional Al content delays the N-loss during annealing, it has a significant improvement on the oxidation resistance. These results are also justified by others [168, 175–177].

1.7.2. Conclusion

As a conclusion, the Cr/CrN/AlCrN multilayers system on cutting tools during turning of Ti alloy will be studied. In the following chapters the optimization of the Cr, CrN and AlCrN

monolayers is presented. Then the influence of the multilayer architecture on their properties is shown. The optimal mono and multilayers were applied on carbide pins for tribological tests to determine the best CrN-based system to be tested on carbide tools under traditional MWF (flood) and cryogenic assisted machining.

1.8. Résumé du Chapitre 1

Ce chapitre présente l'état de l'art sur le procédé de coupe des métaux, l'usinage cryogénique, l'alliage de titane Ti6Al4V, la tribologie, l'usure des outils, les matériaux d'outils en général, et en particulier les avancées récentes dans les revêtements durs de protection des outils de coupe (monocouches, systèmes multicouches).

Ainsi, l'usinage des métaux et plus particulièrement le procédé de tournage sont décrits en détails. Les fluides de coupe tels que les huiles entières ou non ont été abordées puisque l'objectif de cette étude est de les remplacer. En effet, les problèmes liés à ces lubrifiants (sur l'environnement mais aussi sur la santé) sont connus. C'est pourquoi l'objectif à moyen termes est de les remplacer par des lubrifiants tels que l'azote ou le CO₂ liquide. Ainsi, l'historique de la cryogénie et de son apport comparé aux lubrifiants utilisés actuellement en industrie a été fait suivi par un état de l'art, depuis la fin des années 90, de l'assistance cryogénique en usinage. S'en suit un rappel sur la matière usinée : l'alliage de titane Ti6Al4V et de son usinabilité qui demande d'avoir des outils très résistants notamment à l'abrasion. De ce fait, l'usure des outils de coupe et les bases de la tribologie ont été abordées (conditions de contact, COF, usure des outils etc). Un rappel a également été fait sur le matériau de l'outil lui-même (ie. Le carbure de tungstène et ses propriétés). Enfin, il est connu que les revêtements durs sont une solution pour assurer une bonne résistance à l'abrasion aux outils de coupe et ainsi une durée de service maximale. Un état de l'art sur les procédés de dépôts sous vide et plus particulièrement la pulvérisation magnétron a donc été fait, suivi par un historique des revêtements appliqués sur des outils de coupe depuis la fin des années 60, que ce soit des revêtements mono ou multicouches. Enfin, sont abordés les travaux de recherche qui ont impliqués des revêtements sur des outils de coupe lors d'usinage cryogénique. Finalement, l'expérience du LABOMAP en revêtements durs couplée à l'état de l'art réalisé ont permis de proposer les revêtements à étudier à savoir, des revêtements multicouches de type Cr/CrN/AlCrN.

Chapter 2. Experimental methods

2.1. Introduction

This chapter presents all the experimental devices and the characterization methods that were utilized during this research work. The first part concerns the coating deposition technique and their characterization methods. The second part concerns the assembly of tribological test system, tool wear test system and their analysis methods.

2.2. PVD deposition system

2.2.1. General view of PVD system

The PVD magnetron system is presented in *Figure 20*. It is designed and commissioned as an industrial deposition machine in LABOMAP in order to realize PVD coatings under vacuum environment on big and complex geometries of substrates. The machine is composed of a power-supply coupled with an automate and of a semi industrial chamber.

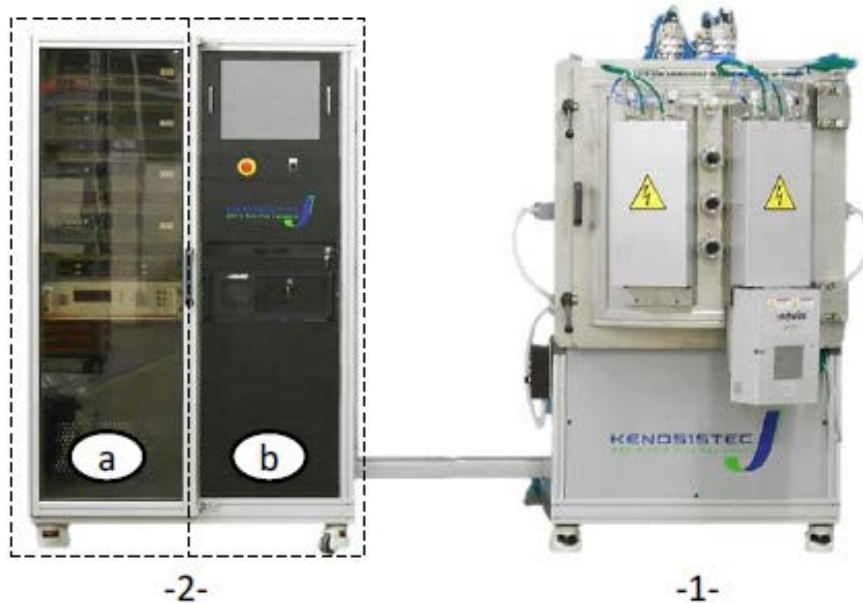


Figure 20. Deposition system of KENOSISTEC-KS40V-113K12, 1) chamber, 2-a) power supply and 2-b) automate [178]

Figure 21 illustrates the scheme of the operative part (chamber). It presents the constitution of the chamber with the accessories such as pumps, pressure gauges, valves, gas line etc. The semi-cylindrical chamber measures 730 mm of diameter, 780 mm of height and about 340 liters of volume. Two pumps equip this machine: the primary mechanical scroll pump (SCROLLVAC, Oerlikon Vacuum-SC60D) and a turbo-molecular pump (TURBUVAC MAG integra). The pumping speed of the primary pump is 20 l/s, while the pumping speed of turbo-

molecular pump is 1700 l/s. This pump system permits to reach a high vacuum until 10^{-7} mbar (10^{-5} Pa).

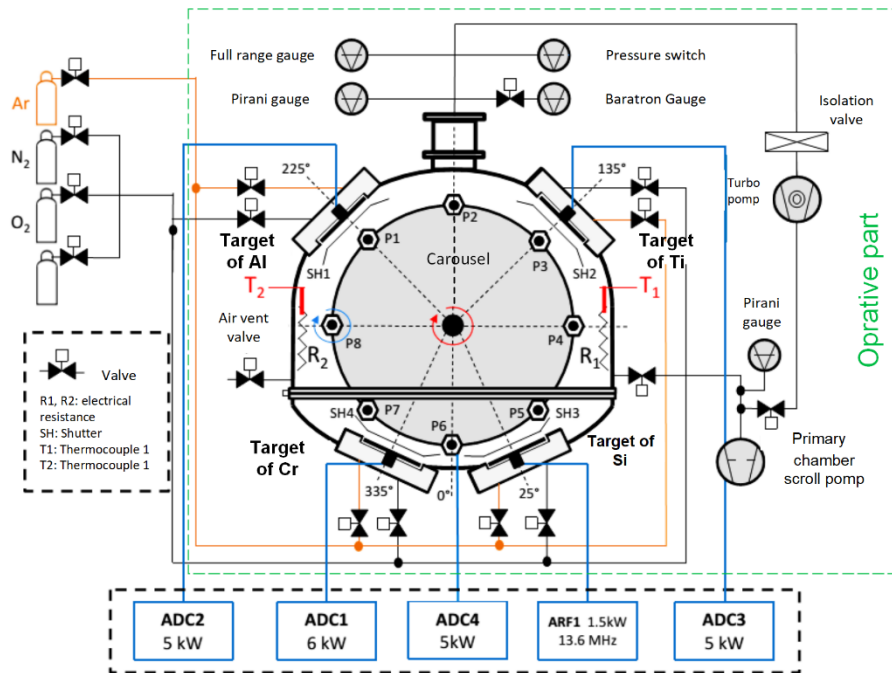


Figure 21. Operating system diagram of KENOSISTEC-KS40V-113K12 [178]

Four rectangular flat magnetron cathodes are located in 4 sides of the deposition chamber, at relative angle of 25° , 135° , 225° and 335° . The deposition mode could be radio frequency (RF), direct current (DC) or pulsed DC. The standard metal target dimensions are $16'' \times 5''$ with a thickness of 6.35 mm. The distance between the target and the rotating substrate holder is 120 mm. The substrate holder is a planetary double rotating carousel. The carousel is constituted with one main central vertical axis and others are vertical axis satellites around the main central vertical axis. The carousel is also linked with a power supply ADC4 to clean and/or to provide a bias voltage on substrates. A 3D scheme (Figure 22) illustrates the substrate holders and the targets.

Two electrical resistances are equipped near the wall of the chamber to heat until 400°C , they are controlled by the thermocouples (T_1 and T_2) with a servo system.

The power supply is constituted of an ADC1 (DC-6000W) generator, an ADC2 and an ADC3 (DC-5000W) generators. The command system is a computer-controlled software. The all operative part and power supply part can be controlled with this software, all the data during deposition (pressure, applied power, voltage, current, time, gas flow, temperature, rotating speed of carousel, etc.) are saved each 8 seconds.

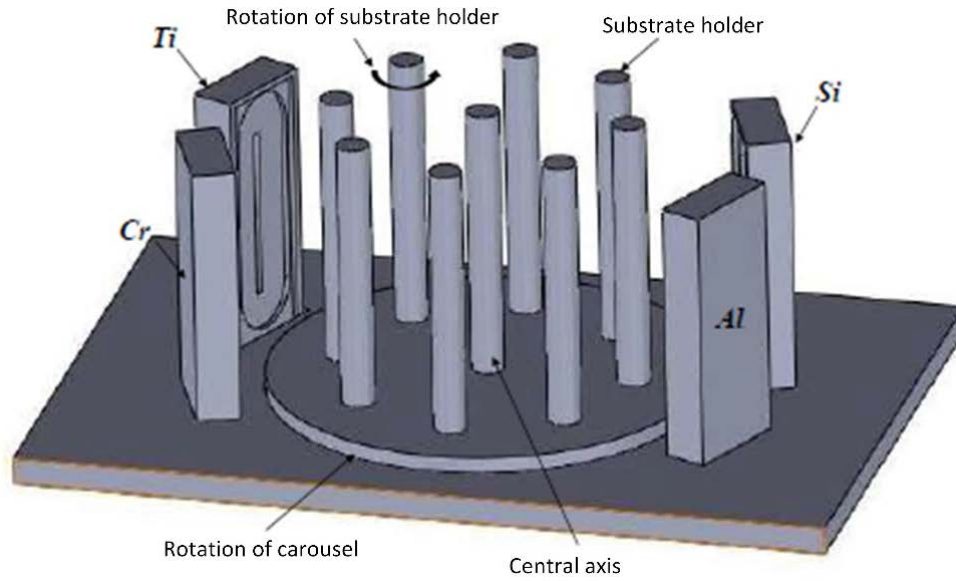


Figure 22. Planetary carousel system and targets [111]

2.2.2. Substrates and targets

2.2.2.1. Substrates materials

Silicon (100) and WC-Co specimens are used as substrates. Their dimensions and geometry are listed in *Table 4*.

Table 4. Geometry and dimension of substrates

Material	Geometry	Dimensions (mm ³)	Applications
Si (100)		15×15×0.4	Thickness, surface morphology, cross-section images/microstructure, residual stress, hardness, elastic modulus
WC-Co		15×15×5	Chemical composition, surface morphology, structure, XPS, hardness, elastic modulus, adhesion, tribological behavior, thermal properties

The geometry and dimension of substrates for calculating the residual stress was determined by Ardigo et al. [179]. They demonstrated that the deformation of substrate is influenced by the

shape of specimen. The silicon specimens were cut with a diamond stylus on disc. The WC substrates dimensions are adapted to the characterizations like nanoindentation, scratch-test and rotative tribometer. The arithmetic mean roughness R_a of WC substrate is 0.19 μm , the one for mirror-polished is 6 nm (used for some scratch tests and nanoindentation). It is noteworthy that the chemical composition of the WC substrates is the same as the pins used in tribological tests on CNC machine (see Chapter 4).

2.2.2.2. Substrates cleaning

There are two steps to clean the substrates. The first is a chemical cleaning (*ex-situ*): the specimens go through an acetone ($\text{C}_3\text{H}_6\text{O}$, 99.5 %, $d = 58.08 \text{ g/mol}$) bath (10 min) then in an ethanol ($\text{C}_2\text{H}_6\text{O}$, 95%) bath (10 min). This process removes the organic contaminations such as the resin, the grease, the hydrocarbons, etc.

The second step is an ionic cleaning (*in-situ*), also called ‘etching’. During this process the substrates are etched by argon ions to remove the oxide layers. The momentum transported by the argon ions strips the undesired layers or particles absorbed at the surface of substrates. The ionic cleaning conditions are listed in *Table 5*.

Table 5. Etching condition for the substrates

Gas	Pressure ($\times 10^{-3}$ mbar)	Flow rate (sccm)	Substrate bias voltage (V)	Time (min)
Argon	7	150	-700	5

2.2.2.3. Targets cleaning

Etching is also applied to clean the targets. The process cleans the contaminated layer coming from previous depositions under reactive gas like nitrogen, oxygen, etc. as well as the oxidation during opening of the chamber. The cleaning conditions of the targets are listed in *Table 6*.

Table 6. Etching condition for the targets

Target	Gas	Flow rate (sccm)	Pressure (10^{-3} mbar)	Target bias voltage (V)	Power (W)	Time (min)
Cr	Argon	100	5	-340	500	10
Al		100		-340	500	10

2.3. Coating Characterizations

In this section, we present the characterization techniques we used to determine the properties of the coatings. We detail the principle of each technique, the equipment and trademark/model used. More specifically, we will describe scanning electron microscopy, X-ray photoelectron spectroscopy, X-ray diffraction, optical profilometry, nanoindentation, scratch-test, rotative tribometry, stress determination and modulated photothermal radiometry.

2.3.1. Surface morphology: Scanning electron microscope

The scanning electron microscope (SEM) is a technique based on interaction between radiation and materials [180]. The specimens are placed in vacuum where the pressure is about 10^{-4} to 10^{-5} Pa. An electron beam scans this specimen and several types of signals will be issued, which related to several radiations (*Figure 23 a*), interaction is not only on the surface but like a volume of pear under the impact point (*Figure 23 b*), where the scanning length is about 500 nm to 1 μm depending on the electron beam energy. The emissions in a SEM are as follows:

- The secondary electrons are emitted very close to the specimen surface. An oscilloscope pipe modulates the electron beam to signal, it is synchronized with the incident beam. The image will be shown completely after a period of scanning. Images could reach high magnification and quality (about 10 to 100 000 times).
- The backscattered electrons are reflected out of the specimen interaction volume by elastic scattering interactions with specimen atoms. Their energy is related to the atomic density of the specimen. The image constituted could show the distribution of heavy atoms in specimen, since heavy atoms backscatter more strongly than light atoms, thus brighter pixels appear in the image.
- The X photons emitted from the atoms of the specimen are characteristic radiations. These photons present continuous spectrum and characteristic line spectrum, the last one could tell the identity of the elements from specimen. Thickness of the emission zone impacted by the electron beam is about 1 μm . The detection system produces a signal proportional to the photons X, then the signal amplified and digitalized will be treated in a multichannel analyzer [181].

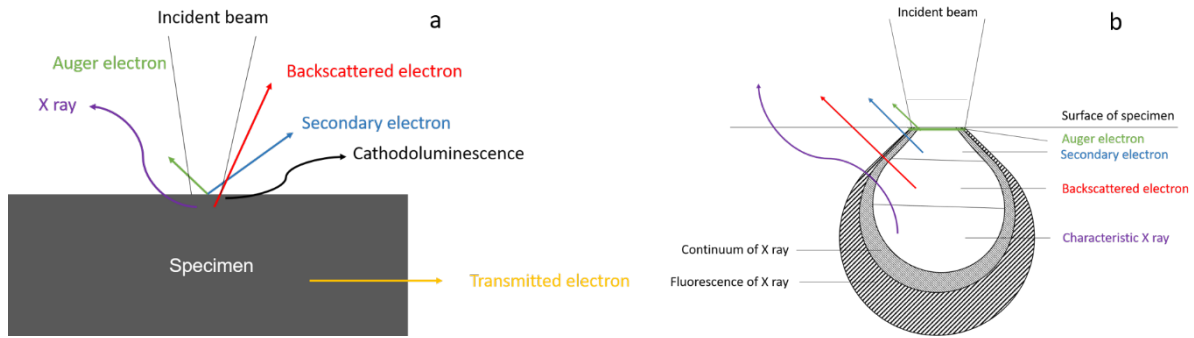


Figure 23. a) Interaction between radiation and material, b) Interaction zone between radiation and material [182]

In the current study, a high-resolution HRSEM (JEOL JSM 7610F) is used to observe the cross-section and surface morphology of the coatings. This SEM is equipped with an EDS microanalysis for qualitative and quantitative chemical analysis. The EDS is constituted with a diode that could receive the entire X-ray spectrum. A multichannel analyser classifies the occurrence number (quantitative information) of received energy (qualitative information) on each level, then it rebuilds the emission spectrum of specimen.

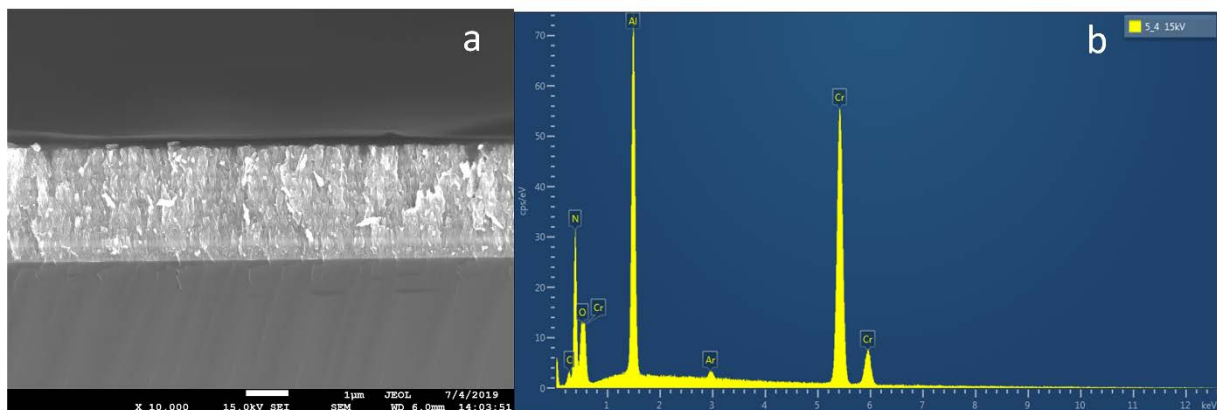


Figure 24. Example of: a) cross-section and b) EDS spectra of a CrN/CrAlN multilayer

This technique permits to obtain information on the surface morphology, the microstructure, the qualitative density, the chemical composition, the thickness and the architecture of multilayers. Figure 24 presents the obtained cross-section and EDS results from SEM of a developed multilayer.

2.3.2. Chemical composition: X-ray photoelectron spectroscopy

X-ray Photoelectron Spectroscopy (XPS) was developed in the 1960s by Siegbahn's group in Sweden [183, 184]. Its use became widespread for surface analysis. The technique is described as follows: when light irradiates the surface of a specimen, atoms of the sample will interact with the incident photons. Then the electrons may absorb enough energy to escape from the

atomic orbital, this energy is called binding energy of the electron. This energy is specific both to element and the atomic orbital where the electron comes from. Kinetic energy of emitted photoelectrons is evaluated by a spectrometer and the binding energy is determined by Equation 8 (equation of conservation of energy).

$$E_k = h\nu + E_B + \phi \quad \text{Equation 8}$$

where E_k is the kinetic energy of the photoelectrons in eV, h is Planck's constant (6.626×10^{-34} J·s), ν is the frequency of the X-ray in Hz, E_B is the binding energy in eV, ϕ is the work function term that depends on both spectrometer and material.

The emission process is illustrated in Figure 25. When energy of a photon is absorbed by an atom it causes the ejection of a photoelectron from an orbital (K for example). Next, the transition from an electron on external orbitals (L for example) to the vacant state causes the relaxation of the ion excited by the photoemission. The extra energy caused by this de-excitation release in a way of fluorescence (photon emission) or ejection of an Auger electron. This one is detected but not studied.

Characterizations of the chemical composition of the coatings were performed by XPS using an Al K α X-ray source at 1486.6 eV. Electron detection was provided by a hemispheric analyzer CLAM 4 MCD (Thermo VG Scientific). Photoelectrons were collected with an analyzer slit of 2 mm and a pass energy of 100 eV for survey spectra and of 20 eV for the spectral ranges corresponding to Cr2p, Al2p, N1s and O1s lines. Argon ion bombardments were carried out with an accelerating voltage of 500 eV during 2 min, following by 5 keV during 6 min. The etched depth is estimated to 32 nm.

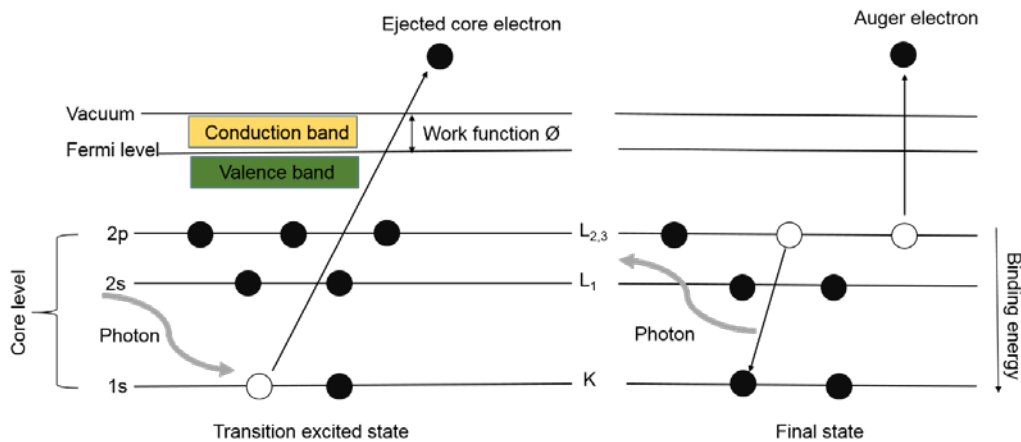


Figure 25. XPS emission process [112, 153]

This technique permits to obtain the bonding energy of the coatings and thus a more accurate chemical composition of the synthesized material in comparison to EDS microanalysis.

2.3.3. Structure :X-ray diffraction

The X-ray diffraction technique (XRD) is well known and widely used. It is a non-destructive method that permits to study the crystallography and structure of thin films. When X-ray beam irradiates the surface of a material, the crystalline plans of this material diffract the electromagnetic beam (*Figure 26*). The atoms in a lattice should be regular and well-ranged. To be detected, the incident angle should be in respect of certain angles, given by Bragg's law *Equation 9*.

$$2d_{hkl} \sin \theta = n\lambda \quad \text{Equation 9}$$

where d_{hkl} (\AA) is the interplanar distance separated by Miller index (h, k, l); θ ($^\circ$) is the incident angle; λ (\AA) is the wavelength of X-ray beam; n is an integer number, it equals to 1 generally. With the knowledge of the peaks position and intensity, one could determine the presence of the phase, the residual stress, the lattice parameter and the grain size.

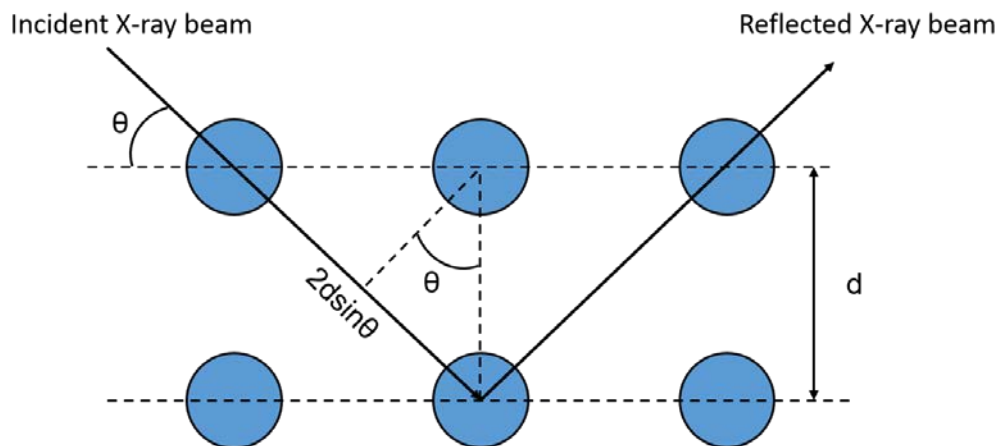


Figure 26. Principle of X-ray diffraction

The $\theta/2\theta$ Bragg-Brentano configuration is the most used configuration, which is presented in *Figure 27*. Normally, the configuration is less and less sensitive when the thickness of the film is very thin. This is because the X-ray penetrate more into the substrate rather than into the film.

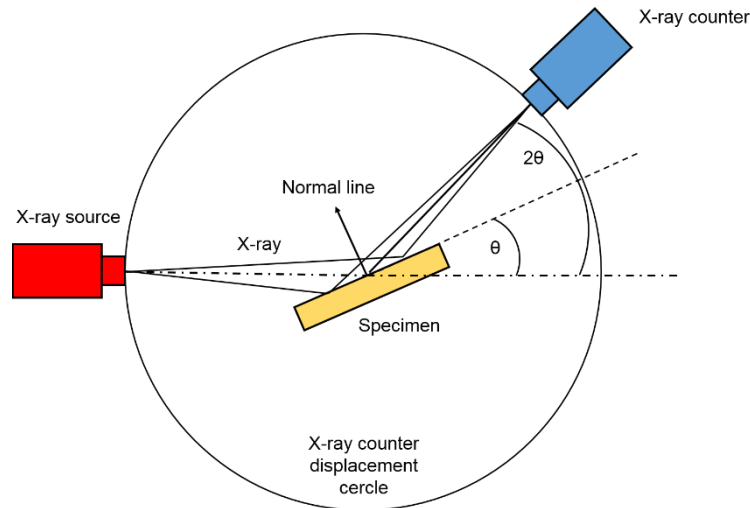


Figure 27. Bragg-Brentano configuration

The diffraction analysis was performed by a diffractometer (INEL XRG-3000) with a maximum power of 3000 W, monochromatic silicon plane, CPS 120 diffractometer with curved detector over 2 theta angular range of 120°, theoretical 2 theta resolution of 0.29°, K_{α} Co radiation source of 0.178897 nm. The voltage and current applied on the cobalt source are 24 kV and 24 mA, respectively. The incident angle is fixed at 5° for each measurement. The quality of the measurement carried out by this machine is sufficient to identify the crystalline phases and the preferred orientation of the grain. It should be pointed out that with this diffractometer, the accuracy should be taken into account because the height of the samples could not be fixed as it should. Also, the grain size is estimated by applying the Debye-Scherrer formula (Equation 10):

$$\tau = \frac{K\lambda}{\beta \cos \theta} \quad \text{Equation 10}$$

where τ is the mean size of the ordered crystalline domains in nm, it's equal or smaller to the grain size; K is a dimensionless shape factor, generally it equals to 0.94 but varies with the crystallite shape; λ is the X-ray wavelength in Å; β is the line broadening at FWHM (full width half the maximum intensity); θ (°) is the incident angle.

This technique permits to obtain the crystallography and structure of the thin films. The grain size was estimated with the Debye-Scherrer formula.

2.3.4. Residual stress: Optical profilometer

An optical profilometer (VEECO Wyko NT-1100) is available at LABOMAP. This apparatus permits to measure thickness and residual stress of the coatings on silicon substrate.

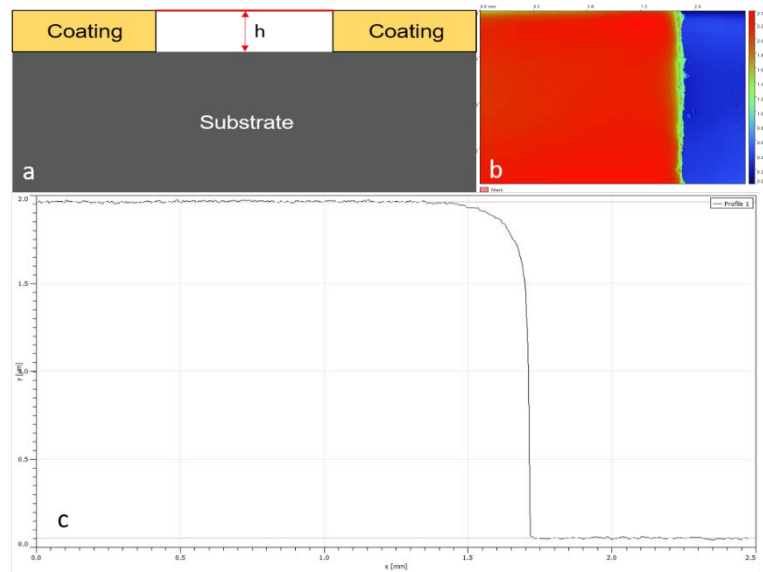


Figure 28. Method to determine the thickness of coatings on silicon substrate

The thickness could be determined by measuring the height differential between a deposition and a mask, as shown in *Figure 28*. Before deposition, an aluminum adhesive tape was stucked on a silicon substrate as a mask (*Figure 28 (a)*). This difference of height between coating and mask could be measured by the optical profilometer (*Figure 28 (b)*), then the different height of the coating and substrate could be exploited by a software such as Gwyddion (*Figure 28 (c)*). Residual stress exists on all the materials, not only for thin films. For example, a workpiece after welding presents locally some residual stress. In the case of thin film, the residual stress is sometimes on prominent place, concerning the integrity of the whole microstructures.

Generally, the residual stress could be divided into 3 groups [185]. First group includes the macroscopic residual stress. Second group includes the residual stress on scales of grains, the different constitution of grains, their orientation and their size are issued of the residual stress. Third group includes the microscopic residual stress that may be due to the presence of the interstitial elements, the gap or other defects within the crystallites.

For massive materials, the most used methods for measuring the residual stress are X-ray diffraction (XRD) or hole-drilling technique. For thin films, one can use grazing angle diffraction or interferometry (curvature method). This last technique was used in our research work.

In the case of thin films, there are three types of residual stress:

- Thermal residual stress
- Intrinsic residual stress
- Structural residual stress (which are negligible in our case)

The thermal residual stress could be expressed by different dilatation coefficients between each material. This residual stress could be created from the deformation of the different elements in cooling procedure. This type of residual stress is in first group because it affects the structure by a global manner. The intrinsic residual stress is formed during the preparation of the thin films, during their growth. It is divided into the three types of stresses. It's difficult to separate the origin of the intrinsic residual stress from the others, but it is known that it could come from defect, gap, contamination, diffusion of oxygen into the layer causing expanded volume, different size of the atoms, dislocation of interface in the monocrystalline etc.

The simplest way to measure residual stress is to measure the deflection of specimen as illustrated in *Figure 29*.

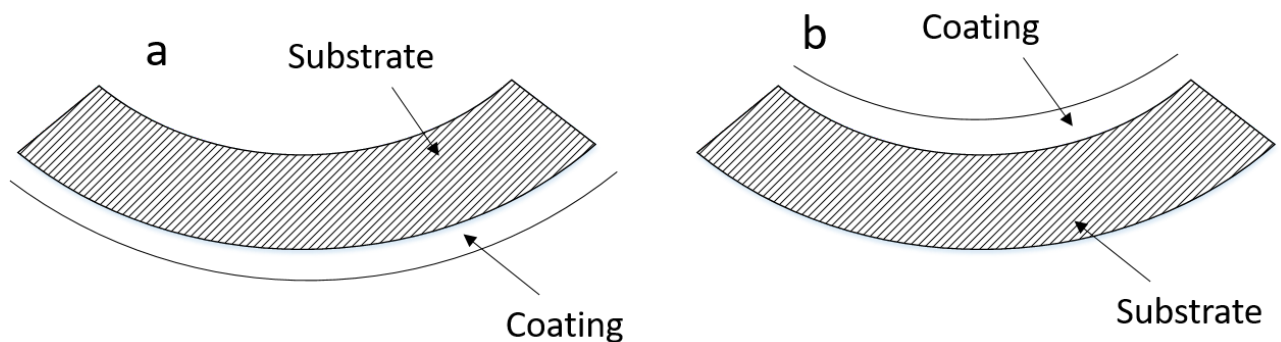


Figure 29. Deformation of coating-substrate: a) compressive residual stress and b) tensile residual stress [112]

The residual stress σ of coatings on silicon wafer was determined by Stoney formula (*Equation 11*) [186]:

$$\sigma = \pm \frac{E_s}{6(1 - \nu_s)} \frac{h_s^2}{h_f} \left(\frac{1}{R} - \frac{1}{R_0} \right) \quad \text{Equation 11}$$

where E_s is the elastic modulus of substrate; ν_s is the Poisson ratio of the substrate, which equals to 0.28; h_s and h_f are the thickness of the substrate and coating, respectively. h_s equals to 380 μm . R and R_0 are the curvature of the silicon after and before deposition, respectively. The curvatures and the thickness of the films are measured by optical profilometer, the curvature is measured with 'Stiching' mode. The two main curvatures in *Equation 11* are chosen automatically by post-treatment program Gwyddion as shown in *Figure 30*.

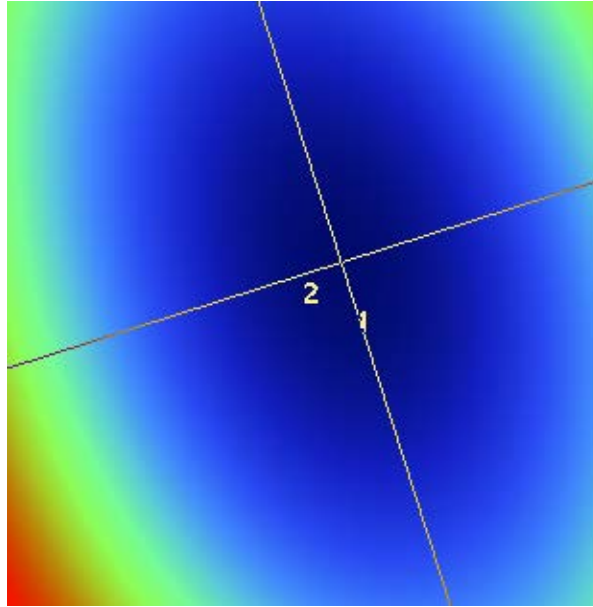


Figure 30. Post-treatment example of curvature measurement

This technique permits to obtain the residual stress.

2.3.5. Hardness and elastic modulus: Nanoindentation

The hardness is defined as the resistance of local penetration by other materials. The hardness is representative of the mechanical resistance, the abrasion resistance, etc. The hardness H could be expressed as the resistance of plastic deformation caused by an indenter according to *Equation 12*:

$$H = \frac{P_{max}}{A} \quad \text{Equation 12}$$

where P_{max} is the maximum force applied by the indenter, A is the residual deformation surface calculated after indentation.

For thin films, the most appropriate manner to measure the hardness and elastic modulus is nanoindentation. Regarding of their small thickness, the influence of the substrate occurs when applying a significant effort. Synthetically, a load/unloading cycle is applied on the surface of the tested material, then the plastic and elastic response is observed after this cycle. In nano-metric scale, Oliver et al. [187] developed a method to measure the reduced elastic modulus and hardness.

Figure 31 illustrates the load/unload cycle of nanoindentation, the plastic deformation leaves a residual displacement h_f on the surface. The slope of tangent on unloading curve represents the stiffness S of material.

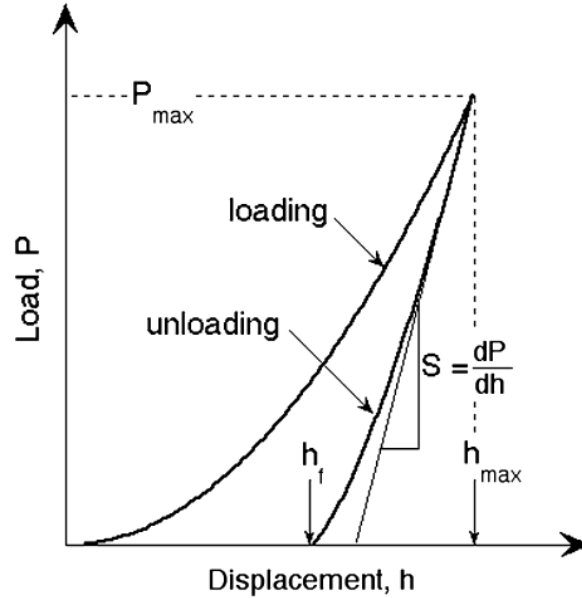


Figure 31. Schematic illustration of indentation load–displacement data [188]

The reduced elastic modulus is thus expressed in Equation 13:

$$E_r = \frac{s\sqrt{\pi}}{2\sqrt{A}} \quad \text{Equation 13}$$

where A is the projected contact surface determined by the depth h_c and the geometry of the indenter. h_{max} is the real penetration depth when maximum load is applying, it can be expressed as follows in Equation 14:

$$h_c = h_{max} - h_s \quad \text{Equation 14}$$

where h_s is the displacement of elastic deformation as shown in Figure 32. h_s varies according to the geometry of the indenter and it is expressed in Equation 15:

$$h_s = \varepsilon \frac{P_{max}}{S} \quad \text{Equation 15}$$

where ε is a constant value that depends on indenter geometry, it equals to 1 when the indenter is circular, 1.034 when the indenter is triangular, 1.012 when the indenter is a square.

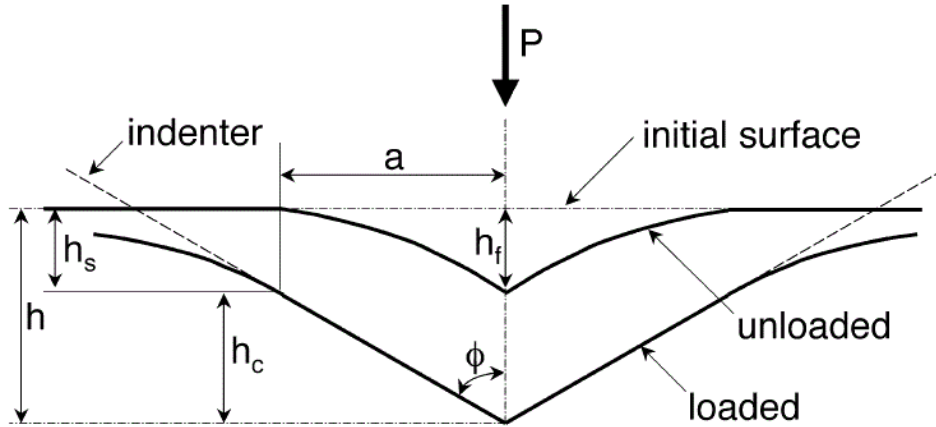


Figure 32. Cross-section of indentation process showing the parameters characterizing the contact geometry [188]

Then the elastic modulus E of specimen is calculated by Equation 16:

$$\frac{1}{E_r} = \frac{1 - \nu^2}{E} + \frac{1 - \nu_i^2}{E_i} \quad \text{Equation 16}$$

where E and ν are elastic modulus and Poisson coefficient of specimen, respectively. E_i and ν_i are elastic modulus and Poisson coefficient of indenter, respectively. The hardness is calculated from the penetration depth h_c and the stiffness S .

A Nano-indenter (XP MTS) in MSMP of the Arts et Métiers campus of Lille was used in our current study to determine the mechanical properties (hardness and elastic modulus) of the coating. This Nano-indenter is equipped with a Berkovich (pyramid triangle) indenter that is able to reach a small penetration of several nanometers, controlled by a dynamic contact mode. In this mode the indenter is controlled by the loading/unloading cycles to calibrate the depth of penetration, the resolution of the vertical displacement is lower than 0.01 nm; the resolution of the applied force of indenter is 1 μ N; the maximum penetrating depth is 15 μ m and maximum force is 10 mN.

Continuous stiffness measurement (CSM) permits to measure the stiffness of the specimen [189]. The hardness and the elastic modulus could be saved directly during this procedure as a function of displacement of the indenter until a maximum penetration depth of 15 μ m. 12 indentations were performed on each coating according to their thickness. The evolutions of hardness and elastic modulus are traced by the average of these results. According to the

literature [190], the values of hardness and elastic modulus are determined on the average curve corresponding to 10% of penetration depth for hardness and 5% of penetration depth for elastic modulus, these percentages aim to diminish the influence of the substrate.

This technique permits to obtain the mechanical properties of thin films such as hardness and elastic modulus.

2.3.6. Adhesion: Scratch test

The adhesion of a coating depends on its structure, its intrinsic mechanical properties as well as the coating/substrate couple. Adhesion is an important parameter because it links directly to the performance of the coating during metal cutting process. If the adhesion of coating is not strong, the notion 'protective coating' is not validated.

The most employed method to test the adhesion of coating is scratch test. This test aims to judge the quality of the coating/substrate couple. The material should stand with an external mechanical solicitation or a residual stress effect, adhering on substrate to play its role of protection. During the test, cracking is formed into the layer before the total delamination of the coating from the substrate. Considering that the critical loads generally appear in the domain of plastic deformation, the analysis is difficult to realize. The test machine usually equips several sensors, such as the friction sensor, acoustic emission sensor, depth sensor etc. These sensors help to detect the critical load by the acoustic emission, friction force and penetration depth. The critical load can be also verified by observing its crack mode alongside the scratch path by optical microscopy. *Figure 33* presents a typical graph of friction force and acoustic emission obtained by scratch test and the critical load confirmed by observation under optical microscope. The critical load Lc_1 presents the occurrence of cracking located on the board of scratch track, where the crack is perpendicular to the scratch track. The critical load Lc_2 presents the total delamination of coating.

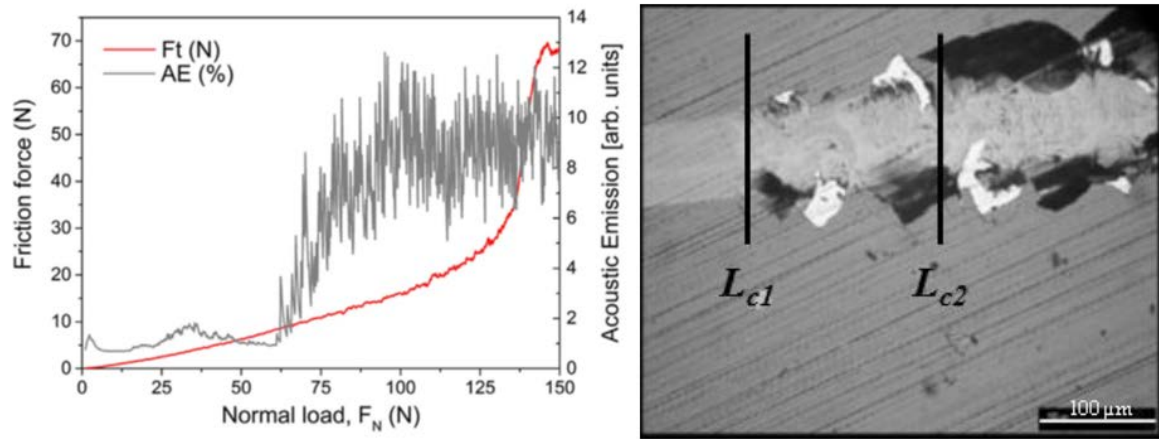


Figure 33. Typical friction force and acoustic emission curve obtained after scratch test and observation of scratch path under optical microscope [151, 191]

The equipment is a ‘Scratch Tester Millenium 200’ located in MSMP (campus of Lille). It is equipped with an optical microscope, a detector of acoustic emission and a tangential force sensor. The indenter is a diamond Rockwell tip with an angle of 120° on the tip of cone, a radius of 0.2 mm. Scratch-test was performed 3 times on each coating with a length of 5 mm and a progressive load from 5 N to 100 N. The loading speed is 100 N/min and the sliding speed is 5 mm/min. The critical load was determined with an implemented microscope and a platform fixes the sample integrated with ruler. Further observation and analysis of the sliding tracks were realized by an optical microscope (OLYMPUS BX51M) in LABOMAP.

The adhesion property could be also compared with the work of adhesion W_{ad} mentioned in the model of Bull and Rickerby [192]. The work of adhesion is calculated by Equation 17. Although this model does not take the internal residual stress into consideration [193], but it still makes a comparison of the adhesion for different coatings:

$$W_{ad} = 3.307 \cdot 10^{11} \frac{hLc_2}{d^4E} \quad \text{Equation 17}$$

where W_{ad} is the work of adhesion in J/m², h is the thickness of the coating in μm, Lc_2 is the critical load in N, d is the width of the track when Lc_2 occurs in μm, E is the elastic modulus in kg/mm².

This technique permits to obtain the adhesion property of the as-deposited coatings as well as the work of adhesion thanks to the Bull and Rickerby model.

2.3.7. Tribology: Rotative tribometer

The essential of the tribometry is to define the behavior of a material submitted under certain cycles of friction against a counterpart, as well as determining the friction coefficient. The friction coefficient is a wide-spread property for qualifying and quantifying the behavior of the contact surface, although this value is strongly dependent on the test conditions and on the two materials in contact. The objective of this test is to determine the friction coefficient and the wear resistance of coated tungsten carbide against a Ti6Al4V ball (6 mm of diameter). The equipment used is a continuous rotative tribometer (TriboX, CSM Instruments) located at the LABOMAP.

Before each test, the ball and the substrate are cleaned by ethanol and deionized water to remove any impurities, which could modify the nature of the contact between the two counterparts. The test conditions are the following: a normal load of 10 N, a cycle radius of 4 mm, a sliding speed of 10 cm/s, a sliding distance of 100 m and about 4000 sliding cycles. The tests were conducted at ambient temperature without lubricant.

The wear track on the coatings was observed with the optical profilometer and SEM to compare and determine the wear volume (or wear rate). The wear volume V of the ball is considered as a spherical cap, which could be calculated by measuring its height and diameter, as shown in *Equation 18* and *Equation 19*:

$$h = R - \sqrt{R^2 - \frac{D^2}{4}} \quad \text{Equation 18}$$

$$V = \frac{\pi h}{6} \left(\frac{3D^2}{4} + h^2 \right) \quad \text{Equation 19}$$

where h is the height of the cap, R is the radius of the ball, D is the diameter of the cap (measured by an optical microscope).

The wear volume of coated tungsten carbide was calculated according to Archard [194] by multiplying the perimeter of the wear track and the average of 3 sections on wear volume. The section area is given by *Equation 20* while the *Equation 21* presents sum of the section:

$$A_i = \frac{(y_{i+1} + y_i)}{2} \times (x_{i+1} - x_i) \quad \text{Equation 20}$$

$$A_j = \sum_i^j A_i \quad \text{Equation 21}$$

where x represents abscissa and y represents ordinate, A is the area section.

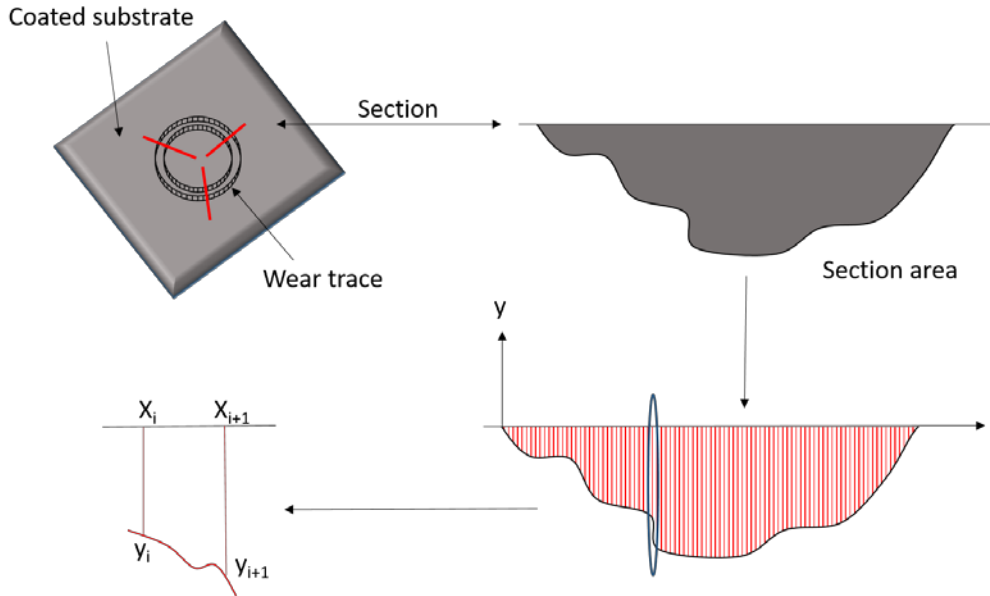


Figure 34. Method to calculate the wear volume

Figure 34 shows how to calculate the wear volume from each section area of the wear track. The abscissa and the ordinate are fixed by measurement with the optical profilometer, then the wear volume could be calculated with the help of Equation 20 and Equation 21. The wear rate is calculated by the determined wear volume (mm^3) divided by the applied normal force (N) and the sliding distance (m).

This technique permits to obtain the wear resistance of the as-deposited coating against the counterpart, to obtain the friction coefficient and study the tribological behaviour between the coating and the counterpart.

2.3.8. Thermal properties: Modulated photothermal radiometry

As foregoing mentioned, the thermal property of the coating is a main property for our work because the developed coating acts as a thermal diffusion barrier to protect the cutting tool from either too high or too low temperature and thermal shocks during cryogenic assisted machining of Ti6Al4V alloy. Machining process will cause significant rise of temperature up to 500°C [195]. The heating generated during machining Ti6Al4V is hardly taken away by chips, then the cutting tools is overheated, which is the main reasons of rapid tool wear.

A thermal characterization bench for thin layers (MPTR) (Figure 35) in Institute I2M-University of Bordeaux was used to determine the thermal properties of the coatings and WC substrates.

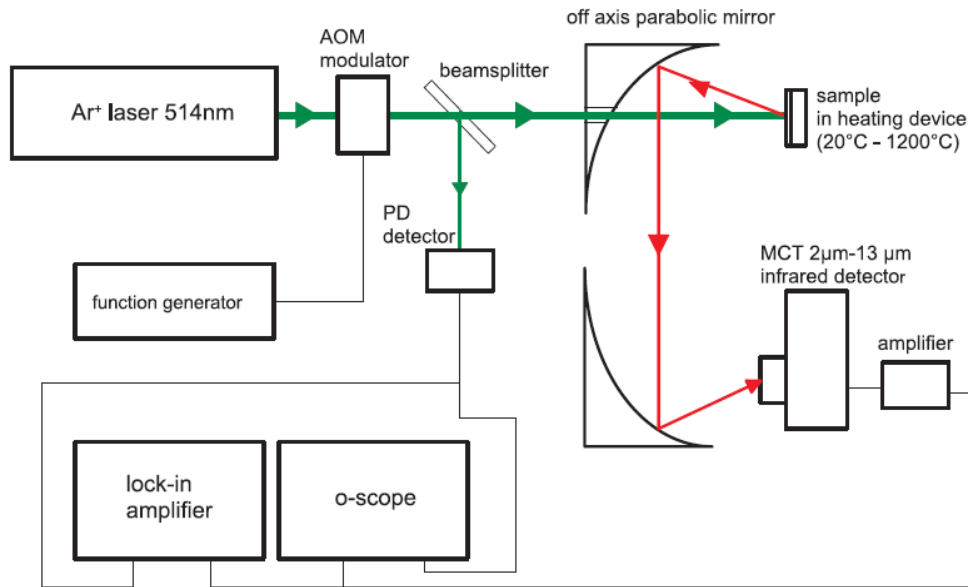


Figure 35. Modulated photothermal radiometry experimental setup [196]

The machine is able to operate from ambient temperature until 1200°C. The heat source is a continuous Ar⁺ laser of 514 nm wavelength and 1.7 W maximum power. The laser beam is modulated in intensity by an acousto-optic modulator in the range 1-100 kHz and is brought to the sample surface by a set of mirrors. On the spot of 1 mm in diameter at 1/e² of the laser beam, it has a Gaussian profile of power distribution. An infrared HgCdTe detector is responsible to measure the thermal response, the permitted wavelength is between 2 to 13 μm. The parabolic mirror collects the emitted infrared radiation then focus it on the detector. The detected zone is a circle of 1 mm on the heated sample. The phase lag between the reference signal from a photodiode and the signal from infrared detector is measured by a lock-in amplifier [196, 197]. The temperature variation ΔT generated by the modulated laser was small, it is assumed that the heat transfer is linear and radiative emission ΔT is linear proportional to the heat. Since the thermal diffusion length $\sqrt{a_s/\pi f}$, with a_s is the thermal diffusivity of the substrate and f the explored frequency range in 1-100 kHz, is very small compared to the substrate thickness, the substrate can be considered semi-infinite media. Regarding the thickness of the coatings, at the lowest frequency, the heat conduction in the specimen can be considered as one-dimensional (1D). The thermal quadruples in 1D [198] is used to modulate the thermal system, the measured

average temperature on the sample θ_s according to the heat flux φ in frequency domain $\omega - 2\pi f$ and j imaginary unit is written in *Equation 22*:

$$\theta_s(j\omega) = (Z_s^\infty(j\omega) + R_{th})\varphi(j\omega) \quad \text{Equation 22}$$

where $Z_s^\infty(j\omega) = \sqrt{a_s/j\omega}/k_s$, k_s is the thermal conductivity of substrate. The thermal resistance of the coatings is written in *Equation 23*:

$$R_{th} = \frac{h_d}{k_d} + R_{ds} \quad \text{Equation 23}$$

where h_d is the thickness of the coating, k_d is the thermal conductivity of the coating and R_{ds} is the thermal contact resistance between the interface of coating and substrate.

The phase lag is an argument of the transfer function $Z(j\omega)$ according to angular frequency $\omega - 2\pi f$. By using minimizing Levenberg-Marquardt algorithm, the R_{th} could be calculated from the measurement of phase from lock-in amplifier and the calculated phase from the transfer function [196].

In this work, the WC substrate, the optimal CrN, AlCrN monolayers and three as-deposited multilayers on WC substrates were analysed by the foregoing introduced technique. The thermal resistance thus the thermal conductivity of these as-deposited coatings were determined.

Table 7. Summary of the coatings' characterization techniques

Properties	Methods	Locations
Thickness	SEM, optical profilometer	Arts et Métiers - Cluny
Surface morphology	SEM, optical profilometer	Arts et Métiers - Cluny
Chemical Composition	EDS XPS	Arts et Métiers – Cluny LICB-UBFC-Dijon
Residual stress	Optical profilometer	Arts et Métiers - Cluny
Friction coefficient / wear resistance	Ball-on-disc tribometer	Arts et Métiers - Cluny
Structure	XRD	ECAM-Lyon
Hardness / elastic modulus	Nanoindentation	MSMP-Lille
Adherence	Scratch-test	MSMP-Lille
Thermal conductivity	MPTR	Arts et Métiers – Bordeaux

2.4. Experimental setup for tribological tests

The tribological tests were conducted on SOMAB T500 CNC lathe machine, the assembly of tribological tests is presented in *Figure 36*, the pin is mounted on a laboratory-made tribometer adapted to the tribological tests, the detail of the tribometer is presented in *Appendix A*. The pin's technical design is shown in *Appendix B*. Then the tribometer is mounted on a piezoelectric dynamometer Kistler 9121, the acquisition card is NI cDAQ-9174, the sampling frequency was set to 2 kHz. The normal force (F_n), the tangential force (F_t) and the feed force (F_f) were measured by this dynamometer, they are represented by F_x , F_z and F_y respectively in *Figure 36*. The MWF fluid used is Blaster B-Cool 755 (7%) mixed with water (93%). The LN2 container is placed on a balance to control the flow rate on time. The delivery pipe is a flexible PA12 of diameter 8 mm, which is often used for high pressure nature gas distribution for thermo-purpose. It is covered by PE foam insulation sleeve. The pressure of flood is 7.25 bar. The pressure of LN2 is 4 bar and the flow rate is 2 l/min. The contact pressure between pin and bar is controlled by external supply of CO2 pressurized gaz. The tribometer and dynamometer is covered by an isothermal material to avoid the coolant influencing the sensitive acquisition system. The rotation of the workpiece is counter clock, the nozzle is placed in front of the pin to simulate the cooling effect in chip evacuation direction during machining process.

The detail of the nozzle position is presented in *Figure 37*. As already optimized by P. Lequien [61]: the nozzle outlet diameter is 3 mm; the distance between the nozzle and the pin is 2 mm; the distance from nozzle to workpiece is 2 mm (as the piston of tribometer moves back 3 mm

in experience, the pre-setup distance before tests is 5 mm); the projection angle between the pin and the workpiece is 15° , which means the nozzle tilted 75° from the pin.



Figure 36. The assembly of tribological tests



Figure 37. Nozzle position in MWF and cryogenic assisted tribological tests

In order to eliminate the potential influence of surface roughness, the surface preparation for tribological tests aims to obtain the same conditions as Courbon et al. [62]. The R_a of Ti6Al4V bar was controlled to 0.1 μm . According to *Equation 24*, where R_a is the arithmetic average roughness (μm), f is the feed (mm/rev), r_ϵ is the nose radius (μm). An insert reference number CNGG 1204 08-SGF H13A from Sandvik Coromant was chosen to prepare and refresh the bar surface.

$$R_a = 1000 \frac{f^2}{18\sqrt{3}r_\epsilon} \quad \text{Equation 24}$$

2.5. Experimental setup for tool wear

The tool wear tests were conducted on SONIM T9 CNC lathe machine (*Figure 38*). The cutting force (F_c), the thrust force (F_t) and the feed force (F_f) were measured by the same dynamometer as in tribological test. The tool wear was monitored with a laboratory-made integrated wear scope (IWS), which permits to measure the flank wear on the spot without demounting the insert. This system takes pictures of worn tool when each critical machining time is achieved, then the picture will be treated with a program to determine the tool wear. The general experimental set-up of wear test is similar to that of tribological tests. The Ti6Al4V bar is divided into 3 parts in order to test 3 different inserts. The liquid nitrogen delivery nozzle is integrated on tool holder that developed during P. Lequien [61] PhD work. Both the rake face and the flank face are injected directly with liquid nitrogen, the diameter of the nozzle is 3 mm and 1.2 mm, respectively. The tool holder is presented in *Appendix C*. The pressure of flood is 3.2 bar. The pressure of LN2 is 4 bar and the flow rate is 2 l/min and 1.5 l/min for two nozzles, respectively.

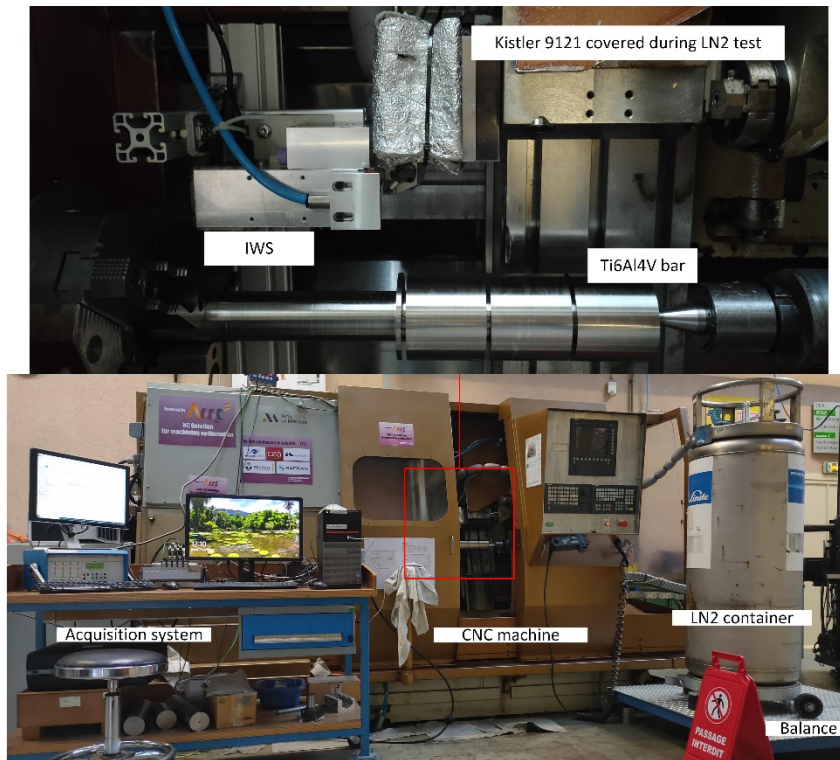


Figure 38. SONIM CNC lathe machine and the assembly of tool wear tests

2.6. Preparation of the pins and inserts for temperature measurements

During tribological tests and tool wear tests, the temperature was measured by a thermocouple type K (Type 12R 12-k-150-118-0.5-2i-3p21-2.5m A27KX-Drain wire to be connected to the sheath). To permit the measurement, a hole of 0.8 mm diameter was drilled to insert the thermocouple of 0.5 mm diameter. The pins and cutting tools were drilled by a drilling EDM machine Agie Charmilles DRILL 20 (cf. *Figure 39*), the setup and the electrode are also presented in this figure. The position of the thermocouple is depicted in *Figure 40*. For the pin, the hole was drilled at the bottom of the cylindrical body. The distance between the thermocouple and the contact point between the workpiece and the pin is 1.53 mm. Then, the thermocouple is fixed by a metallic adhesive tape. In the case of the insert, the hole is drilled on the opposite side to the rake face. The distance between the hole and the cutting edge is 1 mm.

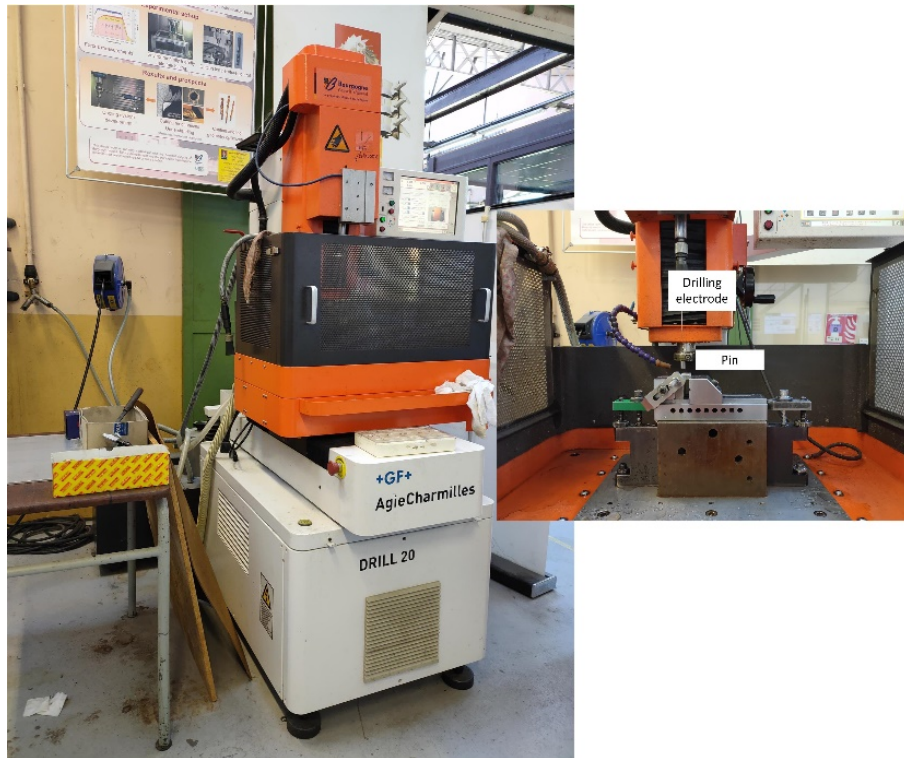


Figure 39. Drilling EDM machine and drilling position on pins and cutting tools

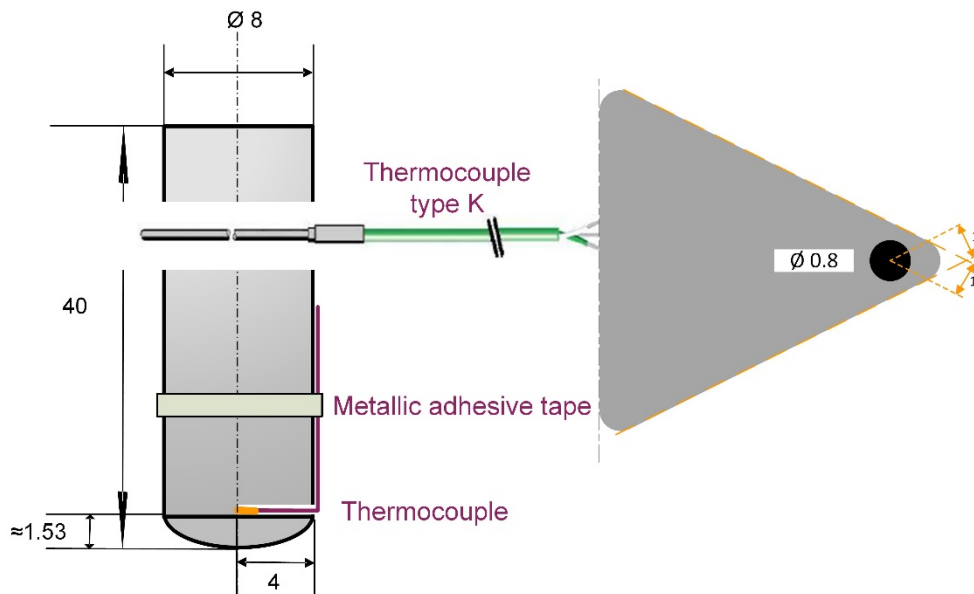


Figure 40. Detail of thermocouple position in the pin and in the insert

2.7. Characterization methods

2.7.1. Micro-hardness and microstructure of the work material

The homogeneity of the titanium bar was at first verified by micro-hardness instrument Wilson Hardness Tukon™ 1202, in its axial and longitudinal direction. Indeed, it should be altered several times during tribological tests and machining tests. A Knoop indenter was used, the force applied is 50 gf (1 gf = 9.8 mN). 20 points for each series of test were performed. The distance between each imprints is 1.5 times of the imprints size. The average hardness in longitudinal direction was 3.43 GPa and in axial direction was 3.38 GPa. The micro-hardness do not exhibit significant variation comparing both directions.

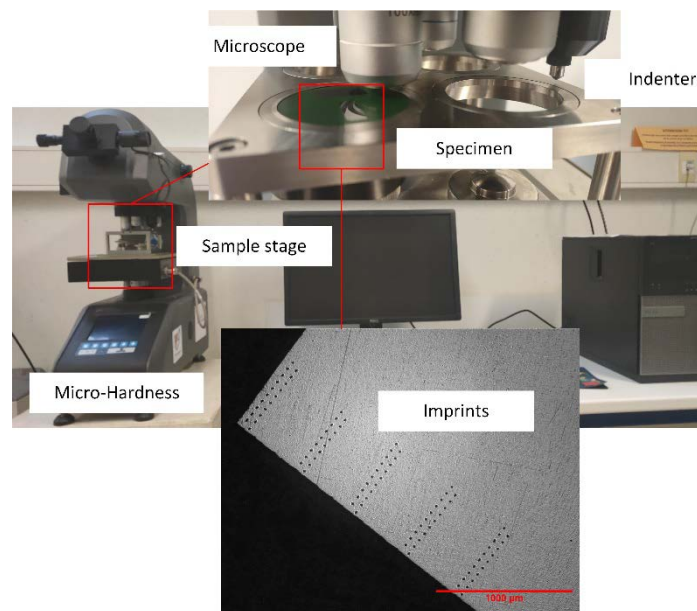


Figure 41. Micro-hardness of Ti6Al4V bar

The microstructure was also observed by an optical microscope OLYMPUS BX51M, as shown in Figure 42. ($\alpha+\beta$) phase are evenly distributed on longitudinal and axial section of Ti6Al4V bar. The α phase shows equiaxed microstructure and β shows lamellar microstructure.

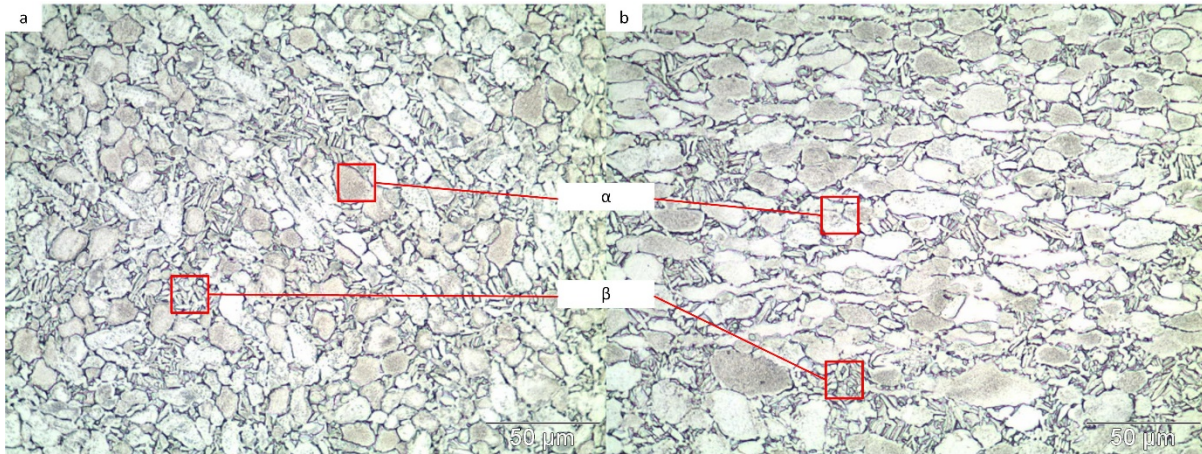


Figure 42. Microstructure of Ti6Al4V bar on a) longitudinal and b) axial section

2.7.2. Observation of the work material (Ti6Al4V) adhesion to the pins

The work material (Ti6Al4V) adhesion to the pins after the tribological tests was observed using optical microscope Keyence VHX 1000 (Figure 43), and quantified using dynamic focusing microscope Alicona InfiniteFocus (Figure 44).

Keyence device is equipped with a CCD or CMOS sensor for detecting surface image. This technic allows us to have an instant idea about what happened during tests and gives the surface state data for results exploitation.

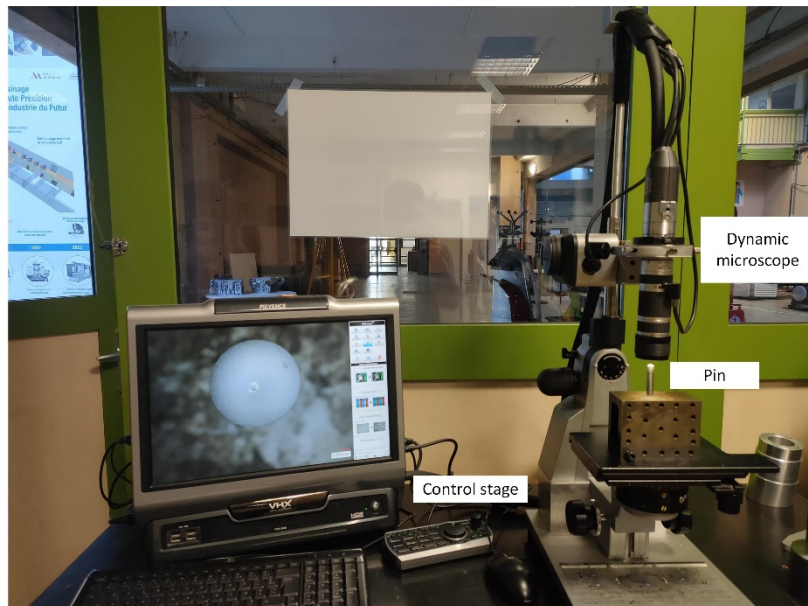


Figure 43. Optical surface observation setup with the digital microscope Keyence

Alicona is a non-contact, optical 3-dimensional microscope. 3D topography and surface roughness measurement with color information can be obtained by this system. The

magnification is $\times 10$ and exposition time is about 5ms. The adhesion volume on the pin was calculated by scanning the pins before and after tribological tests, the method of calculation is presented in *Appendix D*.

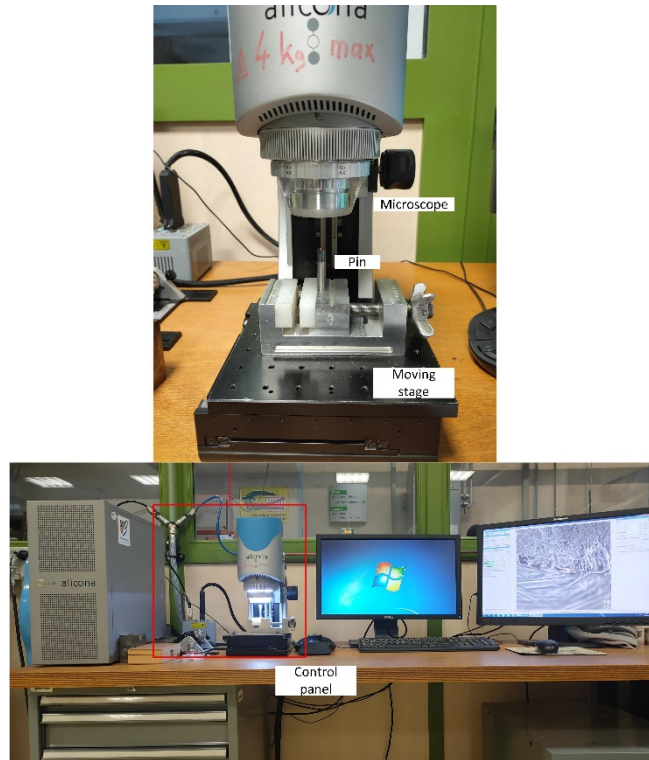


Figure 44. Alicona 3D measurement system

2.7.3. Pin's profile inspection

A vertical profile projector Delta METROLOGIE VB12 series was used to measure the curvature of the pins before and after deposition to ensure the quality of the pins and the regular geometry of each pin's spherical surface, as shown in *Figure 45*. The pin's spherical part was measured 6 times on the border to obtain the curvature. The magnification is $\times 50$. 3 random pins were selected for each coating.

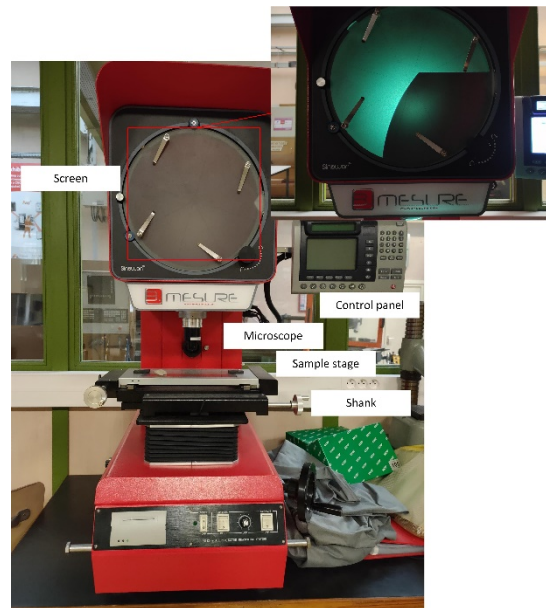


Figure 45. Vertical profile projector

2.7.4. Surface roughness measurements

To measure the surface roughness of the pins before and after coating the dynamic focusing microscope *Alicona InfiniteFocus* (Figure 44) was used. The magnification is $\times 10$ and exposition time is about 5 ms. The one-dimensional evaluation length is 3 mm and the cut-off wavelength is 0.8 mm, each result was revealed after 6 times measurements. The roughness was extracted after remove the curvature profile from the data.

As far as the surface roughness of the workpiece is concerned, a contact profilometer Somicronic Surfascan was used both to measure the surface roughness of the workpiece during the tribological tests, and of the workpiece during the tool wear tests (Figure 46). The chosen stylus series number ST 260 has a 90° tilt angle and $2 \mu\text{m}$ radius point. The base length is 0.25 mm and the evaluation length is 1.25 mm. A 50% Gauss filter is used with $\lambda_c=0.8$.

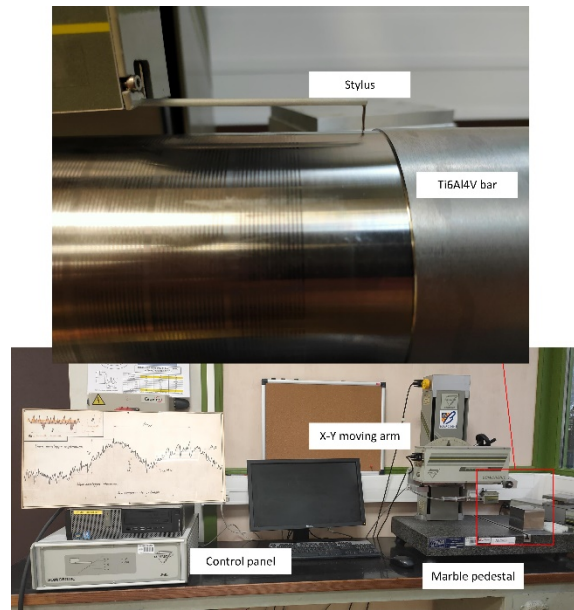


Figure 46. Contact profilometer Surfscan

2.8. Résumé du Chapitre 2

Ce chapitre présente tous les dispositifs expérimentaux et les méthodes de caractérisation qui ont été utilisés au cours de ce travail de recherche. La première partie concerne la technique de dépôt des revêtements et leurs méthodes de caractérisation. La deuxième partie concerne l'assemblage du système de test tribologique, du système de coupe des métaux et de leurs méthodes d'analyse.

Ainsi nous avons dans un premier temps détaillé le système de dépôts PVD industriel sur lequel nous avons réalisé nos revêtements mono et multicouches. Le principe de fonctionnement, les éléments constituant ce système et ses caractéristiques ont été explicités. Nous nous sommes ensuite intéressés aux substrats utilisés lors de cette étude : silicium et carbure de tungstène (dimensions, géométries) mais également procédure de nettoyage ex-situ et in-situ. Le nettoyage in-situ des cibles avant chaque dépôt a également été abordé. Afin de caractériser les propriétés de nos revêtements sur les différents substrats, nous avons fait appel à de nombreuses méthodes complémentaires qui sont résumées dans le *Table 8*.

Table 8. Techniques de caractérisation des couches minces utilisées lors de notre étude

Propriétés	Méthodes	Lieux
Epaisseur	MEB, profilomètre optique	Arts et Métiers - Cluny
Morphologie de surface	MEB, profilomètre optique	Arts et Métiers - Cluny
Composition chimique	EDS XPS	Arts et Métiers – Cluny LICB-UBFC-Dijon
Contraintes résiduelles	Profilomètre optique	Arts et Métiers - Cluny
Coefficient de frottement / résistance à l'usure	Tribométrie bille-disque	Arts et Métiers - Cluny
Structure	DRX	ECAM-Lyon
Dureté / module d'élasticité	Nanoindentation	MSMP-Lille
Adhérence	Scratch-test	MSMP-Lille
Conductivité thermique	MPTR	Arts et Métiers – Bordeaux

Systématiquement, pour chacune de ces techniques nous avons rappelé le principe de fonctionnement, le modèle et la marque de l'équipement utilisé, les conditions d'analyse ou de test et les propriétés obtenues.

Dans la seconde partie de ce chapitre 2 nous avons détaillé les assemblages des tests tribologiques ou d'usure sur la machine d'usinage utilisée que ce soit sous émulsion ou sous cryogénie. La mise en place des thermocouples à l'extrémité des pions (pour les tests de tribologie) et des inserts carbure (pour les tests d'usure) a été explicitée. Nous avons également donné nos résultats de caractérisations des barres de Ti6Al4V qui vont être utilisées pour les tests de tribologie et d'usure. Enfin, les différents microscopes ou appareils qui nous ont servi à déterminer la rugosité des pions/inserts avant et après dépôt, mais également l'usure des pions/inserts, l'adhérence/transfert de matière après les tests de tribologie sont listés.

Chapter 3. Optimization of Cr-based mono and multilayers

3.1. Introduction

To optimize the multilayer films to be synthesized on carbide inserts for the machining of Ti6Al4V under cryogenic assistance, we first have to determine the deposition conditions to obtain Cr, CrN and AlCrN layers presenting a good adhesion, but also good tribological and mechanical properties. One objective of this study was also to verify the reproducibility and results of Aouadi [111]. Indeed, Aouadi obtained very good results for Cr/CrN/CrAlN multilayers, however these coatings have not yet been applied on cutting tools. Thanks to our work, we are going to verify the reproducibility of the monolayers obtained in our industrial PVD system to develop multilayers that will be tested on carbide inserts. A comparison of CrAlN and AlCrN monolayers is also presented here.

In this chapter, the development of chromium underlayers, CrN, CrAlN and AlCrN layers produced by magnetron sputtering are presented. We first developed chromium films according to the deposition conditions of Aouadi [111]. The objective is to obtain an adherent chromium layer on WC and Si substrates.

For CrN coatings, we varied the deposition temperature and substrate bias voltages. The substrate-holder rotation speed was fixed at 1.5 rpm according to Aouadi [111] results. The aim is to study the influence of the deposition temperature and substrate bias voltage on the physico-chemical, structural, mechanical and tribological properties of the CrN films.

Then we will present the development of CrAlN and AlCrN layers. Indeed, first we want to verify the CrAlN coatings properties according to Aouadi [111]. We studied the influence of the Al content on the properties of the CrAlN layers. After the Al content optimized, we fixed it and studied the influence of substrate bias voltage and deposition temperature on the AlCrN monolayers properties.

Finally, we developed new Cr-based multilayers such as Cr/CrN/CrAlN and Cr/CrN/AlCrN by varying the number of monolayers (or number of interfaces) and the thickness of each CrN/CrAlN or CrN/AlCrN pair. The influence of these two parameters on the multilayers' properties was studied.

3.2. Optimization of the monolayer films

3.2.1. Cr underlayer

3.2.1.1. Deposition conditions

Chromium was chosen to perform as an underlayer between the substrate and the desired coating system. The deposition condition was maintained as in [111]. The improvement of adhesion provided by this layer was proved by several researchers [164, 199–201]. Hong et al. [164] showed that the critical load L_{c2} increased from 30 N to 50 N for CrAlSiN coating by adding a chromium underlayer. Li et al. [199] demonstrated that for TiN nanocomposite coating deposited on stainless steel the complete delamination occurred at 29.1 N instead of 15.8 N without underlayer.

The Cr coating's deposition conditions are listed in *Table 9*.

Table 9. Deposition conditions of the Cr underlayer

Cr	
Argon flow (sccm)	100
Working pressure (Pa)	0.5
Power applied on chromium target (W)	1500
Average current on chromium target (A)	4.04
Substrate-holder rotation speed (rpm)	1.5
Deposition time (min)	120
Deposition temperature (°C)	300
Substrate bias voltage (V)	-500

Besides, Herr and Broszeit [202], observed that the film adhesion continuously increased from ambient temperature to 650°C. Broszeit et al. [201] realized TiN and CrN coatings by PVD with different deposition temperatures. Increasing the temperature from 200°C to 750°C, leads to an increase of the critical load L_{c2} from 37 N to 41 N.

Applying a substrate bias voltage has a significant influence on the adhesion of the coatings, as presented in several works [203–205]. Ye et al. [205] proved that the density of the Cr coating is lower when applying low substrate bias voltage. As a consequence, the adhesion is improved. On the other hand, elevated bias voltage will decrease the adhesion of the coating on substrate due to high interfacial stress [206]. According to the above-mentioned results and to Aouadi

[111], we decided to choose a deposition temperature of 300°C and -500 V as substrate bias voltage.

The rotation speed of the substrate-holder was also fixed to 1.5 rpm according to the work of Aouadi [111]. Indeed, with this rotation speed we are sure to avoid multilayer structure, especially in the case of the ternary coatings (CrAlN and AlCrN).

3.2.1.2. Physico-chemical properties

3.2.1.2.1. Chemical composition by EDS

The chemical composition of the Cr underlayer on WC substrate was obtained by EDS. Slight oxygen content (6.2 at.%) is present in this layer, and about 94 at.% purity of chromium was obtained. This quantity of oxygen is negligible for mechanical applications.

3.2.1.2.2. Surface morphology and microstructure

Figure 47 shows the surface morphology and cross-section of the Cr underlayer.

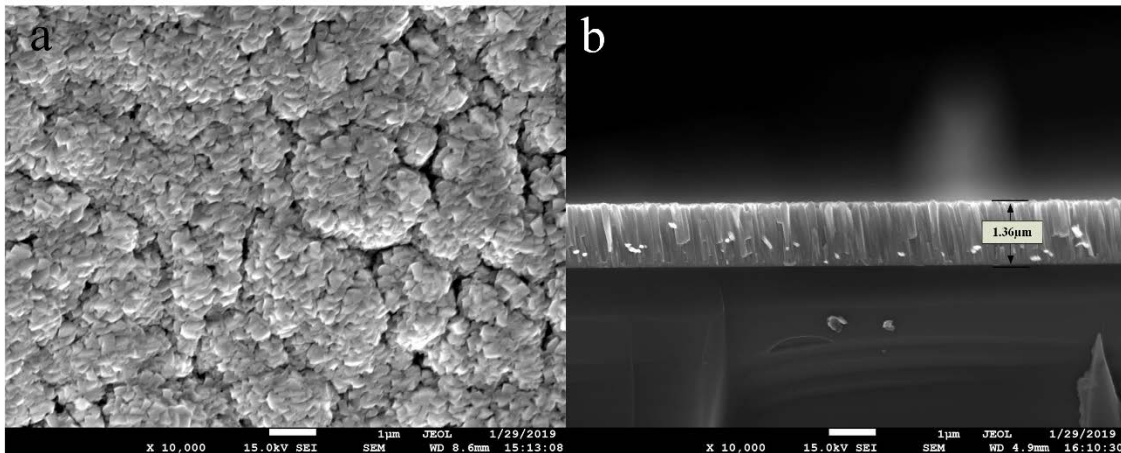


Figure 47. a) SEM images of the Cr underlayer surface morphology on WC substrate and b) cross-section of the Cr underlayer on silicon substrate

On WC substrate, packages of pyramidal columns top are observed in Figure 47a. As expected, at a medium substrate bias voltage of -500 V, this layer also presents some pores. The cross-section on (100) silicon substrate of the Cr underlayer exhibits the well-known columnar structure (Figure 47b). Referencing to the structure zone model (SZM) of Mahieu [207], this morphology may be attributed to Zone I_c (Figure 48).

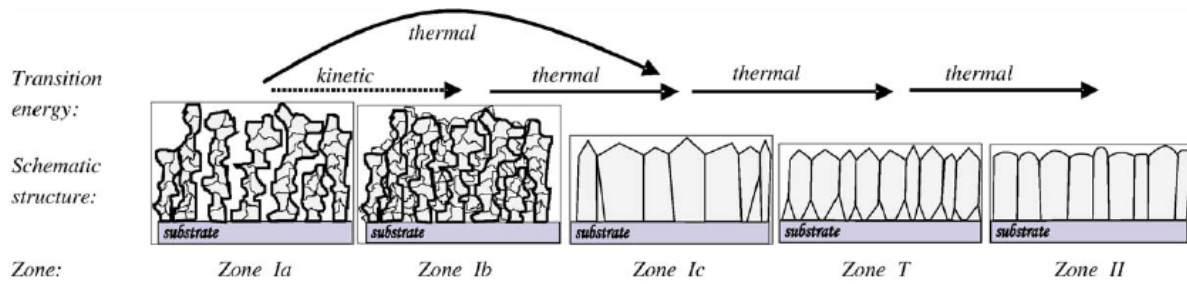


Figure 48. Schematic view of extended SZM [207]

The elevated temperature induces the thermal mobility of the adatoms to nucleate and form crystalline islands, the grains are faceted to constitute faceted columns. The voids between columns are filled thanks to adatoms mobility, the columns are separated by grain boundaries rather than voids. Despite of this phenomenon, there is still competition between columns growth: the tallest columns are able to overgrow the others to create shadow effect. The thickness of the Cr layer determined by SEM observation is $1.36 \mu\text{m}$. The deposition rate of Cr is then of $11.33 \text{ nm}\cdot\text{min}^{-1}$.

3.2.1.2.3. Structure

Figure 49 presents the XRD patterns of the Cr-coated and uncoated WC substrate. The main Cr underlayer diffraction peak was detected at 51.5° and attributed to the (110) orientation. The (110) theoretical peak according to (ICDD 00-006-0694) card is at 52.04° . It is well known that the pure chromium coating has a (110) preferential crystalline orientation [208]. It also presents minor (211) and (200) diffraction peaks at 97.99° and 75.72° , respectively. According to the (110) narrowness diffraction peak, the Cr underlayer is well crystallized.

The grain size was calculated according to the Debye Scherrer formula [209] (Equation 10). In these deposition conditions, the Cr underlayer presents a small grain size of 9.74 nm calculated from the (110) diffraction peak.

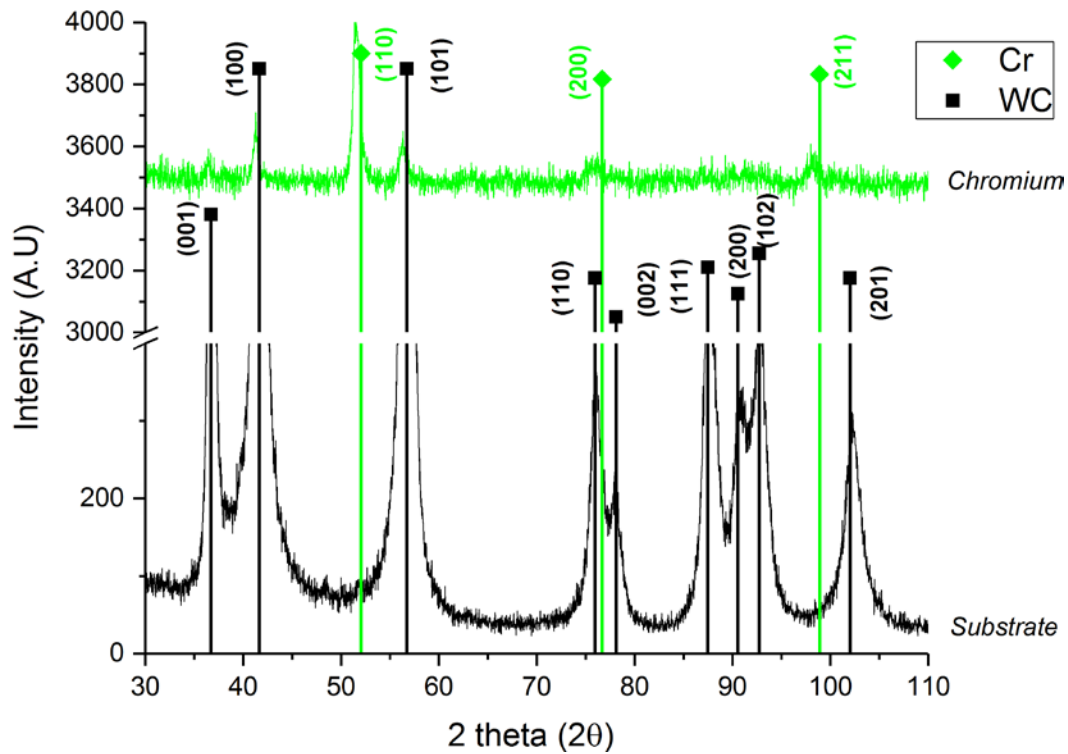


Figure 49. XRD pattern of the Cr underlayer and the WC substrate

3.2.1.3. Tribological properties

The wear resistance of the Cr underlayer was studied by rotative tribometry against a Ti6Al4V ball. The roughness, friction coefficient, wear volume and wear rate of the Cr underlayer are listed in *Table 10*.

Table 10. Tribological properties of the chromium underlayer

Roughness R_a (μm)	Friction coefficient	Wear volume (mm^3)	Wear rate ($\text{mm}^3 \cdot \text{m}^{-1} \cdot \text{N}^{-1}$)
0.18	0.51	0.05	5.32×10^{-5}

The Cr layer is not very rough and presents an acceptable coefficient of friction (0.51). The wear track of chromium and WC substrate are shown in *Figure 50*. One can note that for tungsten carbide the main wear mechanism is adhesion wear and there is a build-up effect on raw substrate. The wear volume on raw substrate is hard to determine. The SEM image of the wear tracks are presented in *Appendix E*. Darbeida et al. [210] examined the wear rate between Cr coating with several variation of hardness and WC ball as counterpart. They found for a Cr pure coating with a hardness of 6 GPa, a wear rate of $0.6 \text{ mm}^3 \cdot \text{m}^{-1} \cdot \text{N}^{-1}$ and a friction coefficient

of 0.6. The higher wear rate compared to current study may be due to the different type of counterpart.

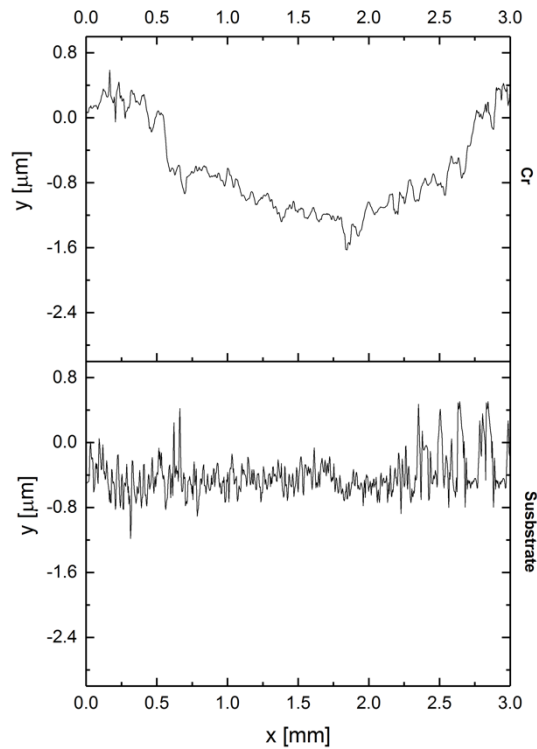


Figure 50. Wear track of the Cr underlayer and WC substrate

3.2.1.4. Mechanical properties

The residual stress, hardness, elastic modulus, hardness/elastic modulus ratio and critical loads (Lc_1 and Lc_2) are listed in Table 11.

Table 11. Mechanical properties of the Cr underlayer

Properties	Residual stress (MPa)	Hardness (GPa)	Elastic modulus (GPa)	H^3/E^2 ($\times 10^{-3}$)	Lc_1 (N)	Lc_2 (N)
Coating Cr	222.8	5.9	170	7	9.45	31.62

The Cr coating presents a tensile stress of around 223 MPa, a hardness and elastic modulus of 5.9 and 170 GPa, respectively. Darbeida et al. [210] compared the residual stress and hardness of chromium coatings deposited by several methods: a Cr coating obtained by magnetron sputtering has a hardness of 6 GPa and residual stress of 136 MPa. The residual stress of the obtained Cr films varies within ± 1 GPa, their hardness varies from 5 to 20 GPa. Komiya et al. [211] showed that the hardness of a Cr coating deposited by electrochemically plated method

has a hardness of 8.9 GPa. Hollow cathode deposited Cr coatings exhibits 3.4 GPa and 2.4 GPa at 190°C and 520°C, respectively, under a substrate bias voltage of -50 V. Nilsson et al. [212] reported that the elastic modulus of chromium decreases with its thickness. A chromium film of 83 nm has an elastic modulus lower than 100 GPa, while the bulk elastic modulus is around 250 GPa. Lintymer et al. [213] showed that the elastic modulus of chromium thin film deposited by glancing angle deposition (GLAD) varied from 94 GPa to 210 GPa. This huge variation was mainly attributed to the zigzag microstructure produced by the GLAD process, e.g. the porosity has a crucial influence on the elastic modulus. The plastic deformation resistance given by hardness and elastic modulus ratio is low, but considering as the first/base layer of the total future coatings, its influence on their global mechanical properties is negligible. It seems that the Cr layer has an acceptable adhesion on the WC substrate. Indeed, the critical loads, L_{c1} and L_{c2} , are 9.45 N and 31.62 N, respectively according to *Figure 51*.

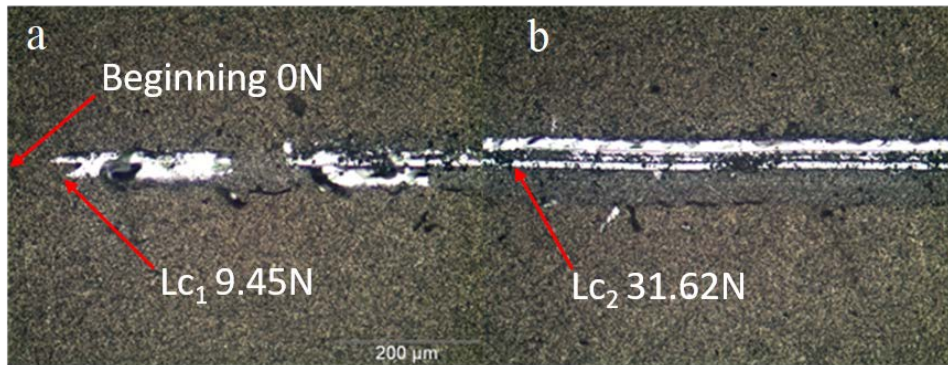


Figure 51. Optical images of L_{c1} and L_{c2} critical loads for the Cr underlayer

Guilbaud et al. [208] studied pure chromium coatings shows tensile stress and a critical load L_{c2} of around 11 N. They also demonstrated the correlation between residual stress and adhesion. Indeed, when the intrinsic stress continuously decreased, the critical load of chromium film increased from 11 to 18 N. The relatively good and acceptable L_{c2} critical load of as-deposited Cr underlayer can be due to its low tensile residual stress. This is a main result as this Cr underlayer will be at the interface of all the substrates we studied (silicon, WC) whatever the architecture of the multilayers.

3.2.1.5. Partial conclusion

The chromium underlayer was studied for the purpose of providing a good adhesion between the substrate and the coatings we studied (especially for multilayers). Indeed, pure chromium underlayer significantly improves the performance of the desired coatings, especially their adhesion on many different substrates [163, 164, 199, 200, 208, 210, 211, 214–218]. We

obtained almost pure chromium thin films (Cr 94 at.%) by DC magnetron sputtering with an acceptable adhesion ($Lc_2 = 31.62$ N) on tungsten carbide substrate, a low friction coefficient (0.51) and wear rate ($5.32 \times 10^{-5} \text{ mm}^3 \cdot \text{m}^{-1} \cdot \text{N}^{-1}$) after being in rubbing with Ti6Al4V ball. Finally, the Cr layers was well crystallized, showed the (110) preferred orientation with a grain size of around 10 nm and has a relative porosity. All the above-mentioned results obtained on as-deposited Cr coating on WC substrate confirmed Aouadi [111] results about Cr coating on steel substrate. Thus, as expected, the Cr coating is adherent whatever the type of substrate or its roughness.

3.2.2. CrN coatings

3.2.2.1. Deposition conditions

In this part we will develop CrN coatings. We began by studying the influence of the deposition temperature and of the substrate bias voltage on the chemical composition, microstructure and crystallography of CrN layers on WC substrates. The mechanical properties of the CrN layers were also investigated.

To achieve these coatings, we varied the deposition temperature and the substrate bias voltage, while the other deposition parameters are fixed. The working pressure is 0.5 Pa and the power applied to the chromium target is 1500 W (i.e. ~ -385 V). The deposition time is 360 min. During deposition, the substrate-holder rotation speed is 1.5 rpm according to Aouadi [111] and with an Ar+N₂ mixture defined by Moones [219]. *Table 12* summarizes the deposition conditions of the CrN films studied.

Table 12. Deposition conditions of the CrN monolayers

CrN						
Argon flow (sccm)	60					
Nitrogen flow (sccm)	53					
Working pressure (Pa)	0.5					
Power applied on chromium target (W)	1500					
Substrate-holder rotation speed (rpm)	1.5					
Average current on chromium target (A)	3.9					
Deposition time (min)	360					
Temperature (°C)	Ambient	Ambient	150	300	300	300
Substrate Bias Voltage (V)	0	-500	-500	-500	-250	0

3.2.2.2. Physico-chemical properties

3.2.2.2.1. Deposition rate and thickness of the CrN layers

The thickness of the CrN coatings varies from 2.03 to 3.26 μm (*Table 13* and SEM cross section images in section 3.2.2.2.3 of this Chapter), which means that the deposition rate varies from 5.7 to 9.1 $\text{nm}\cdot\text{min}^{-1}$.

Table 13. Deposition rate and thickness of the CrN monolayers

Temperature (°C)	Ambient		150	300		
Substrate Bias Voltage (V)	0	-500		-250	0	
Thickness (μm)	3.26	2.59	2.46	2.03	2.76	2.65
Deposition rate ($\text{nm}\cdot\text{min}^{-1}$)	9.1	7.2	6.8	5.7	7.7	7.4

These results are consistent with those obtained by Aouadi [111]. It is noteworthy that he realized CrN layers with a substrate-holder rotation speed of 3 rpm, instead of 1.5 rpm. His deposition rate of the CrN layer synthesized at -500 V and 300 °C is 7.25 $\text{nm}\cdot\text{min}^{-1}$ while we found 5.7 $\text{nm}\cdot\text{min}^{-1}$. It suggests that the rotation speed of the substrate-holder influences the deposition rate and thickness of the coatings. Indeed, the exposure of the substrate in front of the Cr target is longer in the case of the highest substrate-holder rotation speed. Considering the deposition time of six hours for all the coatings, the thickness of the CrN layers decreases while the temperature and bias voltage increase. The effect of the substrate bias is representative of the well-known resputtering process [220] that occurs when the species acting during the

deposition are too energetic. In the case of the temperature effect, one can suppose that the layers are densified at high deposition temperature by the increase of the adatoms mobility.

3.2.2.2. Chemical composition

Table 14 shows the chemical composition of the CrN monolayers on tungsten carbide obtained by EDS microanalyses.

Table 14. Chemical composition of the CrN monolayers

Deposition temperature (°C)	Substrate bias voltage (- V)	Cr at.%	N at.%	O at.%	N/Cr
Ambient	0	45.2	42.5	12.3	0.94
	500	49.9	45.8	4.3	0.92
150		49.8	46.3	3.9	0.93
300		49.8	46.7	3.5	0.94
	250	48.5	47	4.5	0.97
	0	46.8	45.2	8	0.97

Figure 52 illustrates the evolution of the chemical composition of CrN monolayers as a function of the deposition temperature and substrate bias voltage.

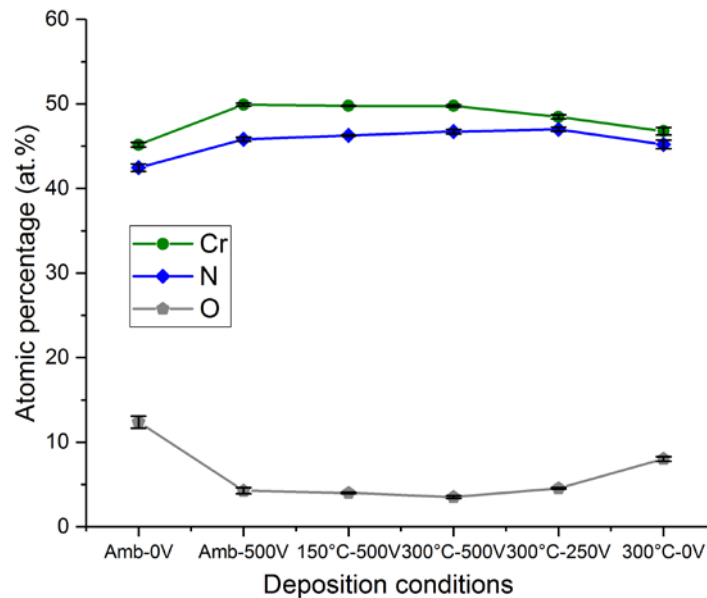


Figure 52. Chemical composition of the CrN monolayers as a function of the deposition temperature and substrate bias voltage

According to the EDS analyzes, all the CrN coatings are almost stoichiometric, especially when the oxygen content is the lowest (3.5 at.%). The decrease of the oxygen content may be related to the substrate bias voltage. A study on ZrNO [221] reported the reduction of oxygen fraction with the increase of the substrate bias voltage. This phenomenon was explained by the preferential re-sputtering of oxygen [222] caused by the lower bond strength of the Zr-O atomic bond in comparison to the Zr-N one [223]. Nevertheless, it seems that the deposition temperature has also an influence on the oxygen content even if it is not so obvious (*Table 14, Figure 52*).

According to these results, the deposition conditions to obtain a CrN layer almost stoichiometric and with a low oxygen content are -500 V and 300°C.

XPS analyzes were performed at the ICB laboratory of the University of Burgundy on CrN layer obtained at 300°C-500V on WC substrate. The experimental was as follows: X-ray source Al K α 1 (1486.7 eV), a spot of 200 μ m, 50 W, 15 kV and a pass energy of 187 eV/58.7 eV for spectra/windows. The carbon and oxygen contents after 2 min of sputtering at 500 eV and 6 min at 2 keV were still high (25.4 and 11 at.% respectively). The second sputter cleaning was realized during 10 min at 2 keV and 20 min at 4 keV. The XPS spectra are presented in *Figure 53*.

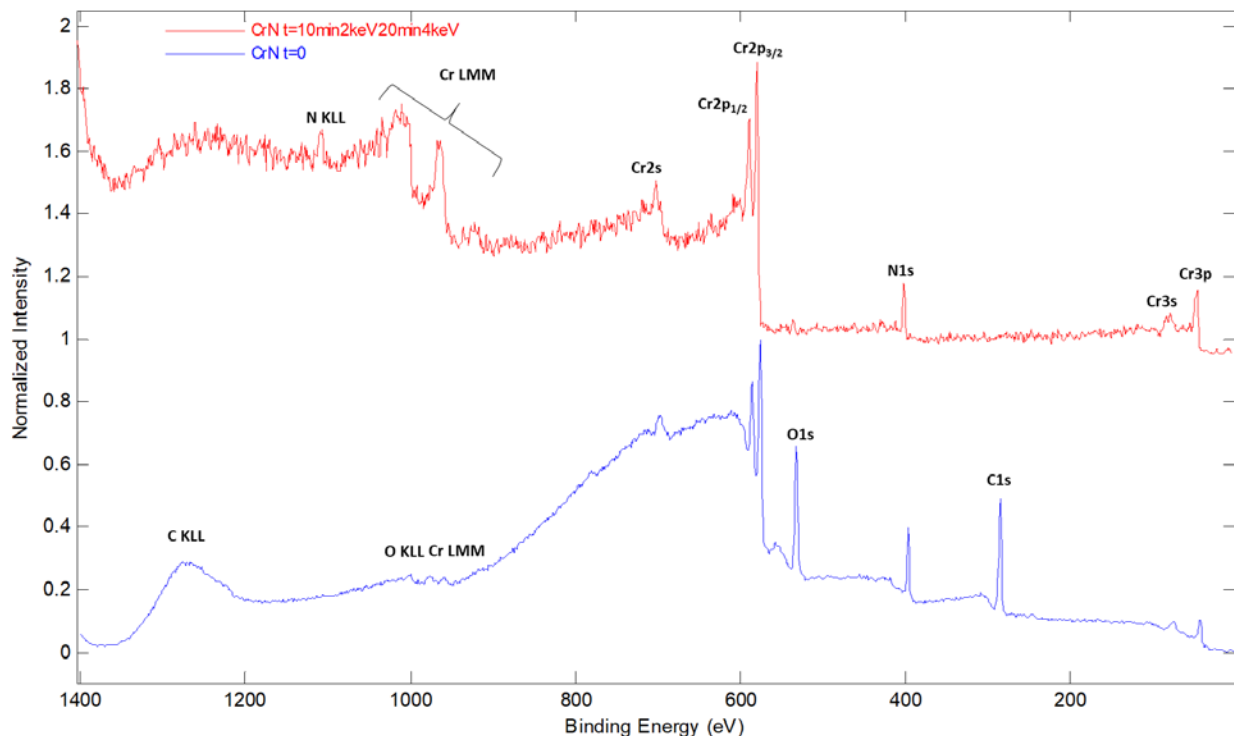


Figure 53. XPS spectra of the CrN monolayers (300°C-500V) on WC substrate

The $\text{Cr}2p_{3/2}$ has a binding energy of 575,3 eV. According to Wagner and Muilenberg. [224], CrN has a $\text{Cr}2p_{3/2}$ binding energy of 575,5 eV. Besides the N1s at 397,2 eV corresponds to numerous nitrides including chromium nitride CrN at 397 eV [225] and Cr_2N at 397.4 eV [226]. The atomic composition of the CrN layers after the second XPS analysis are summarized in *Table 15*.

Table 15. Chemical composition of the CrN monolayer (300°C-500V) by XPS

Cr at. %	N at. %	O at. %	C at. %	N/Cr
45.3	50	2	2.7	1.1

The chemical composition results obtained from EDS and XPS are different. Indeed, EDS is a volume (depth of 500 nm to 1 μm) and semi-quantitative analysis while XPS is a surface (depth of dozens to several dozen nanometers) and quantitative analysis. We observe that the nitrogen was underestimated while the oxygen was overestimated in EDS, comparing to the results from XPS. The N/Cr ratio is 1.1, so the CrN layers are slightly over-stoichiometric in nitrogen. Moreover, if nitrogen only has one Cr as a neighbor, the N1s spectrum should be symmetric. *Figure 54* confirms that we can have a slight presence of Cr_2N . As the intensity of Cr_2N is much smaller than that of CrN, we can assume that an almost pure cubic phase of chromium nitride was synthesized.

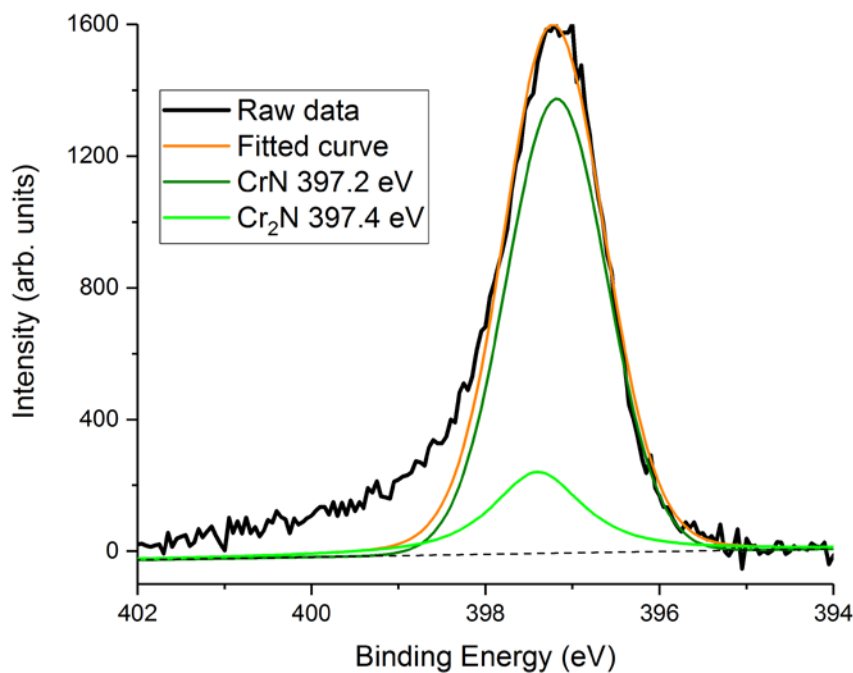


Figure 54. XPS N1s spectra of the CrN monolayer (300°C-500V) on WC substrate

3.2.2.2.3. Surface morphology and microstructure

Figure 55 and Figure 56 show the surface morphology of the CrN coatings on tungsten carbide and silicon substrates.

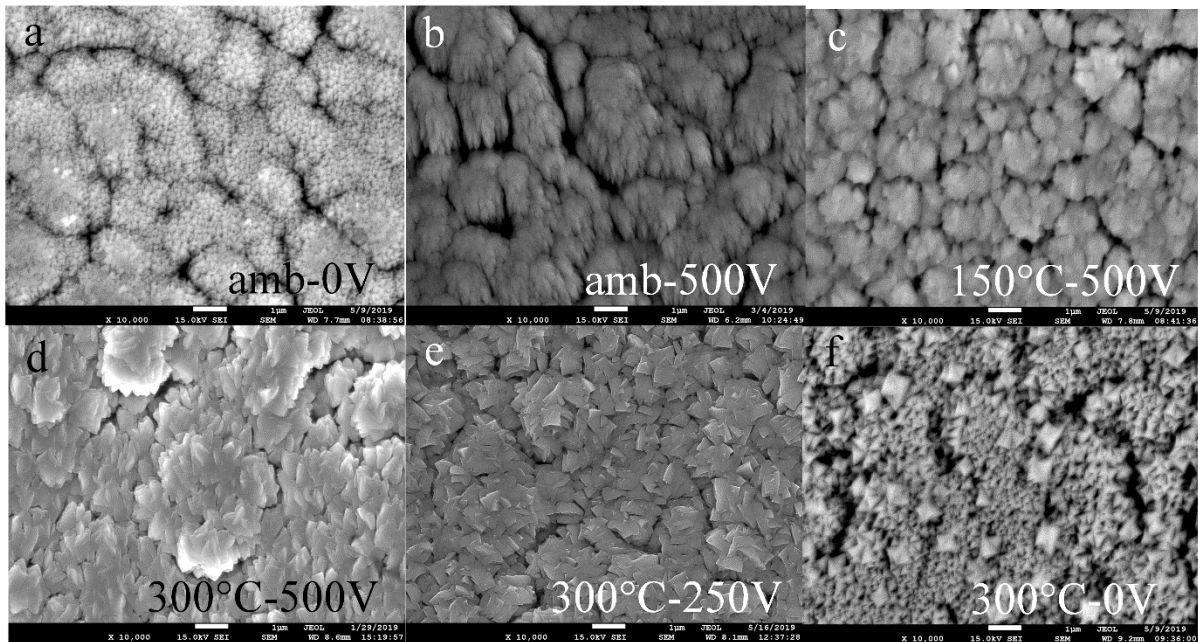


Figure 55. Surface morphology of the CrN monolayers on WC substrates: a) amb-0V, b) amb-500V, c) 150°C-500V, d) 300°C-500V, e) 300°C-250V and f) 300°C-0V

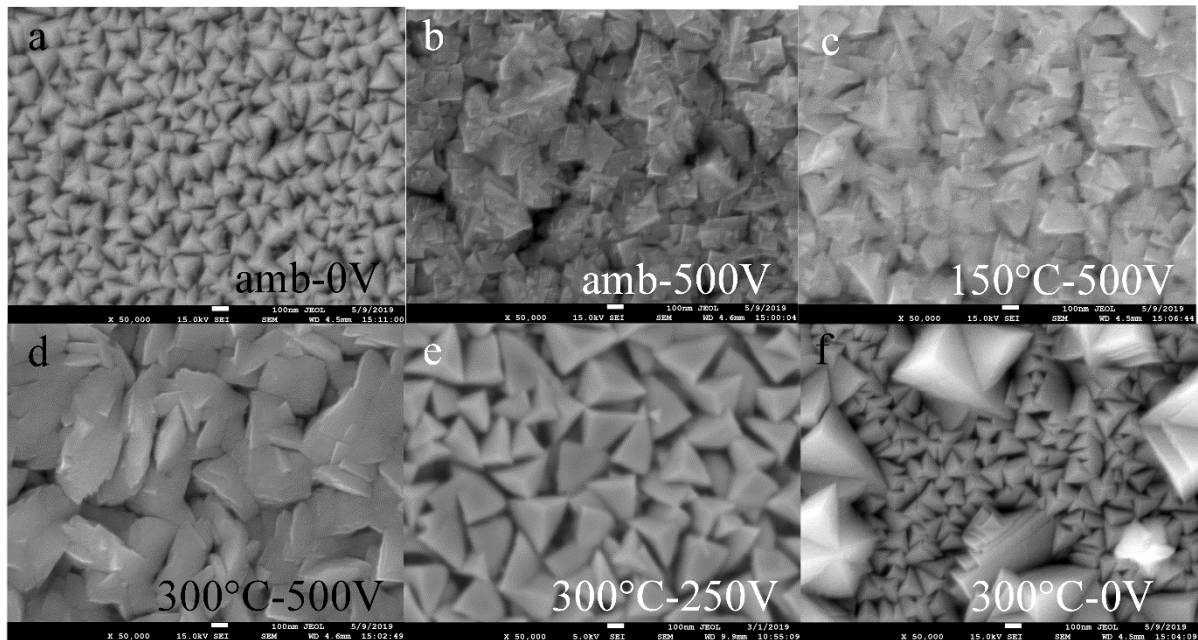


Figure 56. Surface morphology of the CrN monolayers on silicon substrates: a) amb-0V, b) amb-500V, c) 150°C-500V, d) 300°C-500V, e) 300°C-250V and f) 300°C-0V

On WC substrates, most of the surface morphology looks like cauli-flower. Nevertheless, some pyramidal tops of columns are visible for the layers synthesized at 300°C with a substrate bias

voltage of -500 V (*Figure 55d*) or -250 V (*Figure 55e*). At ambient temperature the coating obtained without bias voltage (*Figure 55a*) presents large clusters of columns while the one obtained at -500 V (*Figure 55b*) is denser. As far as the influence of the deposition temperature is concerned, it is obvious that the coatings get denser and reduce their porosity when the temperature increases (*Figure 55 b and d*). When the deposition temperature is 300 °C, substrate bias voltages of -500 V (*Figure 55d*) and -250 V (*Figure 55e*) induced a dense structure and similar column size. In the case of the CrN layer realized at 300°C without bias voltage (*Figure 55f*), we notice macro-particles, an irregular surface morphology and a non-negligible porosity. This is mainly due to the lack of bias voltage on substrate, as already studied by other researchers [203, 216, 227]. It is then predictable that the CrN layers obtained at 300°C with a substrate bias voltage should have the highest hardness.

Mirror-polished silicon substrates were used to better observe the influence of the deposition temperature and the substrate bias voltage on the CrN layers surface morphology (*Figure 56 a-f*). In contrast to the layers realized on rough WC substrate, all the CrN layers developed on mirror-polished silicon substrate present columns with a pyramidal top and are more or less dense. The CrN layer obtained without heating nor substrate bias voltage presents the smaller column size (*Figure 56a*). The lack of energy is probably responsible for this result. Indeed, when we increase the substrate bias voltage (*Figure 56b*) or the temperature (*Figure 56f*), it is obvious that a mixture of small and big columns appears. When the substrate bias voltage is fixed to -500 V, the CrN layers synthesized at 150°C (*Figure 56c*) or 300°C (*Figure 56d*) present a homogeneous and dense surface morphology. Besides, when the deposition temperature is fixed to 300°C, the layers realized with a substrate bias voltage (*Figure 56 d and e*) have a homogeneous and dense surface morphology.

The increase in column size with increasing substrate bias voltage is a consequence of the high mobility of adatoms due to the energy of the ions [228–230]. According to the above-mentioned results, it is obvious that a high deposition temperature and substrate bias voltage permit to get a dense and homogeneous CrN layer. *Figure 57* shows the cross-section of the CrN coatings on silicon substrate.

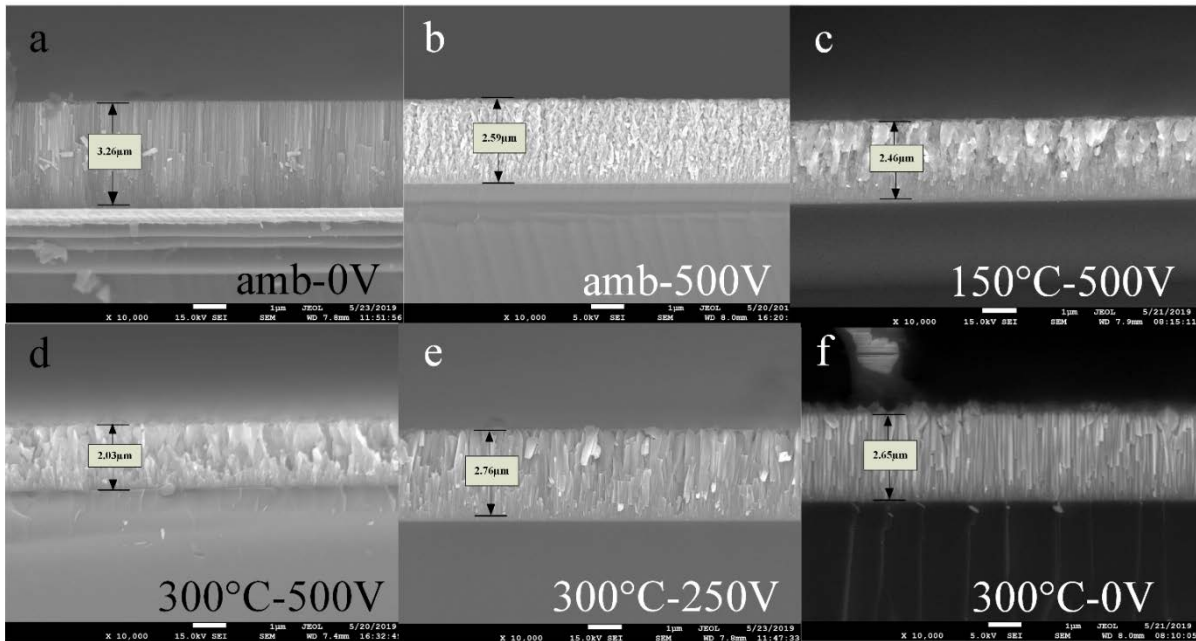


Figure 57. Cross-section of the CrN monolayers on Silicon substrate obtained at: a) amb-0V, b) amb-500V, c) 150°C-500V, d) 300°C-500V, e) 300°C-250V and f) 300°C-0V

The densest structures appear in *Figure 57 c, d and e*. The substrate bias voltage generally creates harder and denser structures according to Berg et al. [231]. The change of temperature has also an influence on the microstructure. As a matter of fact, a denser structure could appear after “heat treatment” during the sputtering [202]. One can also notice that these cross-section observations confirm the previous surface morphology analyses.

3.2.2.2.4. Structure

The XRD analyses have been made on WC coated substrates. According to the (ICDD 00-011-0065) card, we observe only the cubic phase of CrN for all coatings, no hexagonal Cr₂N diffraction peaks are present regarding of XRD patterns (*Figure 58*).

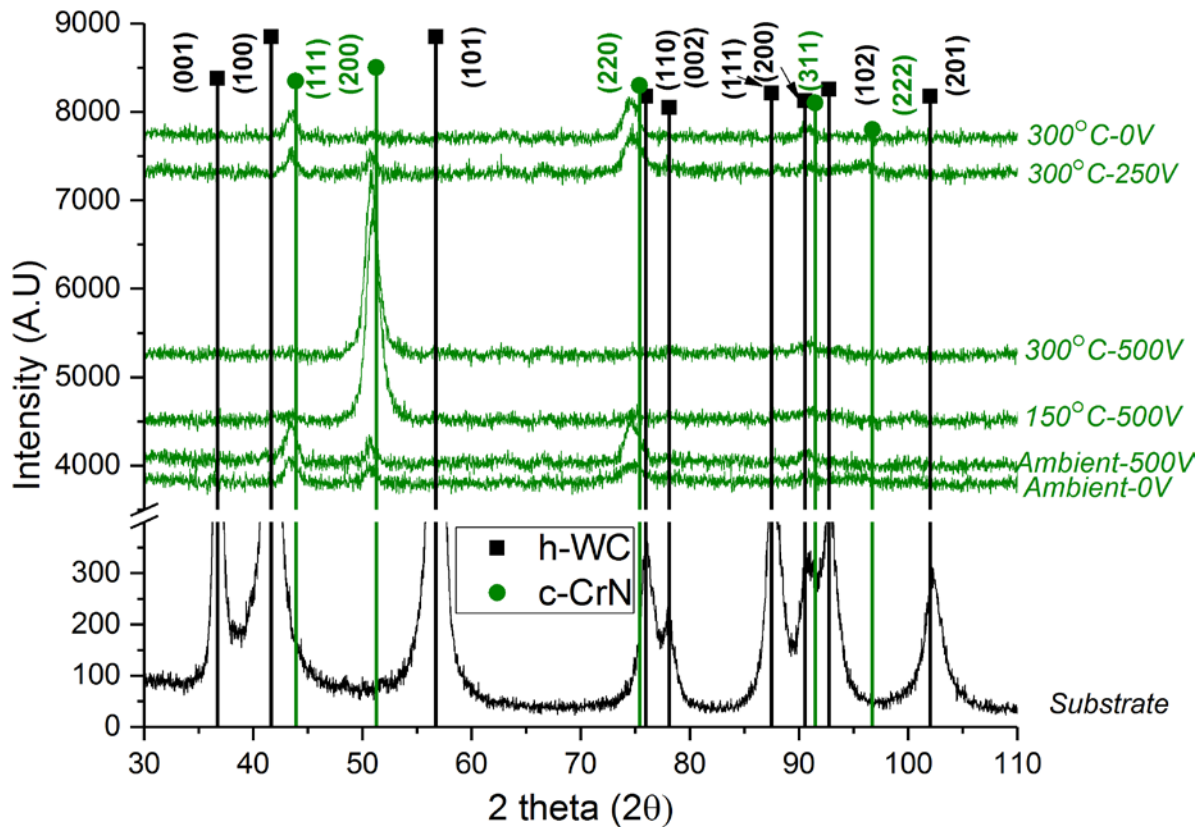


Figure 58. XRD patterns of CrN monolayers.

When the deposition temperature is fixed (at 300°C or ambient temperature), the CrN layers are well crystallized for the highest substrate bias voltage, e.g. -500 V. Besides, we observe that the preferred orientation changed when the substrate bias voltage increases. At ambient temperature, the CrN layer presents a major (220) diffraction peak at 74.62° with -500V substrate bias voltage, while it presents a major (111) diffraction peak at 43.43° without substrate bias. We can suppose that the energy brought thanks to the substrate bias voltage increases the atoms mobility and modify the grain orientation (surface energy model [232, 233] or strain energy model [234]). At 300°C when the substrate bias voltage increased from -250 to -500 V, the (220) and (111) orientations completely disappeared and the (200) plans are major. The CrN coatings are then oriented according to the denser (200) plans containing mainly the Cr atoms. When we compare the influence of the substrate bias voltage, it is obvious that the orientation of the CrN layers depends on the deposition temperature and that these both parameters are related. Indeed, at ambient temperature, the influence of the substrate bias voltage is low while it is important at 300°C. If we now observe the influence of the temperature at a substrate bias voltage of -500 V, it is clearly shown that temperature is a main parameter to modify the crystalline orientation of the CrN layers.

In conclusion, whatever the temperature higher than the ambient one, the (200) orientation is obtained for the highest substrate bias voltage (-500 V). Moreover, whatever the substrate bias voltage, the same crystalline orientations are obtained at ambient temperature. Finally, it is obvious that the substrate bias voltage has a higher influence than the deposition temperature because the XRD patterns obtained for the couples 300 °C/-500 V and 150 °C/-500 V are very similar.

It is noteworthy that the CrN diffraction peaks are all shifted on the left in comparison to their theoretical position. According to the Bragg's law [235] it means that d_{hkl} increases and that these coatings should present tensile stresses.

We also compared our CrN layers preferred orientation with the ones developed by Aouadi [111]. It is interesting to note that he obtained CrN layers with a (111) preferred orientation and not (200). We can suppose that this is caused by the different substrate-holder rotation speeds as already observed by Yousaf et al. [236] and Tian et al. [237]. Indeed, Aouadi realized his CrN coatings with a rotation speed of 3 rpm while we fixed our own at 1.5 rpm according to his optimization of CrAlN coatings. According to Pelleg et al. [238], the evolution of the texture of thin films is related to the minimization of free energy. This energy is made up of surface energy and strain energy. In the case of nitrides, if the surface energy dominates then the preferential orientation is (200). However, if the strain energy dominates then the preferred orientation is (111). So, we can confirm that our CrN layers obtained at 300 °C and -500 V have a surface energy higher than their strain energy. Surface energy is explained by Steckelmacher [239] as a work done that quantifies the disruption of intermolecular bonds that occurred with the existence of a new surface.

Finally, we calculated the grain size thanks to the Debye-Scherrer formula (*Equation 10*). *Table 16* summarizes the calculated grain size of the CrN monolayers as a function of the deposition conditions.

Table 16. Grain size of the CrN monolayers

Deposition conditions	Grain size (nm)	Diffraction peak as reference
Ambient-0V	8.37	111
Ambient-500V	6.99	111
150°C-500V	6.65	200
300°C-500V	7.07	200
300°C-250V	5.17	220
300°C-0V	7.01	220

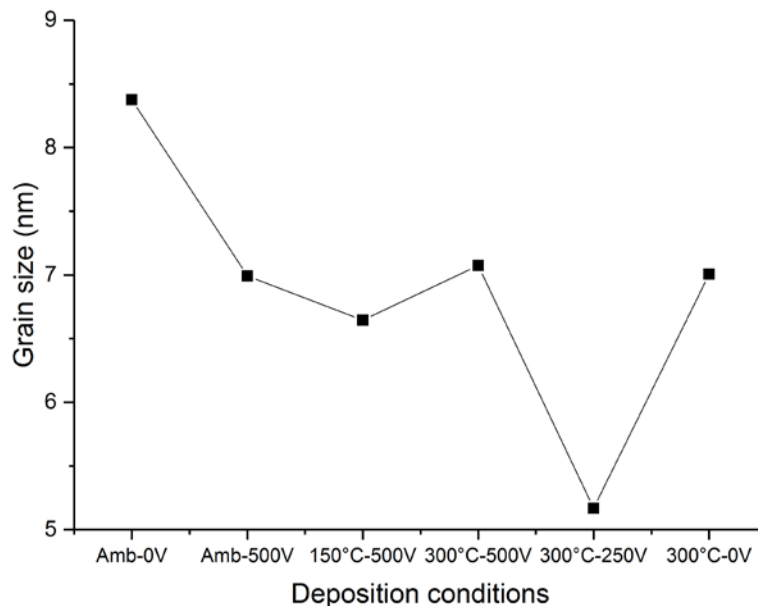


Figure 59. Grain size of the CrN monolayers as a function of the deposition conditions

We observe that whatever the deposition conditions the grain sizes of the CrN monolayers are very similar and varies from 5.17 to 8.37 nm (Figure 59). Considering the (111) plans at ambient temperature, the grain size decreases when the bias voltage increases. We observe the same result in the case of the (220) plans at 300 °C and when the substrate bias increases from 0 to -250 V. As observed also by Aouadi [111], increasing the substrate bias voltage can cause the creation of defects resulting from enhanced ion bombardment. Defects in the sputtered film prevent particle migration to grain boundaries [240]. In addition, the increase in the number of surface defects allows the presence of more preferential nucleation sites which can lead to a decrease in grain size [241]. Now if we consider the (200) diffraction plans, we can note that for a fixed substrate bias, the grain size shortly increases with the deposition temperature: 6.65

nm at 150 °C-500 V and 7.07 nm at 300 °C-500 V. Similar results were obtained by Li et al. [242] in the case of TiN composite films. It is noteworthy that Aouadi [111] got a grain size of 21 nm for his CrN layers realized with a substrate holder rotation speed of 3 rpm while the grain size of our own CrN coatings obtained at 1.5 rpm is around 7 nm. Martín-Tovar et al. [243] observed similar results for Al-doped ZnO thin films prepared by rf-sputtering. They explained that “as the rotation velocity increases, there is a decrement in the value of the FWHM, reaching its minimum for the sample grown at” the highest “substrate velocity”, which means that the substrate rotation improves the crystallinity of the thin films. Thus, we verified the FWHM of the (111) diffraction peak of the CrN layer of Aouadi is 0.45° while the FWHM of the (200) diffraction peak of as-deposited CrN layer is 3 times higher (1.6°).

3.2.2.3. Tribological properties

To study the effect of CrN deposition on the friction coefficient, we performed friction tests in a ball-on-disc configuration. A Ti6Al4V ball rubs on a sample of coated WC substrate. The tests are carried out in air, at room temperature and without lubrication. The friction speed is 10 cm/s and the distance traveled by the Ti6Al4V ball is 100 m. The SEM image of the wear tracks are presented in *Appendix E*. The friction coefficient is shown in *Figure 60* and varies from 0.4 to 0.5.

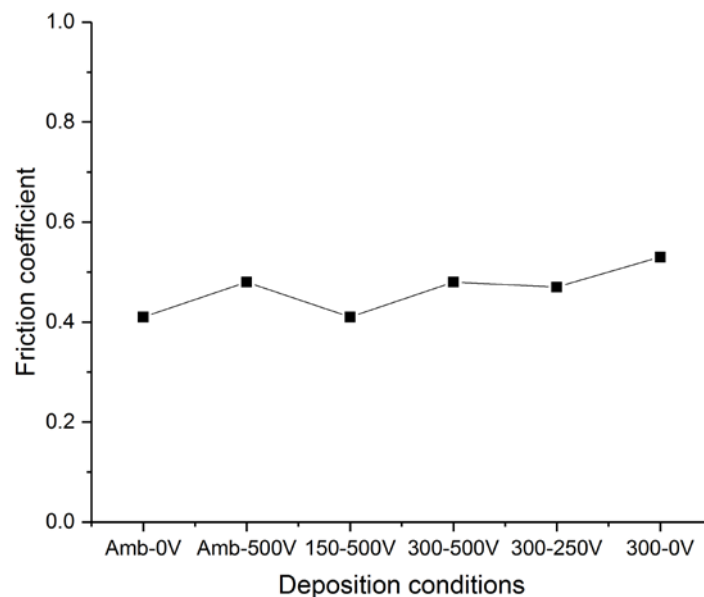


Figure 60. Friction coefficient of CrN monolayers as a function of the deposition conditions

Similar values were obtained by Tlili [244] who got a coefficient of friction of CrN of 0.58, Benlatreche [151] and Aouadi [111] found a coefficient of friction of almost 0.55. One can notice that the COF does not depend on the deposition temperature or the substrate bias voltage.

Figure 61 illustrates the calculated wear rate according to Archard [194].

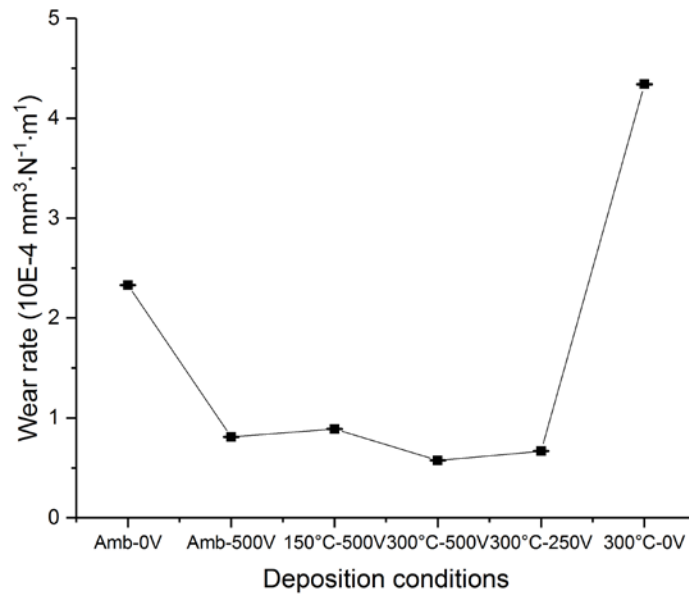


Figure 61. Wear rate of the CrN monolayers as a function of the deposition conditions

The wear rates are summarized in Table 17.

Table 17. Wear rates of the CrN monolayers

Deposition conditions	Ambient-0V	Ambient-500V	150°C-500V	300°C-500V	300°C-250V	300°C-0V
Wear rate ($\times 10^{-4} \text{mm}^3 \cdot \text{m}^{-1} \cdot \text{N}^{-1}$)	2.33	0.81	0.89	0.58	0.67	4.34

The wear tracks are presented in Figure 62.

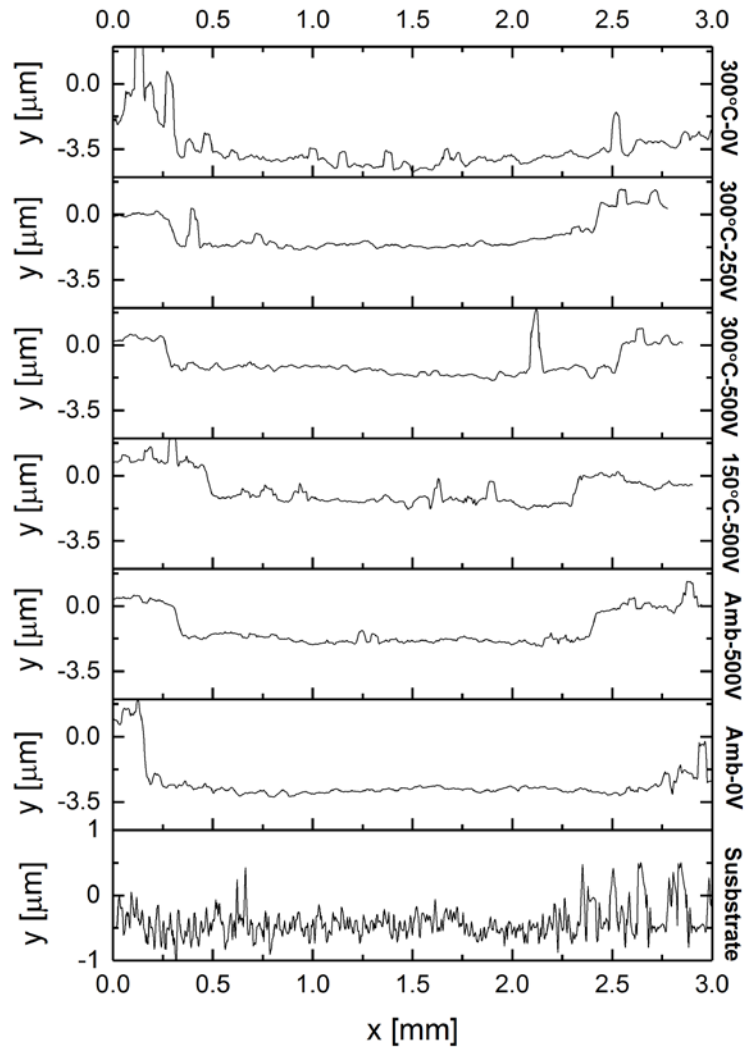


Figure 62. Wear tracks of the CrN monolayers as a function of the deposition conditions

The coatings obtained without substrate bias voltage whatever the deposition temperature have the higher wear rates ($2.33 \times 10^{-4} \text{ mm}^3 \cdot \text{N}^{-1} \cdot \text{m}^{-1}$ and $4.34 \times 10^{-4} \text{ mm}^3 \cdot \text{N}^{-1} \cdot \text{m}^{-1}$). The coatings realized at higher temperature or with a substrate bias voltage present a wear rate 10 times lower than these two coatings. Romero et al. [245] have shown that the wear rate decreases when the bias voltage of the substrate increases. The substrate bias voltage influenced the wear resistance in the contrary to the deposition temperature. These results are consistent with the work of Ye et al. [205]. Indeed, Kok et al. [216] asserted that wear of coatings correlates well with friction performance, especially films with lower coefficients of friction experience low wear rates. This can be explained by a better adhesion and hardness of the four coatings obtained with a substrate bias voltage (see Chapter 3, section 3.2.2.4.2 and 3.2.2.4.3).

It is noteworthy that our CrN monolayers are less wear resistant (wear rate in order of $10^{-4} \text{ mm}^3 \cdot \text{N}^{-1} \cdot \text{m}^{-1}$) than the CrN monolayers (wear rate in order of $10^{-8} \text{ mm}^3 \cdot \text{N}^{-1} \cdot \text{m}^{-1}$) developed by

Aouadi [111]. This can be explained by the influence of the substrate rotation speed as showed Yousaf et al. [236]. They observed a higher wear resistance for AlTiN/MoN multilayers obtained by cathodic arc ion-plating at 1 and 4 rpm while the coatings obtained at 2, 3 and 5 rpm are less wear resistant. These results are probably also influenced by the deposition technique (energy of the particles, incident angle of the different species, etc.).

3.2.2.4. Mechanical properties

3.2.2.4.1. Residual stress

The residual stresses of the CrN monolayers were determined by measuring the radius of curvature of the samples after deposition on silicon. Optical profilometer profiles of the samples before and after deposition were carried out. The radii of curvature are then calculated with the Gwyddion software.

The residual stress of the CrN coatings are presented in *Table 18* and *Figure 63*.

Table 18. Residual stress of the CrN monolayer as a function of the deposition conditions

Deposition conditions	Ambient -0 V	Ambient T°-500V	150°C-500V	300°C-500V	300°C-250V	300°C-0V
Residual stress (MPa)	24.5	70.8	48.8	40.2	22.1	18.6

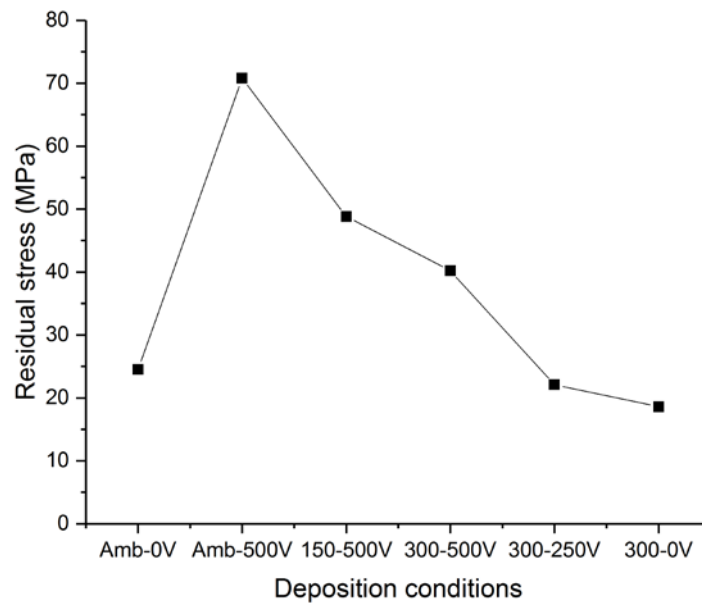


Figure 63. Residual stress of the CrN monolayers as a function of the deposition conditions

All the CrN monolayers have tensile stress varying from 18.6 MPa to 70.8 MPa. We corroborate here the XRD patterns that showed us that the stress should be tensile as the diffraction peaks were shifted on the left of their theoretical position (*Figure 58*). In *Figure 63* it is obvious that the increase of the bias voltage from 0 to -500 V at ambient temperature results in the increase of the tensile stress from 24.5 MPa to 70.8 MPa. A similar result is observed when the temperature is fixed to 300°C and when the bias voltage varies from 0 to -500 V. The residual stress varies from 18.6 to 40.2 MPa. Nevertheless, if the bias voltage is fixed to -500 V and for a deposition temperature increasing from ambient to 300°C, the residual stress decreases from 70.8 to 40.2 MPa. It is then obvious that the bias voltage increases the residual stress while the temperature reduces it. Similar results were observed by Kong et al. [246] for CrN layers deposited on stainless steel and Si (111) substrates via medium frequency magnetron sputtering under a systematic variation of the substrate bias voltage.

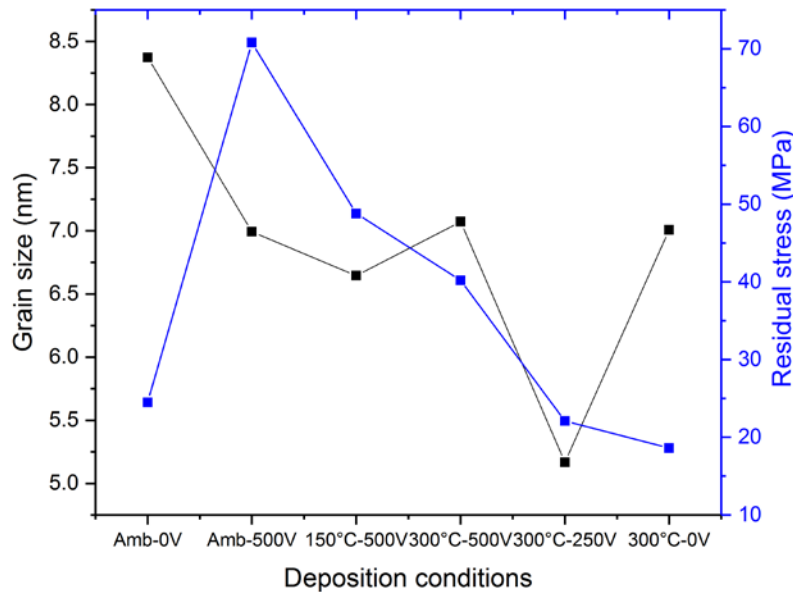


Figure 64. Grain size and residual stress of the CrN monolayers

It is obvious in *Figure 64* that the grain size is inversely proportional to the residual stress of almost all of the CrN monolayers. This result shows that the intrinsic stress of the CrN monolayers is governed by the grain size. From this result we can conclude that in the CrN coatings, larger grains correspond to lower intrinsic stresses. This is especially the case for the following CrN coatings obtained at a fixed deposition temperature and when the substrate bias increases (*Figure 64*). Espinoza-Beltran et al. [247] explained that this behavior can be due to the increase of the kinetic energy of the particles impacting the coating; as a consequence, there is an increase in the surface mobility of the atoms forming the coating, leading to larger crystallites and lower intrinsic stresses.

It is noteworthy that we obtained a tensile residual stress of 40.2 MPa for the coating obtained at 300°C and -500 V while Aouadi [111] observed a twice higher tensile stress of around 80 MPa. Wang et al. [248] showed that in the case of TiC/GLC composites obtained by magnetron sputtering, the internal stress increase with the substrate rotation speed. They explained that “the bombardment was enhanced since the kinetic energy of as-grown surface was raised by increasing rotational speed, which result in the internal stress increased with rotational speed”.

3.2.2.4.2. Hardness and elastic modulus

The results from nanoindentation are first calculated by an implement model, the wide spread Olivier & Pharr method [187], then post-treated by another method [249] and further fitted in a multilayer model [250]. The results of nanoindentation tests realized on coated silicon substrates are shown in *Figure 65*.

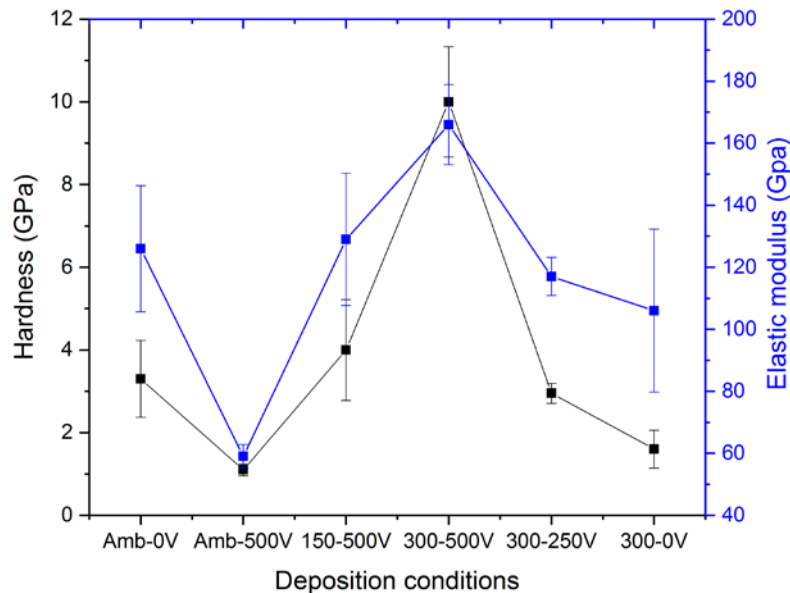


Figure 65. Hardness and elastic modulus of the CrN monolayers under different coating conditions on silicon substrate

The hardness of the CrN coatings varies from 1.1 GPa to 10 GPa, while the elastic modulus varies from 59 GPa to 166 GPa. The values of hardness, elastic modulus and H^3/E^2 , which is a plastic deformation resistance indicator, are listed in *Table 19*.

Table 19. Hardness, elastic modulus, elastic and plastic deformation resistance H/E and H³/E² of the CrN monolayers on silicon substrate and mirror-polished WC substrate

Mechanical properties		H (GPa)	E (GPa)	H/E (×10 ⁻²)	H ³ /E ² (×10 ⁻³)
Deposition conditions					
On Si substrate	Ambient-0V	3.3	126	2.6	2.2
	Ambient-500V	1.1	59	1.9	0.4
	150°C-500V	4	129	3.1	3.9
	300°C-500V	10	166	6	36.3
	300°C-250V	2.95	117	2.5	1.9
	300°C-0V	1.6	106	1.5	0.4
On mirror- polished WC	300°C-500V	16.2	346	4.7	35.5
	300°C-250V	6.2	263	2.4	3.4

The coating obtained at 300°C and -500 V presents the highest hardness, elastic modulus as well as the highest H³/E² ratio.

These values of hardness and elastic modulus are in contradiction to other studies, which reported that the hardness of CrN coatings are generally around 20 GPa or even higher [112, 251–254], while the elastic modulus are generally between 230-400 GPa for an arc-evaporated CrN coating [252, 255]. The reason of this hardness and elastic modulus difference may be due to the change of deposition technique and substrate. According to Broszeit et al. [201], hardness lower than 10 GPa is obtained in rotatory PVD system. Besides Wilson et al. [116] also reported a hardness of 6 GPa for CrN coating deposited on Ti6Al4V substrate. Panich et al. [256] explained that structural and properties difference could be the result of the variation of adatom energy with substrate-target distance. It is noteworthy that Aouadi [111] obtained CrN layers with a hardness of 22 GPa and an elastic modulus of 240 GPa with a substrate rotation speed twice higher than ours. Similar results were observed by Tian et al. [237]

As expected from SEM observations (*Figure 55d*) we confirmed here that the CrN layer obtained at 300°C and -500 V is the harder.

It is obvious on *Figure 65* that the hardness and elastic modulus increase with the substrate bias voltage. Previous work [257] explained this increase by the energies of ions that bombard the substrate. On the other hand, the hardness and elastic modulus increase with the deposition temperature. Ming et al. [258] deposited BN coatings by MW-ECR radio frequency (RF)

magnetron sputtering. They observed that the hardness of BN films shows a progressive increase as the temperature increases. Balakrishnan et al. [259] reported an increasing hardness of the coatings with increasing deposition temperature owing to higher packing density and crystallinity. We confirm here the XRD and SEM observations results: the denser and well crystallized CrN layers are the one obtained at the highest deposition temperature of 300°C.

The nanoindentation tests were also conducted on two mirror-polished WC substrates synthesized at 300°C but with a substrate bias voltage of -250 and -500 V. Relatively higher hardness and elastic modulus are obtained, as shown in *Table 19*. While the H^3/E^2 indicator is similar to the ones on silicon substrate.

According to Zegtouf et al. [260] “The resistance to contact damage depends not only on the hardness of the films but on the H/E and H^3/E^2 ratios too. The H/E ratio is a good reference of the amount of strain in a film without the appearance of permanent deformation. The H^3/E^2 ratio (i.e. elastic strain to failure) is an estimation of the resistance to plastic deformation and to predict their resistance to wear during contact events. In order to provide a better resistance, the thin films must have a high H/E and H^3/E^2 ”. The H/E and H^3/E^2 ratios of the CrN monolayers of this study are presented in *Table 19*. As the substrate bias voltage increases, we can see that the strain of a film and its resistance to wear increase. The maximum values of H/E and H^3/E^2 ratio are found for the CrN monolayer obtained for -500 V at 300 °C whatever the substrate (*Table 19*).

Figure 66 illustrates the hardness and residual stress of CrN monolayers deposited on silicon.

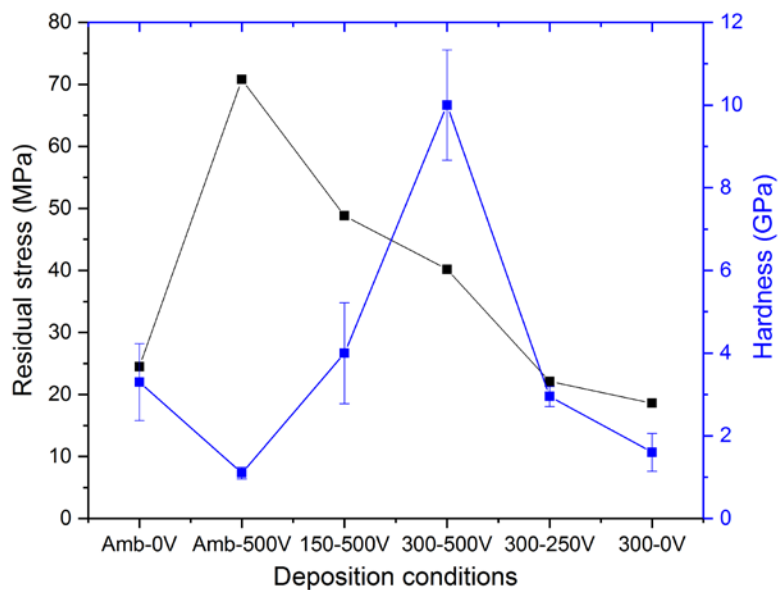


Figure 66. Residual stress and hardness of the CrN monolayers on silicon substrate

When the substrate bias is fixed to -500 V, the residual stress decreases when the deposition temperature increases while the hardness increases. According to Escobar et al. [261] at low temperature “the calculated stress is normally associated with intrinsic stresses because the thermal expansion factor (extrinsic stress) is generally low compared to that produced by the deposition process (intrinsic stress). Nucleation processes for crystal growth are not relaxation mechanisms because of the high energy of the deposition process and the poor mobility of adatoms caused by the low values”. This leads to high stresses. Then when the deposition temperature increases, “the adatoms increase in mobility, so do the relaxation processes and defects due to film densification and impurity evaporation decrease. Therefore, lower intrinsic stresses are generated”. As far as the hardness is concerned, it increases with the deposition temperature, this result can be explained by the grain size evolution (“inverse Hall-Petch effect”). “Hall-Petch establishes an inverse dependence between the domain size and the material hardness. This dependence is caused by the limitation of dislocations in movement due to high density at the boundary”. In our case, the grain size increases as the hardness in some deposition conditions according to the “inverse Hall-Petch effect” (at ambient temperature when the substrate bias decreases from -500 to 0 V, at -500 V when the deposition temperature increases from 150 to 300 °C and at 300 °C when the substrate bias increases from 250 to 500 V *Figure 67*).

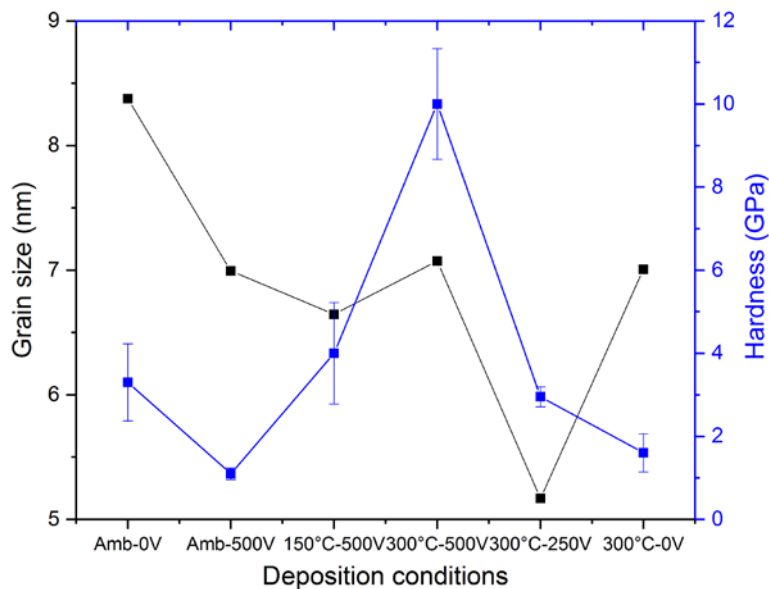


Figure 67. Grain size and hardness of the CrN monolayers

Nevertheless, when the deposition temperature is fixed to 300°C, the hardness and the residual stress increase with the substrate bias voltage. We can confirm here that the main residual stress

are the thermal ones as explained above when the temperature and substrate bias are high while the hardness is still a result of the inverse Hall-Petch effect.

The correlation between plastic deformation resistance and wear rate is illustrated in *Figure 68*.

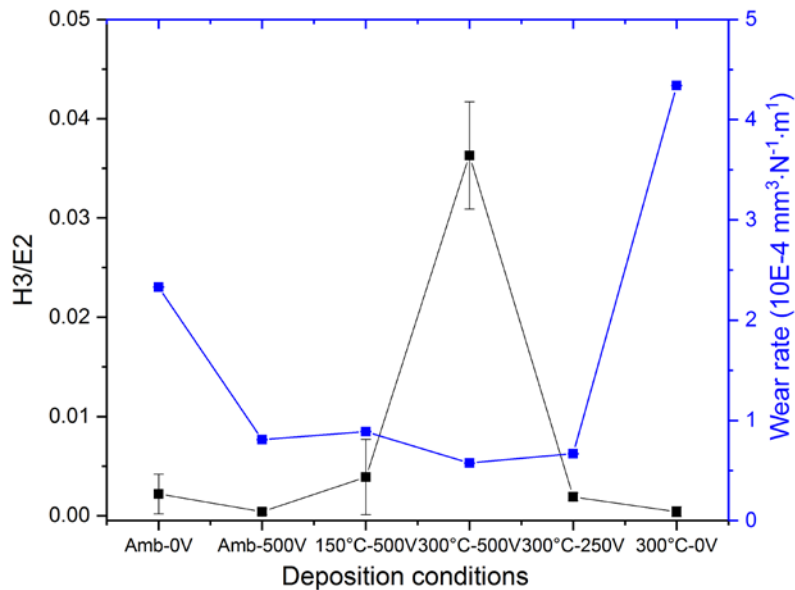


Figure 68. Wear rate and plastic deformation resistance of the CrN monolayers

It is obvious that the CrN layer showing the best plastic deformation is the one obtained at 300°C and -500 V.

3.2.2.4.3. Adhesion

The failure mode of Bull [262] will be used to identify the damages of the coatings during scratch-tests (*Figure 69*).

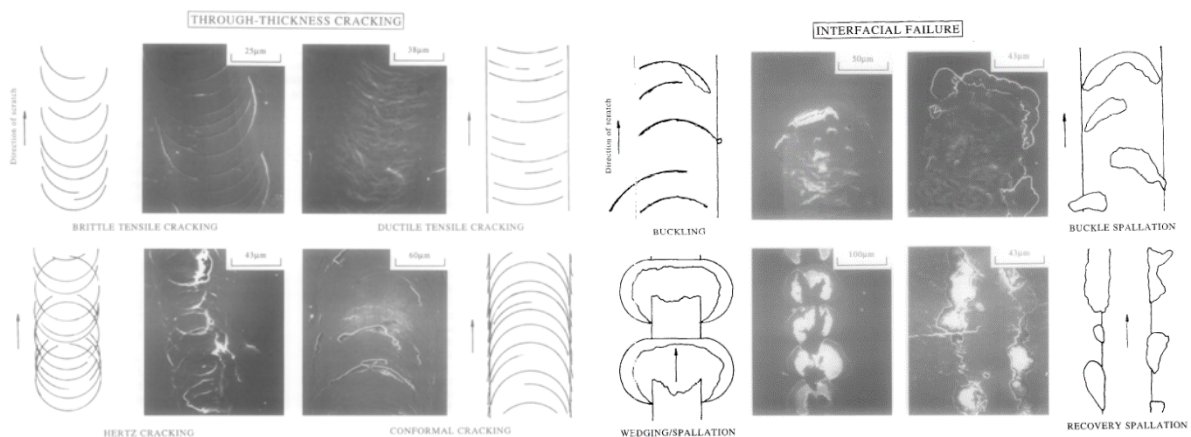


Figure 69. Classification of different failure mode of thin films after scratch test [262]

CrN monolayers present a buckling crack mode (*Figure 71*, *Figure 72* and *Figure 73*). Localized regions containing interfacial defects allow the coating to buckle in response to the

stress applied during the scratch-test. This failure mode typically appears as curved cracks extend to the edges of the scratch track.

Table 20 summarizes the critical loads and work of adhesion of the CrN monolayers.

Table 20. Critical load and work of adhesion of CrN monolayers

Deposition conditions \ Properties	Ambient -0V	Ambient -500V	150°C -500V	300°C -500V	300°C -250V	300°C -0V
L_{c1} (N)	6	7	9	20	10	6
L_{c2} (N)	9	32	38	43	20	15
W_{ad} (J/m ²)	4.3	14.6	7.6	4.5	12.9	23.16

The model of Bull and Rickerby [192] is employed to reveal the adhesion performance of coatings by the work of adhesion W_{ad} . The work of adhesion is calculated by Equation 17.

The residual stress and the work of adhesion of CrN monolayers under different deposition conditions are represented in Figure 70.

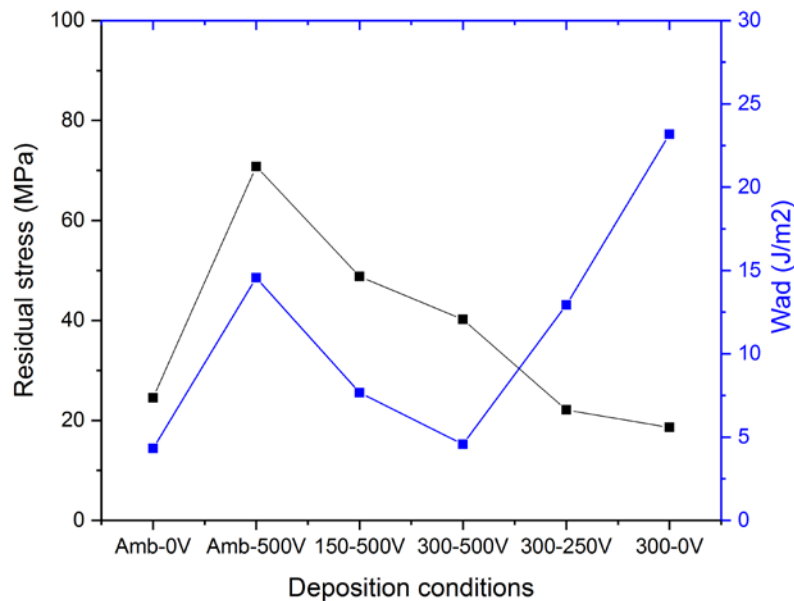


Figure 70. Relation between residual stress and work of adhesion work for CrN monolayers

When the substrate bias voltage is fixed at -500 V, increasing the deposition temperature results in a decrease of the work of adhesion, as well as the residual stress. When the deposition temperature is fixed at 300°C, decreasing the substrate bias voltage results in the work of adhesion increase while the residual stress decreases.

We verified here the results of Nouveau [112] who observed also in the case of CrN layers realized by RF magnetron sputtering that the critical loads are related reversely to the work of adhesion.

According to *Table 20*, the highest critical loads are obtained for the monolayer synthesized at 300°C and -500 V. We verify here that the substrate rotation speed has no influence on the adhesion of the layers as Aouadi [111] got the same Lc2 critical load for his own CrN layer synthesized at 3 rpm instead of 1.5 rpm as we did. One can also note that all the layers synthesized at the highest substrate bias voltage have the highest Lc2 critical load.

Figure 71, *Figure 72* and *Figure 73* present the optical images where the critical loads took place on rough and mirror-polished WC substrate, respectively.

The CrN monolayer synthesized at 300°C and -500 V shows plastic deformation until 20 N when first crack appears. We can observe a wedging spallation according to Bull [262]. Then it exhibits some regular internal cracks until about 50 N before the total delamination of the coating from the substrate occurs. Some recovery spallation is also observed according to Bull [262]. Concerning the CrN coating obtained at 300°C and -250 V, internal cracks appear at the very beginning of the scratch test and then propagate all along the track.

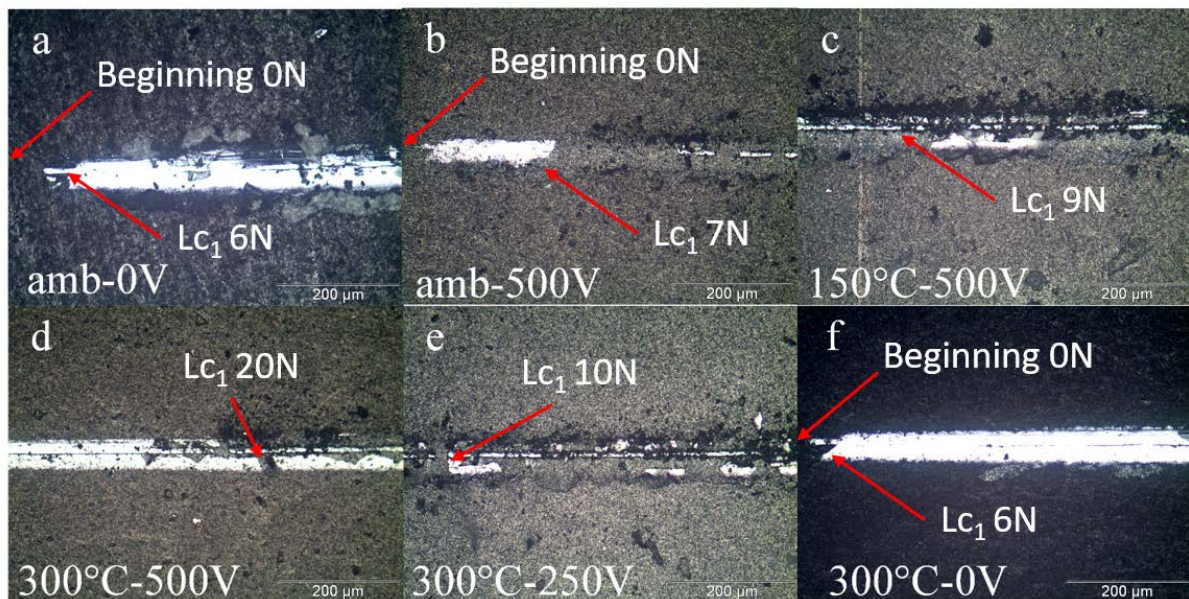


Figure 71. Optical images of critical load Lc1 of the CrN monolayers on rough WC substrate obtained at: a) Ambient-0V, b) Ambient-500V, c) 150°C-500V, d) 300°C-500V, e) 300°C-250V, f) 300°C-0V

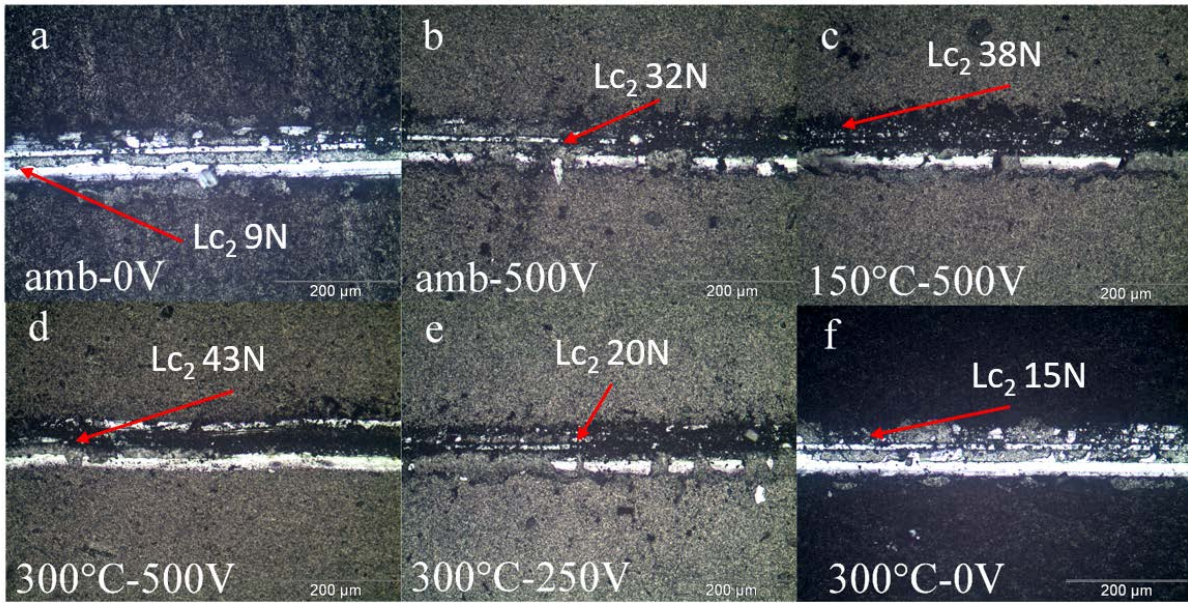


Figure 72 Optical images of critical load L_{c2} of the CrN monolayers on rough WC substrate obtained at: a) Ambient-0V, b) Ambient-500V, c) 150°C-500V, d) 300°C-500V, e) 300°C-250V, f) 300°C-0V

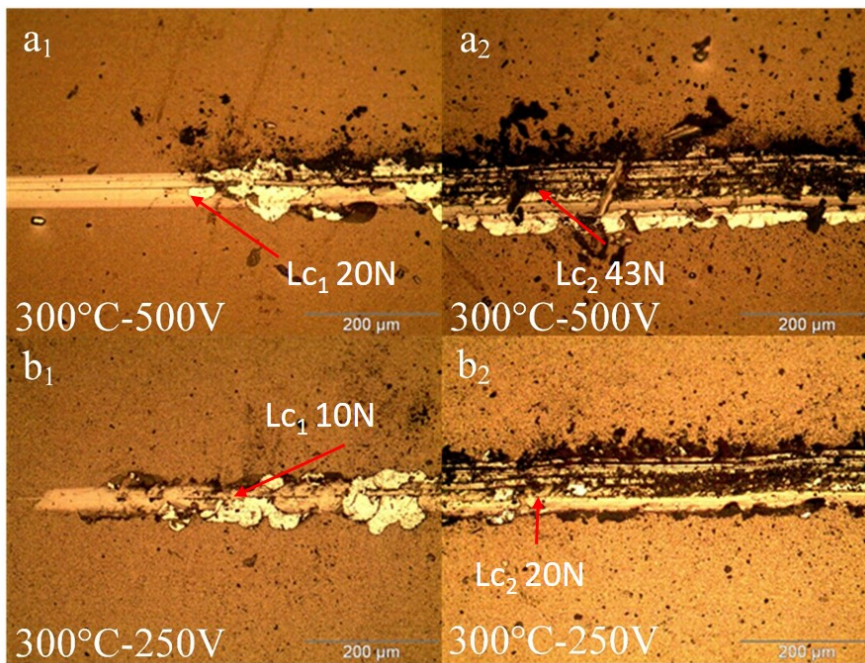


Figure 73. Optical images of critical loads of the CrN monolayers obtained on WC polished substrates at: a1) L_{c1} 300°C-500V, a2) L_{c2} 300°C-500V, b1) L_{c1} 300°C-250V and b2) L_{c2} 300°C-250V

Figure 74 illustrates the evolution of the CrN monolayers critical loads as a function of the deposition conditions.

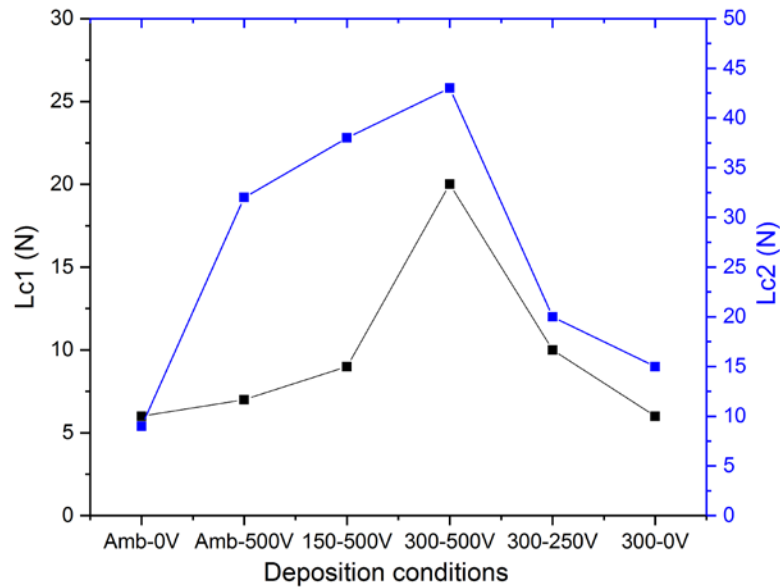


Figure 74. Critical loads of the CrN monolayers as a function of the deposition conditions

A better adhesion appears for the CrN monolayer synthesized at 300°C and -500V with a L_{c2} up to 43 N. It is obvious on *Figure 74* that the adhesion, L_{c1} and L_{c2} critical loads, increases with the substrate bias voltage and the deposition temperature. Niu et al. [263] studied Ti–Zr–N (multi-phase) films prepared by cathodic vacuum arc technique with different substrate bias voltage (0 to -500 V). They showed that the pack density, bombardment and implantation effect are enhanced with the increase of substrate bias voltage, which results in the improvement of adhesion strength.

To explain the influence of the deposition temperature on the adhesion of the CrN monolayers, Thouless model [264, 265] pointed out that the adhesion energy is directly proportional to the elastic modulus of the coatings as we verified on *Figure 75*. It must be also pointed out on the adhesion energy or interfacial energy which determines the spallation of the coatings from the substrate. From *Figure 75*, it is clear that the coatings deposited at 300°C has the highest elastic modulus (166 GPa). Therefore, both the critical load and adhesion energy suggest that the coating deposited at 300°C and -500 V has better adhesion strength (*Figure 74* and *Figure 75*).

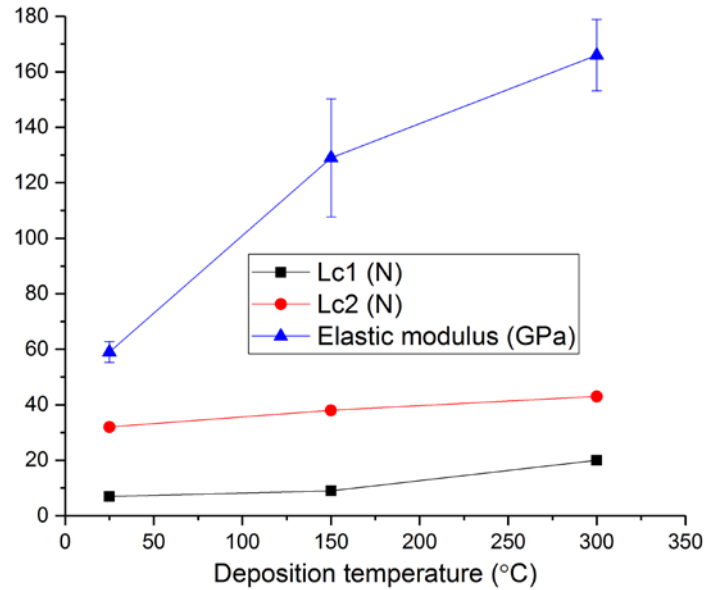


Figure 75. Evolution of the Lc1, Lc2 critical loads of the CrN monolayers and their elastic modulus as a function of the deposition temperature

3.2.2.5. Partial conclusion

In this part we developed CrN monolayers by varying the deposition temperature and substrate bias voltage. The influence of both deposition parameters was shown. Moreover, mostly we verified the results obtained previously by Aouadi [111]. When we obtained different results, we showed the influence of the substrate rotation speed. According to its properties, the CrN monolayer deposited under 300°C and -500V exhibits a (200) preferred crystalline orientation, it is well crystallized, it has a dense surface morphology and small top column size (grain size of around 7 nm). Concerning its mechanical properties, it presents the highest hardness and elastic modulus, the best plastic deformation resistance and has a very good adhesion up to 43 N (Lc2) and finally the lowest wear rate of $0.58 \times 10^{-4} \text{ mm}^3 \cdot \text{m}^{-1} \cdot \text{N}^{-1}$. This optimized CrN monolayer will be realized in the different multilayers we are going to present in the multilayers section.

3.2.3. Cr_{1-x}Al_xN coatings

3.2.3.1. Optimization of the Al content

In this part, we will develop CrAlN films by reactive magnetron sputtering. The objective is to study the effect of the Al content in the layer on its structural, mechanical and tribological properties. The substitution of chromium from Cr-N matrix by additional aluminum shall

improve the performance of the coating as mentioned in Chapter 1, but also by Schmitt [266]. For concentrations below 70 at.%, most authors agree that CrAlN is an exceptional candidate for severe applications such as large-scale machining speed. This is similar in the case of adding aluminum into TiN. A lot of researchers have proved this phenomenon [169, 171, 176, 267, 268]. In the same time, the limit of Al content in the matrix is about $x = 0.64$ where the hexagonal phase of AlN will appear and reduce the performance of the coating [176, 177, 269]. The CrN carried out under a substrate bias voltage of -500 V and a deposition temperature of 300°C (previous section) was used as a reference.

3.2.3.1.1. Deposition conditions

The deposition conditions of the $Cr_{1-x}Al_xN$ monolayers are listed in *Table 21*.

Table 21. Deposition conditions of the $Cr_{1-x}Al_xN$ monolayers at different target power density

	Fixed current		Fixed power	
Argon flow (sccm)	60		68.8 Aouadi [111]	60
Nitrogen flow (sccm)	53		33.3 Aouadi [111]	53
Cr target power density (W/cm ²)	1.29	1.3	2.91	0.96
Alr target power density (W/cm ²)	4.81	6.81	1.94	2.91
Deposition time (min)	120		120	360
DF (Duty factor)	0.6			
Frequency (kHz)	100			

We varied the current and the power applied on the chromium or aluminum targets. The target power density was calculated from these data in *Table 21* and the surface dimension is given in Chapter 2, section 2.2.1. When the current is fixed, a variation of the power is observed, consequently an average value of the power is used for the calculation of the target power density. The Ar and N₂ flow rate was 60 sccm and 53 sccm, respectively. The working pressure was 5.10^{-3} mbar, the substrate bias voltage was -500 V and the deposition temperature was 300 °C. During the optimization of his $Cr_{1-x}Al_xN$ monolayers, Aouadi [111] kept a substrate rotation speed of 3 rpm and applied an argon flow rate of 68.8 sccm and a nitrogen flow rate of 33.3 sccm. We studied the same deposition conditions for one $Cr_{1-x}Al_xN$ layer except that we applied a substrate rotation speed of 1.5 rpm instead of 3. Then, we could compare our results with his own and verify the influence of the substrate rotation speed. However, with the PVD KENOSISTEC-KS40V-113K12 system, the automate process accepts only the power applied

on the targets as a control parameter. Then for more convenient experiences, especially during the future complex process of multilayer deposition, the study of $\text{Cr}_{1-x}\text{Al}_x\text{N}$ shifts on a fixed power.

Here we introduce a new parameter: the duty factor (DF). This is due to the well-known poisoning phenomenon during the synthesis of AlN coatings. At the beginning of our experiments, a strong arcing problem, damaging the PVD system, was detected when applying high current on the Al target. Arcing problem is a very common issue when sputtering Al targets in a nitride atmosphere [270]. The main reason is due to a glow discharge and arcs formation. It is separated into two stages: the first stage is the primary transition from normal gas state to a glow discharge; photoelectric current will be generated at the cathode when an electric field is applied between two electrodes in gas. The second stage is ions impact on the cathode and the photoelectric effect of the photons generated in the discharge that are main contributors. This second stage happens frequently to allow the regeneration of the primary electrons to insure a permanent glow discharge. The micro-arcs appeared on the surface and near-surface of the target as well as on the substrate, as shown in *Figure 76*.

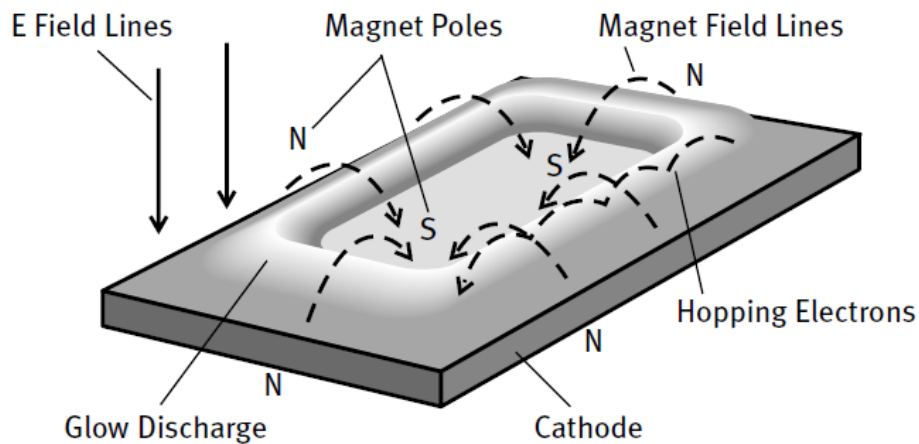


Figure 76. Glow discharge at the surface field of a target [270]

The solution to reduce the arc rate has been introduced by Carter et al. and School [271, 272]. They suggested to use a pulsed-DC current. It will then induce three new parameters: frequency (f), reverse time (t_{rev}) and duty factor (DF). The duty factor is calculated by *Equation 25*:

$$DF = \frac{\frac{1}{f} - t_{rev}}{\frac{1}{f}} \tag{Equation 25}$$

In this study, the DF factor equals to 0.6, the reverse time and frequency are set to 4 μ s and 100 kHz, respectively to avoid the arcing problem.

Nevertheless, the arcing problem still occurred. The counting of the hard arc number displayed on machine panel is almost the same when high current is applied on aluminum target. The fixed power (1500W, 2.91 W/cm²) applied on the Al target results lower power density than the fixed current (e.g. 2500W, 4.82 W/cm²), relative low power density helps to reduce the micro-arc issue. Besides the power entry values are needed for developing the multilayers with the help of automate procedure. Our objective was to obtain CrAlN layers with significant Al content variation, the further work was not focused on the reduction of the arc.

3.2.3.1.2. Physico-chemical properties

3.2.3.1.2.1. Deposition rate and thickness of the CrAlN layers

The thickness and deposition rate obtained from the SEM cross-section observations of the CrAlN coatings (*Figure 85*) are listed in *Table 22*. The thickness of the CrAlN layers varies from 0.88 to 1.41 μ m.

Table 22. Thickness and deposition rate of the Cr_{1-x}Al_xN monolayers as a function of the targets power density

Cr target power density (W/cm ²)	2.91 Aouadi [111]	0.96	1.29	1.3
Al target power density (W/cm ²)	1.94 Aouadi [111]	2.91	4.81	6.81
Deposition time (min)	120	360	120	120
Thickness (μ m)	1.01	1.41	0.88	1.26
Deposition rate (nm.min ⁻¹)	8.42	3.92	7.33	10.5

The deposition rate for the CrAlN monolayer obtained with a Cr target power density of 2.91 W/cm² and an Al target power density of 1.94 W/cm² is 8.42 nm.min⁻¹. Aouadi [111] obtained a very close deposition rate even with a rotation speed twice higher than our own: 8.66 nm.min⁻¹. The rotation speed of the substrate holder does not seem to have any influence in this case. Besides, when the Cr target power density is divided by a factor of 3, the deposition rate is very low (3.92 nm.min⁻¹) even if the Al target power density increased from 1.94 to 2.91 W/cm². This is explained by the sputter yield that is twice higher for chromium than for aluminum [274] : the sputter yield of Cr etched under Ar⁺ incident ions at 200 eV is 0.67 while the one of Al is

0.35. As expected, the targets power density has a high influence on the deposition rate of the CrAlN layers.

According to *Figure 77*, it is obvious that the deposition rate varies with the Cr and Al target density.

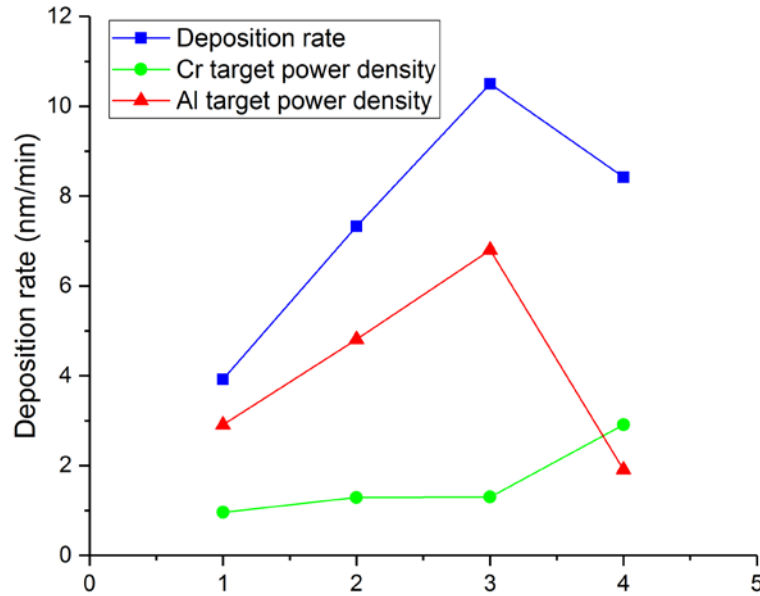


Figure 77. Deposition rate of the $Cr_{1-x}Al_xN$ monolayers as a function of the targets power density

In the three first cases, it increases with the power densities, nevertheless, for the layer obtained at 1.91 W/cm² on the Al target and 2.91 W/cm² on the Cr target, the deposition rate decreases. This can be explained by the fact that this coating has been realized with a different Ar/N₂ flow rate ratio: 68.8/33.3 instead of 60/53. Besides, as the Cr target density increases for this layer, the Al target density drastically decreases. As a result of both deposition conditions changes, the deposition rate decreases.

3.2.3.1.2.2. Chemical composition by EDS microanalyses

Table 23 summarizes the chemical composition of the CrAlN monolayers obtained on WC substrate as a function of the deposition conditions. The Al content vary from 13.6 to 73.9 at.% which is a significant range to determine the optimal Al content. We observe that the CrAlN monolayers have a very good quality with no more than 2.7 at.% of oxygen. The nitrogen content is also almost the same for all the CrAlN coatings. It varies from 45.4 to 47.1 at.%.

Table 23. Chemical composition of the $Cr_{1-x}Al_xN$ monolayers

Cr target density (W/cm ²)	Al target density (W/cm ²)	Cr (at.%)	Al (at.%)	N (at.%)	O (at.%)	Al/(Cr+Al) ($\times 10^{-2}$)	Al/Cr
2.91	1.94	44.8	7.1	45.4	2.7	13.6	0.16
1.29	4.81	23.0	29.9	47.1	0.0	56.5	1.3
0.96	2.91	20.5	32.8	46.6	0.1	61.5	1.6
1.3	6.8	14.1	40.1	45.8	0.0	73.9	2.84
Aouadi [111]	Aouadi [111]	41.35	6.9	46	6.9	14.3	0.17

As expected, when the Cr target power density decreases and the Al target power density increases, the Cr content decreases while the Al one increases (Figure 78 and Table 23). We have clearly here a representation of the Cr substitution by Al atoms in the CrAlN ternary coatings.

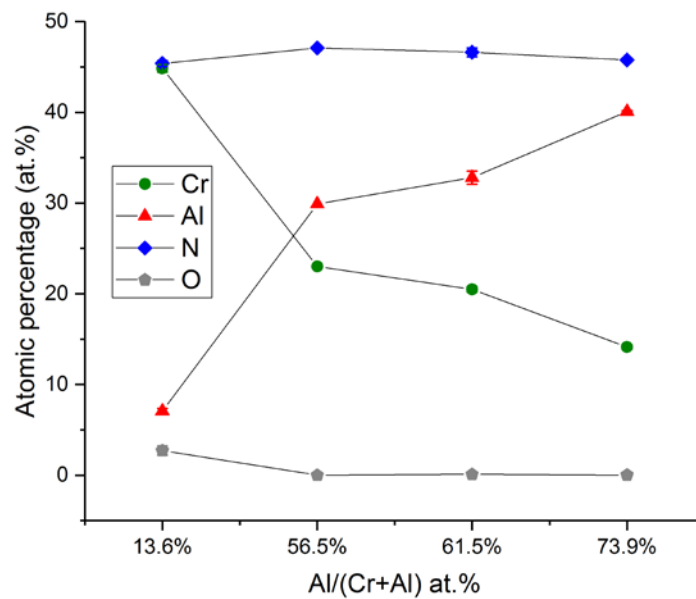


Figure 78. Chemical composition of $Cr_{1-x}Al_xN$ monolayers as a function of the Al content

Finally, the reproducibility of the CrAlN deposition process was verified. Indeed, Aouadi [111] obtained a chemical composition of 41.35 at.%, 6.9 at.%, 46 at.% and 6.9 at.% of Cr, Al, N and O, respectively, in his own layer realized at 3 rpm. The substrate rotation speed does not seem to have an influence on the chemical composition of the CrAlN layers except for the oxygen content that is 3 times higher. Indeed, as the substrate is faster, it is more exposed to the unused targets of our PVD system and to the walls of the chamber that most of the time contain impurities such as oxygen or carbon.

3.2.3.1.2.3. Chemical composition by XPS analyses

As our objective is to develop CrAlN monolayers on WC substrate with the Al/(Al+Cr) ratio of about 0.6, we realized XPS analyses on the coatings that have an Al/(Cr+Al) ratio of 61.5×10^{-2} (Figure 79) and 73.9×10^{-2} (Figure 80 and Figure 81).

For the CrAlN layer with 61.5 at.% of Al, argon ion bombardments were carried out as described in Table 24.

Table 24. Chemical composition of the CrAlN layer with 61.5 at.% of Al from XPS

Etching conditions	Etched thickness	% C1s	% O1s	% N1s	% Al2p	% Cr2p	Al/(Cr+Al) ($\times 10^{-2}$)	Al/Cr
Before etching	0	25.1	25.3	29.7	11.7	8.3	58.5	1.41
After etching at 500eV- 2min	~ 2 nm	9.9	26.3	30	22.1	11.7	65.4	1.89
After etching at 500eV- 2min + 2keV- 2min	~ 12 nm	5	16.9	34.9	25.8	17.5	59.6	1.47
After etching at 500eV-2min + 2keV- 6min	~ 32 nm	3.6	11.4	38.2	27.6	19.3	58.8	1.43
	EDS results (at.%)	-	0.1	46.6	32.8	20.5	61.5	1.6

The Al/(Cr+Al) ratio is 58.8×10^{-2} not so close to the one obtained by EDS (61.5×10^{-2}). As there was still a no negligible amount of C and O in this layer, another etching at 4 keV during 10 minutes was realized. The Cr2p_{3/2}, Al2p_{3/2}, N1s and O1s spectra are illustrated in Figure 79. As a conclusion for this CrAlN layer, the Al content should be close to 60 at.%.

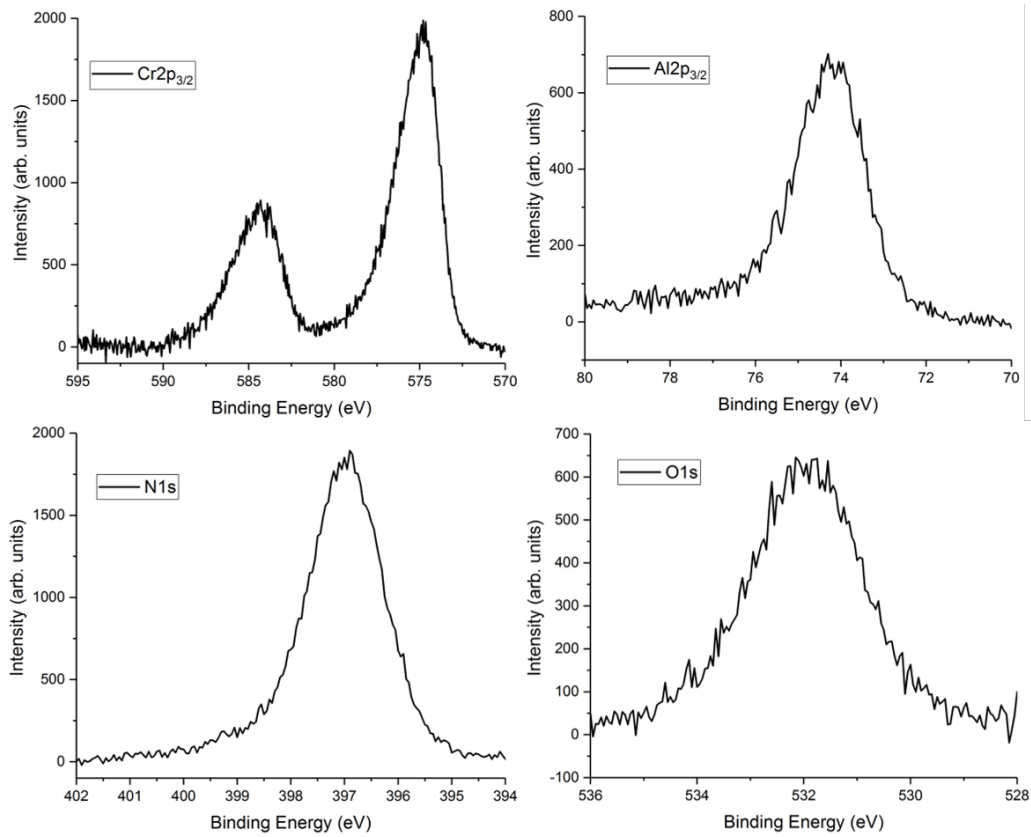


Figure 79. XPS analyses of the CrAlN monolayer with 61.5 at.% of Al

XPS analyze under the same etching parameters was carried out on the CrAlN layer containing 73.9 at.% of Al. The main spectra are shown in Figure 80 while the Cr_{2p_{3/2}}, Al_{2p_{3/2}} and N_{1s} spectra are shown in Figure 81.

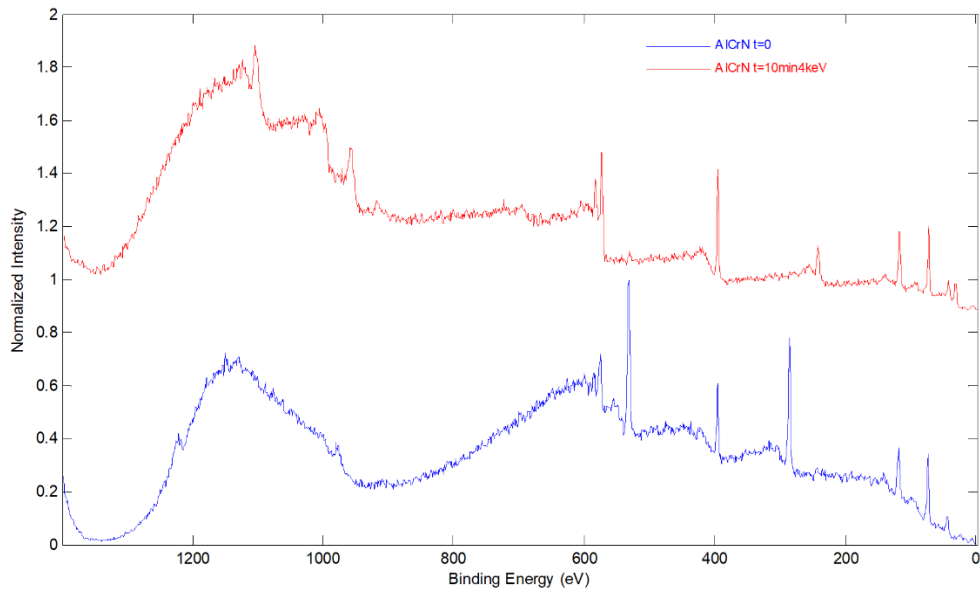


Figure 80. XPS spectra of the CrAlN monolayer containing 73.9 at.% of Al

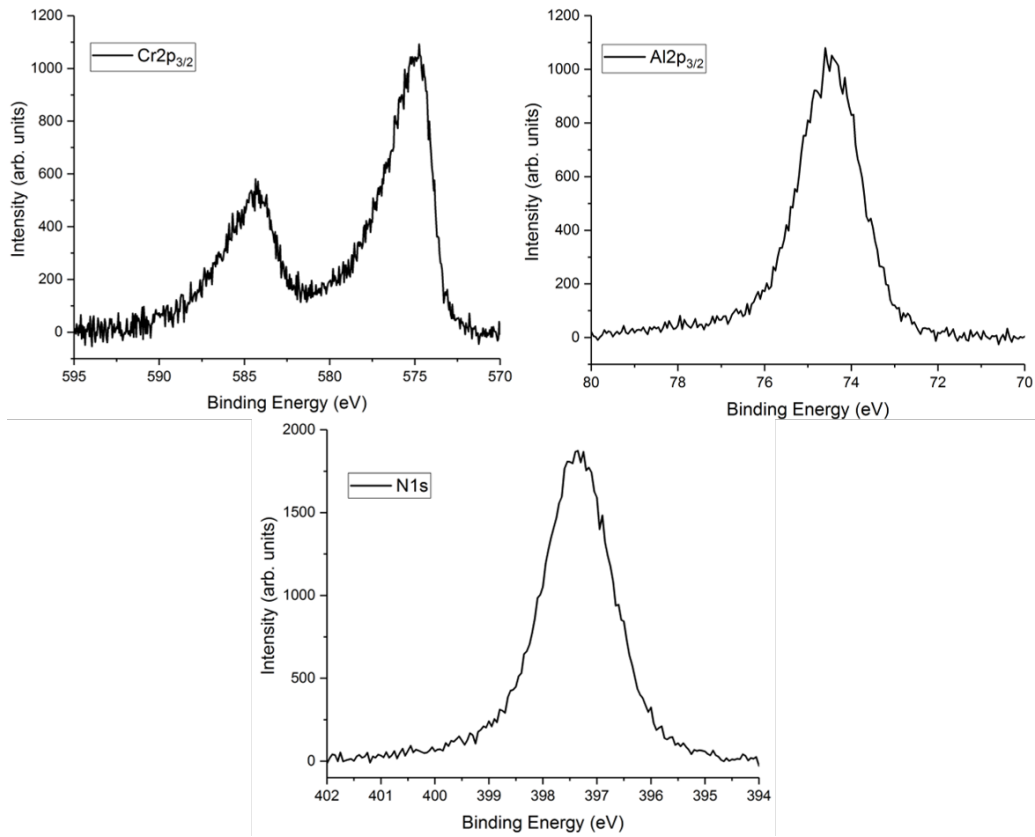


Figure 81. XPS analyses of the CrAlN monolayer with 73.9 at.% of Al.

The chemical composition after the last etching is given in Table 25.

Table 25. Chemical composition of the CrAlN layer with 73.9 at.% of Al from XPS analyses

	Cr (at.%)	Al (at.%)	N (at.%)	O (at.%)	Al/(Cr+Al) ($\times 10^{-2}$)	Al/Cr
EDS	14.1	40.1	45.8	0.0	73.9	2.84
XPS	11.7	43.3	43.2	1.8	78.7	3.7

As mentioned in section 3.2.2.2.2, the XPS results are different from the EDS results because XPS is a quantitative analyses while EDS is a semi-quantitative one.

The positions of the peaks are always relatively approximate because of their greater or lesser widths. The bibliography is rich and therefore presents results which may be contradictory. In Figure 79 and Figure 81, we observe the C1s peak at 285 eV probably carbon graphite pollution [275]. For the CrAlN layer with 61.5 at.% of Al, the Al_{2p_{3/2}} peak is at 74.25 eV, for the CrAlN layer with 73.9 at.% of Al, the Al_{2p_{3/2}} peak is at 74.5 eV, these can be attributed to AlN (at 74.4 eV) according to McGuire et al. [276]. The Cr_{2p_{3/2}} is detected at 575.3 eV for both layers, which probably corresponds to the cubic CrN phase (at 575.5 eV) according to Wagner et al.

[277]. As the amount of oxygen in our layers is very low, even in the CrAlN layer with 61.5 at.% of Al after the entire etching, we can suppose that there is no or a small amount of oxide in our CrAlN layers. Finally, the deconvolution of N1s peaks for both CrAlN monolayers is shown in *Figure 82*. For CrAlN with 61.5 at.% of Al, CrN and AlN are present at 396.8 eV [225] and 397.3 eV [278], respectively. For CrAlN with 73.9 at.% of Al, Cr₂N and AlN are detected at 397.4 eV [226, 278] while CrN is detected at 396.8 eV. As already discussed at the beginning of this section (3.2.3.1), when the aluminum content exceeds about 64 at.% of the (Cr+Al) matrix, hexagonal AlN is present instead of cubic AlN, thus the substitution of Cr forms hexagonal Cr₂N in this monolayer.

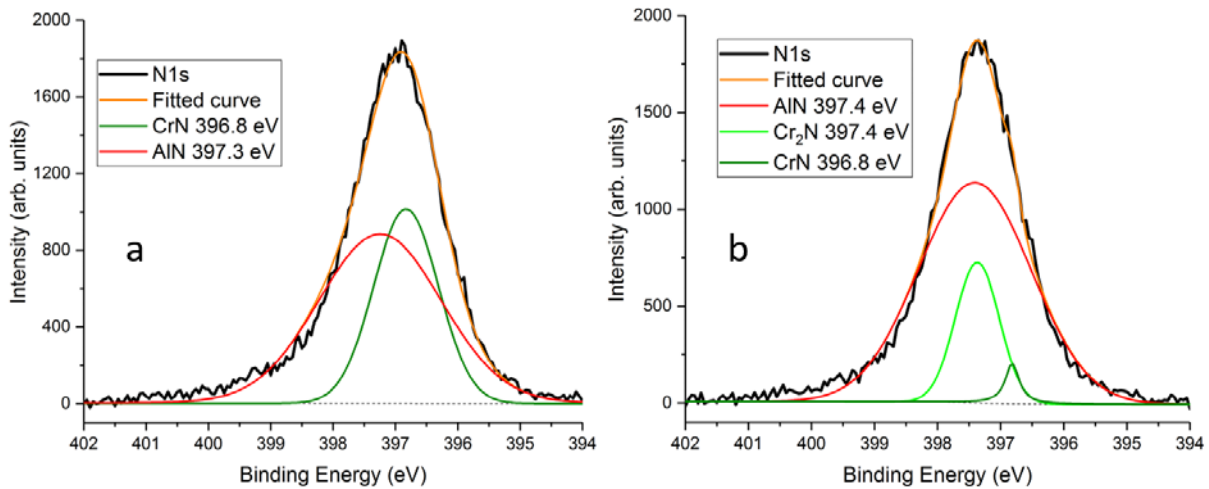


Figure 82 Deconvolution of N1s peaks: a) 61.5 at.% of Al, b) 73.9 at.% of Al

To conclude, these analyses confirm the mixture of CrN and AlN in our CrAlN layers, if there are oxides of the two metals, they are probably at the grain boundaries but in a slight proportion. The XRD should confirm this result. Moreover the XPS chemical compositions confirm the ones obtained by EDS and for the continuation of this work, a CrAlN layer with an Al content close to 60 at.% will be used to insure good mechanical properties to the mono and multilayers [266].

In the following, to lighten the name of the Cr_{1-x}Al_xN layers we studied, the *x* values will be: 0.14, 0.57, 0.62 and 0.74.

3.2.3.1.2.4. Surface morphology and microstructure

Figure 83 and *Figure 84* shows the surface morphology of the Cr_{1-x}Al_xN coatings on WC and silicon substrate. Adding aluminum content in the Cr-N system changes its topography. Indeed, larger clusters appear while aluminum is added into Cr-N. Meanwhile, Cr_{1-x}Al_xN layers exhibit different surface morphology at low (0.14), medium (0.57 and 0.62) and high (0.74) aluminum

content. At low aluminum content (0.14) in CrN, we observe a porous surface like in the case of the CrN layers. The CrAlN layers with medium Al content (*Figure 83 b and c*) have a similar surface morphology with no apparent porosity. The CrAlN layer with the highest Al content (0.74) presents sharp and small columnar clusters and an irregular surface. The clusters seem inhomogeneous; this may be due to the co-existence of cubic and hexagonal AlN phases.

On silicon substrate (*Figure 84 a*), the CrAlN layer with 14 at.% of Al presents pyramidal and porous top columns.

The porosity is well seen in *Figure 85a*. Aouadi [111] and Tlili [244] observed also a pyramidal and porous microstructure for their CrAlN layer containing 11 and 13 at.% of Al, respectively. The CrAlN with 57 or 62 at.% of Al seem very dense as confirmed on *Figure 85b and c*. The CrAlN layer with 74 at.% of Al presents the well-known columnar and porous structure (*Figure 85d*).

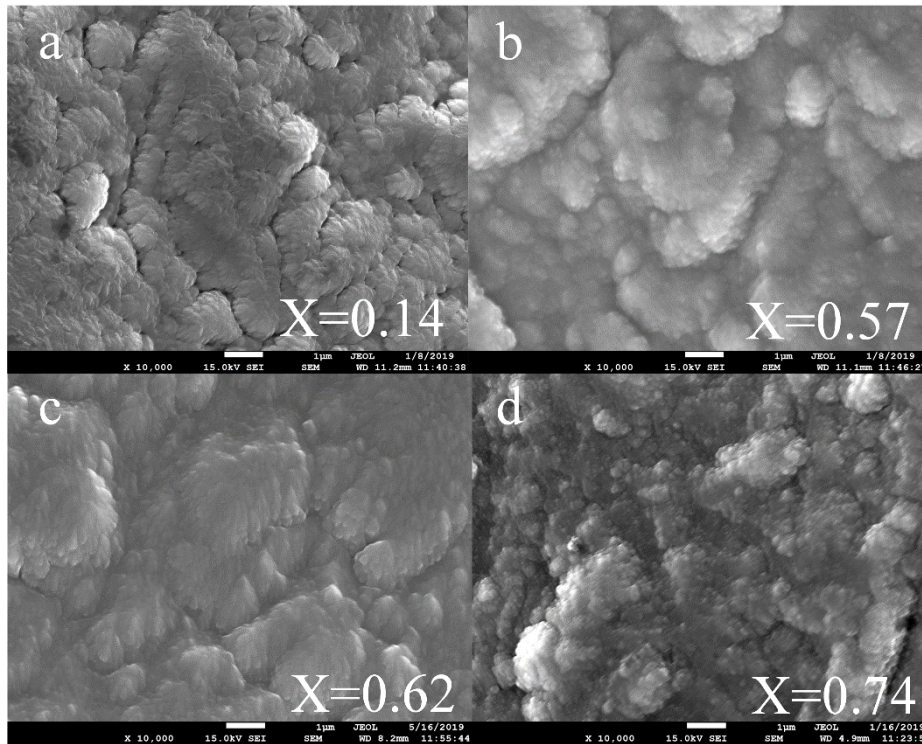


Figure 83 Surface morphology of $Cr_{1-x}Al_xN$ monolayers on WC substrate with varied Al content: a) $x=0.14$, b) $x=0.57$, c) $x=0.62$, and d) $x=0.74$

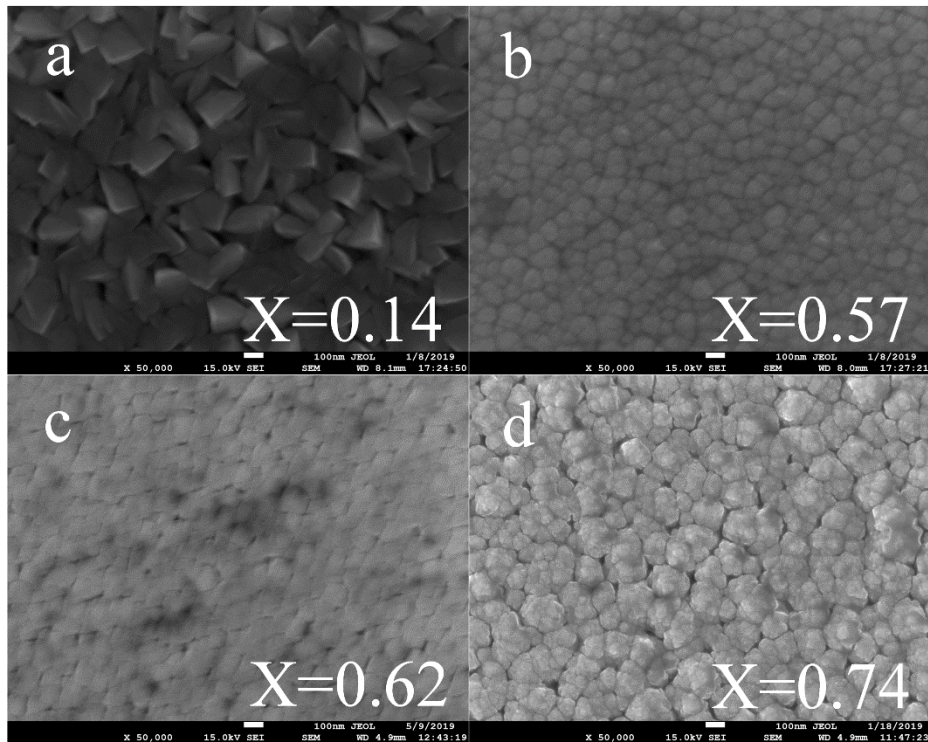


Figure 84 Surface morphology of $Cr_{1-x}Al_xN$ monolayers on silicon substrate with varied Al content: a) $x=0.14$, b) $x=0.57$, c) $x=0.62$ and d) $x=0.74$

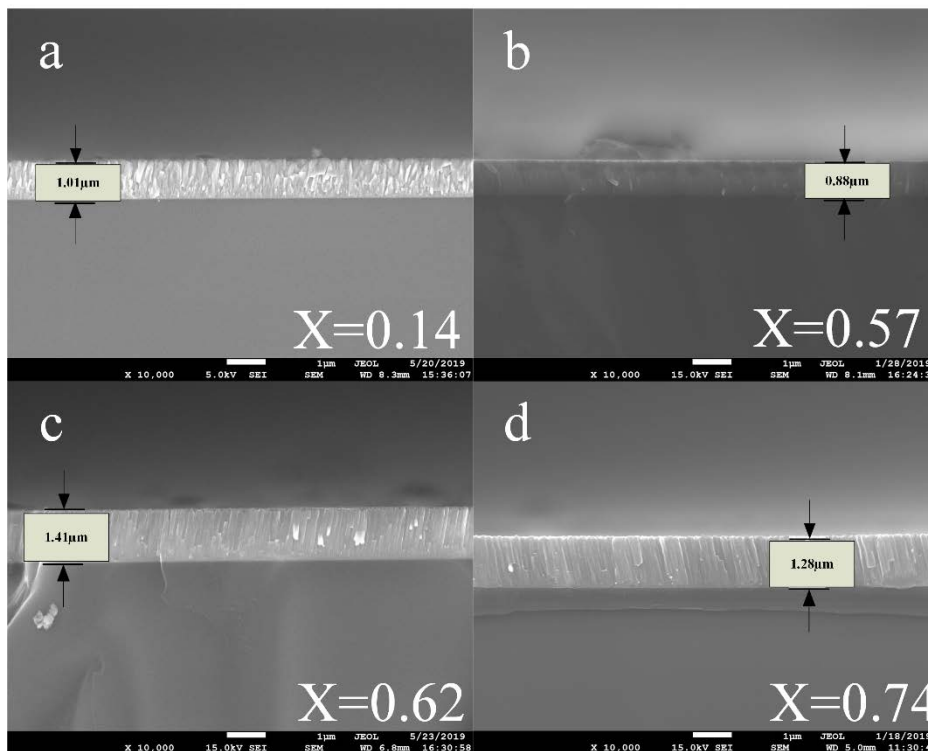


Figure 85. Cross-section images of $Cr_{1-x}Al_xN$ monolayers on silicon substrate with varied Al content: a) $x=0.14$, b) $x=0.57$, c) $x=0.62$ and d) $x=0.74$

If we compare the CrAlN of $x = 0.57$ or 0.62 with the CrN obtained at $300\text{ }^{\circ}\text{C}$ and -500 V (Figure 57d), it is obvious that the columns size of the CrAlN layers are smaller than the one of the CrN layer. Reiter et al. [170] observed a dense and granular morphology for CrN and CrAlN films. They explained that the additional Al increases the density of the layers and decreases the grain size. Lin et al. [167] found that all their CrAlN layers have a columnar structure and that the size of the lattice decreases from CrN to CrAlN (58.5 at.% of Al). On the other hand, it begins to increase from 64 at.% of Al. The effect of the Al content on column size is due to the crystalline change of the layers. These hypotheses will be investigated in the following paragraph dealing with the layers structure and grain size of the CrAlN layers.

3.2.3.1.2.5. Structure

The XRD analyses have been made on WC coated substrates (Figure 86).

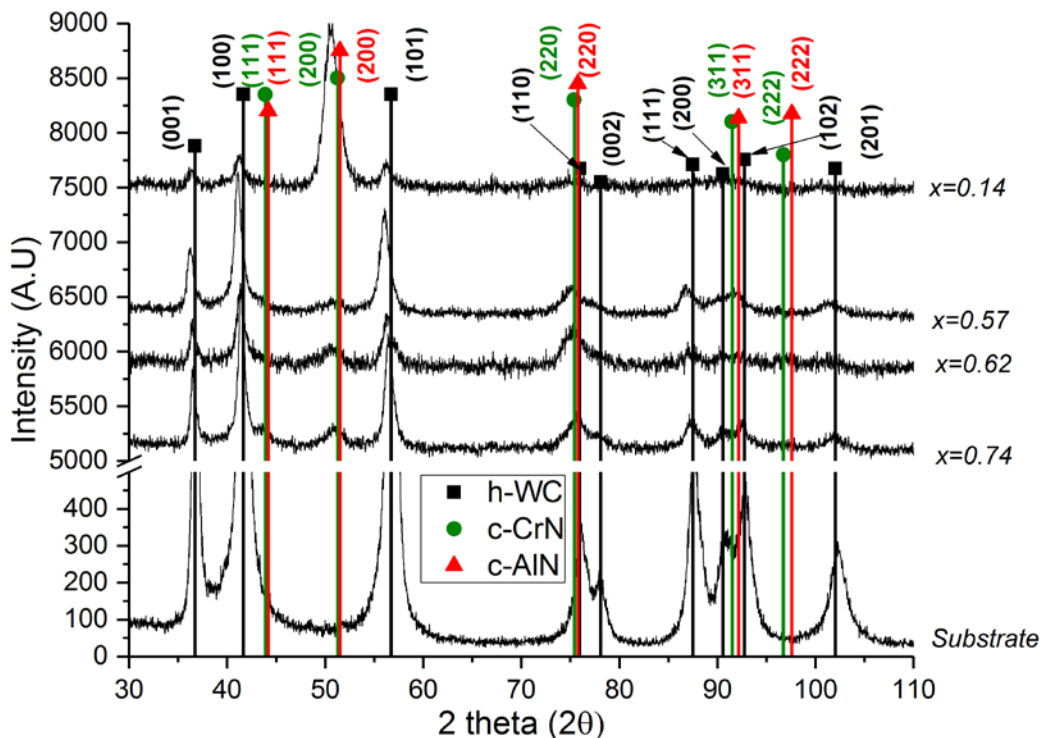


Figure 86. XRD patterns of the $\text{Cr}_{1-x}\text{Al}_x\text{N}$ monolayers with varied Al content

For an Al content of 14 at.%, a major (200) diffraction peak at 50.6° probably mainly attributed to the cubic CrN phase is shown. The theoretical position of the (200) CrN and (200) AlN diffraction peaks is 51.26° (ICDD 00-011-0065 card) and 51.47° (ICDD 00-025-1495 card), respectively. Then, according to the shift of our diffraction peaks on the left of the theoretical peaks' positions, our CrAlN layer should present some tensile stress.

For an Al content from 57 to 74 at.%, we observe a main (220) diffraction peak and a minor (200) one. Nevertheless, almost all the cubic AlN and CrN peaks are superposed or closed to the tungsten carbide substrate diffraction peaks. This is not easy to define the crystalline orientation of the CrAlN layers. Moreover, other researchers [167, 171] reported that when the aluminum content exceeds 64 at.%, the hexagonal AlN phase should be detected. This is may be the case for the CrAlN layer obtained at 74 at.% of Al even if we don't detect it. The reason could be due to the fine grain size of the AlN and the presence of boundaries, which causes difficulty for XRD analysis to detect it. So, the cubic AlN and CrN phases are detected, no obvious hexagonal AlN phase is observed in *Figure 86*.

Lin et al. [167] pointed out that when Al concentration is below 58.5 at.%, the preferred crystalline orientation is (200). When the percentage is beyond this value, the orientation is both in (111) and (200) texture. In our case, we have a (200) preferred orientation for low Al content, a (220) and minor (311) and (200) crystalline orientations for medium Al content. For the highest Al content, we have a (220), (200) and a minor (111) crystalline orientation. We can suppose that the CrAlN layers result of the coupling of two FCC phases, AlN and CrN, "which generate a conjugate complex where the Al and Cr atoms are located in the reticular positions and the aluminum atoms (Al) are replaced for the (Cr) atoms while the nitrogen is located interstitial positions of the CrAlN crystal. Furthermore, to date, the letters of the crystalline structure of the chromium aluminum nitride (CrAlN) have not been reported in the international indexing archive" according to Correa et al. [279].

At 11 at.% of Al in his CrAlN layers, Aouadi [111] observed a (200) preferred orientation of the cubic CrN phase and a minor (101) cubic AlN diffraction peak. This is probably due to the fact that he realized his coating with a substrate rotation speed of 3 rpm while we applied a rotation speed of 1.5 rpm as explained in Chapter 3, section 3.2.2.2.4.

The grain size was calculated thanks to the Debye-Scherrer formula (*Equation 10*) as mentioned above in the Cr underlayer paragraph. *Table 26* and *Figure 87* summarize the calculated grain size of the CrAlN layers as a function of the Al content.

Table 26. Grain size and diffraction peaks of the $Cr_{1-x}Al_xN$ monolayers

Al content (at.%)	Grain size (nm)	Diffraction peak as reference	Diffraction peaks detected by XRD
13.6	5.6	200	(200)
56.5	4.19	220	(220) (311) (200)
61.5	3.68	220	(220) (311) (200)
73.9	5.34	220	(220) (311) (111)

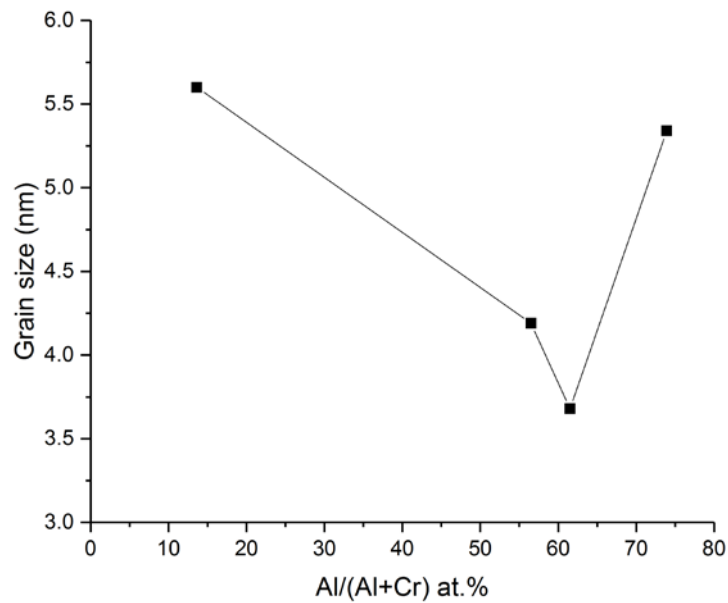


Figure 87. Grain size of the $Cr_{1-x}Al_xN$ monolayers at different Al content

The grain size of CrAlN layers are very small and even smaller than the CrN ones. An identical behavior is observed in the study by Reiter et al. [170] where the calculation of the crystallite size using the Rietveld method gives values of 12 nm for CrN and 6 nm for CrAlN, i.e. twice as small. The grain size of the CrAlN layer containing 62 at.% of Al is 3.68 nm, while it is 5.34 nm for the layer containing 74 at.% of Al. A similar result was obtained by Aouadi [111] who showed that the grain size for the CrAlN film with an Al content of 11 at.% is 38 nm while it is 77 nm for the CrAlN film with a Al content of 24 at.%. This can also be due to the change of crystallite orientation: (111) instead of (200) which are denser plans. We verify here that the columns diameter observed in cross section images in *Figure 85* results from a structure and grain size change. The CrAlN layers obtained with the medium Al content are the densest because of the smaller grain size and as a consequence, the smaller columns diameter.

Finally, Aouadi [111] obtained bigger grain size (38 nm) for a CrAlN layer with 11 at.% of Al than as-deposited layer with 14 at.% of Al because again, this is the effect of a twice faster substrate rotation speed (see Chapter 3, section 3.2.2.2.4).

3.2.3.1.3. Tribological properties

To study the effect of the Al content on the friction coefficient of CrAlN layers, we performed friction tests in a ball-on-disc configuration. A Ti6Al4V ball rubs on a sample of coated WC substrate. The tests are carried out in air, at room temperature and without lubrication. The friction speed is 10 cm/s and the distance traveled by the Ti6Al4V ball is 100 m. The SEM images of the wear tracks are presented in *Appendix E*. The friction coefficient is shown in *Figure 88* and varies from 0.43 to 0.52. It is similar to the CrN layers. One can notice that the COF does not depend on the Al content.

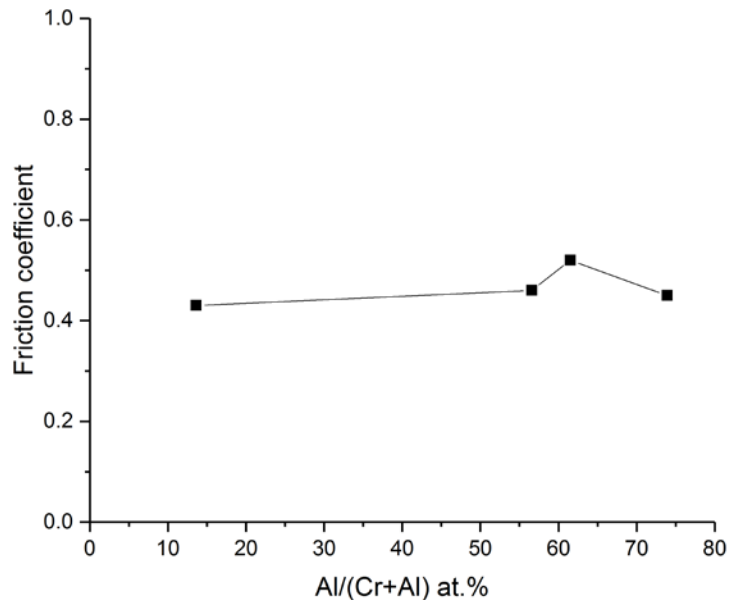


Figure 88. Friction coefficient of the $Cr_{1-x}Al_xN$ monolayers at different Al content

Aouadi [111] and Benlatreche [151] obtained higher coefficient of friction for CrAlN films from 0.6 to 0.8. This can be explained first by the fact that Benlatreche realized his CrAlN layers with a PVD system that produced rougher CrAlN layers. In the case of Aouadi [111], he obtained a COF of 0.8 for the CrAlN layer containing 11 at.% of Al. This is probably due to a higher grain size (28 nm) in comparison to our own (5.6 nm). Bigger grains tend to increase the surface roughness and as a consequence, the friction coefficient. Indeed, Pengfei et al. [280] showed that when the grain size of CrCN coatings becomes smaller, the surface becomes smoother which helps to reduce the friction coefficient. Schmitt [266] also obtained a COF of around 0.8 for his CrAlN layer during linear tribometer alternative tests.

Figure 89 illustrates the calculated wear rate according to Archard [194] as a function of the Al content in the CrAlN layers.

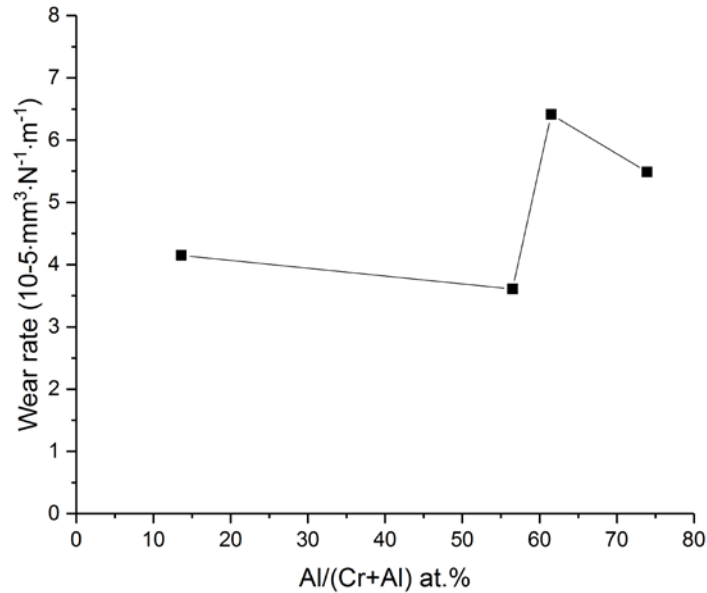


Figure 89. Wear rate of the $Cr_{1-x}Al_xN$ monolayers at different Al content

The wear rates are summarized in Table 27 and the wear tracks are presented in Figure 90.

The wear rates of the CrAlN layers are similar whatever the Al content (Figure 89 and Table 27). Indeed, the grain size of these CrAlN layers is finally very close too and they have a similar coefficient of friction. The CrAlN layers are more wear resistant than the CrN layers as also observed by Schmitt [266].

Nevertheless, in Figure 90 this is obvious that the wear track for the CrAlN layer containing 14 at.% of Al is the widest. At 57 at.% of Al, the CrAlN coating has an irregular wear track profile, which may result from the adhesion of titanium materials. The CrAlN coating with the highest amount of Al (74 at.%) has the deepest wear track, which predicts its poor wear resistance. To confirm these results, we determined the mechanical (residual stress, hardness and elastic modulus) properties of the CrAlN layers in the following paragraph.

Table 27. Wear rate of the $Cr_{1-x}Al_xN$ monolayers

Al content (at. %)	13.6	56.5	61.5	73.9
Wear rate ($\times 10^{-5} \text{ mm}^3 \cdot \text{m}^{-1} \cdot \text{N}^{-1}$)	4.15	3.61	6.41	5.49

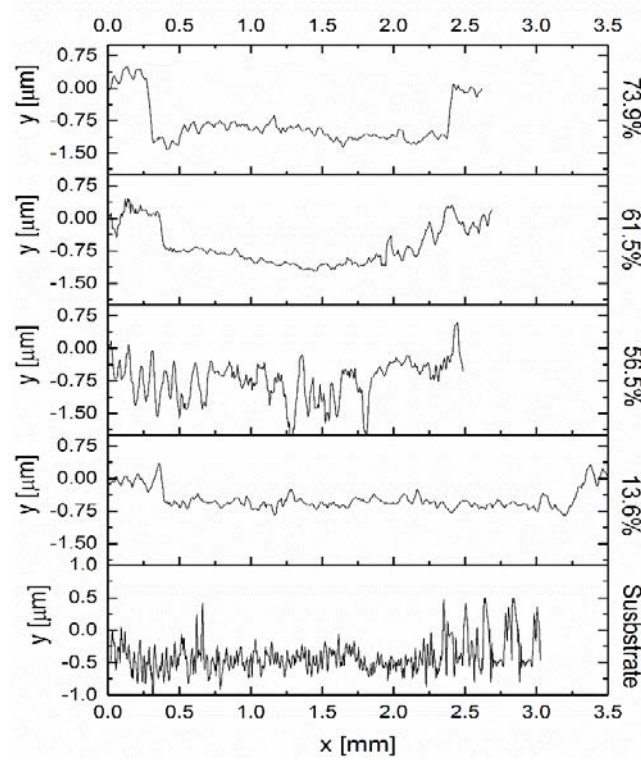


Figure 90. Wear tracks of the $Cr_{1-x}Al_xN$ monolayers at different Al content and of the WC substrate

3.2.3.1.4. Mechanical properties

3.2.3.1.4.1. Residual stress

Table 28 and Figure 91 show the evolution of the residual stress vs. the aluminum content in the $Cr_{1-x}Al_xN$ monolayers.

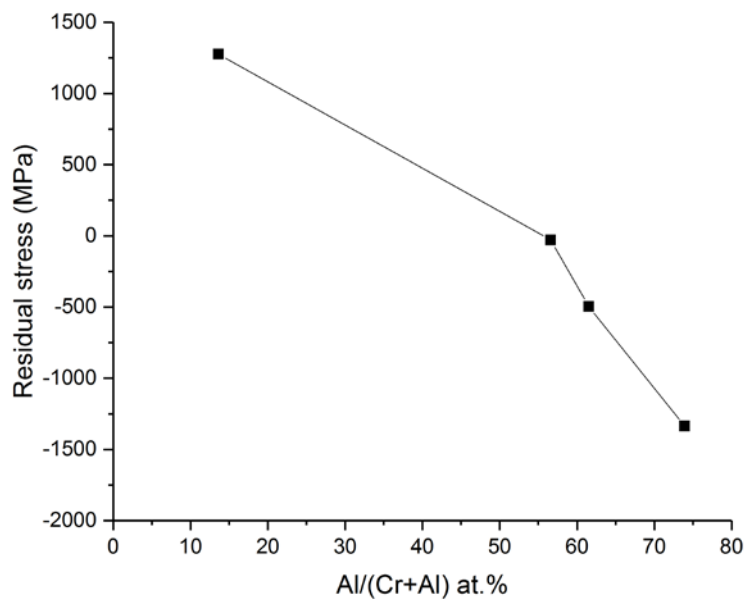


Figure 91. Residual stress of the $Cr_{1-x}Al_xN$ monolayers at different Al content

Table 28. Residual stress of the $Cr_{1-x}Al_xN$ coatings at different Al content

Al content (at.%)	13.6	56.5	61.5	73.9
Residual stress (MPa)	1276.7	-28.1	-495.6	-1336.2

As expected from the XRD patterns, the CrAlN layers do not have tensile stress except the one with the lowest Al content. Indeed, this layer shows the highest shift on the left of the (200) diffraction peak and presents as expected tensile stress. The stress change from tensile stress (14 at.% of Al) to compressive stress when adding aluminum content. For $x = 0.14$, the ternary coating has a tensile stress of 1.28 GPa; when $x = 0.57$ and $x = 0.62$, the coating has a compressive stress of -28.1 MPa and -495.6 MPa, respectively; further additional aluminum increase the residual stress to -1.34 GPa when $x = 0.74$. These values are smaller than the ones obtained by Lin et al. [167]. Reiter et al. [170] have shown that the residual stresses increase as a function of the percentage of Al. This increase was explained by the dissolution of Al atoms in the cubic structure of CrN which causes the latter to distort and deform due to the difference in atomic radius between Cr and Al. Moreover, this increase in compressive stresses may be due to the formation of defects during the growth phase of the layers. Indeed, defects such as stacking defects and trapped atoms can produce deformation of the crystal lattice, which generates compressive stresses as observed by Hong et al. and Nouveau et al. [281, 282].

Our CrAlN layer with 14 at.% of Al has a tensile stress of around 1.28 GPa while the CrAlN layer of Aouadi [111] containing 11 at.% of Al presented compressive stress of around -80 MPa. Again, we show here the effect of the substrate rotation speed on the CrAlN layers properties. Martín-Tovar et al. [243] highlighted that in the case of Al-doped ZnO thin films prepared by rf-sputtering, the crystallinity was greatly influenced by the substrate rotation favoring the formation of larger crystallite sizes which contributes to the reduction of the tensile stress contribution from crystalline boundaries. In our case, our CrAlN layer has a grain size of 5.6 nm, around 7 times lower than Aouadi's layer (38 nm). In *Figure 92*, it is obvious that there is a correlation between the grain size and the residual stress of the CrAlN layers.

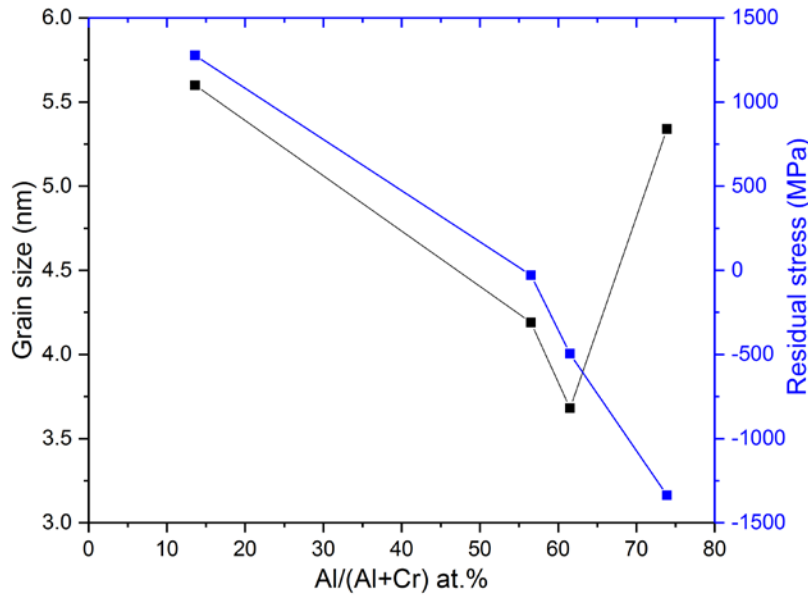


Figure 92. Grain size and residual stress of the $Cr_{1-x}Al_xN$ monolayers at different Al content

Indeed, the highest grain size corresponds to the highest tensile and compressive stress. Except for the layer containing 74 at.% of Al, the grain size decreases as the stress varies from 1.28 to -0.5 GPa. Quek et al. [283] demonstrated that different regimes of grain size effect on yield stress exist : Regime I is the classical Hall-Petch regime dominated by dislocation pile-up against GB (grain boundaries)s; Regime III is the inverse Hall-Petch regime dominated by lattice dislocation emission from triple junctions as a result of GB sliding; and an intermediate regime II where pure GB sliding dominates. Their model shows that the inverse Hall-Petch behavior can be obtained through a relief of stress buildup at GB junctions from GB sliding by emitting dislocations from the junctions. The yield stress is shown to vary with grain size, d , by a $d^{1/2}$ relationship when grain sizes are very small which is our case (grain size < 10 nm). We verify here the “inverse Hall-Petch” effect: the lower the grains, the lower the residual stress. In the case of the layer with 74 at.% of Al one can suppose that the presence of a mixture of the cubic and the hexagonal AlN phases could be responsible for the increase of the grain size and of the compressive stress. This should be confirmed by other characterizations such as grazing XRD or Raman spectroscopy.

3.2.3.1.4.2. Hardness and elastic modulus

The results of nanoindentation tests carried out on coated silicon substrates are shown in *Figure 93*.

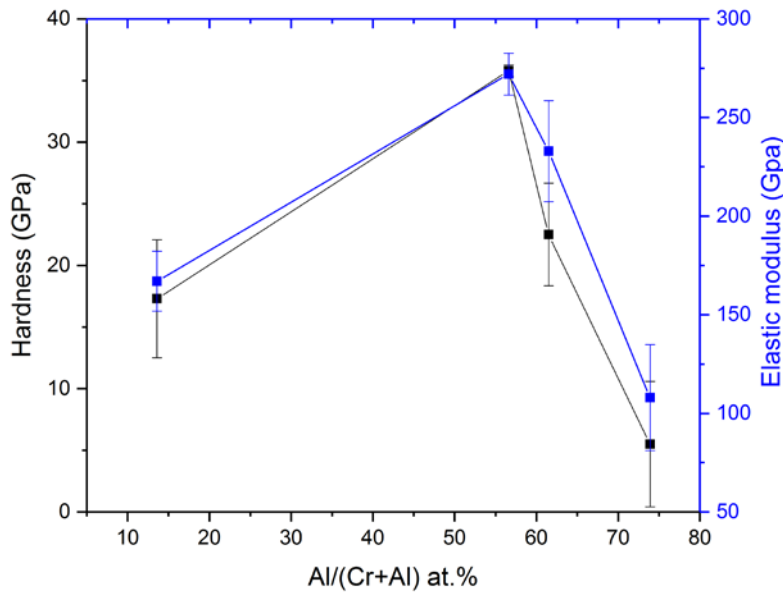


Figure 93. Hardness and elastic modulus of the $Cr_{1-x}Al_xN$ monolayers at different Al content on silicon substrate

The hardness of the CrAlN coatings varies from 5.5 GPa to 35.8 GPa, while the elastic modulus varies from 108 GPa to 272 GPa. The values of hardness, elastic modulus and plastic deformation resistance indicators are listed in Table 29.

Table 29. Hardness, elastic modulus, elastic and plastic deformation resistance H/E and H^3/E^2 of $Cr_{1-x}Al_xN$ monolayers with varied Al content

Mechanical properties Al content (at.%)	H (GPa)	E (GPa)	H/E ($\times 10^{-2}$)	H^3/E^2 ($\times 10^{-2}$)
13.6	17.3	167	10.4	18.57
56.5	35.8	272	13.4	62.02
61.5	22.5	233	9.7	20.98
73.9	5.5	108	5.1	1.43

Adding Al to the Cr-N system improves its hardness. Indeed, all the CrAlN films showed higher hardness and elastic modulus compared to those of CrN (Table 19). According to Barshilia et al. [284], this increase in hardness can be attributed to the small inter-atomic distance of the CrAlN films and the solid solution hardening. The coating containing 57 at.% of Al presents the highest hardness (35.8 GPa), elastic modulus (272 GPa) as well as the highest H/E (0.134) and H^3/E^2 (0.62) ratios. Ding et al. [285] showed similar results, where the H^3/E^2 ratio is the highest (0.45) when $x = 0.62$, as well as the hardness gets the maximum value of 40 GPa. The

CrAlN layer with 62 at.% of Al presents acceptable hardness, elastic modulus and wear resistance values. The lowest values were obtained at 14 and 74 at.% of Al in the CrAlN layers. The evolution of the hardness and elastic modulus of CrAlN films as a function of the percentage of Al has been reported in several studies [167, 170, 285], where it was found that the additional Al improves the mechanical properties of the film. From certain levels of Al, the AlN phase is found dominant in the CrAlN layers, which reduces the hardness and elastic modulus due to the difference in mechanical properties of the CrN and AlN phases [170]. These results corroborate the SEM observations in *Figure 85*. Indeed the denser coatings are the ones that have the highest hardness, etc. For his CrAlN layer with 11 at.% of Al, Aouadi [111] got a hardness of around 24 GPa and a elastic modulus of almost 285 GPa. This is probably the result of the variation of the substrate's rotation speed.

Figure 94 illustrates the comparison of the hardness and residual stress of CrAlN monolayers deposited on silicon. The results show a correlation between hardness and residual stress.

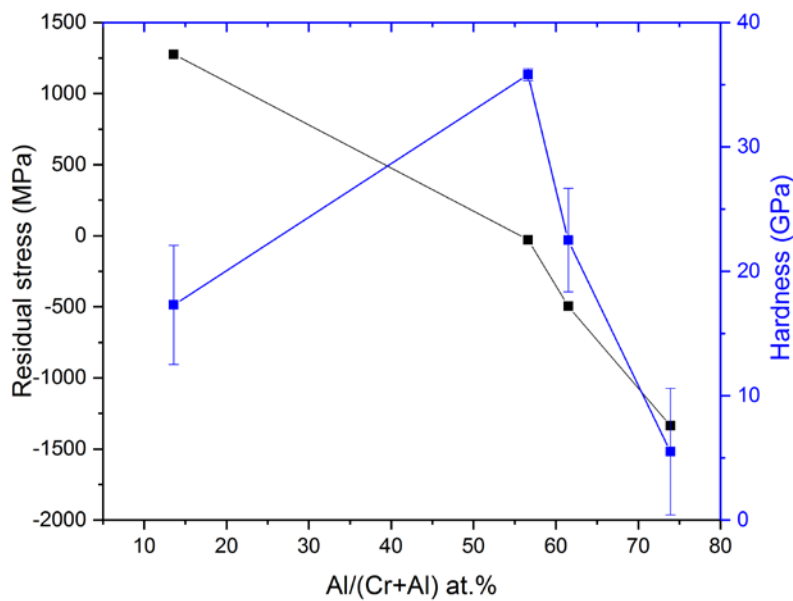


Figure 94. Correlation between residual stress and hardness of $Cr_{1-x}Al_xN$ monolayers at different Al content

The hardness seems to be low when the residual stresses are the highest (tensile and compressive). Aouadi [111] observed the same tendency for his own CrAlN layers with different Al content: the hardness was inversely proportional to the stress. When the stress is the lowest, about -28 MPa, the hardness goes up to 35.8 GPa. When the residual stresses increase from -28 MPa to -1.33 GPa, the hardness decreases from 35.8 to 5.5 GPa.

The relation between the grain size and the hardness is illustrated in *Figure 95*.

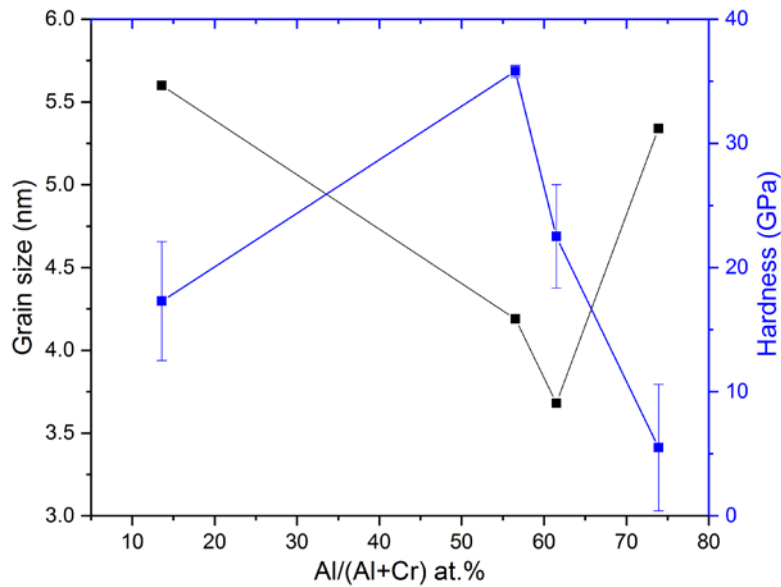


Figure 95. Grain size and hardness of the $Cr_{1-x}Al_xN$ monolayers at different Al content

We verify here the “Hall-Petch” effect: the larger the grains, the lower the hardness.

The wear rates of the CrAlN monolayers are illustrated in Figure 96.

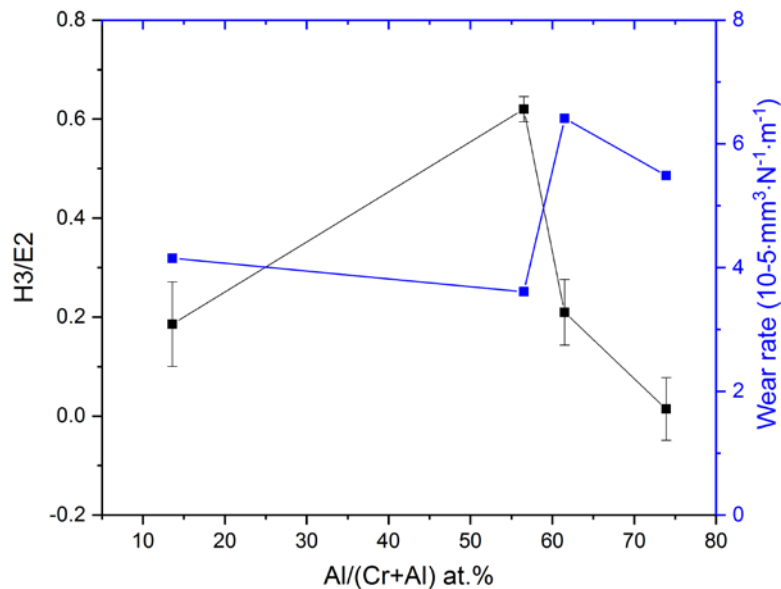


Figure 96. Correlation between plastic deformation resistance and wear rate of the $Cr_{1-x}Al_xN$ monolayers at different Al content

As expected, the higher the H^3/E^2 ratio, the lower the wear rate. The CrAlN layer showing the best plastic deformation is the one obtained with 57 at.% of Al. It is noteworthy that the CrAlN layer containing 62 at.% of Al presents a relative low plastic deformation resistance and the highest wear rate. This can be explained by a higher COF, a smaller grain size, and especially higher compressive stresses. These properties all together could lead to decrease the plastic

deformation and to weaken this layer in comparison to the one obtained with 57 at.% of Al, but also to the others.

3.2.3.1.4.3. Adhesion

The failure mode of Bull [262] was used to identify the damages of the coatings during scratch-tests. Some recovery spallation is observed for all the CrAlN coatings according to Bull [262]. The scratch tracks of these layers are presented in *Figure 97*.

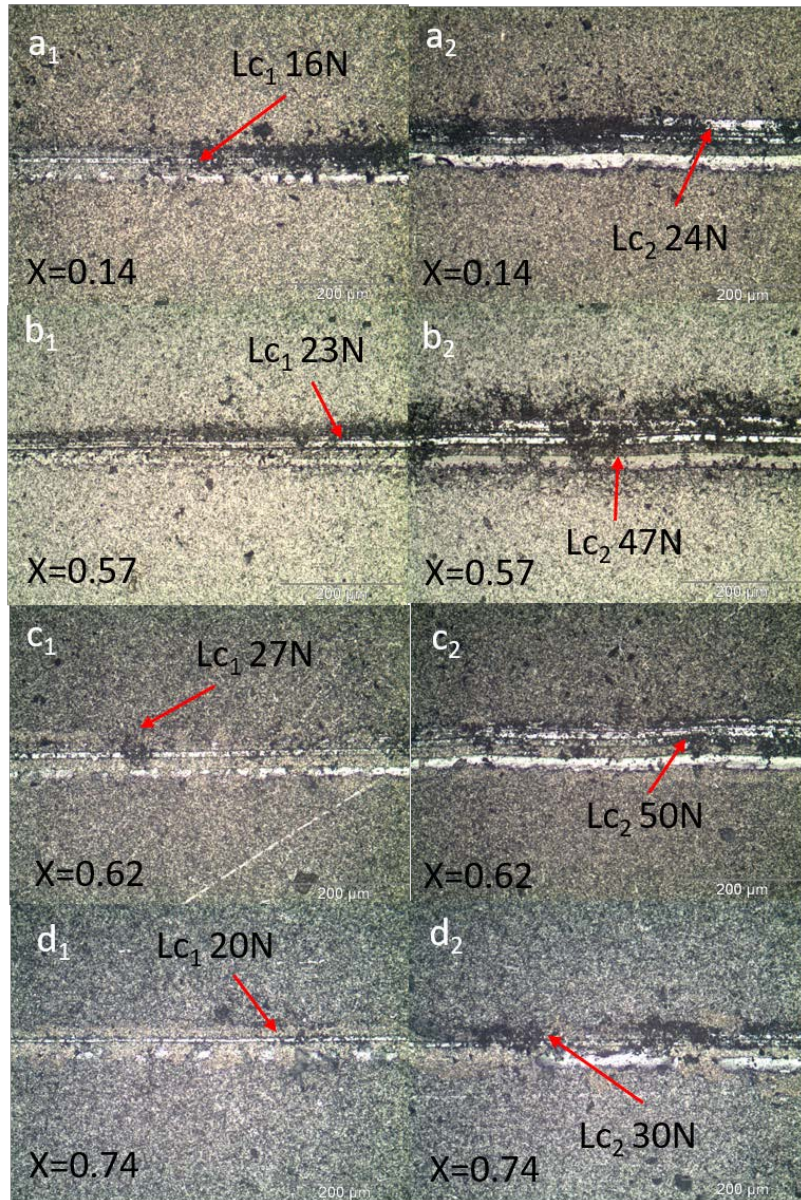


Figure 97. Optical images of critical load of the $Cr_{1-x}Al_xN$ monolayers on WC substrate: a1) Lc_1 $x=0.14$, a2) Lc_2 $x=0.14$ b1) Lc_1 $x=0.57$, b2) Lc_2 $x=0.57$, c1) Lc_1 $x=0.62$, c2) Lc_2 $x=0.62$, d1) Lc_1 $x=0.74$ and d2) Lc_2 $x=0.74$

The critical loads and the work of adhesion of CrAlN coatings with different Al content are presented in *Table 30* and in *Figure 98*.

Table 30. Critical loads and work of adhesion of Cr_{1-x}Al_xN coatings at different Al content

x value	0.14	0.57	0.62	0.74
Lc ₁ (N)	16	23	27	20
Lc ₂ (N)	24	47	50	30
W _{ad} (J/m ²)	2.36	1.36	1.39	2.66

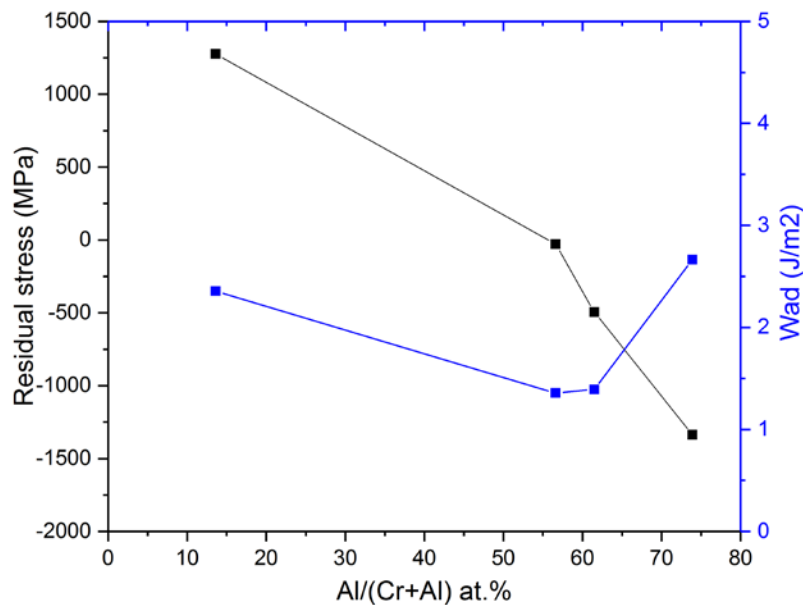


Figure 98. Correlation between residual stress and work of adhesion of the Cr_{1-x}Al_xN monolayers at different Al content

The highest work of adhesion corresponds to the highest residual stresses (tensile and compressive) according to *Figure 98*; higher work of adhesion corresponds to the lower adhesion. We verified here, as in the case of our CrN coatings, Nouveau [112] who observed also in the case of CrN layers synthesized by RF magnetron sputtering that the critical loads are related reversely to the work of adhesion (*Table 30*).

The highest critical loads are obtained for the coating with 57 and 62 at.% of Al (*Figure 99*).

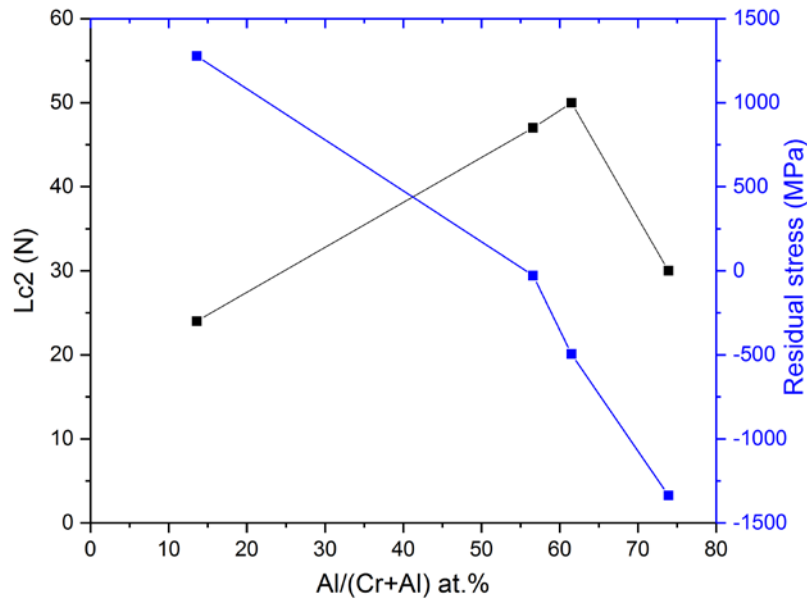


Figure 99. Critical loads of the $Cr_{1-x}Al_xN$ coatings at different Al content at different Al content

We verify here that the substrate rotation speed has an influence on the adhesion of the layers. As Aouadi [111] got 55N of Lc2 for his CrAlN layer with 11 at.% of Al at 3 rpm instead of 1.5 rpm, the last contains 14 at.% of Al. The force required to tear off the layer from its substrate (Lc2) for the optimal CrN film is in the order of magnitude of 43 N (Figure 74). However, that of the more adherent CrAlN films varies between 47 and 50 N.

These results also correlate with the work of Benlatreche [151] who made CrAlN layers by RF dual magnetron sputtering by varying the voltage applied to the Al target. The decrease in the effort required to tear off the layer with increasing Al level is attributed to its microstructure [286]. Indeed, the CrAlN films with an Al content of 57 or 62 at.% have the most dense structure (Figure 85) and their grain size are 4.19 and 3.68 nm, respectively. This dense structure has strong intercolumnar bonds, therefore strong resistance to the formation of intercolumnar cracks. Also, Li et al. [287] explained the evolution of the force required to tear off the layer from its substrate (Lc2) by the evolution of the grain size. They showed that as the grain size increases, Lc2 decreases. To show clearly this relation of the grain size with the Lc2 for the CrAlN layers, we multiplied the grain size by a factor of 2 in Figure 100.

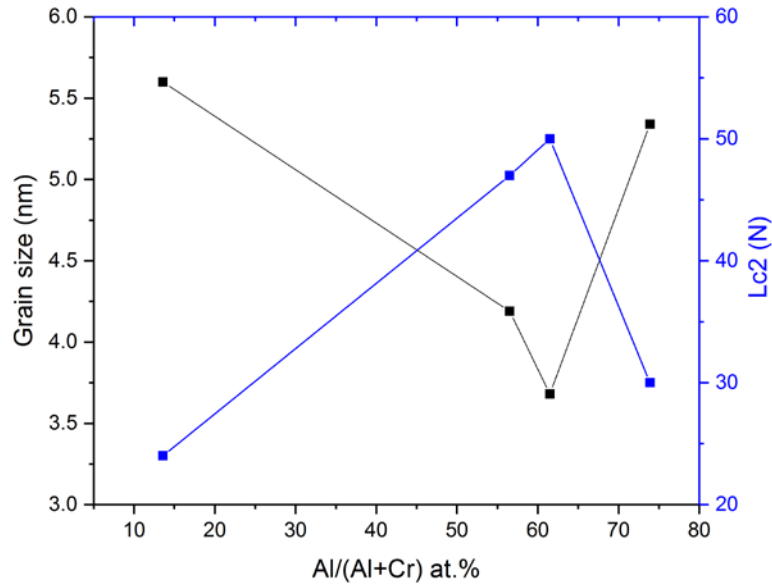


Figure 100. Evolution of the Lc2 critical load of the $Cr_{1-x}Al_xN$ monolayers and their grain size (x_2) as a function of the Al content

Moreover, the layer with $x = 0.14$, as well as the one with $x = 0.74$, have relatively low critical loads probably due to their high tensile or compressive residual stress (± 1.5 GPa). According to Kim and Lee. [288], Lc2 is inversely proportional to the residual stress, which may explain the low value obtained at $x = 0.14$ and 0.74 because this is where the stress is maximum (Figure 101). In addition, samples with low stress have better adhesion than those with high stress.

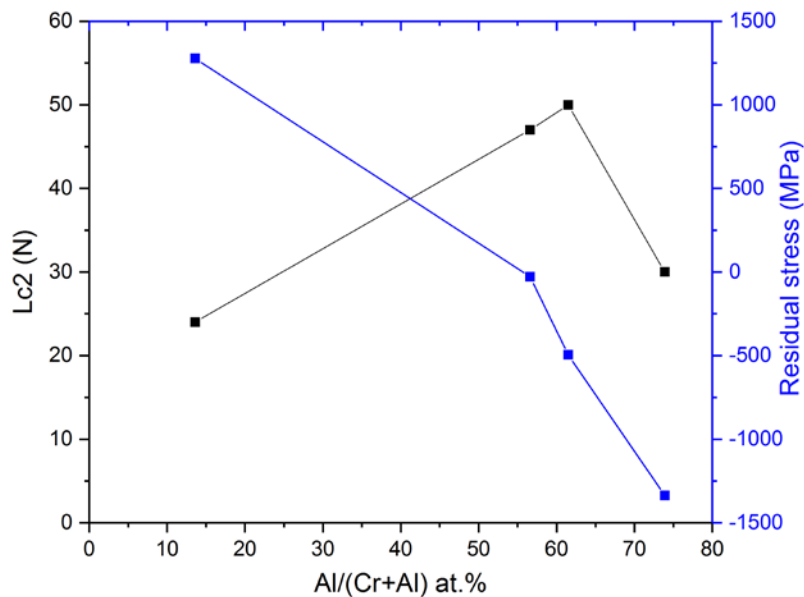


Figure 101. Correlation between residual stress and critical load of the $Cr_{1-x}Al_xN$ coatings at different Al content

3.2.3.1.5. Partial conclusion

In this section, we developed CrAlN monolayers by varying the Al content to determine the optimal composition to be applied in the following section (AlCrN monolayers). The influence of this parameter was shown. Moreover, we verified the results obtained previously by Aouadi [111]. When we obtained different results, we showed the influence of the substrate rotation speed. According to their properties, the CrAlN monolayers obtained with 57 and 62 at.% of Al exhibit the same crystalline orientation, have a dense surface morphology, small column size and grain size. Concerning their mechanical properties, the layer with 57 at.% of Al presents the highest hardness and elastic modulus, the best plastic deformation resistance and has a very good adhesion up to 47 N (Lc2) and finally the lowest wear rate. This optimized CrAlN monolayer should be our choice in the different multilayers that we are going to present in the multilayers section. Nevertheless during the deposition process when $x = 0.57$, a high current was fixed on the aluminum target, which was unfortunately significantly damaged. Indeed, with a high current applied on the aluminum target, we poisoned it by nitrogen in a very short time, which is not a sustainable way for PVD coatings. Then even if the layer obtained for $x = 0.62$ has a low plastic deformation resistance, it presents the best adhesion and similar physico-chemical and mechanical properties with the layer obtained for $x = 0.57$. Besides, it has been synthesized at a fixed power on the aluminum target (*Table 21*) which reduces the target damage during the PVD process. For all the above-mentioned reasons, we decided to choose as the optimal Al content, $x = 0.62$ for the following study about the optimization of AlCrN monolayers by varying the substrate bias voltage and the deposition temperature.

3.2.3.2. Optimization of the substrate bias voltage and deposition temperature

In the previous section we optimized the Al content in CrAlN layers as 62 at.% obtained with the following deposition parameters: Ar flow = 60 sccm, N₂ flow = 53 sccm, Cr target power = 500 W, Al target power = 1500 W, working pressure = 5.10^{-3} mbar, substrate rotation speed = 1.5 rpm. Indeed, it is obvious in *Figure 102* that an Al content of around 60 at.% permits to have the highest hardness at low and high temperature, which will be the case during the tribological and tool wear tests under flood or LN₂ cooling conditions.

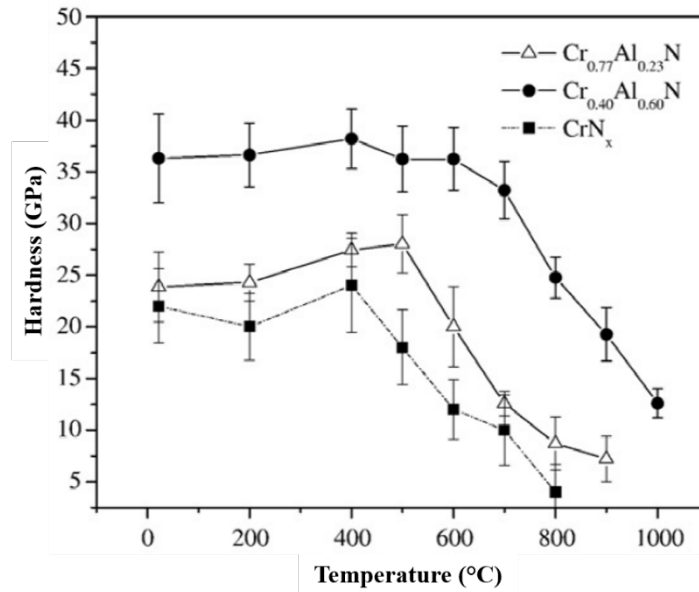


Figure 102. Hardness of CrN and CrAlN layers as a function of the temperature [230]

Then, in the following sections, as we have more Al than Cr in the layers, we will name them AlCrN.

3.2.3.2.1. Deposition conditions

In this section we will develop AlCrN coatings on WC substrates according to the deposition parameters summarized in Table 31. The deposition temperature and the substrate bias voltage varied while all the other parameters were fixed. The deposition time was adjusted to obtain similar thickness for all the AlCrN layers.

Table 31. Deposition conditions of the AlCrN monolayers

AlCrN						
Argon flow (sccm)	60					
Nitrogen flow (sccm)	53					
Working pressure (mbar)	$5 \cdot 10^{-3}$					
Power applied on chromium target (W)	500					
Power applied on aluminum target (W)	1500					
Substrate-holder rotation speed (rpm)	1.5					
Deposition time (min)	180	300	300	360	300	300
Temperature (°C)	Ambient	Ambient	150	300	300	300
Substrate Bias Voltage (V)	0	-500	-500	-500	-250	0

3.2.3.2.2. Physico-chemical properties

3.2.3.2.2.1. Deposition rate and thickness of the AlCrN layers

The thickness of the coatings varies from 1.06 to 1.71 μm (*Table 32* and SEM cross section images in section 3.2.3.2.2.3), which means that the deposition rate varies from 3.07 to 6.9 $\text{nm}\cdot\text{min}^{-1}$.

Table 32. Deposition rate and thickness of the AlCrN monolayers

Temperature ($^{\circ}\text{C}$)	Ambient		150	300		
Substrate Bias Voltage (V)	0	-500		-250	0	
AlCrN thickness (μm)	1.24	1.27	1.06	1.41	1.15	1.71
Deposition rate ($\text{nm}\cdot\text{min}^{-1}$)	6.9	4.23	3.53	3.07	3.83	5.7

At a substrate bias voltage of -500 V and a deposition time of 300 min, the deposition rate decreases from 4.23 to 3.53 $\text{nm}\cdot\text{min}^{-1}$ when the deposition temperature increases from the ambient to 150 $^{\circ}\text{C}$. We probably improve the densification of the layers thanks to a higher adatoms mobility when the temperature increases. Moreover, at a deposition time of 300 min and a deposition temperature of 300 $^{\circ}\text{C}$, when the substrate bias voltage increases from 0 to -250V, the deposition rate decreases from 5.7 to 3.83 $\text{nm}\cdot\text{min}^{-1}$ probably because of the re-sputtering phenomena as observed in the case of the CrN monolayers. To conclude, even if we tried to adjust the deposition time, it is not so easy to obtain similar thicknesses as we varied also two other parameters. Nevertheless, we will consider for the following section that our thicknesses are in the same order of magnitude because we have a difference lower than 1 μm (650 nm).

3.2.3.2.2.2. Chemical composition by EDS microanalyses

Table 33 shows the chemical composition of the AlCrN monolayers obtained on tungsten carbide.

Table 33. Chemical composition of the AlCrN monolayers

Deposition conditions	Atomic percentage (at.%)					
	Cr	Al	N	O	Al/(Cr+Al) ($\times 10^{-2}$)	Al/Cr
Amb-0V	18.4	29	36.7	16.1	62	1.58
Amb-500V	20.3	32.2	44	3.6	61.3	1.59
150°C-500V	19.3	34.7	45.4	0.5	64.3	1.80
300°C-500V	20.5	32.8	46.6	0.1	61.5	1.60
300°C-250V	19.7	32.7	45.1	2.5	62.4	1.66
300°C-0V	18.9	30.5	39.1	11.5	61.7	1.61

Figure 103 illustrates the evolution of the chemical composition of AlCrN monolayers as a function of the deposition temperature and substrate bias voltage.

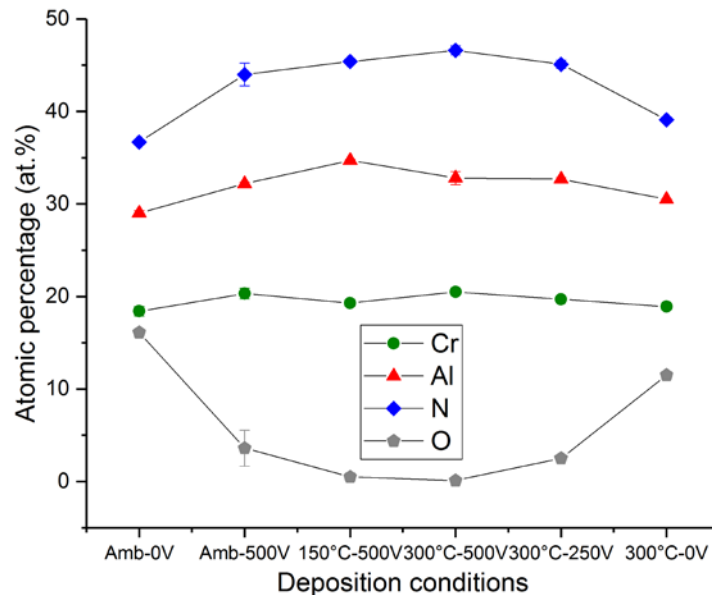


Figure 103. Chemical composition of the AlCrN monolayers as a function of the deposition temperature and substrate bias voltage

According to Table 33 and Figure 103, all the AlCrN coatings have a stable Cr (average of 19.5 at.%), Al (average of 32 at.%) and N (average of 42.9 at.%) content. As the average of the Al/(Al+Cr) ratio is 0.62, we can name our AlCrN layers as follows: Al₆₂Cr₃₈N. As in the case of our CrN monolayers, we observed the decrease of oxygen content related to the increase of substrate bias voltage and deposition temperature. This phenomenon was explained as the preferential re-sputtering of oxygen in comparison to the metallic elements [221–223].

3.2.3.2.2.3. Surface morphology and microstructure

Figure 104 and Figure 105 show the surface morphology of the AlCrN coatings on tungsten carbide and silicon substrates.

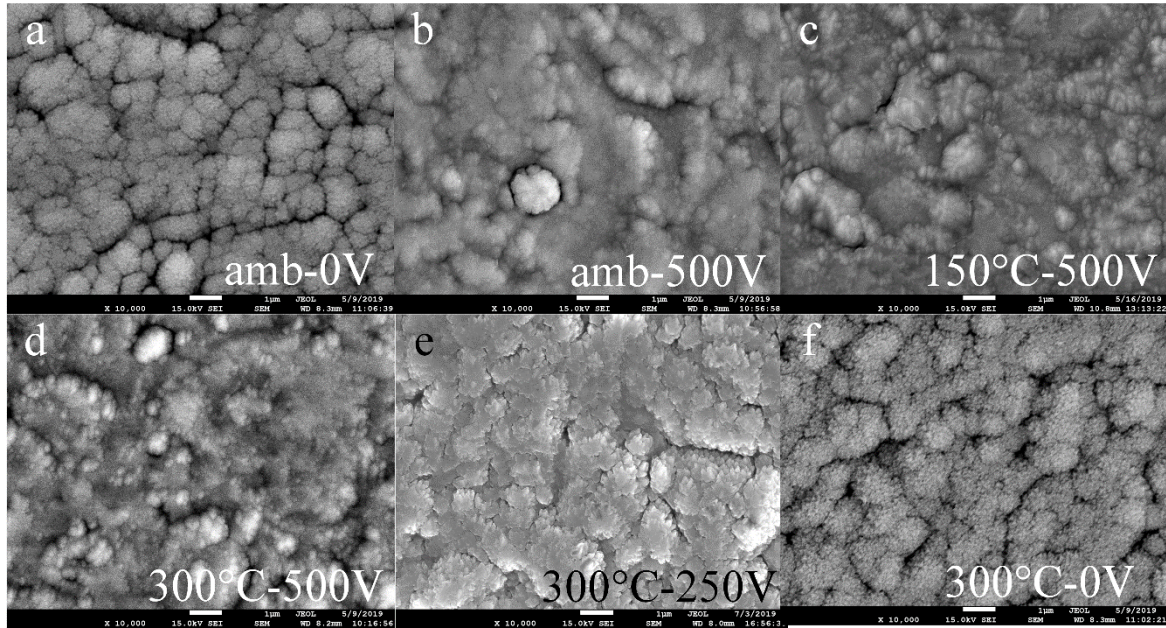


Figure 104. Surface morphology of the AlCrN monolayers on WC substrate a) amb-0V, b) amb-500V, c) 150°C-500V, d) 300°C-500V, e) 300°C-250V and f) 300°C-0V

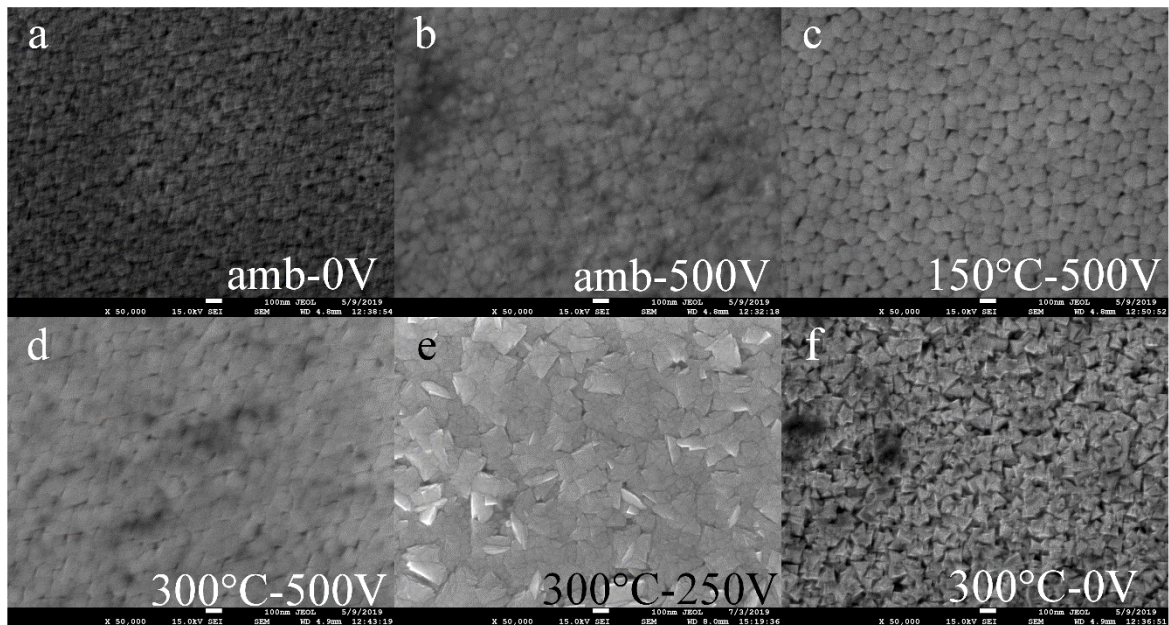


Figure 105 Surface morphology of the AlCrN monolayers on silicon substrate a) amb-0V, b) amb-500V, c) 150°C-500V, d) 300°C-500V, e) 300°C-250V and f) 300°C-0V

In Figure 104, most of the surface morphology looks like cauli-flower on a rough substrate such as WC. The layers obtained without substrate bias voltage present substrate bias voltage

present a similar surface morphology with a high porosity (*Figure 104a and f*). This is mainly due to the lack of bias voltage on substrate, as already studied by other researchers [203, 216, 227] and observed in the case of the CrN monolayers. For the coatings synthesized at -500 V, the surface morphology is very heterogeneous and rough (*Figure 104b, c and d*). The layer obtained at 300 °C and -250 V presents a homogenous surface morphology with low porosity (*Figure 104e*). At ambient temperature the coating obtained without bias voltage (*Figure 104a*) presents large cluster of columns, while the one obtained at -500 V (*Figure 104b*) is denser. As far as the influence of the deposition temperature is concerned, it is obvious that the coatings get denser and reduce their porosity when the temperature decreases (*Figure 104b, c and d*). When we fixed the deposition temperature to 300°C, we observed that for a substrate bias voltage of -500 V (*Figure 104d*) and -250 V (*Figure 104e*), the coatings showed a dense structure. It seems that the films are more compact with a substrate bias voltage. It is then predictable that the AlCrN layers obtained at 300°C with a substrate bias voltage of -250 or -500 V should have the highest hardness.

Because of the roughness of the WC substrates, the AlCrN layers were also synthesized on mirror-polished silicon substrates, to better observe the influence of the deposition temperature and the substrate bias voltage on their surface morphology (*Figure 105 a-f*).

In contrast to the layers synthesized on the WC substrate, all the AlCrN layers developed on mirror-polished silicon substrate present a homogenous surface morphology. The AlCrN layer obtained without heating and substrate bias voltage presents the smaller grain size (*Figure 105a*). The lack of energy is probably responsible for this result. Indeed, when we increase the substrate bias voltage (*Figure 105b*) or the temperature (*Figure 105f*), it is obvious that bigger grains are obtained. When we fixed the substrate bias voltage to -500 V, the AlCrN layers synthesized at 150 °C (*Figure 105c*) or 300 °C (*Figure 105d*) present a similar grain size but the one synthesized at 300 °C seems denser. Besides, when we fixed the deposition temperature to 300 °C, the layers with a substrate bias voltage (*Figure 105d and e*) are denser. Moreover, the AlCrN layer obtained at 300 °C and -250 V has bigger grains than the one we got at 300 °C and -500 V and with some pyramidal top of columns. We verify here what we observed from the CrN monolayers: the increase in grain size with increasing substrate bias voltage is a consequence of the high mobility of adatoms due to the high energy of the ions [228–230]. Nevertheless, as the coating synthesized at -250 V has bigger grains than the one obtained at -500 V, we can expect a different structure for these two AlCrN coatings. Besides, the AlCrN coating synthesized at 300 °C and -250V should be more crystallized than the other one.

According to the above-mentioned results, it is obvious that a high deposition temperature and substrate bias voltage would permit to get a dense and homogeneous AlCrN layer on silicon substrates.

Figure 106 shows the cross-section of the AlCrN coatings on silicon substrate.

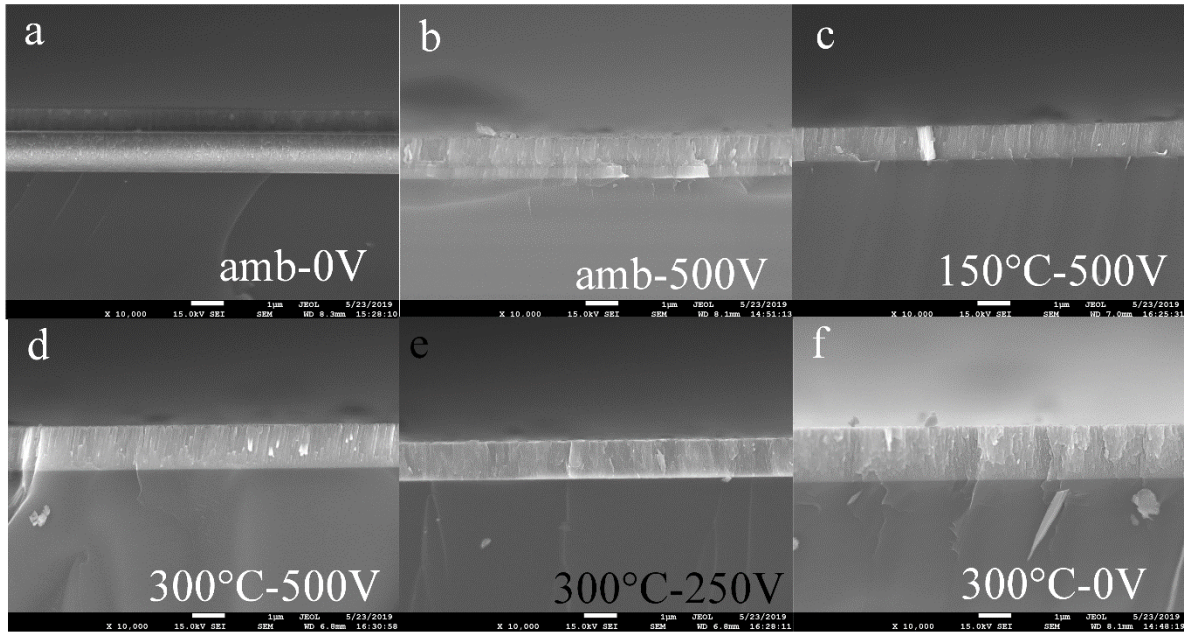


Figure 106. Cross-section of the AlCrN monolayers on Si obtained at: a) amb-0V, b) amb-500V, c) 150°C-500V, d) 300°C-500V, e) 300°C-250V and f) 300°C-0V

The densest structures appear in Figure 106d and e. The substrate bias voltage generally creates a structure much harder and denser according to Berg et al. [231], as also shown in the case of the CrN monolayers. We also verified that for the AlCrN layers, the temperature has an influence on the microstructure as explained by Herr et al. [202].

We are now going to verify the structure and grain size of the AlCrN layers in the following section.

3.2.3.2.2.4. Structure

The XRD analyses have been made on WC coated substrates. According to the (ICDD 00-011-0065) and (ICDD 00-025-1495) cards, we observe only the cubic phase of CrN and AlN for all coatings, no hexagonal Cr₂N or AlN diffraction peaks are present regarding of XRD patterns (Figure 107).

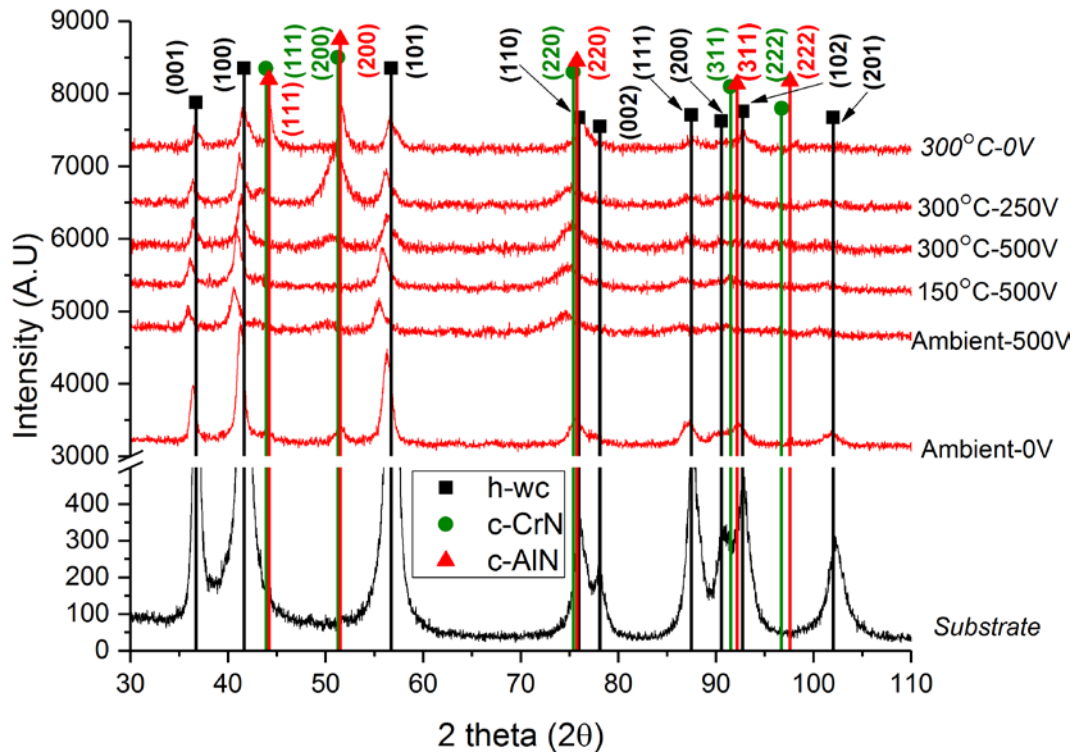


Figure 107. XRD patterns of AlCrN monolayers with different deposition conditions

The AlCrN layer synthesized at 300 °C-0 V presents a major (200) and (111) diffraction peaks at 51.68 and 44.27°, respectively. It also shows a minor (220) diffraction peak at 76.51°. The theoretical (111), (200) and (220) diffraction peaks positions are 43.88 and 44.17°, 51.26 and 51.47°, and finally 75.38 and 75.75° according to the (ICDD 00-011-0065) and (ICDD 00-025-1495) cards for CrN and AlN, respectively. Then we can expect some compressive stresses in this AlCrN layer as its diffraction peaks are shifted to higher angles. When we increase the substrate bias voltage to -250 V, we still have a main (200) diffraction peak located at 51.09°. A minor (111) diffraction peak is also detected at 43.57° and maybe a (220) diffraction peak at 74.98°, but here the influence of the substrate is possible. It is expected the tensile stresses for this layer as its diffraction peaks are shifted to lower angle positions. At the highest substrate bias voltage of -500 V, one can suppose that we have a (220) diffraction peak at 75.3° and a (200) diffraction peak at 50.88°. It seems that the AlCrN coatings change their structure when the substrate bias voltage increases. As observed for our CrN monolayers, the energy brought thanks to the substrate bias voltage increases the atoms mobility and modifies the grain orientation, this is explained by the surface energy model [232] or strain energy model [234]. The experimental diffraction peaks are close or between the CrN and AlN theoretical diffraction positions, so we can consider that our AlCrN layers are solid solutions of Al atoms in substitution in the CrN lattices.

Moreover, we observed that the orientation of the AlCrN layers depends on the substrate bias voltage, but also on the deposition temperature and that these both parameters are correlated. Indeed, at ambient temperature, the influence of the substrate bias voltage is low while it is important at 300°C. The AlCrN layer synthesized at amb-0V have a (220) and a (111) diffraction peaks at 51.53° and 44.12°, respectively. When the substrate bias voltage increases up to -500 V, the XRD spectrum is very similar to the one of the layer obtained at 300 °C-500 V. Furthermore, at ambient temperature, the substrate bias voltage has a small influence on the layers structure while it is more obvious when the deposition temperature is 300 °C. When the substrate bias voltage is fixed to -500 V, no effect of the temperature is observed when it increases from ambient to 300 °C. Besides as expected, the layers are more crystallized when the deposition temperature is high, except at the highest substrate bias voltage. Well crystallized AlCrN monolayers are the ones obtained at 300°C-0V and 300°C-250V.

We calculated the grain size thanks to the Debye-Scherrer formula (*Equation 10*). *Table 34* summarizes the calculated grain size of the AlCrN monolayers as a function of the deposition conditions. *Figure 108* illustrates the grain size of the AlCrN monolayers.

The grain size varies from 2.66 to 7.94 nm. These results corroborate what we observed by SEM (*Figure 104*). Besides the grain size of the AlCrN layers is lower than the CrN layers one (from 5.17 to 8.35 nm) as also observed by Schmitt [266].

Table 34. Grain size of the AlCrN monolayers

Deposition conditions	Grain size (nm)	Diffraction peak as reference
Ambient-0V	6.24	200
Ambient-500V	4.70	200
150°C-500V	2.66	220
300°C-500V	4.96	200
300°C-250V	4.12	200
300°C-0V	7.94	200

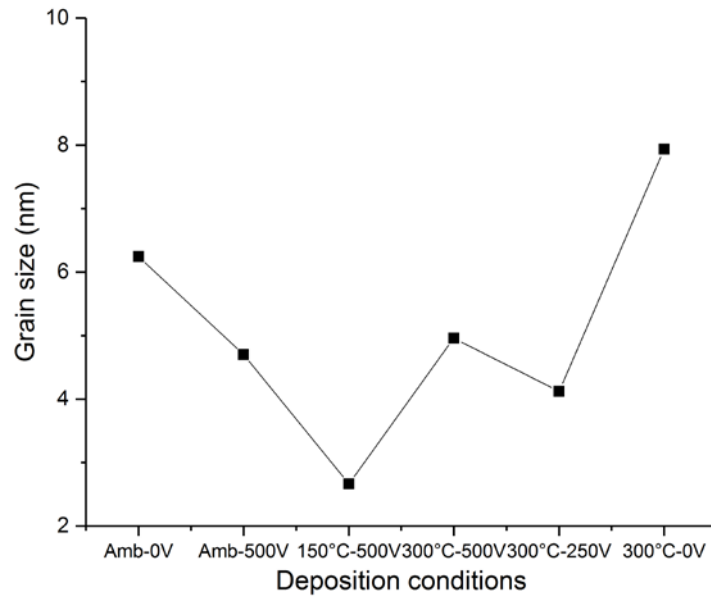


Figure 108. Grain size of the AlCrN monolayers as a function of the deposition conditions

Considering the (200) plans at ambient temperature, the grain size decreases when the bias voltage increases. Same result was observed in the case of the (200) plans at 300 °C and when the substrate bias increases from 0 to -250 V or from 0 to -500 V. As also observed by Aouadi [111], increasing the bias voltage of the substrate can cause the creation of defects resulting from enhanced ion bombardment as also explained by Lee et al. [240] and Sundgren et al. [241]. As far as the deposition temperature is concerned and if only the (200) diffraction plans is considered, we can note that for a fixed substrate bias of -500 V, the grain size shortly increases with the deposition temperature: 4.70 nm at ambient-500 V and 4.96 nm at 300°C-500 V. Similar results were obtained by Li et al. [242]. As the grain size of the layer obtained at 150 °C-500 V has been calculated with the (220) diffraction peak, it was not compared to the others as this diffraction peak can also be due to the substrate. Mainly, we observed the same tendency for the CrN and the AlCrN grain size as a function of the deposition temperature and substrate bias voltage.

3.2.3.2.3. Tribological properties

To study the effect of Al₆₂Cr₃₈N deposition conditions on their friction coefficient, we performed friction tests in a ball-on-disc configuration. A Ti6Al4V ball rubs on a sample of coated WC substrate. The tests are carried out in air, at room temperature and without lubrication. The friction speed is 10 cm/s and the distance traveled by the Ti6Al4V ball is 100 m.

The friction coefficient is shown in *Figure 109* and is around 0.5 whatever the deposition conditions.

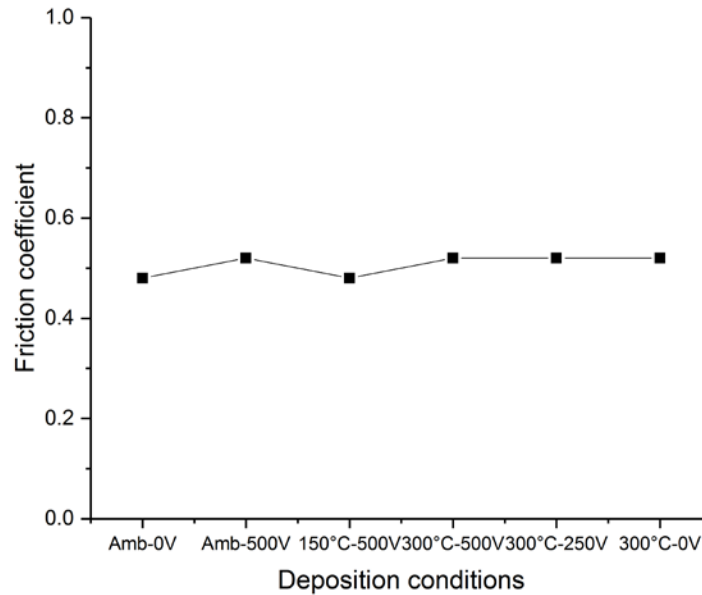


Figure 109. Friction coefficient of AlCrN monolayers as a function of the deposition conditions

Similar values were obtained by Benlatreche [151] who obtained a coefficient of friction of CrAlN with 51 at.% of Al synthesized by RF magnetron sputtering, around 0.65. Uchida et al. [289] obtained a friction coefficient between 0.5–0.8 for all deposited Cr₇₀Al₃₀N films synthesized by a cathodic arc ion plating without lubrication. Correa et al. [279] got a friction coefficient without lubrication of 0.65 for their Cr_{40.27}-Al_{38.01}-N_{21.72} coatings synthesized by DC magnetron sputtering. Gong et al. [290] observed for Cr₃₀Al₇₀N coatings synthesized by cathodic arc evaporation (CAE) on carbide substrates with a chemical composition close to our AlCrN layers, a friction coefficient of 0.6-0.65, similar to ours. One can notice that the COF does not depend on the deposition temperature or the substrate bias voltage.

The wear rates are summarized in *Table 35*.

Table 35. Wear rate of the AlCrN monolayers

AlCrN	Ambient -0V	Ambient -500V	150 -500V	300 -500V	300 -250V	300 -0V
Wear rate ($\times 10^{-5} \text{ mm}^3 \cdot \text{m}^{-1} \cdot \text{N}^{-1}$)	3.11	6.36	2.66	2.65	2.02	5.38

The wear tracks determined by optical profilometry are depicted in *Figure 110*.

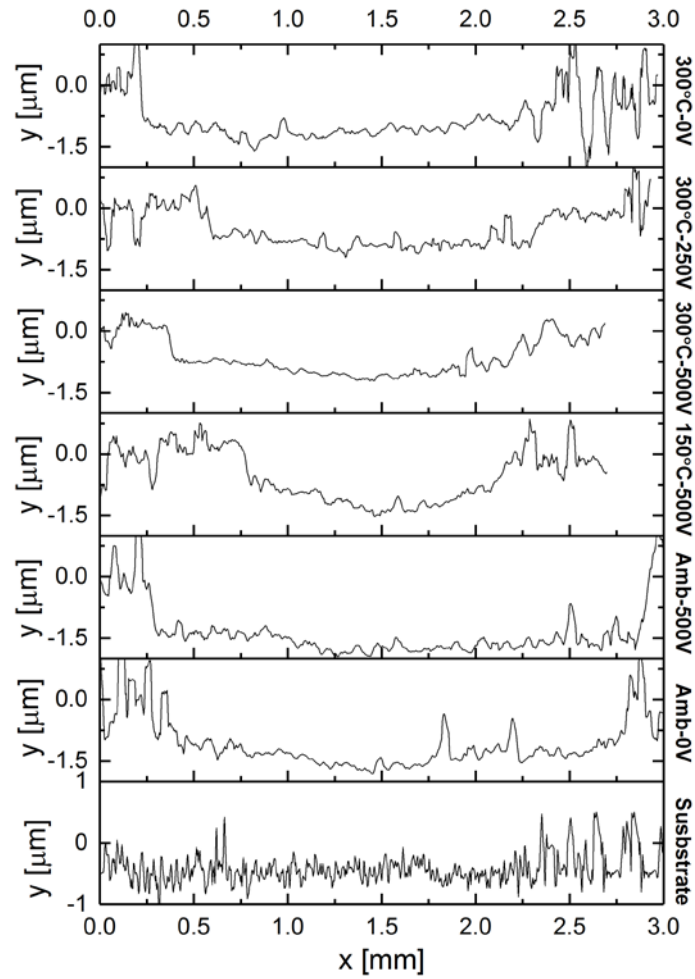


Figure 110. Wear tracks of the AlCrN monolayers as a function of the deposition conditions

Figure 111 illustrates the calculated wear rates according to Archard [194].

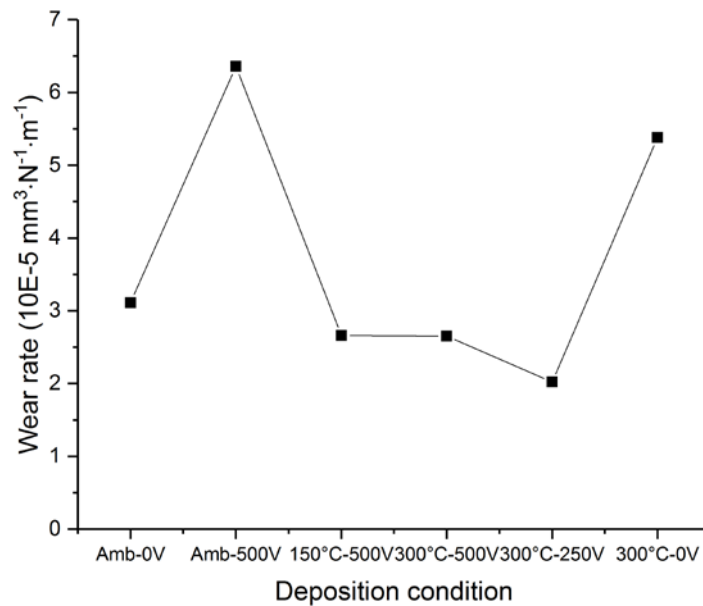


Figure 111. Wear rate of the AlCrN monolayers as a function of the deposition conditions

According to *Table 35* and *Figure 111*, at ambient temperature, applying a substrate bias voltage of -500 V tends to double the wear rate from 3.11 to $6.36 \times 10^{-5} \text{mm}^3 \cdot \text{N}^{-1} \cdot \text{m}^{-1}$. Nevertheless, at high deposition temperature, applying a substrate bias voltage of -250 V permits to decrease the wear rate from 5.38 to $2.02 \times 10^{-5} \text{mm}^3 \cdot \text{N}^{-1} \cdot \text{m}^{-1}$. As in the case of our CrN monolayers, we observed that the wear rate decreases when the substrate bias voltage increases [245]. It seems that thanks to a good compromise between the temperature and substrate bias voltage, we have the lowest wear rates (from 2.02 to $2.66 \times 10^{-5} \text{mm}^3 \cdot \text{N}^{-1} \cdot \text{m}^{-1}$). Kok et al. [216] asserted that wear of coatings correlates well with friction performance. As we have the same low COF for all of our AlCrN layers, we can expect a better adhesion and hardness for the coatings that have the lowest wear rates (see Chapter 3, section 3.2.3.2.4.2 and 3.2.3.2.4.3). It is also noteworthy that the AlCrN present lower wear rates than the CrN layers (see Chapter 3, section 3.2.2.3).

3.2.3.2.4. Mechanical properties

3.2.3.2.4.1. Residual stress

The residual stresses in the AlCrN layers were determined by measuring the curvature of the samples after deposition on silicon. Optical profilometer profiles of the samples before and after deposition were measured. The radii curvature are then extracted with the Gwyddion software. The residual stress of the AlCrN coatings are presented in *Figure 112* and *Table 36*.

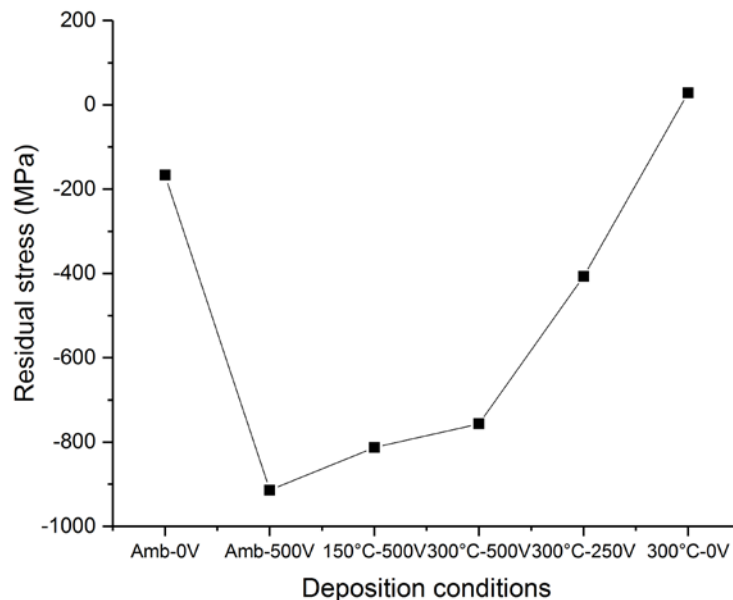


Figure 112. Residual stress of the AlCrN monolayers as a function of the deposition conditions

Table 36. Residual stress of AlCrN monolayers as a function of the deposition conditions

Deposition conditions	Amb-0 V	Ambient -500V	150°C -500V	300°C -500V	300°C -250V	300°C-0V
Residual stress (MPa)	-166.3	-914	-813.2	-756.7	-407.3	28.6

All the AlCrN layers have compressive stress varying from -914 MPa to -166.3 MPa except the layer synthesized at 300°C-0V that has tensile stress of 28.6 MPa. We do not corroborate here the XRD patterns that showed us the stress should be tensile or compressive as the diffraction peaks are shifted on the left or on the right of their theoretical position (Figure 107). Indeed, the layer synthesized at 300°C-0V should have compressive stress while it is tensile and the layer obtained at 300°C-250V should have tensile stress while it is compressive.

It is obvious in the case of AlCrN layers that at ambient temperature and 300°C, the stress increases with the substrate bias voltage (*Figure 112*) from -166.3 to -914 MPa and from 28.6 to -756.7 MPa. It is the same for our CrN layers and this is explained by the thermal stress domination when a substrate bias voltage is applied, as shown also by Kong et al. [246]. Besides if the bias voltage is fixed to -500 V and for a deposition temperature increasing from ambient to 300°C, the residual stress decreases from -914 to -756.7 MPa.

It is then obvious that the bias voltage increases the residual stress while the temperature reduces it, as it was the case for the CrN layers. It is also noteworthy that the AlCrN stress behave the same as the CrN layers ones, shown in *Figure 113* where the AlCrN stress are in absolute values.

Furthermore, Schmitt [266] compared the Al-N and Cr-N bonds length in their face-centered cubic configuration, for which nitrogen occupies the octahedral sites formed by Al and Cr. Calculation shows that Al-N bonds are shorter (2.02 Å) than Cr-N bonds (2.07 Å). The CrAlN structure is thus composed of face-centered cubic meshes, in which the aluminum atoms replace the chromium. The smaller dimension of Al-N bonds tends to contract the mesh, which sees its parameter decrease. This structure, strongly out of equilibrium, is stabilized by the combined effect "long" Cr-N bonds and "shorter" Al-N bonds. This can explain why we observed compressive stress instead of tensile stress as expected from the XRD results. Indeed, as we have more Al than Cr in our AlCrN layers, we can suppose that we have more Al-N than Cr-N bonds that contract the lattice and then induces compressive stress.

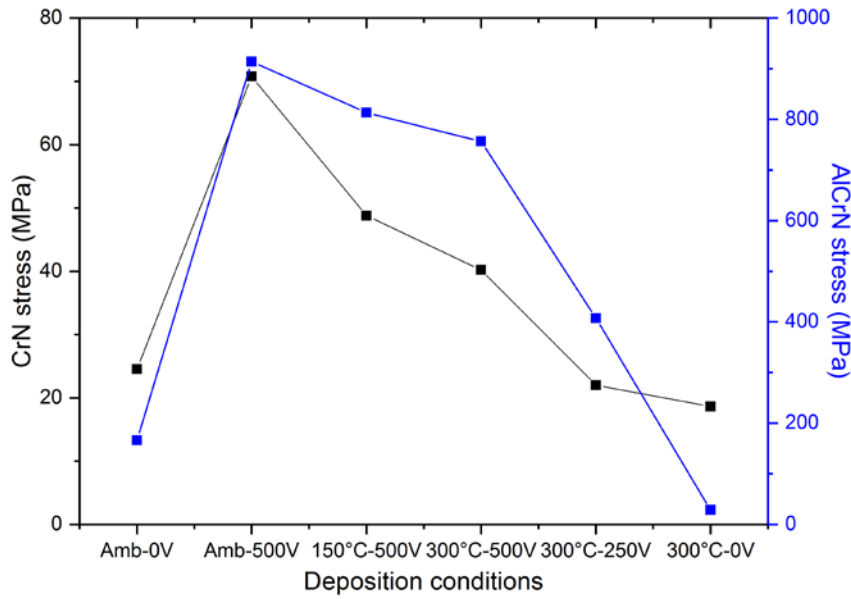


Figure 113. Residual stress of the CrN and AlCrN monolayers as a function of the deposition conditions

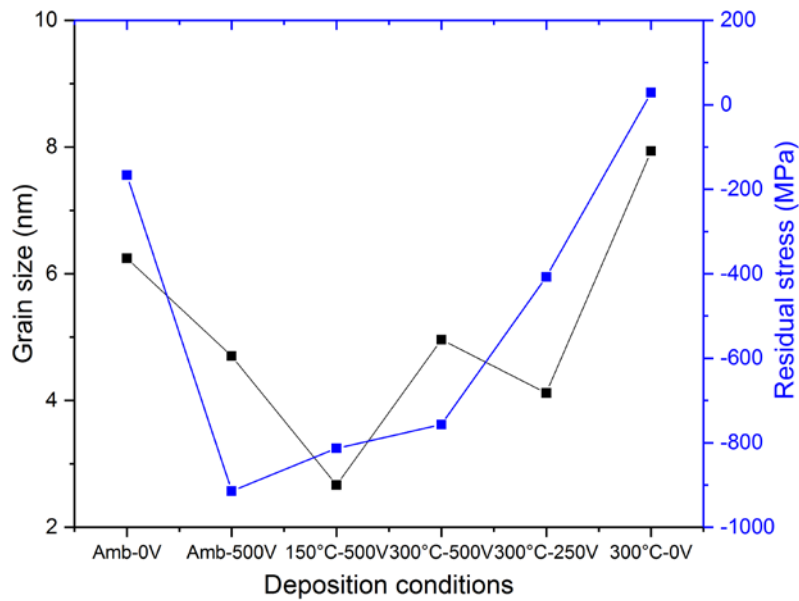


Figure 114. Grain size and residual stress of the AlCrN monolayers

It is obvious in Figure 114 that the grain size is inversely proportional to the residual stress of almost all of the AlCrN layers. This result shows that the intrinsic stress of the AlCrN layers is governed by the grain size. From this result we can conclude that in the AlCrN coatings, larger grains correspond to lower intrinsic stresses. This was also the case for the CrN coatings and was explained by the increase of the kinetic energy of the particles impacting the coating [247].

3.2.3.2.4.2. Hardness and elastic modulus

The results of nanoindentation tests carried out on coated silicon substrates are shown in *Figure 115*.

To verify the hardness values on silicon, nanoindentation was also carried out on mirror-polished WC substrate in the case of the AlCrN layer synthesized at 300°C-250V. Very similar values were obtained for this layer. The hardness of the AlCrN coatings varies from 2.2 GPa to 25.8 (on Si) or 26.4 (on WC) GPa, while the elastic modulus varies from 43.3 GPa to 233 GPa. The values of hardness, elastic modulus and H^3/E^2 are listed in *Table 37*.

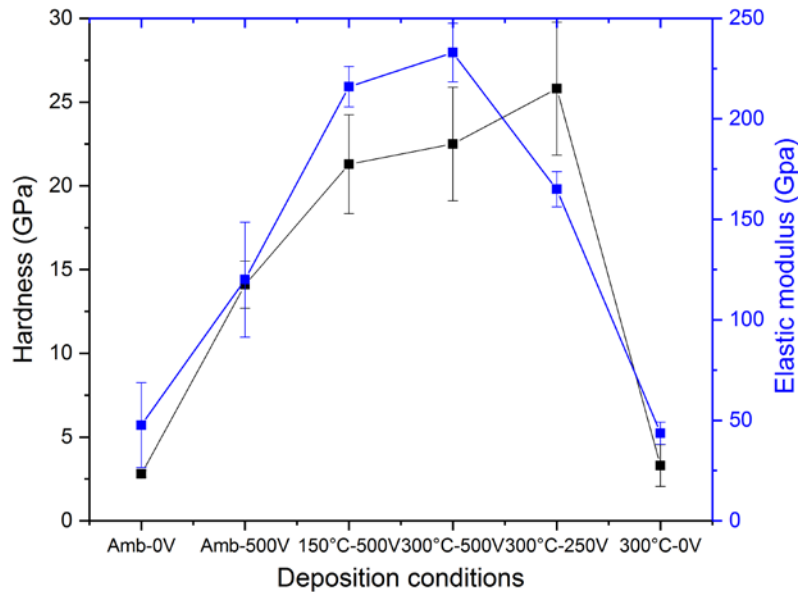


Figure 115. Hardness and elastic modulus of the AlCrN monolayers as a function of the deposition conditions on silicon substrate

In comparison, Gong et al. [290] got an average hardness of 18.9 GPa for their Al₇₀Cr₃₀N layers synthesized on sintered carbide substrates. The coating obtained at 300 °C and -250 V presents the highest hardness and H^3/E^2 ratio whatever the substrate and an acceptable elastic modulus of 165-170 GPa.

Table 37. Hardness, elastic modulus, elastic and plastic deformation resistance H/E and H³/E² of the AlCrN monolayers on silicon and mirror-polished WC substrate

Mechanical properties Deposition conditions	H (GPa)	E (GPa)	H/E (×10 ⁻²)	H ³ /E ² (×10 ⁻²)
Ambient-0V	2.8	47.6	5.9	0.97
Ambient-500V	14.1	120	11.75	19.47
150°C-500V	21.3	216	9.9	20.71
300°C-500V	22.5	233	9.7	20.98
300°C-250V (Silicon)	25.8	165	15.6	63.08
300°C-250V (WC)	26.4	170	15.5	63.67
300°C-0V	3.3	43.6	7.6	1.89

As in the case of the CrN layers, it is obvious on *Figure 115* that the hardness and elastic modulus of the AlCrN layers increase with the substrate bias voltage. Bendavid et al. [257] explained this result by the increase of the ions energies that bombard the substrate. On the other hand, the hardness and elastic modulus increase with the deposition temperature. Balakrishnan et al. [259] reported an increasing hardness of the coatings with increasing deposition temperature owing to higher packing density and crystallinity. We confirm here the XRD and SEM observations results: the denser and well crystallized AlCrN layers are the one obtained at the highest deposition temperature of 300 °C. Indeed, as expected from SEM observations (*Figure 104d and e*), we confirmed here that the AlCrN layers obtained at 300°C-250 V and 300°C-500 V are the harder.

Figure 116 illustrates the comparison of the hardness and residual stress of AlCrN monolayers deposited on silicon. The results show a correlation between hardness and residual stress. When the substrate bias voltage is fixed to -500 V, the residual stress decreases when the deposition temperature increases while the hardness increases. We observed the same phenomena in the case of the CrN layers. According to Escobar et al. [261], when the deposition temperature increases, “the adatoms increase in mobility, so do the relaxation processes and defects due to film densification and impurity evaporation decrease. Therefore, lower intrinsic stresses are generated”.

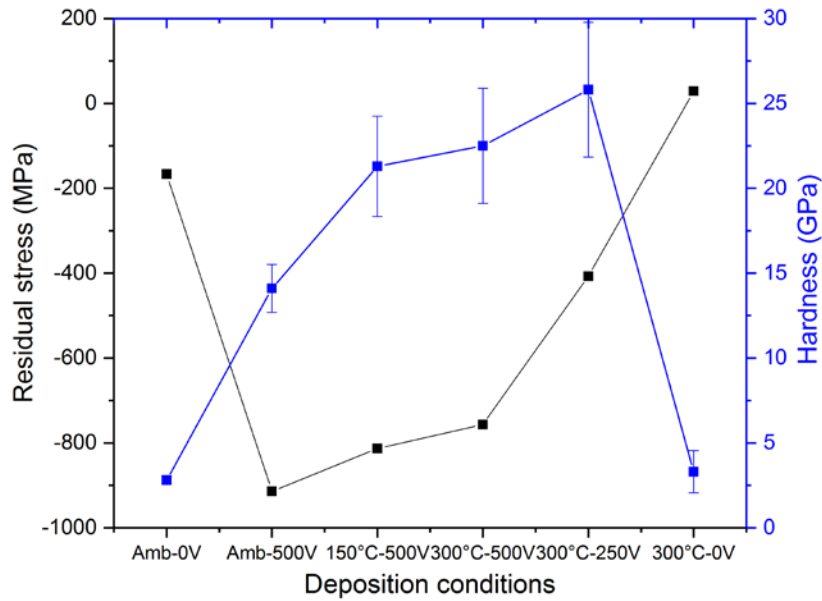


Figure 116. Correlation between residual stress and hardness of the AlCrN monolayers

Concerning the hardness, it increases with the deposition temperature (Figure 116), this result can be explained by the grain size evolution (“Hall-Petch effect”). Indeed, the grain size is inversely proportional to the hardness as illustrated in Figure 117.

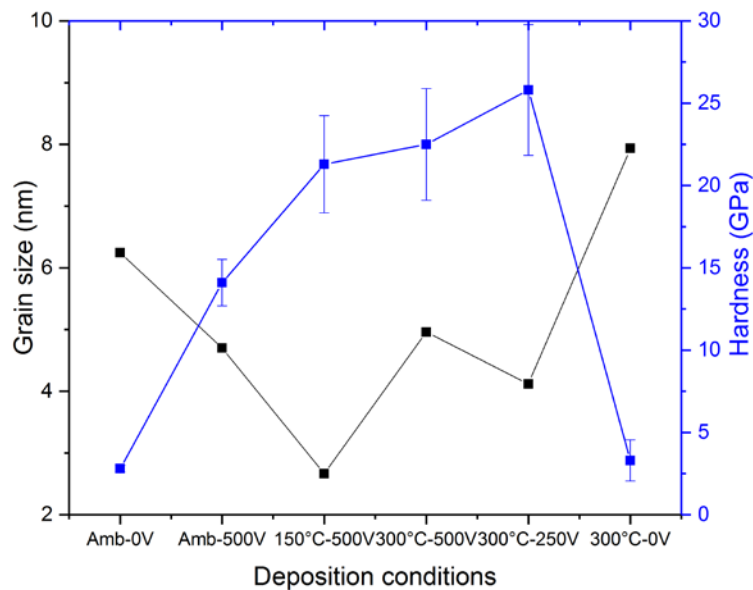


Figure 117. Grain size and hardness of the AlCrN monolayers

Nevertheless, when the deposition temperature is fixed to 300°C, the hardness and the residual stress increase with the substrate bias voltage. We can confirm here that the main residual stress are the thermal ones when the temperature and substrate bias voltage are high, while the hardness is a result of the Hall-Petch effect.

The correlation between plastic deformation resistance and wear rate is illustrated in *Figure 118*.

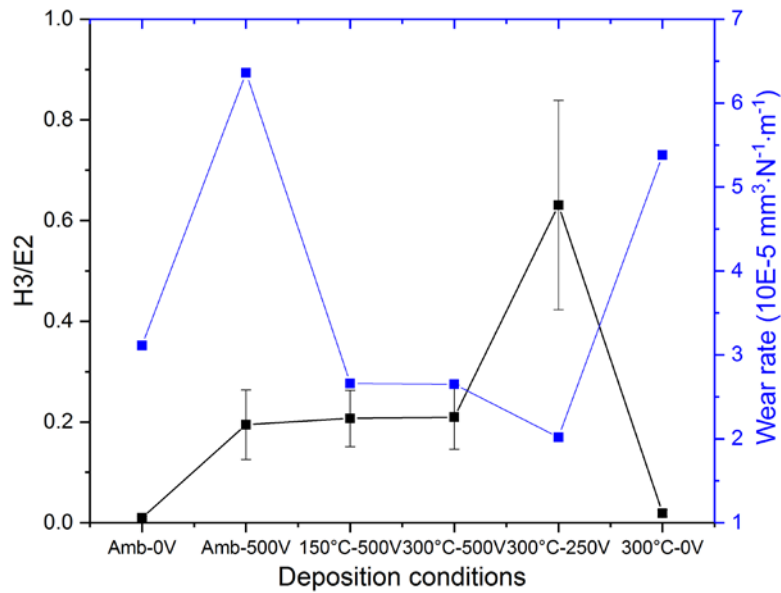


Figure 118. Wear rate and plastic deformation resistance of the AlCrN monolayers

We verify that the AlCrN layer obtained at 300°C-0V has a high wear rate because of the lowest plastic deformation resistance. It is also obvious, that the AlCrN layer obtained at 300 °C and -250 V shows the best plastic deformation resistance and the lowest wear rate. Nevertheless, the correlation between plastic deformation resistance and wear rate is not so obvious in the case of the AlCrN layers than it was in the case of the CrN ones.

3.2.3.2.4.3. Adhesion

Figure 119 and

Figure 120 show the critical loads of the AlCrN monolayers obtained on rough WC substrate. The failure mode of Bull [262] will be used to identify the damages of the coatings during scratch-tests.

Some recovery spallation is observed for all the AlCrN coatings according to Bull [262].

In *Figure 121a1*, on mirror-polished WC substrates, it seems that we have a wedging spallation mode when it reaches the Lc1 critical load for the AlCrN layer obtained at 300°C-250V. Recovery spallation is observed at the Lc2 critical load (*Figure 121a2*).

Table 38 summarizes the critical loads and work of adhesion for each coating as determined in *Figure 119*,

Figure 120 and *Figure 121*.

We mostly verified here the results of Nouveau [112] who observed also in the case of CrN layers synthesized by RF magnetron sputtering that the critical loads are related reversely to the work of adhesion.

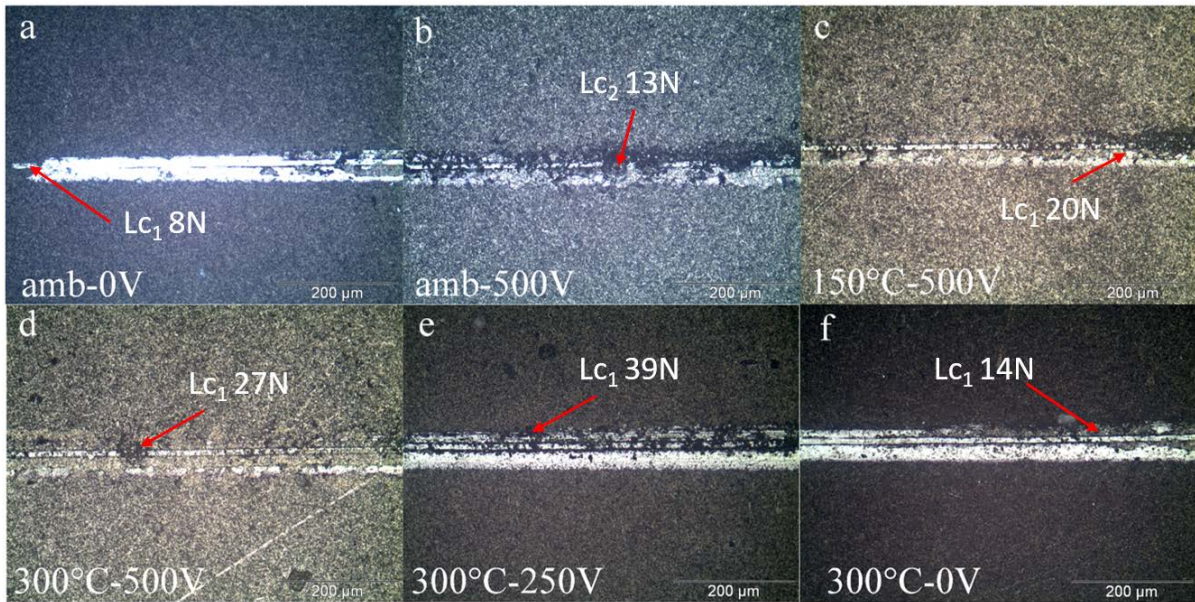


Figure 119. Optical images of the critical load Lc_1 of the AlCrN monolayers on rough WC substrate: a) Ambient-0V, b) Ambient-500V, c) 150°C-500V, d) 300°C-500V, e) 300°C-250V, f) 300°C-0V

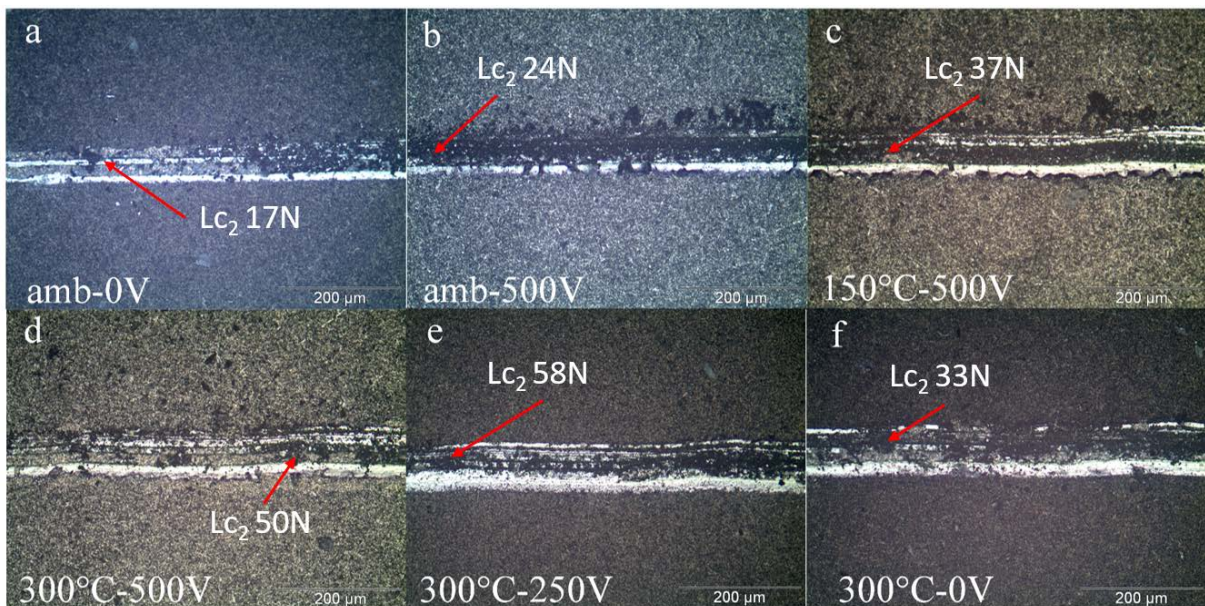


Figure 120 Optical images of the critical load Lc_2 of the AlCrN monolayers on rough WC substrate: a) Ambient-0V, b) Ambient-500V, c) 150°C-500V, d) 300°C-500V, e) 300°C-250V, f) 300°C-0V

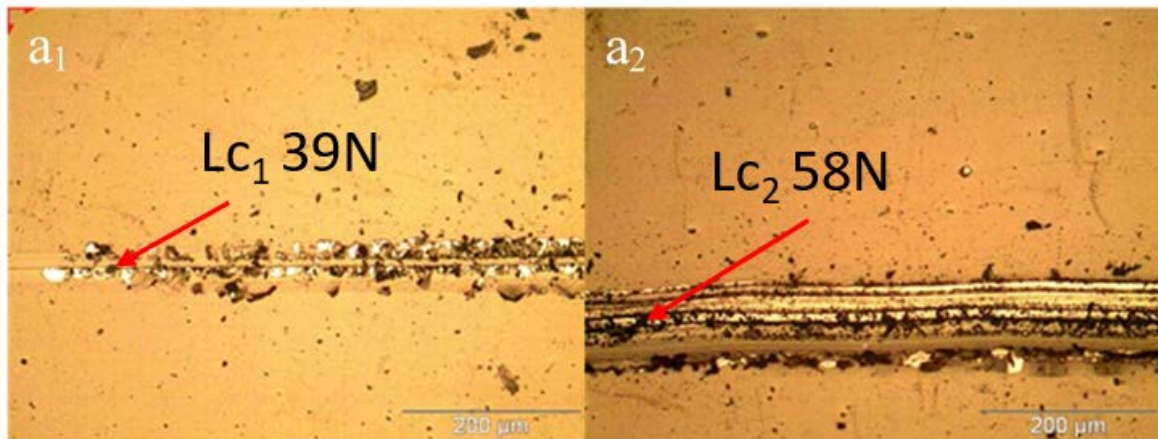


Figure 121. Optical images of the critical loads of AlCrN monolayers obtained at 300°C-250V on polished substrate: a1) Lc1 and a2) Lc2

Table 38. Critical load and work of adhesion of AlCrN monolayers

Properties \ Deposition conditions	Deposition conditions					
	Ambient -0V	Ambient -500V	150°C -500V	300°C -500V	300°C -250V	300°C -0V
Lc ₁ (N)	8	13	20	27	39	14
Lc ₂ (N)	17	24	37	50	58	33
W _{ad} (J/m ²)	6.5	3.09	6.32	1.39	4.05	10.55

As in the case of the CrN layers, when the deposition temperature is fixed (to ambient or 300°C), increasing the substrate bias voltage results in a decrease of the work of adhesion and in an increase of the residual stress. Nevertheless, the influence of the deposition temperature is not so obvious. Indeed, when the substrate bias voltage is fixed to -500 V, the stress decreases when the deposition temperature increases. But it is only the case for the work of adhesion when the deposition temperature varies from ambient to 150°C, it decreases also as the stress when the deposition temperature increases up to 300°C.

As expected, the highest work of adhesion corresponds to the lowest residual stresses (tensile and compressive) according to Figure 122.

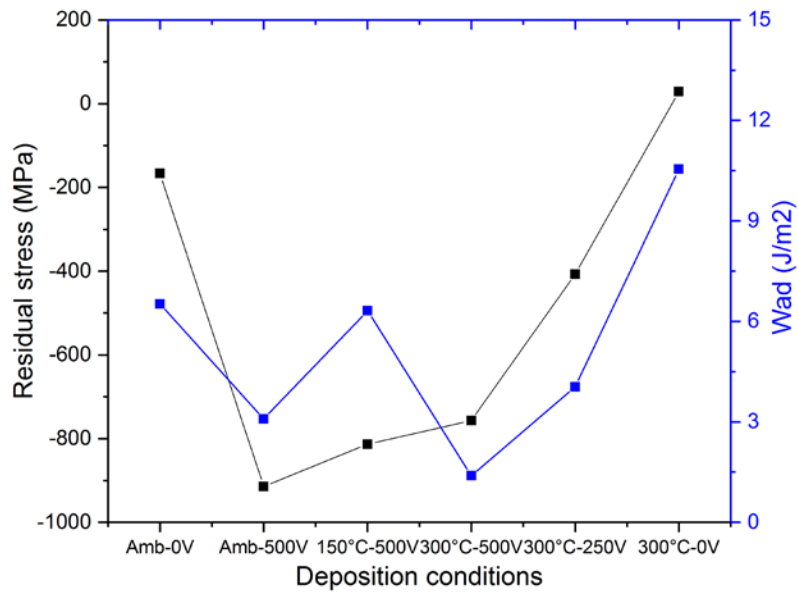


Figure 122. Relation between residual stress and work of adhesion of AlCrN monolayers obtained on silicon substrate

Figure 123 presents the critical loads of AlCrN monolayers as a function of the deposition conditions.

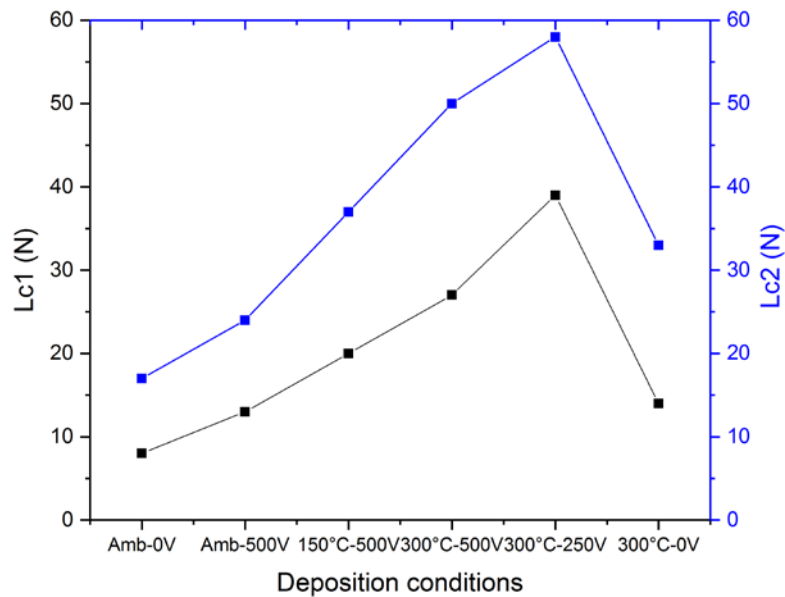


Figure 123. Critical loads of AlCrN monolayers

A better adhesion appears for the AlCrN monolayer synthesized at 300 °C and -250 V with a Lc2 up to 58 N. In comparison, Gong et al. [290] got similar results with an angular cracking of 58 N and a transverse cracking of 65 N for their Al₇₀Cr₃₀N layers synthesized on sintered carbide substrates. Besides, most of the AlCrN layers present a better adhesion than the CrN layers whatever the deposition conditions.

It is obvious in *Figure 123* that the adhesion, Lc1 and Lc2 critical loads, increases with the substrate bias voltage and the deposition temperature. The temperature and bias voltage both have positive impacts on adhesion property of the AlCrN layers. We previously mentioned, in the case of the CrN layers, that Niu et al. [263] showed that the pack density, bombardment and implantation effect are enhanced with the increase of substrate bias voltage. It results in the improvement of adhesion strength for Ti–Zr–N (multi-phase) films prepared by cathodic vacuum arc technique with different substrate bias voltage(0 to -500 V). To explain the influence of the deposition temperature on the adhesion of the AlCrN coatings, Thouless [264] and Toonder et al. [265] pointed out that the adhesion energy is directly proportional to the elastic modulus of the coatings as verified in *Figure 124*.

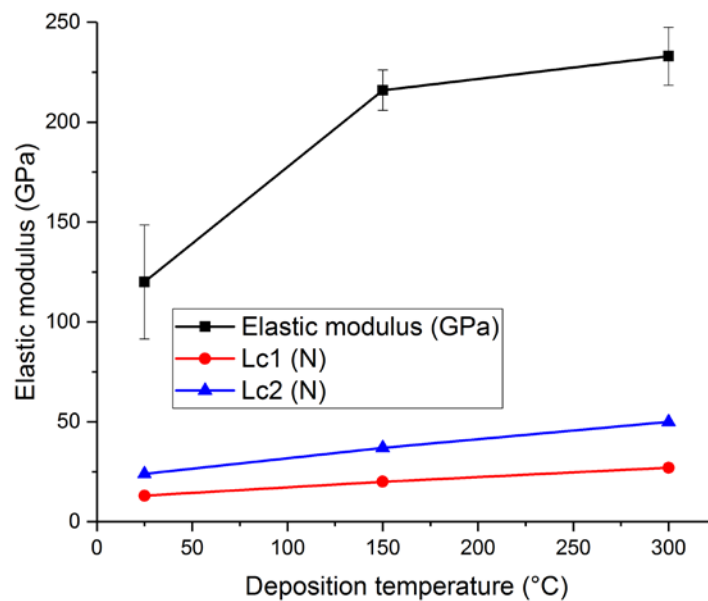


Figure 124. Evolution of the Lc1, Lc2 critical loads and elastic modulus of the AlCrN monolayers as a function of the deposition temperature at a substrate bias voltage of -500V

From *Figure 124*, it is clear that the coatings deposited at 300°C has the higher elastic modulus (233 GPa). Therefore, both the critical load and adhesion energy suggest that the coating deposited at 300 °C and -250 V has a better adhesion strength (*Figure 123*).

Furthermore, as previously observed from the CrAlN layers with different Al content, it is verified that the evolution of the force required to tear off the AlCrN layer from its substrate (Lc2) is correlated to the evolution of the grain size [287]. Indeed, when the grain size increases, the Lc2 critical load decreases as shown in *Figure 125*.

Moreover, in contrary to the CrAlN layers, it is obvious in *Figure 126* that the stress and the critical load Lc2 behave the same.

Indeed, the critical load increases when the stress increases. In addition, samples with low stress have better adhesion than those with high stress. Such results were observed by Lin et al. [291] for aluminum oxide films on glass substrates. They concluded that “the adhesion strength of aluminum oxide films on glass increases as compressive residual stresses because of the resistance to the tensile cracking failure provided by the compressive residual stress in the films”. Then, it should be interesting to verify by SEM observations if we have tensile cracks for the AlCrN layers presenting compressive stress.

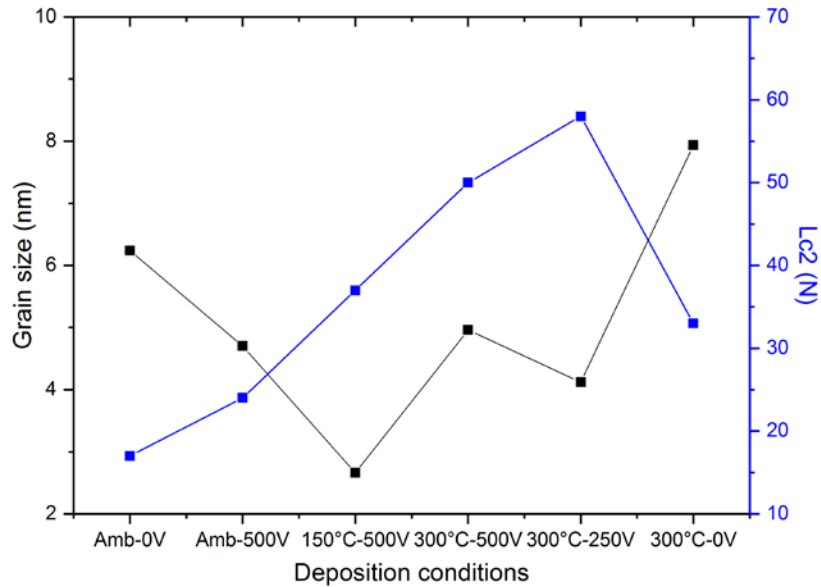


Figure 125. Evolution of the L_{c2} critical load of the AlCrN monolayers and the grain size as a function of the deposition conditions

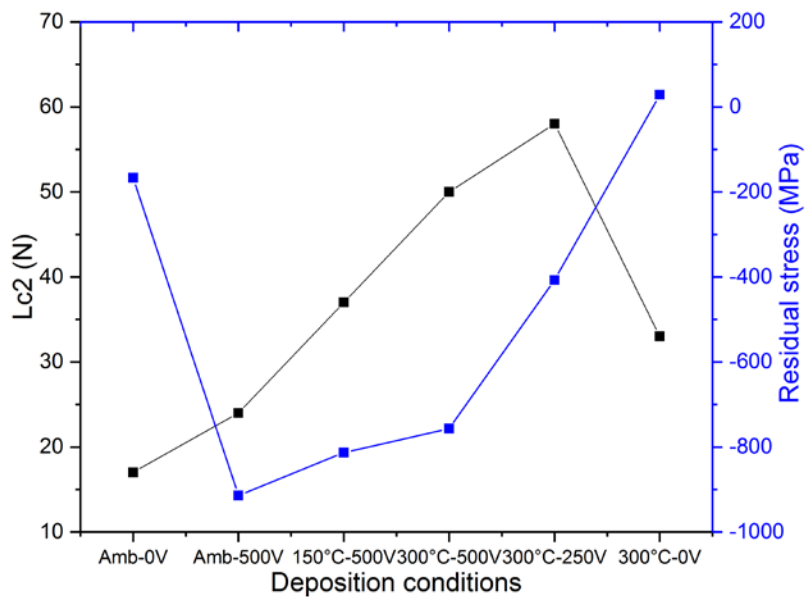


Figure 126. Correlation between residual stress and critical load L_{c2} of the AlCrN monolayers

3.2.3.2.5. Partial conclusion

In this section we developed AlCrN monolayers by varying the deposition temperature and substrate bias voltage. The influence of these parameters on the coatings' properties was shown. Indeed, high deposition temperature and substrate bias voltage would permit to get a dense and homogeneous AlCrN layer on silicon substrates. For the AlCrN layers, the temperature has an influence on the microstructure.

The crystalline orientation of the AlCrN layers depends on the substrate bias voltage but also on the deposition temperature and these both parameters are correlated. The grain size decreases when the bias voltage increases and the deposition temperature decreases. Concerning the mechanical properties of the AlCrN layers: their COF does not depend on the deposition temperature or the substrate bias voltage and was around 0.5. All the AlCrN layers have compressive stress varying from -914 MPa to -166.3 MPa except the layer realized at 300°C-0V that has tensile stress of 28.6 MPa. The temperature and bias voltage have both positive impacts on adhesion property of the AlCrN layers. We also showed that for the AlCrN layers, the Hall-Petch effect governs their hardness.

Moreover, mostly we verified the results of AlCrN with the CrN monolayers. Indeed, it has been shown that the substrate bias voltage increases the residual stress while the deposition temperature reduces it. Most of the AlCrN layers present a better adhesion than the CrN layers whatever the deposition conditions.

According to their properties, the stoichiometry of the AlCrN layers is Al₆₂Cr₃₈N. In XRD we observe only the cubic phase of CrN and AlN for all coatings, no hexagonal Cr₂N or AlN diffraction peaks are present. The experimental diffraction peaks are close or between the CrN and AlN theoretical diffraction positions, so we can consider that the AlCrN layers are solid solutions of Al atoms in substitution in the CrN lattices.

The AlCrN layer synthesized at 300°C-250 V is well crystallized, presents the highest hardness and H³/E² ratio whatever the substrate, an acceptable elastic modulus of 165-170 GPa, the best plastic deformation resistance, the lowest wear rate and best adhesion with a Lc2 up to 58 N.

This AlCrN optimized monolayer (300°C-250 V) will be applied in the synthesis of the Cr/CrN/AlCrN multilayers, which will be presented in the following section.

3.3. Cr/CrN/AlCrN and Cr/CrN/CrAlN multilayers

We are now going to introduce the development of our multilayers. The main idea is to combine irreconcilable properties in a single material. Indeed, the multilayer coatings can have new

properties or even an improved behavior compared to the monolayers of which they are composed. Our objective is to develop a coating with a good adhesion, a good wear resistance and a good thermal stability.

We recall that an almost pure chromium thin films was obtained by DC magnetron sputtering with an acceptable adhesion on tungsten carbide substrate, a low friction coefficient and wear rate after being in contact with Ti6Al4V ball. The CrN monolayer deposited under 300°C and -500 V, exhibits a (200) preferred crystalline orientation, is well crystallized, has a dense surface morphology and small top column size. Concerning its mechanical properties, it presents the highest hardness and elastic modulus, the best plastic deformation resistance and has a very good adhesion up to 43 N (Lc_2), the lowest wear rate of $0.58 \times 10^{-4} \text{ mm}^3 \cdot \text{m}^{-1} \cdot \text{N}^{-1}$. Finally, the $\text{Al}_{62}\text{Cr}_{38}\text{N}$ layer synthesized at 300 °C-250 V is well crystallized, presents the highest hardness whatever the substrate, an acceptable elastic modulus of 165-170 GPa, the best plastic deformation resistance, the lowest wear rate and best adhesion with a Lc_2 up to 58 N.

Thus, we are going to synthesize multilayers such as Cr/CrN/AlCrN and study the effect of the number of interfaces of and of their thickness on the physico-chemical, structural, tribological and mechanical properties. Besides, the best Cr/CrN/CrAlN multilayer obtained by Aouadi [111] was also deposited on WC substrate as a reference and will be compared to our coatings.

3.3.1. Deposition conditions

We studied three types of multilayers architectures as shown in *Figure 127*. All the multilayers are composed of a Cr underlayer and the repetition of the CrN/AlCrN pair. Whatever the multilayer, each CrN/AlCrN pair has the same chemical composition and the Cr underlayer is about 200 nm thick. This thickness for the underlayer was selected because the R_a of substrate is around 200 nm. Bouzakis et al. [162] studied the effectiveness of Cr/CrN underlayer to improve the adhesion property and cutting performance of cemented carbide substrate. Their conclusion is that the underlayer should be adapted to the substrate's surface roughness. Besides, Hong et al. [164] made a study on mechanical properties of CrAlSiN with different Cr underlayer thickness. They observed that the hardness of the coating gradually decreased with increasing the Cr underlayer thickness, as well as the adhesion. The total thickness is pre-set to about 3 μm for each type of multilayers as this is a well-known optimal thickness on cutting tools as observed by Nouveau [112]. Indeed, a lower thickness would not be efficient while a

higher one could tend to diminish the cutting angle of the cutting tools and decrease their service life.

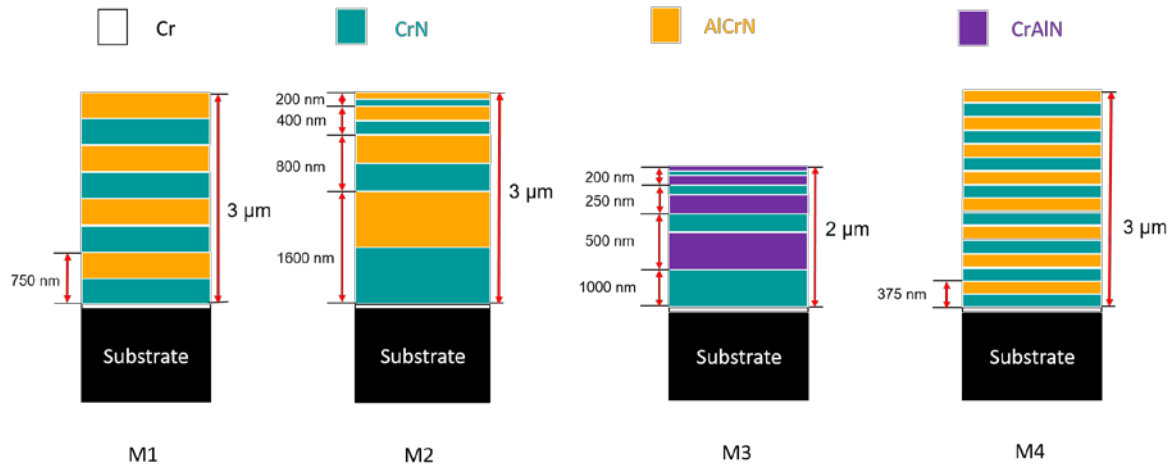


Figure 127. Architecture of the multilayers

As far as the CrN/AlCrN architectures are concerned, we can summarize them as follows:

-M1 is made of 4 pairs of CrN/AlCrN, 750 nm thick each

-M2 is made of 4 pairs of CrN/AlCrN with decreasing thickness from the substrate interface to top surface. The thickness of each CrN/AlCrN pair is 1600 nm, 800 nm, 400 nm and 200 nm from the bottom to the top of the multilayer. Moreover, we wanted to verify and compare the AlCrN ternary coating with the CrAlN one of Aouadi [111]. This is why we have two similar multilayers: M2 is the Cr/CrN/AlCrN multilayer while M3 is a 2 μm Cr/CrN/CrAlN multilayer.

-M4 is made of 8 pairs of CrN/AlCrN, 375 nm thick each.

The deposition conditions of the multilayers are listed in *Table 39*. For M3, we repeated the deposition conditions of Aouadi [111] to realize his best Cr/CrN/CrAlN multilayer. The deposition conditions that differ from ours are clearly shown in *Table 39*. Indeed, argon and nitrogen flow, the power applied on the Cr and Al targets for the ternary monolayer, the deposition time for each binary/ternary pair and the substrate bias voltage were different. Besides Aouadi realized his coatings on 90CrMoV8 steel, not on carbide substrate. As a consequence, the thickness of his Cr underlayer is 150 nm instead of 200 nm for our multilayers. When the comparison our results with the one of Aouadi is made, the differences will be taken into consideration.

Table 39. Deposition conditions of the multilayers

Multilayer		M1	M2	M3 Repetition of Aouadi [111]	M4
Argon flow (sccm)	Cr	100		92	100
	CrN	60		68.6	60
	AlCrN	60		-	60
	CrAlN	-		68.6	-
Nitrogen flow (sccm)		53		33.3	53
Working pressure (Pa)		0.5			
Power applied on the chromium target (W)	Cr	1500			
	CrN	1500			
	AlCrN	500		-	500
	CrAlN	-		1500	-
Power applied on the aluminum target (W)		1500		1000	1500
Substrate rotation speed (rpm)		1.5			
Deposition time (min)	Cr	15		10	15
	CrN	45×4	90/45/25/20*	60/30/15/12*	25×8
	AlCrN	75×4	150/75/40/30*	-	40×8
	CrAlN	-	-	60/30/15/12*	-
Deposition temperature (°C)		300			
Substrate bias voltage (V)	Cr	-500			
	CrN	-500			
	AlCrN	-250		-	-250
	CrAlN	-		-500	-

* The deposition time presented for M2 and M3 are the deposition time for each monolayer from the thicker to the thinner.

3.3.2. Physico-chemical properties

3.3.2.1. Deposition rate and thickness

Our objective was to obtain a total thickness of 3 μm for the Cr/CrN/AlCrN multilayers and of 2 μm for the Cr/CrN/CrAlN one. Finally, according to the SEM cross section images in *Figure 130*, the thickness of the Cr/CrN/AlCrN multilayers varies from 2.44 to 2.55 μm while the Cr/CrN/CrAlN multilayer is 1.85 μm . Then, even if the work is on an industrial PVD system with an automatic process, we show here that the system was well controlled to get similar thicknesses for the Cr/CrN/AlCrN multilayers and a Cr/CrN/CrAlN one close to 2 μm . The deposition rate is from 4.8 to 5 $\text{nm}\cdot\text{min}^{-1}$ for the Cr/CrN/AlCrN multilayers while it is 7.6 $\text{nm}\cdot\text{min}^{-1}$ for the Cr/CrN/CrAlN ones. This can be explained by the higher Cr content in the CrAlN ternary monolayers in comparison to the AlCrN ones and the higher sputtering yield of Cr in comparison to the Al one.

3.3.2.2. Chemical composition by EDS microanalyses

The chemical composition is quantitatively determined by EDS profiles made on silicon (100) substrates cross sections. The profiles of each element are depicted in *Figure 128* and compared with the expected architectures of the Cr/CrN/AlCrN or Cr/CrN/CrAlN layers.

It is obvious in *Figure 128*, that the repetitions of CrN/AlCrN or CrN/CrAlN pairs are well present in all the multilayers according to what was expected from *Figure 127*. Indeed, it is clearly verified the thickness of each multilayer but also the thickness of each monolayer. It is verified that M1 and M4 are homogenous in thickness and that the monolayers thickness decreases according to the expectation. The nitrogen percentage is almost constant all along the profiles, which indicates that the nitrogen flow is well controlled by the automate process during the CrN/AlCrN and CrN/CrAlN pairs deposition. The oxygen content is below 10 at.% for all multilayers synthesized. Nevertheless, as mentioned in the previous sections, regarding the XPS results, the oxygen detected by EDS may be overestimated. Another interesting observation is that for M1, the chemical composition of Al in AlCrN almost reaches 60 at.% ($\text{Al}/(\text{Al}+\text{Cr})$ at.%), while for M2 and M3, the Al content decreases with the AlCrN and CrAlN thickness, respectively. For M4, the Al content falls to about 40 at.% ($\text{Al}/(\text{Al}+\text{Cr})$ at.%). This may be explained by the SEM scanning beam limit. Indeed, the width of the beam is about 500 nm, as mentioned in Chapter 2, when the thickness of CrN/AlCrN pair is below this value, an interaction between two pairs may occur and then the quantitative evaluation of the chemical composition can be distorted.

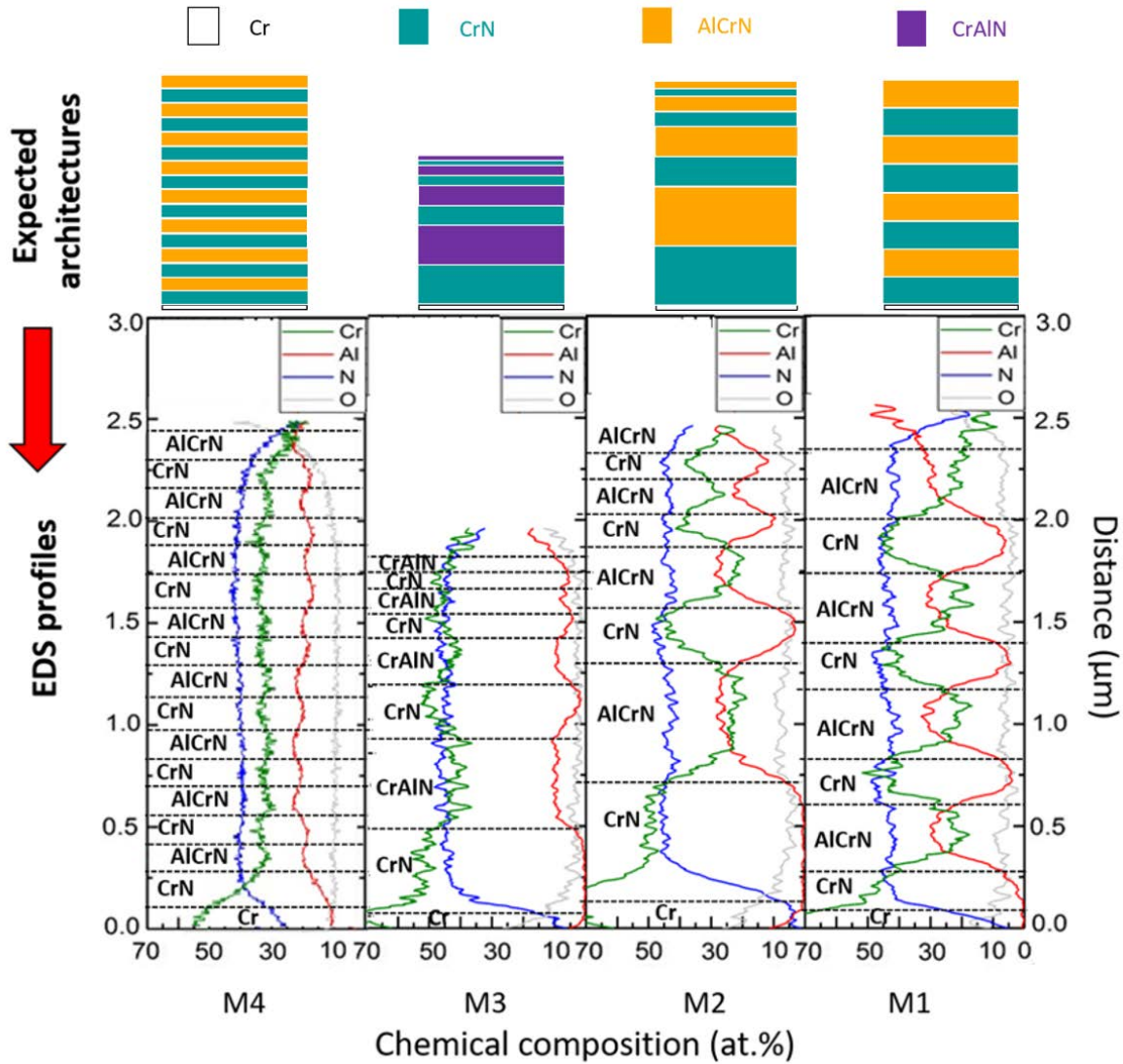
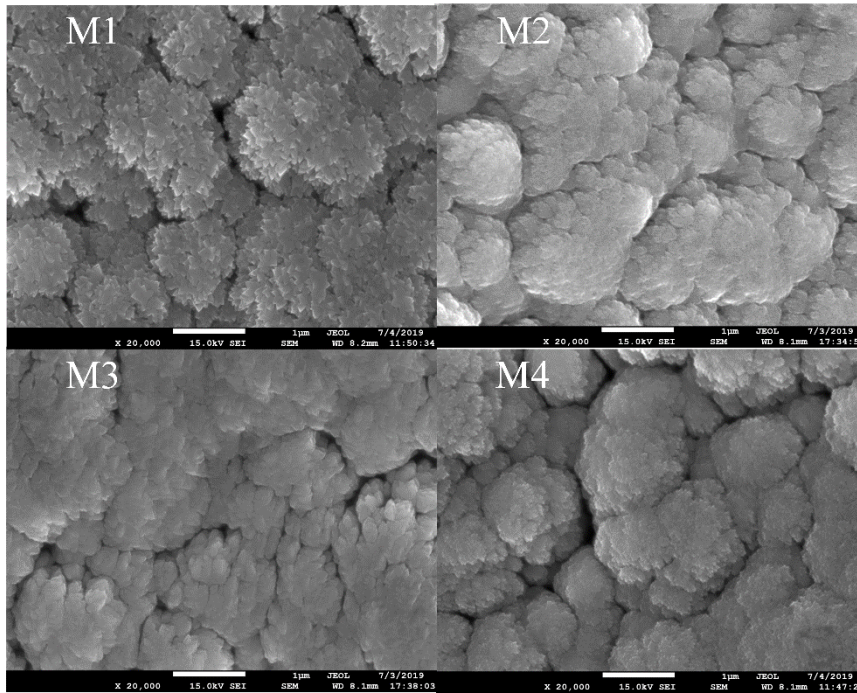


Figure 128. Chemical composition of multilayers (cross-section EDS scanning profiles)

3.3.2.3. Surface morphology and microstructure

Observations of the surface morphology of the Cr/CrN/AlCrN and Cr/CrN/CrAlN multilayers were carried out by SEM-FEG at high resolution. *Figure 129* shows the surface morphology of multilayers on rough and mirror-polished WC substrates.

Rough WC substrates



Mirror-polished WC substrates

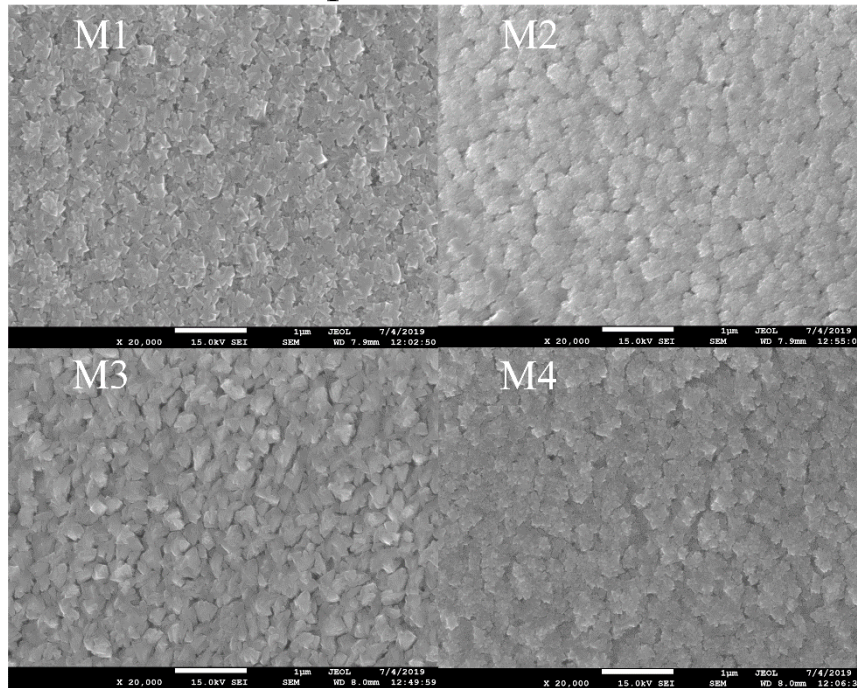


Figure 129. Surface morphology of multilayers on rough and mirror-polished WC substrates

On rough WC substrates, we note that the morphology of multilayer coatings is of columnar type. Most of the surface morphologies looks like cauli-flower, are homogenous with low porosity as it was the case for the AlCrN layers obtained at 300 °C-250 V (Figure 104e). Some

pyramidal tops are visible only for M1 for a thicker top AlCrN layer. The three other multilayers with an AlCrN or a CrAlN top layer of around 200 nm present similar surface morphologies. It is obvious, on mirror-polished WC substrates, that the top AlCrN layers are denser than the top CrAlN one. The intrinsic properties of the Cr/CrN/AlCrN and Cr/CrN/CrAlN multilayers should differ. Besides, as we have here a smooth substrate, the columns clusters of each multilayer are smaller. We can also observe more pyramidal tops than on the rough substrate. Moreover, the surface morphology of the M2 multilayer is close to the surface morphology observed for a AlCrN monolayer obtained at 300 °C-250 V on a mirror-polished silicon substrate (*Figure 105e*).

Figure 130 shows the cross-section of the multilayers on silicon substrate. As already observed by Aouadi [111], all films show a dense, columnar structure which is comparable to studies conducted by Barshilia et al. and Okumiya et al. [126, 157].

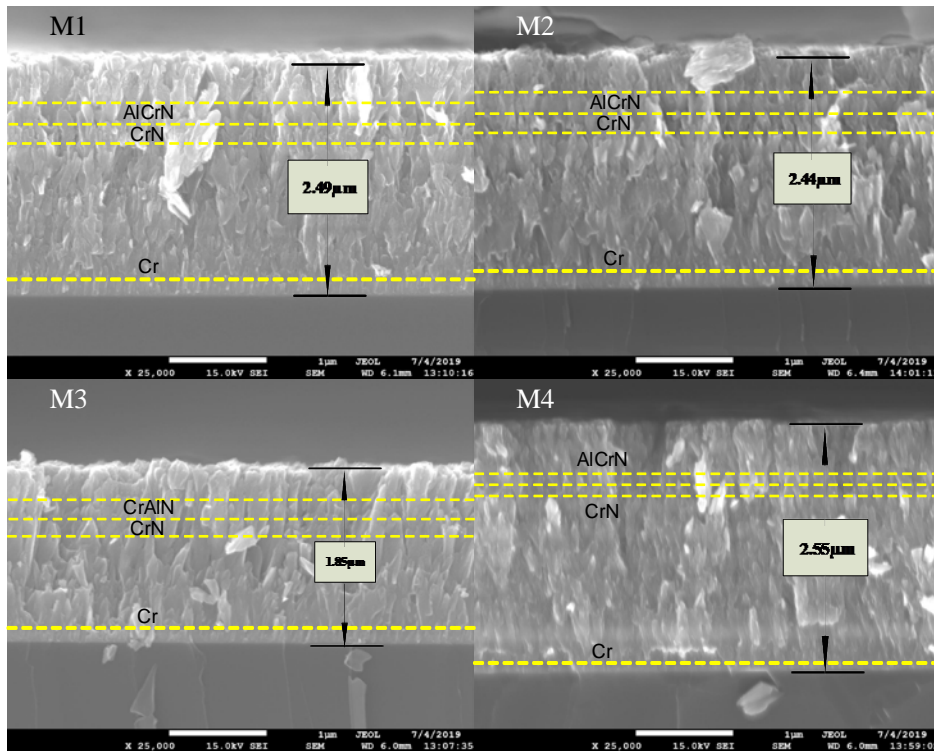


Figure 130. Cross section of the multilayers on silicon substrates

As shown in *Figure 130*, the CrN/AlCrN or CrN/CrAlN pairs can be observed, even if the contrast between these layers is not high. The Cr underlayer is the first layer bonded to the substrate and its thickness is around 160 ± 20 nm. Furthermore, regarding all the multilayers produced, at the interface between the coating and the substrate, we observe that the grain size of the Cr layer is very small and that this layer is very dense. This zone is formed at the beginning of the PVD process when the temperature and the mobility of the adsorbed atoms are

low. Thus, a large number of small grains are formed. Then, during the deposition and due to the growth of the other monolayers, grains of larger size and with a preferential orientation are formed. Therefore, we can conclude about the existence of small columns at the Cr / substrate interface and then large grains for the other successive monolayers as explained by Wiecinski et al. [292].

We are now going to verify the structure and grain size of the multilayers in the following section.

3.3.2.4. Structure

The XRD analyses have been made on WC coated substrate (Figure 131).

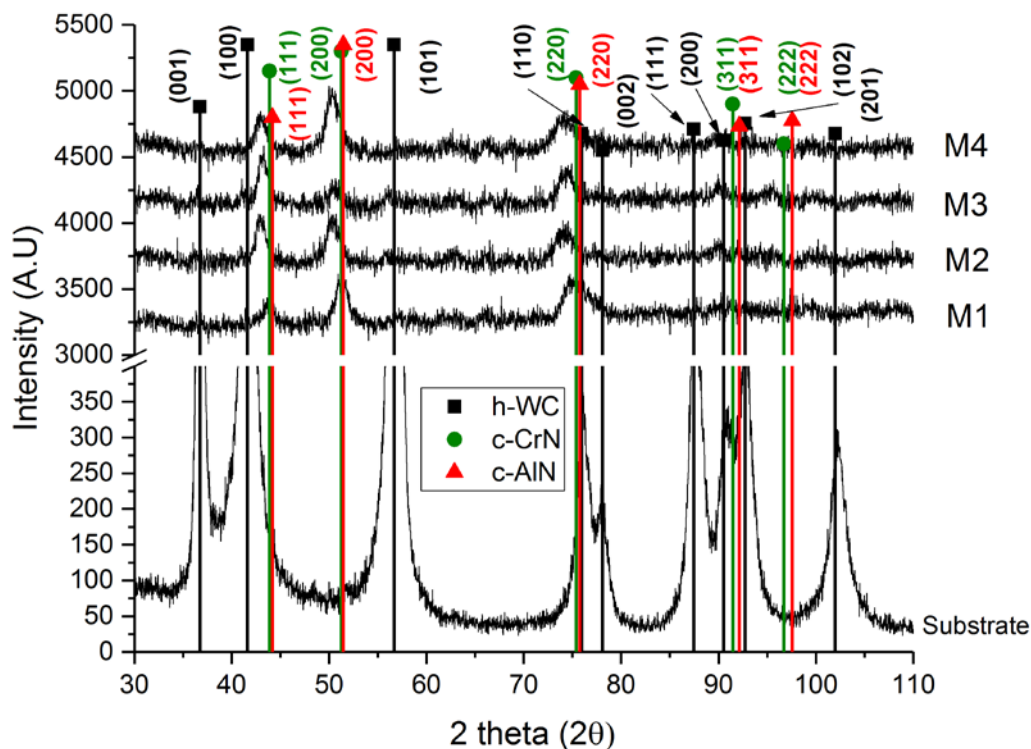


Figure 131. XRD patterns of the multilayers

As the multilayers are composed of CrN/AlCrN or CrN/CrAlN pairs, their XRD patterns show the same peaks positions as the monolayers. Thus, according to the (ICDD 00-011-0065) and (ICDD 00-025-1495) cards, we observe only the cubic phase of CrN and AlN for all multilayers. The M1 presents a major (200) at 51.27°, (220) at 75.34° and a minor (111) diffraction peak at 43.72°. The M2 coating presents (111) and (200) major diffraction peaks at 43.06 and 50.48°, respectively. It also shows a non-negligible (220) diffraction peak at 74.25°. The M4 multilayer has a main (200) diffraction peak at 50.26°. It also shows the (111) and (220) diffraction peaks at 43.06 and 74.25°, respectively. The M1 and M4 multilayers both

present a major (200) diffraction peak while the M2 has similar (111) and (200) diffraction peaks intensity. The difference between M1 and M4 multilayers is the number of interfaces, even if, the CrN and AlCrN thickness in all these coatings is the same (*Figure 127*). That is why they present very similar XRD patterns. Therefore, we can conclude that the number of interfaces does not have any influence on the multilayers structure. This is not the case for the different thickness of each monolayer. Indeed, the M2 multilayer should have also a similar total thickness of CrN and AlCrN than the M1 and M4 multilayers, but it has a different XRD pattern. This architecture (variation of the monolayers thickness) seems to favor (111) and (200) orientations. It means that the monolayers thickness has an influence on their growth mechanism and as a consequence, on their crystalline orientations. Indeed, Ellis et al. [293] explained that “the (111)-to-(100) texture transformation has been attributed to a competition between strain energy and interface energy. In FCC materials, the (111) orientation has the lowest interface energy, while the (100) orientation has the lowest biaxial modulus. Thus, the interface energy per unit volume decreases as the inverse of the film thickness, while, at a given strain, the strain energy per unit volume is constant with film thickness. This model therefore predicts that a critical thickness exists, below which a film should adopt (111) fiber texture to minimize interface energy, and above which it should adopt a (100) fiber texture to minimize strain energy”. As a matter of fact, as the monolayers thickness is decreased in the M2 multilayer, we have more (111) orientations than the two other multilayers, while the (200) orientation is still present.

The M3 multilayer presents a (111) major diffraction peak at 43.17° and minor (200) and (220) diffraction peaks at 50.7 and 74.47° , respectively. Similar results were found by Aouadi [111]. Thus, we verify here the reproducibility of the Cr/CrN/CrAlN multilayer deposition conditions. In *Table 40* are listed the theoretical and experimental diffraction peaks position detected in the multilayers and the calculated grain size thanks to the Debye-Scherrer formula (*Equation 10*). All the diffraction peaks are shifted to smaller 2θ positions compared to CrN and AlN theoretical positions, which means that the multilayers may have tensile stress according to Bragg's law.

The grain size of the multilayers with CrN/AlCrN pairs is very similar because it only varies from 5.51 to 5.95 nm, whatever the number of interface and the CrN/AlCrN pairs thickness.

Table 40. Theoretical and experimental diffraction peaks position and grain size of as-deposited multilayers

Coatings \ 2θ (°)	(111)	(200)	(220)	Grain size (nm)	Diffraction peaks as reference
CrN (theoretical)	43.88	51.26	75.38	-	-
AlN (theoretical)	44.17	51.47	75.75	-	-
M1	43.72	51.24	75.34	5.57	(200)
M2	43.06	50.48	74.25	5.95	(200)
M3	43.17	50.7	74.47	9.35	(111)
M4	43.06	50.26	74.25	5.51	(200)

We verify here the SEM observations shown in *Figure 129*. In the contrary, the M3 with CrN/CrAlN pairs has a higher grain size of 9.35 nm (*Figure 132*).

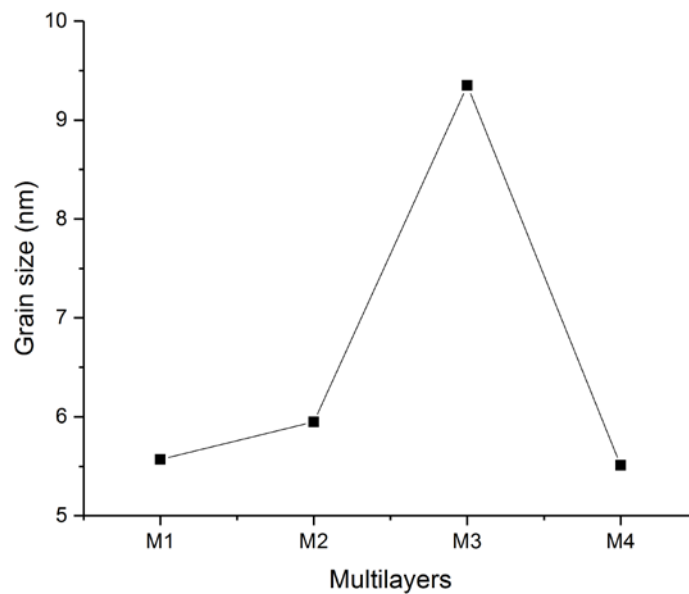


Figure 132. Grain size of the multilayers

We also verify here the SEM surface morphology previously mentioned (*Figure 129*). This is consistent with other studies on AlCrN and CrAlN coatings. Indeed, because of the substitution of Cr atoms by Al atoms, the lattice is smaller. Lin et al. [167] found a continuous decrease of lattice parameter from pure CrN coatings to AlCrN with 58.5 at.% of Al. Moreover, Hasegawa

and Suzuki [267] or Reiter et al. [170] observed similar results: in the last case, the lattice parameter decreases from pure CrN to fcc AlCrN coatings containing 71 at.% of Al. The multilayer M3 has a grain size of only 9.53 nm, while Aouadi [111] obtained by AFM a grain size of around 31 nm for his multilayer. It could be explained by the fact that we did not use the same technique to determine the grain size of the coatings (AFM and XRD/Debye Scherrer).

3.3.3. Tribological properties

The friction tests were conducted with a Ti6Al4V ball against coated WC substrates. The applied normal force is 10 N, the friction speed is 10 cm/s, the sliding distance is 100 m and about 4000 cycles were realized. No lubricant was used. The SEM images of the wear tracks are presented in *Appendix E*.

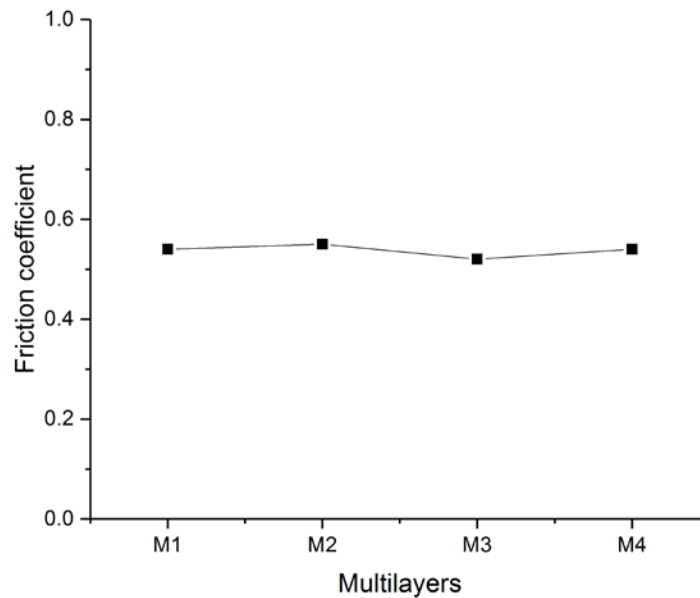


Figure 133. Friction coefficient of the multilayers

As shown in *Figure 133*, the friction coefficient varies from 0.52 to 0.55. Whatever the multilayers architecture, there is no influence. As expected, the COF of the multilayers is similar to the COF of the AlCrN and CrAlN monolayers (around 0.5, see *Figure 109* and *Figure 88*). Aouadi [111] found a higher friction coefficient (0.68) for his Cr/CrN/CrAlN multilayer. However, he used an alumina ball and different friction conditions: an applied normal load of 5 N and a sliding speed of 2 cm/s.

The wear rate is presented in *Figure 134* and in *Table 41*.

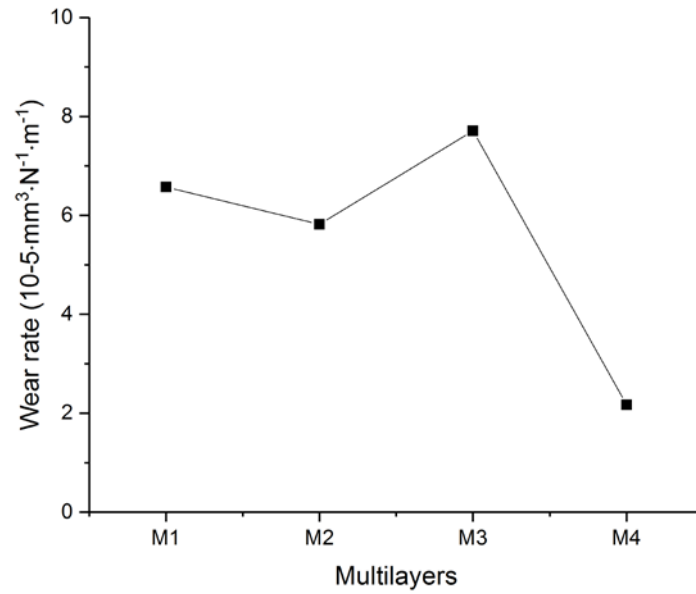


Figure 134. Wear rate of the multilayers

Table 41. Wear rate of the multilayers

Multilayer	M1	M2	M3	M4
Wear rate ($\times 10^{-5} \text{ mm}^3 \cdot \text{m}^{-1} \cdot \text{N}^{-1}$)	6.57	5.82	7.71	2.17

The multilayers have a wear rate in the same order of magnitude ($\times 10^{-5} \text{ mm}^3 \cdot \text{m}^{-1} \cdot \text{N}^{-1}$) as that of the AlCrN or CrAlN monolayers (Figure 111 and Figure 89). We can expect hardness for the multilayers close to the one of the monolayers. The highest wear rate belongs to M3 and the lowest one belongs to M4. Comparing M1 and M4 multilayers, increasing the number of interfaces improves the tribological behavior of multilayers [111, 158, 292]. Indeed, the interfaces interact with the dislocations and the propagation of cracks. An increase in the number of interfaces increases the number of barriers to crack propagation. As a result, the wear resistance increases. We thus observe that the wear rate of multilayers decreases when the number of interfaces increases.

When we compare M1 and M2, the wear rate is lower when the CrN/AlCrN pairs thickness progressively decreases. This result has also been observed by Aouadi [111].

Comparing the M2 and M3 multilayers, a higher wear rate is obtained for the last one. The better performance of M2 is attributed to the replacement of CrAlN monolayer by AlCrN monolayer. As mentioned in the $\text{Cr}_{1-x}\text{Al}_x\text{N}$ section, the increasing Al content in the CrN matrix will increase its mechanical and thermal properties, thus increase its tribological properties.

3.3.4. Mechanical properties

3.3.4.1. Residual stress

The residual stresses in the multilayers were determined by measuring the curvature of the samples before and after deposition on silicon.

The residual stresses of the multilayers are presented in *Figure 135* and *Table 42*.

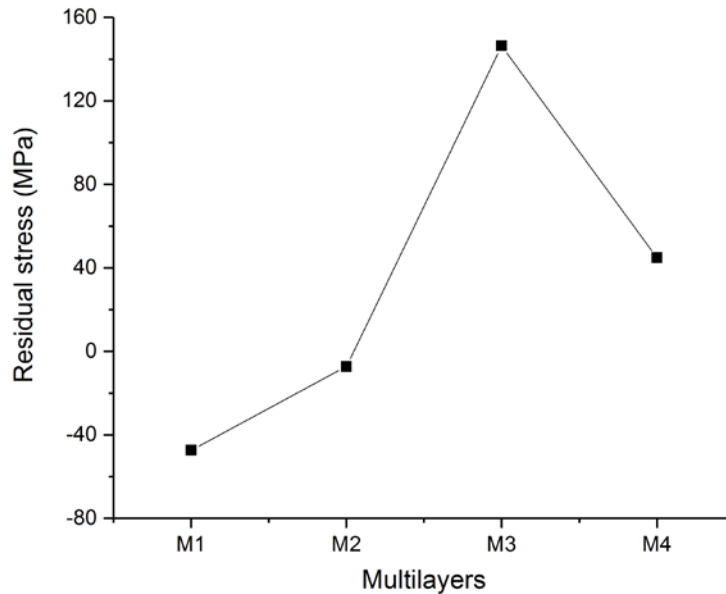


Figure 135. Residual stress of the multilayers

All the multilayers present lower stress than the AlCrN or CrAlN monolayers. Only the CrN 300 °C-500 V presents low tensile residual stress such as M4.

Table 42. Residual stress of the multilayers

Multilayer	M1	M2	M3	M4
Residual stress (MPa)	-47.4	-7.3	146.4	44.8

According to the XRD patterns (*Figure 131*), we expected tensile stress for all the multilayers. But, this is not the case for M1 and M2, that have low compressive stress (*Table 42*). This can be explained by Schmitt [266] in the case of AlCrN monolayers. Indeed, because of their architecture, one can suppose that M1 and M2 present in their total volume more Al-N bonds than Cr-N bonds leading to compressive stress instead of tensile stress. Furthermore, when we decrease the CrN/AlCrN pairs thickness in M2, the compressive stress decrease (-7.3 MPa) in comparison to M1 stresses (-47.4 MPa). Aouadi [111] observed the same trend in the case of Cr/CrN/CrAlN multilayers.

Besides, we notice that by increasing the number of interfaces of multilayer coatings (comparing M1 and M4), the stress change from compressive to tensile. This is probably due to the existence of more interfaces in M4. Indeed, the interfaces between the layers can lead to stress relaxation and energy dissipation. Thus, their presence absorbs the residual stresses during the growth phase of the film [294, 295].

The M3 multilayer exhibits tensile stress of 146.4 MPa, in good agreement with Aouadi [111] who calculated a tensile stress of about 112 MPa for the same multilayer.

Figure 136 presents the grain size and the residual stresses of the multilayers. As in the case of the CrN and CrAlN monolayers, we observe here that the grain size is proportional to the residual stress (“inverse Hall-Petch effect”) as previously explained by Quek et al. [283].

We verify here the “inverse Hall-Petch” effect: the lower the grains, the lower the residual stress.

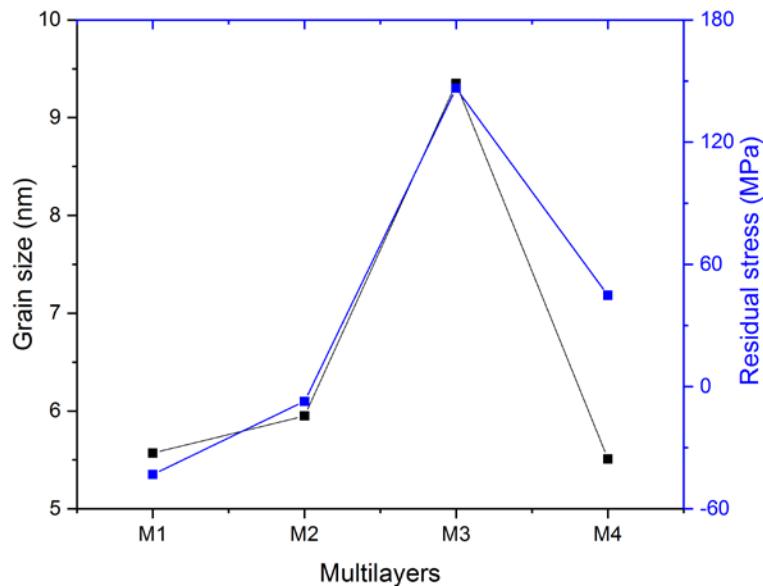


Figure 136. Grain size and residual stress of the multilayers

3.3.4.2. Hardness and elastic modulus

The results of nanoindentation tests carried out on coated mirror-polished WC substrates are shown in Figure 137.

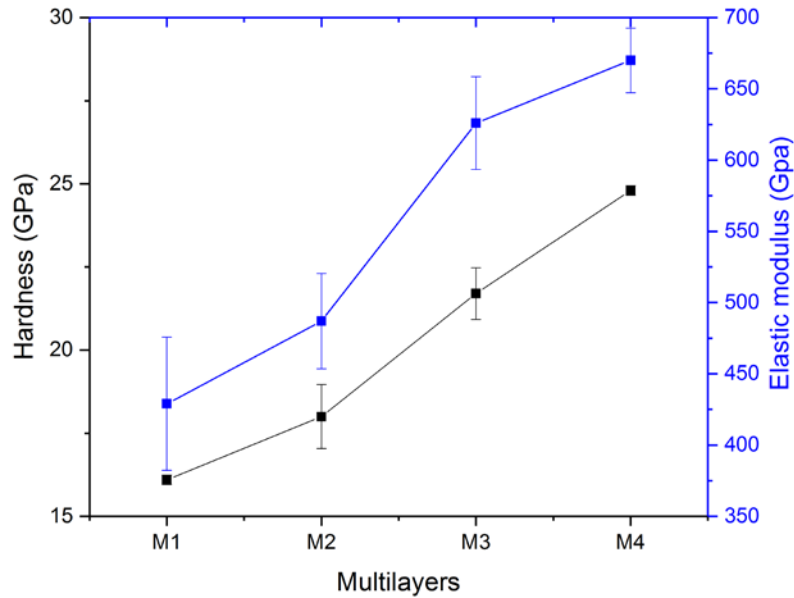


Figure 137. Hardness and elastic modulus of the multilayers

The values of hardness, elastic modulus, H/E and H^3/E^2 are listed in Table 43.

Table 43. Hardness, elastic modulus, elastic and plastic deformation resistance H/E and H^3/E^2 of the multilayers on WC substrates

Multilayer	H (GPa)	E (GPa)	$H/E (\times 10^{-2})$	$H^3/E^2 (\times 10^{-2})$
M1	16.1	429	3.75	2.27
M2	18	487	3.70	2.46
M3	21.7	626	3.47	2.61
M4	24.8	670	3.70	3.40

The hardness of the multilayers varies from 16.1 GPa to 24.8 GPa, while their elastic modulus varies from 429 GPa to 670 GPa. As expected, the hardness of the multilayers is in the same order of magnitude than the monolayers' hardness. Nevertheless, as the number of interfaces increases from M1 to M4, the hardness, elastic modulus, as well as the plastic deformation resistance increase. Many studies have proven the advantage of increasing number of interfaces: the mechanical properties like plastic deformation resistance of coatings will increase, and thus, enhance the wear resistance [158]. The hardness and elastic modulus will increase too, according to the studies of Mori et al. [296] and Yousaf et al. [118]. This can be explained by the fact that the numerous interfaces serve to prevent the sliding of dislocations and prevent the growth of column grains through the layers. Blocking dislocations due to column-to-column discontinuity contributes to hardness improvement [295, 297].

When we compare the M1 and M2, a slight increase of the hardness (from 16.1 to 18 GPa) and of the elastic modulus (from 429 to 487 GPa) was observed. Thus, the thickness decrease of the CrN/AlCrN pairs does not have a lot of effect on the hardness and elastic modulus.

Besides, one can note that the hardness of the M3 multilayer is similar to the one of the M2 while its elastic modulus is much higher (626 instead of 487 GPa). This can be explained by the fact that the elastic modulus of the AlCrN monolayers is lower (170 GPa) (Table 37) than the one of the CrAlN monolayers (233 GPa) (Table 29).

Finally, in his study, Aouadi [111] obtained a Cr/CrN/CrAlN multilayer with a hardness of 43 GPa, about twice higher than the multilayer M3, but with a lower elastic modulus of 402 GPa instead of 626 GPa. This result is probably due to the different deposition conditions Aouadi employed in comparison to ours. Indeed, Yousaf et al. [236] explained that not only grain size, but also inter-diffusion and interface state must be considered to explain the evolution of hardness, elastic modulus and their dependence on process parameters. All diffusion processes between monolayers inevitably lead to degradation of mechanical properties. Therefore, the diffusion at the interfaces can be a reason for the reduction of the hardness of the M2 multilayer in comparison to the M3 one.

Figure 138 illustrates the comparison of the hardness and residual stress of the multilayers deposited on mirror-polished WC and silicon substrate, respectively.

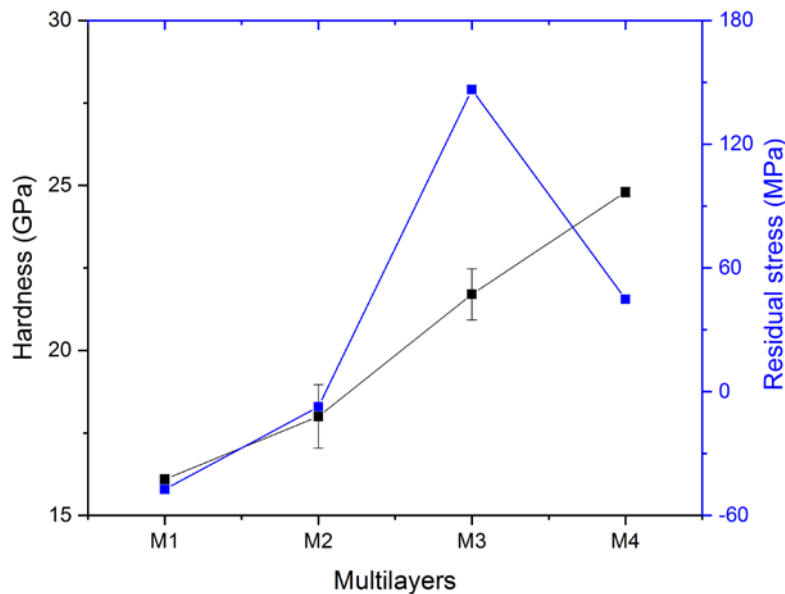


Figure 138. Correlation between residual stress and hardness of the multilayers

The results show a correlation between hardness and residual stress. The hardness seems to be low when the residual stresses are the highest (tensile or compressive). When the stress is the highest, 146.4 MPa, the hardness is 21.7 GPa. Then when the residual stresses decrease from

146.4 MPa to 44.8 GPa, the hardness increases from 21.7 to 24.8 GPa. We observed the same trend for the compressive stresses. Aouadi [111] observed the same tendency for his CrAlN layers with different Al content: the hardness was inversely proportional to the stress.

The relation between the grain size and the hardness is illustrated in *Figure 139*.

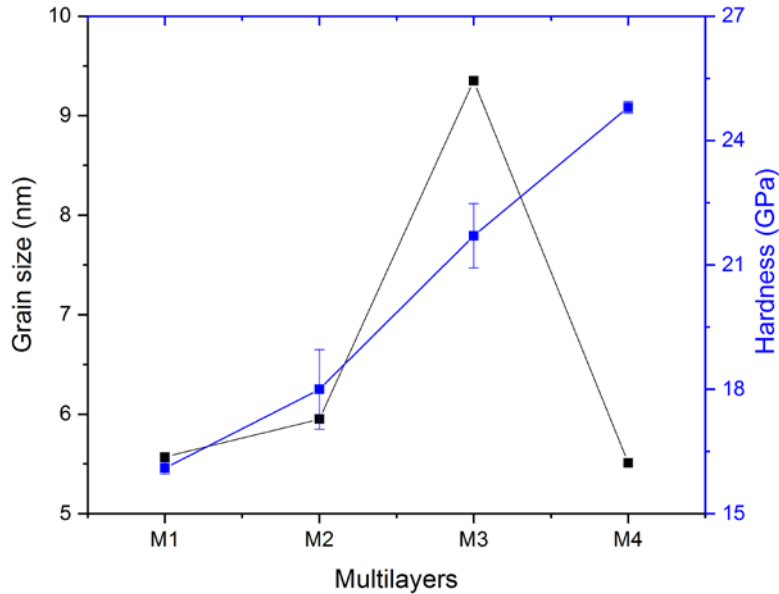


Figure 139. Grain size and hardness of the multilayers

We verify here the “inverse Hall-Petch” effect: the lower the grains, the lower the hardness except for the M4 where we obtained the highest hardness for a small grain size. Nevertheless, this result is logical: as grains size is small, we expect a higher hardness. This multilayer seems to follow the “Hall-Petch” effect in contrary to the others. This may be caused by the number of interfaces that is twice higher than the other coatings [111].

The correlation between plastic deformation resistance and wear rate is illustrated in *Figure 140*.

We verify that the M4 multilayer has the lowest wear rate because of its highest plastic deformation resistance. The correlation between plastic deformation resistance and wear rate permits to confirm that the number of interfaces is a main parameter to obtain coatings with a low wear rate in comparison to the CrN/AlCrN or CrN/CrAlN pairs thickness. Aouadi [111] observed the same results for his Cr/CrN/CrAlN multilayers.

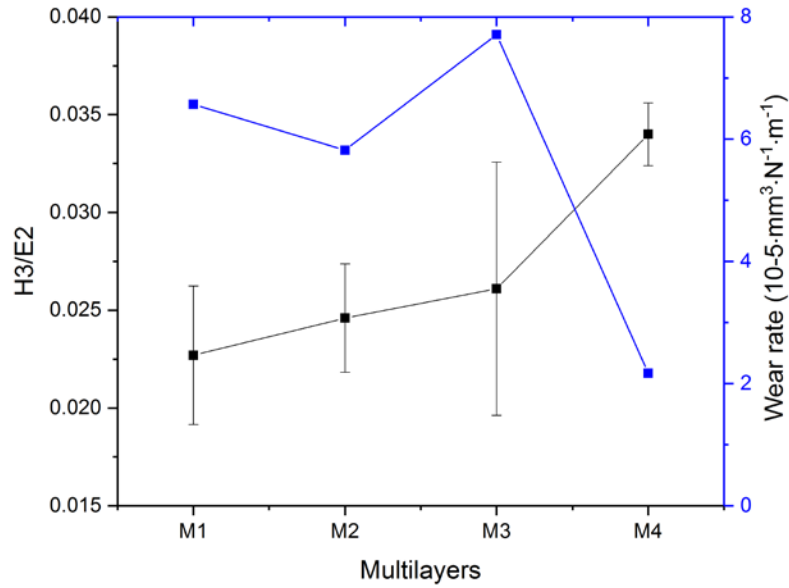


Figure 140. Wear rate and plastic deformation resistance of the multilayers

3.3.4.3. Adhesion

Figure 141 shows the scratch track of the multilayers obtained on mirror-polished WC substrates. Compared to the failure mode of Bull [262], the M1 exhibits buckle spallation failure mode (at Lc_1) and then recovery spallation mode (at Lc_2).

Moreover, the M2 and M3 seems less adherent than M4 as they present recovery spallation from Lc_1 . The M4 shows wedging spallation mode (at Lc_1) and recovery/wedging spallation modes (at Lc_2).

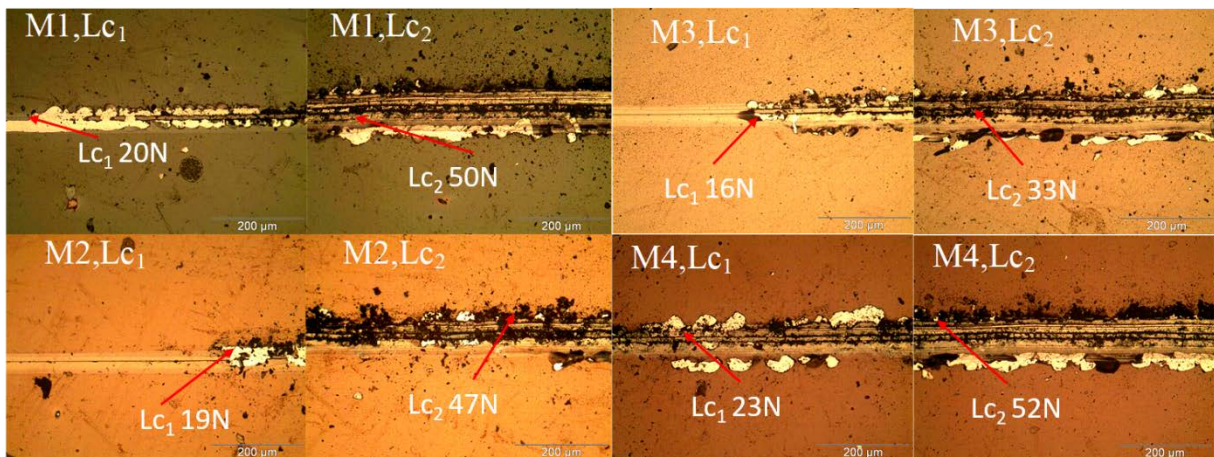


Figure 141. Optical images of the critical loads (Lc_1 and Lc_2) of the multilayers

Table 44 summarizes the critical loads and work of adhesion for each multilayer.

Table 44. Critical loads and work of adhesion of the multilayers

Multilayer	M1	M2	M3	M4
Lc1 (N)	20	19	16	23
Lc2 (N)	50	47	33	52
Wad (J/m ²)	1.32	1.52	0.43	0.61

Figure 142 presents the correlation between residual stress and work of adhesion.

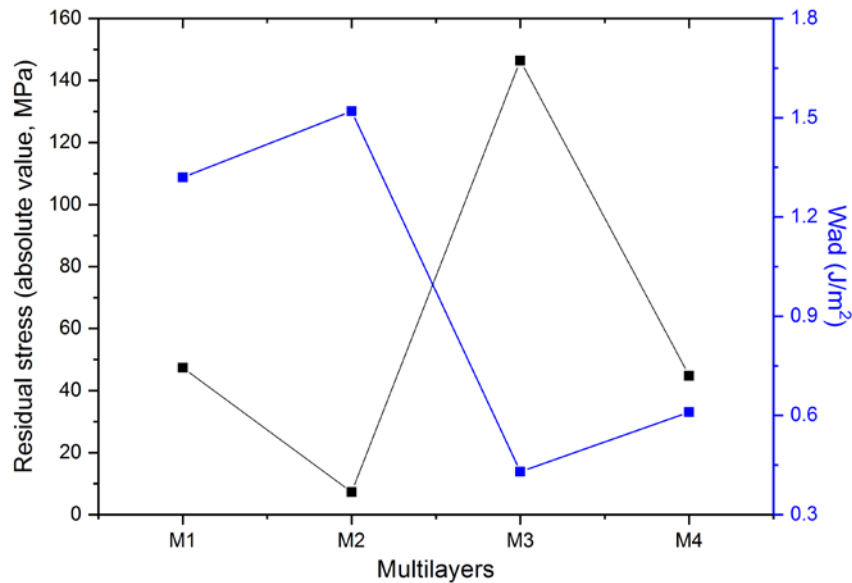


Figure 142. Relation between residual stress (absolute values) and adhesion work of the multilayers

The increasing number of interfaces reduces the work of adhesion for similar absolute stress which indicates the improvement of adhesion in the case of the M4. In the contrary, the decrease of the CrN/AlCrN pairs thickness, increases the work of adhesion and the stress decreases. Indeed, the adhesion of the M2 is lower than the one of M1. Finally, if we compare M2 to M3, we do not verify that the Cr/CrN/CrAlN multilayer has a higher adhesion strength, as its work of adhesion is the lowest. Nevertheless, it is well verified here that the work of adhesion behaves inversely to the residual stresses (tensile and compressive) as already observed in the case of the AlCrN monolayers.

It is obvious in Figure 143, that M4 has the best adhesion as it is constituted of twice number of interfaces in comparison to M1. Even if the adhesion of M4 is slightly higher than that of M1, Mori et al. [296] and Yousaf et al. [118] already observed this effect of the interface number in multilayers. When the CrN/AlCrN pairs thickness decreases, the adhesion of M2 is similar to the M1 one. But, the M3 multilayer has the lowest adhesion in comparison to others.

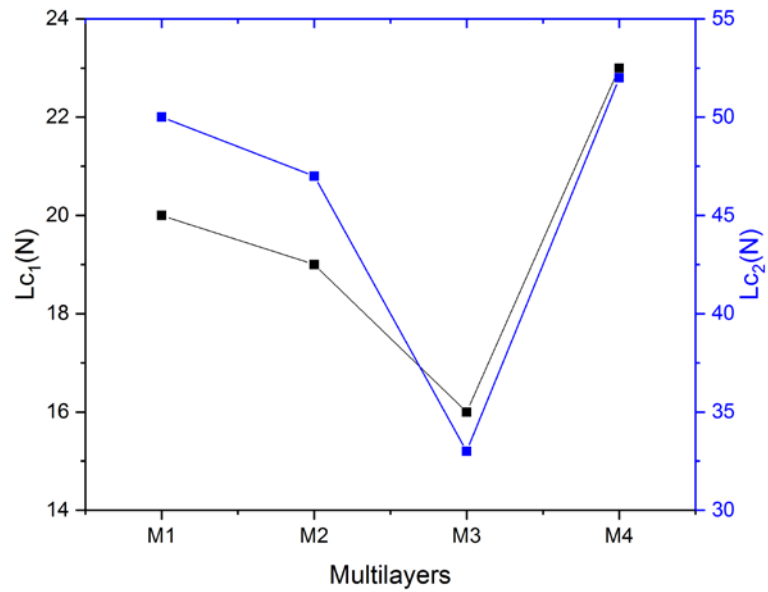


Figure 143. Critical loads of the multilayers

Furthermore, as previously observed for the CrAlN layers with different Al content, it is verified that the evolution of the force required to tear off the multilayers from their substrate (L_{c2}) is correlated to the evolution of the grain size [287]. Indeed, when the grain size increases, the L_{c2} critical load decreases as shown in Figure 144.

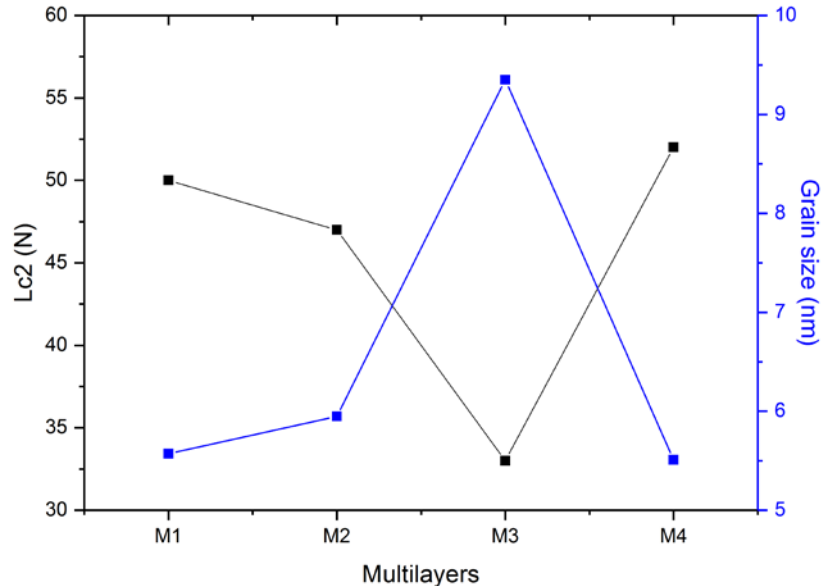


Figure 144. Evolution of the L_{c2} critical load of the multilayers and their grain size

Moreover, as in the case of the AlCrN monolayers, it is obvious in Figure 145, that the stress and the critical load L_{c2} behave the same, when we compare M1 to M4 or M1 to M2. Indeed, the critical load increases when the stress increases. In addition, samples with low stress have better adhesion than those with high stress. Such results were observed by Lin et al. [291].

Nevertheless, when we compare M2 to M3, it is the inverse: the stress increases while the Lc_2 decreases as in the case of the CrAlN monolayers as already shown by Kim et al. [158].

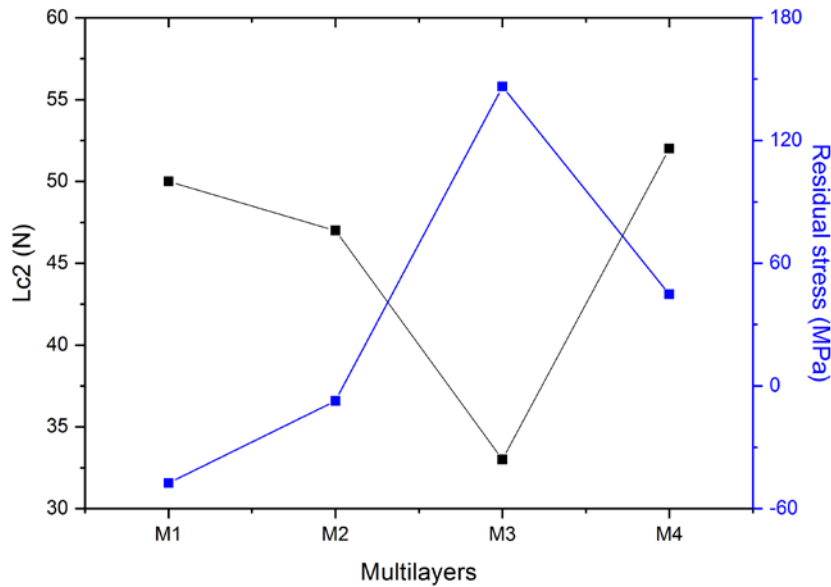


Figure 145. Correlation between residual stress and critical load Lc_2 of the multilayers

3.3.5. Thermal properties

Thermal property is a main parameter for the mono and multilayers as they will be applied in cryogenic assisted machining. Thus, thermal resistance measurement of the optimized CrN monolayer but also of M2, M3 and M4 multilayers were performed. The thermal conductivity was then measured by the MPTR method introduced in Chapter 2. The results are illustrated in Figure 146 and summarized in Table 45.

The thermal properties of AlCrN monolayers was not obtained by this method due to its optical transparency. Miao et al. [298] showed that the AlCrN with high Al content (above 64 at.%) has high transmissivity and is totally transparent in visible wavelength scale (300-800 nm), which indicates that it is also transparent in near IR scale (closed to 700 nm). Thus, the thermal conductivity of the AlCrN monolayer comes from the literature [299], where the thermal conductivity of CrAlN was measured with Al content varying from 0 to about 71.4 at.%. Besides, AlCrN coating are known to have a good thermal stability. Tlili et al. [300] reported that the thermal conductivity of CrAlN (Al content varying from 5 to 30 at.%) is from $4.5 \text{ W}\cdot\text{m}^{-1}\cdot\text{K}^{-1}$ to $2.8 \text{ W}\cdot\text{m}^{-1}\cdot\text{K}^{-1}$ and its thermal diffusivity is from $8\times 10^{-7} \text{ m}^2\cdot\text{s}^{-1}$ to $4\times 10^{-7} \text{ m}^2\cdot\text{s}^{-1}$. Willmann et al. [177] reported that with 56 at.% of Al the AlCrN coating undergoes annealing temperature until $900 \text{ }^\circ\text{C}$ without decomposition and keeps high hardness around 30 GPa, while a Al content of 68 at.% AlCrN coating exhibits formation of hexagonal (h) AlN before $700 \text{ }^\circ\text{C}$.

The thermal conductivity of our coatings varies from 1 to 2.72 $\text{W}\cdot\text{m}^{-1}\cdot\text{K}^{-1}$, that is much lower than the WC substrate one. The coatings show low and close thermal conductivity, which may indicate that the architecture of multilayers has no significant influence on thermal properties. To have more information about the effect of the interfaces, we need to have thermal conductivity of the M1 to compare with the M4 multilayer.

When we compare M2 and M3, the multilayer composed of CrN/CrAlN pairs has a slight lower thermal conductivity. This may be due to its higher grain size or its (111) preferred orientation according to the XRD patterns.

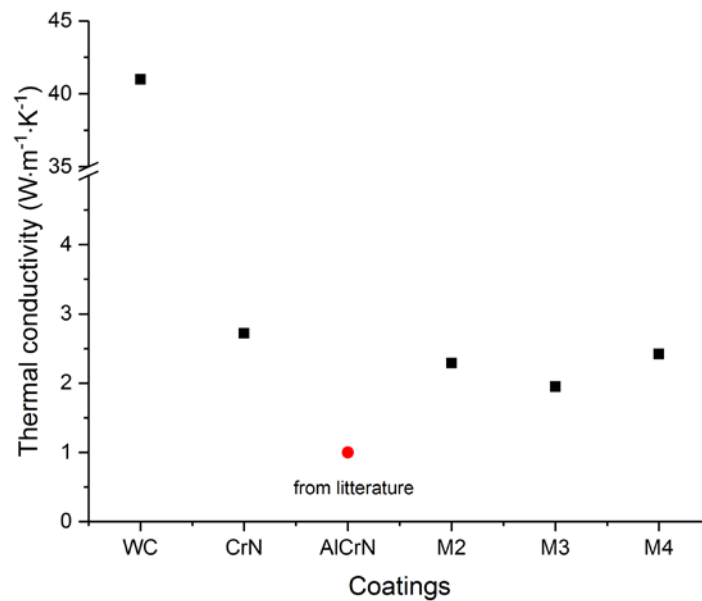


Figure 146. Thermal conductivity of as-deposited monolayers and multilayers (substrate as reference)

Table 45. Thermal conductivity of as-deposited monolayers and multilayers (WC substrate as reference)

Coatings	WC	CrN	AlCrN	M2	M3	M4
Thermal conductivity ($\text{W}\cdot\text{m}^{-1}\cdot\text{K}^{-1}$)	41	2.72	1 (from literature)	2.29	1.95	2.42

3.3.6. Partial conclusions

In this section, we developed Cr/CrN/AlCrN and Cr/CrN/CrAlN multilayers by varying the CrN/AlCrN pairs number or thickness. The influence of these parameters was shown. Indeed, the deposition process of as-deposited multilayers are verified by EDS profiles. This permits also to verify their chemical composition. The thickness and deposition rate of the multilayers were verified by SEM observations: the thickness of the multilayers varies from 1.85 to 2.55

µm. The multilayers have columnar and dense microstructure. According to XRD, the multilayers are well crystallized and composed of cubic CrN and AlN phases. Their friction coefficient is in the range of 0.52-0.55. The intrinsic stress of the multilayers is low (from -47.4 to 146.4 MPa). Their hardness and elastic modulus evolve with the number of interfaces. The adhesion failure mode is different among the multilayers, when M1 exhibits buckle spallation, others exhibit recovery spallation mode. The thermal properties are excellent for all as-deposited coatings, which predicts a good prominent performance in cryogenic assisted machining.

As far as the number of interfaces is concerned, it is obvious that M4 multilayer would perform better than the M1 one. Moreover, the M2 should be chosen in comparison to the M3 according to its higher mechanical and tribological properties. Nevertheless, in the following chapter, the optimized CrN and AlCrN monolayers, M2 and M4 multilayers are going to be tested under flood and LN2 cooling conditions, in tribological tests on a CNC machine. This aims to verify and confirm our choice of the coatings, which will be further used for evaluating the tool life in tool wear tests.

3.4. Conclusions

In Chapter 3, our objectives were:

- to optimize Cr underlayer to get an adhesive coating as it will be the first layer in contact with the WC substrates
- to optimize the CrN monolayers with good mechanical and tribological properties
- to optimize the Al content in CrAlN monolayers to develop AlCrN ones
- to optimize the AlCrN monolayers with good mechanical and tribological properties
- to develop new Cr/CrN/AlCrN multilayers and to verify the Cr/CrN/CrAlN multilayer properties obtained previously by Aouadi [111].
- to compare the multilayers physico-chemical, structural, mechanical, tribological and thermal properties in order to choose the best coatings to be applied on carbide pins for tribological tests (Chapter 4) and on carbide inserts for tool wear tests (Chapter 5).

The conclusions of the Chapter 3 are as follows:

Cr underlayer

We obtained almost pure chromium thin films by DC magnetron sputtering with an acceptable adhesion on tungsten carbide substrate, a low friction coefficient and wear rate after being in

contact with Ti6Al4V ball. The Cr layer was well crystallized, showed the (110) preferred orientation with a grain size around 10 nm and has a relative porosity. Thus, as expected, the Cr coating are adherent whatever the type of substrate or its roughness.

CrN monolayers

CrN monolayers were synthesized by varying the deposition temperature and substrate bias voltage. The influence of both deposition parameters was shown. Moreover mostly we verified the results obtained previously by Aouadi [111]. When we obtained different results, the influence of the substrate rotation speed was shown. According to its properties, the CrN monolayer deposited under 300 °C and -500 V exhibits a (200) preferred crystalline orientation, is well crystallized, it has a dense surface morphology and small top column size. Concerning its mechanical properties, it presents the highest hardness and elastic modulus, the best plastic deformation resistance and has a very good adhesion up to 43 N (Lc_2) and finally the lowest wear rate $0.58 \times 10^{-4} \text{ mm}^3 \cdot \text{m}^{-1} \cdot \text{N}^{-1}$. This optimized CrN monolayer will be used in the different multilayers.

CrAlN monolayers

We developed CrAlN monolayers by varying the Al content to determine the optimal chemical composition to be applied in the AlCrN monolayers. The influence of this parameter was shown. Moreover mostly we verified the results obtained previously by Aouadi [111]. When we obtained different results, the influence of the substrate rotation speed was shown. According to their properties, the CrAlN monolayers obtained with 57 and 62 at.% of Al exhibit the same crystalline orientation, have a dense surface morphology, small column size and grain size. Concerning their mechanical properties, the layer with 57 at.% of Al presents the highest hardness and elastic modulus, the best plastic deformation resistance and has a very good adhesion up to 47 N (Lc_2) and finally the lowest wear rate. This optimized CrAlN monolayer should be our choice. Nevertheless, during the deposition process of $x = 0.57$ we fixed a high current on the aluminum target that was unfortunately significantly damaged. Indeed, with a high current applied on the aluminum target, we poisoned it by nitrogen in a very short time, which is not a sustainable way for PVD coating. Then even if the layer obtained for $x = 0.62$ has a low plastic deformation resistance, it presents the best adhesion and similar physico-chemical and mechanical properties with the layer obtained for $x = 0.57$. Besides, it has been synthesized at a fixed power on the aluminum target which reduces the target damage during

the PVD process. For all the above-mentioned reasons, we decided to choose as the optimal Al content, $x = 0.62$ for the study about the optimization of AlCrN monolayers by varying the substrate bias voltage and the deposition temperature.

AlCrN monolayers

We developed AlCrN monolayers by varying the deposition temperature and substrate bias voltage. The influence of these parameters was shown. Indeed, high deposition temperature and substrate bias voltage would permit to get a dense and homogeneous AlCrN layer on silicon substrates. For the AlCrN layers, the temperature has an influence on the microstructure. The crystalline orientation of the AlCrN layers depends on the substrate bias voltage but also on the deposition temperature and these both parameters are correlated. The grain size decreases when the bias voltage increases and the deposition temperature decreases. Concerning the mechanical properties of our AlCrN layers: their COF does not depend on the deposition temperature or the substrate bias voltage and was around 0.5. All the AlCrN layers have compressive stress varying from -914 MPa to -166.3 MPa except the layer realized at 300°C-0V that has tensile stress of 28.6 MPa. The deposition temperature and substrate bias voltage both have positive impacts on adhesion property of the AlCrN layers. We also showed that for the AlCrN layers, the “Hall-Petch effect” governs their hardness. Moreover, mostly we verified the results of the CrN monolayers. Indeed, it has been shown that the substrate bias voltage increases the residual stress while the temperature reduces it. Most of the AlCrN layers present a better adhesion than the CrN layers whatever the deposition conditions.

According to their properties, the stoichiometry of our AlCrN layers is $\text{Al}_{62}\text{Cr}_{38}\text{N}$. In XRD we observe only the cubic phase of CrN and AlN for all coatings, no hexagonal Cr_2N or AlN diffraction peaks are present. The experimental diffraction peaks are close or between the CrN and AlN theoretical diffraction positions, so it is considered that the AlCrN layers are solid solutions of Al atoms in substitution in the CrN lattices.

The AlCrN layer realized at 300 °C-250 V is well crystallized, presents the highest hardness whatever the substrate, an acceptable elastic modulus of 165-170 GPa, the best plastic deformation resistance, the lowest wear rate and the best adhesion with a Lc_2 up to 58 N.

Thus, the optimized AlCrN monolayer (300 °C-250 V) has been applied in the synthesis of the Cr/CrN/AlCrN multilayers.

Multilayers

We synthesized Cr/CrN/CrAlN and Cr/CrN/AlCrN by varying the CrN/AlCrN or CrN/CrAlN pairs thickness and number. As far as the number of interfaces is concerned, it is obvious that M4 multilayer would perform better than the M1 one. Moreover, the M2 should be chosen in comparison to the M3 according to its higher mechanical and tribological properties. Nevertheless, all the optimized monolayers and M2, M4 multilayers will be tested on carbide pins in tribological tests against Ti6Al4V alloy.

Finally, the main question is: what is the contribution of using a multilayer instead of a monolayer?

To answer this question, we summarized all the mono and multilayers properties in *Table 46*.

Table 46. Properties of the mono and multilayers

	Bad	Acceptable	Good					
Coatings	Cr	CrN	AlCrN	M1	M2	M3	M4	
Deposition rate (nm/mn)	-	5.7	3.83	4.8-5	4.8-5	7.6	4.8-5	
Microstructure	and porous	Columnar with small pores	Columnar and dense					
Grain size (nm)	9.74	7.07	4.12	5.57	5.95	9.35	5.51	
COF	0.51	0.5	0.5	0.52-0.55	0.52-0.55	0.52-0.55	0.52-0.55	
Wear rate (10 ⁻⁵ mm ³ /(m·N))	5.32	5.8	2.02	6.57	5.82	7.71	2.17	
Stress (MPa)	222.8	40.2	-407.3	-47.4	-7.3	146.4	44.8	
Hardness (GPa)	5.9	16.2	26.4	16.1	18	21.7	24.8	
Elastic modulus (GPa)	170	346	170	429	487	626	670	
H ³ /E ²	0.007	0.0355	0.6367	0.0227	0.0246	0.0261	0.0340	
Lc2 (N)	31.6	43	58	50	47	33	52	
W _{AD} (J/m ²)	-	4.5	4.05	1.32	1.52	0.43	0.61	
Thermal conductivity (W/m/K)	-	2.72	1	-	2.29	1.95	2.42	

According to *Table 46*, the multilayers do not have a high deposition rate except M3 but their deposition rate is higher than the AlCrN monolayers. Besides, multilayers are of a great interest because they have a columnar dense microstructure, a small grain size, a small wear rate in the case of the M4, an acceptable hardness and a high elastic modulus, a good adhesion (except M3), and as a consequence a low work of adhesion. The plastic deformation resistance is only acceptable for the M4 multilayer. Furthermore, the multilayers have a low thermal conductivity. Finally, it is obvious from *Table 46* that the most interesting multilayer is the M4 one and that the worst is the M3 one.

In the following Chapter 4, we are going to introduce the tribological tests that carried out thanks to a laboratory-made tribometer with coated and uncoated-carbide pins against Ti6Al4V alloy bars. According to the results we could choose the best coatings to be tested in tool wear tests under flood and LN2 cooling conditions in turning of Ti6Al4V alloy.

3.5. Résumé du Chapitre 3

Les objectifs du Chapitre 3 étaient les suivants :

- optimiser la sous-couche de Cr pour obtenir un revêtement adhérent car ce sera la première couche en contact avec les substrats de WC
- optimiser les monocouches de CrN avec de bonnes propriétés mécaniques et tribologiques
- optimiser la teneur en Al dans les monocouches CrAlN pour développer celles en AlCrN
- optimiser les monocouches d'AlCrN avec de bonnes propriétés mécaniques et tribologiques
- développer de nouvelles multicouches Cr/CrN/AlCrN et vérifier les propriétés des multicouches Cr/CrN/CrAlN obtenues précédemment par Aouadi [111].
- comparer les propriétés physico-chimiques, structurales, mécaniques, tribologiques et thermiques des multicouches en vue de choisir les meilleurs revêtements à appliquer sur les pions carbure pour les essais de tribologie (Chapitre 4) et sur les plaquettes carbure pour test d'usure des outils (Chapitre 5).

Les conclusions du Chapitre 3 sont les suivantes :

Sous-couche de Cr

Nous avons obtenu des couches minces de chrome presque pur par pulvérisation magnétron DC avec une adhérence acceptable sur substrat de carbure de tungstène, un faible coefficient de

frottement et un faible taux d'usure après avoir été en contact avec la bille Ti6Al4V. Les couches de Cr étaient bien cristallisées, présentaient l'orientation préférentielle (110) avec une taille de grain d'environ 10 nm et avaient une porosité relative. Ainsi, comme attendu, les revêtements de Cr sont adhérents quel que soit le type de substrat ou sa rugosité.

Monocouches de CrN

Des monocouches de CrN ont été réalisées en faisant varier la température de dépôt et la tension de polarisation du substrat. L'influence des deux paramètres de dépôt a été montrée. De plus, nous avons également vérifié les résultats obtenus précédemment par Aouadi [111]. Lorsque nous avons obtenu des résultats différents, nous avons montré l'influence de la vitesse de rotation du substrat. Selon ses propriétés, la monocouche de CrN déposée sous 300 °C et -500 V présente une orientation cristalline préférentielle (200), est bien cristallisée, elle a une morphologie de surface dense et des colonnes fines. Concernant ses propriétés mécaniques, elle présente la dureté et le module d'élasticité les plus élevés, la meilleure résistance à la déformation plastique et possède une très bonne adhérence jusqu'à 43 N (Lc2) et enfin la plus faible vitesse d'usure $0,58 \times 10^{-4} \text{ mm}^3 \cdot \text{m}^{-1} \cdot \text{N}^{-1}$. Cette monocouche de CrN optimisée sera donc réalisée dans les différentes multicouches.

Monocouches de CrAlN

Nous avons développé des monocouches de CrAlN en faisant varier la teneur en Al pour déterminer la composition optimale à appliquer dans les monocouches d'AlCrN. L'influence de ce paramètre a été montrée. De plus, nous avons également vérifié les résultats obtenus précédemment par Aouadi [111]. Lorsque nous avons obtenu des résultats différents, nous avons montré l'influence de la vitesse de rotation du substrat. Selon leurs propriétés, les monocouches de CrAlN obtenues avec 57 et 62 % at. d'Al présentent la même orientation cristalline, ont une morphologie de surface dense et une taille de grain faible. Concernant leurs propriétés mécaniques, la couche à 57 % at. d'Al présente la dureté et le module d'élasticité les plus élevés, la meilleure résistance à la déformation plastique et possède une très bonne adhérence jusqu'à 47 N (Lc2) et enfin la vitesse d'usure la plus faible. Cette monocouche de CrAlN optimisée devrait être notre choix. Néanmoins lors du processus de dépôt lorsque $x = 0,57$ nous avons fixé un courant élevé sur la cible en aluminium qui a malheureusement été fortement endommagée. En effet, avec un fort courant appliqué sur la cible en aluminium, nous l'avons empoisonnée à l'azote en très peu de temps, ce qui n'est pas une voie durable pour le

revêtement PVD. Alors, même si la couche obtenue pour $x = 0,62$ a une faible résistance à la déformation plastique, elle présente la meilleure adhérence et des propriétés physico-chimiques et mécaniques similaires avec la couche obtenue pour $x = 0,57$. En outre, elle a été réalisée à une puissance fixe sur la cible en aluminium, ce qui réduit les dommages de la cible pendant le procédé PVD. Pour toutes les raisons mentionnées ci-dessus, nous avons décidé de choisir comme teneur optimale en Al, $x = 0,62$ pour l'étude sur l'optimisation des monocouches d'AlCrN en faisant varier la tension de polarisation du substrat et la température de dépôt.

Monocouches de AlCrN

Nous avons développé des monocouches d'AlCrN en faisant varier la température de dépôt et la tension de polarisation du substrat. L'influence de ces paramètres a été montrée. En effet, une température de dépôt et une tension de polarisation du substrat élevées permettraient d'obtenir une couche d'AlCrN dense et homogène sur des substrats de silicium. Pour nos couches d'AlCrN, la température a une influence sur la microstructure. L'orientation cristalline des couches d'AlCrN dépend de la tension de polarisation du substrat mais aussi de la température de dépôt et ces deux paramètres sont corrélés. La taille des grains diminue lorsque la tension de polarisation augmente et que la température de dépôt diminue. Concernant les propriétés mécaniques de nos couches d'AlCrN : leur COF ne dépend ni de la température de dépôt ni de la tension de polarisation du substrat et était d'environ 0,5. Toutes les couches d'AlCrN ont des contraintes de compression variant de -914 MPa à -166,3 MPa sauf la couche réalisée à 300°C-0V qui a des contraintes en tension de 28,6 MPa. La température de dépôt et la tension de polarisation du substrat ont toutes deux un impact positif sur les propriétés d'adhérence des couches d'AlCrN. Nous avons également montré que pour nos couches d'AlCrN, l'« effet Hall-Petch » régit leur dureté. De plus, nous avons également vérifié les résultats que nous avons obtenus pour nos monocouches de CrN. En effet, il a été montré que la tension de polarisation augmente la contrainte résiduelle alors que la température la diminue. La plupart de nos couches d'AlCrN présentent une meilleure adhérence que nos couches de CrN quelles que soient les conditions de dépôt.

D'après leurs propriétés, la stœchiométrie de nos couches d'AlCrN est $Al_{62}Cr_{38}N$. En DRX, nous observons uniquement la phase cubique de CrN et AlN pour tous les revêtements, aucun pic de diffraction de Cr_2N ou d'AlN hexagonal n'est présent. Les pics expérimentaux de diffraction sont proches ou entre les positions de diffraction théoriques de CrN et AlN, on peut

donc considérer que nos couches AlCrN sont des solutions solides de substitution d'atomes d'Al dans le réseau du système Cr-N.

La couche d'AlCrN réalisée à 300 °C-250 V est bien cristallisée, présente la dureté la plus élevées quel que soit le substrat, un module d'Young acceptable de 165-170 GPa, la meilleure résistance à la déformation plastique, le taux d'usure le plus faible et une bonne adhérence avec un Lc2 jusqu'à 58 N.

Ainsi, la monocouche optimisée AlCrN (300 °C-250 V) a été appliquée dans la synthèse des multicouches Cr/CrN/AlCrN.

Multicouches

Nous avons réalisé des couches de type Cr/CrN/CrAlN et Cr/CrN/AlCrN en faisant varier l'épaisseur et le nombre de chaque paire CrN/AlCrN ou CrN/CrAlN. En ce qui concerne le nombre d'interfaces, il est évident que la multicouche M4 serait plus performante que M1. De plus, M2 est plus performante que M3 car elle présente des propriétés mécaniques et tribologiques plus élevées. Néanmoins, toutes les monocouches optimisées et les multicouches M2 et M4 seront testées sur des pions en carbure lors d'essais de tribologie contre l'alliage Ti6Al4V.

Enfin, la question principale est : quel est l'apport d'une multicouche par rapport à une monocouche ?

Pour répondre à cette question, nous avons résumé toutes les propriétés des mono et multicouches dans le *Tableau 47*.

Tableau 47. Propriétés des mono et multilcouches

Dépôts	Cr	CrN	AlCrN	M1	M2	M3	M4
Vitesse de dépôt (nm/mn)	-	5.7	3.83	4.8-5	4.8-5	7.6	4.8-5
Microstructure	Colonnaire et poreuse	Colonnaire et poreuse	Colonnaire et dense				
Taille de grain (nm)	9.74	7.07	4.12	5.57	5.95	9.35	5.51
COF	0.51	0.5	0.5	0.52-0.55	0.52-0.55	0.52-0.55	0.52-0.55
Vitesse d'usure ($\times 10^{-5}$ mm ³ /(m*N))	5.32	5.8	2.02	6.57	5.82	7.71	2.17
Contraintes résiduelles (MPa)	222.8	40.2	-407.3	-47.4	-7.3	146.4	44.8
Dureté (GPa)	5.9	16.2	26.4	16.1	18	21.7	24.8
Module d'élasticité (GPa)	170	346	170	429	487	626	670
H ³ /E ²	0.007	0.0355	0.6367	0.0227	0.0246	0.0261	0.0340
Lc2 (N)	31.6	43	58	50	47	33	52
W _{AD} (J/m ²)	-	4.5	4.05	1.32	1.52	0.43	0.61
Conductivité thermique (W/m/K)	-	2.72	1	-	2.29	1.95	2.42

D'après le *Tableau 47*, les multicouches n'ont pas une vitesse de dépôt élevée sauf M3 mais leur vitesse de dépôt est plus élevée que les monocouches d'AlCrN. Par ailleurs, les multicouches présentent un grand intérêt car elles présentent une microstructure colonnaire dense, une faible taille de grain, une faible vitesse d'usure dans le cas de M4, une dureté acceptable et un module d'Young élevé, une bonne adhérence (sauf pour M3), et par conséquent un faible travail d'adhérence. La résistance à la déformation plastique n'est acceptable que pour la multicouche M4. De plus, les multicouches ont une faible conductivité thermique. Enfin, il ressort du *Tableau 47* que la multicouche la plus intéressante est M4 et que la moins performante est M3. Dans le chapitre 4 suivant, nous allons introduire les essais de tribologie que nous avons réalisés grâce à un tribomètre de laboratoire avec des pions en carbure revêtus et non revêtus contre des barres d'alliage de Ti6Al4V. En fonction des résultats que nous obtiendrons, nous pourrons choisir les meilleurs revêtements à tester lors du test d'usure contre Ti6Al4V sous émulsion et LN2.

Chapter 4. Tribological analysis

4.1. Introduction

Tribological behaviour is a complex phenomenon that happens in every single machining operation, causing severe tool wear and failure. Recent developments in cryogenic assisted machining as potential alternative to classical MWF have shown a huge interest in limiting the tool wear in machining of difficult to cut materials.

The objective of the tribological tests presented in this chapter is to analyse the performance of the coatings developed in this thesis in terms of friction coefficient, volume of build-up material (adhesion) to the tool, and tool temperature. This analysis will be performed for two cooling/lubrication strategies: LN2 and traditional MWF consisting of oil-water mixture (emulsions). A dedicated home-made tribometer will be used to conduct the tribological tests using coated and uncoated pins in contact with a workpiece in Ti6Al4V alloy, under several sliding speeds and two contact pressures.

These tribological tests should permit to select the best coatings that will be used in the cutting inserts for further tool wear analysis. Moreover, the obtained friction coefficients could be further implemented into metal cutting models to predict the machining outcomes, including surface integrity of the machined parts and tool wear.

4.2. Determination of contact conditions in machining of Ti6Al4V alloy

The contact between the tool and the workpiece/chip in machining is affected by several parameters, including: the sliding speed, contact pressure, contact temperature and the surface roughness of the tool. The objective of this section is to determine the values of these parameters that are representative of machining of Ti6Al4V titanium alloys using cemented carbide tools. In particular, this study is focused on the tool-chip contact due to the extreme contact conditions (high pressure and high temperatures) observed at this contact compared to the tool-workpiece one [301].

4.2.1. Determination of the sliding speeds

The sliding speed of the chip against the tool rake face is different from the cutting speed. As shown in Figure 147, a layer of material is separated from the workpiece by the action of the tool to form the chip. The formed chips are generally thicker than the uncut chip layer, while

the volume is preserved. Thus, the chip compression ratio (CCR) is presented the following equation [302]:

$$\zeta = \frac{h_1}{h} = \frac{V_c}{V_1} \quad \text{Equation 26}$$

where ζ is CCR, h and h_1 are uncut chip thickness (mm) and chip thickness, respectively. V_c and V_1 are the cutting speed and chip velocity (m/min), respectively.

As the pin-on-bar tribological tests is used to simulate the chip-tool contact behavior in machining, the sliding velocity, V_s , is equivalent to the chip velocity, V_1 . Considering that the average CCR in orthogonal cutting of Ti6Al4V alloy using uncoated cemented carbide tools is about 1.5 (see Figure 148) [303], the sliding speeds can be determined for various cutting speeds using *Equation 26*, as listed in Table 48. The large range of cutting speeds aims to determine the influence of this parameter to the tribological behavior of coatings. It is worth to point out that the upper value of the cutting speed is a bit higher for machining Ti6Al4V alloy using commercial cemented carbide cutting tools. The main reason for this is to evaluate the tribological performance of the new coatings for more aggressive cutting conditions than those used today for commercial coatings.

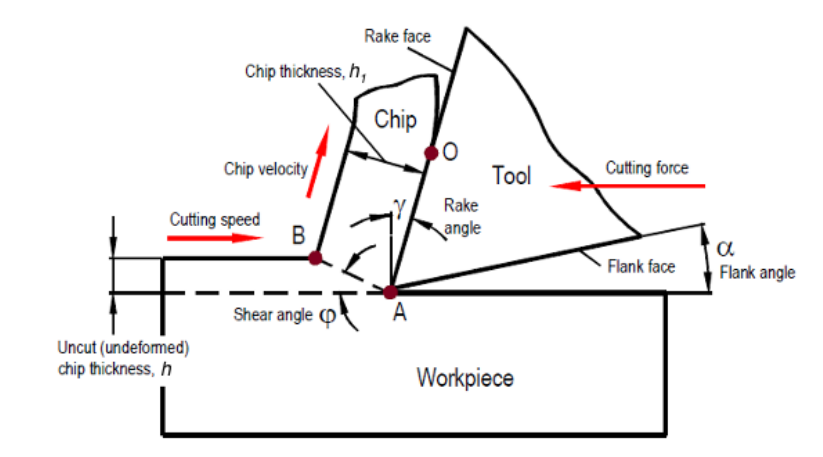


Figure 147. Single-shear plan model [10].

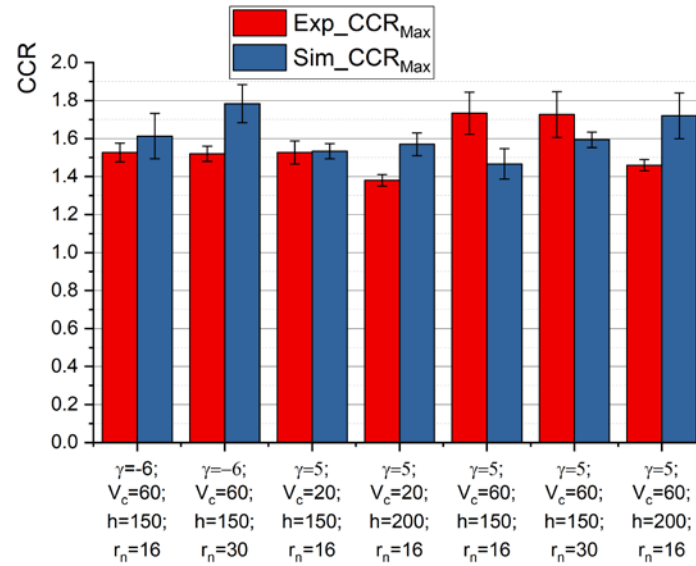


Figure 148. Chip compression ratio (CCR) in orthogonal cutting of Ti6Al4V alloy using uncoated cemented carbide tools [303]

Table 48. Sliding velocities and correlated cutting speeds determined in tribological tests

Cutting speed (m/min)	15	30	60	90	120	150
Sliding velocity (m/min)	10	20	40	60	80	100

4.2.2. Determination of the normal force acting in the pins

Figure 149 shows the procedure used for determining the normal force to be applied into the pins in the tribological tests. The first step of this procedure consists of gathering the forces, CCR and the tool-chip contact lengths generated by orthogonal cutting tests of Ti6Al4V alloy using cemented carbide tools. Based on the measured cutting (F_c) and thrust (F_t) forces, the normal force (F_{ny}) to the tool rake face is calculated using the forces diagram for orthogonal cutting, known from many publications [301, 302]. Then, the average contact pressure (P_{ny}) between the tool and the chip is calculated by dividing the normal force by the tool-chip contact area. The next step consists into calculate the normal force necessary to be applied to the pins ($F_{n,pin}$) to reach a contact pressure at the pin-workpiece interface (P_{pob}) equals to that pressure calculated from the cutting tests (P_{ny}).

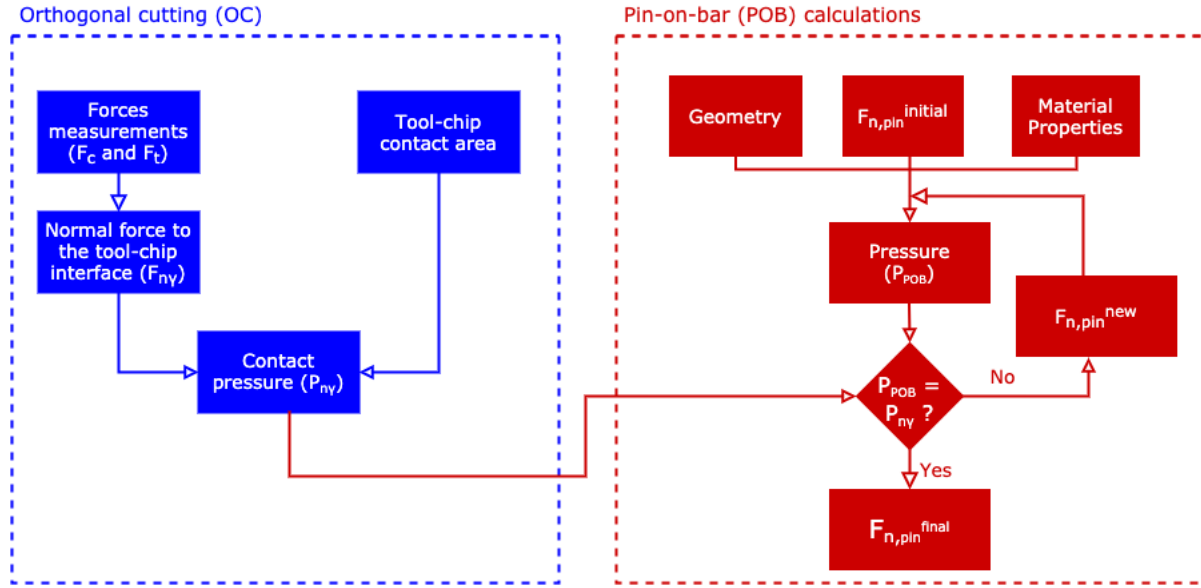


Figure 149. Flowchart of the procedure to determine the normal force to be applied into the pins.

4.2.2.1. Determination of the contact pressure in machining of Ti6Al4V alloy

Data from orthogonal cutting tests conducted by Outeiro et al. [304] was used in the procedure described above to calculate the normal forces acting on the pins during the tribological tests. This data is presented in *Table 49*, corresponding to two tests conducted with two cutting speeds, keeping constant the other cutting regime parameters. The force diagram shown in *Figure 150* was used to calculate the normal force applied to the tool rake face $F_{n\gamma}$, using the measured cutting and thrust forces and the equations derived from this figure (*Equation 27* to *Equation 29*) [301]. Then, the contact pressure is calculated by dividing the normal force $F_{n\gamma}$ by the tool-chip contact area (*Equation 31*). This area is the product of the contact length l_c (*Equation 30*, taken from [301]) by the width of cut b .

$$R = \sqrt{F_c^2 + F_t^2} \quad \text{Equation 27}$$

$$F_{n\gamma} = R \cdot \sin \left[\frac{\pi}{4} + (\phi - \gamma) \right] \quad \text{Equation 28}$$

$$\phi = \tan^{-1} \left(\frac{\cos \gamma}{\zeta - \sin \gamma} \right) \quad \text{Equation 29}$$

$$l_c = h \cdot \zeta^{1.5} \quad \text{Equation 30}$$

$$P_{ny} = \frac{F_{ny}}{l_c b}$$

Equation 31

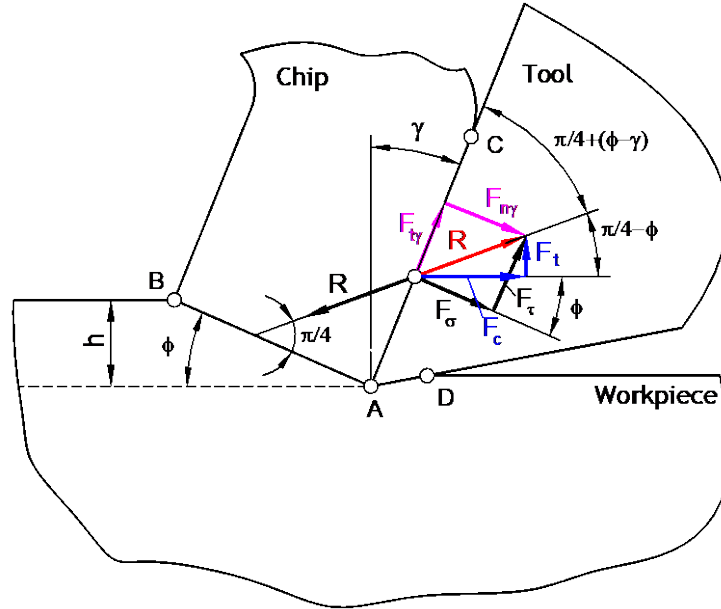


Figure 150. Force diagram in orthogonal cutting [301].

For the cutting conditions listed in Table 49, the average contact pressure in orthogonal cutting of Ti6Al4V alloy for the selected cutting conditions is 1188 MPa. Therefore, a reference average contact pressure around 1000 MPa is suitable for the tribological tests.

Table 49. Experimental data taken from the work of Outeiro et al. [304].

No.	Cutting speed v (m/min)	Uncut layer thickness h (mm)	Width of cut b (mm)	Rake angle γ_0 ($^\circ$)	Flank angle α_0 ($^\circ$)	Edge radius r_n (μm)	Cutting force F_c (N)	Thrust force F_f (N)	Compressive chip ratio γ (CCR)
Test1	55	0.15	4	6	7	30	1125	650	1.5
Test2	90	0.15	4	6	7	30	1100	630	1.4

Table 50. Determination of the contact pressure.

No.	Resultant force R (N)	Contact length l_c (mm)	Normal force F_{ny} (N)	Contact Pressure P (MPa)
Test1	1299	0.276	1252	1136
Test2	1268	0.248	1233	1240

4.2.2.2. Determination of the normal force acting in the pins

Since the geometry of cutting tools and pins are different, the values of the normal forces presented in *Table 50* are not the same of those to be applied in tribological tests, for the same contact pressures. Therefore, the normal force acting in the pins should be calculated.

Initially, two analytical models of the pin-on-bar test are developed using the Hertz theory for both elastic and elastoplastic contact. However, these models considered only the indentation in a static contact between two spheres, so the sliding was neglected, which does not represent exactly the physical phenomenon occurring in the pin-on-bar test. Therefore, an inverse approach consisting of conducting numerical simulations of the pin-on-bar tests is applied by varying the normal force until the contact pressure at the pin-workpiece interface (P_{pob}) is equal to that pressure calculated from the cutting tests (P_{ny}).

A model of the pin-on-bar test is developed and simulated using Abaqus FEA (implicit) software. A 2D model is shown in *Figure 151*, where the pin in uncoated cemented carbide and having a radius of 6 mm is sliding over a flat workpiece in Ti6Al4V alloy having a rectangular shape with 10 mm length and 4 mm height. The workpiece is fixed at its bottom side and the pin is allowed to slide over the top surface of the workpiece in the x-direction at a constant speed (the sliding speed). Amongst the sliding speeds shown in *Figure 148*, five of them are used in the simulations of pin-on-bar: 10, 20, 40, 60 and 80 m/min. Due to the convergence issues, the application of a force in the pin is replaced by a displacement imposed to the pin in the direction normal to the workpiece surface until reach the desired normal force.

The materials of the workpiece and pin are considered as isotropic. The elastic properties of the Ti6Al4V alloy are taken from Cheng et al. [305], while the elastic properties of the pin are obtained from several studies found in the literature [50, 306, 307]. The Johnson-Cook [308] plasticity model without the temperature term is used to represent the plastic behavior of the Ti6Al4V alloy, as described by *Equation 32*:

$$\tilde{\sigma} = (A + m\varepsilon_p^n) \left[B + C \ln\left(\frac{\dot{\varepsilon}}{\dot{\varepsilon}_0}\right) \right] \quad \text{Equation 32}$$

where the first term ($A + m\varepsilon_p^n$) represents the strain hardening effects, and the second term $\left[B + C \ln\left(\frac{\dot{\varepsilon}}{\dot{\varepsilon}_0}\right) \right]$ the strain-rate effect. ε_p and $\dot{\varepsilon}$ are the plastic strain and strain rate, respectively. The coefficients A , B , C and n of this plasticity model were determined from quasi-

static and dynamic (different strain-rates) compression tests conducted over samples from the same bar used in the tribological tests. The mechanical properties of both workpiece and pin are listed in *Table 51*.

Table 51. Mechanical properties of the pin and workpiece used in the pin-on-bar model[309].

	Ti6Al4V	WC
Density (Kg/m ³)	4420	13967
Elastic modulus (GPa)	114	627.5
Poisson's ratio	0.31	0.25
Coefficients of the plasticity model	$A = 619, B = 639, C = 0.0214$ $n = 0.124, m = 0.666, \dot{\epsilon} = 0.001 \text{ s}^{-1}$	

The friction coefficient in function of the sliding speed was taken from the work of Courbon et al. [62], obtained for the same pin and workpiece materials using similar tribological tests. This friction coefficient can be represented by the following equation:

$$\mu = a + b \cdot \ln(V_s) \quad \text{Equation 33}$$

where V_s is the sliding speed and a and b are constants, equal to 0.359 and -0.042 , respectively. The simulation is divided into 2 steps: indentation and sliding. In the indentation step the pin penetrates a given depth into the workpiece to reach the suitable average contact pressure. Then, in the sliding step the pin slides 10 mm over the workpiece top surface in the x-direction at constant sliding speed. After the simulation, the contact pressure is extracted from the model and compared with that obtained by orthogonal cutting. If they are different, the penetration depth is modified, and a new simulation is performed. This procedure is applied until both contact pressures be similar, and consequently the normal force acting in the pin is obtained. Both pin and workpiece are meshed with four-node plane stress element type (CPS4R). A thin layer of 0.2 mm thickness is partitioned on top of the workpiece to refine the mesh. A maximum element size of 1 mm and 0.5 mm are used for the pin and workpiece, respectively. To determine the minimum element size, the influence of element size on the results is studied, as described below. In addition, since the model is a simplification of the pin-on-bar geometry (initial bar diameter is equal to 80 mm), the influence of the equivalent radius used in the Hertz

theory [310, 311] is also presented below. After this, simulations are conducted for the 5 sliding speeds mentioned above.

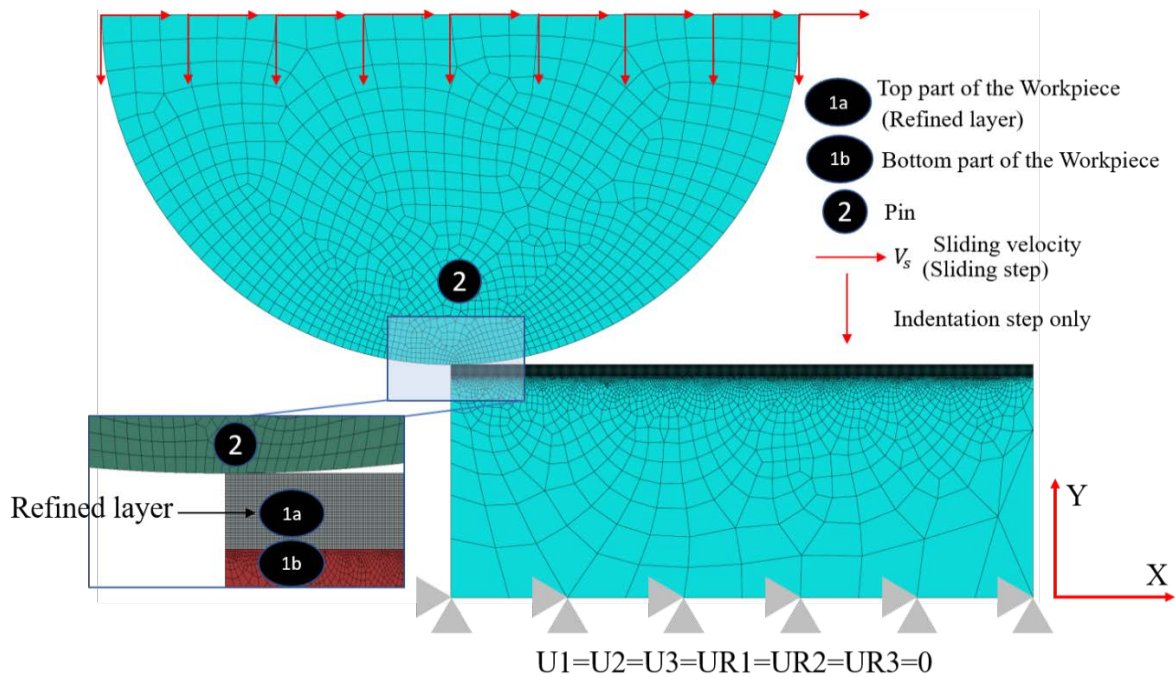


Figure 151. Model and mesh of the pin-on-bar tribological test.

Determination of the minimum element size

Four levels of mesh sizes were studied to verify their influence on the results, as shown in Table 52. As shown in Figure 151, the minimum element size of the pin is located in the bottom of the spherical part in contact with the workpiece. On the workpiece side, the elements with minimum size are located at the top surface of the workpiece within a thin layer of 0.2 mm thickness in contact with the pin.

Table 52. Minimum element size tested pin and workpiece

	Minimum element size (µm)			
	Mesh 200P-40W	Mesh 100P-20W	Mesh 50P-10W	Mesh 25P-5W
Pin	200	100	50	25
Workpiece	40	20	10	5

As shown in Figure 152 and in Figure 153, the largest combination of minimum element size Pin (P)-Workpiece (W) (200 µm for the pin and 40 µm for the workpiece) presents the largest

discrepancy on normal force and contact stress compared to other three element sizes. The average contact stresses are 1059 MPa, 1003 MPa, 907 MPa and 781 MPa for the mesh sizes 25P-5W, 50P-10W, 100P-20W and 200P-40W, respectively. The two finest combinations of minimum element size of 25P-5W and 50P-10W generate similar normal force of 439 N and 436 N, respectively. Considering the accuracy of the results and the computational time, the combination of minimum element size 50P-10W is chosen for the simulations to calculate the normal force acting in the pins for different sliding speeds.

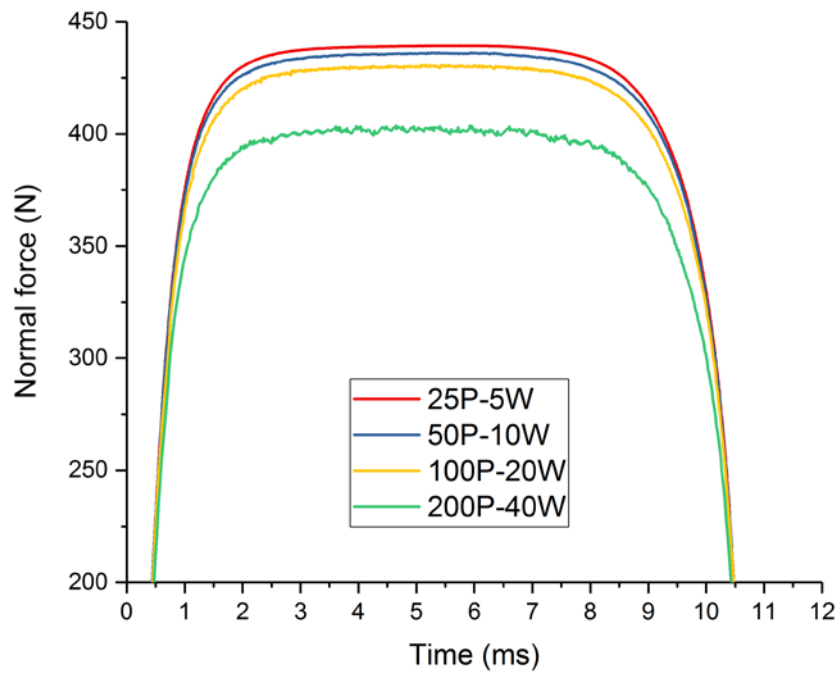


Figure 152. Normal forces in function of the time for several minimum element size.

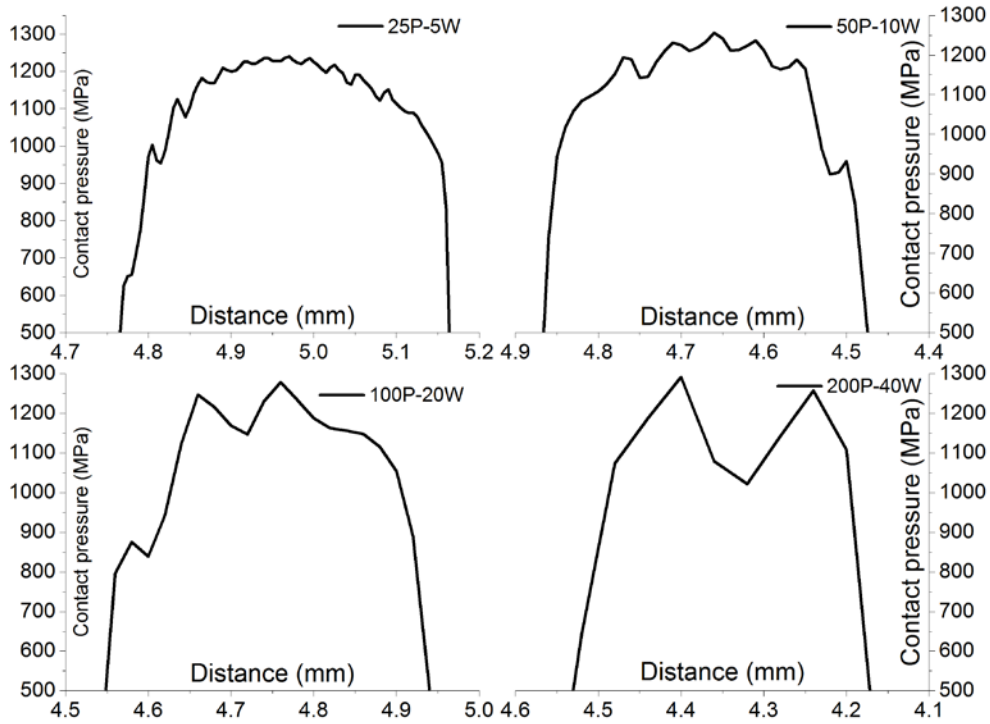


Figure 153. Contact stress distribution in function of the minimum element size.

Influence of the equivalent radius in the results

Ti6Al4V bar is machined several times during tribological tests to obtain a new surface for the pin-on-bar tests, thus the diameter of the bar will be reduced from an initial one of 80 mm to 56 mm. Furthermore, the simulated model is based on a sphere-plane contact, while the actual pin-on-bar tests are conducted using spherical pins sliding over a cylindrical workpiece. Therefore, when the pin is sliding over the bar is “seeing” a curved surface with a given radius. In order to verify the influence of this geometrical effect on the simulated results, an equivalent radius (R_{eq}) is calculated using Equation 34 based on the Hertz contact theory [310, 311]:

$$R_{eq} = \frac{1}{\frac{1}{R_{pin}} + \frac{1}{R_{work}}} \quad \text{Equation 34}$$

where R_{pin} and R_{work} are the radius of the pin and workpiece, respectively. The equivalent radius (R_{eq}) calculated considering the bar with an initial diameter of 80 mm and a final one of 56 mm are listed in Table 53. Consequently, numerical simulations with the optimized mesh (50P-10W) were performed using pins with these two equivalent radii, completed with a third

simulation using a pin with the original radius of 6 mm. As shown in Figure 154, the normal forces for these three different radii corresponding to the original pin radius of 6 mm, equivalent pin radius of 5.2 mm and of 5 mm are 436 N, 414 N and 406 N, respectively. Moreover, the distributions of the contact stresses are almost the same, as shown in Figure 155. To conclude, the numerical model using a spherical pin sliding against a flat surface can be used to simulate the real pin-on-bar test using a pin with its original radius of 6 mm, since the error does not exceed 7%.

Table 53. Equivalent radius (R_{eq}) calculated considering the bar with an initial diameter of 80 mm and a final one of 58 mm.

Bar radius (mm)	40 (initial)	28 (final)
Pin radius (mm)	6	6
Equivalent pin radius (R_{eq}) (mm)	5.2	5

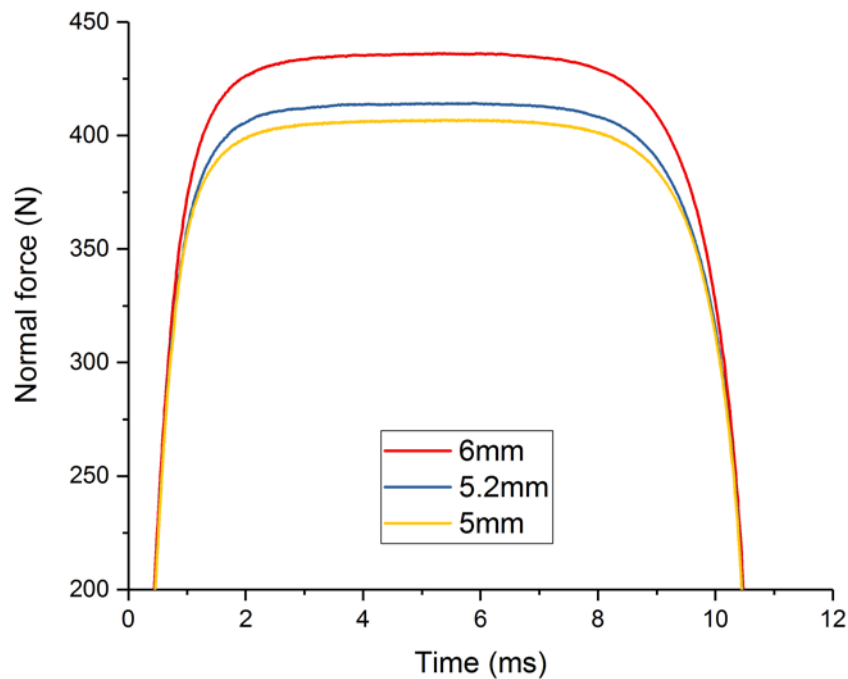


Figure 154. Normal forces in function of the time for different pin radius.

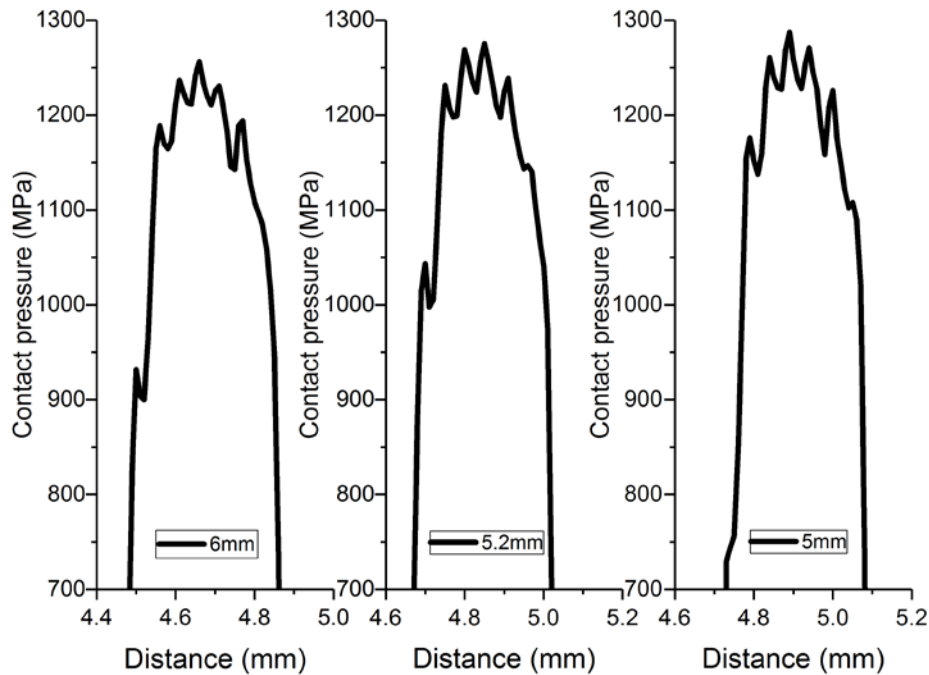


Figure 155. Contact stress distribution for different pin radius.

Determination of the normal force acting in the pins for different sliding speeds

After analyzing the effects of minimum element size and equivalent radius on the results, five numerical simulations using five sliding speeds are performed to determine the normal forces able to reproduce a reference average contact pressure around 1000 MPa determined from orthogonal cutting. The results are shown in *Figure 156* concerning to the normal force applied to the pin along its axis and *Figure 157* shows the corresponding contact pressure generated by these normal forces, for several sliding speeds. *Figure 157* shows that the maximum contact pressures are closed to 1260 MPa, with an average pressure of 989 MPa. These figures also shows that the sliding speed has a small effect on the normal force and contact pressure. The normal force varies from 423N for lowest speed of 10 m/min to 437N for highest speed of 100 m/min, which corresponds to a variation of 14N. The average contact pressure varies from 975 MPa for the lowest speed of 10 m/min to 1006 MPa for the highest speed of 100 m/min, which corresponds to a variation of 31 MPa.

Based on this analysis, it was decided to apply a normal force of 300 N during the tribological tests, which corresponds to an average contact pressure of 872 MPa.

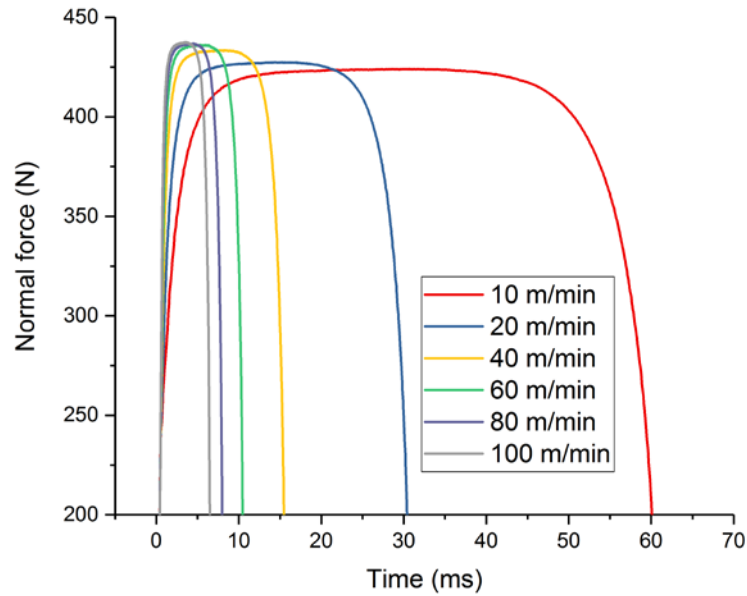


Figure 156. Normal forces in function of the time for several sliding speeds.

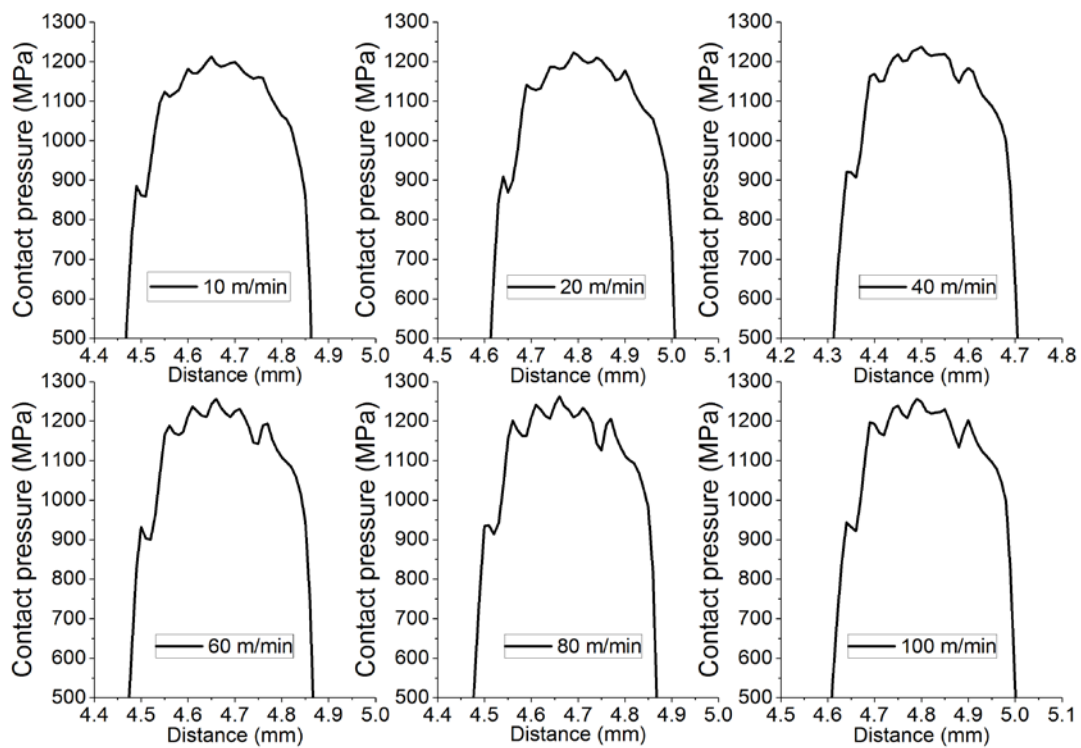


Figure 157. Contact stress distribution for several sliding speeds.

4.3. Surface roughness of the pins

The roughness of the pins was measured after the depositions using dynamic focusing microscope *Alicona InfiniteFocus*. The arithmetic average roughness of uncoated and coated

pins varies from 0.5 to 0.71 μm , the root mean square roughness varies from 0.63 to 0.91 μm , the maximum height varies from 3.64 to 6.21 μm . The coatings slightly increase the roughness of the pins according to R_a and R_q , although the coatings follow the surface topography of substrate, this may be due to the triangle tips of the coatings. The roughness of AlCrN monolayer and M2, M4 multilayers are almost the same, because the top layer of them is AlCrN monolayer. The maximum height reveals that the AlCrN is rougher than the other coated pins. The SEM images of the coated pins are presented in *Figure 200 of Appendix F*. This figure shows that the AlCrN monolayer has more randomly small particles on the surface compared to the other coatings. Indeed, M2 and M4 multilayers present less particles than the AlCrN and the CrN monolayer, they are relatively homogenous among all the coatings. This may be due to the unstable micro-arc phenomenon that occurs during deposition of AlCrN monolayer. The quantity and distribution of these small particles justifies the observed surface roughness values between different coatings.

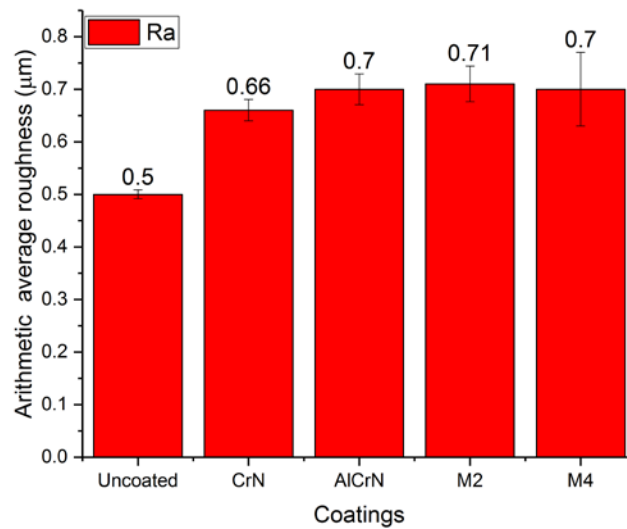


Figure 158. Arithmetic average roughness (R_a) of the pins for different coatings.

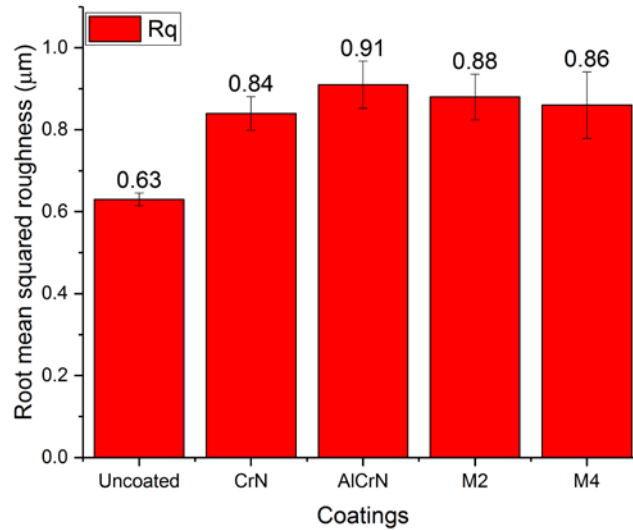


Figure 159. Root mean square roughness (R_q) of the pins for different coatings.

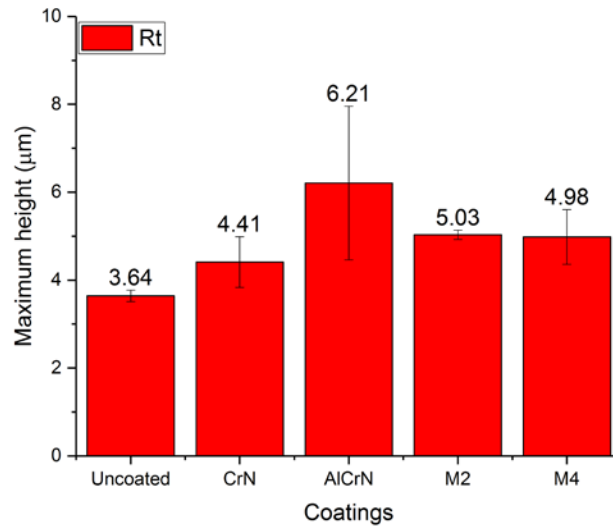


Figure 160. Maximum height of the roughness profile (R_t) of the pins for different coatings.

4.4. Design of experiments

Design of experiments (DoE) is one powerful statistical method when dealing with many variables (factors) and corresponding values (levels), which results in a huge number of experiments. It allows the establishment of statistical correlation between a set of input factors and output responses.

Based on the number of pin-on-bar process variables and corresponding values, the multilevel factorial design was selected for analysing the tribological behaviour of the coatings under flood and LN2 cooling/lubrication conditions. The multilevel factorial design is a $N = u^k$ factorial experiment used to investigate the effects of one or more factors on the response in u levels. When the factor number k is more than one, these factors can influence the response

individually as well as jointly. Factorial experiments include all possible factor combinations in experimental design when there is no order of testing restrictions. Details about the multilevel factorial design applied to metal cutting can be found in this reference [301].

The DoE is composed by 3 factors (sliding speed, coating type and MWF) and several levels listed in *Table 54*. The contact pressure was not included in this DoE, since at this stage it was assumed a constant contact pressure and equal to 872 MPa. Each condition was tested twice (one repetition) corresponding to a total of 120 tests. The outputs are the normal and tangential forces, the friction coefficient, and the volume of build-up layer of Ti6Al4V alloy in the pins. Temperature was also measured (twice) but only for the sliding speed of 60 m/min. The measured average normal force applied on these tests is 316 N, with average contact pressure of 877 MPa. The maximum average normal force applied is 393 N, with average contact pressure of 971 MPa. The minimum average normal force applied is 266 N, with average contact pressure of 839 MPa.

Table 54. Factors and levels used in the multilevel factorial DoE.

Factors	Levels
Sliding speed (m/min)	10, 20, 40, 60, 80 and 100
Coating Type	No coating (uncoated pin), CrN, AlCrN, M2 and M4
MWF	LN2 and Flood

To evaluate the influence of the contact pressure, additional 12 tests were performed by applying a normal force of 1400 N to the pins, which corresponds to an average contact pressure of 1329 MPa, calculated using the numerical model presented previously. These additional tests are shown in *Table 55*. The sliding distance for each tribological test is equal to 4 m.

Table 55. Additional tests for an average contact pressure of 1329 MPa.

No.	Sliding speed (m/min)	Coating type	MWF
1	10	Uncoated	LN2
2	20	Uncoated	LN2
3	40	Uncoated	LN2
4	60	Uncoated	LN2
5	80	Uncoated	LN2
6	100	Uncoated	LN2
7	20	Uncoated	Flood
8	60	Uncoated	Flood
9	100	Uncoated	Flood
10	20	M2	Flood
11	60	M2	Flood
12	100	M2	Flood

4.5. Results of the tribological tests

In this section the results from the tribological tests concerning to the apparent friction coefficient, forces, temperatures, and the volume of build-up layer of Ti6Al4V alloy in the pins will be presented and discussed.

Based on the measurements of the tangential and normal force during the tribological tests, the apparent friction coefficient was determined. *Figure 161* shows the friction coefficient in function of the sliding speed, for different coatings, for both MWF (flood and LN2) and for an average contact pressure of 872 MPa. This figure shows that the apparent friction coefficient decreases as the sliding speed increases until about 60-80 m/min, then it increases as the sliding speed increases up to 100 m/min. Similar results were also obtained by Meier et al. [312] by an in-process (cutting) open tribometer to determine the friction coefficient between the Ti6Al4V alloy and a 6 mm diameter pins coated with a AlTiN coating, using several pin axial (normal) forces (between 5N and 400 N), and under dry and lubricated (oil) conditions. Like the present work, they also found that the apparent friction coefficient shows a minimum value for intermediate sliding speeds when 100 N of normal force. According to Meier et al. [312], the increase of the friction coefficient for higher sliding speeds is may due to higher shear forces at

higher relative speeds and a stronger adhesion of the workpiece material to the pins. This strong adhesion at higher speeds was observed in the present tribological tests, as shown in *Figure 162*. This figure shows a strong increase of the volume of build-up layer of Ti6Al4V alloy in the pins for sliding speeds greater than 60-80 m/min, for both flood and LN2 coolant/lubricant conditions. Nevertheless, the uncoated pin seems to present a lower adhesion of Ti6Al4V alloy under LN2 cooling condition (*Figure 162 b*) which can be explained by its lower roughness as shown above in section 4.3 of this chapter. This volume is higher when LN2 is applied compared to the flood.

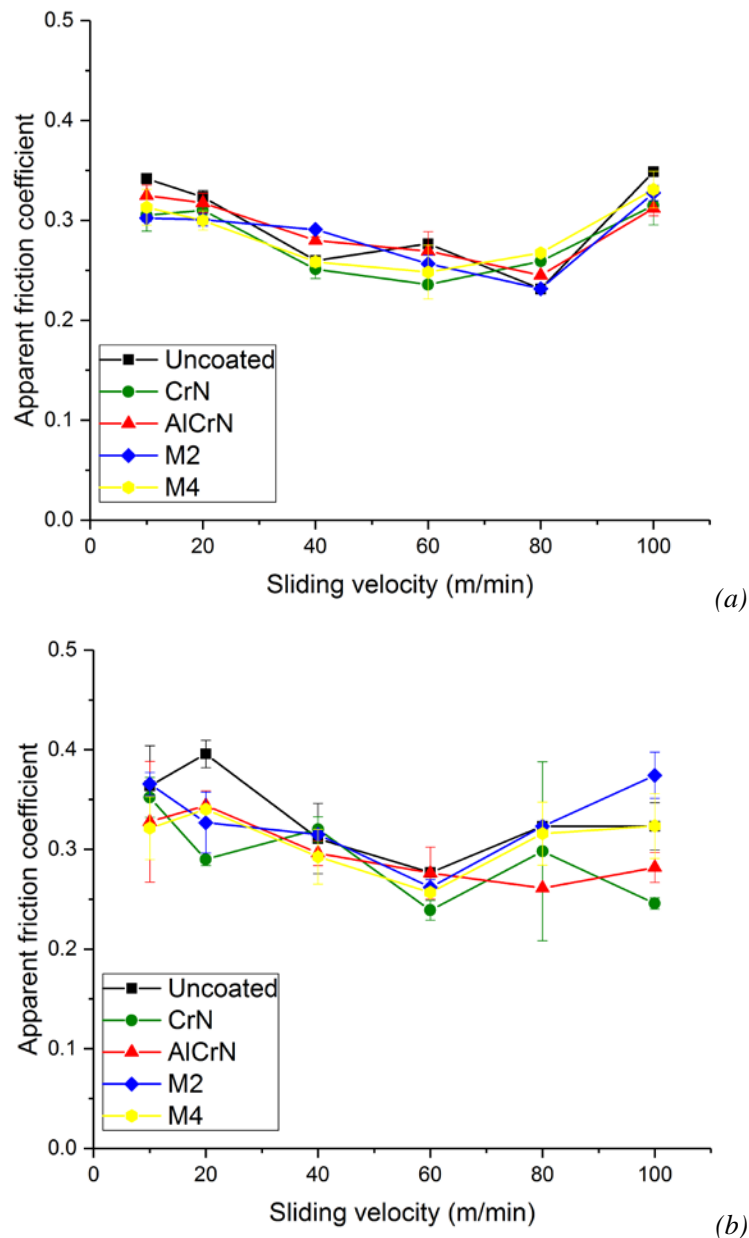


Figure 161. Apparent friction coefficient in function of the sliding speed and for different coatings, for (a) flood and b) LN2 (average contact pressure of 872 MPa).

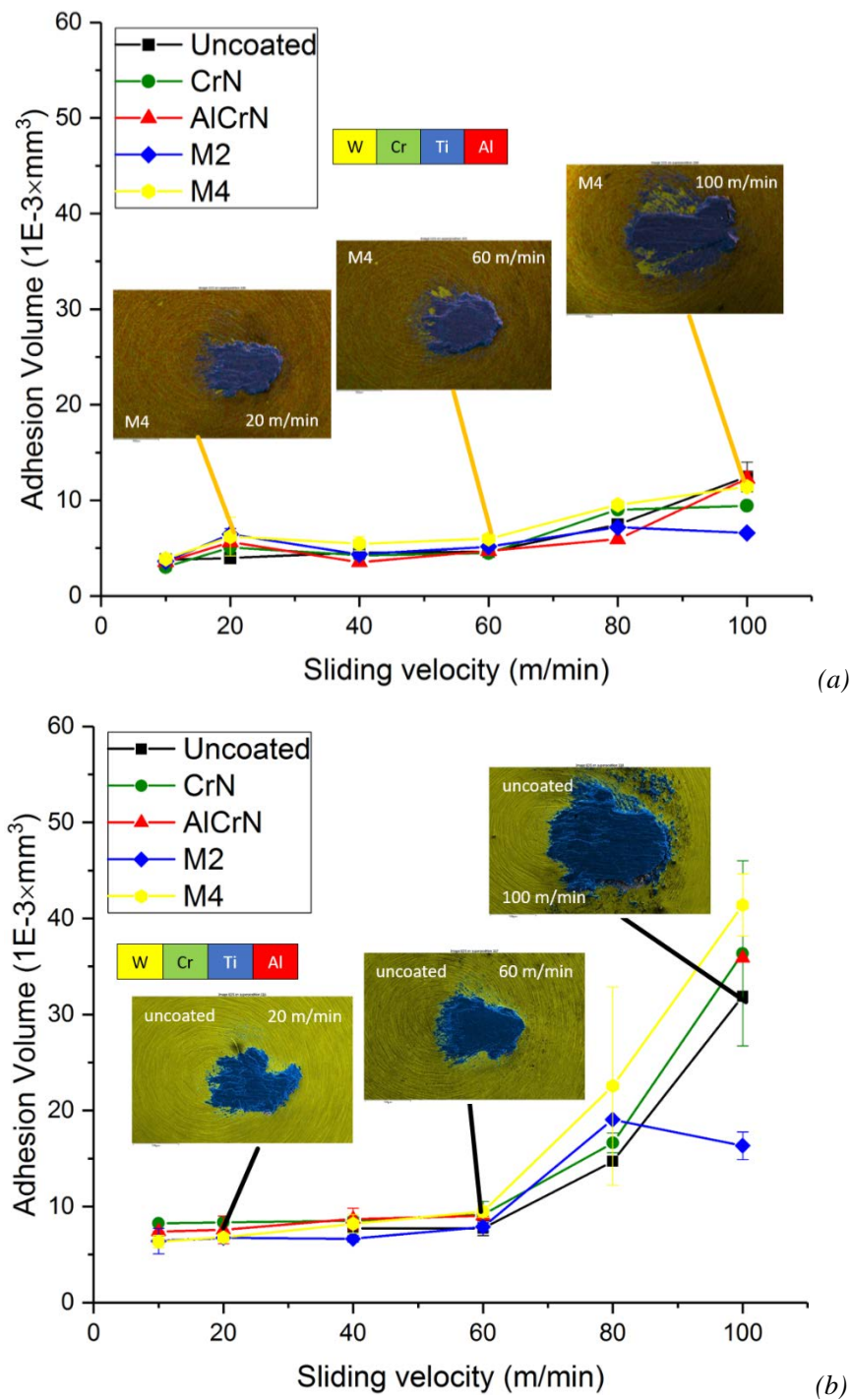


Figure 162. Volume of build-up layer of Ti6Al4V alloy in the pins in function of the sliding speed and for different coatings, for (a) flood and (b) LN2 (average contact pressure of 872 MPa).

As far as the average contact pressure is concerned, increasing the pressure from 872 MPa to 1329 MPa reduces the apparent friction coefficient, as shown in Figure 163 for uncoated and coated pins (M2) and both MWF. In particular, the apparent friction coefficient decreases

monotonically with the sliding speed when the higher pressure is used and for both MWF. Similar results were also obtained by Meier et al. [312]. However, this reduction of the apparent friction coefficient is not followed by a reduction of the volume of build-up layer of Ti6Al4V alloy in the pins, but the opposite is observed as shown in *Figure 164*.

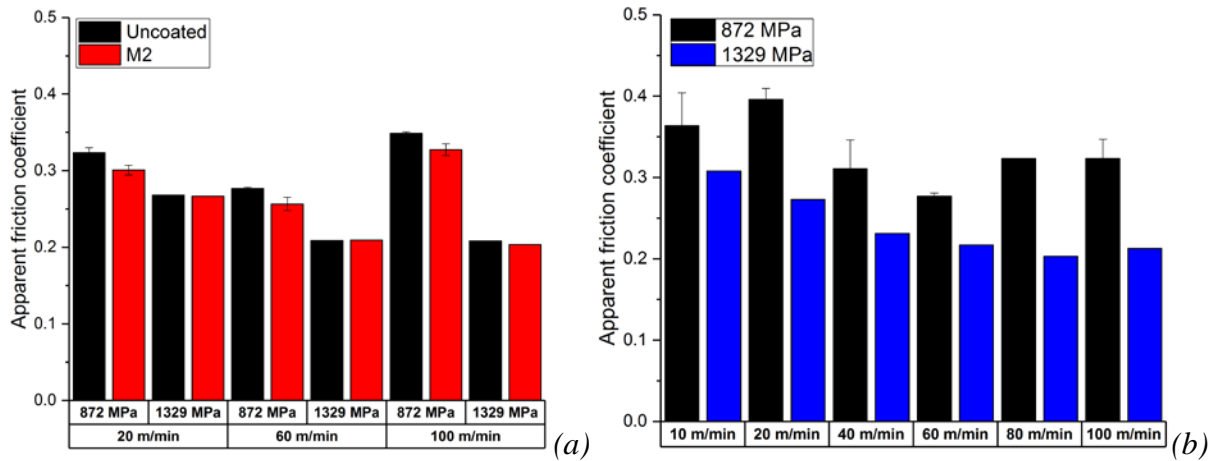


Figure 163. Apparent friction coefficient in function of the sliding speed, for two average contact pressures (872 MPa and 1329 MPa), and for a) flood conditions using coated (M2) and uncoated pins, and b) for LN2 conditions using uncoated pins.

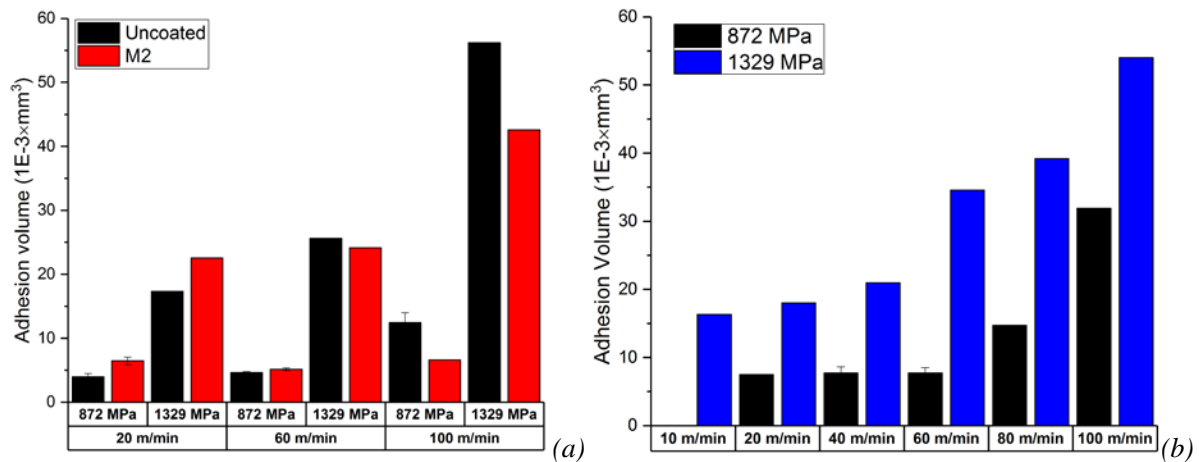


Figure 164. Volume of build-up layer of Ti6Al4V alloy in the pins in function of the sliding speed, for two average contact pressures (872 MPa and 1329 MPa), and for a) flood conditions using coated (M2) and uncoated pins, and b) for LN2 conditions using uncoated pins.

The apparent friction coefficients between the uncoated pins and the Ti6Al4V alloy for an average contact pressure of 1329 MPa and under LN2 cooling conditions were compared with those obtained by Courbon et al. [62], as shown in *Figure 165* for different sliding speeds. The present work has generated apparent friction coefficients about 20% higher than those found

by Courbon et al. [62]. This difference can be due to the different contact conditions (pressure, temperature, etc) between the present tribological tests and those performed by Courbon et al. [62], because the application of the LN2 (including the flow characteristics), pin diameter and normal force are not the same of present tribological tests. Despite these differences, both curves of the apparent friction coefficient follow the same trend with the sliding speed, which confirms the good accuracy of the apparent friction coefficients determined in the present work.

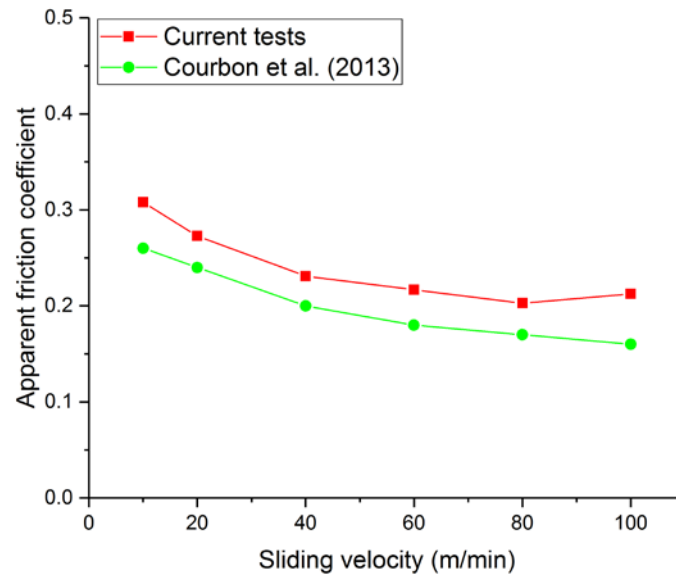


Figure 165. Apparent friction coefficient in function of the sliding speed obtained by current tribological tests and from the Courbon et al. [62] (Uncoated pin; average contact pressure of 1329 MPa; LN2 cooling).

As far as the coating is concerned, and regardless the MWF used in the tribological tests, *Figure 161* and *Figure 162* do not reveal any evident effect of the coating on the apparent friction coefficients and volume of build-up layer of Ti6Al4V alloy in the pins, respectively. As far as the temperature in the pins is concerned, some differences amongst each coating can be seen in *Figure 166*. This figure shows the temperature in the pins for different coatings and for both MWFs, at average contact pressure of 872 MPa and a sliding speed of 60 m/min. These temperatures were extracted from the curves of the temperature in function of the time, acquired during the tribological tests (see *Appendix H*, corresponding to a cutting time of 3.5 seconds for all the coatings shown in *Figure 166*).

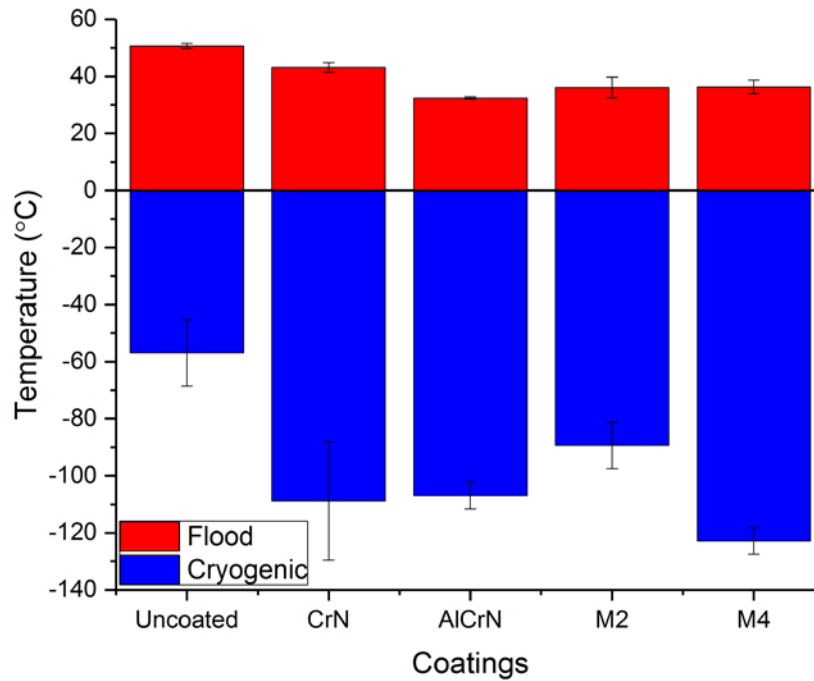


Figure 166. Temperature in the pins for different coatings (average contact pressure of 872 MPa and a sliding speed of 60 m/min)

This temperature is higher and positive for flood conditions when compared to LN2 cooling, where the temperature is negative. Moreover, this temperature is higher for the uncoated pins, regardless the MWF. The lower temperature in the pins depends on the coating and MWF used in the tribological tests. For flood conditions, the lowest temperature is observed for the AlCrN coating, followed by the M2 and M4. For LN2 cooling conditions, the lowest temperature is observed for the M4 coating, followed by the CrN, AlCrN and M2.

Nevertheless, from the thermal perspective the coated pins perform better than the uncoated one, because their temperature is closer to the MWF temperature compared to the uncoated pin temperature. Indeed, it seems that coated pins are less affected by the heat generated by friction at the pin-bar interface when compared to the uncoated one.

4.6. DoE analysis and discussion

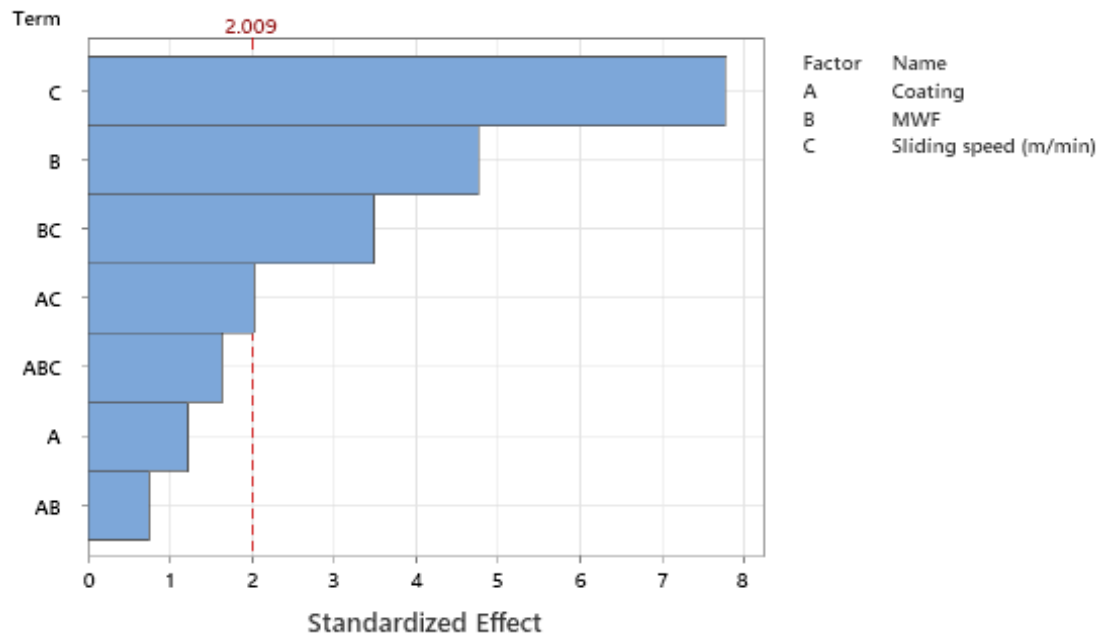
In this section the analysis of the DoE presented in Section 4.4 is performed with the following objectives:

- 1) to identify the relevant factors affecting the apparent friction coefficients and the volume of build-up layer of Ti6Al4V alloy in the pins.
- 2) to determine the influence of these relevant factors on the apparent friction coefficient and the volume of build-up layer of Ti6Al4V alloy in the pins.

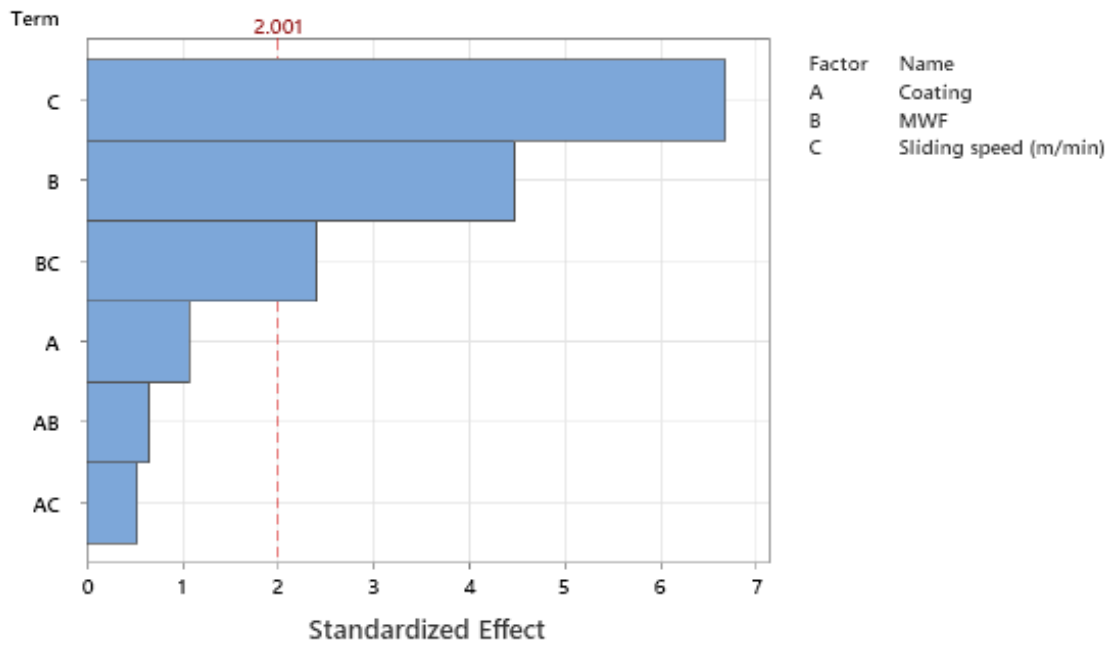
This DoE analysis is performed using the *Minitab*TM statistical software. The first step consists into identify the significant factors affecting the apparent friction coefficient and the volume of build-up layer of Ti6Al4V alloy in the pins and their interactions using the Pareto analysis. As shown in *Figure 167*, the significant factors are the type of MWF (flood vs LN2), the sliding speed and its interaction. The type of coating does not have any significance, confirming what was already mentioned in the previous section. As we can find in *Figure 161* and *Figure 162*. The apparent friction coefficient varies within 0.05 under flood conditions and varies within 0.1 under cryogenic conditions for all pins. Similar small variation is found for build-up layer of Ti6Al4V.

Figure 168 shows a graphical representation of the influence of the significant factors (MWF, sliding speed and their interactions) on the apparent friction coefficient. *Figure 168a* shows that the apparent friction coefficient is higher for cryogenic (LN2) cooling when compared to flood conditions. This can be explained by the fact that no lubricant is used under cryogenic cooling with LN2. This figure also shows a decrease of the apparent friction coefficient with the sliding speed until 60 m/min, followed by an increase until 100 m/min. This confirms the previous results, and the justification for this behavior of the apparent friction coefficient with the sliding speed can be attributed to the increase of the adhesion after 60 m/min. *Figure 168b* shows the interaction between the type of MWF and sliding speed. This figure shows for almost the sliding speeds (except for 100 m/min) the apparent friction coefficient is higher for cryogenic (LN2) cooling when compared to flood conditions.

Figure 169 shows a graphical representation of the influence of the significant factors on the volume of build-up layer of Ti6Al4V alloy in the pins. This volume of build-up layer can be used to estimate the amount of adhesion of Ti6Al4V alloy in the pins. *Figure 169a* shows that adhesion is higher for cryogenic (LN2) cooling when compared to flood conditions. Again, this can be explained by the fact that no lubricant is used under cryogenic cooling with LN2. This figure also shows that adhesion is almost constant until a sliding speed of 60 m/min, followed by a fast increase of adhesion beyond 60 m/min until 100 m/min. *Figure 169b* shows that adhesion is higher for cryogenic (LN2) cooling when compared to flood conditions regardless the sliding speed, which confirms the previous results.



(a)



(b)

Figure 167. Pareto analysis of the factors affecting the (a) apparent friction coefficient and (b) volume of build-up layer of Ti6Al4V alloy in the pins.

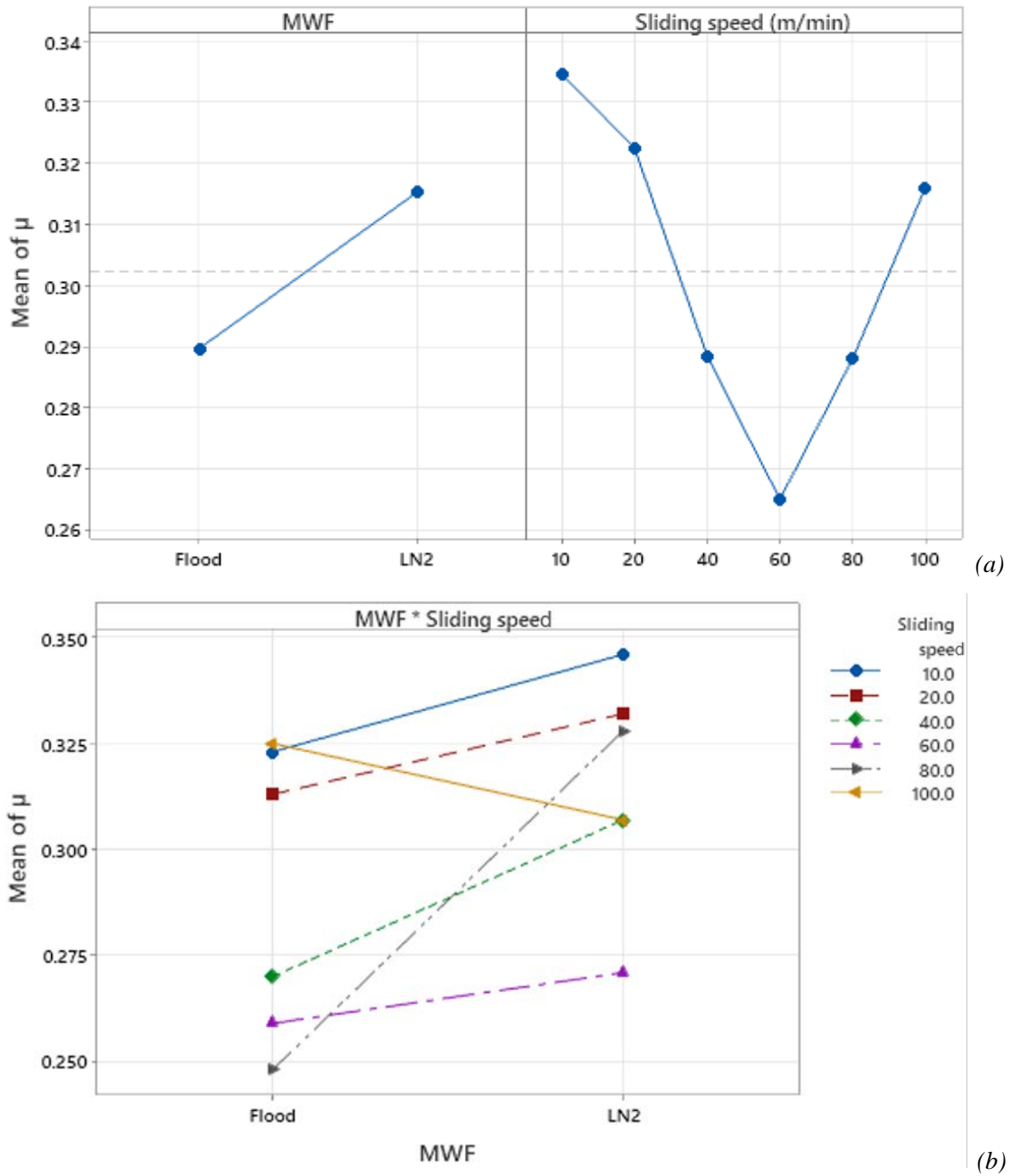


Figure 168. Influence of the (a) type of MWF and sliding speed, and (b) their interactions on apparent friction coefficient.

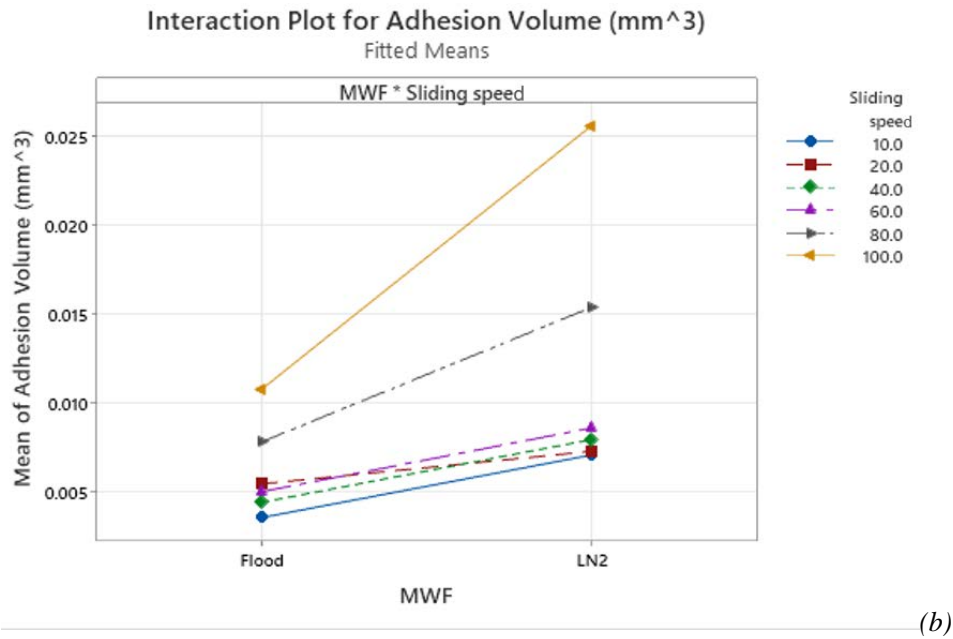
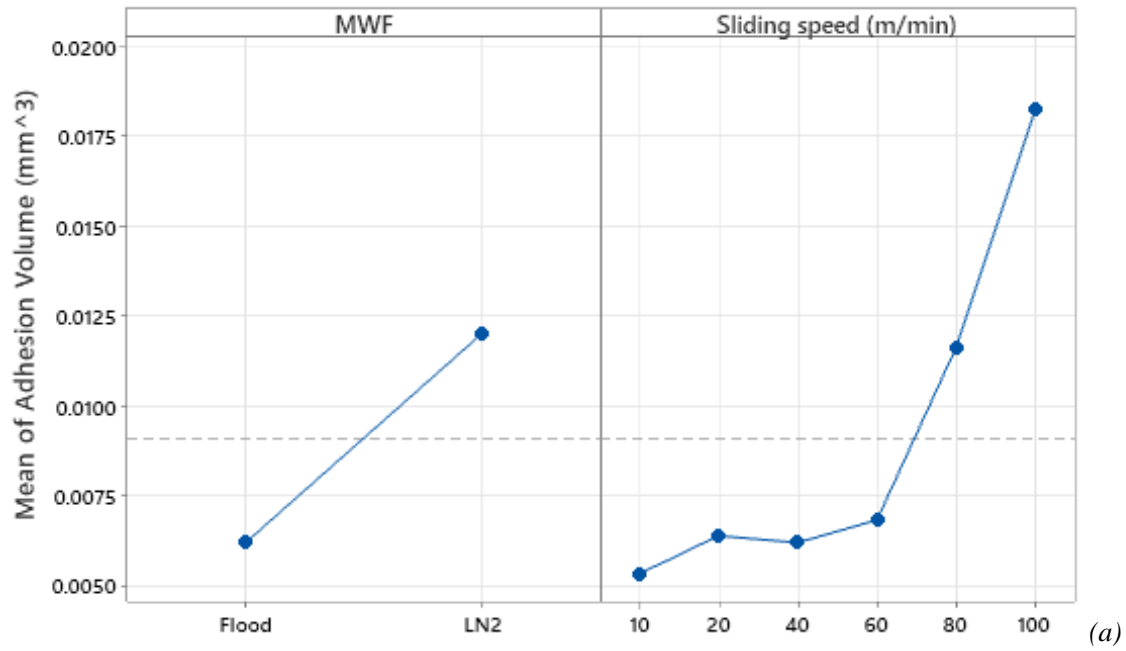


Figure 169. Influence of the (a) type of MWF and sliding speed, and (b) their interactions on the volume of build-up layer of Ti6Al4V alloy in the pins.

Figure 169b shows that adhesion is higher for cryogenic (LN2) cooling when compared to flood conditions regardless the sliding speed, which confirms the previous results.

To determine the optimal type of MWF and sliding speed for a reduced adhesion of Ti6Al4V material to the pins and thus the apparent friction coefficient, an optimization analysis was performed using Minitab™ software. The results are presented in Table 56, which permit to

conclude that flood conditions and a sliding speed of 60 m/min should be used to reduce the adhesion of Ti6Al4V material to the pins and consequently the apparent friction coefficient.

Table 56. Optimized type of MWF and sliding speed for a reduced adhesion of volume of Ti6Al4V material to the pins and apparent friction coefficient.

MWF	Sliding speed (m/min)	Adhesion Volume (mm³) - Fit	μ - Fit	Composite Desirability
Flood	60	0.00507	0.259	0.864

4.7. Conclusion

The objective of the tribological tests presented in this chapter is to analyse the performance of the coatings developed in this thesis in terms of apparent friction coefficient, volume of build-up material (adhesion) to the pins, and their temperature. This analysis was performed for two cooling/lubrication strategies: LN2 and flood (oil-water mixture). A special designed pin-on-bar tribometer to reproduce the contact conditions in machining is used to conduct the tribological tests using uncoated and coated pins in contact with a workpiece in Ti6Al4V alloy, under several sliding speeds and two contact pressures. Four coatings are selected for the tribological tests: CrN, AlCrN, M2 and M4.

This chapter starts with the determination of the values of the parameters affecting the contact between the Ti6Al4V titanium alloys and the cemented carbide tools, in particular the sliding speeds and the contact pressure. These values are determined based on experimental data from orthogonal cutting tests and the single-shear plane analytical model. This permitted to obtain the sliding speeds between 10 and 100 m/min and a reference average contact pressure around 1000 MPa, to be used in the pin-on-bar tribological tests. Since the contact geometry in machining is not the same as in tribological tests, a numerical model of the pin-on-bar was developed using Abaqus FEA software. The model was optimized considering the influence of the element size and equivalent radius in the results. This model permitted to obtain the normal force of 300 N to be applied to the pins, which corresponds to an average contact pressure of 872 MPa.

Then, a multilevel factorial design of experiments (DoE) was built which is composed by a total of 120 tests. Additional 12 tests were performed to investigate the influence of the contact pressure on the results. The results have shown that for both cooling/lubrication strategies the coating does not have any relevant effect in the apparent friction coefficient. However, the

apparent friction coefficient decreases as the sliding speed increases until about 60-80 m/min, then it increases with the sliding speed until 100 m/min. Their values are generally higher under LN2 when compared to flood conditions. The increase of the apparent friction coefficient after 60-80 m/min is related to the increase of the adhesion of Ti6Al4V alloy to the pins for both cooling/lubrication strategies, even if this adhesion is higher for the LN2 cooling due to the absence of lubricant. Increasing the contact pressure from 872 MPa to 1329 MPa decreases the apparent friction coefficient, although the adhesion is higher for 1329 MPa. The temperature measurements in the pins show that it is lower for the coated pins compared to the uncoated one. The lowest pin temperature under flood conditions is obtained for the AlCrN coating, while this lowest temperature under LN2 cooling is obtained for the M4 coating.

The chapter ends with the analysis of the DoE and the determination of the contact conditions to reduce the adhesion of Ti6Al4V material to the pins and the apparent friction coefficient. The analysis of the DoE permitted to identify the sliding speed and the cooling/lubrication strategy as the two main factors influencing the friction coefficient and the adhesion of Ti6Al4V alloy to the pins, while the type of coating as no relevant effect. It confirms that the apparent friction coefficient decreases with the increase of the sliding speeds until around 60 m/min, then it increases up to 100 m/min. The adhesion volume is almost constant until a sliding speed of 60 m/min, then it increases up to 100 m/min. LN2 cooling leads to higher apparent friction coefficient and adhesion volume than the flood conditions, which is attributed to the lack of lubricant in LN2. Finally, an optimization analysis permits to conclude that flood conditions and a sliding speed of 60 m/min should be used to reduce the adhesion of Ti6Al4V material to the pins and consequently the apparent friction coefficient.

The analyse conducted in this chapter did not permit to identify the best coatings that will be applied to the cutting inserts for the tool wear tests in turning. However, we decided to select both M2 and M4 multilayers based on the global results obtained in this and previous chapters.

4.8. Résumé du Chapitre 4

L'objectif des essais tribologiques présentés dans ce chapitre est d'analyser les performances des revêtements développés dans cette thèse en termes de coefficient de frottement, de volume de matériau rapporté à l'outil (adhésion) et de la température de l'outil. Cette analyse sera effectuée pour deux couples de refroidissement/lubrification : l'azote liquide (LN2) et l'émulsion (mélange huile-eau). Un tribomètre pion-barre capable de reproduire les conditions

de contact lors de l'usinage a été utilisé pour réaliser les essais tribologiques en utilisant des pions non revêtus et revêtus en contact avec une pièce en alliage de titane Ti6Al4V, à plusieurs vitesses de glissement et deux pressions de contact. Quatre revêtements sont sélectionnés pour les essais tribologiques : CrN, AlCrN, M2 et M4.

Ce chapitre commence par la détermination des valeurs des paramètres affectant le contact entre les alliages de titane Ti6Al4V et les outils en carbure cémenté, en particulier les vitesses de glissement et la pression de contact. Ces valeurs sont déterminées sur la base des données expérimentales des essais de coupe orthogonale et du modèle analytique du plan de cisaillement. Ceci a permis d'obtenir des vitesses de glissement comprises entre 10 et 100 m/min et une pression de contact moyenne de référence autour de 1000 MPa, à appliquer dans les essais tribologiques pion-barre. Comme la géométrie de contact en usinage n'est pas la même que dans les essais tribologiques, un modèle numérique de l'essai pion-barre a été développé avec le logiciel Abaqus. Le modèle a été optimisé en tenant compte de l'influence de la taille de l'élément et du rayon équivalent sur les résultats. Ce modèle a permis d'obtenir la force normale à la surface de la pièce (barre) de 300 N à appliquer sur les pions, qui génère la même pression de contact moyenne de 827 MPa.

Ensuite, un plan d'expériences multifactoriel a été construit, composé d'un total de 120 tests. Douze essais supplémentaires ont été effectués pour étudier l'influence de la pression de contact sur les résultats. Les résultats ont montré que le revêtement n'a pas d'effet significatif sur le coefficient de frottement apparent pour les deux couples de refroidissement/lubrification. Cependant, le coefficient de frottement apparent diminue lorsque la vitesse de glissement augmente jusqu'à environ 60-80 m/min, puis il augmente avec la vitesse de glissement jusqu'à 100 m/min. Leurs valeurs sont généralement plus élevées sous LN2 par rapport aux émulsions. L'augmentation du coefficient de frottement apparent après 60-80 m/min est liée à l'augmentation de l'adhésion de l'alliage Ti6Al4V sur les pions pour les deux couples de refroidissement/lubrification, même si cette adhésion est plus élevée pour le LN2 en raison de l'absence de lubrifiant. L'augmentation de la pression de contact nominale de 872 MPa à 1329 MPa diminue le coefficient de frottement apparent, bien que l'adhésion soit plus élevée pour 1329 MPa. Les mesures de température dans les pions montrent que cette température est plus basse pour les pions revêtus par rapport aux pions non revêtus. Ainsi, les revêtements fonctionnent comme barrière thermique contre la chaleur générée pendant les essais tribologiques. La température du pion la plus basse est obtenue pour le revêtement AlCrN en

utilisant des émulsions, tandis que la température la plus basse en utilisant le LN2 est obtenue pour le revêtement M4.

Le chapitre se termine par l'analyse du plan d'expériences et la détermination des conditions de contact pour réduire l'adhésion de l'alliage Ti6Al4V sur les pions et le coefficient de frottement apparent. L'analyse du plan d'expériences a permis d'identifier la vitesse de glissement et le couple de refroidissement/lubrification comme les deux principaux facteurs influençant le coefficient de frottement et l'adhésion de l'alliage Ti6Al4V sur les pions, tandis que le type de revêtement n'a pas d'effet pertinent. Cette analyse confirme que le coefficient de frottement apparent diminue avec l'augmentation des vitesses de glissement jusqu'à environ 60 m/min, puis il augmente jusqu'à 100 m/min. Le volume d'adhésion est presque constant jusqu'à une vitesse de glissement de 60 m/min, puis il augmente jusqu'à 100 m/min. Le refroidissement par LN2 conduit à un coefficient de frottement apparent et à un volume d'adhésion plus élevés que les émulsions, ce qui est attribué à l'absence de lubrifiant dans le LN2. Enfin, une analyse d'optimisation a permis de conclure qu'une vitesse de glissement de 60 m/min sous émulsions devrait être utilisée pour réduire l'adhésion du matériau Ti6Al4V sur les pions et par conséquent, le coefficient de frottement apparent.

L'analyse menée dans ce chapitre n'a pas permis d'identifier les meilleurs revêtements qui seront appliqués aux plaquettes pour les essais d'usure en tournage. Cependant, nous avons décidé de sélectionner les revêtements M2 et M4 sur la base des résultats globaux obtenus dans ce chapitre et les chapitres précédents.

Chapter 5. Tool wear analysis

5.1. Introduction

Since the objective of this PhD study is to develop new tool coatings for reducing tool wear in cryogenic assisted machining of Ti6Al4V, tool wear tests and analysis need to be conducted to evaluate the life of coated cemented carbide tools using the developed multilayers M2 and M4 under cryogenic conditions. The obtained tool will be compared with the standard machining conditions of this alloy using uncoated cemented carbide with flood conditions. This chapter begins with the description of the tool wear tests, including experimental setup, work material, machining conditions.

5.2. Tool wear tests and results

5.2.1. Description of the tool wear tests

Tool wear is investigated in turning of Ti6Al4V alloy using cryogenic cooling (LN₂) and flood (mixture of oil and water) as MWFs. The workpiece was prepared by dividing it in three sections one per insert as shown in *Figure 170*. These wear tests are performed using uncoated and coated cemented carbide inserts. The uncoated inserts are CNMG 12 04 08 SM grade H13A from Sandvik, and they are considered as reference for machining Ti6Al4V alloy under flood conditions. The coated inserts use the same substrate of the uncoated ones, and they are coated using the multilayer M2 and M4 coatings. The tool holder used is a PCLNL 2525M-12-JHP from Iscar used in a previous PhD thesis of Pierre Lequien [61]. By default, this holder allows to deliver the MWF to the rake face. However, it is modified to deliver the MWF also to the tool flank face. Details about this holder is presented in *Appendix C*. These tests are conducted in the SONIM CNC lathe machine model T9. This machine is equipped with an experimental setup to measure the forces and tool wear as described in Chapter 2. The cutting conditions used in the tool wear tests are summarized in *Table 57*. The cutting regime parameters were chosen based on toolmaker recommendations and on the results from tool-work material pair (NF E66-520-4 “*Domaine de fonctionnement des outils coupants - Couple outil-matière - Partie 4 : mode d'obtention du couple outil-matière en tournage*”) tests performed by Lequien [61].

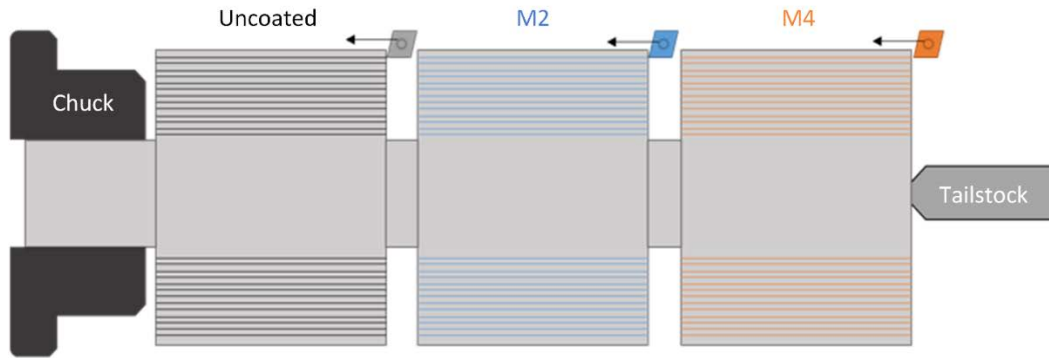


Figure 170. Schematic representation of the workpiece preparation for the tool wear tests.

Table 57. Cutting conditions used in the tool wear tests.

Inserts	CNMG 12 04 08 SM substrate H13A CNMG 12 04 08 SM substrate H13A + M2 coating CNMG 12 04 08 SM substrate H13A + M4 coating		
Tool holder	PCLNL 2525M-12-JHP		
Cutting regime parameters	$V_c = 90$ m/min	$f = 0.2$ mm/rev	$a_p = 1$ mm
Flood conditions	Mixture of Blaster B-Cool 755 oil (7%) and water (93%) Pressure = 3.2 bar Nozzle diameter (rake face) = 3 mm Nozzle diameter (flank face) = 1.2 mm Temperature = 20°C		
LN2 conditions	Liquid Nitrogen (LN2) Pressure = 4 bar Nozzle diameter (rake face) = 3 mm Nozzle diameter (flank face) = 1.2 mm Temperature = -193°C		
Tool geometry (ISO 3002/1982)	Tool cutting edge radius (r_n) = 26.3 μm (uncoated), 27.4 μm (M2 coating) and 28.3 μm (M4 coating)		
	Tool nose radius - r_ϵ (mm) = 0.8		
	Normal rake angle (γ_n) = -6°		
	Normal flank angle (α_n) = 6°		
	Tool wedge angle (β_n) = 90°		
	Cutting edge inclination angle (λ_s) = -6°		
	Tool cutting edge angle (κ_r) = 95°		
	Tool minor cutting edge angle (κ'_r) = 5°		
Tool included angle (ϵ_r) = 80°			

Tool wear tests were conducted based on the standard ISO 3685:1993 (reviewed and confirmed in 2017) “Tool-life testing with single-point turning tools” and ANSI/ASME “Tool Life Testing with Single-Point Turning Tools” (B94.55M-1985, reaffirmed 2014). According to these standards, the major cutting edge of the tool is divided into three regions as shown in *Figure 171*:

- Region C is curved part of the cutting edge at the tool corner;
- Region B is the remaining straight part of cutting edge behind zone C;
- Region N extends beyond the area of mutual contact between the tool workpiece for approximately 1 to 2 mm along the major cutting edge. The wear is of notch type. But for the current study, we don't consider this type of wear.

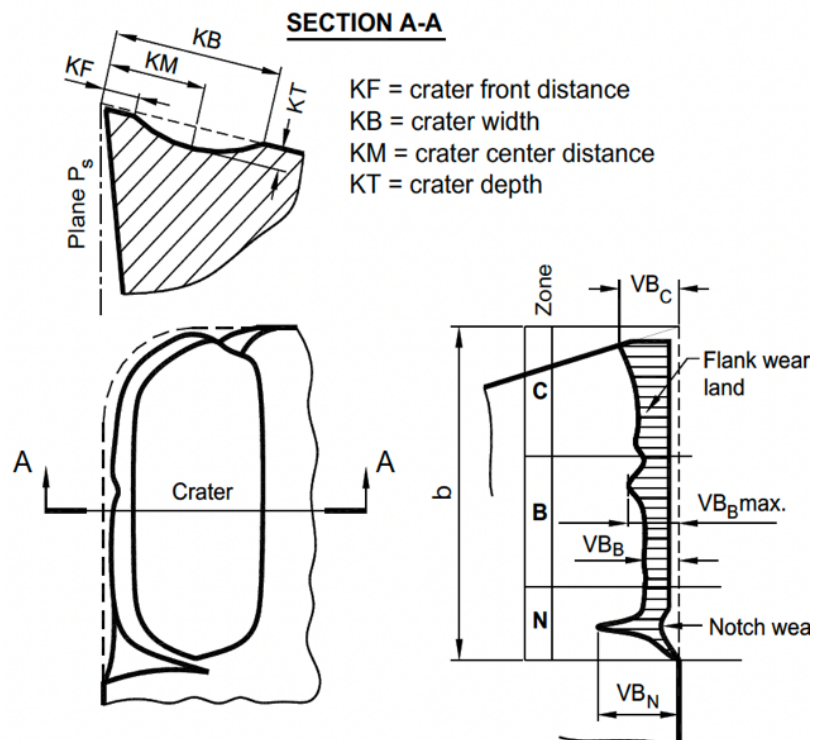


Figure 171. Types of wear in turning tools.

The criteria recommended by the standard ISO 3685:1993 to define the effective tool life for cemented carbides tools are:

- 1) $VB_B = 0.3$ mm, or
- 2) $VB_{Bmax} = 0.6$ mm, if the flank is irregularly worn, or
- 3) $KT = 0.06 + 0.3 \cdot f$, being f the feed

However, due to the high time and resources consuming (specially the LN2 consumption) typical of the tool wear tests, and the high part quality requirements of the aerospace industry, the limiting values of VB are reduced. Moreover, the standard does not mention anything about the criterium for VB_C . Therefore, we propose the following criteria to evaluate the tool life for the current tool wear tests (the first that is occurring):

- 1) $VB_B = 0.2$ mm, or
- 2) $VB_{Bmax} = 0.3$ mm, if the flank is irregularly worn, or
- 3) $VB_C = 0.3$ mm, or
- 4) Cutting edge chipping/tool breakage.

5.2.2. Results and discussion

Figure 172 shows the flank face of the new and worn uncoated inserts. Due to the low depth of cut (1 mm) compared to the nose radius (0.8 mm), most of the wear is concentrated in the nose region. Moreover, the wear pattern in zone B seems to be regular, so the VB_B should be suitable to represent the wear in zone B. Therefore, tool wear will be evaluated in zone B near the corner zone using VB_B parameter but also in the insert corner (zone C) using the VB_C parameter.

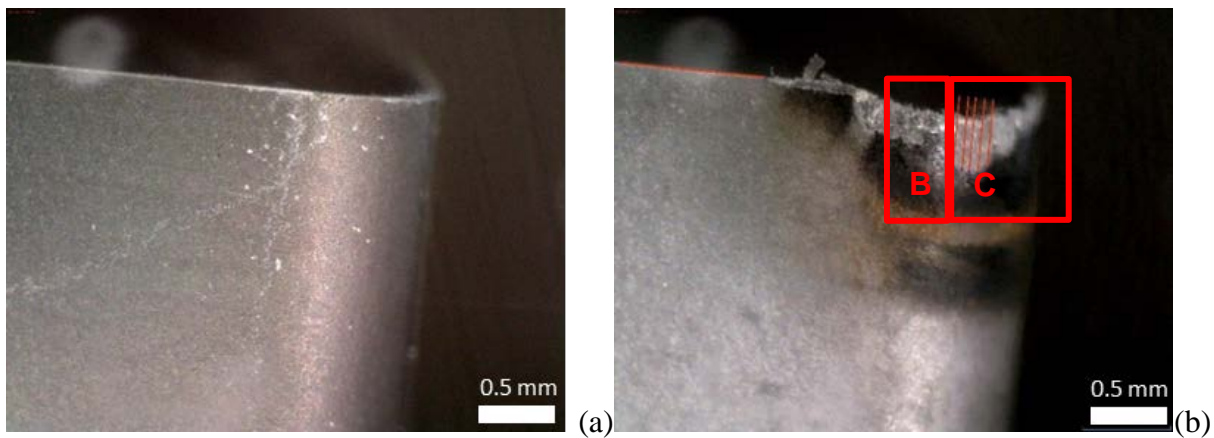


Figure 172. Uncoated inserts (a) new and (b) worn showing the tool wear (VB) measurements.

5.2.2.1. Cryogenic conditions

Figure 173 shows the tool flank wear curves for zone B (VB_B) in function of the time for the three inserts under cryogenic cooling conditions. These curves show that tool flank wear increases in the same way regardless the insert type. M2 seems to have a slightly lower tool wear at initial stage of cutting process compared to other inserts, but after 7.5 min all inserts have almost the same behavior. These three inserts reach the tool life criterium of VB_B almost

simultaneously in about 12 min, although M4 coated insert seems to reach the tool life criterium a little bit earlier than M2 and uncoated ones, but this difference is negligible.

As far as the tool wear curves for the zone C is concerned (VB_C), *Figure 174* shows that tool flank wear increases faster for the uncoated and coated M4 insert when compared to the M2. Therefore, uncoated and coated M4 inserts reach the tool life criterium for VB_C at about 8.4 min and 9 min, against 11.2 min for the M2 one, respectively. The M2 coating improves tool life of about 2.8 min compared to uncoated one, while the M4 coating shows no relevant improvement. *Figure 175* summarizes the overall tool life defined in section 5.2.1, for the three inserts under cryogenic cooling conditions. Observing this figure and considering the proposed criteria to evaluate tool life, we can conclude that the longest tool life is obtained using the M2 insert (11.2 min), followed by the M4 insert (9 min) and finally the uncoated insert (8.4 min).

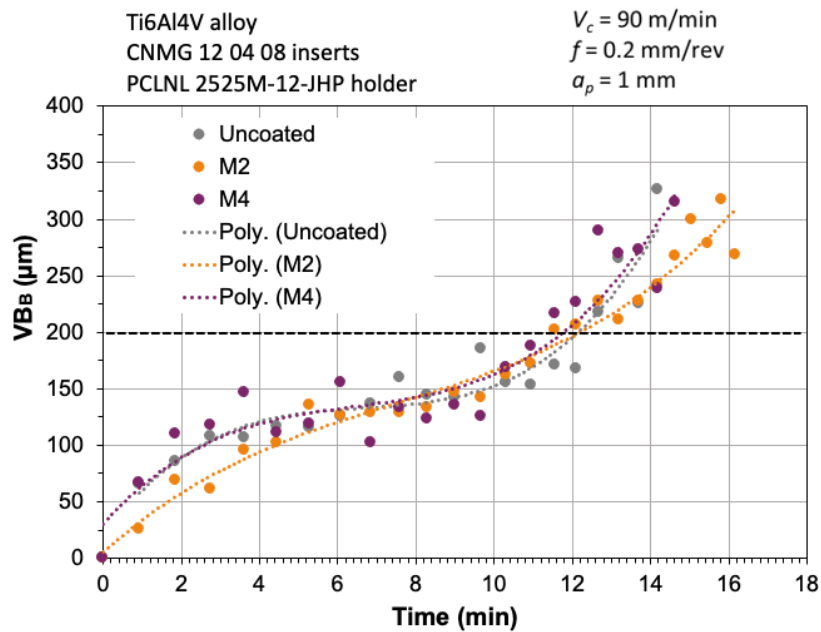


Figure 173. Tool flank wear VB_B in function of the time for the three inserts under cryogenic cooling.

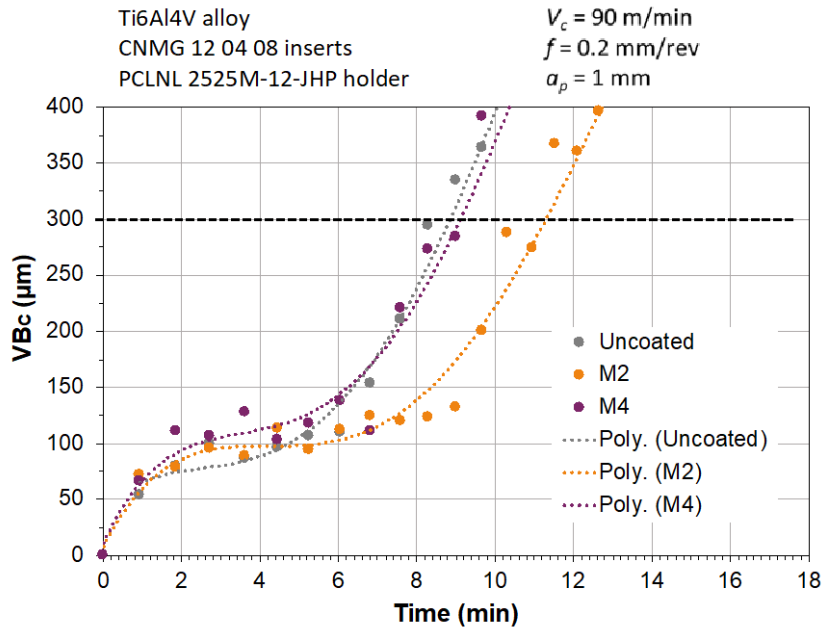


Figure 174. Tool flank wear VB_c in function of the time for the three inserts under cryogenic cooling.

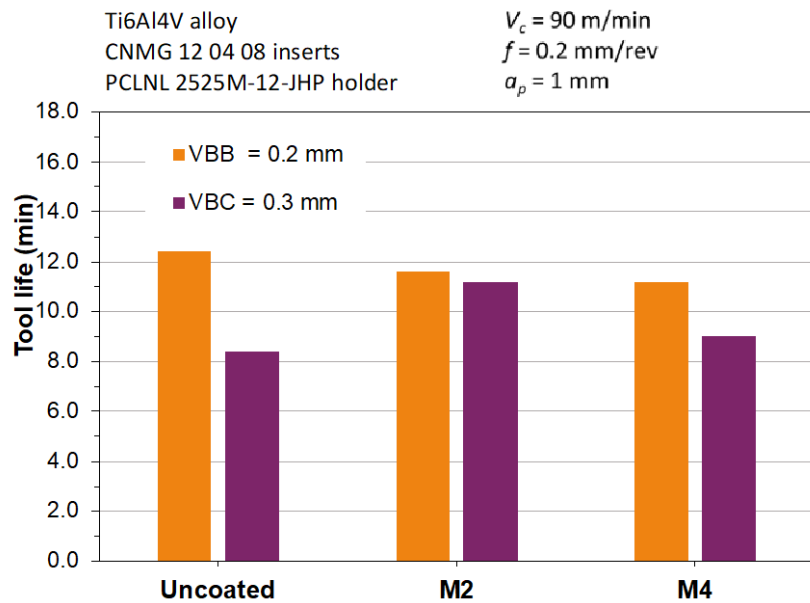


Figure 175. Tool life for the three inserts under cryogenic cooling (uncoated = 8.4 min, M2 = 11.2 min and M4 = 9 min).

Figure 176 shows the pictures of the worn inserts at the end of the wear tests under cryogenic cooling conditions taken using Alicona InfiniteFocus equipment. Figure 177 shows the pictures of the same inserts taken using SEM, completed with the distributions of the elements on the tool rake face measured by EDS shown in Appendix I. As can be seen in these figures, crater

wear, flank wear and nose wear are the principal types of wear for all the inserts. The proper indicator to compare the tool life is still the VB_B and VB_C .

As can be seen in *Figure 177*, the low magnification SEM images show adhesion of Ti6Al4V on the tool rake face and on tool nose region for all the inserts. Some coating abrasion is observed for M2 and M4 multilayer coated inserts (*Figure 177 (b) (c)*). Therefore, two main mechanisms are contributing for tool wear: abrasion and adhesion.

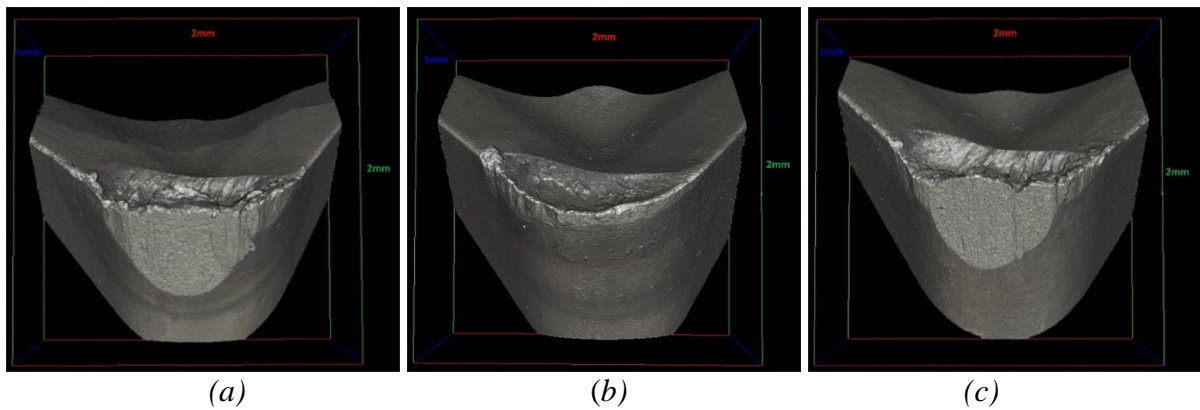


Figure 176. Worn inserts at the end of the wear tests using LN2: a) uncoated, b) M2 and c) M4.

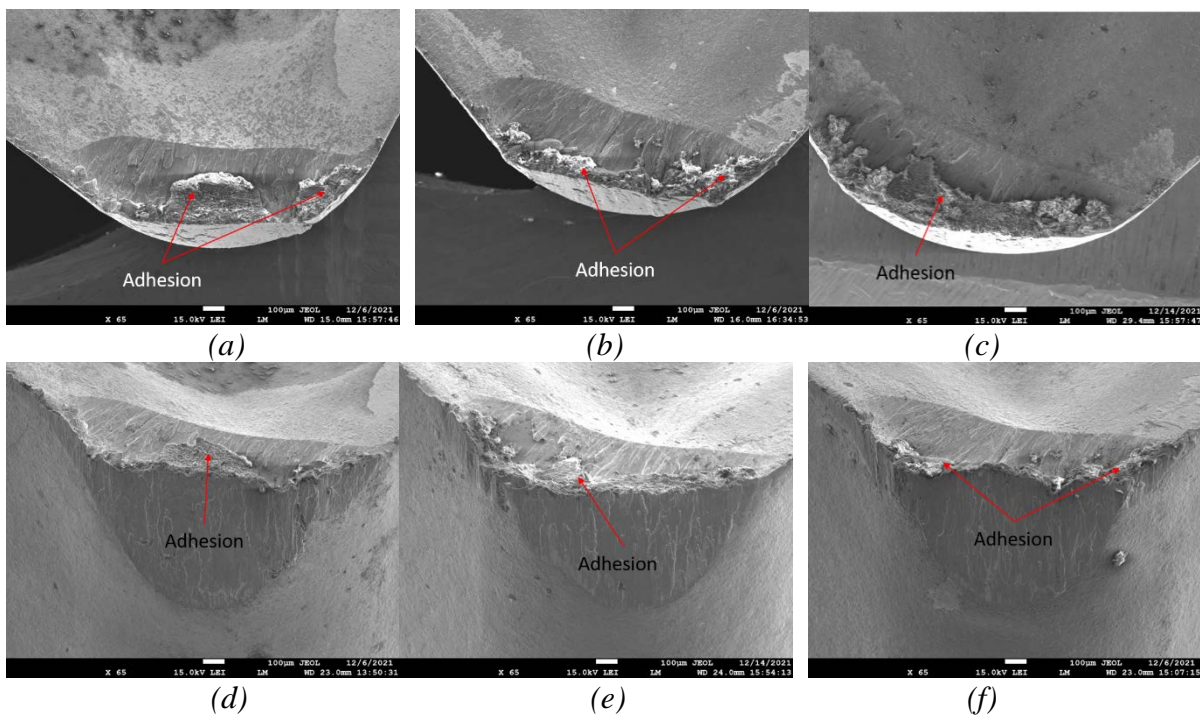


Figure 177. Worn inserts at the end of the tests using LN2: a) rake face of uncoated, b) rake face of M2, c) rake face of M4, d) nose region of uncoated, e) nose region of M2, f) nose region of M4.

Figure 178 shows the temperature measured by the thermocouples embedded in the cutting insert (see Chapter 2 for the detail). All inserts exhibit a maximum temperature at the beginning of the tests. Then, the temperature stabilizes around -58°C , -60°C and -80°C for uncoated, M2

and M4 coated inserts, respectively. The M4 insert exhibits the lowest temperature with a difference of about 20 °C. Tool temperature results are in accordance with the temperature in the pins measured in tribological tests, suggesting that the M4 coating is the best one for the same reason mentioned in Chapter 4.

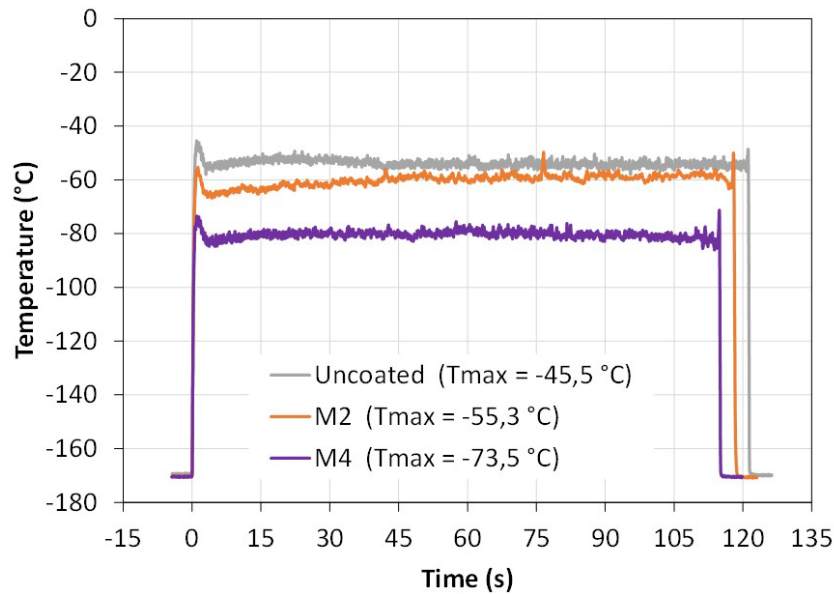


Figure 178. Tool temperature for the uncoated, M2 and M4 coated inserts under cryogenic cooling.

5.2.2.2. Flood conditions

To compare the performance of the coated inserts M2 and M4 under cryogenic cooling with the standard machining conditions of this alloy using flood conditions, the same tool wear tests were performed for flood. *Figure 179* shows the tool wear curves for zone B (VB_B) in function of the time for the three inserts under flood conditions. Surprisingly, these curves show that tool wear increases faster for the coated M2 insert when compared to the uncoated one, reaching the tool life using the VB_B criterium in only 4.4 min. For the other inserts, they have very similar tool wear evolution until reaching the tool life criterion of VB_B , which is slightly higher for the M4 (about 9.2 min) when compared to the uncoated insert (about 8.6 min).

As far as the tool wear curves for the zone C is concerned (VB_C), *Figure 180* shows that the tool wear rate of M4 and uncoated inserts is initially very low or almost constant, increasing faster after 4 min of cutting time and reaching the tool life criterion of VB_C . The tool life using the VB_C criterium is slightly higher for the M4 (about 8.6 min) when compared to the uncoated insert (about 8 min). The tool wear tests for the M2 insert were not sufficient long to determine the tool life using the VB_C criterium. However, following the trend of the wear curve of the M2

inserts, we estimate that the tool life of this insert will be higher (about 10.6 min) when compared to the other inserts.

Figure 181 summarizes the tool life using both VB_B and VB_C criteria for the three inserts under cryogenic cooling. Observing this figure and considering the proposed criteria to evaluate tool life, we can conclude that the longest tool life is obtained using the M4 insert (8.6 min), followed by the uncoated insert (8 min) and finally the M2 insert (4.4 min).

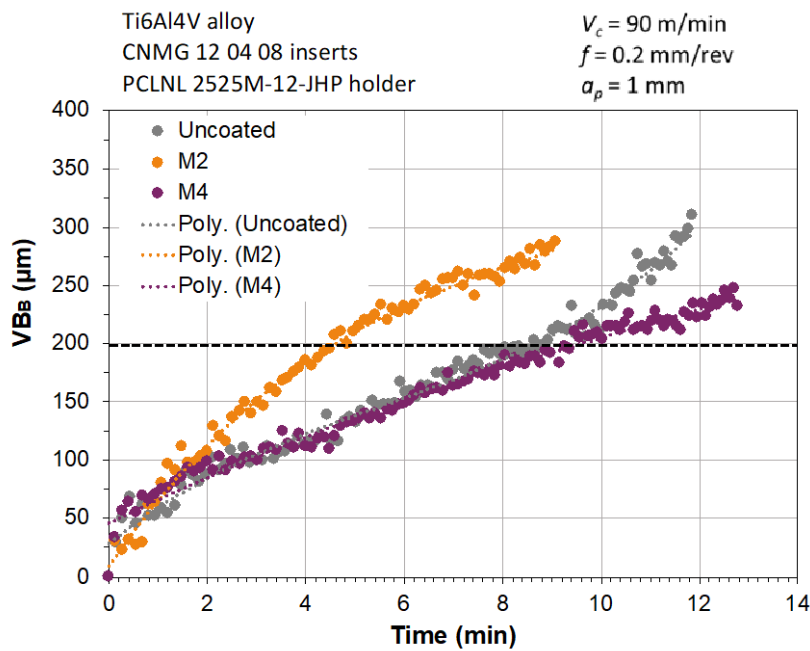


Figure 179. Tool flank wear VB_B in function of the time for the three inserts under flood conditions.

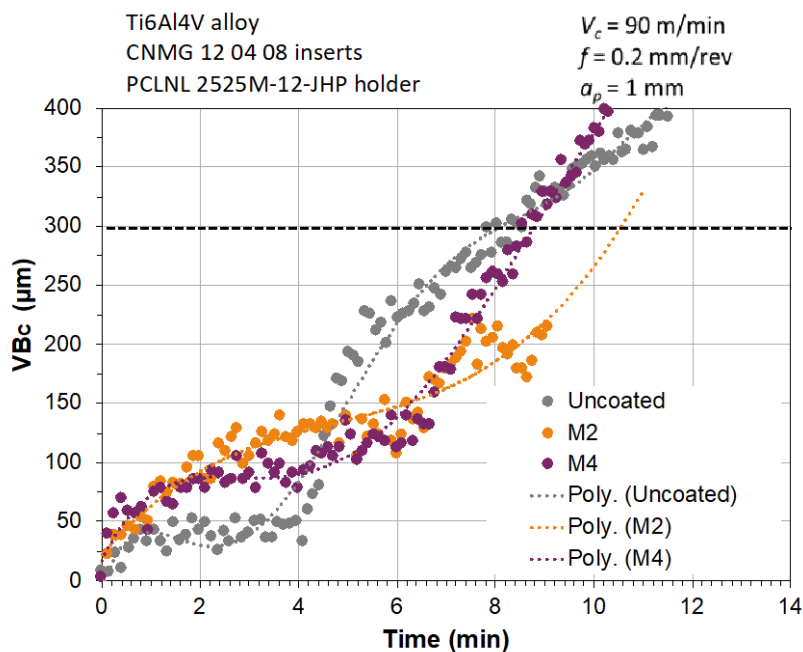


Figure 180. Tool flank wear VB_C in function of the time for the three inserts under flood conditions.

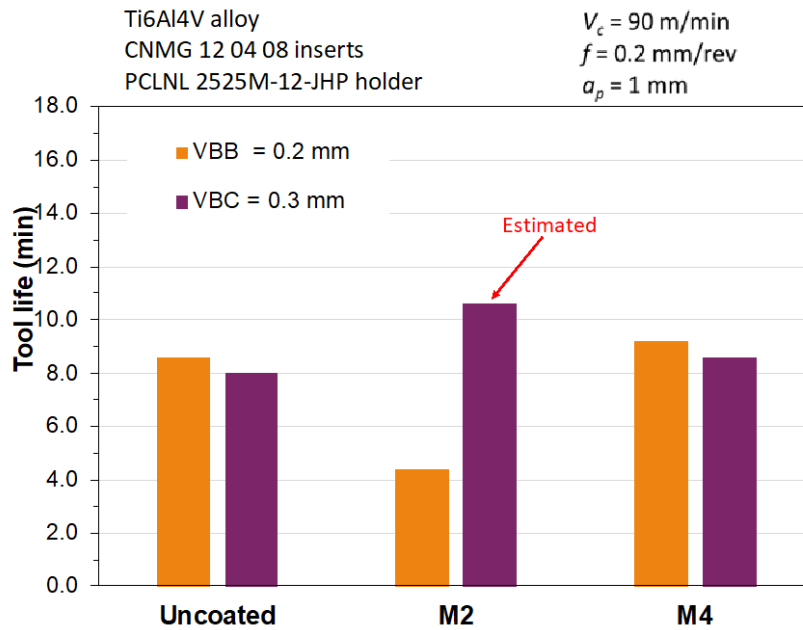


Figure 181. Tool life for the three inserts under flood conditions (uncoated = 8 min, M2 = 4.5 min and M4 = 9 min).

Figure 182 shows the worn inserts at the end of the tests under flood conditions taken using Alicona InfiniteFocus equipment. Figure 183 shows the same using SEM analysis, completed with the distributions of the elements on the tool rake face measured by EDS shown in Appendix I. Like for cryogenic cooling, these figures show that crater wear, flank wear and nose wear are the principal types of wear for all the inserts. Again, the proper indicator to compare the tool life is still the VB_B and VB_C .

As can be seen in Figure 183, the low magnification SEM images show some adhesion of Ti6Al4V on the tool rake face and on tool nose region for all the inserts, although this adhesion is lower than that observed under cryogenic cooling. This lower adhesion using flood conditions when compared to the cryogenic cooling was also observed on the pins used in the tribological tests. Some coating abrasion is observed for both M2 and M4 coated inserts (Figure 183 (b) (c)). Finally, like for the cryogenic cooling the two main mechanisms that are contributing for tool wear are abrasion and adhesion.

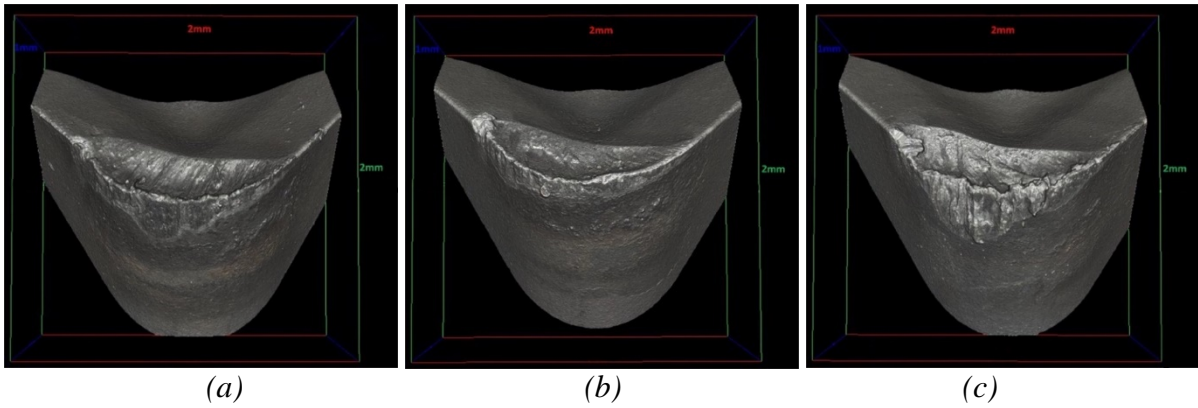


Figure 182. Worn inserts at the end of the tests under flood conditions: a) uncoated, b) M2 and c) M4.

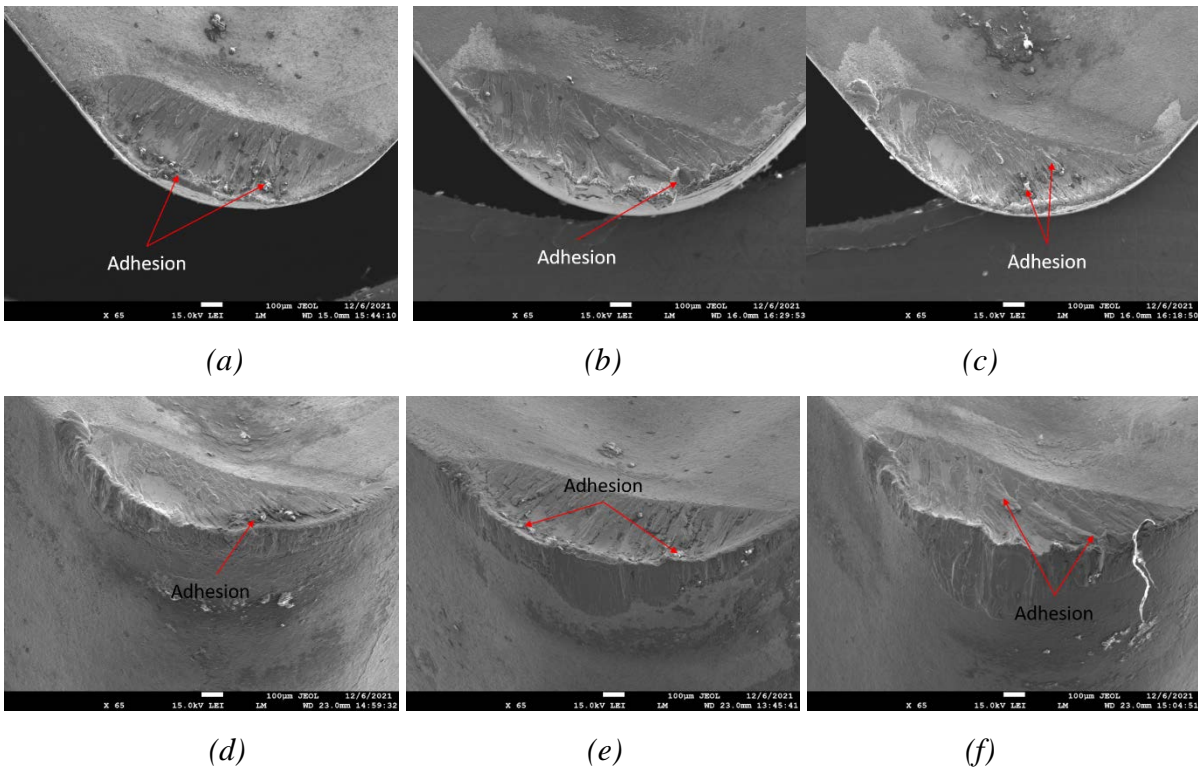


Figure 183. Worn inserts at the end of the tests under flood conditions: a) rake face of uncoated b) rake face of M2 c) rake face of M4 d) nose region of uncoated e) nose region of M2 f) nose region of M4.

As shown in *Figure 184*, the tool temperature in flood conditions starts to be stable until 30 s for all the inserts, followed by high oscillations until the end of the tests. The average temperature in the stable region is 65°C for both M2 and M4 inserts, and 51°C for uncoated insert. Contradictory to the results from tribological tests, the uncoated insert exhibits the lowest temperature, though the difference between the coated and uncoated inserts is only 14°C. Besides, a sudden increase of the tool temperature was observed for the uncoated and M4 inserts

between 75s to 90s. This is probably due to a small displacement of thermocouple inside the hole during tool wear tests.

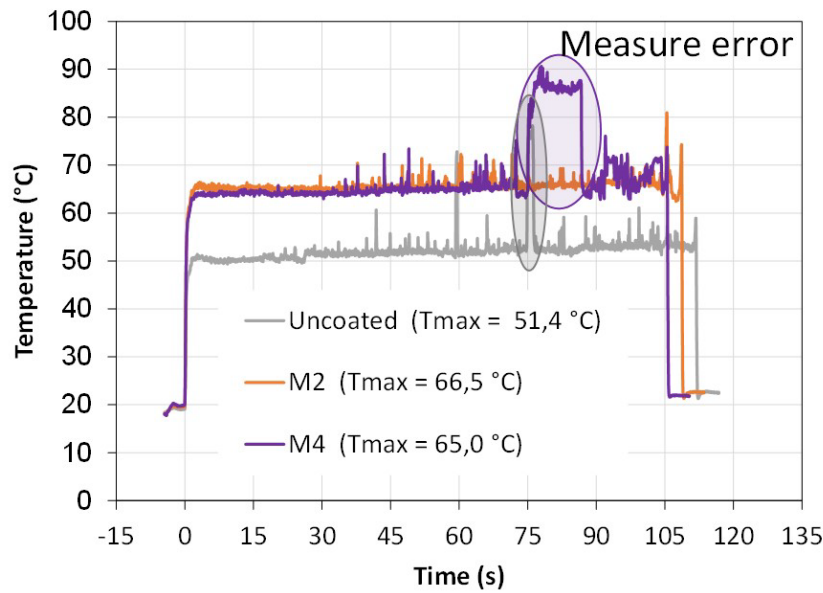


Figure 184. Tool temperature for the uncoated, M2 and M4 coated inserts under flood conditions.

5.2.2.3. Cryogenic vs flood

Figure 185 summarizes the tool life for the three inserts under cryogenic (LN₂) and flood conditions. This figure shows that regardless the insert type, the tool life in turning of Ti6Al4V alloy is higher under cryogenic cooling when compared to the flood conditions. This result agrees with several studies presented in the literature [46, 48, 313–315] in machining this alloy. Moreover, the insert with the M2 coating has the longest tool life of about 11.2 min until reach the VB_C criterium of 0.3 mm; tool life of the M2 inserts under cryogenic cooling increases about 33% when compared to the uncoated insert, for the same cooling conditions. As also seen in Figure 186, tool life of the M2 insert under cryogenic cooling increases about 155% when compared to the tool life for the same insert in flood conditions.

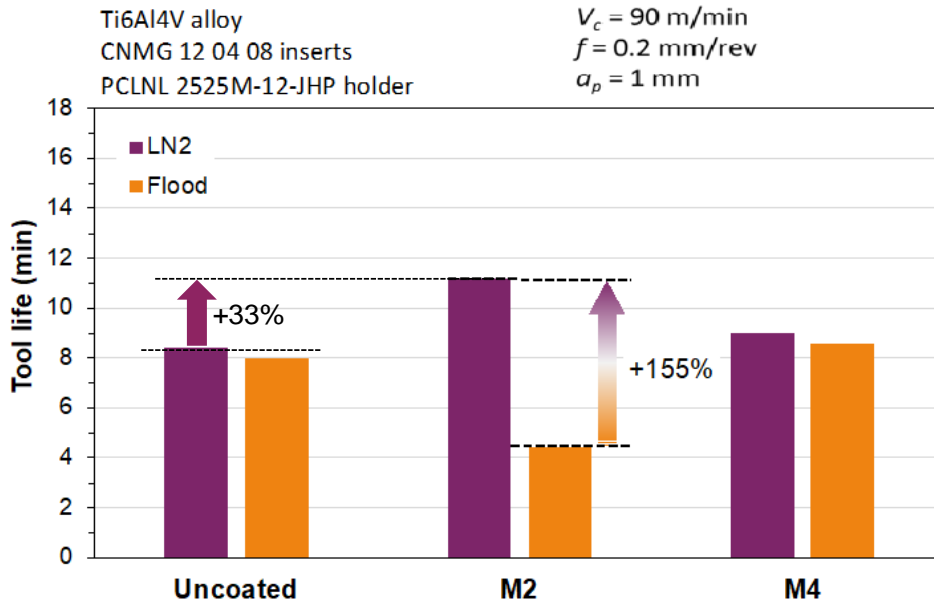


Figure 185. Summary of tool life for the three inserts under cryogenic (LN2) and flood conditions.

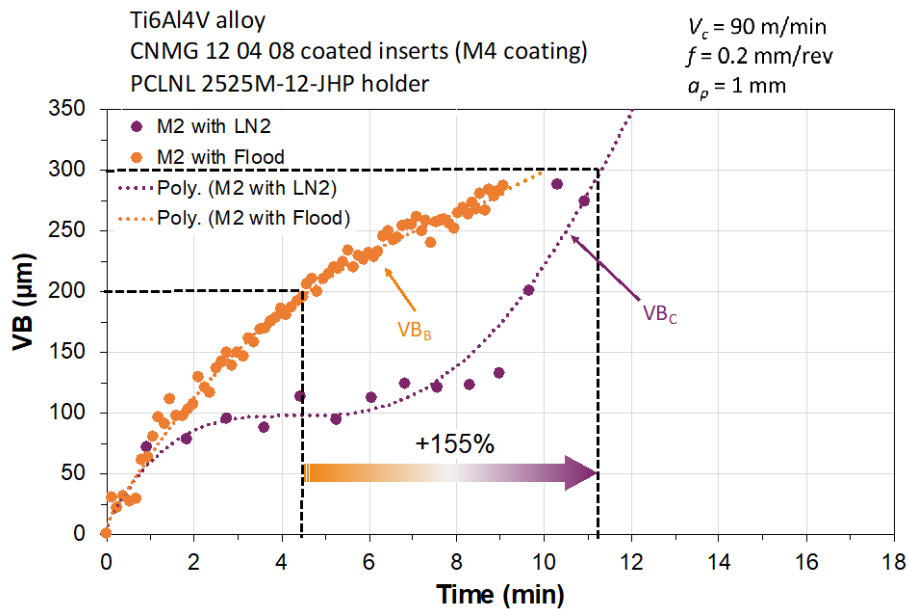


Figure 186. Tool wear VB_B and VB_C as a function of the time for the M2 insert under flood and LN2 conditions, respectively.

5.3. Statistical analysis

This section aims to identify the relation between tool flank wear (VB_B and VB_C) and other machining outcomes (forces and roughness of the machined surface), and to build models for predicting the flank wear in function of the (relevant) machining outcomes that are strong correlated with the tool wear.

5.3.1. Statistical approach

The statistical approach is composed by several steps as shown in *Figure 187*. Two kinds of statistical methods are used: Pearson's correlation analysis and *Principal Component Analysis (PCA)*.

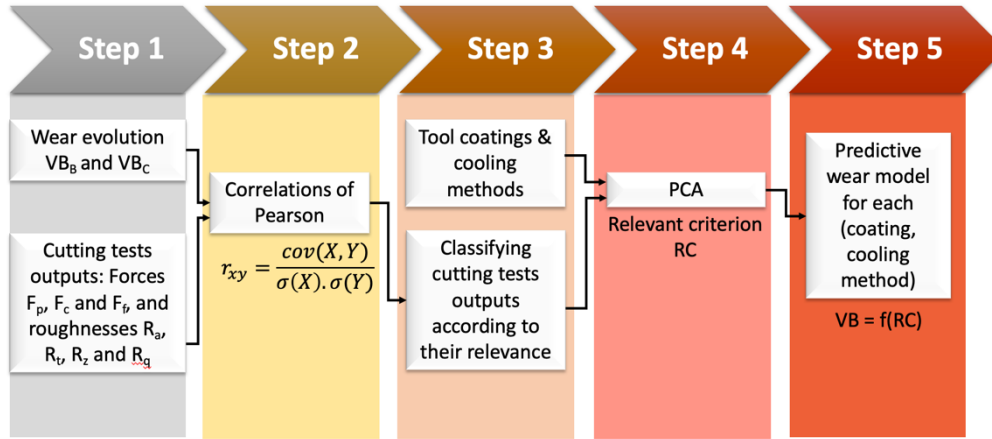


Figure 187. Statistical approach.

5.3.1.1. Pearson's correlation analysis

Correlation analysis, called the correlation of Bravais-Pearson, consists in studying the correlation between two or more statistical variables or random entities: it is a quantification of the relationship potentially existing between two variables by the coefficient r_{xy} calculated as follows:

$$r_{xy} = \frac{cov(X, Y)}{\sigma(X) \cdot \sigma(Y)} \quad \text{Equation 35}$$

with σ the standard deviation and $cov(X, Y)$ the covariance of the variables X and Y . For this study, the variable X corresponds to a parameter of the quantity qualifying wear evolution (VB_C and VB_B). The variable Y corresponds to an output of the cutting test (Cutting force F_c , feed force F_f , thrust force F_t , surface arithmetic roughness R_a and surface roughness at maximum height R_t). The correlation coefficient is unitless, what allows the comparison between the variables. Each measurement is normalized and defined between -1 and 1. The correlation coefficient aims firstly to characterize a linear relationship, either positive or negative. The more it is near 1 (absolute value), the more the relationship is strong. A zero r_{xy} signifies the absence of any correlation.

5.3.1.2. Principal Component Analysis (PCA)

It is possible to have an idea about criteria following the evolution of flank wear. However, the definition of the parameter the most reflecting wear needs a mathematical method. A principal component analysis method applied to our trials results is then necessary. For that, values of the different parameters in addition to the associated VB must be written in a table.

The next organization chart presents the Principle of the Principal Component Analysis (PCA) method explained by Denguir et al. [316]. As we have a high number of surveyed variables (7 for both MWF and LN2), and the complete number of wear tests, it is impossible to report the found results step by step (*Figure 188*).

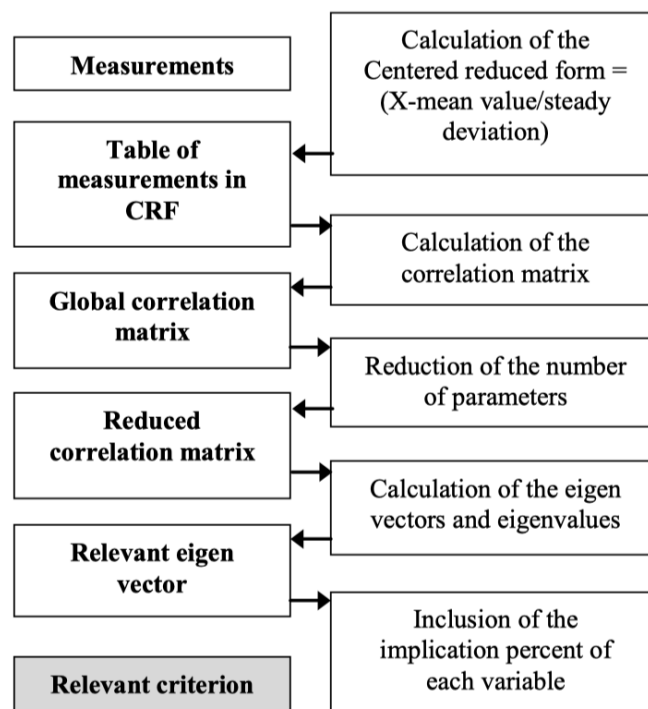


Figure 188. Principle of the PCA applied to a simple sample [316].

Correlation analysis permitted the identification of the influent parameters regarding tool wear evolution. This analysis requires to follow a procedure composed by several steps.

The first step consists in gathering all the experimentally measured values concerning wear evolution (VB_B and VB_C in function of the cutting time) and cutting tests output for each used tool coating. The experimental results corresponding to flank wear, cutting forces and surface roughness cover a full design of experiments DoE.

Table 58. Order of the tool coatings used in the wear tests.

Test N°	Coating	Lubrication
1	Uncoated	Emulsion
2	M2	Emulsion
3	M4	Emulsion
4	Uncoated	LN2
5	M2	LN2
6	M4	LN2

The second step consists into calculating Pearson's correlations for each pair (output parameter / flank wear entity). Results are presented in section 5.3.2.1. It is worthy to remind that a positive value of the correlation coefficient corresponds to an evolution of the pair in the same direction, and that a negative value corresponds to opposite evolution.

The third step consists in identifying outputs having correlation coefficients higher than 0.7 (absolute value).

In the fourth step, selected parameters become the object of the PCA in function of the cutting tool coating and the cooling method. The process as described in *Figure 188* is then applied and the Relevant Criteria RC modeled for each case.

In the fifth step, according to the RC models found, flank wear entities VB_B and VB_C are written in function of RC. Finally, the predictive model $VB = f(\text{output components})$ can be written for each pair (coating, cooling method).

5.3.2. Results of the statistical analysis

At first, Pearson's correlation coefficient between the results of the flank wear evolution and the corresponding forces and roughness are calculated to evaluate which outputs follow a comparable evolution to tool wear. Then, thanks to PCA, the relevant criterion for each tool coating/cooling pair is revealed. Finally, a predictive model is built for each pair using the relevant criteria.

5.3.2.1. Results of the Correlations of Pearson

The correlation coefficients revealed that, for all pairs tool coating/cooling method as shown in *Table 59*, force components evolution during wear tests are highly correlated to flank wear evolution in both cases of VB_B and VB_C .

Table 59. Pearson's correlations between cutting tests output and tool flank wear.

Test N°		F_c	F_t	F_f	R_a	R_t
1	VB_C	0.966	0.904	0.932	0.421	0.543
	VB_B	0.965	0.924	0.947	0.487	0.754
2	VB_C	0.770	0.640	0.832	0.039	0.069
	VB_B	0.785	0.597	0.834	0.172	0.326
3	VB_C	0.947	0.975	0.994	0.088	0.272
	VB_B	0.975	0.870	0.924	-0.858	-0.765
4	VB_C	0.753	0.968	0.975	-	-
	VB_B	0.748	0.806	0.833	-	-
5	VB_C	0.736	0.991	0.989	-	-
	VB_B	0.795	0.917	0.925	-	-
6	VB_C	0.714	0.930	0.965	-	-
	VB_B	0.691	0.812	0.965	-	-

5.3.2.2. Centered reduced form

The centered reduced form is written basing on the mean value and the steady deviation (σ) of a serial measurement x_i . The new variable X_i becomes then without unit (*Equation 36*).

$$X_i = \frac{x_i - \bar{X}}{\sigma} \quad \text{Equation 36}$$

The use of this form allows the summation of entities with different physical significations without losing sense. In fact, a table is elaborated regrouping comparable values for each tool coating/cooling method pair. *Table 60* corresponding to M2 insert using LN2 pair is given here as an example. Here, only variables having a correlation coefficient with VB exceeding 60% are conserved, that we took this scale as a limit in the repartition of the coefficients.

Table 60. Centered Reduced table corresponding to the M2 insert, LN2 cooling (unitless).

Time (min)	Length (m)	VB_B	VB_C	F_t	F_r	F_c
0.0	0.0	-1.97	-1.33	-1.51	-1.69	-4.02
0.9	70.0	-1.31	-1.02	-0.85	-0.87	-0.47
1.9	140.0	-0.97	-0.89	-0.88	-0.74	-0.23
2.7	210.0	-1.18	-0.87	-0.79	-0.78	-0.67
3.6	280.0	-0.87	-0.88	-0.86	-0.80	-0.39
4.5	350.0	-0.65	-0.84	-0.88	-0.80	-0.52
5.3	420.0	-0.47	-0.69	-0.97	-0.75	0.23
6.1	490.0	-0.65	-0.82	-0.72	-0.78	-0.16
6.8	560.0	-0.44	-0.73	-0.75	-0.78	-0.39
7.6	630.0	-0.52	-0.80	-0.74	-0.79	-0.38
8.3	700.0	-0.34	-0.64	-0.67	-0.73	-0.20
9.0	770.0	-0.39	-0.72	-0.61	-0.71	-0.16
9.7	840.0	-0.39	-0.64	-0.34	-0.40	-0.15
10.3	910.0	-0.15	-0.20	-0.19	-0.23	0.04
10.9	980.0	-0.13	0.06	0.06	-0.01	0.18
12.1	1120.0	0.32	0.42	0.25	0.31	0.34
12.7	1190.0	1.48	0.52	0.41	0.42	0.37
13.2	1260.0	0.50	0.62	0.45	0.49	0.37
13.7	1330.0	0.50	0.80	0.74	0.86	0.54
14.2	1400.0	1.29	0.97	1.00	1.17	0.67
14.6	1470.0	1.08	1.26	1.31	1.37	0.88
15.1	1470.0	1.66	1.40	1.49	1.50	0.91
15.5	1470.0	0.63	1.37	1.59	1.55	1.06
15.8	1470.0	1.66	1.67	1.50	1.40	1.07
16.2	1470.0	1.32	1.97	1.96	1.79	1.09

Basing on values in centered reduced form, linear correlation coefficients are calculated. Results are gathered in a symmetric square matrix called correlation matrix for each tool coating/cooling method pair. *Table 61* corresponding to M2 insert/LN2 pair is given here as an example.

Table 61. Correlation matrix corresponding to the coating M2 insert, LN2 cooling.

	VB_b	VB_c	F_t	F_f	F_c
VB_b	1.0000	0.9506	0.9395	0.9432	0.8142
VB_c	0.9506	1.0000	0.9905	0.9886	0.7365
F_t	0.9395	0.9905	1.0000	0.9952	0.7559
F_f	0.9432	0.9886	0.9952	1.0000	0.7850
F_c	0.8142	0.7365	0.7559	0.7850	1.0000

Now parameters implication percentage should be defined. For that, eigenvalues and eigenvectors of the simplified matrix should be calculated.

Table 62. Eigenvectors and eigenvalues corresponding to the correlation matrix (M2 insert, LN2 cooling).

	fact 1	fact 2	fact 3
F_t	0.5919	-0.4231	-0.6860
F_f	0.5977	-0.3405	0.7257
F_c	0.5406	0.8396	-0.0510
	eigenvector 1	eigenvector 2	eigenvector 3

The analysis of the linear correlation matrix allows calculation of its eigenvectors and eigenvalues as in the example in *Table 62*. Eigenvectors are called factors. Eigenvalues are reflecting the amount of information included in every factor. After ranking them, we can analyze these results. As we see in *Table 63*, the first factor of its own represents 90% of the information. It is so the relevant criterion.

Table 63. Eigen values and their implication percentage for wear tests with (M2 insert, LN2 cooling).

	fact 1	fact 2	fact 3
Eigenvalues	2.6955	0.3007	-0.0037
Information (%)	90%	10%	0%

According to the previous paragraph, we choose factor 1 as a relevant criterion RC. So,

$$RC = 0.5919F_t + 0.5977F_f + 0.5406F_c \quad \text{Equation 37}$$

To give a physical signification to the coefficients of the relevant criterion, we will come back to a percentage of the whole information. i.e: With a coefficient of 0.5919, F_t represents 34,2%

of Fact1, F_f 34,5%, and F_c 31,2%. (cf. *Table 64*). However, factor 1 bis, like factor 1, represents 90% of the information as it is associated to the first eigenvalue (cf. *Table 63*). By multiplying every value of the factor 1 bis by 0.9, we will get the percentage of the total information included in every variable. (cf. *Table 64*).

Table 64. Percentage of implication of every variable in fact1 (M2 insert, LN2 cooling).

	fact 1	fact 1 bis (%)	Total info (%)
F_t	0.5919	34.2	30.7
F_f	0.5977	34.5	31.1
F_c	0.5406	31.2	28.1

Now the expression of the relevant criterion for the pair (M2 insert, LN2 cooling) becomes:

$$RC = 0.307F_t + 0.311F_f + 0.281F_c \quad \text{Equation 38}$$

Let's check that the VB can effectively be characterized by this criterion. For that, we will just see correlation coefficients relating RC to VB_B and VB_C . They are equal to 92,9% and 96%, respectively.

As correlation is very high (>90%), RC characterizes the flank wear VB in a reliable way. We can calculate the linear relation between RC and VB:

$$VB_B = 1.1141RC (R^2 = 0.903) \quad \text{Equation 39}$$

$$VB_C = 1.1254RC (R^2 = 0.921) \quad \text{Equation 40}$$

Replacing RC by its expression presented in the previous paragraph, VB can be described by an equation in function of the other inputs in centered reduced form:

$$VB_B = 0.343F_t + 0.346F_f + 0.313F_c \quad \text{Equation 41}$$

$$VB_C = 0.346F_t + 0.349F_f + 0.316F_c \quad \text{Equation 42}$$

Finally, to be able to use this wear model, the coefficients of the expression of VB must correspond to the normal form, and not the centered reduced form. For that reason, the full

expression must be multiplied by the steady deviation of the VB results used initially for the coefficients identification, plus the average value of the results used initially for the coefficients identification too.

$$(VB_B - 166.88)/85.3 = 0.343 \cdot ((F_t - 336)/223) + 0.346 \cdot ((F_f - 393)/232) + 0.313 \cdot ((F_c - 483)/120) \quad \text{Equation 43}$$

$$(VB_C - 276.56)/202.88 = 0.346 \cdot ((F_t - 336)/223) + 0.349 \cdot ((F_f - 393)/232) + 0.316 \cdot ((F_c - 483)/120) \quad \text{Equation 44}$$

The final model becomes the following:

$$VB_B (\mu m) = 0.1312 \cdot F_t (N) + 0.1272 \cdot F_f (N) + 0.2225 \cdot F_c (N) - 35 \quad \text{Equation 45}$$

$$VB_C (\mu m) = 0.3148 \cdot F_t (N) + 0.3052 \cdot F_f (N) + 0.5342 \cdot F_c (N) - 207 \quad \text{Equation 46}$$

The accuracy of this model can be checked for each (coating, cooling method) pair.

5.3.2.3. Forces based flank wear models for each (coating, cooling method) pair

The statistical method (PCA) described above was applied to each (coating, cooling method) pair, and has resulted into the following forces-based flank wear models, as described in the following table.

The results issued from the models based on forces components are then compared with the experimental results, as shown in the following figures (*Figure 189-Figure 194*). The wear models for each coating/cooling pair are listed in *Table 65*.

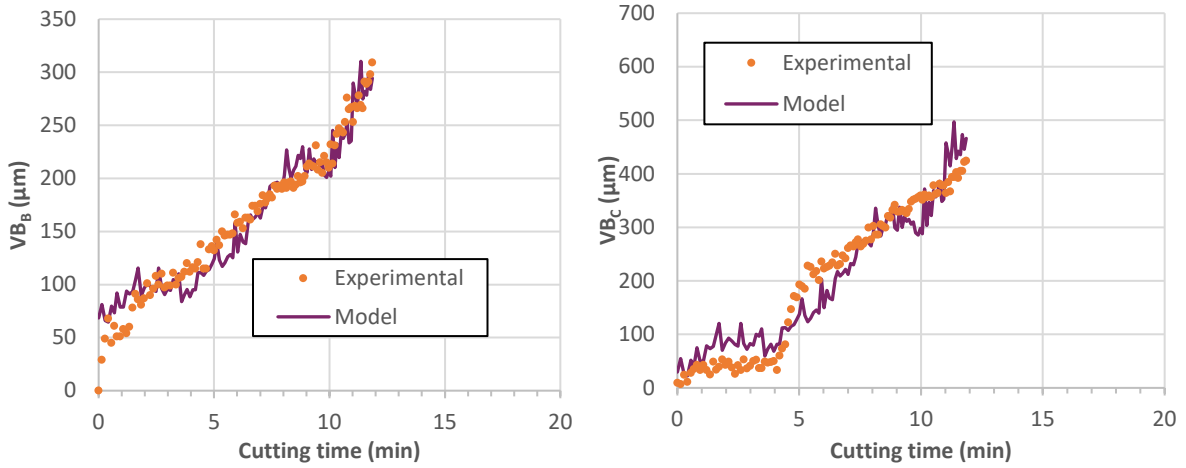


Figure 189. Comparing results issues from experimental measurements and forces based models concerning VB_B and VB_C of the uncoated insert during tests under flood conditions.

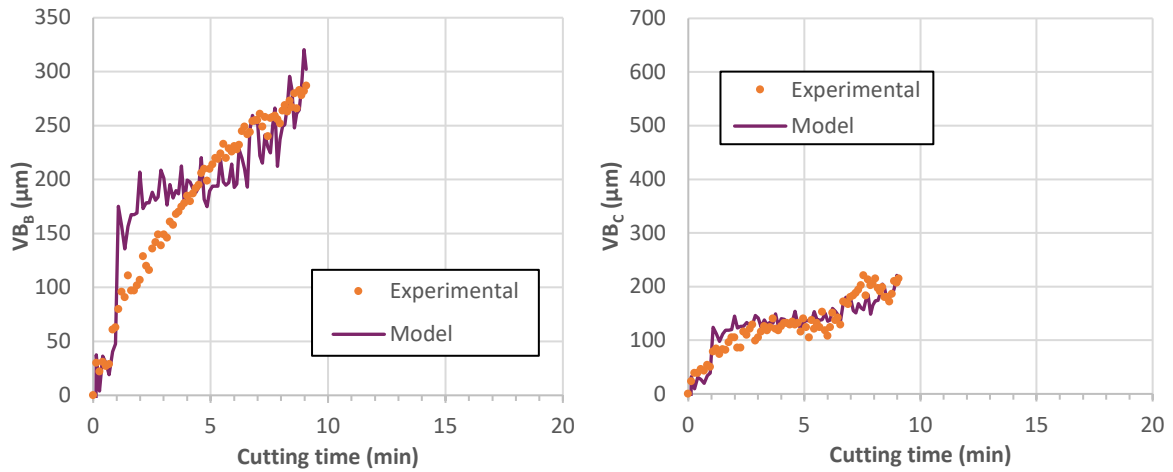


Figure 190. Comparing results issues from experimental measurements and forces-based models concerning VB_B and VB_C of the M2 insert during tests under flood conditions.

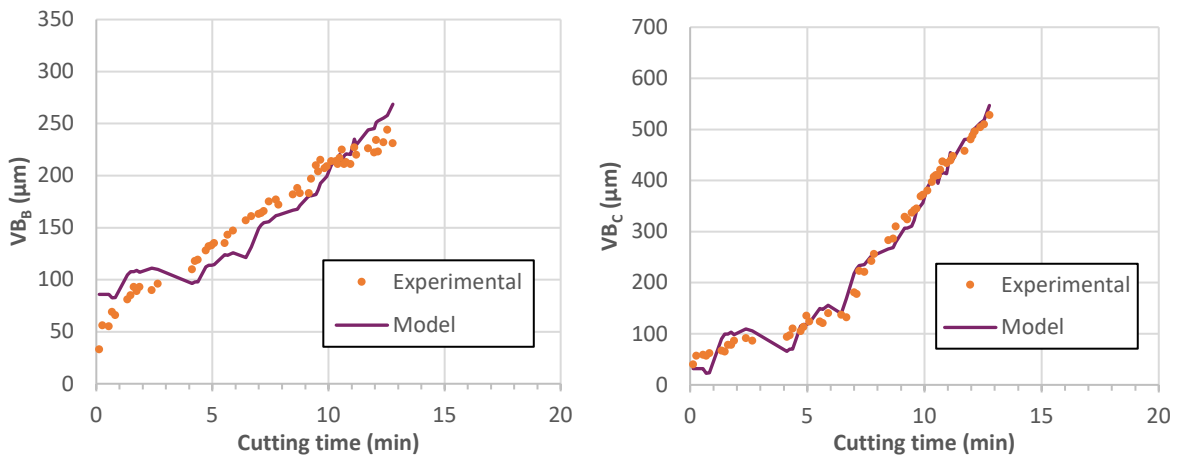


Figure 191. Comparing results issues from experimental measurements and forces-based models concerning VB_B and VB_C of the M4 insert during tests under flood conditions.

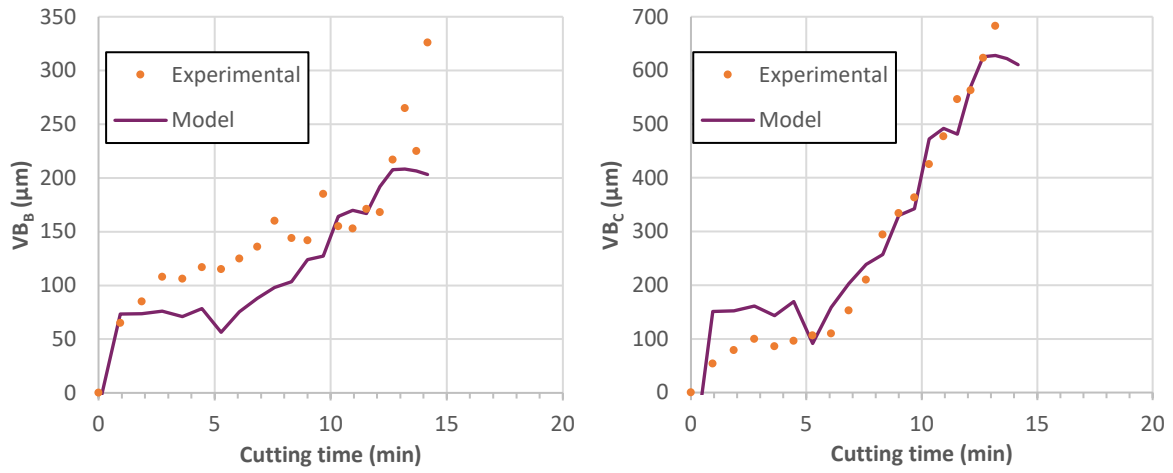


Figure 192. Comparing results issues from experimental measurements and forces based models concerning VB_B and VB_C of the uncoated insert during tests under LN2.

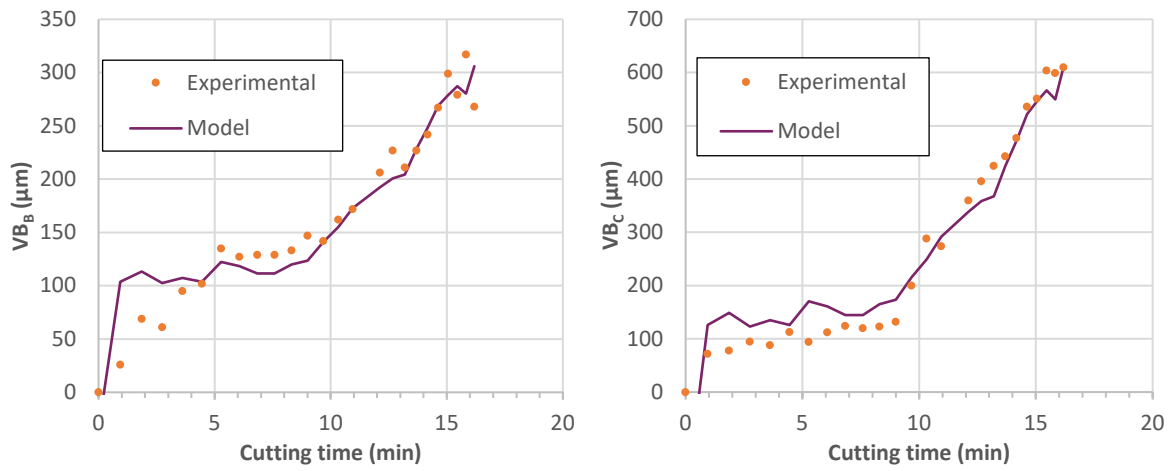


Figure 193. Comparing results issues from experimental measurements and forces-based models concerning VB_B and VB_C of the M2 insert during tests under LN2.

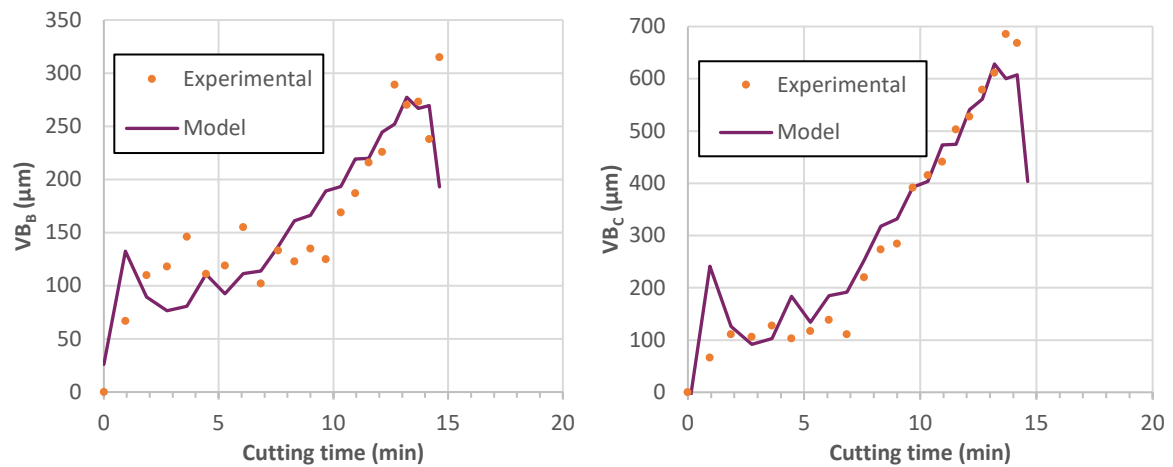


Figure 194. Comparing results issues from experimental measurements and forces-based models concerning VB_B and VB_C of the M4 insert during tests under LN2.

Table 65. Forces based flank wear models for three types of inserts and two lubrication/cooling strategies.

Coating, cooling	Flank wear VB models
Uncoated, emulsion	$VB_B (\mu\text{m}) = 0.5257 \cdot F_t(\text{N}) + 0.3123 \cdot F_f(\text{N}) + 0.6284 \cdot F_c(\text{N}) - 289$ $VB_C (\mu\text{m}) = 1.016 \cdot F_t(\text{N}) + 0.6035 \cdot F_f(\text{N}) + 1.2142 \cdot F_c(\text{N}) - 661$
M2, emulsion	$VB_B (\mu\text{m}) = 1.4868 \cdot F_t(\text{N}) + 0.8305 \cdot F_f(\text{N}) + 0.5244 \cdot F_c(\text{N}) - 427$ $VB_C (\mu\text{m}) = 0.9926 \cdot F_t(\text{N}) + 0.5545 \cdot F_f(\text{N}) + 0.35 \cdot F_c(\text{N}) - 278$
M4, emulsion	$VB_B (\mu\text{m}) = 0.2181 \cdot F_t(\text{N}) + 0.1217 \cdot F_f(\text{N}) + 0.2981 \cdot F_c(\text{N}) - 65$ $VB_C (\mu\text{m}) = 0.5728 \cdot F_t(\text{N}) + 0.3194 \cdot F_f(\text{N}) + 0.9485 \cdot F_c(\text{N}) - 421$
Uncoated, LN2	$VB_B (\mu\text{m}) = 0.0947 \cdot F_t(\text{N}) + 0.0884 \cdot F_f(\text{N}) + 0.1373 \cdot F_c(\text{N}) - 15$ $VB_C (\mu\text{m}) = 0.3344 \cdot F_t(\text{N}) + 0.3123 \cdot F_f(\text{N}) + 0.4848 \cdot F_c(\text{N}) - 160$
M2, LN2	$VB_B (\mu\text{m}) = 0.1312 \cdot F_t(\text{N}) + 0.1272 \cdot F_f(\text{N}) + 0.2225 \cdot F_c(\text{N}) - 35$ $VB_C (\mu\text{m}) = 0.3148 \cdot F_t(\text{N}) + 0.3052 \cdot F_f(\text{N}) + 0.5342 \cdot F_c(\text{N}) - 207$
M4, LN2	$VB_B (\mu\text{m}) = 0.109 \cdot F_t(\text{N}) + 0.106 \cdot F_f(\text{N}) + 0.158 \cdot F_c(\text{N}) + 26$ $VB_C (\mu\text{m}) = 0.2913 \cdot F_t(\text{N}) + 0.2836 \cdot F_f(\text{N}) + 0.4213 \cdot F_c(\text{N}) - 43$

5.4. Conclusions

In this chapter, tool wear tests were performed in turning of Ti6Al4V using uncoated and coated M2 and M4 inserts, under both flood (traditional MWF) and cryogenic (LN2) conditions. Tool wear measurement was conducted using both a home-made tool wear inspection system integrated into a SONIM CNC lathe machine model T9 and using optical microscope Keyence VHX 1000. Tool life was determined based on ISO 3685:1993 using reduced VB values.

Tool wear results have shown that for cryogenic cooling the longest tool life is obtained using the M2 insert (11.2 min), followed by the M4 insert (9 min) and finally the uncoated one (8.4 min). SEM analysis of worn inserts reveals that all inserts show the same wear modes under cryogenic cooling, including crater, flank and nose wear. SEM analysis also revealed adhesion of Ti6Al4V material into the tool, suggesting that the main wear mechanism is abrasive and adhesive wear. Tool temperature is around -58°C , -60°C and -80°C for uncoated, M2 and M4 coated inserts, respectively.

Concerning to the traditional MWF (flood), the longest tool life is obtained using the M4 insert (8.6 min), followed by the uncoated insert (8 min) and surprisingly the M2 insert got the lowest tool life (4.4 min). The main reason for this worse tool life for the M2 coated insert can be due to chemical reactions between the emulsion and the thin top CrN and AlCrN monolayers of M2 as this is well known in the case of MoS₂ that is completely dissolved into emulsion. Indeed, one can suppose that some chemical elements (such as oxygen, acid or base) of the emulsion

react with the CrN and AlCrN layers as they are very thin and as a consequence, damage them. As they are thicker in the case of the M4 multilayer, maybe these chemical reactions don't have the time to damage completely the CrN and AlCrN top monolayers. It should be interesting to make some tribocorrosion tests under an emulsion atmosphere to verify this hypothesis. The tool wear modes and mechanisms for the inserts under flood conditions are similar to those of cryogenic cooling, but with less titanium adhesion to the inserts. Surprisingly, tool temperature is higher for both M2 and M4 inserts (around 65°C) compared to the uncoated insert (and 51°C). This can be due to the chemical reactions mentioned above that act at the coating surface between the emulsion and the CrN/AlCrN top layer, especially if these reactions are exothermic.

Depending on the insert material, the tool life under LN2 cooling is similar or higher than that obtained under flood conditions. Tool life is almost the same for both LN2 and flood conditions using coated M4 and uncoated inserts (difference is lower than 5%). However, tool life increases dramatically for the M2 insert when the traditional MWF is replaced by LN2 (about 155%). This can be explained by the different monolayers architecture between M2 and M4. Indeed, in M2 we decreased the CrN/AlCrN pair thickness from the substrate to the top surface of the coating. Then, the thermal conductivity is not the same at the interface Cr/CrN/AlCrN / substrate and at the top CrN/AlCrN pair. It is known that the thermal conductivity is higher when the thickness of the coatings increases [317]. To summarize, the M2 multilayer has a low thermal conductivity into its top layer and is very efficient to protect the cutting tool during the machining tests under LN2. In comparison, the M4 multilayer has the same thermal conductivity in all of its CrN/AlCrN pairs, so it is less efficient to protect the cutting tool under LN2.

This chapter ends with the identification of the relation between tool flank wear (VB_B and VB_C) and other machining outcomes (forces and roughness of the machined surface) by applying the Pearson's correlation analysis. This analysis was performed for the three types of inserts and both lubrication/cooling couples. The results have shown a strong correlation between the flank wear and forces (with coefficients higher than 85%). The statistical analysis also permitted to build models for predicting the flank wear in function of the measured forces using the Principal Component Analysis (PCA) methodology.

5.5. Résumé du Chapitre 5

Dans ce chapitre, des essais d'usure ont été réalisés en tournage du Ti6Al4V en utilisant des plaquettes non-revêtues et revêtues avec les revêtements M2 et M4. Ces essais ont été réalisés avec des émulsions et avec le refroidissement cryogénique (LN2). L'usure en dépouille (VB) des outils a été mesurée à l'aide d'un système de contrôle de l'usure intégré dans le tour CNC SONIM modèle T9 et à l'aide d'un microscope numérique Keyence VHX 1000. La durée de vie des outils a été déterminée en se basant sur la norme ISO 3685:1993, mais en utilisant des valeurs de VB plus réduites.

Les résultats de l'usure ont montré qu'avec le refroidissement cryogénique la durée de vie la plus longue est obtenue en utilisant la plaquette M2 (11,2 min), suivie par la plaquette M4 (9 min) et enfin la plaquette non revêtue (8,4 min). L'analyse MEB des plaquettes usées révèle que toutes les plaquettes présentent les mêmes modes d'usure sous refroidissement cryogénique, y compris l'usure en cratère, en dépouille et sur le bec. L'analyse MEB a également révélé l'adhésion du Ti6Al4V sur l'outil, ce qui suggère que les principaux mécanismes d'usure sont l'usure par abrasion et par adhésion. La température de l'outil est d'environ -58°C pour les plaquettes non revêtues, et -60°C et -80°C pour les plaquettes revêtues avec les revêtements M2 et M4, respectivement.

En ce qui concerne les émulsions, la durée de vie la plus longue est obtenue en utilisant la plaquette M4 (8,6 min), suivie par la plaquette non revêtue (8 min) et, étonnamment, la plaquette M2 a obtenu la durée de vie la plus faible (4,4 min). La principale raison de cette durée de vie plus faible pour la plaquette revêtue M2 peut être due aux réactions chimiques entre l'émulsion et les minces monocouches de CrN et d'AlCrN à la surface de M2, comme cela est bien connu dans le cas du MoS₂ qui est complètement dissous lorsqu'il est utilisé sous émulsion. En effet, on peut supposer que certains éléments chimiques (tels que l'oxygène, un acide ou une base) de l'émulsion réagissent avec les couches de CrN et d'AlCrN car elles sont très fines et par conséquent, les endommagent. Comme elles sont plus épaisses dans le cas de la multicouche M4, peut-être que ces réactions chimiques n'ont pas le temps d'endommager complètement les monocouches CrN et AlCrN de surface. Il devrait être intéressant de faire des tests de tribocorrosion sous émulsion pour vérifier cette hypothèse. Les modes et mécanismes d'usure des plaquettes sont similaires à ceux du refroidissement cryogénique, mais avec moins d'adhésion du titane aux plaquettes. De manière surprenante, la température de l'outil est plus élevée pour les plaquettes M2 et M4 (environ 65°C) par rapport à la plaquette non revêtue

(51°C). Cela peut être dû aux réactions chimiques mentionnées ci-dessus qui agissent à la surface du revêtement entre l'émulsion et la couche supérieure CrN/AlCrN, surtout si ces réactions sont exothermiques.

Selon le matériau de la plaquette, la durée de vie de l'outil sous refroidissement LN2 est similaire ou supérieure à celle obtenue avec les émulsions. La durée de vie de l'outil ne change pratiquement pas avec le fluide de coupe (émulsions vs LN2) pour les plaquettes M4 revêtues et non revêtues (la différence est inférieure à 5%). Cependant, la durée de vie de l'outil augmente considérablement pour la plaquette M2 lorsque les émulsions sont remplacées par le LN2 (environ 155%). Cela peut s'expliquer par l'architecture différente des monocouches entre M2 et M4. En effet, dans M2, nous avons diminué l'épaisseur des paires CrN/AlCrN du substrat à la surface supérieure du revêtement. Ainsi, la conductivité thermique n'est pas la même à l'interface Cr/CrN/AlCrN/substrat et au niveau de cette bicouche CrN/AlCrN supérieure. Il est connu que la conductivité thermique est plus élevée lorsque l'épaisseur des revêtements augmente [315]. Pour résumer, la multicouche M2 a une faible conductivité thermique dans sa couche supérieure et est donc très efficace pour protéger l'outil de coupe lors des tests d'usinage sous LN2. En comparaison, la multicouche M4 a la même conductivité thermique dans toutes ses paires CrN/AlCrN, donc elle est moins efficace pour protéger l'outil de coupe sous LN2.

Ce chapitre se termine par l'identification de la relation entre l'usure en dépouille (VB_B et VB_C) et les autres résultats de l'usinage (efforts et rugosité de la surface usinée) en appliquant l'analyse de corrélation de Pearson. Cette analyse a été réalisée pour les trois types de plaquettes et les deux couples de lubrification/refroidissement. Les résultats ont montré une forte corrélation entre l'usure en dépouille et les efforts (avec des coefficients de corrélation supérieurs à 85%). L'analyse statistique a également permis de construire des modèles pour prédire l'usure en dépouille en fonction des efforts mesurés en utilisant la méthodologie de l'analyse de la composante principale (ACP).

Conclusions and perspectives

1. General conclusion

The objective of this research work is to develop and to characterize new multilayer coatings produced by reactive magnetron sputtering, to be used in the cutting tools for machining of Ti6Al4V under cryogenic cooling conditions.

The state of the art (Chapter 1) points out the need to develop new tool materials for the cryogenic assisted machining of titanium alloys for the following main reasons. First, for health and environmental reasons, there are a need to replace the actual metal working fluids, composed by a mixture of oil or chemical fluid and water, by eco-friendly cutting fluids like the liquid nitrogen (LN₂) and the liquid CO₂. Second, since titanium alloys is a difficult-to-cut material, the cutting temperature and the contact stresses between the tool and the workpiece/chip generated during cutting are very high, significantly reducing the tool life. Third, today, there are no suitable tool material (including coatings) for machining difficult-to-cut materials under cryogenic cooling conditions. Therefore, there are a need to develop new tool materials (including coatings) for cryogenic assisted machining of difficult-to-cut materials. As it is known, hard coatings are a solution to ensure good abrasion resistance to cutting tools and thus to increase tool life. Therefore, a state of the art on vacuum deposition processes and more particularly magnetron sputtering was presented. A review on the (single and multilayer) coatings used in the cutting tools since the end of the 1960s was performed. Finally, the experience of LABOMAP in hard coatings coupled with the state of the art allowed us to propose the coatings to be studied in this thesis, namely multilayer coatings of the Cr / CrN / AlCrN type.

Chapter 3 is devoted to the optimization of monolayers of Cr, CrN, CrAlN and AlCrN. First, almost pure chromium thin films by DC magnetron sputtering with an acceptable adhesion on tungsten carbide substrate, a low friction coefficient and wear rate after being in contact with Ti6Al4V ball was obtained. The Cr layer was well crystallized, showed the (110) preferred orientation with a grain size around 10 nm and has a relative porosity. Thus, as expected, the Cr coating is adherent whatever the type of substrate or its roughness. Then, Cr-N system was studied, in particular the effect of substrate bias voltage and deposition temperature on film properties. This permitted to verify the results obtained previously by Aouadi [111]. The different results can be explained by the effect of the substrate rotation speed. According to its

properties, the CrN monolayer deposited under 300 °C and -500 V exhibits a (200) preferred crystalline orientation, is well crystallized, it has a dense surface morphology and small top column size. Concerning its mechanical properties, it presents the highest hardness and elastic modulus, the best plastic deformation resistance and has a very good adhesion up to 43 N (Lc2) and finally the lowest wear rate $0.58 \times 10^{-4} \text{ mm}^3 \cdot \text{m}^{-1} \text{N}^{-1}$. In conclusion, the application of a bias voltage of -500 V to the substrate and a deposition temperature of 300°C during the development of CrN coatings has led to real improvements in their properties.

Ternary CrAlN monolayers were developed by varying the Al content to determine the optimal composition to be applied in the AlCrN monolayers. As for the case of the CrN monolayers, the results obtained previously by Aouadi [111] were also verified. The different results can be explained by the effect of the substrate rotation speed. According to their properties, the CrAlN monolayers obtained with 57 and 62 at.% of Al exhibit the same crystalline orientation, have a dense surface morphology and small column size and grain size. Concerning their mechanical properties, the layer with 57 at.% of Al presents the highest hardness and elastic modulus, the best plastic deformation resistance and has a very good adhesion up to 47 N (Lc2) and finally the lowest volume rate. Nevertheless, the optimal Al content of $x = 0.62$ was chosen to study the optimization of AlCrN monolayers by varying the substrate bias voltage and the deposition temperature. Indeed, this CrAlN monolayer has a low plastic deformation resistance, but it presents the best adhesion and similar physicochemical and mechanical properties with the layer obtained for $x = 0.57$, and has been realized at a fixed power on the aluminum target which reduces the target damage during the PVD process.

AlCrN was studied by varying the deposition temperature and substrate bias voltage. According to the obtained results, high deposition temperature and substrate bias voltage would permit to get a dense and homogeneous AlCrN layer on silicon substrates. For our AlCrN layers, the temperature has an influence on the microstructure. The crystalline orientation of the AlCrN layers depends on the substrate bias voltage but also on the deposition temperature and these both parameters are correlated. The grain size decreases when the bias voltage increases, and the deposition temperature decreases. Concerning the mechanical properties of our AlCrN layers: their coefficient of friction does not depend on the deposition temperature or the substrate bias voltage and was around 0.5. All the AlCrN layers have compressive stress varying from -914 MPa to -166.3 MPa except the layer realized at 300°C-0V that has tensile stress of 28.6 MPa. The temperature and bias voltage both have positive impacts on adhesion property

of the AlCrN layers. It was shown that for AlCrN layers the “Hall-Petch effect” governs their hardness. Moreover, the results obtained for our CrN monolayers were verified. Indeed, it has been shown that the bias voltage increases the residual stress while the temperature reduces it. Most of AlCrN layers present a better adhesion than CrN layers whatever the deposition conditions.

According to their properties, the stoichiometry of AlCrN layers is Al₆₂Cr₃₈N. According to XRD analyses, we can consider that AlCrN layers are solid solutions of Al atoms in substitution in the CrN lattices. The AlCrN layer realized at 300 °C-250 V is well crystallized, presents the highest hardness and H³/E² ratio whatever the substrate, an acceptable elastic modulus of 165-170 GPa, the best plastic deformation resistance, the lowest wear rate and bests adhesion with a Lc2 up to 58 N. Thus, the optimized AlCrN monolayer (300 °C-250 V) has been applied in the synthesis of the Cr/CrN/AlCrN multilayers.

After optimizing the single-layered coatings of Cr, CrN, CrAlN and AlCrN, the characteristics of alternating architectures by combining the films of CrN and CrAlN or AlCrN and by depositing a Cr underlayer were compared. Cr/CrN/CrAlN and Cr/CrN/AlCrN were obtained by varying the CrN/AlCrN or CrN/CrAlN pairs thickness and number. As far as the number of interfaces is concerned, it is obvious that M4 multilayer would perform better than the M1 one. Moreover, the M2 should be chosen in comparison to the M3 according to its higher mechanical and tribological properties. Nevertheless, all the best monolayers and two multilayers (M2 and M4) were tested on carbide pins during tribological tests against Ti6Al4V alloy.

In conclusion, through this study, we have shown that the assembly according to different types of sequences, periods or thickness of the Cr, CrN, CrAlN and AlCrN layers has properties that would allow to considerably improve the performances of the cutting tools. Besides we confirm the interest of multilayers in comparison to monolayers.

Tribological pin-on-bar tests under flood (mixture oil-water) and cryogenic (LN2) conditions were conducted after optimizing the new hard coatings in Chapter 3. The objective of these tests presented in Chapter 4 is to analyse the performance of the hard coatings in terms of friction coefficient, volume of build-up material (adhesion) to the tool, and tool temperature, using a multilevel factorial design of experiments (DoE). The contact conditions to be applied in these tests were determined based on the experimental data from orthogonal cutting tests and the single-shear plane analytical model, which permitted to obtain the sliding speeds between

10 and 100 m/min and a nominal reference contact pressure of 1000 MPa. Since the contact geometry in machining is not the same as in tribological tests, a numerical model of the pin-on-bar was developed. This model permitted to obtain the normal force of 300 N to be applied to the pins. The results of these tribological tests have shown that: i) the coating does not have any relevant effect in the apparent friction coefficient regardless the cutting fluid; ii) the apparent friction coefficient decreases as the sliding speed increases until about 60-80 m/min, then it increases with the sliding speed until 100 m/min. This increase of the apparent friction coefficient after 60-80 m/min was already observed by other researchers and is related to the increase of the adhesion of Ti6Al4V alloy to the pins for both MWFs; iii) the apparent friction coefficient is generally higher under LN2 compared to flood conditions due to the absence of lubricant in the LN2; iv) increasing the nominal contact pressure from 1000 MPa to 1400 MPa decreases the apparent friction coefficient, although the adhesion is higher for 1400 MPa; v) the temperature is lower for the coated pins than the uncoated one, which is due to the heat flux diminishing effect provided by the coatings during the tribological tests; vi) the analysis of the DoE permitted to identify the sliding speed and MWF as the two main factors influencing the friction coefficient and the adhesion of Ti6Al4V alloy to the pins. This analysis confirms the influence of the type of coating and sliding speed on the apparent friction coefficient and build-up material (adhesion) to the tool observed experimentally; vii) the combination of flood conditions and a sliding speed of 60 m/min permits to reduce the adhesion of Ti6Al4V material to the pins and consequently the apparent friction coefficient.

Finally, tool wear tests were performed in turning of Ti6Al4V using uncoated and coated M2 and M4 inserts, under both flood and cryogenic LN2 conditions. Tool life was determined based on ISO 3685:1993 using reduced VB values. The results of the tool wear have shown that: i) the same wear types were observed under both flood and cryogenic LN2 conditions, including crater, flank and nose wear; ii) the main wear mechanisms are abrasive and adhesive wear, regardless the cutting fluid used; iii) under cryogenic cooling the longest tool life is obtained using the M2 insert (11.2 min), followed by the M4 insert (9 min) and finally the uncoated one (8.4 min); iv) under flood conditions the longest tool life is obtained using the M4 insert (8.6 min), followed by the uncoated insert (8 min) and surprisingly the M2 insert got the lowest tool life (4.4 min); v) the adhesion of Ti6Al4V alloy on the insert is higher for the LN2 compared to flood conditions; vi) tool life under LN2 cooling is similar or higher than that

obtained under flood conditions. Tool life is almost the same for both LN2 and flood conditions using coated M4 and uncoated inserts (difference is lower than 5%). However, tool life increases significantly for the M2 insert when the traditional MWF is replaced by LN2 (about 155%). A statistical analysis permitted to determine a strong correlation between tool flank wear and the machining forces and to build models for predicting the flank wear VB in function of the measured forces.

2. Perspectives

Although this work is promising, it must be continued. Indeed, all the results obtained during this work allow us to offer the following suggestions:

- ✓ Other Cr-based multilayers coatings can be tested: indeed, Al has a low sputtering yield. Thus, it should be interesting to replace it into the Cr-N system by another metal with a higher sputtering yield and that would result in multilayers with properties close to the Cr/CrN/AlCrN ones. The deposition time is a main parameter in industry, and we are obliged to take it into account in the development of new protective coatings.
- ✓ Another solution is also the modification of the substrate surface state to allow a better lubrication by LN2 of the cutting edge. One can suppose that the texturizing of the cutting tool could keep the lubricant longer.
- ✓ The cutting tools suppliers, especially carbide inserts suppliers, are also interested to improve their own products. One solution could be to test WC-Co carbide inserts with another binder than Co or without binder. Indeed, the bad effect of Cobalt on the coatings is well known and the replacement of this element by another could increase the carbide service life thanks to a better adhesion of the protective layers.
- ✓ It should be interesting in a future project to check the affinity of the oil with the tested coatings to explain the observed adhesion and the inefficiency of the coatings under flood conditions. Some tribo corrosion tests under flood and LN2 conditions could be very useful to complete and explain some of the results.
- ✓ The adhesion friction coefficient should be determined based on the apparent friction coefficient, in order to be used in machining models.
- ✓ The tool wear tests should be repeated to verify the obtained results but also during longer times to confirm the hypothesis about multilayer M4 under emulsion.

- ✓ Finally, machining industries are more and more interested now by liquid CO₂ than LN₂ for several reasons. Therefore, the tribological and tool wear tests could be done under liquid CO₂ to compare the results with LN₂. Indeed, to continue this work it will be important to consider the actual industry trends about the future solution to replace the traditional metal working fluids.

References

1. Jerold BD, Kumar MP (2013) The Influence of Cryogenic Coolants in Machining of Ti–6Al–4V. *J Manuf Sci Eng* 135:031005–031005–8. <https://doi.org/10.1115/1.4024058>
2. Outeiro JC, Lenoir P, Bosselut A (2015) Thermo-mechanical effects in drilling using metal working fluids and cryogenic cooling and their impact in tool performance. *Prod Eng Res Devel* 9:551–562. <https://doi.org/10.1007/s11740-015-0619-6>
3. Dieter GE, Bacon D (1988) *Mechanical Metallurgy*. McGraw-Hill
4. (2019) *World Machine Tool Survey*. Gardner Business Media Inc., Cincinnati, OH, USA
5. Díaz J (2020) *Economic & Statistical Toolbox -second quarter*. European Association of the Machine Tool Industries and related Manufacturing Technologies, Cecimo
6. Astakhov VP (2014) *Drills: Science and Technology of Advanced Operations*. CRC Press
7. Astakhov VP (1998) *Metal Cutting Mechanics*. CRC Press
8. Outeiro JC (2020) 11 - Residual stresses in machining. In: Silberschmidt VV (ed) *Mechanics of Materials in Modern Manufacturing Methods and Processing Techniques*. Elsevier, pp 297–360
9. (2014) *N.N. Cutting Tools*. Dedalus Consulting, New York
10. Astakhov VP (2010) *Geometry of Single-point Turning Tools and Drills: Fundamentals and Practical Applications*. Springer-Verlag
11. Debnath S, Reddy MM, Yi QS (2014) Environmental friendly cutting fluids and cooling techniques in machining: a review. *Journal of Cleaner Production* 83:33–47. <https://doi.org/10.1016/j.jclepro.2014.07.071>
12. Shashidhara YM, Jayaram SR (2010) Vegetable oils as a potential cutting fluid—An evolution. *Tribology International* 43:1073–1081. <https://doi.org/10.1016/j.triboint.2009.12.065>
13. Abdalla HS, Baines W, McIntyre G, Slade C (2007) Development of novel sustainable neat-oil metal working fluids for stainless steel and titanium alloy machining. Part 1. Formulation development. *Int J Adv Manuf Technol* 34:21–33. <https://doi.org/10.1007/s00170-006-0585-4>
14. Alves SM, Oliveira JFG de (2008) Vegetable Based Cutting Fluid: An Environmental Alternative to Grinding Process. In: *LCE 2008: 15th CIRP International Conference on Life Cycle Engineering: Conference Proceedings*. pp 664–668

15. Tschätsch H, Reichelt A (2009) Cutting fluids (coolants and lubricants). In: Tschätsch H (ed) Applied Machining Technology. Springer, Berlin, Heidelberg, pp 349–352
16. Jawahir IS, Attia H, Biermann D, et al (2016) Cryogenic manufacturing processes. CIRP Annals 65:713–736. <https://doi.org/10.1016/j.cirp.2016.06.007>
17. Uehara K, Kumagai S (1968) Chip formation, surface roughness and cutting force in cryogenic machining. Ann CIRP 17:409–416
18. Chattopadhyay AB, Bose A, Chattopadhyay AK (1985) Improvements in grinding steels by cryogenic cooling. Precision Engineering 7:93–98. [https://doi.org/10.1016/0141-6359\(85\)90098-4](https://doi.org/10.1016/0141-6359(85)90098-4)
19. Sharma VS, Dogra M, Suri NM (2009) Cooling techniques for improved productivity in turning. International Journal of Machine Tools and Manufacture 49:435–453. <https://doi.org/10.1016/j.ijmachtools.2008.12.010>
20. Park K-H, Yang G-D, Lee M-G, et al (2014) Eco-friendly face milling of titanium alloy. Int J Precis Eng Manuf 15:1159–1164. <https://doi.org/10.1007/s12541-014-0451-5>
21. Lee I, Bajpai V, Moon S, et al (2015) Tool life improvement in cryogenic cooled milling of the preheated Ti–6Al–4V. Int J Adv Manuf Technol 79:665–673. <https://doi.org/10.1007/s00170-015-6849-0>
22. Bordin A, Bruschi S, Ghiotti A, Bariani PF (2015) Analysis of tool wear in cryogenic machining of additive manufactured Ti6Al4V alloy. Wear 328–329:89–99. <https://doi.org/10.1016/j.wear.2015.01.030>
23. Bordin A, Sartori S, Bruschi S, Ghiotti A (2017) Experimental investigation on the feasibility of dry and cryogenic machining as sustainable strategies when turning Ti6Al4V produced by Additive Manufacturing. Journal of Cleaner Production 142:4142–4151. <https://doi.org/10.1016/j.jclepro.2016.09.209>
24. Ayed Y, Germain G, Melsio AP, Kowalewski P (2016) Effect of supply conditions of liquid nitrogen on the cryogenic assisted machining of the Ti64 Titanium alloy. HSM - High Speed Machining 2016:1–3
25. Sadik MI, Isakson S (2017) The role of PVD coating and coolant nature in wear development and tool performance in cryogenic and wet milling of Ti–6Al–4V. Wear 386–387:204–210. <https://doi.org/10.1016/j.wear.2017.02.049>
26. Scurlock RG (1990) A matter of degrees: A brief history of cryogenics. Cryogenics 30:483–500. [https://doi.org/10.1016/0011-2275\(90\)90048-H](https://doi.org/10.1016/0011-2275(90)90048-H)
27. Reitz G (1919) Die Grösse des geistlichen und ritterschaftlichen Grundbesitzes im ehemaligen Kur-Trier. Rheinische Friedrich-Wilhelms-Universität zu Bonn.
28. Machai C, Biermann D (2011) Machining of β -titanium-alloy Ti–10V–2Fe–3Al under cryogenic conditions: Cooling with carbon dioxide snow. Journal of Materials

- Processing Technology 211:1175–1183.
<https://doi.org/10.1016/j.jmatprotec.2011.01.022>
29. Pusavec F, Kramar D, Krajnik P, Kopac J (2010) Transitioning to sustainable production – part II: evaluation of sustainable machining technologies. *Journal of Cleaner Production* 18:1211–1221. <https://doi.org/10.1016/j.jclepro.2010.01.015>
 30. Klocke F, Lung D, Krämer A, et al (2013) Potential of Modern Lubricoolant Strategies on Cutting Performance. *Key Engineering Materials* 554–557:2062–2071. <https://doi.org/10.4028/www.scientific.net/KEM.554-557.2062>
 31. Dhar NR, Paul S, Chattopadhyay AB (2001) The influence of cryogenic cooling on tool wear, dimensional accuracy and surface finish in turning AISI 1040 and E4340C steels. *Wear* 249:932–942. [https://doi.org/10.1016/S0043-1648\(01\)00825-0](https://doi.org/10.1016/S0043-1648(01)00825-0)
 32. Chaharsooghi AS, Dhokia V, Newman S (2014) A Techno-Health Study of the Use of Cutting Fluids and Future Alternatives. pp 625–632
 33. Pusavec F, Krajnik P, Kopac J (2010) Transitioning to sustainable production – Part I: application on machining technologies. *Journal of Cleaner Production* 18:174–184. <https://doi.org/10.1016/j.jclepro.2009.08.010>
 34. Shokrani A, Dhokia V, Newman ST (2012) Environmentally conscious machining of difficult-to-machine materials with regard to cutting fluids. *International Journal of Machine Tools and Manufacture* 57:83–101. <https://doi.org/10.1016/j.ijmachtools.2012.02.002>
 35. Kaganer MG, Ustinovich YV, Kozheurov VI, Levina ZL (1967) Vessels for the storage and transport of liquid oxygen and nitrogen. *Chemical and Petroleum Engineering* 3:918–922. <https://doi.org/10.1007/BF01136404>
 36. Yildiz Y, Nalbant M (2008) A review of cryogenic cooling in machining processes. *International Journal of Machine Tools and Manufacture* 48:947–964. <https://doi.org/10.1016/j.ijmachtools.2008.01.008>
 37. Welsch G, Boyer R, Collings EW (1993) *Materials Properties Handbook: Titanium Alloys*. ASM International
 38. Baudouy B, Defresne G, Duthil P, Thermeau J-P (2014) Propriétés des matériaux à basse température
 39. Ezugwu EO, Wang ZM, Machado AR (1999) The machinability of nickel-based alloys: a review. *Journal of Materials Processing Technology* 86:1–16. [https://doi.org/10.1016/S0924-0136\(98\)00314-8](https://doi.org/10.1016/S0924-0136(98)00314-8)
 40. Hong SY, Zhao Z (1999) Thermal aspects, material considerations and cooling strategies in cryogenic machining. *Clean Products and Processes* 1:107–116. <https://doi.org/10.1007/s100980050016>
 41. Pahlitzsch G (1953) Gases are good cutting coolants. *American Machinist* 97:196

42. Klocke F, Krämer A, Sangermann H, Lung D (2012) Thermo-Mechanical Tool Load during High Performance Cutting of Hard-to-Cut Materials. In: *Procedia CIRP*. pp 295–300
43. Bermingham MJ, Kirsch J, Sun S, et al (2011) New observations on tool life, cutting forces and chip morphology in cryogenic machining Ti-6Al-4V. *International Journal of Machine Tools and Manufacture* 51:500–511. <https://doi.org/10.1016/j.ijmachtools.2011.02.009>
44. Bermingham MJ, Palanisamy S, Dargusch MS (2012) Understanding the tool wear mechanism during thermally assisted machining Ti-6Al-4V. *International Journal of Machine Tools and Manufacture* 62:76–87. <https://doi.org/10.1016/j.ijmachtools.2012.07.001>
45. Sartori S, Moro L, Ghiotti A, Bruschi S (2017) On the tool wear mechanisms in dry and cryogenic turning Additive Manufactured titanium alloys. *Tribology International* 105:264–273. <https://doi.org/10.1016/j.triboint.2016.09.034>
46. Strano M, Chiappini E, Tirelli S, et al (2013) Comparison of Ti6Al4V machining forces and tool life for cryogenic versus conventional cooling. *Proceedings of the Institution of Mechanical Engineers, Part B: Journal of Engineering Manufacture* 227:1403–1408. <https://doi.org/10.1177/0954405413486635>
47. Sun S, Brandt M, Palanisamy S, Dargusch MS (2015) Effect of cryogenic compressed air on the evolution of cutting force and tool wear during machining of Ti-6Al-4V alloy. *Journal of Materials Processing Technology* 221:243–254. <https://doi.org/10.1016/j.jmatprotec.2015.02.017>
48. Venugopal KA, Paul S, Chattopadhyay AB (2007) Tool wear in cryogenic turning of Ti-6Al-4V alloy. *Cryogenics* 47:12–18. <https://doi.org/10.1016/j.cryogenics.2006.08.011>
49. Islam MN, Anggono JM, Pramanik A, Boswell B (2013) Effect of cooling methods on dimensional accuracy and surface finish of a turned titanium part. *Int J Adv Manuf Technol* 69:2711–2722. <https://doi.org/10.1007/s00170-013-5223-3>
50. Combres Y (1999) Propriétés du titane et de ses alliages. *Tech ing, Matér mét* MB5:M557.1-M557.15
51. Cheng W (2019) Modélisation de l'usinage de l'alliage de titane Ti-6Al-4V utilisant un modèle constitutif prenant en compte l'état de contrainte dans la zone de déformation. *These de doctorat, Paris, ENSAM*
52. Peters M, Kumpfert J, Ward CH, Leyens C (2003) Titanium Alloys for Aerospace Applications. *Advanced Engineering Materials* 5:419–427. <https://doi.org/10.1002/adem.200310095>
53. Ulutan D, Ozel T (2011) Machining induced surface integrity in titanium and nickel alloys: A review. *International Journal of Machine Tools and Manufacture* 51:250–280. <https://doi.org/10.1016/j.ijmachtools.2010.11.003>

54. Balasubramanian S, Anand L (2002) Plasticity of initially textured hexagonal polycrystals at high homologous temperatures: application to titanium. *Acta Materialia* 50:133–148. [https://doi.org/10.1016/S1359-6454\(01\)00326-3](https://doi.org/10.1016/S1359-6454(01)00326-3)
55. Donachie MJ (2000) *Titanium: A Technical Guide*, 2nd Edition. ASM International
56. Combres Y (2013) *Traitements thermiques des alliages de titane*
57. Ramirez C (2017) Critères d'optimisation des alliages de TITane pour améliorer leur Usinabilité. Thesis, Paris, ENSAM
58. Campbell FC (2008) *Elements of Metallurgy and Engineering Alloys*. ASM International
59. Hong S, Ding Y (2001) Cooling approaches and cutting temperatures in cryogenic machining of Ti-6Al-4V. *International Journal of Machine Tools and Manufacture* 41:1417–1437. [https://doi.org/10.1016/S0890-6955\(01\)00026-8](https://doi.org/10.1016/S0890-6955(01)00026-8)
60. Bui A, Hébral B, Kircher F, et al (1993) *Cryogénie : propriétés physiques aux basses températures*. 35
61. Lequien P (2017) Etude fondamentale de l'assistance cryogénique pour application au fraisage du Ti6Al4V. Phdthesis, Ecole nationale supérieure d'arts et métiers - ENSAM
62. Courbon C, Pusavec F, Dumont F, et al (2013) Tribological behaviour of Ti6Al4V and Inconel718 under dry and cryogenic conditions—Application to the context of machining with carbide tools. *Tribology International* 66:72–82. <https://doi.org/10.1016/j.triboint.2013.04.010>
63. Field M, Kahles JF (1971) Review of surface integrity of machined components. *Annals of the CIRP* 20:153–163
64. Agrawal C, Khanna N, Pruncu CI, et al (2020) Tool wear progression and its effects on energy consumption and surface roughness in cryogenic assisted turning of Ti-6Al-4V. *Int J Adv Manuf Technol* 111:1319–1331. <https://doi.org/10.1007/s00170-020-06140-w>
65. Shokrani A, Dhokia V, Newman ST (2016) Investigation of the effects of cryogenic machining on surface integrity in CNC end milling of Ti-6Al-4V titanium alloy. *Journal of Manufacturing Processes* 21:172–179. <https://doi.org/10.1016/j.jmapro.2015.12.002>
66. Rech J, Arrazola PJ, Claudin C, et al (2013) Characterisation of friction and heat partition coefficients at the tool-work material interface in cutting. *CIRP Annals* 62:79–82. <https://doi.org/10.1016/j.cirp.2013.03.099>
67. Puls H, Klocke F, Lung D (2012) A new experimental methodology to analyse the friction behaviour at the tool-chip interface in metal cutting. *Prod Eng Res Devel* 6:349–354. <https://doi.org/10.1007/s11740-012-0386-6>
68. M'Saoubi R, Chandrasekaran H (2005) Innovative Methods for the Investigation of Tool-Chip Adhesion and Layer Formation during Machining. *CIRP Annals* 54:59–62. [https://doi.org/10.1016/S0007-8506\(07\)60049-3](https://doi.org/10.1016/S0007-8506(07)60049-3)

69. Kilic DS, Raman S (2007) Observations of the tool–chip boundary conditions in turning of aluminum alloys. *Wear* 262:889–904. <https://doi.org/10.1016/j.wear.2006.08.019>
70. Arrazola PJ, Ugarte D, Domínguez X (2008) A new approach for the friction identification during machining through the use of finite element modeling. *International Journal of Machine Tools and Manufacture* 48:173–183. <https://doi.org/10.1016/j.ijmachtools.2007.08.022>
71. Zemzemi F, Rech J, Ben Salem W, et al (2009) Identification of a friction model at tool/chip/workpiece interfaces in dry machining of AISI4142 treated steels. *Journal of Materials Processing Technology* 209:3978–3990. <https://doi.org/10.1016/j.jmatprotec.2008.09.019>
72. Olsson M, Söderberg S, Jacobson S, Hogmark S (1989) Simulation of cutting tool wear by a modified pin-on-disc test. *International Journal of Machine Tools and Manufacture* 29:377–390. [https://doi.org/10.1016/0890-6955\(89\)90007-2](https://doi.org/10.1016/0890-6955(89)90007-2)
73. Rech J, Claudin C, D’Eramo E (2009) Identification of a friction model—Application to the context of dry cutting of an AISI 1045 annealed steel with a TiN-coated carbide tool. *Tribology International* 42:738–744. <https://doi.org/10.1016/j.triboint.2008.10.007>
74. Zemzemi F, Bensalem W, Rech J, et al (2008) New tribometer designed for the characterisation of the friction properties at the tool/chip/workpiece interfaces in machining. *Tribotest* 14:11–25. <https://doi.org/10.1002/tt.50>
75. Challen JM, Oxley PLB (1979) An explanation of the different regimes of friction and wear using asperity deformation models. *Wear* 53:229–243. [https://doi.org/10.1016/0043-1648\(79\)90080-2](https://doi.org/10.1016/0043-1648(79)90080-2)
76. Smolenicki D, Boos J, Kuster F, et al (2014) In-process measurement of friction coefficient in orthogonal cutting. *CIRP Annals* 63:97–100. <https://doi.org/10.1016/j.cirp.2014.03.083>
77. Bonnet C, Valiorgue F, Rech J, et al (2008) Identification of a friction model—Application to the context of dry cutting of an AISI 316L austenitic stainless steel with a TiN coated carbide tool. *International Journal of Machine Tools and Manufacture* 48:1211–1223. <https://doi.org/10.1016/j.ijmachtools.2008.03.011>
78. Meier L, Schaal N, Wegener K (2017) In-process Measurement of the Coefficient of Friction on Titanium. *Procedia CIRP* 58:163–168. <https://doi.org/10.1016/j.procir.2017.03.212>
79. Ostrovskaia YL, Yukhno TP, Gamulya GD, et al (2001) Low temperature tribology at the B. Verkin Institute for Low Temperature Physics & Engineering (historical review). *Tribology International* 34:265–276. [https://doi.org/10.1016/S0301-679X\(01\)00010-X](https://doi.org/10.1016/S0301-679X(01)00010-X)
80. Gradt T, Schneider T, Hübner W, Börner H (1998) Friction and wear at low temperatures. *International Journal of Hydrogen Energy* 23:397–403. [https://doi.org/10.1016/S0360-3199\(97\)00070-0](https://doi.org/10.1016/S0360-3199(97)00070-0)

81. El-Tayeb NSM, Yap TC, Venkatesh VC, Brevern PV (2009) Modeling of cryogenic frictional behaviour of titanium alloys using Response Surface Methodology approach. *Materials & Design* 30:4023–4034. <https://doi.org/10.1016/j.matdes.2009.05.020>
82. Sadik MI (2014) *An introduction to cutting tools: materials and applications*. Sandvik Coromant
83. Li B (2012) A review of tool wear estimation using theoretical analysis and numerical simulation technologies. *International Journal of Refractory Metals and Hard Materials* 35:143–151. <https://doi.org/10.1016/j.ijrmhm.2012.05.006>
84. Stephenson DA, Agapiou JS (2016) *Metal Cutting Theory and Practice*. CRC Press
85. Trent EM, Wright PK (2000) *Metal Cutting: Fourth Edition*. Butterworth-Heinemann
86. Schultheiss F (2013) *On the Machinability of Ductile and Strain Hardening Materials - Models and Methods for Analyzing Machinability*. Thesis/doccomp, Lund University
87. Taylor FW (1906) *On the art of cutting metals*, 3rd ed. American society of mechanical engineers, l'Université de Californie
88. Kramer BM (1987) On Tool Materials for High Speed Machining. *J Eng Ind* 109:87–91. <https://doi.org/10.1115/1.3187113>
89. Hartung PD, Kramer BM, von Turkovich BF (1982) Tool Wear in Titanium Machining. *CIRP Annals* 31:75–80. [https://doi.org/10.1016/S0007-8506\(07\)63272-7](https://doi.org/10.1016/S0007-8506(07)63272-7)
90. Ezugwu EO, Bonney J, Yamane Y (2003) An overview of the machinability of aeroengine alloys. *Journal of Materials Processing Technology* 134:233–253. [https://doi.org/10.1016/S0924-0136\(02\)01042-7](https://doi.org/10.1016/S0924-0136(02)01042-7)
91. Ezugwu EO, Wang ZM (1997) Titanium alloys and their machinability—a review. *Journal of Materials Processing Technology* 68:262–274. [https://doi.org/10.1016/S0924-0136\(96\)00030-1](https://doi.org/10.1016/S0924-0136(96)00030-1)
92. Dearnley PA, Grearson AN (1986) Evaluation of principal wear mechanisms of cemented carbides and ceramics used for machining titanium alloy IMI 318. *Materials Science and Technology* 2:47–58. <https://doi.org/10.1179/mst.1986.2.1.47>
93. Komanduri R, Reed WR (1983) Evaluation of carbide grades and a new cutting geometry for machining titanium alloys. *Wear* 92:113–123. [https://doi.org/10.1016/0043-1648\(83\)90011-X](https://doi.org/10.1016/0043-1648(83)90011-X)
94. Lueth RC (1974) Determination of Fracture Toughness Parameters for Tungsten Carbide-Cobalt Alloys. In: Bradt RC, Hasselman DPH, Lange FF (eds) *Fracture Mechanics of Ceramics: Volume 2 Microstructure, Materials, and Applications*. Springer US, Boston, MA, pp 791–806

95. Milman YV, Luyckx S, Northrop I (1999) Influence of temperature, grain size and cobalt content on the hardness of WC–Co alloys. *International Journal of Refractory Metals and Hard Materials* 17:39–44. [https://doi.org/10.1016/S0263-4368\(98\)00038-9](https://doi.org/10.1016/S0263-4368(98)00038-9)
96. Saito H, Iwabuchi A, Shimizu T (2006) Effects of Co content and WC grain size on wear of WC cemented carbide. *Wear* 261:126–132. <https://doi.org/10.1016/j.wear.2005.09.034>
97. Zhao Z, Hong SY (1992) Cryogenic properties of some cutting tool materials. *JMEP* 1:705–714. <https://doi.org/10.1007/BF02649252>
98. Lattemann M, Coronel E, Garcia J, Sadik I (2016) Interaction between cemented carbide and Ti6Al4V alloy in cryogenic machining. In: *Proceedings of the 19th Plansee Seminar*. Reutte, Austria
99. Wang H, Webb T, Bitler JW (2015) Study of thermal expansion and thermal conductivity of cemented WC–Co composite. *International Journal of Refractory Metals and Hard Materials* 49:170–177. <https://doi.org/10.1016/j.ijrmhm.2014.06.009>
100. Bouzakis K-D, Michailidis N, Skordaris G, et al (2012) Cutting with coated tools: Coating technologies, characterization methods and performance optimization. *CIRP Annals* 61:703–723. <https://doi.org/10.1016/j.cirp.2012.05.006>
101. Mattox DM (2010) *Handbook of Physical Vapor Deposition (PVD) Processing*. William Andrew
102. Tönshoff HK, Blawit C, Rie KT, Gebauer A (1997) Effects of surface properties on coating adhesion and wear behaviour of PACVD-coated cermets in interrupted cutting. *Surface and Coatings Technology* 97:224–231. [https://doi.org/10.1016/S0257-8972\(97\)00134-5](https://doi.org/10.1016/S0257-8972(97)00134-5)
103. Sproul WD, Legg KO (1995) *Opportunities for innovation: advanced surface engineering*. Technomic Publishing Company
104. Kelly PJ, Arnell RD (2000) Magnetron sputtering: a review of recent developments and applications. *Vacuum* 56:159–172. [https://doi.org/10.1016/S0042-207X\(99\)00189-X](https://doi.org/10.1016/S0042-207X(99)00189-X)
105. Fang B, Zeng Z, Yan X, Hu Z (2013) Effects of annealing on thermoelectric properties of Sb₂Te₃ thin films prepared by radio frequency magnetron sputtering. *J Mater Sci: Mater Electron* 24:1105–1111. <https://doi.org/10.1007/s10854-012-0888-1>
106. Huang H, Luan W, Tu S (2009) Influence of annealing on thermoelectric properties of bismuth telluride films grown via radio frequency magnetron sputtering. *Thin Solid Films* 517:3731–3734. <https://doi.org/10.1016/j.tsf.2009.01.015>
107. Pawlowski L (2003) *Dépôts physiques: techniques, microstructures et propriétés*. PPUR presses polytechniques

108. Constantin DG, Apreutesei M, Arvinte R, et al (2011) MAGNETRON SPUTTERING TECHNIQUE USED FOR COATINGS DEPOSITION; TECHNOLOGIES AND APPLICATIONS. 12:5
109. García J, Collado Ciprés V, Blomqvist A, Kaplan B (2019) Cemented carbide microstructures: a review. *International Journal of Refractory Metals and Hard Materials* 80:40–68. <https://doi.org/10.1016/j.ijrmhm.2018.12.004>
110. Bobzin K (2017) High-performance coatings for cutting tools. *CIRP Journal of Manufacturing Science and Technology* 18:1–9. <https://doi.org/10.1016/j.cirpj.2016.11.004>
111. Aouadi K (2017) Développement d'une nouvelle génération de revêtements ultra-durs. Etude de leur comportement tribologique et anticorrosif. Phdthesis, Ecole nationale supérieure d'arts et métiers - ENSAM
112. Nouveau C (2001) Etude de revêtements durs (CRxNy) obtenus par méthodes PVD: réalisation et caractérisations : applications à l'usinage du bois. Thèse de doctorat, Arts et Métiers ParisTech
113. Sampath Kumar T, Balasivanandha Prabu S, Manivasagam G, Padmanabhan KA (2014) Comparison of TiAlN, AlCrN, and AlCrN/TiAlN coatings for cutting-tool applications. *Int J Miner Metall Mater* 21:796–805. <https://doi.org/10.1007/s12613-014-0973-y>
114. Tsai D-C, Huang Y-L, Lin S-R, et al (2011) Structure and mechanical properties of (TiVCr)N coatings prepared by energetic bombardment sputtering with different nitrogen flow ratios. *Journal of Alloys and Compounds* 509:3141–3147. <https://doi.org/10.1016/j.jallcom.2010.12.026>
115. Venugopal KA, Tawade R, Prashanth PG, et al (2003) Turning of titanium alloy with TiB₂-coated carbides under cryogenic cooling. *Proceedings of the Institution of Mechanical Engineers, Part B: Journal of Engineering Manufacture* 217:1697–1707. <https://doi.org/10.1243/095440503772680622>
116. Wilson A, Matthews A, Housden J, et al (1993) A comparison of the wear and fatigue properties of plasma-assisted physical vapour deposition TiN, CrN and duplex coatings on Ti-6Al-4V. *Surface and Coatings Technology* 62:600–607. [https://doi.org/10.1016/0257-8972\(93\)90306-9](https://doi.org/10.1016/0257-8972(93)90306-9)
117. Xiao B, Li H, Mei H, et al (2018) A study of oxidation behavior of AlTiN-and AlCrN-based multilayer coatings. *Surface and Coatings Technology* 333:229–237. <https://doi.org/10.1016/j.surfcoat.2017.10.078>
118. Yousaf MI, Pelenovich VO, Yang B, et al (2015) Effect of bilayer period on structural and mechanical properties of nanocomposite TiAlN/MoN multilayer films synthesized by cathodic arc ion-plating. *Surface and Coatings Technology* 282:94–102. <https://doi.org/10.1016/j.surfcoat.2015.10.018>

119. Martinez E, Sanjinés R, Karimi A, et al (2004) Mechanical properties of nanocomposite and multilayered Cr–Si–N sputtered thin films. *Surface and Coatings Technology* 180–181:570–574. <https://doi.org/10.1016/j.surfcoat.2003.10.121>
120. Vepřek S, Reiprich S, Shizhi L (1995) Superhard nanocrystalline composite materials: The TiN/Si₃N₄ system. *Appl Phys Lett* 66:2640–2642. <https://doi.org/10.1063/1.113110>
121. Voevodin AA, Prasad SV, Zabinski JS (1997) Nanocrystalline carbide/amorphous carbon composites. *Journal of Applied Physics* 82:855–858. <https://doi.org/10.1063/1.365784>
122. Chu X, Barnett SA, Wong MS, Sproul WD (1993) Reactive unbalanced magnetron sputter deposition of polycrystalline TiN/NbN superlattice coatings. *Surface and Coatings Technology* 57:13–18. [https://doi.org/10.1016/0257-8972\(93\)90331-H](https://doi.org/10.1016/0257-8972(93)90331-H)
123. Helmersson U, Todorova S, Barnett SA, et al (1987) Growth of single-crystal TiN/VN strained-layer superlattices with extremely high mechanical hardness. *Journal of Applied Physics* 62:481–484. <https://doi.org/10.1063/1.339770>
124. Kim GS, Lee SY, Hahn JH, Lee SY (2003) Synthesis of CrN/AlN superlattice coatings using closed-field unbalanced magnetron sputtering process. *Surface and Coatings Technology* 171:91–95. [https://doi.org/10.1016/S0257-8972\(03\)00244-5](https://doi.org/10.1016/S0257-8972(03)00244-5)
125. Park J-K, Baik Y-J (2005) The crystalline structure, hardness and thermal stability of AlN/CrN superlattice coating prepared by D.C. magnetron sputtering. *Surface and Coatings Technology* 200:1519–1523. <https://doi.org/10.1016/j.surfcoat.2005.08.099>
126. Barshilia HC, Deepthi B, Selvakumar N, et al (2007) Nanolayered multilayer coatings of CrN/CrAlN prepared by reactive DC magnetron sputtering. *Applied Surface Science* 253:5076–5083. <https://doi.org/10.1016/j.apsusc.2006.11.021>
127. Cheng YH, Browne T, Heckerman B, Meletis EI (2010) Mechanical and tribological properties of nanocomposite TiSiN coatings. *Surface and Coatings Technology* 204:2123–2129. <https://doi.org/10.1016/j.surfcoat.2009.11.034>
128. Kacsich T, Gasser SM, Garland C, Nicolet M-A (2000) Wet oxidation of Ti₃₄Si₂₃N₄₃ thin films with and without pre-annealing. *Surface and Coatings Technology* 124:162–168. [https://doi.org/10.1016/S0257-8972\(99\)00641-6](https://doi.org/10.1016/S0257-8972(99)00641-6)
129. Yang Q, Zhao LR (2003) Dry sliding wear of magnetron sputtered TiN/CrN superlattice coatings. *Surface and Coatings Technology* 173:58–66. [https://doi.org/10.1016/S0257-8972\(03\)00516-4](https://doi.org/10.1016/S0257-8972(03)00516-4)
130. Rebenne HE, Bhat DG (1994) Review of CVD TiN coatings for wear-resistant applications: deposition processes, properties and performance. *Surface and Coatings Technology* 63:1–13. [https://doi.org/10.1016/S0257-8972\(05\)80002-7](https://doi.org/10.1016/S0257-8972(05)80002-7)
131. Liu Z-J, Liu Z-K, McNerny C, et al (2005) Investigations of the bonding layer in commercial CVD coated cemented carbide inserts. *Surface and Coatings Technology* 198:161–164. <https://doi.org/10.1016/j.surfcoat.2004.10.112>

132. Haubner R, Lessiak M, Pitonak R, et al (2017) Evolution of conventional hard coatings for its use on cutting tools. *International Journal of Refractory Metals and Hard Materials* 62:210–218. <https://doi.org/10.1016/j.ijrmhm.2016.05.009>
133. Matthews A (1985) Titanium Nitride PVD Coating Technology. *Surface Engineering* 1:93–104. <https://doi.org/10.1179/sur.1985.1.2.93>
134. Leyendecker T, Lemmer O, Esser S, Ebberink J (1991) The development of the PVD coating TiAlN as a commercial coating for cutting tools. *Surface and Coatings Technology* 48:175–178. [https://doi.org/10.1016/0257-8972\(91\)90142-J](https://doi.org/10.1016/0257-8972(91)90142-J)
135. Molarius JM, Korhonen AS, Harju E, Lappalainen R (1987) Comparison of cutting performance of ion-plated NbN, ZrN, TiN and (Ti, Al)N coatings. *Surface and Coatings Technology* 33:117–132. [https://doi.org/10.1016/0257-8972\(87\)90182-4](https://doi.org/10.1016/0257-8972(87)90182-4)
136. Aihua L, Jianxin D, Haibing C, et al (2012) Friction and wear properties of TiN, TiAlN, AlTiN and CrAlN PVD nitride coatings. *International Journal of Refractory Metals and Hard Materials* 31:82–88. <https://doi.org/10.1016/j.ijrmhm.2011.09.010>
137. Cselle T, Barimani A (1995) Today's applications and future developments of coatings for drills and rotating cutting tools. *Surface and Coatings Technology* 76–77:712–718. [https://doi.org/10.1016/0257-8972\(96\)80011-9](https://doi.org/10.1016/0257-8972(96)80011-9)
138. Donohue LA, Cawley J, Brooks JS, Münz W-D (1995) Deposition and characterization of TiAlZrN films produced by a combined steered arc and unbalanced magnetron sputtering technique. *Surface and Coatings Technology* 74–75:123–134. [https://doi.org/10.1016/0257-8972\(95\)08298-0](https://doi.org/10.1016/0257-8972(95)08298-0)
139. Jehn HA, Hofmann S, Rückborn V, Münz W (1986) Morphology and properties of sputtered (Ti,Al)N layers on high speed steel substrates as a function of deposition temperature and sputtering atmosphere. *Journal of Vacuum Science & Technology A* 4:2701–2705. <https://doi.org/10.1116/1.573709>
140. Münz W (1986) Titanium aluminum nitride films: A new alternative to TiN coatings. *Journal of Vacuum Science & Technology A* 4:2717–2725. <https://doi.org/10.1116/1.573713>
141. Kusiak A, Battaglia J-L, Rech J (2005) Tool coatings influence on the heat transfer in the tool during machining. *Surface and Coatings Technology* 195:29–40. <https://doi.org/10.1016/j.surfcoat.2005.01.007>
142. Rech J (2006) A multiview approach to the tribological characterisation of cutting tool coatings for steels in high-speed dry turning. *International Journal of Machining and Machinability of Materials* 1:27–44. <https://doi.org/10.1504/IJMMM.2006.010657>
143. Shokrani A, Dhokia V, Muñoz-Escalona P, Newman ST (2013) State-of-the-art cryogenic machining and processing. *International Journal of Computer Integrated Manufacturing* 26:616–648. <https://doi.org/10.1080/0951192X.2012.749531>

144. Rech J, Kusiak A, Battaglia JL (2004) Tribological and thermal functions of cutting tool coatings. *Surface and Coatings Technology* 186:364–371. <https://doi.org/10.1016/j.surfcoat.2003.11.027>
145. Djouadi MA, Beer P, Marchal R, et al (1999) Antiabrasive coatings: application for wood processing. *Surface and Coatings Technology* 116–119:508–516. [https://doi.org/10.1016/S0257-8972\(99\)00236-4](https://doi.org/10.1016/S0257-8972(99)00236-4)
146. Creus J, Idrissi H, Mazille H, et al (1998) Corrosion behaviour of TiN and CrN coatings produced by cathodic arc PVD process on mild steel substrate. *Surface Engineering* 14:432–436. <https://doi.org/10.1179/sur.1998.14.5.432>
147. Navinšek B, Panjan P, Krušič J (1998) Hard coatings on soft metallic substrates. *Surface and Coatings Technology* 98:809–815. [https://doi.org/10.1016/S0257-8972\(97\)00316-2](https://doi.org/10.1016/S0257-8972(97)00316-2)
148. Vetter J, Knaup R, Dweletzki H, et al (1996) Hard coatings for lubrication reduction in metal forming. *Surface and Coatings Technology* 86–87:739–747. [https://doi.org/10.1016/S0257-8972\(96\)03063-0](https://doi.org/10.1016/S0257-8972(96)03063-0)
149. Friedrich C, Berg G, Broszeit E, et al (1997) PVD CrxN coatings for tribological application on piston rings. *Surface and Coatings Technology* 97:661–668. [https://doi.org/10.1016/S0257-8972\(97\)00335-6](https://doi.org/10.1016/S0257-8972(97)00335-6)
150. Navinšek B, Panjan P (1995) Novel applications of CrN (PVD) coatings deposited at 200 °C. *Surface and Coatings Technology* 74–75:919–926. [https://doi.org/10.1016/0257-8972\(95\)08287-5](https://doi.org/10.1016/0257-8972(95)08287-5)
151. Benlatreche Y (2011) Contribution à l'amélioration de la durée de vie d'outils carbure pour l'usinage du MDF (Medium Density Fiberboard) par application de dépôts ternaires (CrAlN, CrVN) et modification de l'arête de coupe. Phdthesis, Arts et Métiers ParisTech
152. Rahil I (2013) Elaboration et caractérisation de revêtements à base de nitrure de chrome, carbonitrure et carbure de titane élaborés par pulvérisation magnétron. Paris, ENSAM
153. Zairi A (2013) Elaboration et Caractérisation de revêtements à base de nitrure de chrome par pulvérisation cathodique magnétron en condition réactive : propriétés mécaniques et tribologiques. Paris, ENSAM
154. Aissani L, Fellah M, Nouveau C, et al (2017) Structural and mechanical properties of Cr–Zr–N coatings with different Zr content. *Surface Engineering* 36:1–9
155. Barshilia HC, Surya Prakash M, Poojari A, Rajam KS (2004) Corrosion behavior of nanolayered TiN/NbN multilayer coatings prepared by reactive direct current magnetron sputtering process. *Thin Solid Films* 460:133–142. <https://doi.org/10.1016/j.tsf.2004.01.096>
156. Warcholinski B, Gilewicz A, Kuklinski Z, Myslinski P (2010) Hard CrCN/CrN multilayer coatings for tribological applications. *Surface and Coatings Technology* 204:2289–2293. <https://doi.org/10.1016/j.surfcoat.2009.12.019>

157. Okumiya M, Griepentrog M (1999) Mechanical properties and tribological behavior of TiN–CrAlN and CrN–CrAlN multilayer coatings. *Surface and Coatings Technology* 112:123–128. [https://doi.org/10.1016/S0257-8972\(98\)00799-3](https://doi.org/10.1016/S0257-8972(98)00799-3)
158. Kim YJ, Byun TJ, Han JG (2009) Bilayer period dependence of CrN/CrAlN nanoscale multilayer thin films. *Superlattices and Microstructures* 45:73–79. <https://doi.org/10.1016/j.spmi.2008.12.020>
159. Bouzakis K-D, Skordaris G, Gerardis S, et al (2010) The effect of substrate pretreatments and HPPMS-deposited adhesive interlayers' materials on the cutting performance of coated cemented carbide inserts. *CIRP Annals* 59:73–76. <https://doi.org/10.1016/j.cirp.2010.03.065>
160. Ehiasarian AP (2010) High-power impulse magnetron sputtering and its applications. *Pure and Applied Chemistry* 82:1247–1258. <https://doi.org/10.1351/PAC-CON-09-10-43>
161. Hovsepiyan PE, Ehiasarian AP, Ratayski U (2009) CrAlYCN/CrCN nanoscale multilayer PVD coatings deposited by the combined High Power Impulse Magnetron Sputtering/Unbalanced Magnetron Sputtering (HIPIMS/UBM) technology. *Surface and Coatings Technology* 203:1237–1243. <https://doi.org/10.1016/j.surfcoat.2008.10.033>
162. Bouzakis K-D, Makrimallakis S, Katirtzoglou G, et al (2010) Adaption of graded Cr/CrN-interlayer thickness to cemented carbide substrates' roughness for improving the adhesion of HPPMS PVD films and the cutting performance. *Surface and Coatings Technology* 205:1564–1570. <https://doi.org/10.1016/j.surfcoat.2010.09.010>
163. Beliardouh NE, Bouzid K, Nouveau C, et al (2015) Tribological and electrochemical performances of Cr/CrN and Cr/CrN/CrAlN multilayer coatings deposited by RF magnetron sputtering. *Tribology International* 82:443–452. <https://doi.org/10.1016/j.triboint.2014.03.018>
164. Hong YS, Kwon SH, Wang T, et al (2011) Effects of Cr interlayer on mechanical and tribological properties of Cr-Al-Si-N nanocomposite coating. *Transactions of Nonferrous Metals Society of China* 21:s62–s67. [https://doi.org/10.1016/S1003-6326\(11\)61062-5](https://doi.org/10.1016/S1003-6326(11)61062-5)
165. Jaffery SHI, Mativenga PT (2012) Wear mechanisms analysis for turning Ti-6Al-4V—towards the development of suitable tool coatings. *Int J Adv Manuf Technol* 58:479–493. <https://doi.org/10.1007/s00170-011-3427-y>
166. Hasegawa H, Kawate M, Suzuki T (2005) Effects of Al contents on microstructures of Cr1–xAlxN and Zr1–xAlxN films synthesized by cathodic arc method. *Surface and Coatings Technology* 200:2409–2413. <https://doi.org/10.1016/j.surfcoat.2004.08.208>
167. Lin J, Mishra B, Moore JJ, Sproul WD (2006) Microstructure, mechanical and tribological properties of Cr1–xAlxN films deposited by pulsed-closed field unbalanced magnetron sputtering (P-CFUBMS). *Surface and Coatings Technology* 201:4329–4334. <https://doi.org/10.1016/j.surfcoat.2006.08.090>

168. Ding X, Zeng XT, Liu YC, et al (2008) Cr_{1-x}Al_xN coatings deposited by lateral rotating cathode arc for high speed machining applications. *Thin Solid Films* 516:1710–1715. <https://doi.org/10.1016/j.tsf.2007.05.019>
169. Mayrhofer PH, Music D, Reeswinkel T, et al (2008) Structure, elastic properties and phase stability of Cr_{1-x}Al_xN. *Acta Materialia* 56:2469–2475. <https://doi.org/10.1016/j.actamat.2008.01.054>
170. Reiter AE, Derflinger VH, Hanselmann B, et al (2005) Investigation of the properties of Al_{1-x}Cr_xN coatings prepared by cathodic arc evaporation. *Surface and Coatings Technology* 200:2114–2122. <https://doi.org/10.1016/j.surfcoat.2005.01.043>
171. Sánchez JE, Sánchez OM, Ipaz L, et al (2010) Mechanical, tribological, and electrochemical behavior of Cr_{1-x}Al_xN coatings deposited by r.f. reactive magnetron co-sputtering method. *Applied Surface Science* 256:2380–2387. <https://doi.org/10.1016/j.apsusc.2009.10.071>
172. Schlögl M, Paulitsch J, Keckes J, Mayrhofer PH (2013) Influence of AlN layers on mechanical properties and thermal stability of Cr-based nitride coatings. *Thin Solid Films* 531:113–118. <https://doi.org/10.1016/j.tsf.2012.12.057>
173. Kawate M, Kimura Hashimoto A, Suzuki T (2003) Oxidation resistance of Cr_{1-x}Al_xN and Ti_{1-x}Al_xN films. *Surface and Coatings Technology* 165:163–167. [https://doi.org/10.1016/S0257-8972\(02\)00473-5](https://doi.org/10.1016/S0257-8972(02)00473-5)
174. He L, Chen L, Xu Y, Du Y (2015) Thermal stability and oxidation resistance of Cr_{1-x}Al_xN coatings with single phase cubic structure. *Journal of Vacuum Science & Technology A* 33:061513. <https://doi.org/10.1116/1.4930424>
175. Reiter AE, Mitterer C, de Figueiredo MR, Franz R (2010) Abrasive and Adhesive Wear Behavior of Arc-Evaporated Al_{1-x}Cr_xN Hard Coatings. *Tribol Lett* 37:605–611. <https://doi.org/10.1007/s11249-009-9557-9>
176. Willmann H, Mayrhofer PH, Persson POÅ, et al (2006) Thermal stability of Al–Cr–N hard coatings. *Scripta Materialia* 54:1847–1851. <https://doi.org/10.1016/j.scriptamat.2006.02.023>
177. Willmann H, Mayrhofer PH, Hultman L, Mitterer C (2008) Hardness evolution of Al–Cr–N coatings under thermal load. *Journal of Materials Research* 23:2880–2885. <https://doi.org/10.1557/JMR.2008.0366>
178. Siad A (2016) Etude numérique et expérimentale de la croissance de couches minces déposées par pulvérisation réactive. Phdthesis, Ecole nationale supérieure d'arts et métiers - ENSAM
179. Ardigo MR, Ahmed M, Besnard A (2014) Stoney Formula: Investigation of Curvature Measurements by Optical Profilometer. *Advanced Materials Research* 996:361–366. <https://doi.org/10.4028/www.scientific.net/AMR.996.361>

180. Doehne E, Stulik DC (1989) APPLICATIONS OF THE ENVIRONMENTAL SCANNING ELECTRON MICROSCOPE TO CONSERVATION SCIENCE. 13
181. Joy DC (1997) Scanning electron microscopy for materials characterization. In: Current Opinion in Solid State and Materials Science. pp 465–468
182. LAGADRILLERE D, QUESADA J (2013) Pratique MEB et microanalyse X - 2013
183. Siegbahn KMB (1971) Electron spectroscopy system with dispersion compensation
184. Siegbahn KMB, Barnett EF (1971) Electron spectroscopy system with a multiple electrode electron lens
185. Inal K, Lebrun JL (1998) Approches numériques et expérimentales du passage micro-macro dans des aciers austéno-ferritiques. J Phys IV France 08:Pr4-69-Pr4-74. <https://doi.org/10.1051/jp4:1998408>
186. Stoney George Gerald, Parsons Charles Algernon (1909) The tension of metallic films deposited by electrolysis. Proceedings of the Royal Society of London Series A, Containing Papers of a Mathematical and Physical Character 82:172–175. <https://doi.org/10.1098/rspa.1909.0021>
187. Oliver WC, Pharr GM (1992) An improved technique for determining hardness and elastic modulus using load and displacement sensing indentation experiments. Journal of Materials Research 7:1564–1583. <https://doi.org/10.1557/JMR.1992.1564>
188. Oliver WC, Pharr GM (2004) Measurement of hardness and elastic modulus by instrumented indentation: Advances in understanding and refinements to methodology. Journal of Materials Research 19:3–20. <https://doi.org/10.1557/jmr.2004.19.1.3>
189. Li X, Bhushan B (2002) A review of nanoindentation continuous stiffness measurement technique and its applications. Materials Characterization 48:11–36. [https://doi.org/10.1016/S1044-5803\(02\)00192-4](https://doi.org/10.1016/S1044-5803(02)00192-4)
190. Rointan FB (2002) Handbook of Hard Coatings: Deposition Technologies, Properties and Applications (Materials and Processing Technology). William Andrew
191. Kabir MS, Munroe P, Zhou Z, Xie Z (2017) Scratch adhesion and tribological behaviour of graded Cr/CrN/CrTiN coatings synthesized by closed-field unbalanced magnetron sputtering. Wear 380–381:163–175. <https://doi.org/10.1016/j.wear.2017.03.020>
192. Bull SJ, Rickerby DS (1990) New developments in the modelling of the hardness and scratch adhesion of thin films. Surface and Coatings Technology 42:149–164. [https://doi.org/10.1016/0257-8972\(90\)90121-R](https://doi.org/10.1016/0257-8972(90)90121-R)
193. Gruss KA, Davis RF (1999) Adhesion measurement of zirconium nitride and amorphous silicon carbide coatings to nickel and titanium alloys. Surface and Coatings Technology 114:156–168. [https://doi.org/10.1016/S0257-8972\(99\)00042-0](https://doi.org/10.1016/S0257-8972(99)00042-0)

194. Archard JF (1953) Contact and Rubbing of Flat Surfaces. *Journal of Applied Physics* 24:981–988. <https://doi.org/10.1063/1.1721448>
195. Lazoglu I, Poulachon G, Ramirez C, et al (2017) Thermal analysis in Ti-6Al-4V drilling. *CIRP Annals* 66:105–108. <https://doi.org/10.1016/j.cirp.2017.04.020>
196. Kusiak A, Martan J, Battaglia J-L, Daniel R (2013) Using pulsed and modulated photothermal radiometry to measure the thermal conductivity of thin films. *Thermochimica Acta* 556:1–5. <https://doi.org/10.1016/j.tca.2013.01.010>
197. Kusiak A, Battaglia J-L, Gomez S, et al (2006) CuO thin films thermal conductivity and interfacial thermal resistance estimation. *The European Physical Journal - Applied Physics* 35:17–27. <https://doi.org/10.1051/epjap:2006064>
198. Maillet D, Andre S, Batsale JC, et al (2000) Thermal quadrupoles: solving the heat equation through integral transforms. Wiley-Blackwell
199. Li D, Guruvenket S, Hassani S, et al (2011) Effect of Cr interlayer on the adhesion and corrosion enhancement of nanocomposite TiN-based coatings deposited on stainless steel 410. *Thin Solid Films* 519:3128–3134. <https://doi.org/10.1016/j.tsf.2010.12.020>
200. Polini R, Barletta M (2008) On the use of CrN/Cr and CrN interlayers in hot filament chemical vapour deposition (HF-CVD) of diamond films onto WC-Co substrates. *Diamond and Related Materials* 17:325–335. <https://doi.org/10.1016/j.diamond.2007.12.059>
201. Broszeit E, Friedrich C, Berg G (1999) Deposition, properties and applications of PVD CrxN coatings. *Surface and Coatings Technology* 115:9–16. [https://doi.org/10.1016/S0257-8972\(99\)00021-3](https://doi.org/10.1016/S0257-8972(99)00021-3)
202. Herr W, Broszeit E (1997) The influence of a heat treatment on the microstructure and mechanical properties of sputtered coatings. *Surface and Coatings Technology* 97:335–340. [https://doi.org/10.1016/S0257-8972\(97\)00196-5](https://doi.org/10.1016/S0257-8972(97)00196-5)
203. Zhang GP, Gao GJ, Wang XQ, et al (2012) Influence of pulsed substrate bias on the structure and properties of Ti–Al–N films deposited by cathodic vacuum arc. *Applied Surface Science* 258:7274–7279. <https://doi.org/10.1016/j.apsusc.2012.03.100>
204. Liu N, Dong L, Li X, et al (2015) Controllable substrate bias voltages effectively tailoring nanocomposite Nb–B–Al–O film properties. *Journal of Alloys and Compounds* 636:363–367. <https://doi.org/10.1016/j.jallcom.2015.02.175>
205. Ye Y, Wang Y, Chen H, et al (2015) Influences of bias voltage on the microstructures and tribological performances of Cr–C–N coatings in seawater. *Surface and Coatings Technology* 270:305–313. <https://doi.org/10.1016/j.surfcoat.2015.02.016>
206. Chang ZK, Wan XS, Pei ZL, et al (2011) Microstructure and mechanical properties of CrN coating deposited by arc ion plating on Ti6Al4V substrate. *Surface and Coatings Technology* 205:4690–4696. <https://doi.org/10.1016/j.surfcoat.2011.04.037>

207. Mahieu S, Ghekiere P, Depla D, De Gryse R (2006) Biaxial alignment in sputter deposited thin films. *Thin Solid Films* 515:1229–1249. <https://doi.org/10.1016/j.tsf.2006.06.027>
208. Guilbaud-Massereau V, Celerier A, Machet J (1995) Study and improvement of the adhesion of chromium thin films deposited by magnetron sputtering. *Thin Solid Films* 258:185–193. [https://doi.org/10.1016/0040-6090\(94\)06360-5](https://doi.org/10.1016/0040-6090(94)06360-5)
209. Thaveedeetrakul A, Witit-anun N, Boonamnuayvitaya V (2012) The role of target-to-substrate distance on the DC magnetron sputtered zirconia thin films' bioactivity. *Applied Surface Science* 258:2612–2619. <https://doi.org/10.1016/j.apsusc.2011.10.104>
210. Darbeida A, von Stebut J, Barthole M, et al (1994) Comparative tribological study of chromium coatings with different specific hardness. *Surface and Coatings Technology* 68–69:582–590. [https://doi.org/10.1016/0257-8972\(94\)90221-6](https://doi.org/10.1016/0257-8972(94)90221-6)
211. Komiya S, Ono S, Umezu N (1977) Hardness and grain size relations for thick chromium films deposited by hollow cathode discharge. *Thin Solid Films* 45:473–479. [https://doi.org/10.1016/0040-6090\(77\)90234-6](https://doi.org/10.1016/0040-6090(77)90234-6)
212. Nilsson SG, Borrísé X, Montelius L (2004) Size effect on Young's modulus of thin chromium cantilevers. *Applied Physics Letters* 85:3555. <https://doi.org/10.1063/1.1807945>
213. Lintymer J, Martin N, Chappe J-M, Takadoum J (2008) Glancing angle deposition to control microstructure and roughness of chromium thin films. *Wear* 264:444–449. <https://doi.org/10.1016/j.wear.2006.08.036>
214. Rouzaud A, Barbier E, Ernoult J, Quesnel E (1995) A method for elastic modulus measurements of magnetron sputtered thin films dedicated to mechanical applications. *Thin Solid Films* 270:270–274. [https://doi.org/10.1016/0040-6090\(95\)06921-6](https://doi.org/10.1016/0040-6090(95)06921-6)
215. Ezazi MA, Quazi MM, Zalnezhad E, Sarhan AAD (2014) Enhancing the tribo-mechanical properties of aerospace AL7075-T6 by magnetron-sputtered Ti/TiN, Cr/CrN & TiCr/TiCrN thin film ceramic coatings. *Ceramics International* 40:15603–15615. <https://doi.org/10.1016/j.ceramint.2014.07.067>
216. Kok YN, Hovsepian PE, Luo Q, et al (2005) Influence of the bias voltage on the structure and the tribological performance of nanoscale multilayer C/Cr PVD coatings. *Thin Solid Films* 475:219–226. <https://doi.org/10.1016/j.tsf.2004.08.042>
217. Schaufler J, Yang G, Durst K, et al (2011) Microscopic study on the interfacial strength of hydrogenated amorphous carbon coating systems. *Surface and Coatings Technology* 205:3429–3433. <https://doi.org/10.1016/j.surfcoat.2010.12.005>
218. Kao WH (2005) Tribological properties and high speed drilling application of MoS₂-Cr coatings. *Wear* 258:812–825. <https://doi.org/10.1016/j.wear.2004.09.045>

219. Houda MOONES (2018) Synthesis of protective coatings on cutting tools for cryogenic machining of titanium alloy: coating characterization and tribological behavior. LABOMAP, ENSAM
220. Kong Q, Ji L, Li H, et al (2011) Composition, microstructure, and properties of CrN_x films deposited using medium frequency magnetron sputtering. *Applied Surface Science* 257:2269–2274. <https://doi.org/10.1016/j.apsusc.2010.09.086>
221. Vaz F, Carvalho P, Cunha L, et al (2004) Property change in ZrN_xO_y thin films: effect of the oxygen fraction and bias voltage. *Thin Solid Films* 469–470:11–17. <https://doi.org/10.1016/j.tsf.2004.06.191>
222. Ohring M (1992) *The Materials Science of Thin Solid Films*. Academic Press, New York
223. Sherman D, Brandon D (2000) *Handbook of Ceramic Hard Materials*. Wiley-VCH, New Jersey
224. Wagner CD, Muilenberg GE (1979) *Handbook of x-ray photoelectron spectroscopy: a reference book of standard data for use in x-ray photoelectron spectroscopy*. Physical Electronics Division, Perkin-Elmer Corp., Eden Prairie, Minn.
225. Latha G, Rajendran N, Rajeswari S (1997) Influence of alloying elements on the corrosion performance of alloy 33 and alloy 24 in seawater. *J of Materi Eng and Perform* 6:743–748. <https://doi.org/10.1007/s11665-997-0076-2>
226. Romand M, Roubin, M. (1976) ESCA STUDIES OF CHROMIUM AND VANADIUM NITRIDES. *Analisis* 4:309
227. Lv Y, Ji L, Liu X, et al (2012) Influence of substrate bias voltage on structure and properties of the CrAlN films deposited by unbalanced magnetron sputtering. *Applied Surface Science* 258:3864–3870. <https://doi.org/10.1016/j.apsusc.2011.12.048>
228. Warcholinski B, Gilewicz A, Ratajski J, et al (2012) An analysis of macroparticle-related defects on CrCN and CrN coatings in dependence of the substrate bias voltage. *Vacuum* 86:1235–1239. <https://doi.org/10.1016/j.vacuum.2011.04.023>
229. Odén M, Ericsson C, Håkansson G, Ljungcrantz H (1999) Microstructure and mechanical behavior of arc-evaporated Cr–N coatings. *Surface and Coatings Technology* 114:39–51. [https://doi.org/10.1016/S0257-8972\(99\)00019-5](https://doi.org/10.1016/S0257-8972(99)00019-5)
230. Lin J, Mishra B, Moore JJ, Sproul WD (2008) A study of the oxidation behavior of CrN and CrAlN thin films in air using DSC and TGA analyses. *Surface and Coatings Technology* 202:3272–3283. <https://doi.org/10.1016/j.surfcoat.2007.11.037>
231. Berg G, Friedrich C, Broszeit E, Berger C (1996) Development of chromium nitride coatings substituting titanium nitride. *Surface and Coatings Technology* 86–87:184–191. [https://doi.org/10.1016/S0257-8972\(96\)03042-3](https://doi.org/10.1016/S0257-8972(96)03042-3)

232. Knuyt G, Quaeys C, D'Haen J, Stals LM (1995) A model for texture evolution in a growing film. *Surface and Coatings Technology* 76–77:311–315. [https://doi.org/10.1016/0257-8972\(95\)02587-1](https://doi.org/10.1016/0257-8972(95)02587-1)
233. Knuyt G, Quaeys C, D'Haen J, Stals LM (1995) A quantitative model for the evolution from random orientation to a unique texture in PVD thin film growth. *Thin Solid Films* 258:159–169. [https://doi.org/10.1016/0040-6090\(94\)06353-2](https://doi.org/10.1016/0040-6090(94)06353-2)
234. Perry A, Valvoda V, Rafaja D (1994) On the residual stress and picostructure of titanium nitride films—II. A picostructural model. *Vacuum* 45:11–14. [https://doi.org/10.1016/0042-207X\(94\)90332-8](https://doi.org/10.1016/0042-207X(94)90332-8)
235. Kacher J, Landon C, Adams BL, Fullwood D (2009) Bragg's Law diffraction simulations for electron backscatter diffraction analysis. *Ultramicroscopy* 109:1148–1156. <https://doi.org/10.1016/j.ultramicro.2009.04.007>
236. Yousaf MI, Pelenovich VO, Yang B, et al (2015) Influence of substrate rotation speed on the structure and mechanical properties of nanocrystalline AlTiN/MoN coatings synthesized by cathodic arc ion-plating. *Surface and Coatings Technology* 265:117–124. <https://doi.org/10.1016/j.surfcoat.2015.01.049>
237. Tian CX, Yang B, Yan SJ, et al (2013) Influence of substrate rotation speed on the structure and mechanical properties of AlTiN/CrN coatings. *Surface and Coatings Technology* 228:S228–S232. <https://doi.org/10.1016/j.surfcoat.2012.05.141>
238. Pelleg J, Zevin LZ, Lungo S, Croitoru N (1991) Reactive-sputter-deposited TiN films on glass substrates. *Thin Solid Films* 197:117–128. [https://doi.org/10.1016/0040-6090\(91\)90225-M](https://doi.org/10.1016/0040-6090(91)90225-M)
239. Steckelmacher W (2001) Introduction to surface and thin film processes. *Vacuum* 62:387–388. [https://doi.org/10.1016/S0042-207X\(00\)00430-9](https://doi.org/10.1016/S0042-207X(00)00430-9)
240. Lee J-W, Tien S-K, Kuo Y-C, Chen C-M (2006) The mechanical properties evaluation of the CrN coatings deposited by the pulsed DC reactive magnetron sputtering. *Surface and Coatings Technology* 200:3330–3335. <https://doi.org/10.1016/j.surfcoat.2005.07.047>
241. Sundgren J-E (1985) Structure and properties of TiN coatings. *Thin Solid Films* 128:21–44. [https://doi.org/10.1016/0040-6090\(85\)90333-5](https://doi.org/10.1016/0040-6090(85)90333-5)
242. Li H, Sun P, Cheng D, Liu Z (2021) Effects of deposition temperature on structure, residual stress and corrosion behavior of Cr/TiN/Ti/TiN films. *Ceramics International* 47:34909–34917. <https://doi.org/10.1016/j.ceramint.2021.09.032>
243. Martín-tovar EA, Daza LG, López-arreguín AJR, et al (2017) Effect of substrate rotation speed on structure and properties of Al-doped ZnO thin films prepared by rf-sputtering. *Transactions of Nonferrous Metals Society of China* 27:2055–2062. [https://doi.org/10.1016/S1003-6326\(17\)60230-9](https://doi.org/10.1016/S1003-6326(17)60230-9)

244. Tlili B (2010) Caractérisation de films durs multicouches élaborés par pulvérisation magnétron. Influence des conditions d'élaboration sur leurs propriétés. Phdthesis, Arts et Métiers ParisTech
245. Romero J, Gómez MA, Esteve J, et al (2006) CrAlN coatings deposited by cathodic arc evaporation at different substrate bias. *Thin Solid Films* 515:113–117. <https://doi.org/10.1016/j.tsf.2006.01.061>
246. Kong Q, Ji L, Li H, et al (2011) Influence of substrate bias voltage on the microstructure and residual stress of CrN films deposited by medium frequency magnetron sputtering. *Materials Science and Engineering: B* 176:850–854. <https://doi.org/10.1016/j.mseb.2011.04.015>
247. Espinoza-Beltrán FJ, Che-Soberanis O, García-González L, Morales-Hernández J (2003) Effect of the substrate bias potential on crystalline grain size, intrinsic stress and hardness of vacuum arc evaporated TiN/c-Si coatings. *Thin Solid Films* 437:170–175. [https://doi.org/10.1016/S0040-6090\(03\)00568-6](https://doi.org/10.1016/S0040-6090(03)00568-6)
248. Wang W, Ji L, Li H, et al (2019) Influence of rotational speed on structure, mechanical and electrical properties of TiC/GLC composite films. *Diamond and Related Materials* 92:65–73. <https://doi.org/10.1016/j.diamond.2018.12.004>
249. Jönsson B, Hogmark S (1984) Hardness measurements of thin films. *Thin Solid Films* 114:257–269. [https://doi.org/10.1016/0040-6090\(84\)90123-8](https://doi.org/10.1016/0040-6090(84)90123-8)
250. Rahmoun K, Iost A, Keryvin V, et al (2009) A multilayer model for describing hardness variations of aged porous silicon low-dielectric-constant thin films. *Thin Solid Films* 518:213–221. <https://doi.org/10.1016/j.tsf.2009.07.040>
251. Rebholz C, Ziegele H, Leyland A, Matthews A (1999) Structure, mechanical and tribological properties of nitrogen-containing chromium coatings prepared by reactive magnetron sputtering. *Surface and Coatings Technology* 115:222–229. [https://doi.org/10.1016/S0257-8972\(99\)00240-6](https://doi.org/10.1016/S0257-8972(99)00240-6)
252. Ichimura H, Ando I (2001) Mechanical properties of arc-evaporated CrN coatings: Part I — nanoindentation hardness and elastic modulus. *Surface and Coatings Technology* 145:88–93. [https://doi.org/10.1016/S0257-8972\(01\)01290-7](https://doi.org/10.1016/S0257-8972(01)01290-7)
253. Ducros C, Benevent V, Sanchette F (2003) Deposition, characterization and machining performance of multilayer PVD coatings on cemented carbide cutting tools. *Surface and Coatings Technology* 163–164:681–688. [https://doi.org/10.1016/S0257-8972\(02\)00656-4](https://doi.org/10.1016/S0257-8972(02)00656-4)
254. He X-M, Baker N, Kehler BA, et al (2000) Structure, hardness, and tribological properties of reactive magnetron sputtered chromium nitride films. *Journal of Vacuum Science & Technology A* 18:30–36. <https://doi.org/10.1116/1.582154>
255. Ehrlich A, Kühn M, Richter F, Hoyer W (1995) Complex characterisation of vacuum arc-deposited chromium nitride thin films. *Surface and Coatings Technology* 76–77:280–286. [https://doi.org/10.1016/0257-8972\(95\)02583-9](https://doi.org/10.1016/0257-8972(95)02583-9)

256. Panich N, Sun Y (2006) Effect of substrate rotation on structure, hardness and adhesion of magnetron sputtered TiB₂ coating on high speed steel. *Thin Solid Films* 500:190–196. <https://doi.org/10.1016/j.tsf.2005.11.055>
257. Bendavid A, Martin PJ, Takikawa H (2000) Deposition and modification of titanium dioxide thin films by filtered arc deposition. *Thin Solid Films* 360:241–249. [https://doi.org/10.1016/S0040-6090\(99\)00937-2](https://doi.org/10.1016/S0040-6090(99)00937-2)
258. Ming'e W, Shuili G, Guojia M, et al (2015) Effects of Deposition Temperature on the Structure and Hardness of BN Films Prepared by a Gradient Temperature Method. *Rare Metal Materials and Engineering* 44:1108–1111. [https://doi.org/10.1016/S1875-5372\(15\)30076-X](https://doi.org/10.1016/S1875-5372(15)30076-X)
259. Balakrishnan G, Tripura Sundari S, Ramaseshan R, et al (2013) Effect of substrate temperature on microstructure and optical properties of nanocrystalline alumina thin films. *Ceramics International* 39:9017–9023. <https://doi.org/10.1016/j.ceramint.2013.04.104>
260. Zegtouf H, Saoula N, Azibi M, et al (2020) Influence of substrate bias voltage on structure, mechanical and corrosion properties of ZrO₂ thin films deposited by Reactive Magnetron Sputter Deposition. *Surface and Coatings Technology* 393:125821. <https://doi.org/10.1016/j.surfcoat.2020.125821>
261. Escobar D, Ospina R, Gómez AG, Restrepo-Parra E (2015) Microstructure, residual stress and hardness study of nanocrystalline titanium–zirconium nitride thin films. *Ceramics International* 41:947–952. <https://doi.org/10.1016/j.ceramint.2014.09.012>
262. Bull SJ (1997) Failure mode maps in the thin film scratch adhesion test. *Tribology International* 30:491–498. [https://doi.org/10.1016/S0301-679X\(97\)00012-1](https://doi.org/10.1016/S0301-679X(97)00012-1)
263. Niu EW, Li L, Lv GH, et al (2008) Characterization of Ti–Zr–N films deposited by cathodic vacuum arc with different substrate bias. *Applied Surface Science* 254:3909–3914. <https://doi.org/10.1016/j.apsusc.2007.12.022>
264. Thouless MD (1998) An analysis of spalling in the microscratch test. *Engineering Fracture Mechanics* 61:75–81. [https://doi.org/10.1016/S0013-7944\(98\)00049-6](https://doi.org/10.1016/S0013-7944(98)00049-6)
265. Toonder JD, Malzbender J, With GD, Balkenende R (2002) Fracture Toughness and Adhesion Energy of Sol-gel Coatings on Glass. *Journal of Materials Research* 17:224–233. <https://doi.org/10.1557/JMR.2002.0032>
266. Schmitt T (2010) Mécanismes de dégradation de revêtements base CrN élaborés par arc-PVD : Intérêt d'une nano-architecture. Phdthesis, Ecole Centrale de Lyon
267. Hasegawa H, Suzuki T (2004) Effects of second metal contents on microstructure and micro-hardness of ternary nitride films synthesized by cathodic arc method. *Surface and Coatings Technology* 188–189:234–240. <https://doi.org/10.1016/j.surfcoat.2004.08.033>

268. Ayako K, Hiroyuki H, Kunihiro Y, Tetsuya S (1999) Effects of Al content on hardness, lattice parameter and microstructure of Ti_{1-x}Al_xN films. *Surface and Coatings Technology* 120–121:438–441. [https://doi.org/10.1016/S0257-8972\(99\)00491-0](https://doi.org/10.1016/S0257-8972(99)00491-0)
269. Chen L, Du Y, Wang SQ, Li J (2007) A comparative research on physical and mechanical properties of (Ti, Al)N and (Cr, Al)N PVD coatings with high Al content. *International Journal of Refractory Metals and Hard Materials* 25:400–404. <https://doi.org/10.1016/j.ijrmhm.2006.11.006>
270. Grove TC (1986) Arcing problems encountered during sputter deposition of aluminum. *Advanced Energy Industries*
271. Carter DC (2008) Arc prevention in magnetron pattering process. In: *Proceedings of the 51st Annual Technical Conference*. pp 380–385
272. Scholl RA (1997) Power systems for reactive sputtering of insulating films. *Surface and Coatings Technology* 93:7–13. [https://doi.org/10.1016/S0257-8972\(97\)00032-7](https://doi.org/10.1016/S0257-8972(97)00032-7)
273. Hsiao Y-C, Lee J-W, Yang Y-C, Lou B-S (2013) Effects of duty cycle and pulse frequency on the fabrication of AlCrN thin films deposited by high power impulse magnetron sputtering. *Thin Solid Films* 549:281–291. <https://doi.org/10.1016/j.tsf.2013.08.059>
274. Simon AH (2018) Chapter 7 - Sputter Processing. In: Seshan K, Schepis D (eds) *Handbook of Thin Film Deposition (Fourth Edition)*. William Andrew Publishing, pp 195–230
275. Poirier DM, Weaver JH (1993) Carbon (as Graphite, Buckminsterfullerene, and Diamond) by XPS. *Surface Science Spectra* 2:232–241. <https://doi.org/10.1116/1.1247704>
276. McGuire GE, Schweitzer GK, Carlson TA (1973) Core electron binding energies in some Group IIIA, VB, and VIB compounds. *Inorg Chem* 12:2450–2453. <https://doi.org/10.1021/ic50128a045>
277. Wagner CD, Riggs WM, Davis LE, et al (1979) Perkin-Elmer Corporation. Physical Electronics Division
278. Taylor JA, Rabalais JW (1981) Reaction of N₂⁺ beams with aluminum surfaces. *J Chem Phys* 75:1735–1745. <https://doi.org/10.1063/1.442251>
279. Correa JF, Aperador W, Caicedo JC, et al (2020) Structural, mechanical and tribological behavior of TiCN, CrAlN and BCN coatings in lubricated and non-lubricated environments in manufactured devices. *Materials Chemistry and Physics* 252:123164. <https://doi.org/10.1016/j.matchemphys.2020.123164>
280. Pengfei H, Bailing J (2011) Study on tribological property of CrCN coating based on magnetron sputtering plating technique. *Vacuum* 85:994–998. <https://doi.org/10.1016/j.vacuum.2011.02.007>

281. Hong SG, Kwon S-H, Kang S-W, Kim KH (2008) Influence of substrate bias voltage on structure and properties of Cr–Mo–Si–N coatings prepared by a hybrid coating system. *Surface and Coatings Technology* 203:624–627. <https://doi.org/10.1016/j.surfcoat.2008.06.125>
282. Nouveau C, Tlili B, Aknouche H, et al (2012) Comparison of CrAlN layers obtained with one (CrAl) or two targets (Cr and Al) by magnetron sputtering. *Thin Solid Films* 520:2932–2937. <https://doi.org/10.1016/j.tsf.2011.11.049>
283. Quek SS, Chooi ZH, Wu Z, et al (2016) The inverse hall–petch relation in nanocrystalline metals: A discrete dislocation dynamics analysis. *Journal of the Mechanics and Physics of Solids* 88:252–266. <https://doi.org/10.1016/j.jmps.2015.12.012>
284. Barshilia HC, Selvakumar N, Deepthi B, Rajam KS (2006) A comparative study of reactive direct current magnetron sputtered CrAlN and CrN coatings. *Surface and Coatings Technology* 201:2193–2201. <https://doi.org/10.1016/j.surfcoat.2006.03.037>
285. Ding X-Z, Zeng XT (2005) Structural, mechanical and tribological properties of CrAlN coatings deposited by reactive unbalanced magnetron sputtering. *Surface and Coatings Technology* 200:1372–1376. <https://doi.org/10.1016/j.surfcoat.2005.08.072>
286. Warcholinski B, Gilewicz A (2013) Effect of substrate bias voltage on the properties of CrCN and CrN coatings deposited by cathodic arc evaporation. *Vacuum* 90:145–150. <https://doi.org/10.1016/j.vacuum.2012.04.039>
287. Li T, Li M, Zhou Y (2007) Phase segregation and its effect on the adhesion of Cr–Al–N coatings on K38G alloy prepared by magnetron sputtering method. *Surface and Coatings Technology* 201:7692–7698. <https://doi.org/10.1016/j.surfcoat.2007.02.044>
288. Kim GS, Lee SY (2006) Microstructure and mechanical properties of AlCrN films deposited by CFUBMS. *Surface and Coatings Technology* 201:4361–4366. <https://doi.org/10.1016/j.surfcoat.2006.08.076>
289. Uchida M, Nihira N, Mitsuo A, et al (2004) Friction and wear properties of CrAlN and CrVN films deposited by cathodic arc ion plating method. *Surface and Coatings Technology* 177–178:627–630. [https://doi.org/10.1016/S0257-8972\(03\)00937-X](https://doi.org/10.1016/S0257-8972(03)00937-X)
290. Gong M, Chen J, Deng X, Wu S (2017) Sliding wear behavior of TiAlN and AlCrN coatings on a unique cemented carbide substrate. *International Journal of Refractory Metals and Hard Materials* 69:209–214. <https://doi.org/10.1016/j.ijrmhm.2017.08.003>
291. Lin CH, Hsiao Lei Wang, Min Hsiung Hon (1996) The effect of residual stress on the adhesion of PECVD-coated aluminum oxide film on glass. *Thin Solid Films* 283:171–174. [https://doi.org/10.1016/0040-6090\(95\)08135-6](https://doi.org/10.1016/0040-6090(95)08135-6)
292. Wiecinski P, Smolik J, Garbacz H, et al (2017) Microstructure and properties of metal/ceramic and ceramic/ceramic multilayer coatings on titanium alloy Ti6Al4V. *Surface and Coatings Technology* 309:709–718. <https://doi.org/10.1016/j.surfcoat.2016.11.003>

293. Ellis EA, Chmielus M, Lin M-T, et al (2016) Driving forces for texture transformation in thin Ag films. *Acta Materialia* 105:495–504. <https://doi.org/10.1016/j.actamat.2015.12.020>
294. Ahmed M (2013) Effect of thermal annealing and carbon implantation on the functional properties of nanocomposite TiSiN coatings on steel. Edith Cowan University
295. Guan X, Wang Y, Zhang G, et al (2017) Microstructures and properties of Zr/CrN multilayer coatings fabricated by multi-arc ion plating. *Tribology International* 106:78–87. <https://doi.org/10.1016/j.triboint.2016.10.036>
296. Mori T, Fukuda S, Takemura Y (2001) Improvement of mechanical properties of Ti/TiN multilayer film deposited by sputtering. *Surface and Coatings Technology* 140:122–127. [https://doi.org/10.1016/S0257-8972\(01\)01021-0](https://doi.org/10.1016/S0257-8972(01)01021-0)
297. Zhang JJ, Wang MX, Yang J, et al (2007) Enhancing mechanical and tribological performance of multilayered CrN/ZrN coatings. *Surface and Coatings Technology* 201:5186–5189. <https://doi.org/10.1016/j.surfcoat.2006.07.093>
298. Miao XS, Chan YC, Pun EYB (1998) Protective AlCrN film for organic photoconductors. *Thin Solid Films* 324:180–183. [https://doi.org/10.1016/S0040-6090\(98\)00374-5](https://doi.org/10.1016/S0040-6090(98)00374-5)
299. Samani MK, Chen GCK, Ding XZ, Zeng XT (2010) Thermal Conductivity of CrAlN and TiAlN Coatings Deposited by Lateral Rotating Cathode Arc. *Key Engineering Materials* 447–448:705–709. <https://doi.org/10.4028/www.scientific.net/KEM.447-448.705>
300. Tlili B, Mustapha N, Nouveau C, et al (2010) Correlation between thermal properties and aluminum fractions in CrAlN layers deposited by PVD technique. *Vacuum* 84:1067–1074. <https://doi.org/10.1016/j.vacuum.2010.01.011>
301. Astakhov VP (2006) *Tribology of Metal Cutting*. Elsevier
302. Zvorykin KA (1896) On the force and energy necessary to separate the chip from the workpiece. *Vetnik Promyslennostie* 123:
303. W. Cheng, J.C. Outeiro (2022) Modelling orthogonal cutting of Ti-6Al-4 V titanium alloy using a constitutive model considering the state of stress. *The International Journal of Advanced Manufacturing Technology* (accepted for publication): <https://doi.org/10.1007/s00170-021-08446-9>
304. Outeiro JC, Umbrello D, M'Saoubi R, Jawahir IS (2015) Evaluation of Present Numerical Models for Predicting Metal Cutting Performance And Residual Stresses. *Machining Science and Technology* 19:183–216. <https://doi.org/10.1080/10910344.2015.1018537>
305. Cheng W, Outeiro J, Costes J-P, et al (2019) A constitutive model for Ti6Al4V considering the state of stress and strain rate effects. *Mechanics of Materials* 137:103103. <https://doi.org/10.1016/j.mechmat.2019.103103>

306. Upadhyaya GS (2001) Materials science of cemented carbides — an overview. *Materials & Design* 22:483–489. [https://doi.org/10.1016/S0261-3069\(01\)00007-3](https://doi.org/10.1016/S0261-3069(01)00007-3)
307. Ruoff AL, Wanagel J (1975) Yield stress of cemented tungsten carbide. *Journal of Applied Physics* 46:4647–4648. <https://doi.org/10.1063/1.321542>
308. Johnson GR, Cook WH (1985) Fracture characteristics of three metals subjected to various strains, strain rates, temperatures and pressures. *Engineering Fracture Mechanics* 21:31–48. [https://doi.org/10.1016/0013-7944\(85\)90052-9](https://doi.org/10.1016/0013-7944(85)90052-9)
309. Melkote SN, Grzesik W, Outeiro J, et al (2017) Advances in material and friction data for modelling of metal machining. *CIRP Annals* 66:731–754. <https://doi.org/10.1016/j.cirp.2017.05.002>
310. HERTZ H (1881) On the contact of elastic solids. *Z Reine Angew Mathematik* 92:156–171
311. Hills DA, Nowell D, Sackfield A (1998) *Mechanics of elastic contacts*, 1993. Butterworth-Heinemann, London) 21:235–237
312. Meier L, Schaal N, Wegener K (2017) In-process Measurement of the Coefficient of Friction on Titanium. *Procedia CIRP* 58:163–168. <https://doi.org/10.1016/j.procir.2017.03.212>
313. Tirelli S, Chiappini E, Strano M, et al (2014) Experimental Comparison between Traditional and Cryogenic Cooling Conditions in Rough Turning of Ti-6Al-4V. *Key Engineering Materials* 611–612:1174–1185. <https://doi.org/10.4028/www.scientific.net/KEM.611-612.1174>
314. Venugopal KA, Paul S, Chattopadhyay AB (2007) Growth of tool wear in turning of Ti-6Al-4V alloy under cryogenic cooling. *Wear* 262:1071–1078. <https://doi.org/10.1016/j.wear.2006.11.010>
315. Venugopal KA, Paul S, Chattopadhyay AB (2004) On Effect of Cryogenic Cooling on Tool Wear in Turning Ti-6Al-4V Alloy. In: *Proceedings of the 34th International MATADOR Conference*. Springer, London, pp 127–132
316. Denguir L a., Besnard A, Fromentin G, et al (2016) Flank wear prediction in milling AISI 4140 based on cutting forces PCA for different cutting edge preparations. *International Journal of Machining and Machinability of Materials* 18:273–287. <https://doi.org/10.1504/IJMMM.2016.076278>
317. Shen X, Nie X, Hu H, Tjong J (2012) Effects of coating thickness on thermal conductivities of alumina coatings and alumina/aluminum hybrid materials prepared using plasma electrolytic oxidation. *Surface and Coatings Technology* 207:96–101. <https://doi.org/10.1016/j.surfcoat.2012.06.009>

Appendix

Appendix A : Tribometer

Figure 195 shows the TAP assembly of pin-on-disc tribological test on CNC turning machine. TAP is a French abbreviation (Tribomètre à Pion), which means tribometer for pin. The tribometer composed of a piston, surrounded and fixed by a casing. The piston can move freely in the casing. The set back of the piston can be fixed by external pressure supply (compressed air, CO₂, etc.). The pin is inserted in the piston by a locking nut. This tribometer work with a force acquisition system like Kistler. The equipment adapts turning and milling.

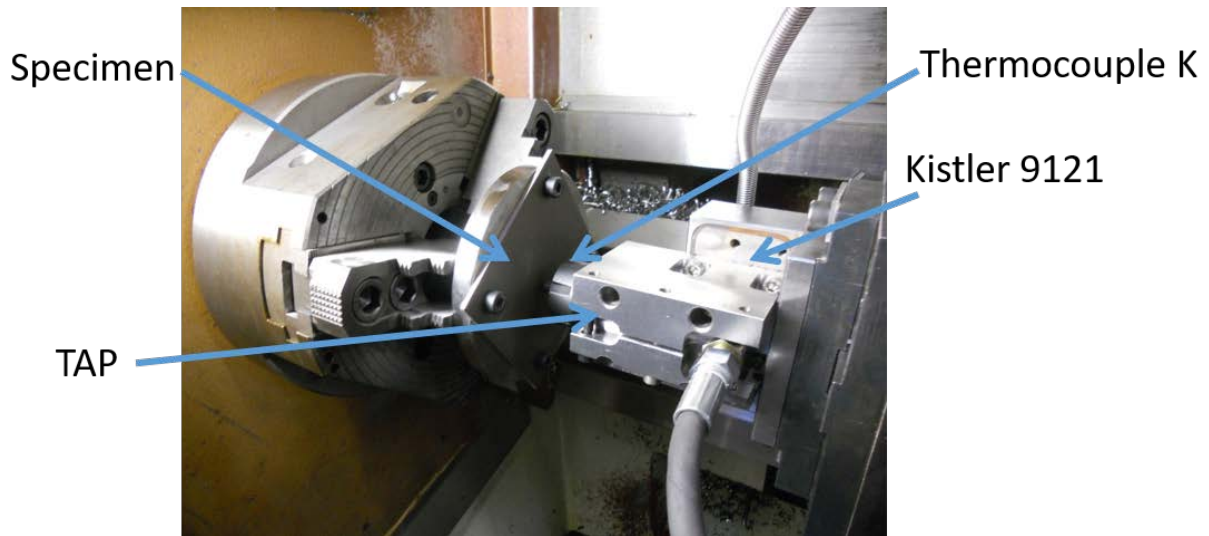


Figure 195. TAP assembly of pin-on-disc tribological test on CNC turning machine (Baizeau, Ramirez, Rossi / Lournand, LABOMAP, Cluny, Arts et Métiers).

Appendix B : Pin technical draw

Figure 196 illustrated the technical draw of pin used in tribological tests. The length of the pin is 40 mm, the diameter is 8 mm. The radius of the sphere part is 6 mm and the arithmetic roughness is $0.4 \mu\text{m}$.

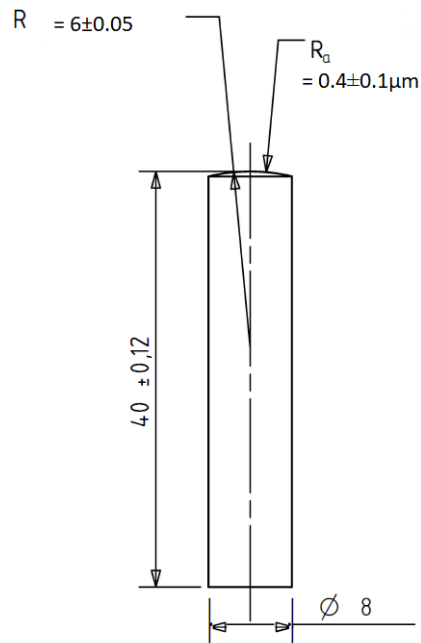


Figure 196. Technical draw of pin used in tribological tests.

Appendix C : Tool holder

The tool holder used in the tool wear tests is a modified PCLNL 2525M-12-JHP used by Lequien [61]. The delivery channels of LN2 is integrated into the tool holder. The LN2 served both the rake face and flank face of the cutting insert, with a diameter of 3 mm and 1.5 mm, respectively.

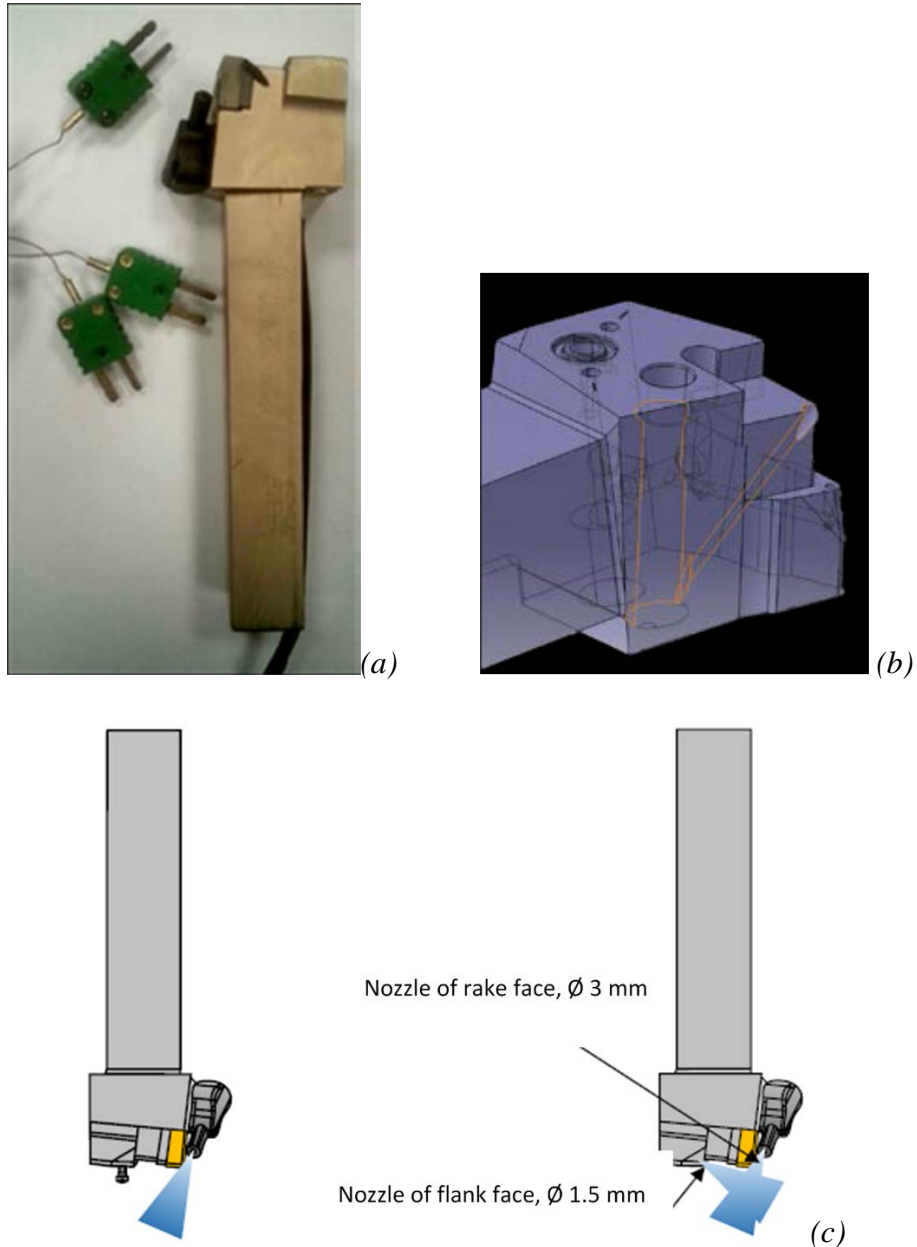


Figure 197. (a) Tool holder PCLNL 2525M-12-JHP, (b) schematic diagram of the channels to deliver the LN2 (c) and the nozzles positions and diameters [61].

Appendix D : Method of determination for adhesion volume

With the help of a home-made Python script integrated in Gwyddion, created by Jean-Marc AUGER, a post-doc in LABOMAP, we are able to determine precisely the adhesion volume on pin's spherical geometry.

The surface 3D information of each pin was measured by *Alicona InfiniteFocus*. Instead of removing the background (curvature part) by fitting a second order polynomial equation (which could be not precise because the center of sphere is hard to find), the principal function of this program is to find exactly the center of sphere, by choosing a large area containing the coordination information and the radius of the pin (*Figure 198 (a)*). Then it subtracts the background. After the treatment, the height information is on a plan (same level of height)(*Figure 198 (b)*), the adhesion volume can be extracted by removing the plan (*Figure 198 (c)(d)*) and the volume is calculated by differential equations.

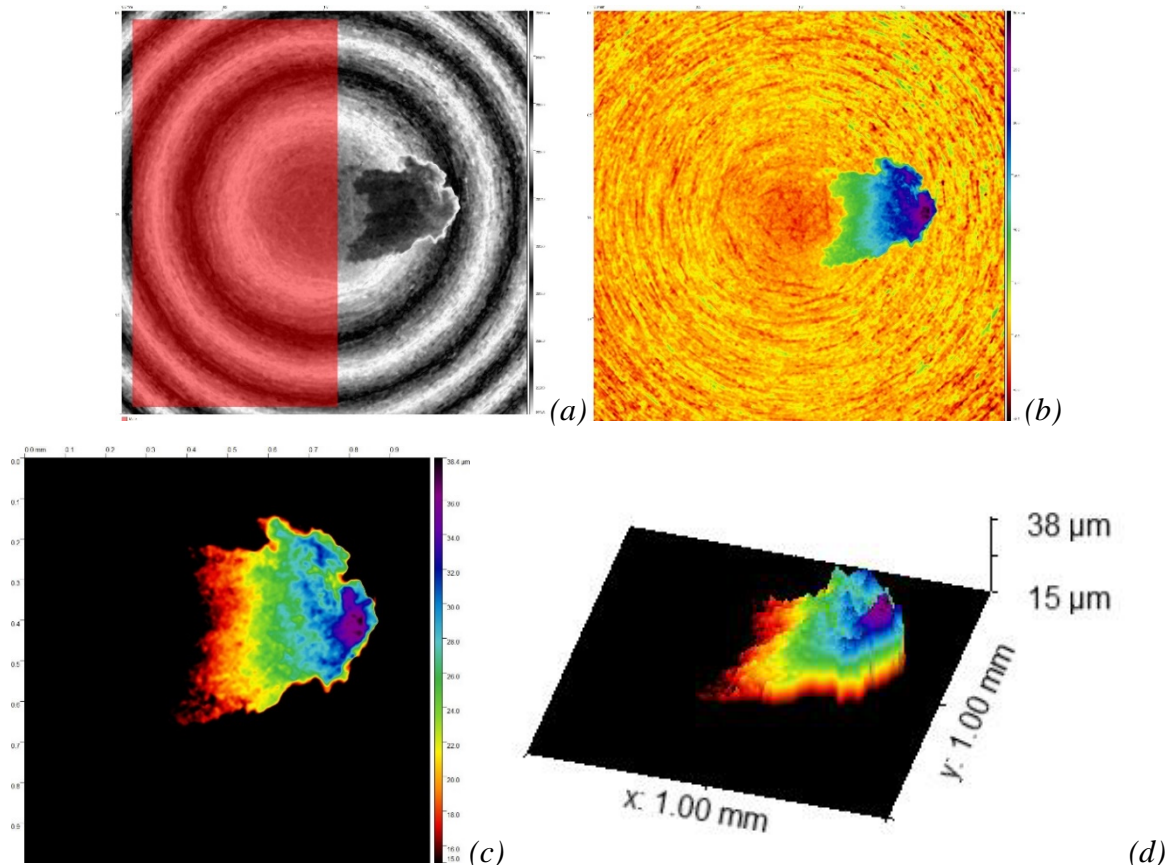


Figure 198. Example of extracting the adhesion volume: a) determination of background, b) information after subtracting background, c) adhesion volume after removing supplementary information d) 3D view of adhesion volume

Appendix E : Wear tracks of pin-on-disc friction tests

Figure 199 shows the wear tracks formed during dry pin-on-disc friction tests on coated substrates. The coatings are: (Figure 199a) Cr underlayer, (Figure 199b) CrN 300°C-500V, (Figure 199c) CrAlN with $x=0.14$, (Figure 199d) AlCrN 300°C-250V. As shown in these pictures, all the coatings are removed after this test, Ti6Al4V adhesion is observed in the wear tracks.

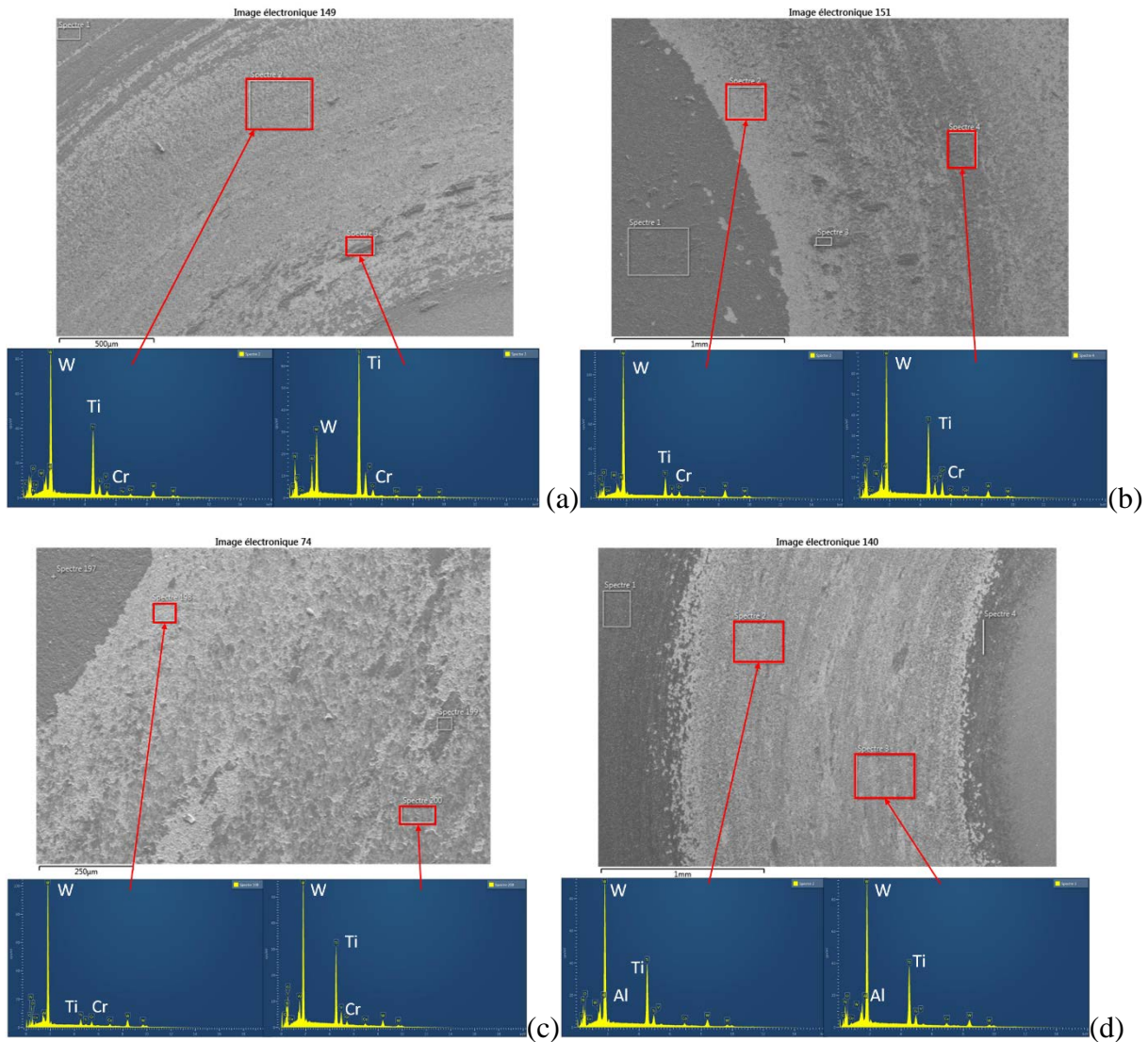


Figure 199. EDS analysis of wear tracks of worn WC substrate coated by: a) Cr underlayer, b) CrN 300°C-500V, c) $Cr_{1-x}Al_xN$ with $x=0.14$ and d) AlCrN 300°C-250V in pin-on-disc friction test without lubricant.

Appendix F : Surface topography of the pins used in the tribological tests

Figure 200 presents the surface topography of coated pins. The coatings follow the substrate texture, since the coatings successfully covers all the sphere surface of the pin, when the trails forms in production of the pins are still visible. The roughness is listed in Table 66. AlCrN monolayer presents the roughest texture when CrN monolayer presents the smoothest texture when we compare the arithmetic average roughness, the root mean square roughness and the maximum height of the surface.

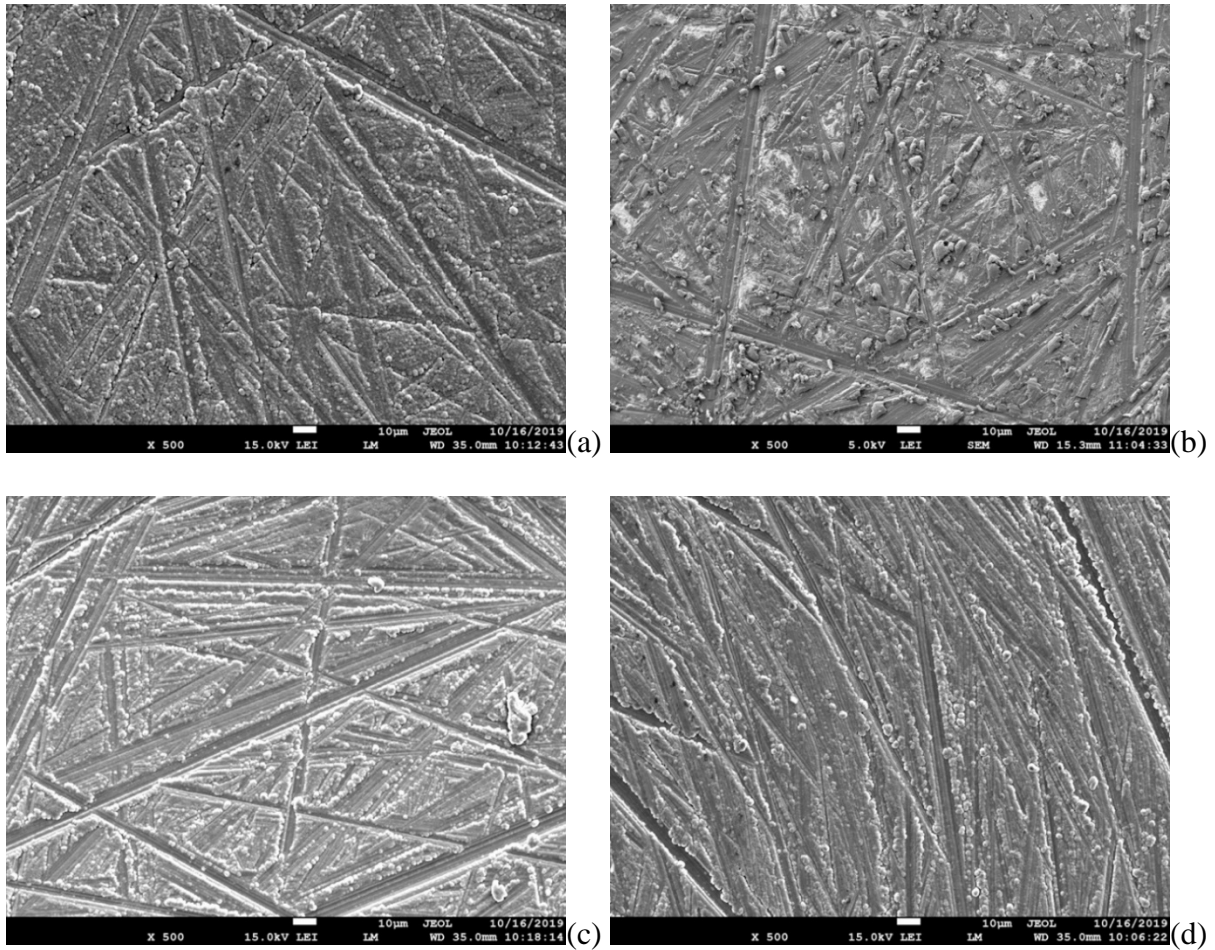


Figure 200. SEM images of the surface morphology of: CrN (a) AlCrN (b) M2 (c) and M4 (d) coated pins

Table 66. Surface roughness of the coated pins.

	CrN	AlCrN	M2	M4
Ra (µm)	0.66	0.7	0.71	0.7
Rq (µm)	0.84	0.91	0.88	0.86
Rt (µm)	4.41	6.21	5.03	4.98

Appendix G : Forces acting in the pins in the tribological tests

Table 67. Surface roughness of the workpiece

N°	1	2	3	4	5	6	7	8	9	10
R _a (μm)	0.21	0.22	0.22	0.23	0.23	0.2	0.22	0.2	0.22	0.25
R _q (μm)	0.26	0.28	0.27	0.28	0.28	0.24	0.27	0.25	0.26	0.29
R _t (μm)	1.16	1.23	1.2	1.21	1.18	1.12	1.14	1.15	1.08	1.36

Forces for flood conditions

Figure 201 illustrates the normal force measured during tribological tests for all pins and sliding speeds for flood lubricant condition. The normal forces decrease generally from 10 m/min to 60 m/min then increase, especially at 100 m/min.

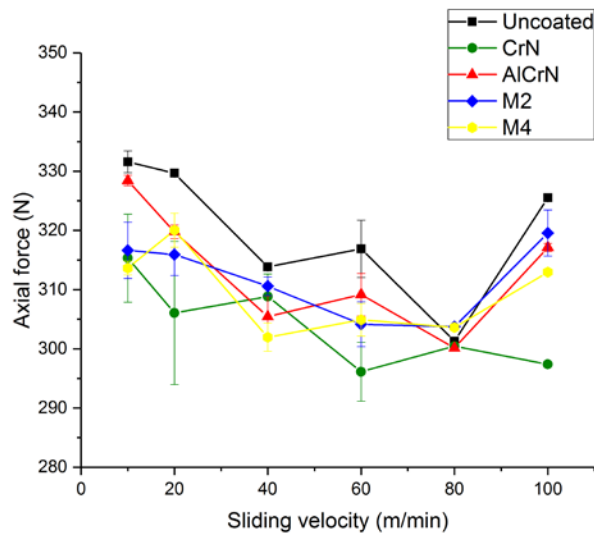


Figure 201. Normal force as a function of the sliding speed and for different coatings in flood conditions (Average contact pressure equals to 872 MPa).

Figure 202 illustrates the tangential force measured during tribological tests for all pins and sliding speeds for flood lubricant condition. The tangential forces decrease generally from 10 m/min to 60 m/min then increase, especially at 100 m/min.

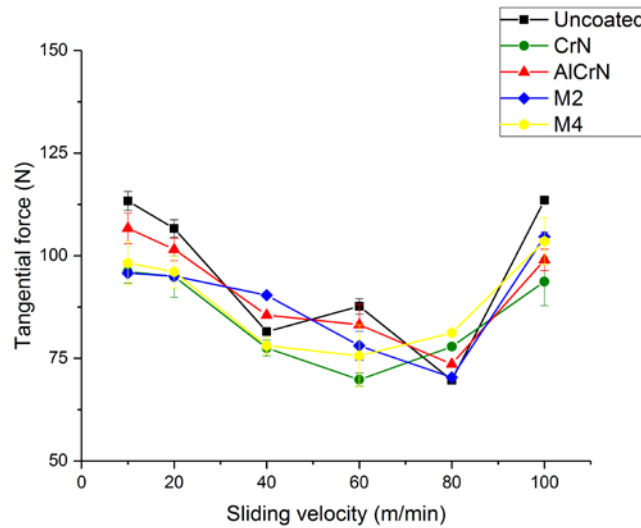


Figure 202. Tangential force as a function of the sliding speed for different coatings in flood conditions (Average contact pressure equals to 872 MPa).

Forces for LN2 conditions

Figure 203 illustrates the normal force measured during tribological tests for all pins and sliding speeds during cryogenic assistance. The normal force in this case is more random than in flood lubricant case, this may reveal the unstable LN2 projection on to the pin.

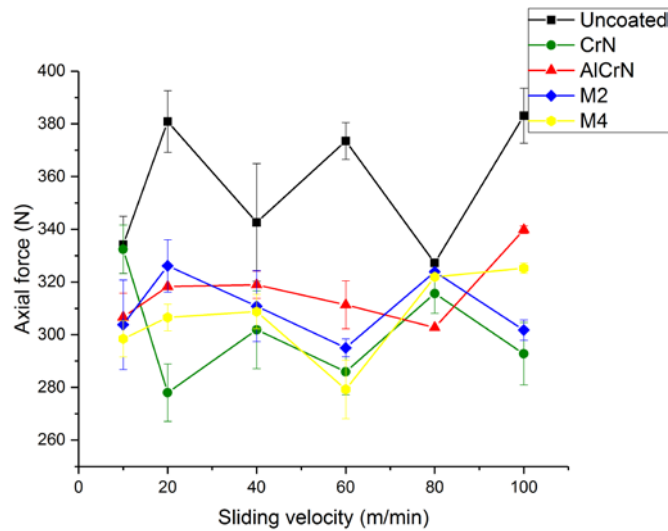


Figure 203. Normal force as a function of the sliding speed for different coatings under LN2 conditions (average contact pressure equals to 872 MPa).

Figure 204 illustrates the tangential force measured during tribological tests for all pins and sliding speeds during cryogenic assistance. The tangential forces decrease generally from 10 m/min to 60 m/min then increase, especially at 100 m/min.

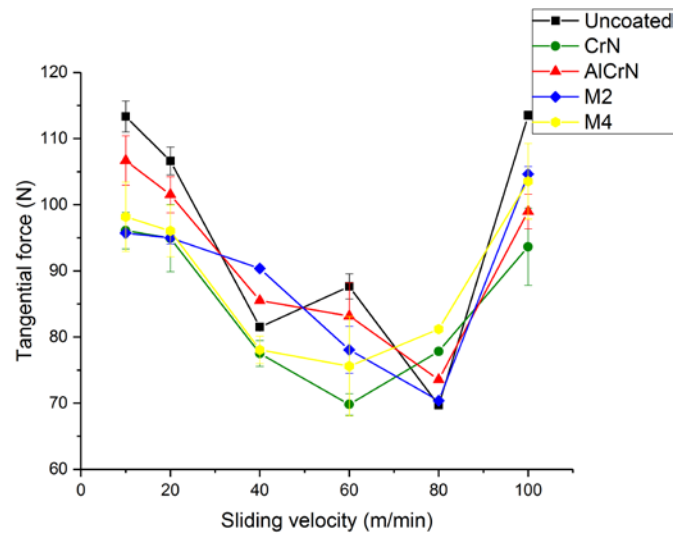


Figure 204. Tangential force as a function of the sliding speed and for different coatings under LN2 conditions (Average contact pressure equals to 872 MPa).

Appendix H : Temperatures of the pins in the tribological tests

Figure 205 and Figure 206 illustrate the curve of the temperature as a function of time detected in all coated and uncoated pins during the tribological tests at a sliding speed of 60 m/min in flood and cryogenic conditions, respectively. The measurement of each type of pin was repeated once. As we can see from Figure 205, during the first 2 s, the temperature varies from 32 to 56°C, then the temperature is relatively stable. The coated pins exhibit lower temperature than uncoated ones. Besides, the AlCrN shows low temperature increasing in both first test and repetition. From Figure 206, the temperature varies from -140 to 40°C during the first 2s. All the curves seem to have further increasing trend. It is noteworthy that the temperature from the beginning of the tests varies (near 30°C) for all tested cases, which is an important factor that influences the measured temperature results, but it cannot be controlled easily during the tests.

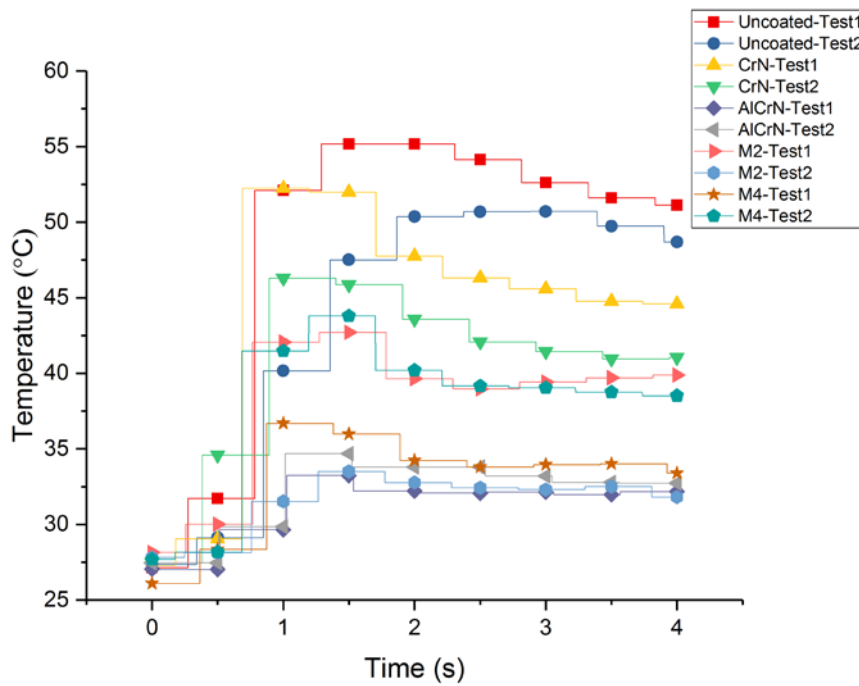


Figure 205. Temperature measured in pins as a function of time for different coatings under flood conditions (Average contact pressure equals to 872 MPa, sliding speed equals to 60 m/min).

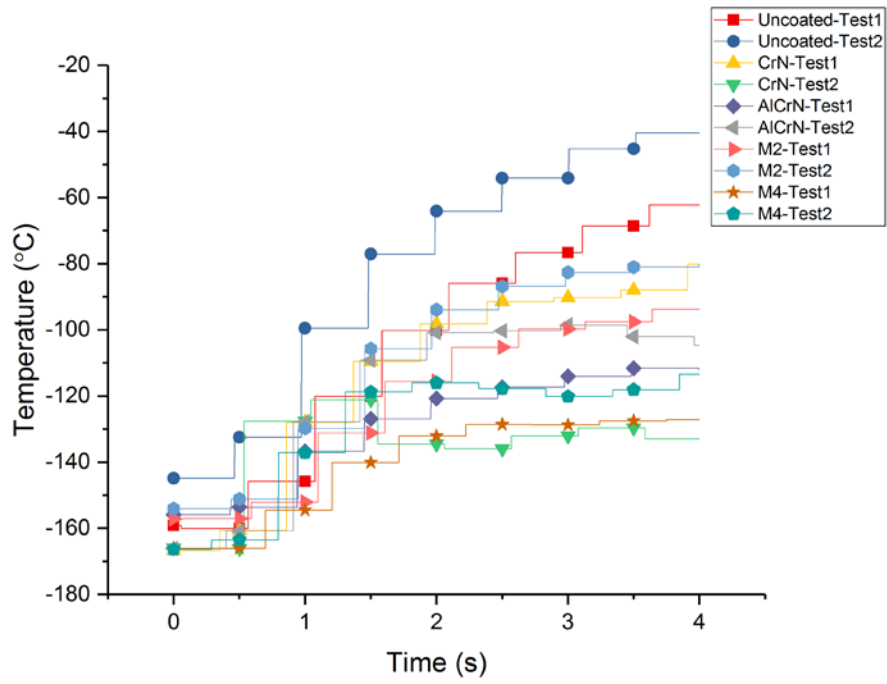


Figure 206. Temperature measured in pins as a function of time for different coatings under LN2 conditions (Average contact pressure equals to 872 MPa, sliding speed equals to 60 m/min).

Appendix I : EDS analysis of worn inserts in tool wear tests

The EDS analysis of uncoated, M2 and M4 coated inserts are presented in *Figure 207* and *Figure 208*. Since the sample holder is on Aluminum, EDS analysis on curved surface causes reflection of beam especially at the cutting edge. Only 3 elements (W, Ti, Cr) are presented as indicators. Ti element is present in all wear craters of the rake face, which proves the adhesion of Ti6Al4V material on the cutting inserts. The coatings are not detected in crater wear except in *Figure 207 (b)* (M2 under cryogenic conditions), where the Cr element is present as the Ti. It is noteworthy that in the same case, the Ti element is present even far away behind the wear crater. One hypothesis is that the wear crater for this case is not so deeper as the others, increasing the chip radius and leading to chip rub behind the wear crater.

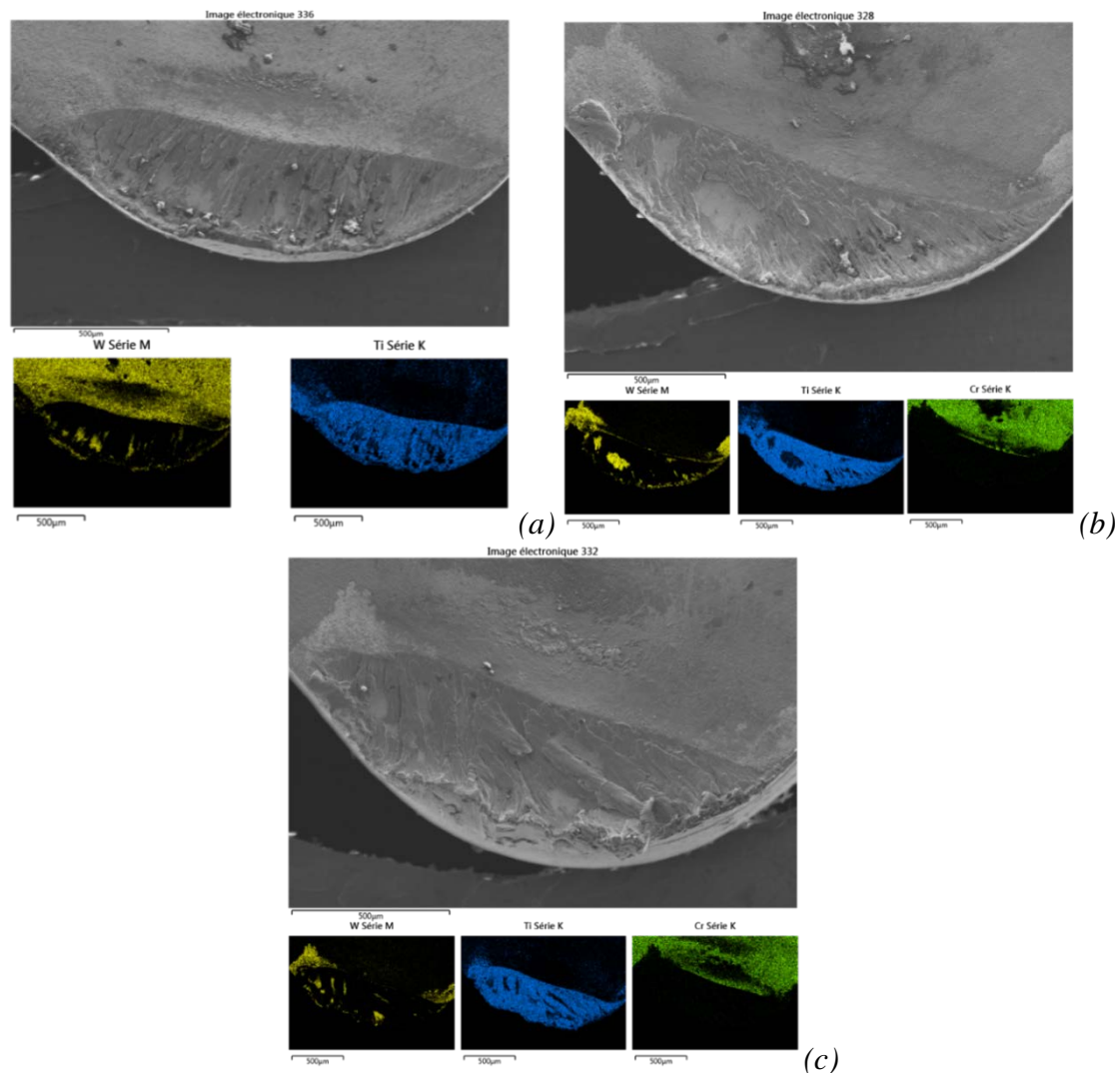


Figure 207. SEM images and EDS cartography of the worn: a) uncoated, b) M2-coated and c) M4-coated inserts at the end of the tests under flood conditions on rake face

Tool materials development for improved performance of cutting tools in cryogenic machining of Aeronautic Alloys

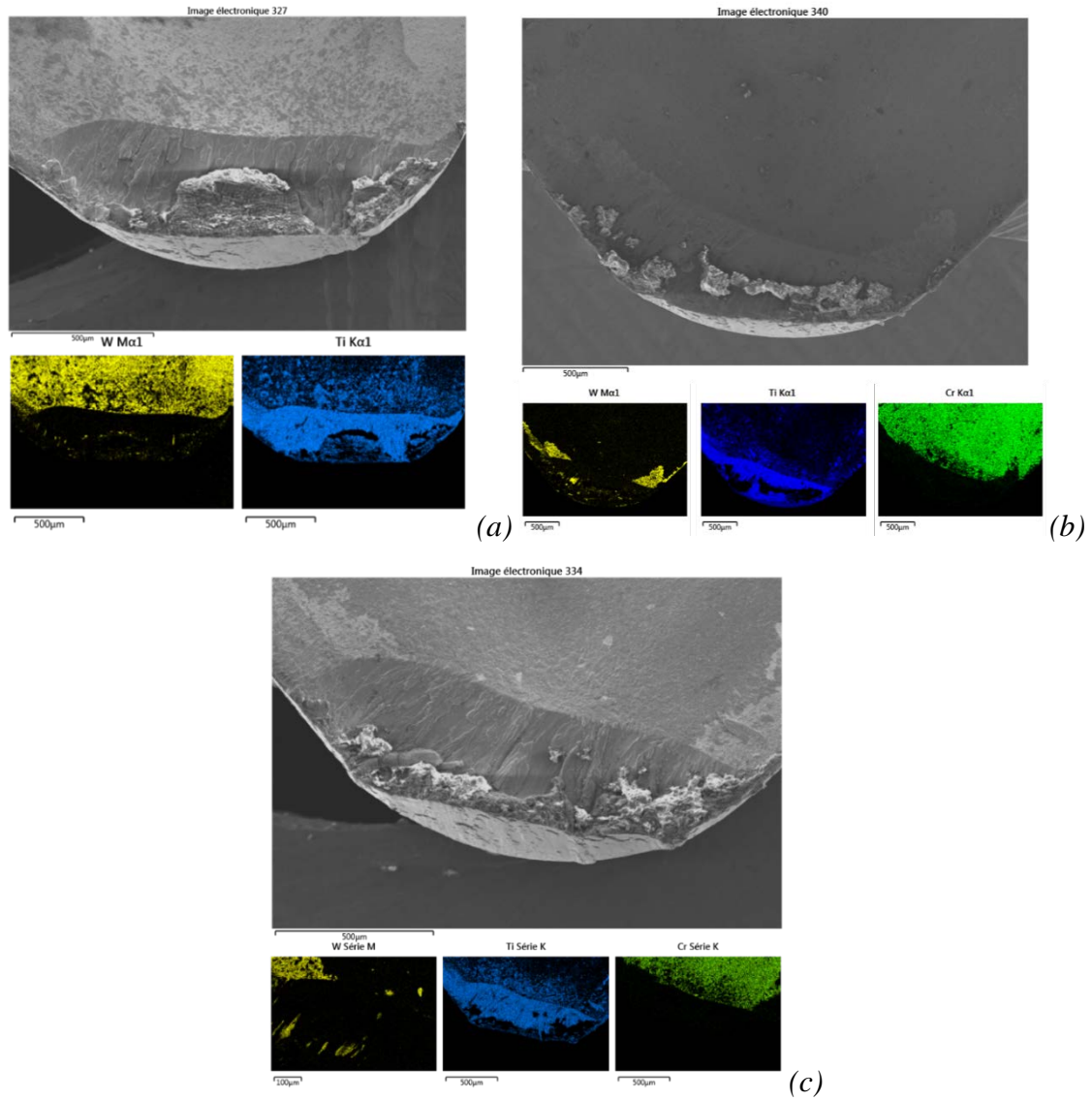


Figure 208. SEM images and EDS cartography of the worn: a) uncoated, b) M2-coated and c) M4-coated inserts at the end of the tests under LN2 conditions

*Tool materials development for improved performance of cutting tools in
cryogenic machining of Aeronautic Alloys*

Développement de nouveaux matériaux de protection pour outils de coupe lors d'usinage cryogénique d'alliages pour l'aéronautique

Résumé

L'objectif de cette étude est de développer une nouvelle génération de revêtements sur outils de coupe pour le tournage de Ti6Al4V sous assistance cryogénique. A cause des conditions de sollicitations sévères que subissent les outils de coupe, les monocouches de base doivent présenter des caractéristiques spécifiques. Ainsi, des couches minces de Cr, CrN, CrAlN et AlCrN ont été déposées sur carbure de tungstène et sur des substrats de silicium par pulvérisation magnétron réactive DC en variant la température de dépôt et la polarisation du substrat. Après avoir optimisé les monocouches, celles-ci ont été associées pour élaborer des multicouches Cr/CrN/AlCrN dont nous avons caractérisé les propriétés physico-chimiques, structurales, mécaniques et tribologiques. Les couches optimales ont été testées avec des essais tribologiques et d'usure en tournage de l'alliage Ti6Al4V sous émulsion et refroidissement cryogénique. Il est démontré que l'application d'un revêtement multicouches apporte des améliorations considérables à la résistance à l'usure des outils carbure en usinage par assistance cryogénique.

Mots clés : Revêtements PVD, Usinage par assistance cryogénique, Alliage de titane Ti6Al4V, Tribologie, Usure d'outil.

Abstract

The objective of this study is to develop a new generation of coatings on cutting tools for turning Ti6Al4V under cryogenic assistance. Because of the severe conditions that the cutting tools are subjected to, the basic monolayers must have specific characteristics. Thus, thin films of Cr, CrN, CrAlN and AlCrN have been deposited on tungsten carbide and on silicon substrates by DC reactive magnetron sputtering by varying the deposition temperature and the polarization of the substrate. After optimizing the monolayers, they were combined to develop Cr/CrN/AlCrN multilayers. Their physicochemical, structural, mechanical and tribological properties were characterized. The optimal layers were investigated by tribological and tool wear tests in turning of Ti6Al4V under both flood and cryogenic LN₂ cooling conditions. The application of a multilayer coating has been shown to provide significant improvements in the wear resistance of cryogenic assisted carbide tools.

Keywords: PVD coatings, Cryogenic Assisted Machining, Ti6Al4V titanium alloy, Tribology, Tool Wear.